Proceedings

3. Internationale Konferenz

# Hybrid

## Materials and Structures

**18.–19. April 2018**

Bremen, ATLANTIC Hotel Universum

https://**hybrid2018.dgm**.de

DGM

# PREFACE
## Hybrid Materials & Structures 2018

**The combination defines it all!**

Again and again innovative materials enable the introduction of new technologies and products. In many cases high performance constructions and components are not possible out of only one material. This is true for vehicles as well as for the mechanical and the constructional engineering. To profit of the specific characteristics of a material, especially in light weight design, the combination of different materials is obligatory. If this compound is achieved through inseparable connections, it is a Multi-Material-Design or Hybrid Structure (remark: The word „Hybrid“ is derived from the greek language and translates as „mixed“). When combining different materials special requirements are given for manufacturing and joining technologies, design methods and several other aspects.

The „Hybrid Materials and Structure 2018“ conference (Hybrid 2018) covers a wide range of topics, starting from the basic materials up to component design, from manufacturing to application and thus creates a basis for a deep understanding of the application specific material and structural behavior.

New: special session: „Multi-Metal-Design“

The combination of different metallic materials within a component offers specific options, concerning aspects of manufacturing and recyclability. Mix-constructions, using several metals, are therefore considered in this conference as well and will be discussed in the special session „Multi-Metal-Design“.

Hybrid 2018 addresses industry as well as academia and emphasizes the strong connection between both. It also encourages participation and acquainting of young engineers, scientists and students.

As location the hanseatic city of Bremen with its historical down town as world heritage has long successful tradition in industrial production of modern mobility applications such as automobiles, aircrafts, satellites and ships and, thus, provides an appropriate atmosphere for the conference.

Within the proceedings each session of the conference is represented by its own chapter. All contributions are checked by the editors for integrity and consistency. However, the individual authors are responsible for the content.

2018: Chapters with manuscripts of the presentations on recent results from research and development are:

**Chapter 1 – Interface, corrosion and residual stresses:**
What are the conditions for compatibility of different materials?

**Chapter 2 – Characterization, destructive and non-destructive testing:**
How to characterize and test hybrid materials?

**Chapter 3 – Manufacturing and processing:**
How to produce and process hybrid structures and materials?

**Chapter 4 – Joining and machining:**
How to join and machine different materials?

**Chapter 5 – Material modelling and simulation:**
How to model and simulate hybrid materials and structures?

**Chapter 6 – Design:**
What is a suitable design and dimensioning method for hybrid structures?

**Chapter 7 – Special session: Multi-metal design:**
What are promising combinations of different metals?

We wish you a lot of new inspirations and solutions for your technical challenges and looking forward to seeing you in Bremen,

*Prof. Dr.-Ing. Joachim M. Hausmann*,
Institut für Verbundwerkstoffe GmbH, Kaiserslautern
*Prof. Dr.-Ing. Marc Siebert*,
PFH – Private Hochschule Göttingen
*Dr.-Ing. Axel von Hehl*
Leibniz-Institut für Werkstofforientierte Technologien - IWT, Bremen

The Conference Chairs and Editors of the proceeding.

# Content

PREFACE **2**

**Chapter 1** – ***Interface, Corrosion And Residual Stresses*** **8**

DIAMOND-LIKE CARBON (DLC) AS ADHESION PROMOTING INTERLAYER IN STEEL / EPOXY-BASED CFRP HYBRID LAMINATES **9**
A. Monden, M.G.R. Sause

FORMING AND CORROSION STABILITY OF A LASER PRETREATED METAL SURFACE –INFLUENCE ON THE PROPERTIES OF METAL-CFRP HYBRID STRUCTURES MADE BY VARTM **17**
C. Zinn, Z. Wang, T. Troester, M. Schaper

IMPACT OF TEMPERATURE AND DEFORMATION GRADIENT ON THE JOINING ZONE FORMATION OF LASER ROLL-BONDED BIMETALS **24**
V. Fux, J. Kaspar, A. Berger, T. Fiebiger, M. Seifert, D. Beitelschmidt

TEXTILE CONNECTION TECHNOLOGY FOR INTERFACES OF FIBRE-REINFORCED PLASTIC-CONCRETEHYBRID COMPOSITES **28**
L. Born, C. Möhl, M. Milwich, G. T. Gresser

CHARACTERIZATION OF RESIDUAL STRESSES IN FIBERMETAL-LAMINATES BY X-RAY DIFFRACTION **34**
A. Busch, P. Brix, R. Brandt

THE CORROSION BEHAVIOR OF MULTICOMPONENT MATERIALS IN DIFFERENT SODIUM CHLORIDE SOLUTIONS **40**
K. Lange, M. Mandel, L. Krüger, M. Ullmann, K. Neh, R. Kawalla, D. Weck, M. Gude, S. Bräunling

**Chapter 2 –** ***Characterization, Destructive And Non-Destructive Testing*** **47**

A SPECIMEN FOR EVALUATING POTTING MATERIALS IN FUNCTIONAL INTE-GRATED DESIGN SOLUTIONS **48**
C. Gundlach, S. Hartwig, M. Mannig, M. Menzel, T. Smatt, K. Dilger

FRACTURE TOUGHNESS AND STRENGTH OF THE INTERFACE OF A GFRP-STEEL-LAMINATE **56**
R. Brandt, A. Busch

ADHESION STUDIES OF THERMOPLASTIC FIBRE-PLASTIC COMPOSITE HYBRID COMPONENTS
PART 1: THERMOPLASTIC-THERMOPLASTIC-COMPOSITES **62**
A. Liebsch, R. Kupfer, M. Krahl, D. R. Haider, W. Koshukow, M. Gude

ADHESION STUDIES OF THERMOPLASTIC FIBRE-PLASTIC COMPOSITE HYBRID COMPONENTS
PART 2: THERMOPLASTIC-METAL-COMPOSITES **68**
D. R. Haider, M. Krahl, W. Koshukow, M. Wolf, A. Liebsch, R. Kupfer, M. Gude

THREE-POINT BENDING TEST ON CFRP-STEEL PROFILE HYBRID STRUCTURES **74**
M. Muth, K. A. Weidenmann

EXPERIMENTAL AND NUMERICAL INVESTIGATIONS ON THE DEFORMATION BEHAVIOR OF FIBER-METAL-ELASTOMER LAMINATES IN 3-POINT BENDING EXPERIMENTS USING DIGITAL IMAGE CORRELATION **81**
V. Sesser, W. V. Liebig, L. Kärger, K. A. Weidenmann

EVALUATION OF BONDING BEHAVIOR IN HYBRID INJECTION MOLDED COMPONENTS BY RIP SHEAR TESTING **88**
A. Geyer, T. Gläßer, R. Schlimper

COMPONENT TESTING OF CONTINUOUSLY AND DISCONTINUOUSLY REINFORCED HYBRID SHEET MOLDING COMPOUNDS (CODICOSMC) **96**
A. Trauth, A. Schubert, D. Bücheler, K. A. Weidenmann

ROBUST AND ADAPTIVE NON DESTRUCTIVE TESTING OF HYBRIDS WITH GUIDED WAVES AND LEARNING AGENTS **104**
S. Bosse, M. Koerdt, A. von Hehl

INVESTIGATION OF FAILURE MECHANISMS IN HYBRID FIBER-REINFORCED PLASTICS BY MEANS OF IN-SITU-CT **114**
F. Bittner, H.-J. Endres

**Chapter 3 – *Manufacturing And Processing*** **120**

IN-SITU PROCESSING OF CAPROLACTAM – T-RTM TECHNOLOGY AS A KEY FOR FULLY AUTOMATED PRODUCTION OF COMPOSITE PARTS **121**
N. Müller

HYBRID FORMING – A COMBINED DEEP DRAWING AND COMPRESSION MOLDING PROCESS FOR FORMING METAL SHEETS WITH THERMOPLASTICS (LFT) TO HYBRID PARTS **128**
X. Fang, T. Kloska

DEVELOPMENT OF FIBRE METAL LAMINATES MADE OUT OF HYBRID SEMI FINISHED PRODUCTS PRODUCED BY A TEXTILE PROCESS **133**
S. Jenkel, P. Schiebel, R. Kösters, A. S. Herrmann

SUITABLE PROCESS FOR MASS PRODUCTION OF HYBRID LAMINATES WITH SENSOR FUNCTIONALITY **140**
A. Graf, R. Decker, V. Kräusel, D. Landgrebe, L. Kroll

EVALUATION OF RELEVANT PROCESS PARAMETERS FOR DIRECTLY CURED THERMOSET COMPOSITES ON METAL PARTS **146**
R. Thomas, S. Wehler, S. Handtke, W. Großmann, F. Fischer

ALCUNNECT - A NEW BIMETAL COMBINATION OF ALUMINIUM AND COPPER **156**
D. Schindler, U. Dreißigacker, J. Ganz, H. Tribus

MANUFACTURING OF BRANCHED STRUCTURES FOR FIBRE-REINFORCED PLASTIC-CONCRETE-HYBRID COMPOSITES **165**
C. Möhl, L. Born, S. Küppers, F. A. Jonas, J. Knippers, M. Milwich, G. T. Gresser

SUSTAINABLE HYBRID COMPOSITES OF CARBON AND NATURAL FIBERS FOR LIGHTWEIGHT COMPONENTS **171**
R. Rinberg, R. Svidler, A.-A. Ouali, M. Klaerner, L. Kroll

FIFDM – MANUFACTURING PROCESS FOR 3D PRINTED FIBER REINFORCED POLYMER COMPOSITES **177**
M. Domm, J. Schlimbach

**Chapter 4 – *Joining And Machining*** **187**

SURFACE PREPARATION OF STEELS BASED ON TUNGSTEN INERT GAS ARC PROCESSING FOR LASER-BASED JOINING OF METAL-PLASTIC COMPONENTS **188**
M.-L. Kohl, K. Schricker, J. P. Bergmann, M. Lohse, M. Hertel, U. Füssel

LASER SURFACE TREATMENT OF CFRP AND TI6AL4V FOR ADHESIVE BONDING OF HYBRID JOINTS **195**
B. Rauh, S. Kreling, H. Fietzek, M. Suess, M. Geistbeck, K. Dilger

COMPARISON OF LASER-BASED JOINING APPROACHES FOR PLASTIC-METAL-HYBRIDS – STRENGTH VS. PROCESS SPEED **203**
K. van der Straeten, C. Engelmann, A. Olowinsky, A. Gillner

CHARACTERIZATION OF THE JOINING ZONE IN LASER DIRECT JOINING BETWEEN THERMOPLASTICS AND METALS **210**
K. Schricker, J. P. Bergmann, M. Hopfeld, L. Spieß

PROCESS CONCEPTS FOR THE MANUFACTURING OF HYBRID COMPOSITES MADE FROM ALUMINUM AND CFRP WITH A POLYMER-BASED DECOUPLING LAYER **216**
A. Schmid, K. Arnaut, J. Clausen, M. Koerdt, A. Struß, F.-J. Wöstmann, M. Busse

BONDING BY MICROBRACING: QUANTIFICATION OF TEMPERATURE INFLUCENCE FOR MULTI-COMPONENT HIGH PRESSURE DIE CASTING **222**
P. Messer, U. Vroomen, A. Bührig-Polaczek

SINGLE SIDE RESISTANCE SPOT WELDING WITH A COAXIAL ELECTRODE ARRANGEMENT FOR JOINING PLASTIC-METALHYBRID STRUCTURES **227**
K. Szallies, M. Bielenin, J. P. Bergmann, C. Neudel

WIRE ARC ADDITIVE MANUFACTURING OF WEAR RESISTANT COMPOUND STRUCTURES BY GAS METAL ARC WELDING **233**
P. Henckell, Y. Ali, J. Reimann, K. Schricker, J. P. Bergmann

**Chapter 5 – *Material Modelling And Simulation*** **239**

OPTIMIZATION-BASED MATERIAL DESIGN OF TAILORED STACKED HYBRIDS FOR FURTHER IMPROVEMENT IN LIGHTWEIGHT CAR BODY STRUCTURES **240**
A. A. Camberg, T. Tröster

COUPLED PROCESS AND STRUCTURE ANALYSIS OF METAL-FRP- HYBRID STRUCTURES **246**
D. Weck, B. Grüber, M. Q. Pham, A. Wolf , S. Bräunling, J.-P. Ziegs, T. Gereke, F. Hirsch, M. Kästner, A. Brosius, C. Cherif, M. Gude

OPTIMISING MECHANICAL INTERLOCKING INTERFACE OF CFRP-(THERMO-PLASTIC/METAL)-HYBRIDS **254**
F. Günther, M. Pohl, V. Kretschmar, G. Scheuermann, M. Stommel

**Chapter 6 – *Design*** **261**

DESIGN AND INTRINSIC PROCESSING OF A HYBRID CFR-TP CONTOUR JOINT WITH A MULTI-SCALE STRUCTURED LOAD INTRODUCTION ELEMENT **262**
V. Würfel, D. Barfuss, R. Grützner, F. Hirsch, M. Gude, R. Müller

EXPERIMENTAL INVESTIGATION OF THE DESIGN CONCEPT FOR A NON-ENGAGING BELLOWS COUPLING MADE OF PREPREG-BASED CARBON FIBER REINFORCED POLYMERS **269**
C. Oblinger, A. Baeten, K. Drechsler

**Chapter 7 – *Special Session: Multi-Metal Design*** **277**

INFLUENCE OF PROCESS PARAMETERS ON THE FATIGUE BEHAVIOR OF STEEL/ALUMINUM HYBRID JOINTS PRODUCED BY MAGNETIC PULSE WELDING **278**
N. Gelinski, D. Huelsbusch, E. Schumacher, S. Böhm, F. Walther

VARIETY OF METAL PROPERTY AND DESIGN COMBINATIONS BY COLD ROLL CLADDING **283**
L.

COLD ROLLING OF COATED STEEL SHEETS AS PRETREATMENT FOR HYBRID COMPONENTS **290**
S. Senge, L. Gerdt, S. Wiesner, M. Öte, K. Bobzin and G. Hirt

POWDER METALLURGICAL COMPONENTS WITH RADIALLY GRADED MATERIAL SYSTEM BY SEGREGATION **296**
Dieter Bohr, Bernd-Arno Behrens, Kai Brunotte

PUMP-OUT EFFECT REDUCTION OF POWER MODULES BY USING HYBRID HEAT SPREADER PLATES **302**
R. Eisele, S. Söhl

**List of Authors** **308**

CHAPTER 1

# INTERFACE, CORROSION AND RESIDUAL STRESSES

# DIAMOND-LIKE CARBON (DLC) AS ADHESION PROMOTING INTERLAYER IN STEEL / EPOXY-BASED CFRP HYBRID LAMINATES

**A. Monden[1*], M.G.R. Sause[1]**

[1]University of Augsburg, Augsburg, Germany

**ABSTRACT:** Four different diamond-like carbon (DLC) coating variants were investigated via different experimental techniques to assess their suitability as adhesion promoting interlayers in intrinsic steel/epoxy-based CFRP hybrid laminates. Sandwich specimens with a symmetrical layup consisting of unidirectional CFRP with a thin, surface modified steel layer in the center plane were investigated. The DLC variants were compared to other types of commonly used surface modifications via SBS (short-beam shear) tests. Subsequently, the two most promising DLC variants (high hardness, DLC-HH and Silicon-doped, DLC:Si) were further investigated. Commonly used testing procedures like DCB (double cantilever beam), ENF (3-point end-notched flexure) and MMB (mixed-mode beam) tests were adapted to assess the fracture toughness at the interface. SBS tests after hot/wet ageing showed a trend from brittle to ductile failure behaviour for DLC-HH and for DLC:Si vice versa. Thus, XPS (X-ray photoelectron spectroscopy) measurements were conducted to detect changes of the surface chemical composition and functional groups caused by hot/wet ageing. Finally, potentiostatic and potentiodynamic measurements proved the corrosion resistance of the DLC variants. The conducted investigations proved a high potential of DLC-coatings as interlayers for metal/epoxy-based CFRP structures.

**KEYWORDS:** CFRP/steel hybrid laminate, surface modification, diamond-like carbon (DLC), fracture toughness, interfacial failure, corrosion resistance

## 1 INTRODUCTION

Reliable use of hybrid structures and materials depends on the availability of mechanically and chemically stable joint technologies for combining fiber reinforced plastics (FRP) and metals [1-4]. While combinations of lightweight metals and FRP are used in aerospace applications, steel is still the most widely used construction material in other fields of engineering, often due to economic reasons. Integration of structural FRP parts in such industrial areas leads inevitably to the challenge of joining these different material classes. Due to their different chemical structure, direct joints of steel and epoxy resin will result in poor adhesion, which leads to the requirement of surface treatments and modifications to achieve a mechanically and chemically stable joint. In case of CFRP, direct contact between carbon-fibers and the surface of the metallic constituent may lead to galvanic corrosion [5, 6]. Using an additional layer of a polymer (e.g. adhesive or resin) or GFRP to insulate the carbon-fibers from the metal surface will usually deteriorate the mechanical properties. Thus, surface modifications applied to the metallic constituent, which are capable of inhibiting galvanic corrosion, are preferred. Diamond-like carbon (DLC) coatings in general are amorphous, metastable carbon-based materials exhibiting a significant ratio of $sp^3$-hybridized C-bonds, which account for the diamond-like properties like high hardness, chemical stability and low electrical conductivity [7, 8]. Therefore, DLC coatings are considered as promising candidate for an interlayer in intrinsic CFRP/metal hybrid laminates. Within this study, four different DLC coating variants were investigated regarding their suitability to fulfill the above-mentioned requirements.

## 2 SCREENING VIA SHORT-BEAM SHEAR TESTS

Within a screening, four different DLC variants were applied to X5CrNi18-10 cold-rolled steel foils of 0.1 mm nominal thickness using a PACVD (plasma-assisted chemical vapour deposition) process. With the choice of

reactive gas (hydrocarbon precursor), the hydrogen content (C/H-ratio) of the coating can be influenced [7, 8]. DLC coatings may be doped with e.g. Silicon to reduce residual stresses of the coating and thus improve adhesion to the steel substrate [8, 9]. Doping may be achieved by using a Silicon containing hydrocarbon precursor. Further, Si-doping may change the surface chemistry regarding steel/DLC and DLC/epoxy adhesion. We investigated two "standard" DLC variants, one with relatively high hardness (DLC-HH) and one with lower hardness (DLC-LH), a multilayer-variant (DLC-ML) consisting of a DLC-HH base layer and a DLC-LH top layer, and a silicon-doped variant (DLC:Si). Typical coating thicknesses are 2 - 3 µm for a monolayer and 5 - 7 µm for the multilayer variant, respectively.
Subsequently, sandwich plates were fabricated using a symmetrical layup consisting of 10 layers of SGL CE 1250-230-39 unidirectional epoxy-based prepreg with a nominal thickness of 0.22 mm per layer in cured state and the DLC coated steel foils laminated at the center plane. A standard curing cycle using 130 °C temperature for 90 min following the materials supplier's recommendations was used. Besides the DLC variants, a variety of commonly used surface modifications was applied to the steel foils prior to co-curing them with the prepreg material to enable a direct comparison [10, 11]. After laminating and curing the sandwich plates, samples of 20 mm length, 10 mm width and 2.4 mm resulting thickness were cut from the cured laminates using a dry diamond saw cutting process to avoid preliminary delamination at the CFRP-metal interface due to moisture expansion or in-take. The surface modifications were compared to an untreated reference (hybrid laminate with cleaned and degreased, "as-received" steel surface) and monolithic CFRP via short-beam shear (SBS) tests [10, 11] following DIN EN 2563. Results of the SBS tests and optical microscopy images of the resultant delamination surfaces are shown in Fig. 1.

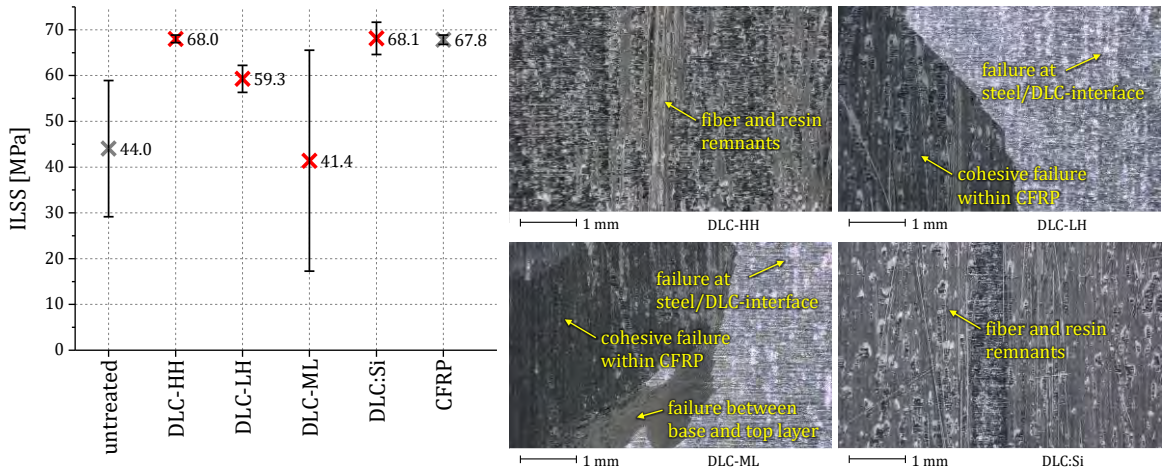


***Fig. 1*** *Apparent interlaminar shear-strength (ILSS) values obtained via SBS tests on three samples each and representative optical microscopy images of the resultant delamination surfaces* [11]

The DLC-LH and DLC-ML variants showed partial failure at the steel/DLC interface, with additional failure between base and top layer for the DLC-ML. DLC-HH and DLC:Si showed mainly cohesive failure within CFRP and at the same time reached ILSS values comparable to the monolithic CFRP. Therefore, those two variants were investigated more closely.

## 3 FRACTURE MECHANICAL CHARACTERIZATION

The fracture toughness at the interface of symmetrical hybrid laminates with DLC-HH and DLC:Si coatings was determined under mode I, mode II and mixed-mode load conditions. In this case, the laminates consisted of 14 layers of the epoxy-based CFRP prepreg and the DLC coated steel foils laminated at the center plane, resulting in a thickness of 3.4 mm. At one side of the steel foil, a precrack was built in using ETFE-foil of 25 µm thickness (Wrightlon® 5200).
DCB tests were conducted in accordance with ASTM D5528. Specimens of 200 mm length, 20 mm width and 50 mm effective precrack length were cut from the cured plates. Force during testing was applied via adhesively bonded load blocks and a crosshead speed of 5 mm/min. Crack tip propagation was recorded using a digital camera system (Zwick VideoXtens) enabling post-evaluation of initiation and propagation values.
In case of ENF tests in accordance with ASTM D7905, specimens of 175 mm length, 20 mm width and 48 mm precrack length (30 mm effective precrack length during fracture testing) were used. Tests were conducted with a crosshead speed of 0.8 mm/min. Delamination initiation was recorded and post-evaluated via digital image correlation (DIC) techniques (GOM ARAMIS 12M) [12].

MMB tests were conducted in accordance with ASTM D6671, and three different mode mixities (Eq. 1) were applied by variation of the lever arm length of the MMB testing apparatus.

$$0 < \frac{G_{\mathrm{II}}}{G} = \frac{G_{\mathrm{II}}}{G_{\mathrm{I}} + G_{\mathrm{II}}} < 1 \qquad (1)$$

Specimens of 150 mm length, 20 mm width and 28 mm effective precrack length were used. Tests were conducted with a crosshead speed of 0.5 mm/min. As for the ENF tests, delamination initiation was recorded and post-evaluated via DIC techniques.

Corrections of the measured (apparent) fracture toughness values are necessary to account for a variety of effects. In case of DCB tests, corrections for large displacements and the stiffening of the specimen by the end blocks are performed according to ASTM D5528. For MMB tests, lever arm weight has to be taken into account, which results in a shift of the intended mode mixities towards higher mode II ratios in the present case. The investigated hybrid laminates exhibit a macroscopically symmetrical layup, whereas failure is initiated at one of the CFRP/steel interfaces and thus asymmetry is introduced in the vicinity of the crack tip. For DCB tests, this asymmetry results in a minor mode II contribution, which can be estimated by the semi-empirical relationship established by MOLLÓN et. al. [13]. In case of MMB tests, similar effects on mode mixity result from the asymmetric failure behavior, which can be estimated using the formalism introduced by SHAHVERDI et. al. [14]. Thermally induced residual stresses resulting from curing at elevated temperatures affect the apparent fracture toughness values and the resultant mode mixities. This influence was quantified using the formulas proposed by YOKOZEKI et. al. [15], which are based on the general relationship introduced by NAIRN [16].

Results shown in Fig. 2 are based on six specimens in case of DCB tests and three specimens in case of MMB and ENF tests, respectively. In case of untreated steel surfaces, purely adhesive failure at the interface was observed for the entirety of investigated mode mixities.

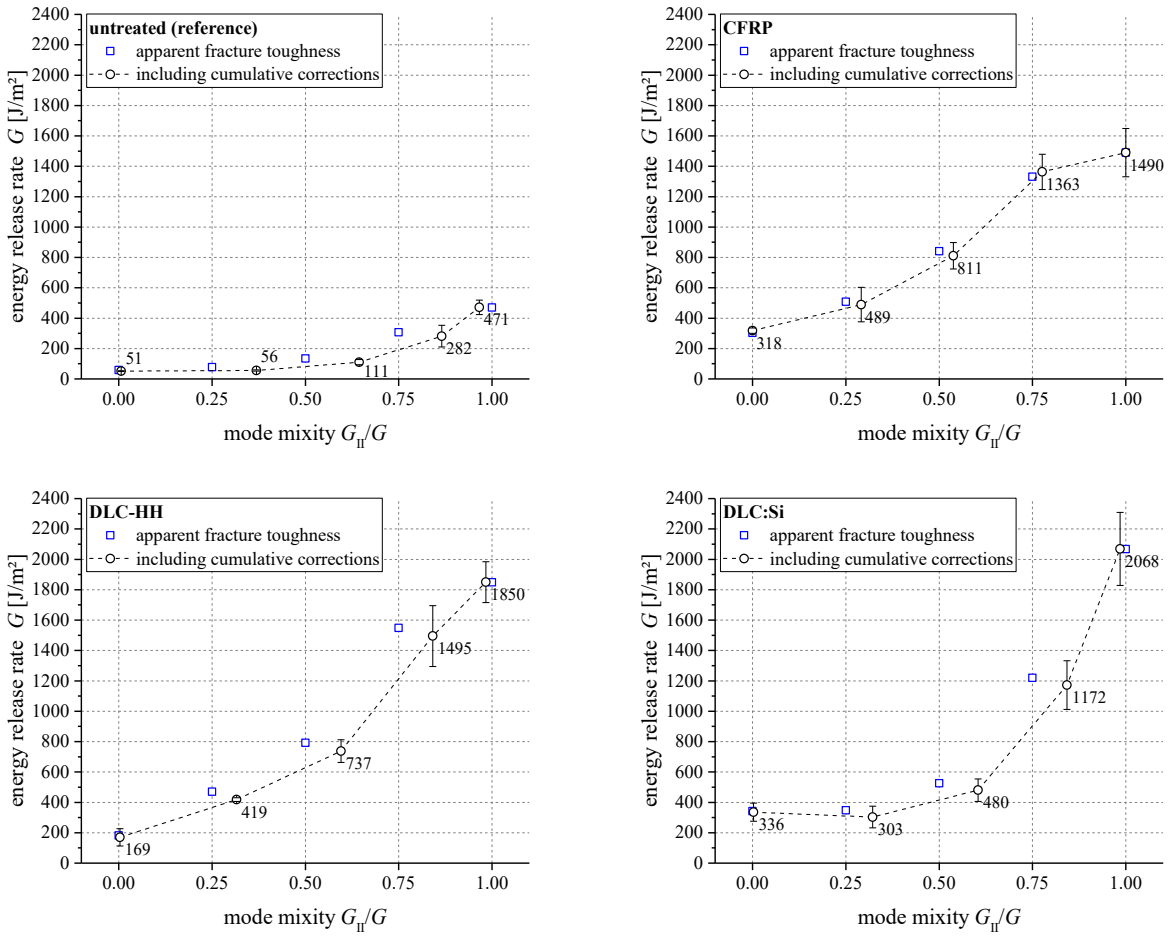


***Fig. 2*** *Fracture mechanics results including apparent fracture toughness values (as measured) and cumulative corrections* [11, 17].

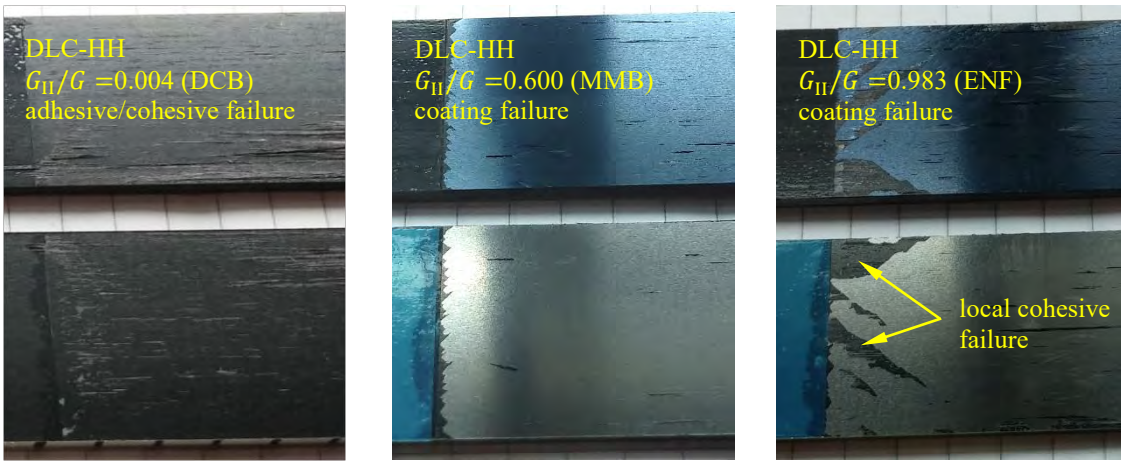


***Fig. 3*** *Fracture surfaces of DLC-HH coated specimens (representative examples)* [11, 17]*. Upper row: CFRP side, lower row: Steel side.*

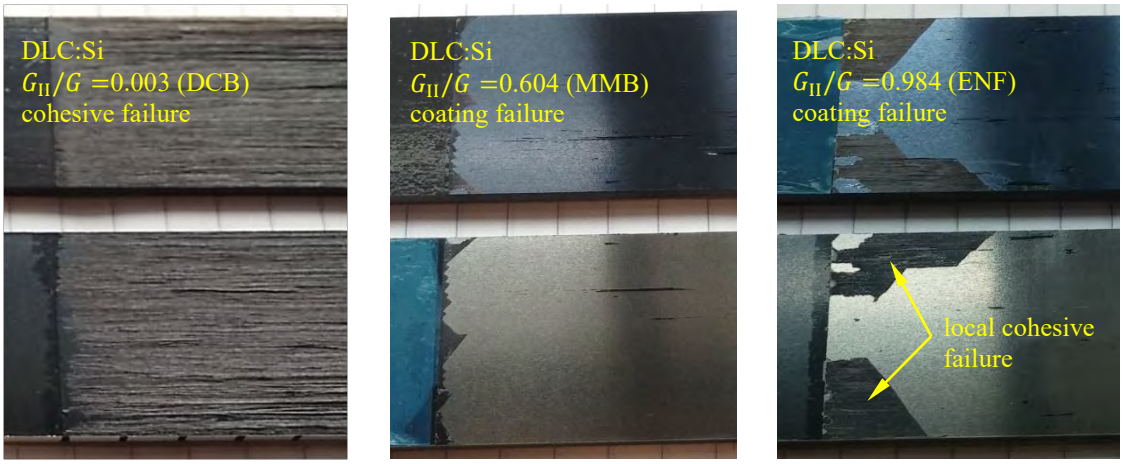


***Fig. 4*** *Fracture surfaces of DLC:Si coated specimens (representative examples)* [11, 17]*. Upper row: CFRP side, lower row: Steel side.*

Mode I fracture toughness was significantly increased by DLC:Si coatings and exceeded the fracture toughness of pure CFRP. Observation of crack surfaces coincides with these findings, exhibiting purely cohesive failure within CFRP (Fig. 4). In the mixed-mode regime, coating failure was observed for both DLC coatings. Fracture toughness values of monolithic CFRP were nearly reached by DLC-HH. Both investigated DLC coatings exceeded the mode II fracture toughness of pure CFRP significantly, but exhibited coating failure at the steel/DLC interface (Fig. 3, 4). Further investigations carried out on combinations of $Al_2O_3$ grit blasting and DLC coatings indicate a further potential of fracture toughness increase mainly in the mode I-dominated regime due to mechanical interlocking [11, 17]. Overall, the investigated DLC coatings proved suitable to improve fracture toughness across the whole range of investigated mode mixities.

## 4 HOT/WET AGEING AND X-RAY PHOTOELECTRON SPECTROSCOPY

To investigate the influence of hot/wet environment on the bonding strength, SBS tests were conducted on specimens after ageing at 85 °C / 85 %RH for 3 and 12 days, respectively. Exemplary shear stress vs. displacement curves are shown in Fig. 5. Interestingly, the failure behaviour changed from brittle to ductile in case of DLC-HH and for DLC:Si vice versa.

To investigate the changes caused by hot/wet ageing, XPS (X-ray photoelectron spectroscopy) measurements on DLC coated steel samples of both variants were conducted before and after ageing at 85 °C / 85 %RH for 14 days.

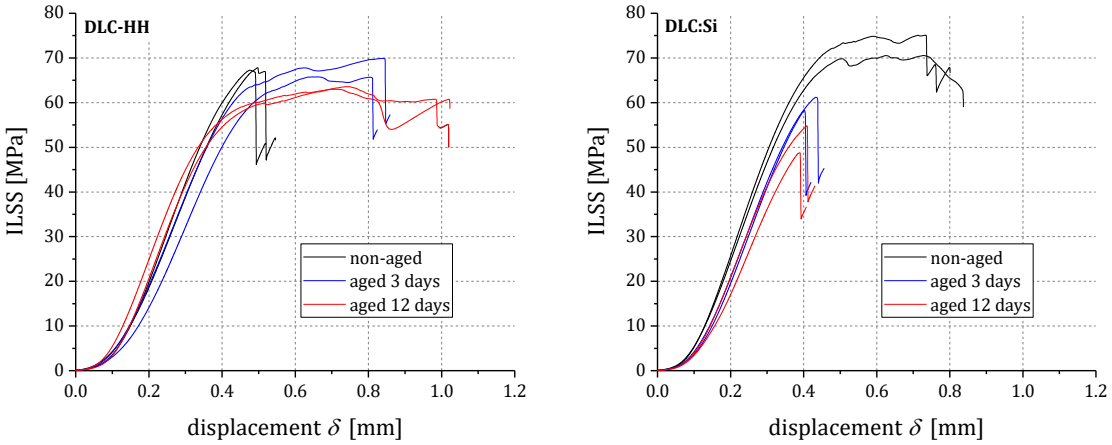


***Fig. 5*** *Exemplary shear stress vs. displacement curves showing contrary effect of hot/wet ageing* [11].

In case of DLC-HH, no significant changes of elementary composition were observed (Table 1), with Oxygen indicating an existence of functional groups. Investigation of the C1s-peak did not show significant changes concerning the existence of functional chemical groups (Table 2). C–C and C–H bonds represent the largest share of chemical bonds determined, which is typical for the DLC type investigated within this study (a-C:H, amorphous Carbon with significant Hydrogen content [7, 8]). The good adhesive properties of DLC towards epoxy resins may be attributed to the existence of functional chemical groups like C–OR, C=O and COOR [18]. As the XPS technique resembles a particularly surface-sensitive spectroscopic technique (information depth ≤ 3 nm [19]), changes at the interface between steel substrate and DLC layer or within the volume of the DLC layer are not accessible. It has already been shown within this paper that the adhesion between steel substrate and DLC coating contributes to the global failure behaviour of the investigated hybrid laminates. Thus, chemical changes at the steel/DLC-interface or within the DLC layer due to hot/wet ageing may alter the failure behaviour.

***Table 1:*** *Elemental composition of DLC-HH before and after hot/wet ageing* [11].

| | C [at%] | O [at%] | N [at%] |
|---|---|---|---|
| DLC-HH non-aged | 87.2 | 10.8 | 1.5 |
| DLC-HH aged 14 days | 87.8 | 11.8 | 0.5 |

***Table 2:*** *Chemical bonds and functional groups determined by investigation of the C1s-peak of DLC-HH before and after hot/wet ageing* [11].

| | C–C [%] | C–H [%] | C–OR [%] | C=O [%] | COOR [%] | Shake-up [%] |
|---|---|---|---|---|---|---|
| DLC-HH non-aged | 52.0 | 34.6 | 7.2 | 3.7 | 1.9 | 0.5 |
| DLC-HH aged 14 days | 52.0 | 34.1 | 7.8 | 3.4 | 2.0 | 0.6 |

In case of DLC:Si, the Silicon-content is clearly detectable and exhibits a stoichiometric composition of $C_{2.65x}Si_x$ in non-aged state and $C_{1.67x}Si_x$ after hot/wet ageing, respectively (Table 3). At the same time, the Oxygen content clearly increases. From Table 4 it can be seen that the share of Si–C- and C–H-bonds at the surface is significantly reduced while the share of C–C-bonds is increased. The share of functional groups (e.g. C–OR, C=O, COOR) does not change significantly. Table 5 shows the oxidation of the present Silicon: The share of $Si(–O)_2$ and $Si(–O)_3$ increases at the expense of Si–C and $Si(–O)_1$. In summary, this indicates a simultaneous breaking up of Si–C-bonds and formation of $SiO_x$-precipitations at or near the DLC-surface, being the governing mechanism altering the global failure behaviour of the laminate towards behaving more brittle. At the same time, the formation of $SiO_x$-precipitations may lead to a concentration gradient inducing diffusion of Silicon towards the surface. In this scenario, the steel/DLC-interface may be depleted from Silicon, deteriorating the adhesive properties at the steel/DLC-interface and thus contributing to the alteration of the global failure behaviour and deteriorating the mechanical properties of the whole laminate.

***Table 3:*** *Elemental composition of DLC:Si before and after hot/wet ageing* [11].

| | C [at%] | O [at%] | N [at%] | Si [at%] |
|---|---|---|---|---|
| DLC:Si non-aged | 58.3 | 15.7 | 4.0 | 22.0 |
| DLC:Si aged 14 days | 45.5 | 24.5 | 2.8 | 27.2 |

***Table 4:*** *Chemical bonds and functional groups determined by investigation of the C1s-peak of DLC:Si before and after hot/wet ageing* [11].

| | Si–C [%] | C–C [%] | C–H [%] | C–OR [%] | C=O [%] | COOR [%] | Shake-up [%] |
|---|---|---|---|---|---|---|---|
| DLC:Si non-aged | 19.1 | 37.6 | 32.4 | 6.3 | 2.1 | 2.6 | - |
| DLC:Si aged 14 days | 11.7 | 53.9 | 21.7 | 8.1 | 2.1 | 2.5 | - |

***Table 5:*** *Chemical bonds and functional groups determined by investigation of the Si2p-peak of DLC:Si before and after hot/wet ageing* [11].

| | Si–C [%] | $Si(–O)_1$ [%] | $Si(–O)_2$ [%] | $Si(–O)_3$ [%] | $Si(–O)_4$ [%] |
|---|---|---|---|---|---|
| DLC:Si non-aged | 40.9 | 41.9 | 5.4 | 11.9 | - |
| DLC:Si aged 14 days | 22.2 | 36.5 | 10.0 | 31.3 | - |

## 5 CORROSION MEASUREMENTS

Besides the adhesion promoting properties of DLC-coatings, their corrosion inhibiting properties are relevant for practical applications. Thus, potentiodynamic and potentiostatic corrosion measurements were conducted on a measurement setup like shown in Fig. 6.

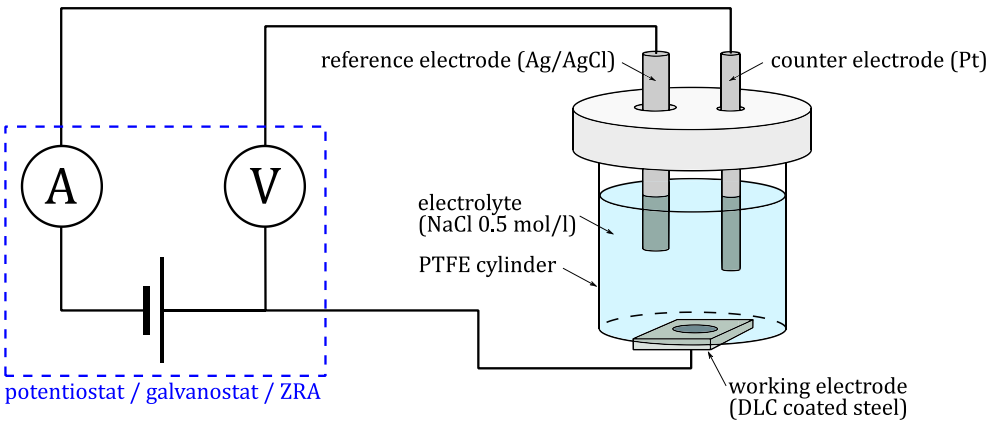


***Fig. 6*** *Schematic of measurement setup used for electrochemical experiments* [11, 20].

The measurement setup shown represents a three-electrode system with the sample used as working electrode. Potentials applied to the sample always have the Ag/AgCl-reference electrode as reference point and electric currents flow solely between sample and Pt-counter electrode. A potentiostat (type Interface 1000, Gamry Instruments) is used to measure or apply electrical currents and voltages, respectively, and can be utilized as potentiostat, galvanostat or zero resistance ammeter (ZRA). Hence, both stable DC voltages can be generated to conduct potentiodynamic polarization scans (PPS), as well as high-precision current measurements of galvanic corrosion processes can be conducted.

For PPS, the sample is polarized either cathodic or anodic via an external, variable voltage. The corresponding currents give information about the extent of the prevailing cathodic or anodic reaction. When plotting the voltage against the logarithmic current (EVANS diagram), characteristic regions may be distinguished. In this study, DLC-HH and DLC:Si coated steel was compared towards CFRP and uncoated steel (X5CrNi18-10) as a reference. From the EVANS diagram shown in Fig. 7 (left) it can be seen that the current is significantly reduced both in the cathodic ($E < E_{corr}$) as well as in the anodic ($E > E_{corr}$) region for both DLC coatings in

comparison to the uncoated steel surface. Both DLC coatings show an atypical trend in contrast to the uncoated steel surface, as passivation does not occur. Instead, the current $I$ just moderately increases with increasing potential difference $E$ even at regions $E \geq 0.5$ V, where pitting corrosion sets in for the uncoated steel surface. No significant increase of electrical current is observable even up to high potential differences, which indicates that pitting was completely inhibited.

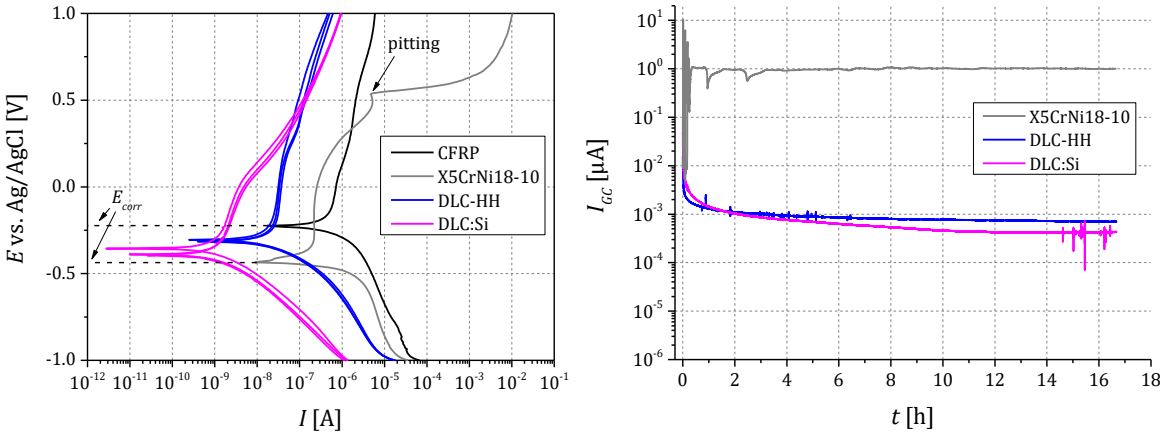


***Fig. 7*** *EVANS diagrams of potentiodynamic polarization scans of three DLC-HH and DLC:Si samples each (left); Galvanic corrosion against CFRP via potentiostatic measurements (right)* [11, 20].

Potentiostatic measurements showed, that the galvanic corrosion current $I_{GC}$ against CFRP was reduced by a minimum of three orders of magnitude compared to an uncoated steel surface by both variants (Fig. 7, right).

## 6 CONCLUSIONS

Four DLC variants were compared against a variety of commonly used surface modification techniques via SBS tests. Among these, the two most promising variants (DLC-HH and DLC:Si) were investigated more detailed via different experimental techniques.

Compared to untreated specimen, DLC coatings showed a significant improvement of interfacial fracture toughness, which could be confirmed by examination of the fracture surfaces, revealing cohesive failure within the CFRP laminate or coating failure, respectively, depending on the applied load condition. Both variants exceeded the Mode II values of monolithic CFRP significantly, whereas the Mode I values of monolithic CFRP were exceeded by DLC:Si. In the mixed-mode regime, values of monolithic CFRP were nearly reached by DLC-HH. Corrections were needed to account for asymmetric failure behaviour and residual thermal stresses, affecting the mode mixities and measured (apparent) fracture toughness values.

SBS tests after hot/wet ageing showed a trend from brittle to ductile failure behaviour for DLC-HH and for DLC:Si vice versa. XPS measurements indicated a formation of $SiO_x$-precipitations at the DLC:Si surface and thus a depletion of the steel/DLC:Si interface from Si accounting for a weakening of this interface.

Potentiostatic and potentiodynamic measurements proved the corrosion resistance of the DLC variants: Pitting corrosion could be inhibited up to high potential differences and corrosion current densities could be reduced by three magnitudes compared to an uncoated steel surface.

The conducted investigations proved a high potential of DLC-coatings as interlayers for metal/epoxy-based CFRP structures. Their application towards hybrid structures based on thermoplastic matrices is currently under investigation.

## 7 ACKNOWLEDGEMENT

This work was conducted within the project “FORCiM³A – Forschungsverbund CFK/Metall-Mischbauweisen im Maschinen- und Anlagenbau“, which was funded by the Bayerische Forschungsstiftung (BFS). The authors take this opportunity to gratefully acknowledge the collaboration with Alexander Hartwig (Anwenderzentrum Material- und Umweltforschung, University of Augsburg), Claus Hammerl (AxynTec Dünnschichttechnik GmbH) and Marcus Kuhn (KUHN Beschichtungen GmbH).

## REFERENCES


[1] Baldan A.: *Review: Adhesively-bonded joints and repairs in metallic alloys, polymers and composite materials: Adhesives, adhesion theories and surface pretreatment.* Journal of Materials Science, 39:1–49, 2004.

[2] Baldan A.: *Review: Adhesively-bonded joints in metallic alloys, polymers and composite materials: Mechanical and environmental durability performance.* Journal of Materials Science, 39:4729–4797, 2004.

[3] Venables J.D.: *Review: Adhesion and durability of metal-polymer bonds.* Journal of Materials Science, 19:2431–2453, 1984.

[4] Sinmazçelik T., Avcu E., Bora M.Ö., Çoban O.: *A review: Fibre metal laminates, background, bonding types and applied test methods.* Materials and Design, 32:3671–3685, 2011.

[5] Tavakkolizadeh M., Saadatmanesh H.: *Galvanic corrosion of carbon and steel in aggressive environments.* Journal Of Composites For Construction, 5(3):200–210, 2001.

[6] Peng Z., Nie X.: *Galvanic corrosion property of contacts between carbon fiber cloth materials and typical metal alloys in an aggressive environment.* Surface and Coatings Technology, 215(0):85–89, 2013.

[7] Robertson J.: *Diamond-like amorphous carbon.* Materials Science and Engineering R, 37:129–281, 2002.

[8] Grill A.: *Diamond-like carbon: state of the art.* Diamond and Related Materials, 8:428–434, 1999.

[9] Damasceno J.C., Camargo Jr S.S., Freire Jr F.L., Carius R.: *Deposition of Si-DLC films with high hardness, low stress and high deposition rates.* Surface and Coatings Technology, 133-134:247–252, 2000.

[10] Monden A., Sause M.G.R., Hartwig A., Hammerl C., Karl H., Horn S.: *Evaluation of Surface modified CFRP-Metal Hybrid Laminates.* In: Proceedings of Euro Hybrid Materials and Structures 2014, 2014.

[11] Monden A.: *Adhäsion zwischen epoxidharzbasiertem CFK und oberflächenmodifiziertem Stahl: Grenzschichtversagen von Hybridlaminaten unter Mode I, Mode II und Mixed-Mode Belastung.* PhD thesis, University of Augsburg, 2016.

[12] Sause M.G.R.: *In Situ Monitoring of Fiber Reinforced Composites.* Springer International Publishing, 2016.

[13] Mollón V., Bonhomme J., Vina J., Argüelles A.: *Theoretical and experimental analysis of carbon epoxy asymmetric dcb specimens to characterize mixed mode fracture toughness.* Polymer Testing, 29:766–770, 2010.

[14] Shahverdi M., Vassilopoulos A.P., Keller T.: *Mixed-Mode I/II fracture behavior of asymmetric adhesively-bonded pultruded composite joints.* Engineering Fracture Mechanics, 115:43–59, 2014.

[15] Yokozeki T., Ogasawara T., Aoki T.: *Correction method for evaluation of interfacial fracture toughness of DCB, ENF and MMB specimens with residual thermal stresses.* Composites Science and Technology, 68:760–767, 2008.

[16] Nairn J.A.: *On the calculation of energy release rates for cracked laminates with residual stresses.* International Journal of Fracture, 139:267–293, 2006.

[17] Monden A., Sause M.G.R., Horn S.: *Surface modified Steel/Epoxy-based CFRP Hybrid Laminates under Mode I, Mode II and Mixed-Mode Load Conditions.* In: Proceedings of 17th European Conference on Composite Materials, 2016.

[18] Moosburger-Will J., Jäger J., Strauch J., Bauer M., Lachner E., Horn S.: *Fiber matrix adhesion in carbon fiber reinforced epoxy resin: influence of surface chemistry and surface morphology.* (to be submitted).

[19] Seah M. P.: *A review of the analysis of surfaces and thin films by AES and XPS*. Vacuum, 34:3-4, 463–478 (1984).

[20] Hartwig A.: *Titandioxid als Korrosionsschutz von X5CrNi18-10 Edelstahl und dessen Einsatzmöglichkeit in CFK-Metall Hybridstrukturen*. PhD thesis, University of Augsburg, 2015.

# FORMING AND CORROSION STABILITY OF A LASER PRE-TREATED METAL SURFACE – INFLUENCE ON THE PROPERTIES OF METAL-CFRP HYBRID STRUCTURES MADE BY VARTM

**C. Zinn[1*], Z. Wang[2], T. Troester[2], M. Schaper[1]**

1 Chair of Materials Science (LWK), Paderborn University, Warburger Straße 100, 33098 Paderborn, Germany

2 Chair for Automotive Lightweight Design (LiA), Paderborn University, Pohlweg 47-49, 33098 Paderborn, Germany

**ABSTRACT:** Today, topics like environmental protection as well as energy and resource efficiency gain increasing importance. Especially in the automotive sector, an enormous effort is undertaken to guarantee an efficient manufacturing of lightweight structures. Thereby, the fabrication of hybrid structures by using innovative processes is currently addressed. One of the toughest challenges is the generation of a strong and durable connection between dissimilar materials. In this study, the forming and corrosion stability of a laser pre-treated metal surface and its influence on the mechanical properties of hybrid structures out of carbon fibre reinforced plastics (CFRP) and a micro-alloyed steel (1.0548) or aluminium alloy 6082 (3.2315) fabricated by a Vacuum Assisted Resin Transfer Moulding (VARTM) process, is presented. The influence of a laser pre-treated surface on a forming process and an exposure in a sodium chloride solution is depicted. The surfaces are optically analysed and the ageing behaviour is investigated.

**KEYWORDS:** VARTM, laser surface pre-treatment, hybrid structures, ageing

## 1 INTRODUCTION

Today, energy and resource efficiency, environmental protection as well as $CO_2$-reduction play a key-role in industrial production, especially in the automotive sector. Due to slight weight savings, the fuel consumption and therefore the $CO_2$ emissions are significantly reduced. Despite huge efforts in a lightweight construction, the average weight of automobiles increased over the past years due to safety and comfort requirements. For a further development novel, innovative and holistic approaches are required.

Therefore, the automotive manufacturers try to integrate materials with a high lightweight construction potential, like high-strength steels, aluminium or magnesium alloys, as well as fibre reinforced plastics (FRP) in their manufacturing processes. In this context, FRP and especially CFRP represent a significant trend in modern automotive applications due to their excellent specific mechanical properties and their enormous lightweight potential. However, the use of CFRP in the automotive sector is predominately limited to prototypes, luxury class or race cars. Only a few automotive manufacturers already set on CFRP in civil cars. As one example, “BMW” employed a full carbon passenger compartment in his “i-series”, which results in an enormous weight reduction but also in high material and production costs [6].

In order to decrease the manufacturing costs and effort as well as to facilitate the integration of FRP structures in established processes, new economic manufacturing processes and efficient material combinations are required. Due to the high price and the low ductility of the high-rigid FRP, it is beneficial to utilize it as a local reinforcement. Prominent examples are the car body structures of the Audi “R8 LMS” and “BMW 7 series” consisting of an aluminium- or a steel-CFRP hybrid construction, respectively. Thanks to the hybrid constructions immense weight savings and increased stiffnesses are achieved [4, 19].

Conventionally, the manufacturing process of metal-CFRP hybrid structures comprises the production of each single component and a following joining procedure (bonding, riveting or screwing) [9, 11, 13]. Further disadvantages, especially of screwing and riveting, are long cycle times, a merely local force transmission [2], a possible damage of the CFRP [14] or contact corrosion between the noble CFRP and the non-noble metal component [5]. Bonded joints enable a huge contact area and eliminate corrosion problematics, but also require a time-consuming additional process step.

At this point, intrinsic manufacturing methods, where the joining process of the complete hybrid structure is integrated in the forming process of the metal and the FRP component, offer a promising alternative. Examples for such procedures are the co-cured bonding, [8] or the well-known autoclave technique, the prepreg-press-technology and resin injection processes [15].
A specific resin injection process, which allows the manufacturing of complex FRP or hybrid structures with high surface qualities in high quantities and short cycle times is presented by the Vacuum Assisted Resin Transfer Moulding (VARTM) process [16, 17]. Conventional VARTM processes are based on the insertion of a dry fibre component (preform) and a subsequent injection of a low viscous thermosetting resin system in an evacuated mould. In this study, a metal-CFRP hybrid structure is manufactured in the VARTM procedure by using a fast-curing epoxy resin system to ensure high strengths and short cycle times.
However, a suitable surface quality of the metal component is essential and has mayor influence on the joint strength between the metal component and the matrix of the CFRP component [10]. Surface pre-treatment is implemented by various methods, like etching, anodizing, plasma spraying or blasting processes [3, 10]. Nevertheless, most of these procedures are time-consuming, environmentally harmful or expensive. An easy and cost-efficient alternative is the laser-induced (nano-) structuring of the metal surface [16]. Thus treated, the surface is increased and open porous with various undercuts and significantly improved adhesion properties and bond strength [1, 10, 12].
Own investigations on laser pre-treated steel (1.0548) and aluminium (3.2315) - CFRP structures under bending [18] and shear load [21] as well as under ageing [20] have shown that both, the joint strength and the corrosion resistance are significantly increased. In all tests, an isolating glass fleece in the metal - CFRP interface area was used to exclude contact corrosion. For a wider use of the laser induced surface pre-treatment of the metal component in complex metal-CFRP hybrid parts, two important aspects are to be examined. First, it should be investigated, if the laser induced oxide layer on the steel or aluminium surface is resistant in a corrosive medium. Therefore, immersion and galvanic corrosion tests are performed. Secondly, it should be analysed, if the laser induced nano-structuring on the metal surface is resistant to forming processes, for it is much easier to pre-treat a 2D metal surface by laser irradiation than a 3D-structure. Both aspects are investigated in this paper.

# 2 EXPERIMENTAL DETAILS

## 2.1 MATERIALS

The materials investigated in this study are the micro-alloyed, fine-grained steel 1.0548 and the aluminium alloy 3.2315 (in the T6 condition). Both alloys are widely used for car body structures in the automotive sector. The material compositions and mechanical properties are shown in **Table 1**.

***Table 1:*** *Chemical composition and mechanical properties of 1.0548 and 3.2315*

| | **Chemical Composition in wt.-%** | | | | | | | | **Mechanical properties** | | |
|---|---|---|---|---|---|---|---|---|---|---|---|
| **1.0548** | C | Si | Mn | P | S | Al | Nb | Ti | $R_m$ **in MPa** | $R_e$ **in MPa** | $A$ **in %** |
| | 0.1 | 0.5 | 1.1 | 0.025 | 0.025 | 0.015 | 0.09 | 0.15 | 470 | 390 | 25-30 |
| **3.2315 (T6)** | Si | Fe | Cu | Mn | Mg | Cr | Zn | Ti | $R_m$ **in MPa** | $R_e$ **in MPa** | $A$ **in %** |
| | 0.7-1.3 | 0.5 | 0.1 | 0.4-1.0 | 0.6-1-2 | 0.25 | 0.2 | 0.1 | 295 | 250 | 8 |

The investigations of the forming stability of the laser induced nano-structuring, is performed on metal sheets with the dimensions of 300 x 300 mm² and a thickness of 2 mm. Some of these sheets are formed to hat profiles with the geometry shown in **Fig. 1**. In order to investigate the corrosion stability of the laser induced nano-structuring, small plates with the dimensions of 20 x 20 mm² and a thickness of 2 mm are used.

## 2.2 LASER PRE-TREATMENT

The surfaces of the aluminium and steel sheets as well as of the hat profiles are pre-treated with a short-pulse ND: $YVO_4$-fibre 3D-laser system “MD-X1520C” from KEYENCE, which has an average output power of 25 W, a wavelength of 1064 nm and pulse frequencies ranging from 0 kHz up to 400 kHz. In addition, it is equipped with an autofocus function and height differences of the specimens are compensable in a range of ±21 mm. In this study, the laser-system operated in the pulsed mode. The parameter settings used are shown in **Table 2**.

***Table 2:*** *Laser parameter settings for 1.0548 and 3.2315*

| Material<br>- | Scan speed<br>in mm/s | Power<br>in % | Frequency<br>in kHz | Track distance<br>in µm | Repetition rate<br>- |
|---|---|---|---|---|---|
| **1.0548** | 700 | 85 | 60 | 60 | 1-8 |
| **3.2315** | 700 | 50 | 30 | 60 | 1-8 |

For the structuring process, the metal sheets and the bottom areas of the hat profiles are placed on a lift table and positioned vertically to the laser optic. For the pre-treatment of the flank areas, the hat profile is placed on a 45 °-angle so that the flank areas are orientated at an angle of 45 ° towards the laser beam. Within the forming tests and the galvanic corrosion tests, the upper sides and in the immersion tests, the entire surface of the specimens, are laser pre-treated.

## 2.3 FORMING TESTS

The forming process is carried out in the same mould, which is typically used for the fabrication of hybrid metal-CFRP structures in the VARTM procedure to guarantee comparability with the conventional process condition. First, the metal sheet is inserted into the bottom tool cavity. To consider the thickness of the generally used CF-preform on top, a 2 mm-thick distance plate is placed on top of the metal sheet. Afterwards, the top cavity is completely closed under a constant pressure for 20 s. Finally, the finished hat profile is removed from the tool cavity. The geometry of the hat profile is shown in **Fig. 1**.

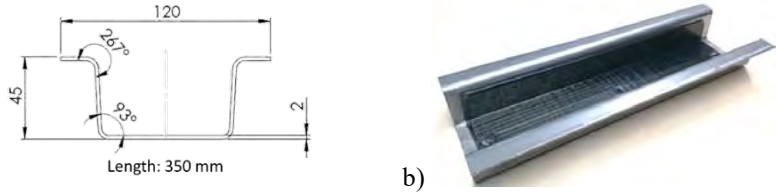


***Fig. 1*** *Geometry of the hat profile (metal component) (a) and example of a complete steel–CFRP hybrid hat profile (b)*

## 2.4 CORROSION TESTS

### 2.4.1 IMMERSION TESTS

Within the immersion tests, the specimens are exposed to a 5 % sodium chloride solution over a time-period of 4 weeks. First, it is analysed, if a (multiple) structuring can improve the corrosion resistance. Therefore, not and 1 to 8 times pre-treated specimens are investigated. Secondly, it is examined, if a (multiple) surface structuring reduces contact corrosion. For this reason, not and (multiple) pre-treated specimens are wrapped with a carbon fibre fabric. Afterwards, the specimens are placed on sample holders at a tilt angle of 15 ° in a box filled with sodium chloride solution. **Table 3** shows the investigated specimen conditions.

***Table 3:*** *Tested combinations in the immersion test: non-structured surfaces and surfaces pre-treated 1-8 times*

| | Reference | 1x | 2x | 4x | 8x |
|---|---|---|---|---|---|
| **1.0548** | x | x | x | x | x |
| **1.0548 + CF** | x | x | x | x | x |
| **3.2315** | x | x | x | x | x |
| **3.2315 + CF** | x | x | x | x | x |

### 2.4.2 GALVANIC CORROSION TESTS

The galvanic corrosion tests are also carried out in a 5 % sodium chloride solution by using a three-electrode cell with a silver/ silver chloride reference electrode, a platinum counter electrode and the specimens as the working electrodes. The three electrodes are connected with a multi-channel potentiostat “MLab 200” from Bank Elektronik. The measurements are performed with a test speed of 1 mV/ s in a range of -500 mV and +500 mV around the open circuit potential (OCP). The OCP is measured for a test period of 10 min with a step size of 100 ms. For all tests, a laser pre-treated area of 20 x 20 mm² is exposed to the electrolyte.

## 2.5 MICROSCOPIC ANALYSIS

After the forming and corrosion tests, the specimens’ surface is investigated by using a scanning electron microscope “Ultra Plus” from Zeiss or a digital microscope “VHX 1000” from KEYENCE, respectively.

# 3 FORMING STABILITY OF LASER PRE-TREATED SURFACES

As a first result, the structuring process of a 2.5D-hat profile is unproblematically possible by using the 3D-laser system. The autofocus function realizes a very even nano-structuring over the entire surface. (**Fig. 2**, left). Regarding the hat profile, which was formed after the laser pre-treatment, some scratches are visible on the surface, but the nano-structuring seems to be intact (**Fig. 2**, right).

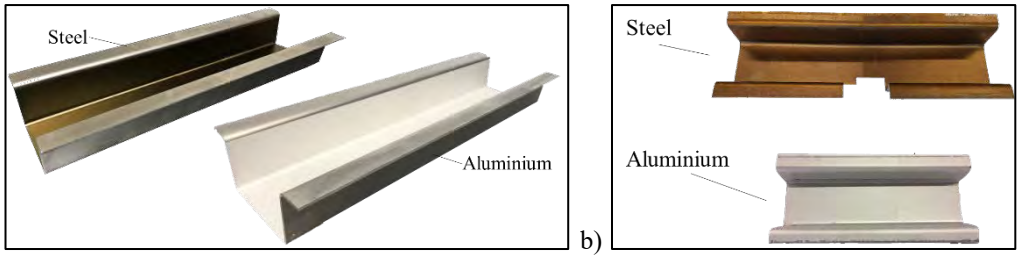


***Fig. 2*** *Laser pre-treated hat profiles: a) pre-treated after the forming process, b) pre-treated before the forming process*

A more detailed SEM-investigation of the nano-structuring on the outer and inner radius of the hat profile confirms this assumption (**Fig. 3**, a)). On the outer radius, fine cracks are visible, but the nano-structure is intact. The nano-structuring is even present in the cracks. Therefore, the cracks are only superficial. Images of the inner radius show fine folds on the surface, but in a higher resolution it is visible that even between and on the fold the nano-structure is defect-free. Thus, the laser-induced nano-structured surface resists extreme forming processes (up to 93 °) so that the laser pre-treatment can be performed prior to the forming process.

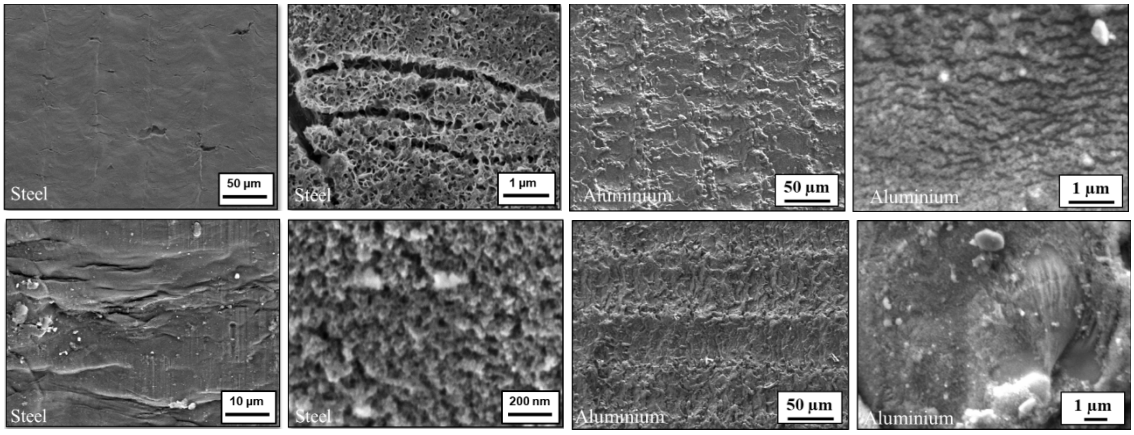


***Fig. 3*** *SEM-images of a) the outer and b) the inner radius of the laser pre-treated steel (left) and aluminium (right) sheets formed to a hat profile*

# 4 CORROSION STABILITY OF THE LASER PRE-TREATED SURFACES

## 4.1 IMMERSION TEST

### 4.1.1 SURFACE QUALITY AFTER 4 WEEKS

The surface quality of the steel and aluminium specimens after an exposure time of 4 weeks in the 5 % sodium chloride solution is shown in **Fig. 4**. Regarding the steel specimens, it is obvious that a multiple laser pre-treatment has no significant effect concerning the corrosion behaviour. Surface corrosion occurs for all specimen types and in a similar amount. The laser structuring is either completely or partly existent on the surface, especially on the surface of the multiple pre-treated specimens. The reduction of the laser structuring, *i.e.* the oxide layer, can be explained as follows: On the one hand, the iron oxide layer is nobler than the base material. Therefore, little defects in the oxide layer lead to an increased reduction, due to the critical anode-cathode relation. On the other hand, the intercrystalline adhesion between iron and the iron oxide layer is generally poor due to their different lattice constants [7].

Concerning the aluminium specimens, the nano-structure is partly intact on all pre-treated specimens and the surface quality is similar for all specimen variants. Homogenous surface corrosion as well as selective corrosion are visible. Nevertheless, it appears that selective corrosion decreases with an increasing number of laser pre-treatment processes. Potentially, the oxide layer of the one or two times pre-treated specimens is very porous and can be disrupted easily, which results in selective corrosion or pitting corrosion. In contrast,

multiple pre-treatment processes can lead to a sealing of the pores and therefore to less selective corrosion as well as reduced pitting corrosion.
In general, a laser-pre-treatment of the steel or aluminium surface has no significant effect regarding the corrosion performance. The existence of the laser structuring on the surface after the immersion test indicates that the laser-induced oxide layer is able to protect the basic material against corrosion. After an exposure time of four weeks, the laser-structuring is still visible on the surface of all pre-treated specimen types.

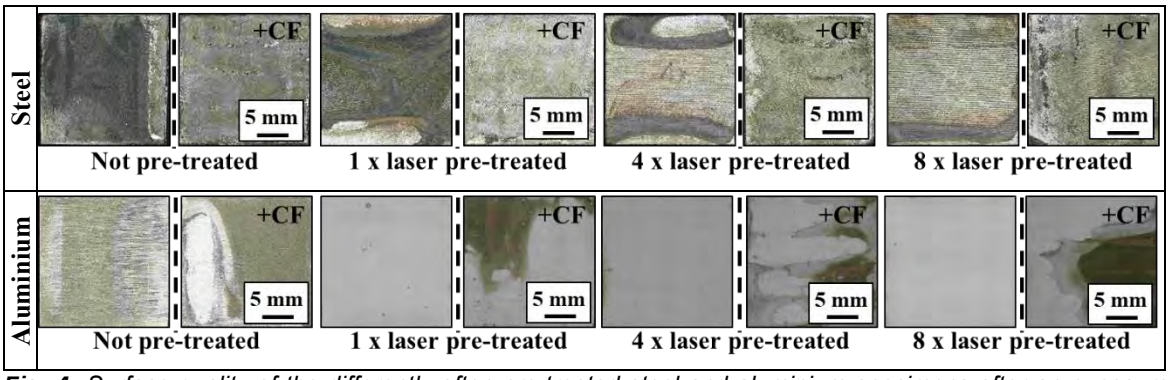


***Fig. 4*** *Surface quality of the differently often pre-treated steel and aluminium specimens after an exposure time of 4 weeks*

### 4.1.2 LOSS OF MASS AFTER 4 WEEKS

The weight loss for each specimen type is shown in **Table 4**.

***Table 4****: Weight loss in percent of the steel and aluminium specimens after an exposure time of 4 weeks: non-structured surfaces and surfaces pre-treated 1-8 times*

| | Reference | 1x | 2x | 4x | 8x |
|---|---|---|---|---|---|
| **1.0548** | 0.44 | 0.41 | 0.39 | 0.41 | 0.44 |
| **1.0548 + CF** | 0.72 | 0.70 | 0.81 | 0.80 | 0.95 |
| **3.2315** | 0.22 | 0.29 | 0.36 | 0.18 | 0.21 |
| **3.2315 + CF** | 1.02 | 1.98 | 1.30 | 1.62 | 1.49 |

The weight loss of the steel specimens is more or less constant for all pre-treatment conditions. Therefore, the laser-pre-treatment has no significant influence on the corrosion performance.
For the aluminium specimens, the weight loss seems to increase due to the laser pre-treatment. However, a clear trend is not visible. Some conditions, *e.g.* four times pre-treated, achieve a reduced weight loss in comparison with the as received condition.
In general, these results indicate that the laser-pre-treatment has no significant influence on the corrosion behaviour of steel and aluminium surfaces.

## 4.2 GALVANIC CORROSION TESTS

Analysing the surface quality of the differently pre-treated steel and aluminium specimens directly after the galvanic corrosion tests, a dependency between the number of repetitions and the corrosion resistance is found (**Fig. 5**, left). The steel specimens, which were pre-treated 4 or 8 times, still show a stable laser structured surface and no visible signs for corrosion. In contrast, the surface of the one-time pre-treated specimen, the nano-structure is mainly detached. The surface of the not pre-treated specimen is matt, rough and uniformly corroded. With regard to the aluminium specimens, the nano-structuring is still present on the surface of all pre-treated specimens. The specimens pre-treated 1 or 8 time(s) reveal more signs for selective corrosion. A possible reason for this is a more open porous surface structure. Summarizing, the two times pre-treated condition seems to be the most stable one. The not-pre-treated aluminium specimens reveal a matt surface with multiple selective corrosion attacks.

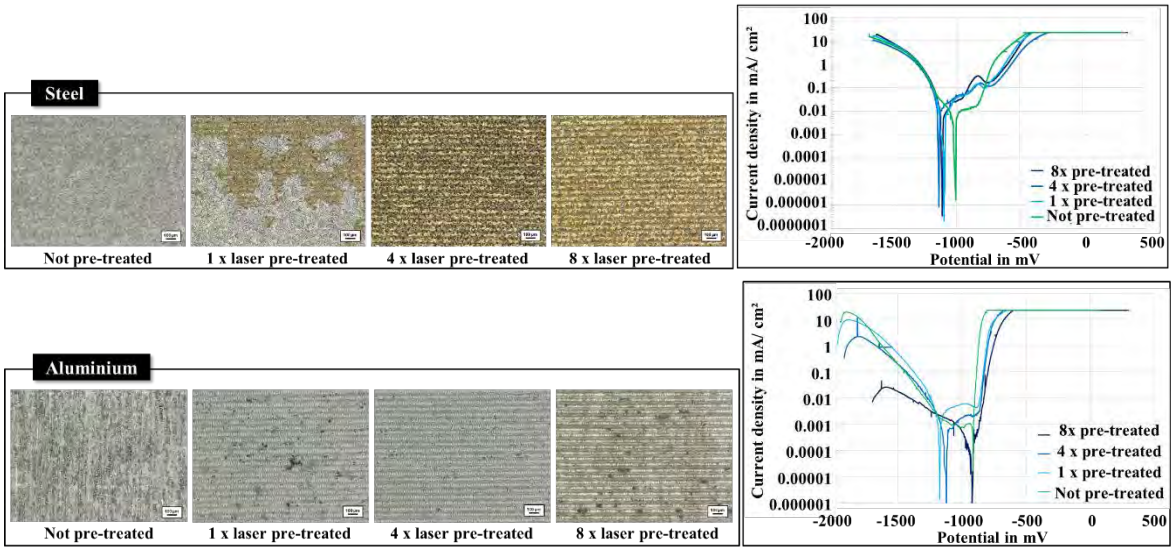


***Fig. 5*** *Surface quality (l.) and current density potential curves (r.) of differently pre-treated steel and aluminium plates*

With only one exception, the current density curves show that the not pre-treated steel and aluminium specimens reveal a more positive OCP (steel ≈ -1000 mV, aluminium ≈ -850 mV) than the pre-treated specimens (**Fig. 5**, right). This means that the corrosion of the pre-treated specimens begins earlier. For both materials, the number of repetitions has no influence on the OCP. For steel, it is approximately -1150 mV and for aluminium about -1200 mV. Despite multiple measurements on different specimens, the eight times pre-treated aluminium specimen exhibits the same OCP than the not pre-treated counterpart. An explanation for this behaviour is complicated. Probably, the chemical composition of the surface is modified by a multiple pre-treatment, but this has to be clarified by further investigations of the chemical composition.
Due to the more negative OCP of the pre-treated surfaces, the potential difference between the metal surface and the carbon fibres, and therefore the risk of contact corrosion increases. However, a detailed analysis of the current density curves shows that the corrosion current density, as a criterion for the corrosion rate, is reduced with increasing repletion rates of the laser pre-treatment. Summarizing, the materials corrode less.

## 5 CONCLUSIONS

Summarizing, two main conclusions can be drawn from these investigations:

- On the one hand, the laser induced nano-structuring on the surface of steel and aluminium specimens resists a forming process up to 93°. Occurring cracks or folds are superficial and, presumably, not critical. Nevertheless, further investigations have to exclude a negative influence on the fatigue performance.
- On the other hand, the laser induced oxide layers are not entirely resistant in sodium chloride solutions. The laser structuring is still visible on parts of the steel or aluminium surface after the exposure time, but it is significantly reduced.

## 6 ACKNOWLEDGEMENT

The authors gratefully acknowledge the financial support of the “Priority Program 1712” provided by the German Research Foundation (DFG).

## REFERENCES

[1] A. Montealegre, M., Castro, G., Rey, P., Arias, J. L., Vázquez, P., and González, M. 2010. SURFACE TREATMENTS BY LASER TECHNOLOGY. *CM* 1, 1, 19–30.
[2] Altmeyer, J., Suhuddin, U., dos Santos, J. F., and Amancio-Filho, S. T. 2015. Microstructure and mechanical performance of metal-composite hybrid joints produced by FricRiveting. *Composites Part B: Engineering* 81, 130–140.
[3] Baburaj, E. G., Starikov, D., Evans, J., Shafeev, G. A., and Bensaoula, A. 2007. Enhancement of adhesive joint strength by laser surface modification. *International Journal of Adhesion and Adhesives* 27, 4, 268–276.

[4] Essbauer, S. 2016. *Produktionsstart der neuen BMW 7er Reihe im Werk Dingolfing*. Accessed 22 January 2018.
[5] Francis, R. 2001. *Galvanic corrosion*. *A practical guide for engineers*. NACE International, Houston, Tex.
[6] Georg K. 2015. *BMW i8 mit 500 PS: 2016: Sportwagen zum Hundertsten.* Accessed 22 January 2018.
[7] Habenicht, G. 2009. *Kleben*. *Grundlagen, Technologien, Anwendungen*. VDI-Buch. Springer Berlin Heidelberg, Berlin, Heidelberg.
[8] Hopmann C., Boettcher A., Fischer K. 2013. Investigations of bonding approaches and initial bond strength for the intrinsic manufacturing of laminar bonded hybrids made of thermoplastic composite and metal. *Journal of Plastics Technology* 9, 253–274.
[9] Huang, Z., Sugiyama, S., and Yanagimoto, J. 2014. Applicability of adhesive–embossing hybrid joining process to glass-fiber-reinforced plastic and metallic thin sheets. *Journal of Materials Processing Technology* 214, 10, 2018–2028.
[10] Kurtovic, A., Brandl, E., Mertens, T., and Maier, H. J. 2013. Laser induced surface nano-structuring of Ti–6Al–4V for adhesive bonding. *International Journal of Adhesion and Adhesives* 45, 112–117.
[11] Lambiase, F. and Di Ilio, A. 2015. Mechanical clinching of metal–polymer joints. *Journal of Materials Processing Technology* 215, 12–19.
[12] Mandolfino, C., Lertora, E., Genna, S., Leone, C., and Gambaro, C. 2015. Effect of Laser and Plasma Surface Cleaning on Mechanical Properties of Adhesive Bonded Joints. *Procedia CIRP* 33, 458–463.
[13] Marannano, G. V. and Pasta, A. 2007. An analysis of interface delamination mechanisms in orthotropic and hybrid fiber-metal composite laminates. *Engineering Fracture Mechanics* 74, 4, 612–626.
[14] Meschut, G., Gude, M., and Augenthaler, F. Geske, V. Evalutation of damage in Carbon-Fibre Composites Induced by self-piercing riveting. *Procedia CIRP* 2014, 18, 186–191.
[15] Neitzel, M., Mitschang, P., and Breuer, U. 2014. *Handbuch Verbundwerkstoffe*. *Werkstoffe, Verarbeitung, Anwendung*. Carl Hanser Fachbuchverlag, s.l.
[16] Wang W., Matsubara T., Takao Y., Yasuda K., Hayashi R. 2015. Effects of curing conditions on the short time co-cure of CFRP-steel hybrid laminates. *Journal of Reinforced Plastics and Composites* 34, 819-829.
[17] Wang Z., Lauter C., Sanitther B., Frantz M., Troester T., Ed. 2015. *Intrinsic Manufacturing of Metal-FRP-Hybrid Structural Automotive Components by Resin Transfer Molding*.
[18] Wang, Z., Bobbert, M., Dammann, C., Zinn, C., Lauter, C., Mahnken, R., Meschut, G., Schaper, M., Troester, T. 2016. Influences of interface and surface pre-treatment on the mechanical properties of metal-CFRP hybrid structures manufactured by Resin Transfer Moulding. *International Journal of Automotive Composite* 2, 3/4, 272–298.
[19] Wolfgang Gomoll. 2015. *Vier Ringe, 610 PS: Hier rast der neue Audi R8*. Accessed 18 July 2016.
[20] Zinn, C. 2017. *Influence of a laser pre-treatment on the mechanical and the corrosion properties of metal-CFRP hybridstructures manufactured by RTM*, Paris.
[21] Zinn, C., Schaper, M., Serna, J., Meiners, D., Wang, Z., Troester, T., Pottmeyer, F., and Weidenmann, K. A. 2016. Shear Edge Tests: A benchmark in investigating the influence of different surface pretreatment methods on the shear stress of metal-CFRP hybrids manufactured by RTM process. *International Journal of Automotive Composites* 2, 3/4, 244–271.

# IMPACT OF TEMPERATURE AND DEFORMATION GRADIENT ON THE JOINING ZONE FORMATION OF LASER ROLL-BONDED BIMETALS

**V. Fux, J. Kaspar, A. Berger, T. Fiebiger, M. Seifert, D. Beitelschmidt**

Fraunhofer IWS Dresden

**ABSTRACT:** The process of laser roll-bonding facilitates the production of bimetals with different geometries and material combinations. Contrasting the classical cold and warm roll-bonding processes, only the surfaces of the two bonding materials to be bonded are heated to the necessary process temperatures using laser energy. As a result, deformation is concentrated on the material volumes near the joining zone. When pairing the materials aluminium and copper, this mechanism becomes visible in metallographic sections. Inclusions containing copper are apparent here in the aluminium near the joining zone. As a result of aluminium flowing against the direction of rolling (formation of a quasi-stationary and convecting bulge), small melt droplets are shorn off the copper surface. At the same time, the melt droplets are integrated into the aluminum. This suppresses the formation of intermetallic phase seams on the material transition making very ductile material composites possible.

**KEYWORDS:** Roll bonding, Plating, Transiton Joint, bimetal-compound, intermetallic phases, bonding mechanism

## 1 INTRODUCTION

A roll-bonding process was developed at the Fraunhofer Institute for Material and Beam Technology Dresden in collaboration with a foreign industrial partner. In contrast to conventional cold or hot-rolled bonding the two bonding partners (bands or square wires) are fed here to the roll gap at an angle of 45° [1-5]. As a result, the inner surfaces of the semi-finished products to be joined become accessible immediately before the roll gap and can therefore be heated to the required process temperature by a linear laser beam (see Fig. 1). Overall deformation therefore remains relatively low (approx. 8-15%).

An inductive preheating facility for the bands or wires is integrated in the pilot plant set up at the IWS. The (optional) preheating of the semi-finished products allows or facilitates the realisation of a large number of material combinations and has a positive effect on the economy of the process at the same time. Preferably narrow semi-finished product contours can be presented with this bonding technology. Fig. 2 shows an example of bimetal cross-sections that can be manufactured using the (with inductive support) laser roll-bonding. They are suitable as a semi-finished products, for example, for friction bearings (steel/copper alloy), contact and connection elements (copper/aluminium) as well as "transition joints" for mixed compounds (steel/aluminium alloy) to be produced by welding.

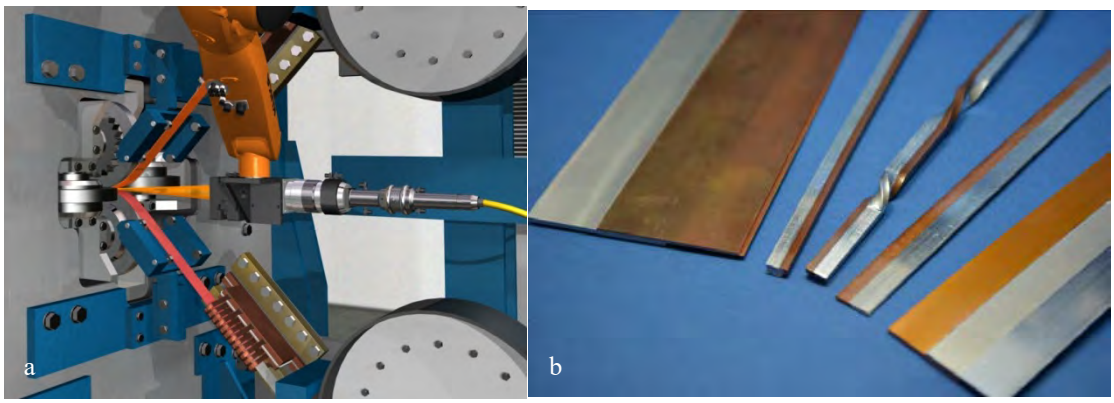


***Fig. 1*** *a) Process principle inductively assisted laser roll bonding b) Examples of laser-rolled bonded bi-metal semi-finished products*

## 2 SPECIAL FEATURES OF THE FORMATION OF THE JOINING ZONE

Generally, the composite bond with all roll-bonding procedures is made from a combination of forming and a diffusion process. While with cold rolling-bonding the final strength of the material bond is usually only achieved by a subsequent annealing process, with hot and laser roll-bonding these mechanisms act simultaneously in a single process step.

From an energy point of view, laser roll-bonding is a short-term process, compared to hot roll-bonding. Heating to process temperature with the laser process concentrates only on the semi-finished products to be joined immediately before rolling. As a result, deformation is only localized on the highly heated areas during rolling. Since the majority of the cross-section portion is hardly deformed, a compensating flow movement of the hot material against the feed movement occurs (see Fig. 2). This effect plays a key role in the formation of highly stressed joining zones of laser roll-bonded bimetals. This disturbs the diffusion-controlled local enrichment of alloy elements on the material transition. It is very critical for the realization of material pairs with a strong tendency to the formation of intermetallic phase seams on the material transition. Examples are the combinations of steel or copper with aluminium materials. As a result, none or only partially developed brittle phases can be observed. Material composites with high strength and high ductility can thus be realised.

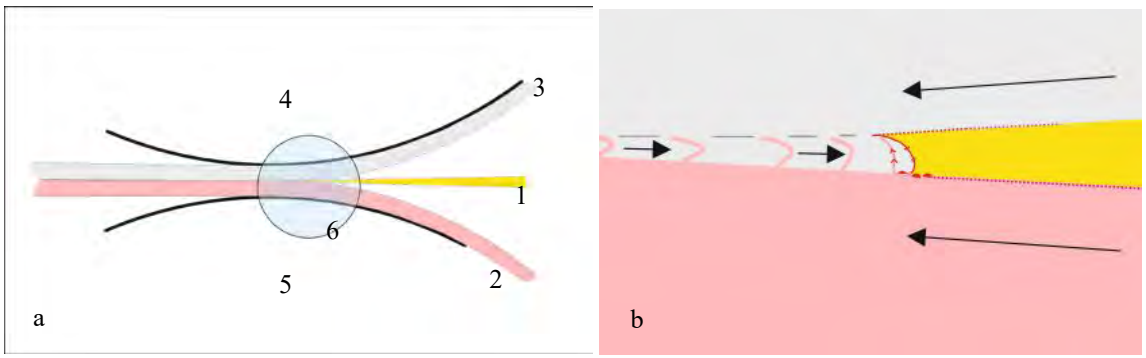


***Fig. 2*** *Principle of laser roll bonding a) Overview, 1 laser beam, 2 copper strip, 3aluminium strip, 4 and 5 rollers, 6 zoom range, b) Transition deformation zone (left) to the laser contact zone (right),*

Metallographic and scanning electron microscopic examinations of joining zones of the material combination of aluminium and copper provide important tools for the description of the above-mentioned mechanism. Already the light microscope images show an astonishing phenomenon in the aluminium near the joining zone. Copper-coloured chill crystal inclusions can be detected at a distance of 100 to 250 µm from the material transition (Fig. 3a). At greater magnification (Fig. 3b) these inclusions can mainly be detected as eutectic ($Al_2Cu$ + Al-mixed crystal) and eutectoid mixtures. The farthest smaller inclusions, showing different sub-eutectic compositions, constitute exceptions (Fig. 4a).

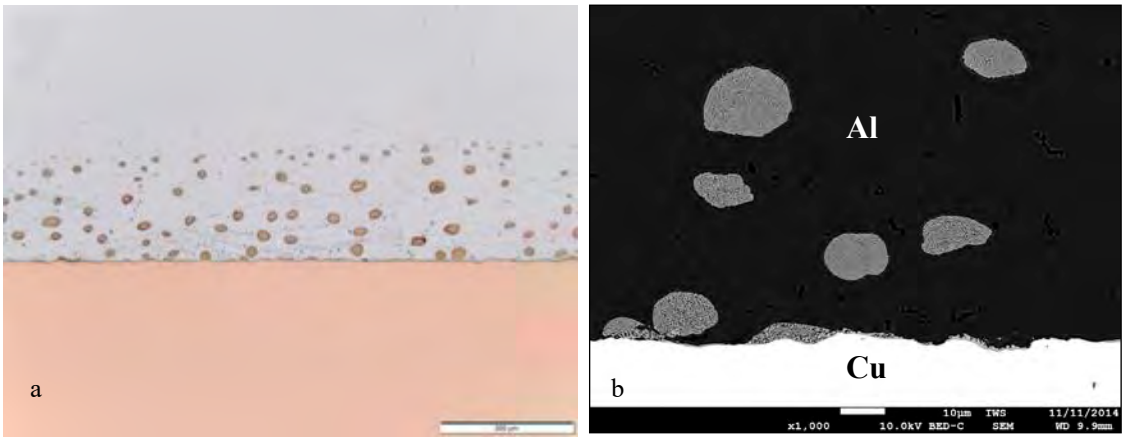


***Fig. 3*** *a) light microscope picture of a Cross section of an AlCu-bimetal b) enlargement with SEM-backscattering- recording*

Except in the inclusions, isolated Cu enrichments appear on the grain boundaries, which are connected again with the inclusions. On the material transition, with the exception of partial phase enrichments, only a very thin phase seam, typical for phase formation at lower temperatures, can be seen. The longitudinal polished sections, Figs. 5a and b, provide an explanation on the origin of the inclusions. They show copper "tubes" in the aluminium that are tapered, leading away from the copper surface at an angle of approx. 15°. They point against the direction of feed, which means that this area of the aluminium material (up to 250 µm) close to the joining zone has moved against the rolling direction. Copper-containing "threads" also appear in the joining zone which seems to delimit this area from the unaffected aluminium.

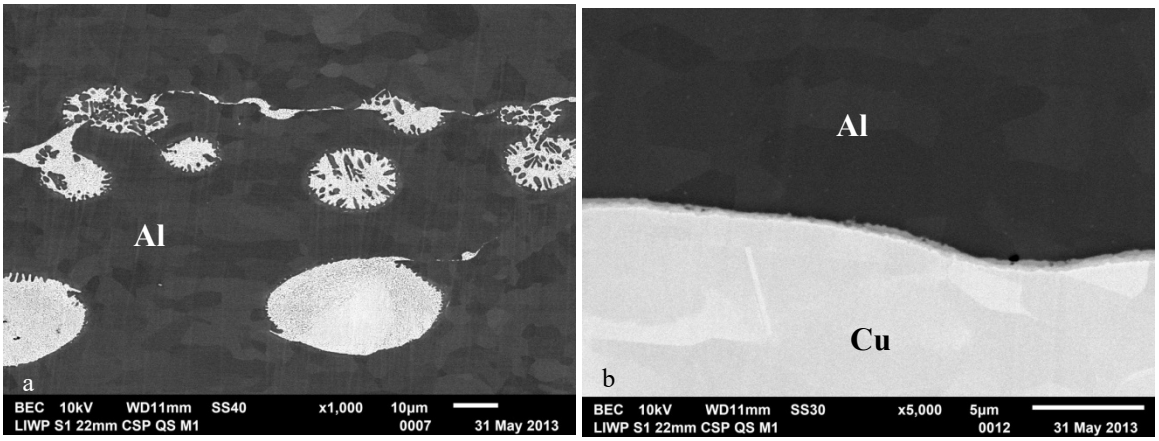


***Fig. 4*** *a) metallografic cross section, rectangular to the rolling direction, SEM –recording of an AlCu-bimatal b) material transition zone*

The large number of analytical investigations shows that a realization of very ductile and thus high-stress composites of this material combination always results in very similar structural characteristics in the joining zone. The material flow of pasty or almost liquid aluminium, which is directed in the opposite direction to the rolling direction, forms a deformation-induced quasi-stationary convective bead, which is pressed out by the rolling gap. The latter obviously shears off small melt droplets from the copper surface. This in turn leads to the uncovering of new, undisturbed but highly active surfaces on the copper side. The most highly heated material areas are transported from the surface to the inside by this mechanism, which means that they no longer have any influence on phase formation at the material transition. This prevents the formation of thicker intermetallic phase seams, which have an unfavourable effect on the composite properties.

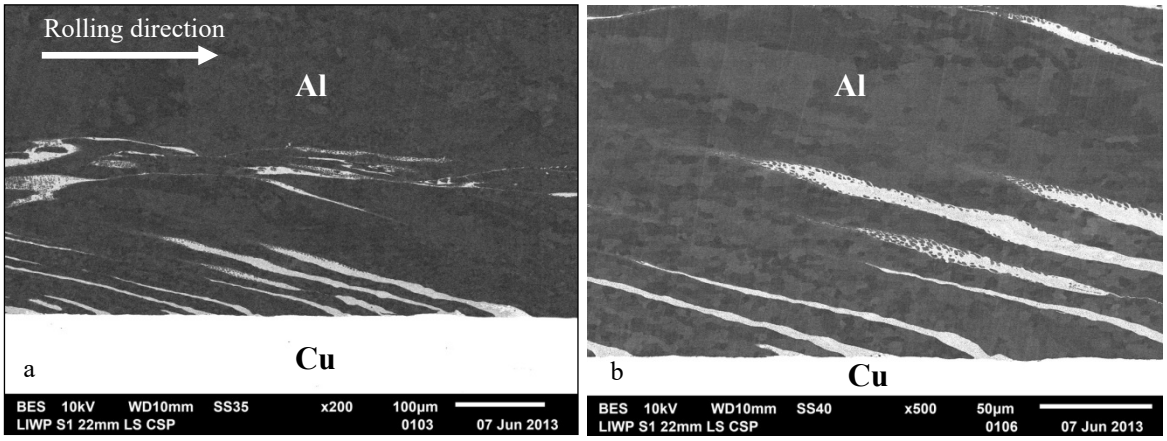


***Fig. 5*** *a) Cut along the rolling direction of AlCu-bonding b) enlargement*

This mechanism is also active in the production of other material pairs. Contrary to the pairing of aluminium and copper it cannot always be observed with the same clarity by means of metallographic examinations. Process observation with a high-speed camera can prove to be more effective at this.

## 3 CONCLUSIONS

The special mode of energy introduction with laser roll-bonding leads to temperature gradients on the semi-finished products to be joined. They cause a deformation-induced material flow in the area of the material transition. This causes CU-rich inclusions in the area of the joining zone of the aluminium when producing al/Cu bimetals. This mechanism prevents the formation of an intermetallic phase seam at the material transition and is therefore responsible for the good composite properties of laser roll-bonded bimetals.

## 4 ACKNOWLEDGEMENT

Part of the investigations was promoted by BMBF via the “Batcon” project, promotion identifier 01MX12055C.

## REFERENCES

[1] Schmitdchen M.: Simulation des Haftungsvorganges in Plattierprozessen. In: Modellierung und Simulation von Prozessen der Stahlerzeugung und Stahlverarbeitung, 210-235, TU Bergakademie Freiberg, Freiberg, 2005.

[2] Bambach M., Pietryga A., Mikloweit A., Hirt A., Karhausen K.: Finite Element Implementation of a Bonding Model and Application to Roll Bonding of Aluminum Sheets of Largely Different Yield In: Material Science Forum Volumes 783-786, pp644-650, 2014.

[3] Bay N., Clemensen C., Juelstrorp O., Wanheim T.: Bond Strength in Cold Bonding. Annals of the CRIP Vol. 34, 221-224, 1985.

[4] Bay N..: Cold pressure welding- the mechanismus governing bonding. In: Journal of Engineering Industry, 121-127, 1979

[5] Knauscher A.: Oberflächenveredeln und Plattieren von Metallen. VEB Deutscher Verlag für Grundstoffindustrie, Leipzig, 1978

# TEXTILE CONNECTION TECHNOLOGY FOR INTERFACES OF FIBRE-REINFORCED PLASTIC-CONCRETE-HYBRID COMPOSITES

**Larissa Born[1*], Claudia Möhl[1], Markus Milwich[2], Götz T. Gresser[1,2]**

[1]Institute for Textile and Fiber Technologies (ITFT), University of Stuttgart, Germany
[2]German Institutes of Textile and Fiber Research (DITF), Denkendorf, Germany

## ABSTRACT:

Based on a textile technology known from carpet manufacturing (tufting) respectively z reinforcement of fibre-reinforced plastics (FRPs), a new process has been developed for interface connections between two FRP component parts: tufting of pre-fabricated FRP pins during preform manufacturing. Both preform and tufting loops are impregnated simultaneously. Afterwards so called “tufting pins” protrude out of plane of the FRP plate or into the inside of a 3D FRP hollow structure, for example a cylindrical component. The hollow structure can be filled with a core material in particular to enhance mechanical properties. In the case of micro-gaps caused e. g. by shrinkage of the material the pins close these micro-gaps between core and FRP-hull or rather maintain mechanical contact between hull and core. In extensive tests the general adhesion properties between pinned FRP and concrete as a filling material as well as the influencing variables of the tufting process with regard to their effects on mechanical parameters were investigated. Decisive influencing factors result both from the textile process as well as the component design. It is shown, how the tension load of a tufted FRP connection increases depending on the reinforcing fibre material as well as the number of tufting pins.

**KEYWORDS:** 3D-reinforcement, carbon, concrete, connection, fibre, fibre-reinforced plastic, FRP, glass, interface, tufting, tufting pin

## 1 INTRODUCTION

For the manufacturing of three-dimensional fibre-reinforced composite components, various textile processes are available, e. g. 3D weaving and braiding. In addition, the reinforcement of 2D textile stacks in the normal direction (z direction) for example by sewing, embroidery or tufting is possible.
Tufting is a textile process originally familiar from carpet manufacturing. In fibre composite technology tufting is used to reinforce multi-layer dry textile preforms in z direction, with subsequent impregnation in a thermoset process [1, 2]. Z-reinforcement improves handling of the stack [3], reduces the risk of delamination and increases impact resistance as well as damage tolerance [4]. In addition, research work on the tufting process aims not only for the general, overall z-reinforcement of fibre-reinforced plastics (FRPs), but aims also to reinforce only local, high loaded, areas. It could be shown that reinforcing a T-profile in the flange edge area with tufting loops limits the delamination failure under tensile stresses [5]. Furthermore, core materials such as foams in sandwich components can also be reinforced by tufting, thus improving the flexural and compressive strength of the final component [6].
In literature, the tufting process is often compared to z-pinning. Via z-pinning metallic or fibre-reinforced rods are integrated through the thickness of a textile stack [7]. In contrast to tufting, z-pinning can also be used to interconnect prepreg layers in z direction and to manufacture lap joint connections between individual FRP components [8]. The improvements of the mechanical properties in the final components are comparable to those of the tufting process: depending on length, thickness and density of the pins, the delamination fracture toughness under static and dynamic load is improved [7, 9, 10, 11].
With the new tufting process, developed at ITFT, it is possible to generate alike connections between FRP components as well as connections between 3D shaped FRP hulls and a component filling consisting of

* Corresponding author: University of Stuttgart, Institute for Textile and Fiber Technologies (ITFT),
Larissa Born, Pfaffenwaldring 9, 70569 Stuttgart; phone 0711-9340-530; fax 0711-9340-663;
larissa.born@itft.uni-stuttgart.de

another material. Filling 3D FRP components with other materials is challenging caused e. g. by shrinkage of the filling material. With tufting pins protruding into the interior of the 3D structure it is possible to bridge micro-gaps between hull and filling. By this technique, it is possible to manufacture fully loadable concrete filled FRP-tubes for the building industry. Even if the concrete shrinks, the pins connect FRP and concrete. This enables a very good load transfer between FRP and concrete and the load bearing capacity can be increased by the complemented strength properties (pressure – concrete/tension – FRP).

## 2 TUFTING PROCESS FOR FRP PINS

Based on the existing one-sided tufting processes with a KUKA-compatible sewing head from KSL-Lorsch "RS 520", a tufting process was developed for tufting pins protruding out of plane from one side of a FRP component. For this purpose, the thread guiding elements of the KSL head were first modified to guide a carbon roving with a fineness of 12 K and 800 tex or glass rovings with a fineness of 600 tex. Within manual preliminary tests it was obvious that this fineness exhibit the best processability for both glass and carbon rovings. The lowest number of filament breaks was measured during processing the rovings with the tufting needle.

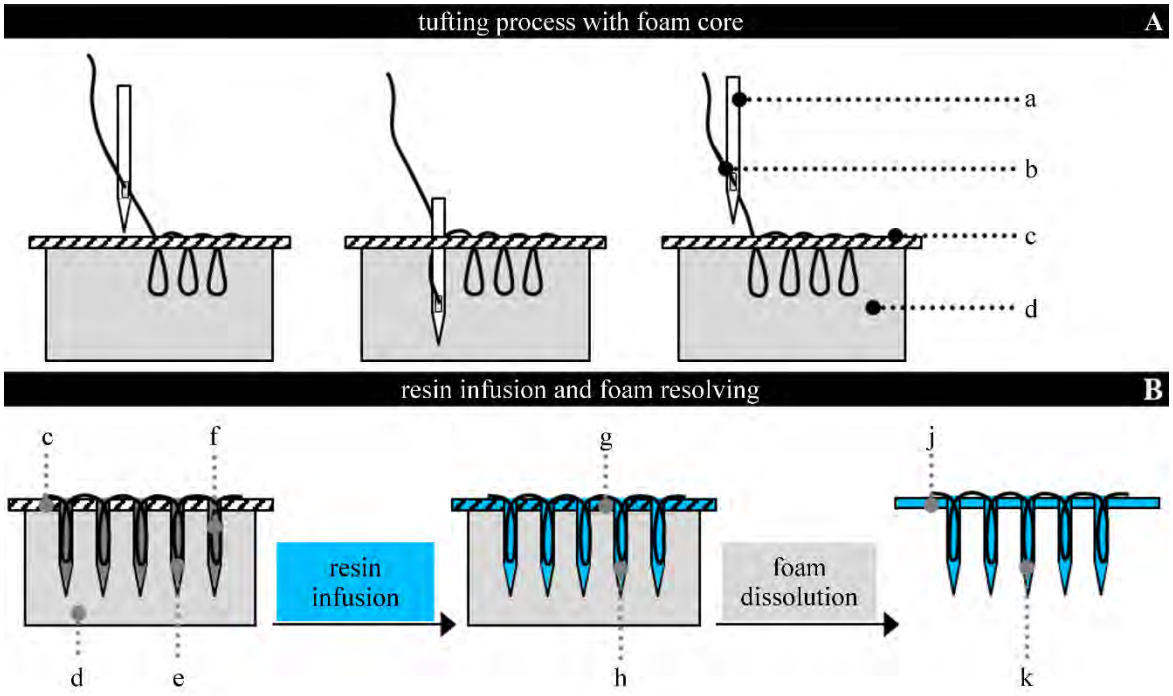


***Fig. 1*** *Adapted tufting process for fabricating tufting pins protruding out of the FRP component plane A: schematic of adapted tufting process with (a) tufting needle, (b) reinforcement thread, (c) textile (stack) and (d) foam; B: schematic of resin infusion of a tufted textile stack for manufacturing FRP components with tufting pins with (c) textile (stack), (d) foam, (e) pinholes, (f) tufted reinforcement thread loops, (g) impregnated textile, (h) resin-filled pinholes, (j) FRP-plate and (k) FRP pin*

For the tufting of FRP-pins, a dry textile stack is draped on a foam base plate or a 3D preform is manufactured onto a three-dimensionally shaped foam core. The tufting needle punctures the foam through the textile (Fig. 1A). Comparable to the process for one-sided tufting to connect multiple textile layers, a thread loop results. Within the adapted process the loop is not mainly formed by the friction between textile layers and thread, but due to the friction between the foam and thread. The penetration depth determines the length of the tufting pins. Afterwards the tufted textile ply structure with the foam is processed in an over- or underpressure process for thermosets (Fig. 1B). Within the experiments presented here, VAP® (vacuum assisted process) [12] is chosen. During the infusion process, the resin not only impregnates the textile layers on the outer side of the foam, but also flows into the puncture holes and thus impregnates the yarn loops (Fig. 1B). After curing of the thermoset, the foam core or the foam base plate is dissolved by solvents from the FRP component. The tufting pins protrude out of plane of the finished component for connection to another component or, in the case of a 3D component, for interfacing to the subsequently filled in (stiffening) core material.

## 2.1 FIBRE, FOAM AND CORE MATERIAL

As reinforcing textiles a carbon fibre multiaxial non-crimp fabric (+45/90/0/-45) with a surface weight of 600 g/m² respectively a glass fibre biaxial non-crimp fabric (±45) with a surface weight of 300 g/m² were chosen. The reinforcement thread is either an 800 tex/12 K carbon roving or a 600 tex glass fibre roving. The resin used for the experiments is an epoxy system of the company Hexion: resin RIMR135 and RIMH137 hardener.
Different foam materials (commercially available EPS foam, commercially available XPS foam, Bio-Foam® (PLA based expanded foam), MONDOMED® PVA foam (C1/B22), FARMfill® Premium (foam based on corn starch), ZealaFoam (biobased EPS foam)) and their suitability for the tufting process were tested. The foam must permit the puncturing of the tufting needle without damaging the reinforcing thread as well as it must be soluble after infusion with epoxy resin. Preliminary tests were carried out manually with different solvents: demineralised water, isopropanol, acetone and ethanol. As result only two were completely soluble after the impregnation with resin (commercially available EPS foam, commercially available XPS foam). However, EPS foam proved to be inappropriate due to separating EPS particles from the foam during the tufting process. Consequently XPS was chosen which is resolved after the infusion with acetone.
After dissolving the foam the FRP component with tufting pins is joined to commercially available concrete with a strength class of C25/30 (DIN EN 206-1)/CT-C35-F6 (based on DIN EN 13813).

## 2.2 MECHANICAL TEST OF SHEAR STRENGTH OF TUFTING CONNECTION

To define potential applications of the new tufting technique, the interface strength between FRP-layer and filling material was mechanically tested. For this issue a tensile/shear double strip test, known from mechanical testing of adhesive bonds and rivets [13], has been conducted according to DIN EN ISO 14589: 2000 and respectively ISO 4587: 2003. The tensile force was measured until maximum load of the connection providing information to what extent forces can be transmitted between core and hull.

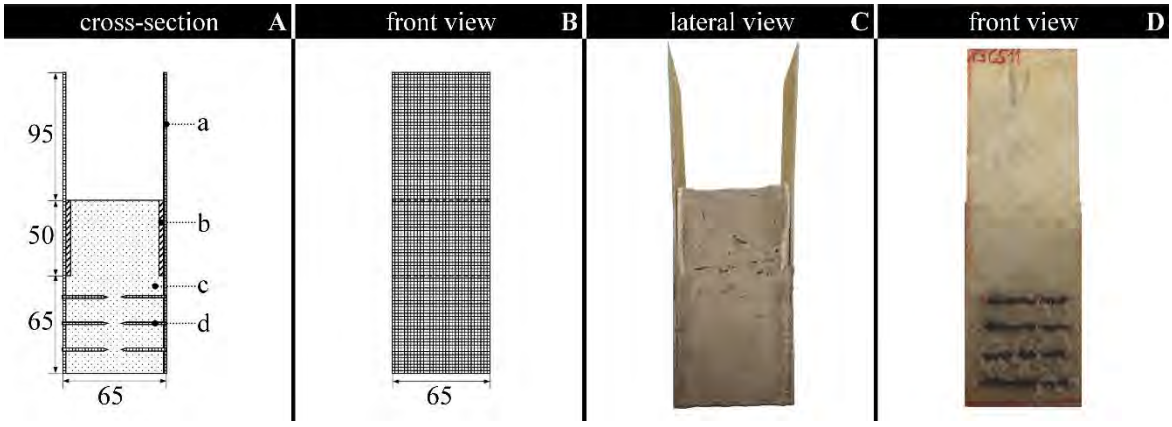


***Fig. 2*** *Test specimen for tensile/shear double strip test, lengths in mm*
*A: schematic cross-section of test specimen for tensile test with (a) tensile strip, (b) EPS foam (spacer, thickness 3 mm), (c) concrete and (d) tufting pins; B: schematic front view of test specimen for tensile test; C: lateral view of a test specimen for tensile/shear double strip test; D: front view of a test specimen for tensile/shear double strip test*

As test specimen, two-dimensional FRP plates (strips) with tufting pins were produced. The dimensions of one strip are 200×65 mm (Fig. 2B). In the lower part of the strip tufting pins were inserted through a surface area of 65×65 mm (Fig. 2A, B, D). Two opposing strips were connected with concrete (Fig. 2A, C), hence the square base area is 65×65 mm. The concrete core is fixed in the testing machine and a tensile force is applied to both strips. In order to prevent a falsification of the results by a failure of the concrete, the concrete is not connected to the strips in a force application length of 50 mm. For this purpose an EPS foam with a thickness of 3 mm is integrated between strips and concrete. To measure the maximum load of the tufting pin connection, only results of test specimens with a shear failure between strips and concrete were valid. Samples with broken strips or concrete are invalid since in this case only the strength of the strips or concrete is measured.
The test speed is 1 mm/min and the clamping length of the strips is 143 mm measured from the bottom side.

# 3 RESULTS AND DISCUSSION

## 3.1 VISUAL EXAMINATION OF THE TUFTING PIN

In preparation of the mechanical tensile/shear double strip tests manual preliminary tests of the tufting process were carried out. The aim was to define a tufting set-up i.e. penetration depth, insertion distance, which provide the best process stability: meaning a minimum of filament breaks and no pull out of the thread loops when the needle punctures the foam to generate the next tufting loop. Since tufting with carbon fibres is more challenging than with glass fibres due to the premature filament breaks, these tests were carried out with the carbon roving on three layers of non-crimp glass fibre fabric. It could be determined that the penetration depth of the needle for generating tufting loops depends on the dimensions of the tufting needle itself. The utilised one has a cross section of 4×1.7 mm at the needle eye and a length of the needle from the tip to the end of the eye of 10 mm. Thereby a manufacturing of tufting loops is only possible starting with a penetration depth of 20 mm.

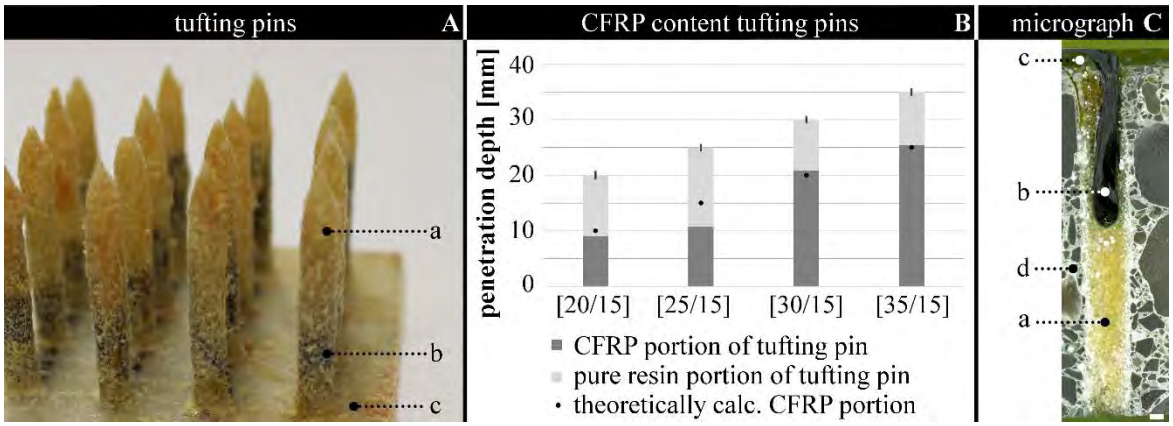


***Fig. 3*** *Visual examination of tufting pins*
*A: tufting pins with (a) pure resin portion of tufting pin, (b) carbon fibre-reinforced plastic (CFRP) portion of tufting pin and (c) glass fibre-reinforced plastic (GFRP) plate; B: diagram of length tufting pin dependant on needle penetration depth, number of measured pins: 6-30, specimen description: [penetration depth/penetration distance]; C: micrograph image of CFPR tufting pin fixed to GFRP plate and embedded in concrete with (a) pure resin portion of tufting pin, (b) CFRP portion of tufting pin, (c) GFRP plate and (d) concrete, scale bar: 1000 µm*

Tufting pins consist of a pure resin portion and a CFRP portion (Fig. 3A). In Fig. 3C a micrograph image of a tufting pin specimen from the double strip test is presented. As described in section 2.2 the pins are positively embedded within the concrete (Fig. 3C). Based on the needle dimensions, a theoretical distribution of resin and CFRP content could be determined by subtracting 10 mm, respectively to the length of the needle tip to the end of needle eye and of the penetration depth of the needle. A comparison of the theoretically calculated fractions of pure resin and CFRP with the real measured values can be seen in Fig. 3B. The results shown allow to conclude that a theoretical calculation of the pin length or pure resin and CFRP fractions in the pin is permitted.

## 3.2 MECHANICAL TEST OF SHEAR STRENGTH OF TUFTING CONNECTION

Based on the preliminary tests, a penetration depth of 40 mm and a puncture distance of 15 mm were set as parameters for tufting the mechanical double strip test specimen. The tufting pins were made of glass fibres and carbon fibres comparatively with four layers of non-crimp carbon fibre fabric for the strips.
The results of the mechanical examination in the tensile/shear double strip test with GFRP pins and CFRP pins can be seen in Fig. 4A. Despite the lateral load of the tufting pins, the carbon fibre pins show in comparison to glass fibre pins a significantly higher resistance to shear failure. Exemplarily values displayed in Fig. 4A for 8 or 12 pins on a surface of 65×65 mm of each strip attached to the concrete core of the test specimen indicate that a connection with CFRP tufting pins can bear up to 17 % (12 pins) respectively 29 % (8 pins) higher tensile loads than GFRP pins.
In addition, the proportion of load bearing capacity to number of pins was mechanically examined. The diagram in Fig. 4B presents a linear dependence between measured tensile force and number of carbon fibre tufting pins. Accordingly, it is possible to accurately predict the strength of a connection of tufting pins for the design of mechanical components.

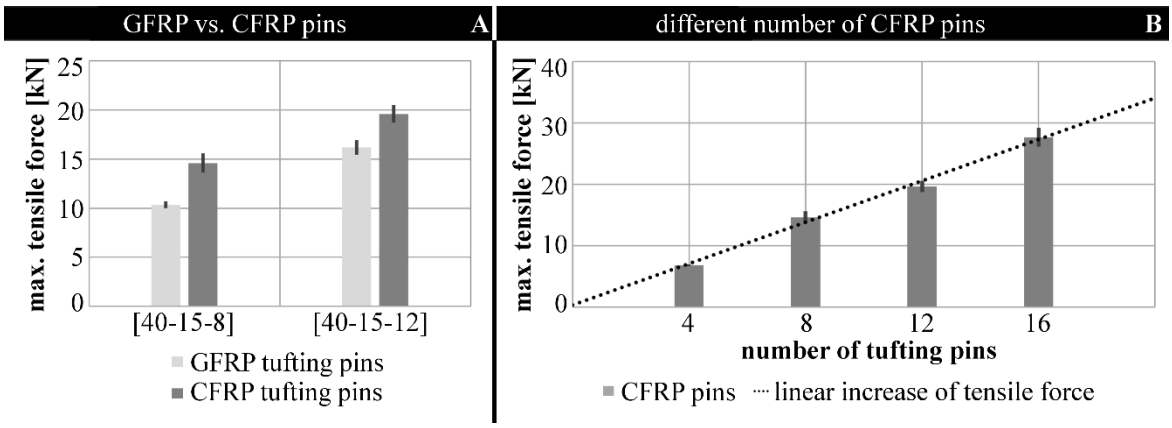


***Fig. 4*** *Results of tensile/shear double strip test*
*A: comparison of maximum tensile force depending on the reinforcing fibre material, specimen number n=10, specimen description: [penetration depth-penetration distance-number of tufting pins];*
*B: increase of max. tensile force depending on number of CFRP tufting pins, specimen number n=10, penetration depth 40 mm and penetration distance 15 mm*

## 4 CONCLUSIONS

The described investigations reveal the potentials of the tufting process to generate interface connection elements for fibre-reinforced plastics. The connection element "tufting pin" has comparable functions and properties, known in literature from z-pins. In contrast to z-pins, tufting pins can be produced in one process step with the FRP component – principally during the pre-forming process. Within optical examinations, the tufting pins were characterised and the reproducibility of their dimensions was ensured. In addition, mechanical tests were performed in an adapted tensile/shear double strip test. The mechanical investigations show a comparison of the load capacity of a GFRP and a CFRP tufting pin connection. An interface connection with CFRP pins can resist higher loads before shear failure. Finally, a linear dependence of load bearing capacity of a tufting connection depending on the applied number of tufting pins was confirmed.

## 5 ACKNOWLEDGEMENT

The authors would like to thank the German Research Foundation (DFG) for funding this work as part of the Transregional Collaborative Research Centre (SFB/Transregio) 141 'Biological Design and Integrative Structures' (project A06). Furthermore we would like to thank all collaborating partners from the University of Freiburg (PBG) and DITF Denkendorf as well as University of Stuttgart (ITFT and ITKE), especially Florian A. Jonas (ITKE) who was particularly involved in the development of the adapted test stand.

## REFERENCES

[1] Cherif C.: *Textile Werkstoffe für den Leichtbau*. Berlin, Heidelberg: Springer Berlin Heidelberg, 2011.
[2] Dell'Anno G., Treiber J. W. G. and Partridge I. K.: *Manufacturing of composite parts reinforced through-thickness by tufting*. In: Robotics and Computer-Integrated Manufacturing 37: 262–272, 2016.
[3] Liu L., Zhang T., Wang P., Legrand X. and Soulat D.: *Influence of the tufting yarns on formability of tufted 3-Dimensional composite reinforcement*. In: Composites Part A: Applied Science and Manufacturing 78: 403–411, 2015.
[4] Liu L., Wang P., Legrand X. and Soulat D.: *Investigation of mechanical properties of tufted composites: Influence of tuft length through the thickness reinforcement*. In: Composite Structures 172: 221–228, 2017.
[5] Cartié D. D. R., Dell'Anno G., Poulin E. and Partridge I. K.: *3D reinforcement of stiffener-to-skin T-joints by Z-pinning and tufting*. In: Engineering Fracture Mechanics 73(16): 2532–2540, 2006.
[6] Henao A., Carrera M., Miravete A. and Castejón L.: *Mechanical performance of through-thickness tufted sandwich structures*. In: Composite Structures 92(9): 2052–2059, 2010.
[7] Mouritz A. P.: *Review of z-pinned composite laminates*. In: Composites Part A: Applied Science and Manufacturing 38(12): 2383–2397, 2007.
[8] Chang P., Mouritz A. P. and Cox B. N.: *Properties and failure mechanisms of z-pinned laminates in monotonic and cyclic tension*. In: Composites Part A: Applied Science and Manufacturing 37(10): 1501–1513, 2006.

[9] Pingkarawat K. and Mouritz A. P.: *Improving the mode I delamination fatigue resistance of composites using z-pins*. In: Composites Science and Technology 92: 70–76, 2014.
[10] Pegorin F., Pingkarawat K., Daynes S. and Mouritz A. P.: *Mode II interlaminar fatigue properties of z-pinned carbon fibre reinforced epoxy composites*. In: Composites Part A: Applied Science and Manufacturing 67: 8–15, 2014.
[11] Pegorin F., Pingkarawat K. and Mouritz A. P.: *Comparative study of the mode I and mode II delamination fatigue properties of z-pinned aircraft composites*. In: Materials & Design (1980-2015) 65: 139–146, 2015.
[12] Henning F. and Moeller E.: *Handbuch Leichtbau: Methoden, Werkstoffe, Fertigung*. München: Hanser, 2011.
[13] Wittel H., Muhs D., Jannasch D. and Voßiek J.: *Roloff/Matek Maschinenelemente*. Wiesbaden: Vieweg+Teubner Verlag, 2011.

# CHARACTERIZATION OF RESIDUAL STRESSES IN FIBER-METAL-LAMINATES BY X-RAY DIFFRACTION

**Arne Busch[1]*, Patrick Brix[1], Robert Brandt[1]**

[1] University of Siegen, Am Eichenhang 50, 57076 Siegen, GERMANY

**ABSTRACT:** The components of a hybrid laminate, for example glass fiber-reinforced plastic and high strength steel, may exhibit different magnitudes of their thermal expansion coefficients and thermally induced residual stresses occur at room temperature. These residual stresses might have a negative effect on the durability of the hybrid laminate so that an analysis of the residual stresses is reasonable. For the residual stress analysis, a $sin^2\psi$-method by means of X-ray diffraction is applied. A hybrid laminate made up by fiber-reinforced plastics and steel has been investigated in order to describe the impact of temperature, fibre material, and volume fraction on the magnitude of the residual stress. Since glass fibers are massively absorbing X-rays, here carbon and aramid fibres are utilized as well. Specimens with the above mentioned material combinations and different laminate designs have been analyzed. The results are compared to an analytical model, which predicts the magnitude of the thermally induced residual stress of a hybrid laminate at room temperature.

**KEYWORDS:** residual stresses, x-ray diffraction, fiber-metal-laminates

## 1 INTRODUCTION

A hybrid laminate made up by fibre-reinforced plastics (FRP) and a metallic component is processed under elevated temperature and pressure in order to properly cure the matrix system. However, the material is generally utilized at significantly lower temperatures, e.g. at room temperature, leading to thermally induced residual stresses by the temperature difference $\Delta T$ due to the individual thermal expansion coefficients $\alpha_i$ of the components of the hybrid laminate denoted by an index $i$. The magnitude of the residual stresses is determined by the temperature difference $\Delta T$, the kind of fibre material, and the volume fractions $\varphi_i$ of the components.

Residual stresses are defined as non-vanishing internal stresses within an enclosed system without any outside loads. The inner loads generated by the residual stresses are in a mechanical equilibrium, i.e. the sum of all inner loads and torques are equal to zero [1]. These residual stresses might have a negative effect on the durability of the hybrid material so that an analysis of the residual stresses is reasonable. There are different approaches to determine residual stresses of the first type I [2] within hybrid laminates:

i. The drill hole method [3].
ii. The $sin^2\psi$-method by means of X-ray diffraction for crystalline materials. This method is state of the art for crystalline metallic materials and can be utilized for partially crystalline polymers or amorphous polymers added with traces of crystalline metallic particles [4, 5].
iii. Specific methods designed for thin, unsymmetrical hybrid laminates utilize the measurement of the temperature dependent curvature of a specimen and the knowledge of the mechanical properties to calculate the average residual stress [6].

In this work the second method serves to measure the residual stress in the metallic part of the hybrid laminates.

# 2 EXPERIMENTAL SETUP

## 2.1 SPECIMEN DESIGN AND PREPARATION

Two different types of specimen designs are considered, namely a) a steel-FRP multi-layer laminate (ML) made up by five layers of steel and six layers of unidirectional FRP and b) a Steel-FRP sandwich specimen (SW) made up by a core of unidirectional FRP with two outer layers of steel (s. Fig. 1). The type ML specimens comprise solely unidirectional carbon-fibre-reinforced plastics (CFRP) as FRP component, whereas two types of SW specimens exit which contains either CFRP or glass-fibre-reinforced plastics (GFRP) as FRP component.

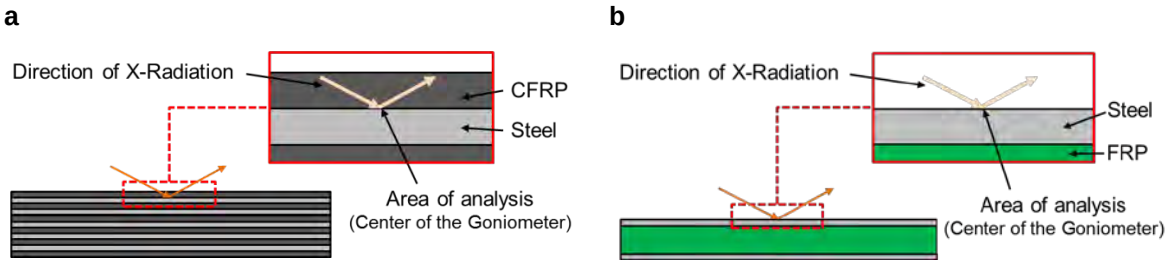


***Fig. 1*** *a) Steel-FRP multi-layer laminate (ML) b) Steel-FRP Sandwich specimen (SW)*

A bainitic steel 51CrV4 represents the metallic component, which is first annealed for 10 $min$ at an elevated temperature $T = 890°C$, then cooled down to $T = 190°C$ in a salt bath, and secondly for 60 $min$ at a temperature $T = 400°C$ in an oven. The setup of all specimens happen by means of a prepreg process. The adhesion between the steel and the FRP layers occurs under elevated temperature and pressure [7]. The specimens dimensions are given by their thickness $t = 5\,mm$ up to $t = 8\,mm$, length $l = 60\,mm$, and width $w = 25\,mm$.

## 2.2 RESIDUAL STRESS MEASUREMENTS

For all measurements a Panalytical Empyrian X-Ray diffractometer with a solid-state hybrid pixel detector has been used. In order to separate the thermally induced residual stresses from the initial residual stresses of the quenched and tempered steel components, a $\omega$-stress measurement geometry has been done upfront. Fig. 2 shows the setup and the parameters used, respectively.

| | |
|---|---|
| X-Radiation: | Cr-Kα |
| Lattice Plane | {211} |
| Omega $\omega$ | -45° to +45° |
| Range $2\theta$ | 149.75° to 162.25° |
| Step Size $\theta$ | 0.05° |
| Cumulative Counts | 10,000 |
| Aperture | 7 mm x 7 mm |

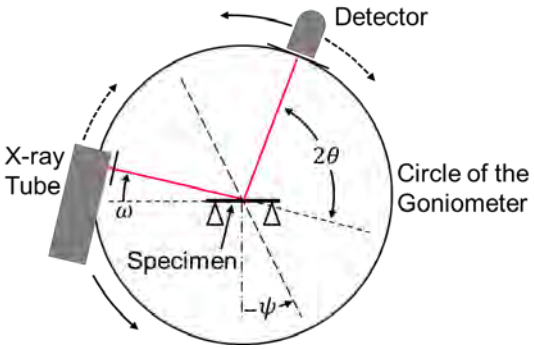


***Fig. 2*** *a) Measurement parameters steel layers b) Setup for the Measurement with $\omega$-stress [8]*

The residual stress measurement of the hybrid specimens happens by means of the $\psi$-stress measurement geometry. Fig. 3 shows the specific parameters and the setup used, respectively.

| | Multi-Layer Laminate (ML) | Sandwich (SW) |
|---|---|---|
| X-Radiation: | Cr-Kα | Cr-Kα |
| Lattice Plane | {211} | {211} |
| $sin^2\psi$ | 0.0 to 0.6 | 0.0 to 0.8 |
| Range $2\theta$ | 151° to 161° | 151° to 161° |
| Step Size $\theta$ | 0.013° | 0.026° |
| Cumulative Counts | min. 1,000 | min. 8,000 |
| Aperture | 10 mm x 10 mm | 7 mm x 7 mm |

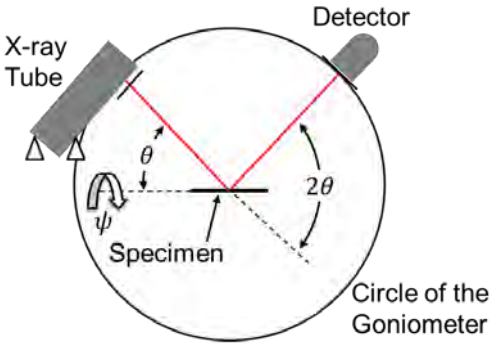


***Fig. 3*** *a) Measurement parameters and b) setup for the Measurement with ψ-stress [8]*

## 3 RESULTS

The surface of the bainitic steel layers are almost free from residual stresses before the assembly of the hybrid specimens since the preliminary measurements comprises a residual stress of only $\sigma_{steel} = 2.9 \pm 11.1\ MPa$. Therefore, the residual stresses which are measured in the steel component of the hybrid laminates represent the thermally induced residual stresses at room temperature after the curing process. Tab. 1 shows the results of the residual stress measurements for the different kinds of materials and specimen designs. The measurement error is small when the residual stress measurement happens at the surface of the SW specimens. However, the measurement error in the ML specimens is significantly higher.

| CFRP - Steel | | | GFRP - Steel | | |
|---|---|---|---|---|---|
| Specimen | Steel Content $\varphi_{Steel}$ [%] | Residual Stress $\sigma_{RS,Steel}$ [MPa] | Specimen | Steel Content $\varphi_{Steel}$ [%] | Residual Stress $\sigma_{RS,Steel}$ [MPa] |
| SW1 | 12.7 | 152.1 ± 3.2 | SW4 | 12.7 | 44.9 ± 3.3 |
| SW2 | 12.7 | 161.9 ± 3.3 | SW5 | 12.7 | 43.4 ± 3.0 |
| SW3 | 8.0 | 189.3 ± 3.2 | | | |
| ML1 | 34.7 | 117.2 ± 28.6 | | | |
| ML2 | 34.7 | 125.2 ± 6.1 | | | |
| ML3 | 34.7 | 121.8 ± 21.1 | | | |
| ML4 | 34.7 | 123.3 ± 17.9 | | | |

***Tab. 1*** *Residual stresses of the hybrid specimens*

## 4 ANALYTICAL MODEL

A quantitative assessment of the magnitude of residual stresses happens at the example of the sandwich specimen type. Fig. 4 shows a half of the symmetrical specimen built up by CFRP and steel.

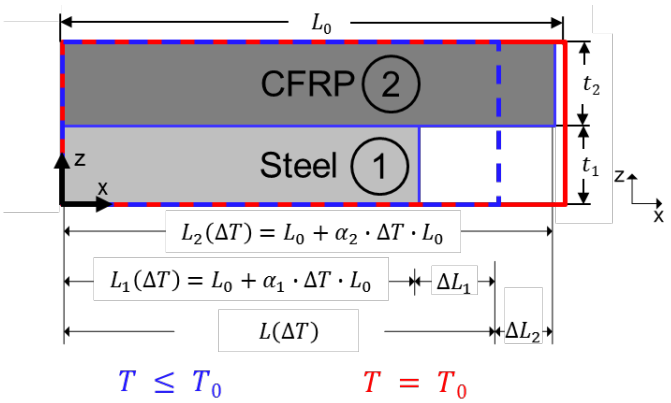


***Fig. 4*** *Symmetrical hybrid specimen at different temperatures*

According to Schürmann [9] the stress free temperature $T_0$ is set to be $T_0 = T_g - 20\ °C$ where $T_g$ denotes the glass transition temperature of the matrix polymer of the FRP. The length $L_0$ of the specimen at the stress free temperature $T_0$ (red boundary) becomes the length $L(\Delta T)$ at a temperature $T < T_0$ (blue boundary) where $\Delta T = T - T_0$ denotes the temperature drop. The residual stresses $\sigma_i$ of the components $i$ are calculated in a two-step procedure. To start with, it is assumed that the layers are not bonded to each other. Then they contract or expand individually to the lengths $L_i(\Delta T)$. With the thermal expansion coefficient $\alpha_i$ of the component $i$ they read

$$L_i(\Delta T) = L_0(1 + \alpha_i \cdot \Delta T). \tag{1}$$

However, the layers are adhesively bonded to each other so that the thermal expansion of the components is matched by this constraint. Hence, the internal strain $\varepsilon_i$ of the component $i$ is to be calculated which is defined by

$$\varepsilon_i(\Delta T) = \frac{L(\Delta T) - L_i(\Delta T)}{L_0}. \tag{2}$$

The value $L(\Delta T)$ is to be determined by the requirement of a mechanical equilibrium. The thickness $t_i$ of the component $i$ provides with the specimen thickness $t$ the volume fraction $\varphi_i$. Together with Young's modulus $E_i$ and the specimens width $w$ the mechanical equilibrium of thermally induced forces $F_i$ leads to

$$\sum_i F_i = \sum_i \varepsilon_i(\Delta T) \cdot E_i \cdot t_i \cdot w = \sum_i \varepsilon_i(\Delta T) \cdot E_i \cdot \varphi_i = 0. \tag{3}$$

Finally, the residual stress $\sigma_i$ then becomes

$$\sigma_i = E_i \cdot \varepsilon_i. \tag{4}$$

This analytical model can be applied to a multi-layer laminate as well. By use of the material specific values of $E_i$ and $\alpha_i$ (s. Tab. 2) the temperature dependent residual stresses $\sigma_i(\Delta T)$ can be estimated (s. Tab. 3). The glass transition temperature $T_g$ of the matrix polymer of the FRP has been measured by means of a dynamic mechanic analysis (DMA) and is set to $T_g = 120°C$.

| Material | Steel | GFRP | CFRP |
|---|---|---|---|
| E-Modulus $E_i$ $[GPa]$ | 206 | 42 | 140 |
| Thermal Expansion Coefficient $\alpha_i$ $[10^{-6}\ 1/K]$ | 12.0 | 7.0 | 0.2 |

***Tab. 2*** *Specific values of the different materials*

| Material Combination | Volume Fraction $\varphi_{steel}$ [%] | Residual Stress in the Steel Layer $\sigma_{steel}$ [MPa] | Residual Stress in the FRP Layer $\sigma_{FRP}$ [MPa] | Residual Stress in the Steel Layer $\sigma_{steel}$ [MPa] |
|---|---|---|---|---|
| | | calculated values | | measured values |
| GFRP - Steel | 12.7 | 48.09 | -7.00 | 44.15 ± 3.3 |
| CFRP - Steel | 8.0 | 172.40 | -14.99 | 189.30 ± 3.2 |
| CFRP - Steel | 12.7 | 160.18 | -23.30 | 157.00 ± 3.3 |
| CFRP - Steel | 34.7 | 109.13 | -57.99 | 121.88 ± 28.6 |

***Tab. 3*** *Mean values of the calculated residual stresses of the steel layers and of the FRP layers*

## 5 CONCLUSION

The residual stress values $\sigma_{steel}$ of the steel component calculated by means of the analytical model and the corresponding average values measured by means of X-Ray diffraction are compared in Fig. 5. The vertical error bars consider the errors of the measurement and the horizontal bars the errors of the calculated values due to errors of input quantities, respectively. The diagram shows up that the correlation between the calculated and the measured values is quite good. Therefore, the analytical model is appropriate for a rough estimate of the residual stresses within the hybrid laminate. However, the specimen SW3 shows a certain deviation, which is not covered by the error of the measurement which is given in Tab. 1 and which is indicated by the vertical error bar in the diagram.

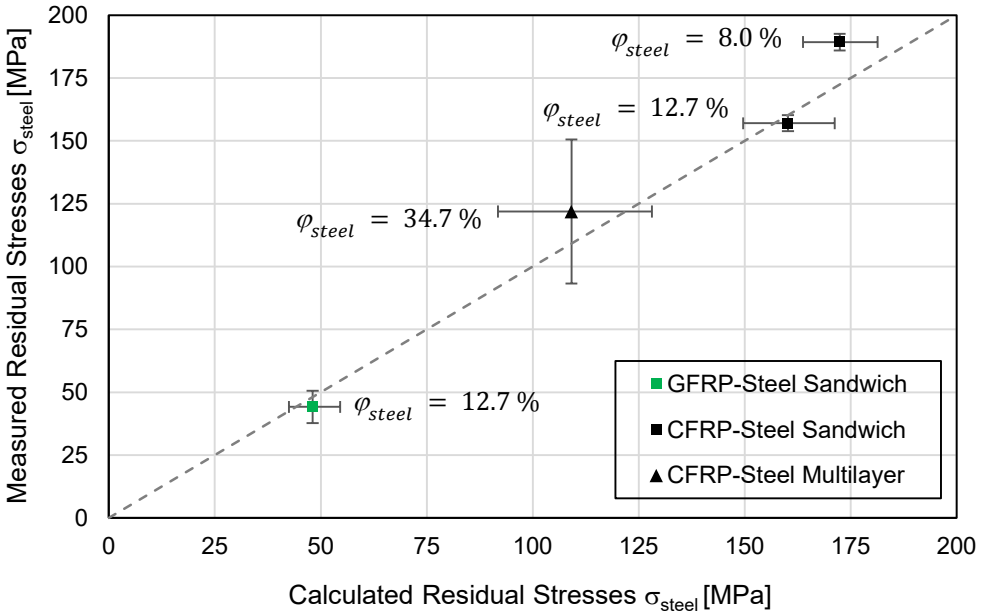


***Fig. 5*** *Comparison of the calculated and measured residual stress values $\sigma_{steel}$ of the steel component at $\Delta T = 80°C$*

The above-mentioned correlation is valid for the multi-layer laminate, too, even though for the measurement by means of the $sin^2\psi$-Method the normal component of the stress tensor is neglected. However, the effect of the normal component to the stress measurement has still to be analysed. Nevertheless, the residual stresses in the inner of the hybrid laminates can be estimated by this analytical approach as well. The validity of this result has to be verified, e.g. by means of a synchrotron experiment.

The analysis of the residual stress shows that the CFRP-steel hybrid laminates with a small volume fraction $\varphi_{steel}$ of steel comprises the highest tensional stresses up to 190 $MPa$ in the steel component. Those values are severe and may harm the strength of the steel component under cyclical loading. In contrast to that, the residual stresses of the steel components in the GFRP-steel hybrid laminates are significantly lower and it is easier to handle these.

## 6 ACKNOWLEDGEMENT

This work is funded by the European Union as a part of the competition “Neue Werkstoffe” EFRE.NRW. Further, the authors gratefully acknowledge the co-operation partner Mubea Fahrwerksfedern GmbH.

## REFERENCES

[1] E. Macherauch, H. Wohlfahrt, U. Wolfstieg: Zur zweckmäßigen Definition von Eigenspannungen, Härterei Technische Mitteilung, 1973.

[2] B. Eigenmann, E. Macherauch: Röntgenographische Untersuchung von Spannungszuständen in Werkstoffen. Teil I, Materialwissenschaft und Werkstofftechnik 26, 1995, pp. 148–160.

[3] A. R. Ghasemi, M. M. Mohammadi: Residual stress measurement of fiber metal laminates using incremental hole-drilling technique in consideration of the integral method, International Journal of Mechanical Sciences 114, 2016, pp. 246–256.

[4] C. S. Barrett, P. Predecki: Stress Measurement in Graphite/Epoxy Uniaxial Composites by X-Rays, Polymer Composites 1, 1980, pp. 2–6.

[5] P. Predecki, C. S. Barrett: Stress measurement in graphite/epoxy composites by X-ray diffraction from fillers, Journal of Composite Materials 13, 1979, pp. 61–71.

[6] R. Prussak, D. Stefaniak, C. Hühne, M. Sinapius: Residual Stresses in Intrinsic UD-CFRP-Steel-Laminates - Experimental Determination, Identification of Sources, Effects and Modification Approaches, MSF 825-826, 2015, pp. 369–376.

[7] A. Busch, R. Brandt: Characterization of the Bonded Connection in Hybrid-Steel-GFRP-Laminates, KEM 742, 2017, pp. 408–415.

[8] DIN EN 15305: Zerstörungsfreie Prüfung - Röntgendiffraktometrisches Prüfverfahren zur Ermittlung der Eigenspannungen. DIN Deutsches Institut für Normung e.V., 2008.

[9] H. Schürmann: Konstruieren mit Faser-Kunststoff-Verbunden, 2nd Ed., Springer, Berlin, Heidelberg, New York, NY, 2007.

# THE CORROSION BEHAVIOR OF MULTICOMPONENT MATERIALS IN DIFFERENT SODIUM CHLORIDE SOLUTIONS

**K. Lange[1*], M. Mandel[1], L. Krüger[1], M. Ullmann[2], K. Neh[2], R. Kawalla[2], D. Weck[3], M. Gude[3], S. Bräunling[4]**

[1]Institute of Materials Engineering, TU Bergakademie Freiberg
[2]Institute of Metal Forming, TU Bergakademie Freiberg
[3]Institute of Lightweight Engineering and Polymer Technology, TU Dresden
[4]Institute of Manufacturing Science and Engineering, TU Dresden

**ABSTRACT:** The electrochemical corrosion behavior of a multicomponent material based on a twin-roll cast (TRC) and hot rolled (HR) AZ31 magnesium alloy sheet and a CFRP (carbon fiber reinforced plastic) was investigated by potentiodynamic polarization in different sodium chloride solutions and by an outdoor exposure test. Due to the variation of the sodium chloride content in the polarization test, the critical concentration for pitting corrosion initiation on the Mg alloy was determined.
For the magnesium alloy sheets in the outdoor exposure test the initiation of pitting corrosion was observed after three months. In consideration of the polarization tests, it is assumed that during the outdoor exposure and caused by wetting and salification, the critical NaCl concentration was reached. This was the concentration where the pitting corrosion was initiated. For the description of the process the Evans droplet model was applied. Moreover, in comparison to the initial magnesium alloy the CFRP-Mg-multicomponent shows no significant corrosive attack after three months outdoor exposure. Based on this results it is concluded, that pit initiation on the unprotected Mg alloy occurs very fast and seems to be unavoidable during outdoor exposure. In the multicomponent the CFRP protects the Mg alloy because of safety shield to an aggressive environment.

**KEYWORDS:** magnesium alloy, polarization, outdoor exposure test, pitting corrosion, CFRP

## 1 INTRODUCTION

Magnesium as the lightest technical used construction metal is in focus of research and technical advancements for several years. There are many positive reasons for the use of magnesium, for example the low density (1.73 g/cm³), which results in a weight saving potential, combined with a high strength and good castability [1,2]. However, magnesium exhibits low formability at room temperature due to its hexagonal (hcp elementary cell) crystal structure. There are less than five slip systems and so the von Mises criterion is unsatisfied [3-5]. Furthermore, the high corrosive susceptibility is undesirable for a commercial application. On the one hand, a possibility is the variation of the alloying components or the change of the ratio of the alloying components. On the other hand, the application of a multicomponent systems consisting of metallic and polymeric materials [6] or magnesium with ceramic layers is possible [7]. The most commonly used magnesium alloy is AZ31 due to its good combination of strength, ductility and weldability as well as its great suitability for rolling and extrusion [8,9].
The plastic component consists of polymeric fibers and a matrix material, which separates and protects the fibers. As reinforcement in polymeric materials a number of additives are used. Glass or carbon fiber reinforced polymers are characterized by an improvement of the strength and stiffness. As a matrix material, duo- or thermoplastics are commonly used in engineering applications. Hence, an opportunity to combine good corrosion resistance and light weight potential with a good strength and ductility represents a CFRP layer (carbon fiber reinforced plastic) with a polyamide matrix (thermoplastic) bonding on a Mg alloy sheet [10-12].
Nevertheless, because of its high electrochemical reactivity the corrosion behavior of magnesium and its alloys is of high interest. In this study, the electrochemical corrosion behavior of the magnesium alloy AZ31 was investigated in sodium chloride solutions of different concentrations to evaluate the critical NaCl con-

centration for a pit initiation. Additionally, the initial magnesium alloy and the alloy laminated with a CFRP were analyzed by an outdoor exposure test under urban climatic conditions. The results of the polarization and outdoor exposure test were correlated to evaluate the corrosion susceptibility of the magnesium alloy and the composite material.

# 2 EXPERIMENTAL

## 2.1 MATERIALS

In this study the twin-roll cast (TRC) and hot rolled (HR) magnesium alloy AZ31 with the chemical composition given in Table 1, and a multicomponent material consisting of an AZ31 sheet and a carbon fiber reinforced plastic (CFRP) layer were used. The TRC technology is developed at the Institute of Metal Forming of the TU Bergakademie Freiberg to produce magnesium strips to standard industrial levels. In this process melt is cast using a casting nozzle in between cooled rolls. By contact with the rolls, the melt rapidly solidifies and a first deformation subsequently occurs. The AZ31 sheet was rolled to 1 mm thickness on a quarto reversing mill [13-15]. Finally, the sheet was heat treated (HT) at 330 °C for 45 min. For the determination of the precipitations X-ray diffraction with grazing incidence angle (GAXRD) was used.
The multicomponent material consisting of AZ31 and CFRP was manufactured in collaboration with the Institute of Lightweight Engineering and Polymer Technology and the Institute of Manufacturing Science and Engineering at the TU Dresden. The CRFP layer is based on organic sheet Tepex® dynalite with PA6-Matrix and reinforcing carbon fibers (fiber volume ratio 50 %). Prior to joining, the mating surface of the AZ31 sheet was ground with corundum particles, cleaned with acetone and coated with silane primer. As well the CFRP sheet was cleaned with acetone. The joining of the thermoplastic CFRP sheet and the AZ31 sheet was done by a hot pressing process under vacuum. The AZ31 sheet was placed on the CFRP sheet, afterwards pressure and temperature were increased up to 8 bar and 250 °C, respectively, and held for 30 minutes. After cooling the multicomponent was cut into samples size of 12.5x12.5 cm.

***Table 1:*** *Chemical composition of the AZ31 TRC+HR+HT sheet in wt.%.*

| Mg | Al | Zn | Mn | Fe | Si |
|---|---|---|---|---|---|
| 95.2 | 3.3 | 0.8 | 0.3 | 0.2 | 0.2 |

## 2.2 ELECTROCHEMICAL MEASUREMENTS AND OUTDOOR EXPOSURE TEST

The AZ31 sheet samples were potentiodynamically polarized in the as-received state in sodium chloride solution with $c_1 = 10^{-4}$ mol/l, $c_2 = 10^{-3}$ mol/l, $c_3 = 10^{-2}$ mol/l, $c_4 = 10^{-1}$ mol/l and $c_5 = 0.885$ mol/l. The polarization was carried out at room temperature with a potentiostat (VSP, BioLogic Science Instruments) using a conventional three-electrode-arrangement with the Mg alloy as the working electrode, a saturated Ag/AgCl-electrode as the reference and a platinum mesh as the counter electrode. The scan rate was 6 mV/min and the polarized area was 1 cm². Before and after the polarization tests the samples were analyzed by electron microscope (MIRA3 TESCAN, SE contrast, 15 kV). In the sodium chloride solutions magnesium forms a crystalline film of MgOH and hydrogen (H) gas [8]. Therefore it was necessary to remove the formed corrosion products before the electron microscopic investigations. The corrosion product removal was carried out by slewing the samples in a cooled 20 %-CrVI-solution for few minutes [16-18]. Afterwards the samples were cleaned with distilled water, ethanol and finally dried.

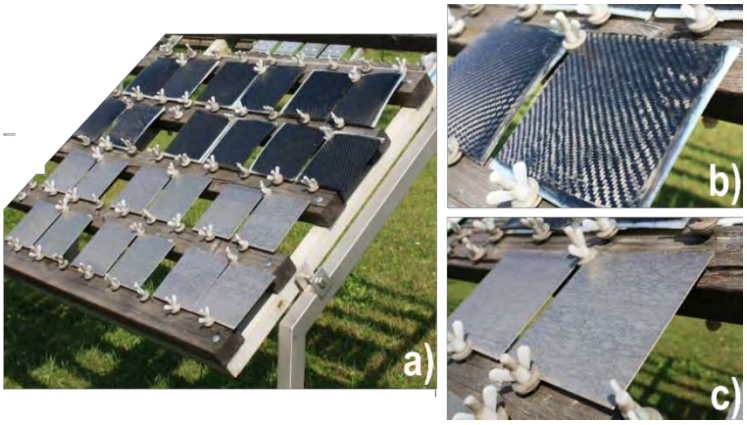


***Fig. 1*** *a) Test-setup for the outdoor exposure test, b) composite material, c) initial AZ31 sheets.*

The outdoor exposure test was carried out on a test station (see Fig. 1**)** in Dresden in collaboration with the Institute for corrosion protection Dresden Ltd (IKS Dresden GmbH). The composite was exposed with the CFRP in front to the weathering side (Fig. 1b). The test started in August 2017.

# 3 RESULTS AND DISCUSSION

## 3.1 POTENTIODYNAMIC POLARIZATION

Potentiodynamic tests carried out in NaCl solutions with various concentrations enable the determination of the corrosion properties of the magnesium alloy AZ31. The polarization curves (Fig. 2) clearly indicate the expected decrease of the corrosion potential $E_{corr}$ and exchange current density $j_{corr}$ with decreasing sodium chloride concentration. The extracted corrosion parameters $E_{corr}$ and $j_{corr}$ are summarized in Table 2. This behavior is in full agreement with the observations by Walke, et al. [9].

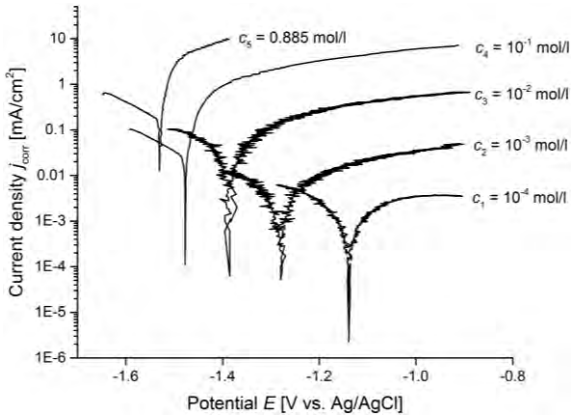


***Fig. 2*** *Potentiodynamic polarization curves of AZ31 in different concentration of sodium chloride solutions.*

***Table 2:*** *Extracted corrosion parameters $E_{corr}$ and $j_{corr}$ for AZ31 for different concentrations of NaCl solutions.*

| *c [mol/l]* | $10^{-4}$ | $10^{-3}$ | $10^{-2}$ | $10^{-1}$ | 0.885 |
|---|---|---|---|---|---|
| $E_{corr}$ *[V vs. Ag/AgCl]* | -1.14 | -1.28 | -1.38 | -1.43 | -1.53 |
| $j_{corr}$ *[µA/cm²]* | 0.79 | 3.35 | 35.26 | 124.18 | 154.03 |

Fig. 3 presents the optical microscopy image (Fig. 3a) of the initial state (before the corrosion) and scanning electron micrographs after the polarization in $c_1 = 10^{-4}$ mol/l (Fig. 3b), $c_2 = 10^{-3}$ mol/l (Fig. 3c), $c_3 = 10^{-2}$ mol/l (Fig. 3d), $c_4 = 10^{-1}$ mol/l (Fig. 3e) and $c_5 = 0.885$ mol/l (Fig. 3f) of the magnesium alloy.

The TRC+HR AZ31 sheets exhibit $Mg_{17}Al_{12}$ and $Al_8Mn_5$ segregations. After the heat treatment (HT) of the AZ31 sheet only the precipitations of the high-temperature phase $Al_8Mn_5$ (Fig. 4) could be detected in the AZ31 sheet [14,19] by GAXRD. For the corrosion behavior, there is no ascertainable effect due to the precipitations. The corrosion attack starts at the grain boundaries with intergranular corrosion (Fig. 4) and a kind of filiform corrosion attack, which is visible in Fig. 3c. Samaniego et al. [20] reported three forms of corrosion: uniform corrosion over the whole area, filiform corrosion and localized corrosion, which depends on surface conditions. The filiform corrosion is a thread-like expression, which depends on the alloying components and the metallic surface. Often, there is an overlapping of filiform corrosion and uniform corrosion, usually in case of non-polished sample surfaces [20]. Filiform corrosion is assumed to proceed on magnesium alloys under relatively resistant oxide film from points where this film is not consistent [21-23]. With an increased NaCl concentration ($c \geq 10^{-3}$ mol/l) a high distribution of pits and filament grooves was observed (Fig. 3c-3f). Pitting corrosion is more predominant with increasing anodic polarization [21]. The grain boundaries are attacked more due to the enhanced activation of the grain bulk. This behavior is similar to studies found elsewhere [17,24,25]. In addition, the presence of impurities, like Fe-particles acting as local cathodes, causes an acceleration of the localized corrosion attack [26]. When the sodium chloride concentration of the solution increases the pitting corrosion attack is strongly increased, which is expressed by larger pit sizes and deepness (Fig. 3f and Fig. 5).

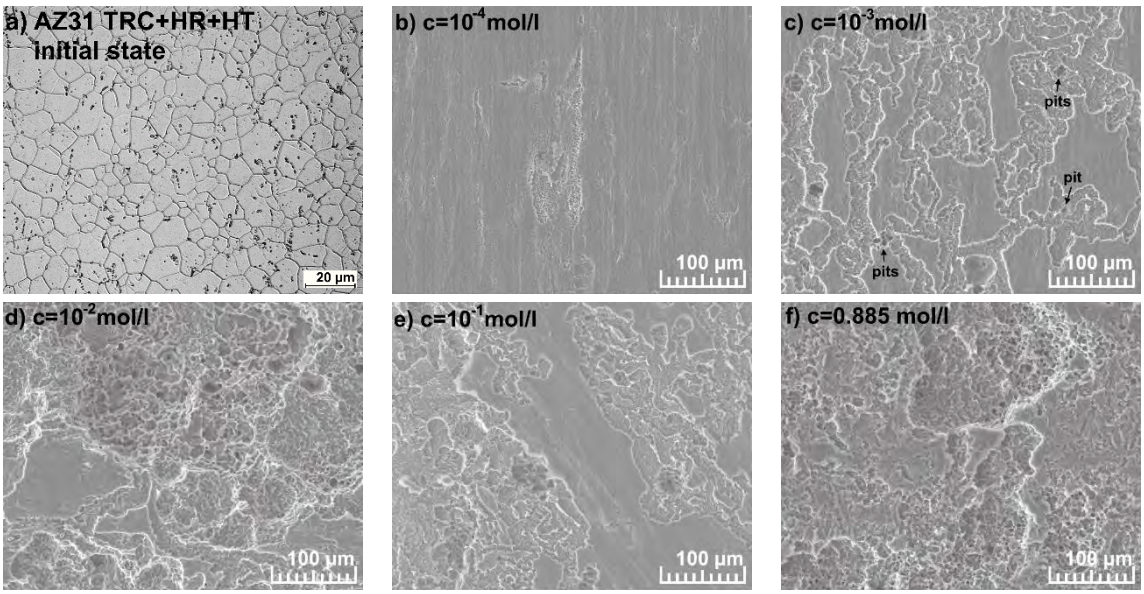


***Fig. 3*** *a) Optical microscopy image of the AZ31 sheet in the initial state; b)-f) scanning electron micrographs of AZ31 (secondary electron (SE) contrast) after electrochemical polarization in different sodium chloride solutions.*

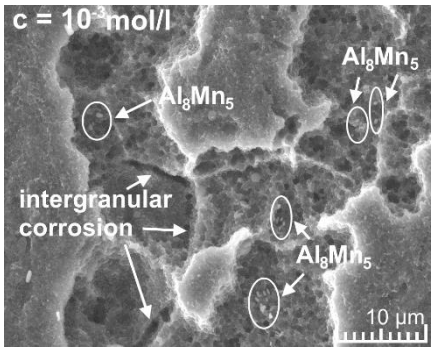


***Fig. 4*** *Scanning electron micrograph (SE contrast) showing intergranular corrosion (IC) after electrochemical polarization of AZ31 in sodium chloride solution c = $10^{-3}$ mol/l.*

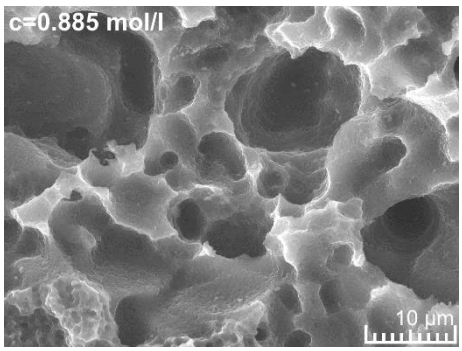


***Fig. 5*** *Scanning electron micrograph (SE contrast) showing pitting corrosion on AZ31 after polarization in 0.885 M NaCl-solution.*

As a main result from the polarization tests it was found that a sodium chloride induced pitting corrosion attack occurs at concentrations with $c > 10^{-3}$ mol/l. For $c = 10^{-4}$ mol/l an initiating attack by intergranular corrosion was identified. Consequently, the critical sodium chloride concentration for pit initiation on the AZ31 magnesium alloy in TRC,HR and HT condition is in the range of $10^{-4}$ mol/l < $c_{crit}$ < $10^{-3}$ mol/l.

### 3.2 OUTDOOR EXPOSURE TESTS

Figure 6 shows the initial AZ31 sheet and the multicomponent material after three months of outdoor exposure. The multicomponent material reveals a partial delamination of the CFRP from the AZ31 sheet, but a significant corrosion attack on both components was not observed. In comparison to the composite, the surface of the initial AZ31 sheet exhibits an intensified oxide film formation. This film formation depends on the interaction with the humidity [27], which is characteristic in rural and most industrial environments [8]. The striation on the AZ31 depends on the manufacturing process. On the one hand, material aggregations can occur on the rolls, which rolled up on the strips during rolling [28]. On the other hand, the striations consist of inverse segregation, which were investigated by Krbetschek et al. [29] for the AZ31 strips.
Main influence factors of the outdoor exposure tests are rain, condensation, air pollution and animal excrements [30]. The detail view, shown in Fig. 7, reveals a ring of salt surrounding a pit. This observation clearly shows that aggressive salt solutions are omnipresent in the environment and unavoidable.

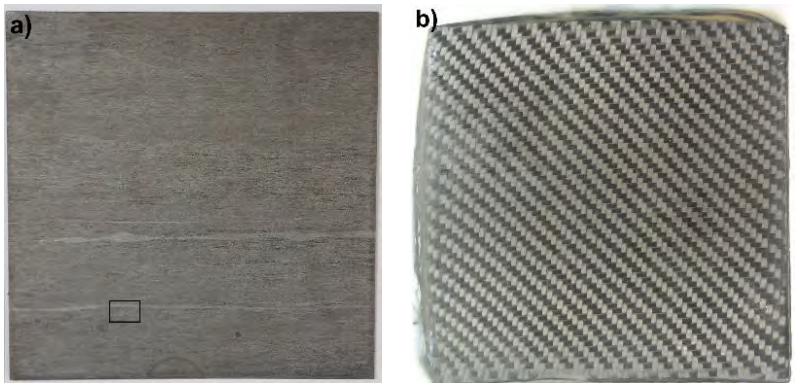


***Fig. 6*** *Samples after three months outdoor exposure test: a) bare AZ31 sheet, b) AZ31-CFRP-multicomponent material. The rectangle indicates the pitting corrosion attack shown in Fig. 7.*

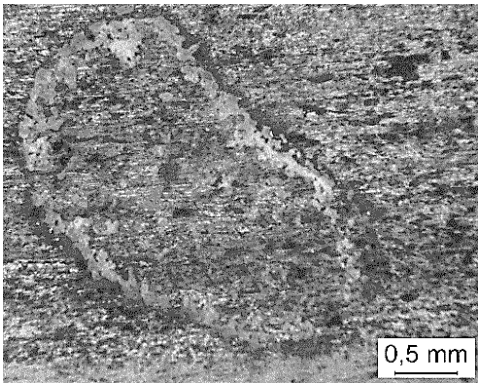


***Fig. 7*** *Optical microscopy image of the salt drop on the sample AZ31 sheet without CFRP-layer after three months outdoor exposure test. It is the marked space in Fig. 6.*

The formation of the salt ring suggests a contamination of the surface by a salt-containing droplet within the three months of outdoor exposure. Although the salt concentration of the droplet is unknown, it is deduced by the results of the polarization test, that a critical concentration of $10^{-4} < c_{crit} < 10^{-3}$ mol/l must have existed. For the explanation of the assumed corrosion process, the Evans droplet experiment was conducted (see Fig. 8). In the model, a droplet with a salt concentration below the critical concentration is assumed for the initial state. At the initial state the salt droplet contacts the surface. Because of lower concentration than $c_{crit}$ the contaminated side is corrosively attacked only by intergranular corrosion. Due to the continuous dehydration of the droplet the salt concentration increases, reaches and exceeds the critical concentration. At this state the pitting corrosion starts at the center of the droplet. The pit growth continues up to steady state or a full dehydration of the droplet.

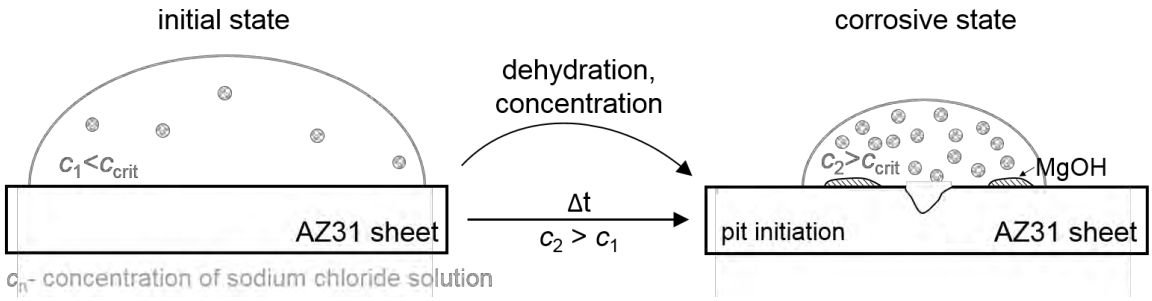


***Fig. 8*** *Schematic representation of the pit growth and dehydration of the droplet according to the Evans droplet model.*

## 4 CONCLUSIONS

In this study, the electrochemical corrosion behavior of a twin-roll cast and hot rolled AZ31 magnesium alloy sheet and a multicomponent material made of the AZ31 sheet and CFRP was investigated by potentiodynamic polarization and an outdoor exposure test. A correlation of the polarization test and the outdoor exposure test depending on the chloride ion concentration was found. The corrosion attack was observed by a concentration of $c = 10^{-4}$ mol/l showed intergranular corrosion and first pits by a concentration of $c = 10^{-3}$ mol/l. Thus, for the polarization tests of the magnesium alloy in different sodium chloride solutions a critical concentration in the range of $10^{-4}$ mol/l $< c_{crit} < 10^{-3}$ mol/l for a pitting corrosion attack is determined. Pitting corrosion was also observed after three months in the outdoor exposure test. For more information about the striation formation and their influence on the corrosion attack further investigation will be done.
Based on the results of the polarization tests, a model adapted from the Evans droplet experiment was established for the explanation of the pitting corrosion attack. Thus, an enhanced pit growth with increasing dehydration of the droplet over a period of time is assumed.

## 5 ACKNOWLEDGEMENT

The authors acknowledge the support of the project “Saxon Alliance for Material- and Resource-Efficient Technologies (AMARETO)” that is funded by the European Union (European Regional Development Fund) and by the Free State of Saxony. Our thanks go to Mrs. E.-M. Kandler and Mrs. C. Krbetschek for their support considering the SEM investigations and helpful discussions, respectively. Thanks go to C. Wüstefeld for the GAXRD measurements.

## REFERENCES

[1] Mordike, B. L.; Ebert, T.: *Magnesium: Properties - applications - potential*, Materials Science and Engineering (A302):37–45, 2001.
[2] Frazier, W. E.; Lee, Eui W.; Donnellan, M. E.; Thompson, J. J.: *Advanced lightweight alloys for aerospace applications*, JOM, 41 (5):22–26, 1989.
[3] Berge, F.; Krüger, L.; Ullmann, M.; Krbetschek, C.; Kawalla, R.: *Anisotropy of the Mechanical Properties of Twin-roll Cast, Rolled and Heat-treated AZ31 as a Function of Temperature and Strain rate*, Materials Today: Proceedings, 2:233–241, 2015.
[4] Tan, C.; Xu S.; Wang L.; Chen Z., Wang F.; Cai H.: *Effect of temperature on mechanical behavior of AZ31 magnesium alloy*, Transactions of Nonferrous Metals Society of China (17):41–45, 2007.
[5] Mises, R. v.: *Mechanik der plastischen Formänderung von Kristallen*, Ingenieurwissenschaftliche Forschungsarbeiten, Band 8 (3):161–185, 1928.
[6] Conceicao, T. F.; Scharnagl, N.; Blawert, C.; Dietzel, W.; Kainer, K. U.: *Corrosion protection of magnesium alloy AZ31 sheets by spin coating process with poly(ether imide) [PEI]*, Corrosion Science, 52 (6):2066–2079, 2010.

[7] Guo, H. F.; An, M. Z.; Huo, H. B.; Xu, S.; Wu, L. J.: *Microstructure characteristic of ceramic coatings fabricated on magnesium alloys by micro-arc oxidation in alkaline silicate solutions*, Applied Surface Science, 252 (22):7911–7916, 2006.
[8] Ghali, E.; Dietzel, W.; Kainer K.-U.: *General and Localized Corrosion of Magnesium Alloys*, Journal of Materials Engineering and Performance, 22 (10):2875–2891, 2013.
[9] Walke, W.; Przondziono; Hadasik, E.; Szala, J.; Kuc, D.: *Corrosion resistance of AZ31 alloy after plastic working in NaCl solutions*, Journal of Achievements in Materials and Manufacturing Engineering (2):132–140, 2011.
[10] Edwards, K. L.: *An overview of the technology of fibre-reinforced plastics for design purposes*, Materials & Design, 19 (1-2):1–10, 1998.
[11] Crawford, R. J.: *Plastics Engineering*. Butterworth-Heinmann, Oxford, 1998.
[12] Arkhurst, B. M.; Kim, J. H.; Lee, M.-Y.: *Hot metal pressing joining of carbon fiber reinforced plastic to AZ31 Mg alloy and the effect of the oxide surface layer on joint strength*, Applied Surface Science):in press, 2017.
[13] Neh, K.; Ullmann, M.; Oswald, M.; Berge, F.; Kawalla, R.: *Twin Roll Casting and Strip Rolling of Several Magnesium Alloys*, Materials Today: Proceedings, 2:45-52, 2015.
[14] Ullmann, M.; Berge, F.; Neh. K; Kawalla, R.: *Development of a rolling technology or twin-roll cast magnesium strips*, Metallurgija, 54 (4):711–714, 2015.
[15] Ullmann, M.; Saleh, H.; Schmitdchen, M.; Kawalla, R.; Vogt, H.-P.: *Improvement of ductility for Twin Roll Cast and rolled AZ31 strips by use of Taguchi method*, Archives of Civil and Mechanical Engineering, 13 (1):1–6, 2013.
[16] Beck, A.: *Magnesium und seine Legierungen*. Springer-Verlag, Berlin, 2001.
[17] Song, G.-L.; Xu, Z.-Q.: *The surface, microstructure and corrosion of magnesium alloy AZ31 sheet*, Electrochimica Acta, 55 (13):4148–4161, 2010.
[18] Lindström, R.; Johansson, L.-G.; Thompson, G. E.; Skeldon, P.; Svensson, J.-E.: *Corrosion of magnesium in humid air*, Corrosion Science, 46 (5):1141–1158, 2004.
[19] Ullrich, C.; Reichel, B.; Rafaja, D.: *Microstructure Development of Twin-roll Cast AZ31 During Deformation*, Materials Today: Proceedings 2S:53-59, 2015.
[20] Samaniego, A.; Llorente, I.; Feliu, S.: *Combined effect of composition and surface condition on corrosion behaviour of magnesium alloys AZ31 and AZ61*, Corrosion Science, 68:66–71, 2013.
[21] Lunder, O.; Lein, J. E.; Hesjevik, S. M.; Aune, T. K.; Nisancioglu, K.: *Corrosion morphologies on magnesium alloy AZ 91*, Materials and Corrosion/Werkstoffe und Korrosion, 45 (6):331–340, 1994.
[22] Schmutz, P.; Guillaumin, V.; Lillard, R. S.; Lillard, J. A.; Frankel, G. S.: *Influence of Dichromate Ions on Corrosion Processes on Pure Magnesium*, Journal of The Electrochemical Society, 150 (4):99–110, 2003.
[23] Williams, G.; Grace, R.: *Chloride-induced filiform corrosion of organic-coated magnesium*, Electrochimica Acta, 56 (4):1894–1903, 2011.
[24] Ben-Haroush, M.; Ben-Hamu, G.; Eliezer, D.; Wagner, L.: *The relation between microstructure and corrosion behavior of AZ80 Mg alloy following different extrusion temperatures*, Corrosion Science, 50 (6):1766–1778, 2008.
[25] Aung, N. N.; Zhou, W.: *Effect of grain size and twins on corrosion behaviour of AZ31B magnesium alloy*, Corrosion Science, 52 (2):589–594, 2010.
[26] Song, G.; Atrens, A.: *Understanding Magnesium Corrosion—A Framework for Improved Alloy Performance*, Advanced Engineering Materials, 5 (12):837–858, 2003.
[27] Ferrando, W. A.: *Review of corrosion and corrosion control of magnesium alloys and composites*, Journal of Materials Engineering, 11 (4):299–313, 1989.
[28] Oswald, M.; Krbetschek, C.; Kawalla, R.: *Technologieentwicklung zum Gieß- und Bandwalzen von Magnesiumlegierungen*. In: Walzen von Flachprodukten, Bauer, H. G.; Schadt (Hrsg.) , Springer Berlin Heidelberg:40–59, 2017.
[29] Krbetschek, C.; Berge, F.; Oswald, M.; Ullmann, M.; Kawalla, R.: *Microstructure Investigations Of Inverse Segregations In Twin-Roll Cast AZ31 Strips*. In: Magnesium Technology 2016 - The Minerals, Metals & Materials Society:369–374, 2016.
[30] Esmaily, M.; Svensson, J. E.; Fajardo, S.; Birbilis, N.; Frankel, G. S.; Virtanen, S.; Arrabal, R.; Thomas, S.; Johansson, L. G.: *Fundamentals and advances in magnesium alloy corrosion*, Progress in Materials Science, 89:92–193, 2017.

CHAPTER 2

# CHARACTERIZATION, DESTRUCTIVE AND NON-DESTRUCTIVE TESTING

# A SPECIMEN FOR EVALUATING POTTING MATERIALS IN FUNCTIONAL INTEGRATED DESIGN SOLUTIONS

**C. Gundlach[1*], S. Hartwig[1], M. Mannig[1], M. Menzel[2], T. Smatt[2], K. Dilger[1]**

[1]Technical University Braunschweig - Institute of Joining and Welding, Germany
[2]Volkswagen AG, Wolfsburg, Germany

**ABSTRACT:** The current state of technology has only limited possibilities for evaluating the suitability of potting materials during the design process of hybrid lightweight components. Looking at innovative hybrid structures in mechanical engineering, there are special requirements when choosing materials together with joining and production techniques. The aim of this work is a simple and cheap mapping of ageing effects in combination with high mechanical loads for evaluating material combinations. A conical specimen consisting of a specially formed metal insert, potted with a polymer to be tested, represents a simplified version of a component's critical area. The mechanical stress levels can be fitted and concentrated using the difference in thermal expansion coefficients based on different metal and geometry combinations of the insert. The ageing process is characterised by e.g. crack initiation and expansion, whereby it is possible to determine fibre content, fibre length and filler content locally. The proposed hybrid specimen allows practical capturing of thermomechanical and chemical ageing by comparing differently aged specimens as well as different material combinations. In particular, material incompatibilities and process vulnerabilities can already be identified during the design stage, where changes are easier than in later development stages of component durability verification. The specimen's low costs enable practical statistics with high significance for evaluation results.

**KEYWORDS:** hybrid test specimen, hybrid design solutions, hybrid lightweight construction, fracture mechanics, ageing of polymers, evaluation of potting polymers

## 1 INTRODUCTION

### 1.1 MOTIVATION

Hybrid material structures increase in importance in today's lightweight design because of their convenient properties. Before starting series production of a new hybrid component, it has to undergo a wide range of testing processes ensuring the durability of the chosen material combination as well as of the whole component. Classical material testing e.g. tensile testing or compact tension testing is not suitable for hybrid material structures because the thermal expansion coefficient $\alpha$ of the chosen materials is not or only insufficiently taken into account. Standardised test methods and specimens for earlier testing are not available, so there is only testing with prototype components as a part of later development stages, which leads to cost and time intensive change processes. That is why basic material characterisation should be extended by test procedures taking place earlier in the development process. For this purpose, the following specimen is proposed and tested for suitability.

### 1.2 GENERAL IDEA

At the current state of technology, there is no test method illustrating property changes of potting materials for combined thermomechanical and chemical ageing. Wittler [1] examines the thermomechanical behaviour of partly potted specimens with cuboid metal inserts. Nevertheless, cracks appear at several places, so the method is not suitable to predict the ageing process of potting polymers. The basic idea of the proposed specimen is to transfer a complex prototype component into a handy replacement structure in shape of a specimen, whereby the special component design is neglected for material characterisation. The specimen forms an All-In-One-Concept that is suitable for existing tests (e.g. Shore-D hardness, change of weight, discolouration) as well as for chemical compatibility (e.g. air, fluid, humidity) and mechanical ageing (e.g. adhesion on metal,

crack initiation). As this approach allows a comprehensive characterisation of hybrid material combinations with only one specimen, it is possible to analyse adhesion properties as well.

### 1.3 CONSTRUCTIONAL APPROACH

The proposed specimen consists of an oval metal insert with a slit surrounded by a polymeric potting material. Dimensions are shown in Fig. 1 for the conical potting and in Fig. 2 for the metal insert. In the side view of the insert it can be seen that there are two plane-parallel areas connected by a ramp with a rise of one material thickness (see the coloured area in Fig. 2). Therefore, there is an asymmetry leading to local concentrated thermomechanical stress within the potting material when loaded. That allows an accelerated testing of mechanical ageing.

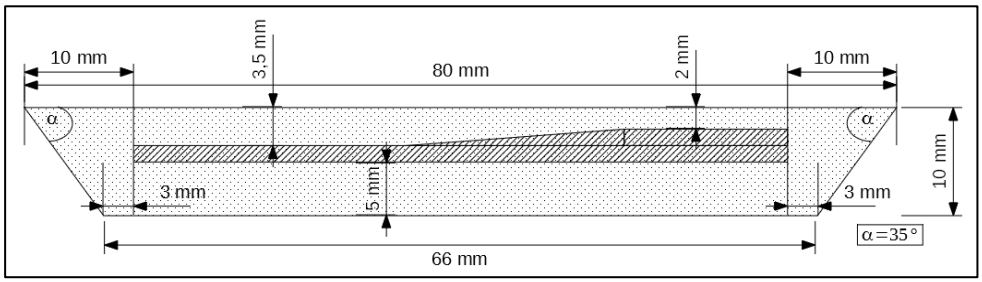


**Fig. 1** *Dimensions of potting polymer*

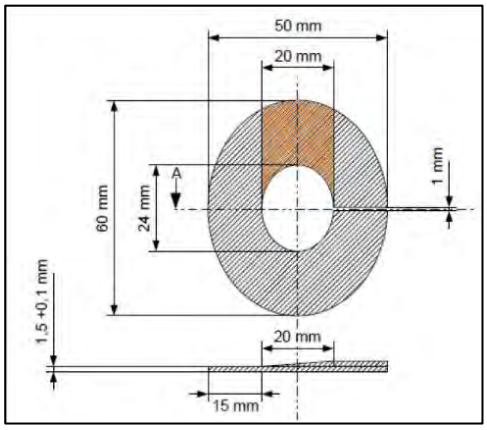


**Fig. 2** *Dimensions of metal insert (coloured area: ramp)*

The idea is to use the differences in the thermal expansion coefficients $\alpha$ of potting and insert material ($\Delta\alpha$ - discrepancy). By choosing certain material combinations, stress levels can be fitted according to the failure limit of the potting polymer to be tested. The thermomechanical behaviour is numerically calculated by FE-simulations. A sensitivity analysis based on FE-simulations is performed concerning the influence factors to evaluate the influence on the results and determine tolerances for production (e.g. polymer height). The final position of the insert was synchronised by determining yield strength $R_{p0,2}$ through tensile testing, so the maximum stress levels of FE-simulation and real testing fit together.

### 1.4 SPECIMEN MANUFACTURING FOR TESTING

For evaluating the proposed constructional approach, specimens have to be built for testing. The challenge is to obtain a potting surrounding the metal insert entirely as well as a reliable height positioning of the insert during manufacturing. A magnetic bearing could let the insert float over the bottom of the potting-form so that the potting polymer could easily flow underneath the insert. However, not all intended insert materials are magnetic. An easier way is introduced for manufacturing the first specimens. The manufacturing process is entirely hand-made, see Fig. 3.

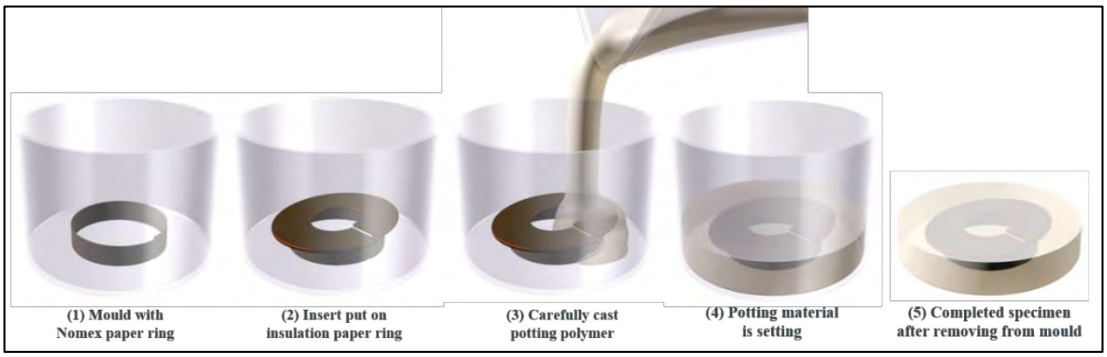


**Fig. 3** *Manufacturing process for first specimen samples*

The insert is placed on a small piece of insulation paper (Nomex paper) set into a circular form and fixed by a paper-fastener. Therefore, the potting is not completely surrounding the insert on the bottom, as seen in Fig. 4. Testing will show if there are any influences on the results. For later versions of the specimen, new manufacturing methods shall improve the potting related to production time and potting quality.

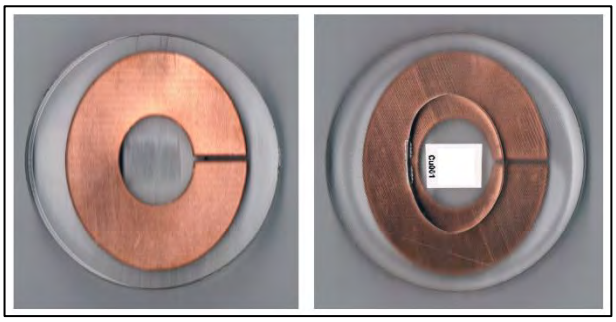

**Fig. 4** *Specimens with transparent potting*

# 2 AGEING AND ANALYSIS

## 2.1 TEST MATRIX AND POSSIBLE INFLUENCE FACTORS

The initial test procedure for the specimen consists of thermomechanical (thermal shocking, step test, high-temperature) and chemical ageing (deposition in Automatic Transmission Fluid ATF). When using thermal shocking, a heavy inhomogeneous temperature distributions result within the specimen because of the fast change between a hot (120 °C respectively 150 °C after 100 cycles) and a cold chamber (-40 °C) and the different thermal conductivities of the materials. The different thermal expansion coefficients lead to high mechanical stress and therefore a fast ageing process. Although the step test uses approximately the same maximum temperatures, mechanical stress will be even lower because the higher thermal exposure time leads to a reduction of local stress peaks due to the possibility of relaxation processes within the specimen. At high-temperature ageing, whether in the air or in oil, there is only one temperature change and the temperature is kept constant for 1000 hours (respectively 1734 hours for oil). Therefore, this test method represents a constant load. In Table 1, the parameters of the applied test methods are summarised.

***Table 1:*** *Applied test methods*

| **Ageing method** | **Temperature** | **Changing time** | **Time/cycles** | **Medium** |
|---|---|---|---|---|
| Thermal shocking | -40 °C / +150 °C | < 10 s [2] | 300 cycles | air |
| Step test | -40 °C / +150 °C | 90 min / 120 min | 300 cycles | air |
| High-temperature | +150 °C | --- | 1000 h | air |
| Transmission Fluid stationary | +150 °C | Oil change each 347 h | 1734 h | Pentosin FFL2 stationary |
| Transmission Fluid stirred | +150 °C | Oil change each 347 h | 1734 h | Pentosin FFL2 stirred |

The evaluation of the specimens before, during and after ageing is performed by visual inspection (crack initiation, discolouration) in accordance with DIN EN ISO 175 [3] as well as by measuring fundamental material properties (hardness, mass). The Shore-D method is chosen for hardness measuring because it is easy to handle via durometer and it is suitable for hard polymers. Shore-D hardness for this work is measured in accordance with DIN EN ISO 868 [4]. To support the results directly obtained from the specimens, FE-simulations and tension tests are used. The simulations are created in ANSYS APDL using Von-Mises-Stress as the fundamental value of interest for evaluation. Mechanical properties of the potting materials (e.g. Young's Modulus, yield strength or elongation at break) by tension tests with appropriate specimens in initial and aged state, whereby the ageing methods are the same like for the proposed specimen, see Table 1.

The quantity of tested specimens is listed in Table 2. In particular, the sample size was limited by available ovens for ageing. For handling all the information obtained by testing, individual DataMatrix-Codes are put on every specimen to store the results in a database.

***Table 2:*** *Sample size with PUR potting for each test method*

| Specimen | Thermal shocking | Step test | High-temperature |
|---|---|---|---|
| Al insert | 7 | 10 | 7 |
| Cu insert | 7 | 10 | 7 |
| Tension | ≥ 5 | ≥ 5 | ≥ 5 |

## 2.2 ANALYSES OF INITIAL AND AGED STATE

In the following, the evaluation focuses on thermomechanical ageing in combination with air for PUR specimens. Fig. 5 shows a PUR specimen in the initial state. Analysis indicates that there are no cracks. On the bottom side, the Nomex paper for height positioning cuts off the potting but causes no cracks. In a side view, it can be seen that the edge on the top is not perfectly smooth which is caused by manufacturing method but it should not have an influence on the results.

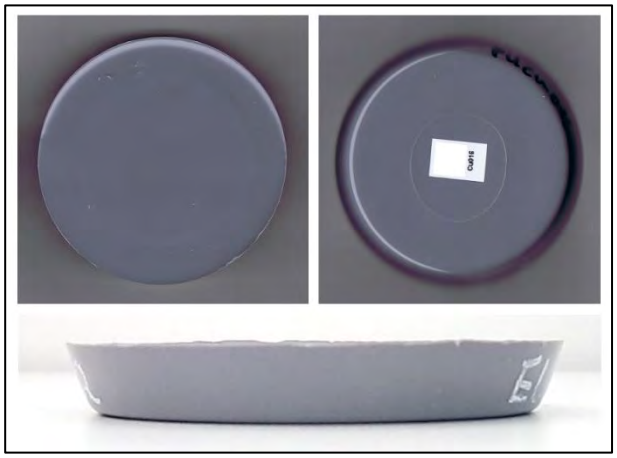

**Fig. 5** *PUR specimen with copper insert in the initial state before testing*

The ageing tests have a very strong influence on the PUR specimens. During thermal shocking, cracks are already appearing after several cycles. The initial crack runs along the insert's inner edge analogous to the FE-simulations. During further cycles, the crack spreads at an angle of 45° towards the surface and when it is reached, crack-spreading is vertical to surface, see Fig. 6.

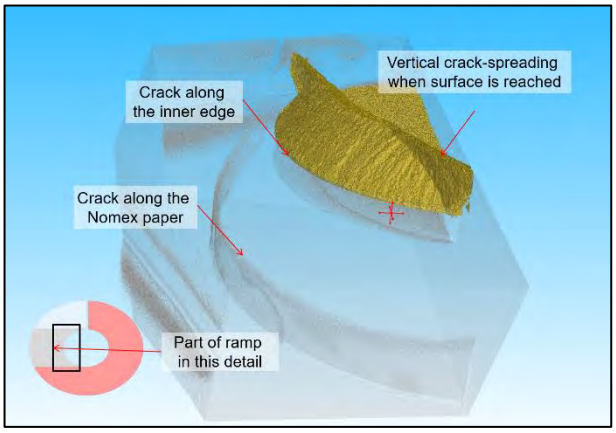


***Fig. 6*** *CT image of crack-spreading for PUR specimen with copper insert after 96 thermal shocking cycles*

The same initial crack pattern is obtained for high-temperature ageing but with shorter crack length because of constant deposition temperature. After further thermal shocking ccycles, additional cracks form along the insert's outer edge, see Fig. 7.

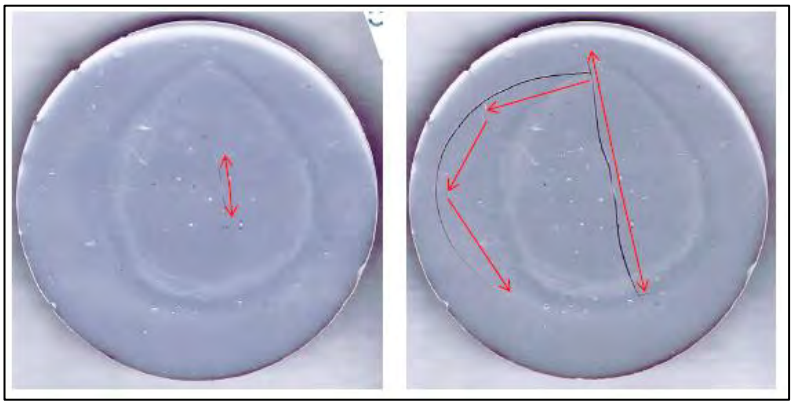

***Fig. 7*** *PUR specimen with copper insert after thermal shocking test. Left: Starting crack at the ramp's inner edge after 13 cycles. Right: Growing crack along insert's outer edge after 48 cycles.*

This pattern can be well described by the FE-simulations (see Fig. 8) in combination with calculated yield strength $R_{p0,2}$ obtained by tensile testing. Due to the difference in the thermal expansion coefficients of copper ($\approx 16.5 \cdot 10^{-6}\ K^{-1}$) and PUR ($\approx 100 \cdot 10^{-6}\ K^{-1}$), mechanical stress appears inside the potting when the specimen is heated up. The area around the inner edge of the insert's ramp shows the highest Von-Mises-Stress at 150 °C caused by leverage effect. The Von-Mises-Stress level is now around yield strength of PUR. Because of the ramp the height of the potting around this area is the lowest and potting is not able to handle plastic deformation. Therefore, the initial crack starts here. With further cycles the potting material is ageing chemically shown by rising hardness and less elongation at break. So additional cracks spread along the stress gradient at the outer edge of the insert because the aged material cannot withstand the stress level anymore and shows a higher crack tendency.

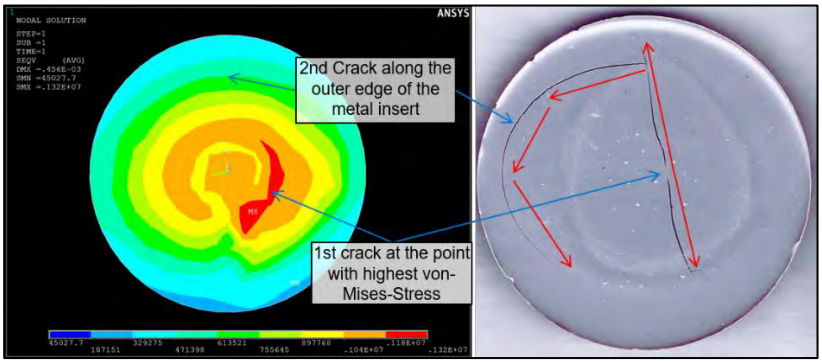


***Fig. 8*** *Comparison between FE-simulation and cracks in PUR specimen with copper insert. Left: Von-Mises-Stress at 150 °C. Right: Cracks in PUR specimen after 48 thermal shocking cycles.*

Looking at the bottom side of the specimen, slight cracking can be detected along the Nomex paper after thermal shocking, see Fig. 9. These cracks start around the same time as the ones on the top side, but do not grow apparently with further thermal shocking cycles. They seem to be caused by shrinkage effects of the potting material due to hardening. Additionally, a cut through a PUR specimen (see Fig. 10) reveals that the cracks on both sides are independent from each other. That is why the influence of the cracks caused by the Nomex paper can be neglected in the first instance.

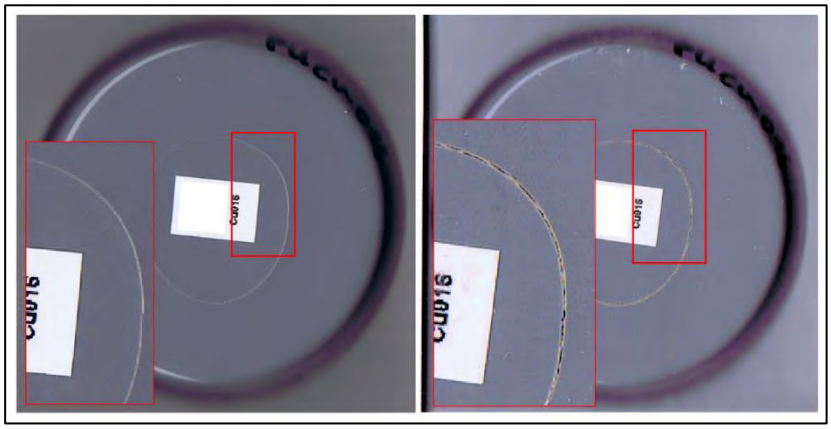

***Fig. 9*** *Bottom side of a PUR specimen before and after thermal shocking. Left: Initial state without any cracks. Left: Slight cracking around the Nomex paper after 13 cycles.*

In general, cracks appear first with specimens having a copper insert due to higher thermomechanical stress inside the potting in comparison to the aluminium insert. As the material pair copper-PUR has a higher difference in thermal expansion coefficients ($16.5 \cdot 10^{-6}\,K^{-1}$ to $100 \cdot 10^{-6}\,K^{-1}$) than aluminium-PUR ($23.1 \cdot 10^{-6}\,K^{-1}$ to $100 \cdot 10^{-6}\,K^{-1}$). Further, that is why crack length is even higher along the outer edge for the copper insert. High-temperature ageing shows the shortest cracks because of constant temperature conditions and therefore lower stress levels in comparison to thermal shocking. Step test is in between them. Additionally, PUR potting delaminates from the copper insert during ageing. A metallographic cutting reveals this area, see Fig. 10.

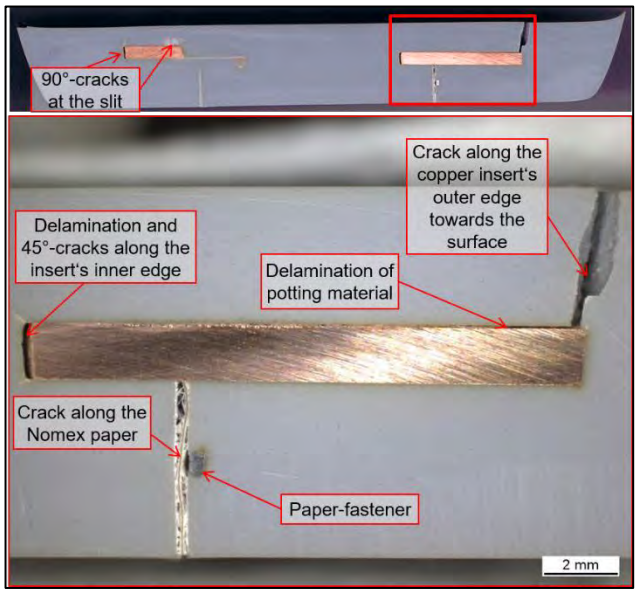


***Fig. 10*** *Cut through an aged PUR specimen with copper insert showing area of delamination*

The analyses show a reproducible crack behaviour for all specimens initiated by copper as well as aluminium insert. Crack patterns of all test variants seem to be nearly similar. Only the point of time for crack initiation differs from each other, see Table 3. Crack length depends on the insert's material as well as the stress level caused by the ageing method. Potting materials can be classified by their crack and ageing behaviour.

***Table 3:*** *Summary of typical damage patterns (point of crack initiation) of specimens before and after ageing*

| **Potting, metal** | **Initial state** | **Air, 150 °C/1000h** | **Step test, < 300 cycles** | **Thermal shocking, < 300 cycles** |
|---|---|---|---|---|
| PUR, Al | Inconspicuous | Inner edge (< 1 h) | Inner edge (50 h) | Inner edge (4 cycles)<br>Outer edge (48 cycles) |
| PUR, Cu | Inconspicuous | Inner edge (<1 h) | Inner edge (50 h) | Inner edge (4 cycles)<br>Outer edge (48 cycles) |

Possible positioning faults of the insert may cause different crack patterns. Having incorrect positioning along the x- or y-axis causes additional cracks at the side edge because the material's thickness is too low to withstand the thermomechanical stress, see Fig. 11. Therefore, tolerances given have to be observed carefully.

***Fig. 11*** *Crack at the outer edge of potting after 13 cycles caused by wrong positioning. Left: X-Ray image. Right: Microscope image.*

## 3 CONCLUSIONS

This paper has provided a hybrid specimen for the evaluation of polymers. The aim was to reproduce their thermomechanical and chemical ageing behaviour in combination with different metals, so hybrid material testing can be fastened in practical use. The test methods implemented on the proposed specimen indicate a reproducible crack behaviour. It is possible to classify different material combinations by their ageing and

crack behaviour. Obviously, certain stress levels can be adjusted by choosing a suitable combination of polymer potting and insert material related to their thermal expansion coefficients. The FE-simulations were able to predict these results. Furthermore, the proposed specimen can be used for already existing standard tests. The most important influence factors are the shape and the height of the polymer potting surrounding the metal insert. Therefore, positioning of the insert should be very precise during production to obtain reproducible results.

## REFERENCES


[1] Wittler, O: *Bruchmechanische Analyse von viskoelastischen Werkstoffen in elektronischen Bauteilen - Dissertation*. Berlin : Fakultät IV - Elektrotechnik und Informatik der Technischen Universität Berlin, 2004

[2] Norm DIN EN 60068-2-14 April 2010. *Umgebungseinflüsse - Teil 2-14: Prüfverfahren - Prüfung N: Temperaturwechsel (IEC 60068-2-14:2009)*

[3] Norm DIN EN ISO 175 März 2011. *Kunststoffe - Prüfverfahren zur Bestimmung des Verhaltens gegen flüssige Chemikalien (ISO 175:2010)*

[4] Norm DIN EN ISO 868 Oktober 2003. *Kunststoffe und Hartgummi – Bestimmung der Eindruckhärte mit einem Durometer (Shore-Härte) (ISO 868:2003)*

# FRACTURE TOUGHNESS AND STRENGTH OF THE INTERFACE OF A GFRP-STEEL-LAMINATE

**Robert Brandt[1*], Arne Busch[1]**

[1] University of Siegen, Am Eichenhang 50, 57076 Siegen, GERMANY

**ABSTRACT:** Unidirectional glass fiber reinforced plastic represents itself as an excellent lightweight material due to its high tensile strength $R_m$ and its low density $\rho$. A major drawback, however, is the relative weakness of the matrix under more complex loading conditions comprising a multi-axial state of stress. Therefore, a local hybridization by use of a more isotropic material, e.g. a high strength steel, seems to be an adequate measure to ensure the robustness of the material. The material testing program sets the focus on the investigation of the strength of the interface between both components. Material tests, like double cantilever beam tests (mode I) and shear tests (mode II), are conducted in order to measure the energy release rate $G_I$ and the shear strength $\tau_s$ of the considered interface at room temperature RT and at an elevated temperature $T = 80°C$. Several methods of surface treatments of the steel layers have been characterized by this approach. The results show up that primers, such as silane, are leading to a good adhesion between the constituents. However, the variation within the data is still significantly higher than for other surface treatment methods. Furthermore, a fiber bridging effect is apparent which leads to an increase of the energy release rate $G_I$with the growth of the length $a$ of the crack. A power law is well suited to describe this strengthening and its exponent $n$ serves as a further measure to describe the strength of the interface. Ageing of the material and testing at an elevated temperature may compromise the performance of the intrinsic hybrid material. Hence, all material tests are conducted by use of intrinsic hybrid specimens in the as manufactured state as well as in an aged state where the ageing has been done by exposing the intrinsic hybrid laminates to water at a temperature $T = 80°C$ for one week.

**KEYWORDS:** Mechanical Properties, Shear Strength, Double Cantilever Beam, Environmental Conditions, Hybrid Laminates, GFRP, Steel

## 1 INTRODUCTION

Intrinsic hybrid materials or laminates mainly consist of a light metal, e.g. aluminum and titanium, and fiber reinforced polymers like glass fiber reinforced plastics (GFRP) or carbon fiber reinforced plastics (CFRP). Other approaches of an intrinsic hybrid laminate consisting of steel and CFRP are known from literature [1, 2, 3].

In this study the intrinsic hybrid laminate is made up by unidirectional GFRP and a high strength steel. Due to the different chemical structures of the components, additional mechanical and chemical treatments are applied to achieve a strong bonding interface. Mechanical adhesion can be enhanced by roughening of the steel surface, i.e. by sand blasting or shot peening. Furthermore, the chemical adhesion between steel and GFRP can be improved by the use of adhesion agents or primers [4]. The chemical primers comprise a functional group which is chemically linked to the steel surface and another group which is chemically linked with the epoxy resin.

Two main load cases are considered for the characterization of the bonding strength of the interface. The fracture toughness, mode I (opening), is evaluated by a double cantilever beam (DCB) test [5] and the shear strength, mode II (sliding), by an Edge-Shear-Test (EST) [6]. These two tests are commonly designed for FRP materials so that modifications are necessary for testing of intrinsic hybrid laminates as well.

# 2 SPECIMEN PREPARATION

## 2.1 MANUFACTURING OF THE SPECIMENS

The intrinsic hybrid laminate specimens are made up by one layer of bainitic steel 51CrV4 and another layer of unidirectional GFRP prepregs, which consist of E-glass fibers and epoxy resin. The fiber volume content of the GFRP is 60 %. The dimensions of each specimen are denoted by its length $l$, thickness $t$, and width $w$. It is here agreed upon that the direction of the dimension length is pointing into the average alignment of the unidirectional glass fibers. The layer thicknesses are $t_{steel} = 1.76\,mm$ for steel and $t_{GFRP} = 3\,mm$ for GFRP, respectively. The synthesis of steel and GFRP happens during the curing step of the prepreg process. The specimens are manufactured in 3 steps which are surface treatment of the steel, synthesis of steel with GFRP in the prepreg process, and finishing of the specimens by cutting them into the final dimensions. The surface treatments are done mechanically by sand blasting of the steel surface, labeled as #SB, to increase the roughness and chemically by using silane and titanium dioxide primers, labeled as #Si and #Ti, to increase the adhesion between steel and epoxy resin. A pure GFRP specimen is serving as a reference, labeled as #GFRP [7].

## 2.2 AGEING

Two types of specimens are prepared for mechanical testing, namely (i) the as manufactured specimens and (ii) aged specimens. Ageing of the specimens means that they are stored into water at an elevated temperature of $T = 80°C$ for one week. These specimens are labeled by the appendix _aged.

# 3 EXPERIMENTAL SETUP

The intrinsic hybrid laminate is exposed to tensional and shear loads, respectively, by using specific material tests. Mode I (opening) fracture toughness of the interface is determined by using a modified DCB-Test according to ASTM D 5528-01 [5]. Mode II (sliding) shear strength is determined by an Edge-Shear-Test, proposed by Weidenmann et al. [6].

## 3.1 MODE I – FRACTURE TOUGHNESS

The effective length $l_{DCB}$ of the double cantilever beam specimen is $l_{DCB} = 163\,mm$ and its width $w = 25\,mm$ (s. Fig. 1). The thickness of the layers $t_{steel}$ and $t_{GFRP}$ , respectively, are chosen such that both cantilevers comprise the same bending stiffness. An initial crack of the length $a_0 = 50\,mm$ is established by means of a thin film for anti-adhesion which is placed between the layers of GFRP and steel before the prepreg process.

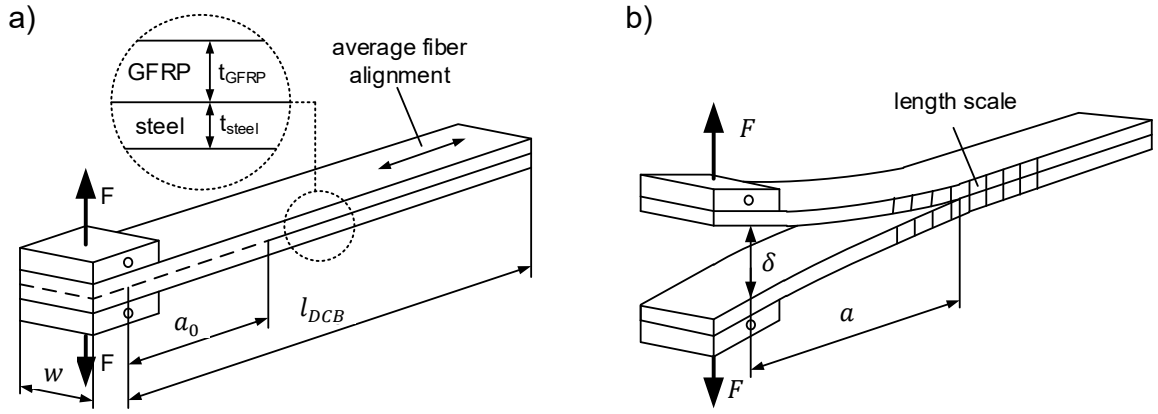


$F$ = load, $w$ = width, $l_{DCB}$ = effective length, $t$ = thickness, $a_0$ = initial crack length, $a$ = total crack length, $\delta$ = crack opening displacement

***Fig. 1*** *Specimen for the DCB-Test a) unloaded b) loaded*

The load F is applied by means of a load block at each layer. The quasi-static, displacement controlled test is conducted at a speed $v_t$ of the traverse between $1\,mm/min < v_t < 3\,mm/min$. A length scale has been applied to the intrinsic hybrid specimens so that the total crack length a can be recorded by means of an external camera system.

### 3.2 MODE II – SHEAR STRENGTH

The dimension of the intrinsic hybrid laminate specimens are given by its width $w = 25\,mm$ and its length $l_{EST} = 10\,mm$ (s. Fig. 2). The specimen is loaded via two pressure plates with an offset $t_{offset}$ of 0.5 up to $1\,mm$. The specimen is applied such that the upper pressure plate solely strains the steel component and the lower plate the GFRP component. The length $l_{EST}$ of the specimen is limited to $l_{EST} \leq 26.7\,mm$ so that it does not fail due to an excessive pressure, but due to the shear stress. The Edge-Shear-Test is a quasi-static, displacement controlled test where the speed of the traverse $v_t$ is $1\,mm/min$.

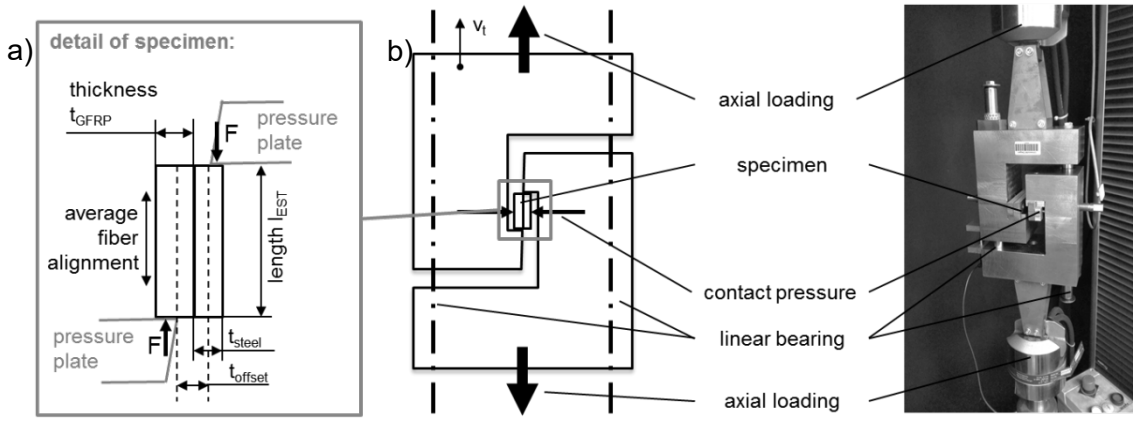


***Fig. 2*** *Test setup of the DCB-Test*

### 3.3 ENVIRONMENTAL CONDITIONS

Testing generally happens at room temperature under dry conditions. However, in order to simulate environmental conditions, the tests have been also performed at an elevated temperature $T = 80\,°C$ under dry conditions as well. For this type of test, a climatic chamber has been installed at the test rig. The specimens, which have been tested at room temperature, are labeled by the appendix _RT and those, which are tested at the elevated temperature, by the appendix _80 °C, respectively.

## 4 RESULTS

The results of the DCB-Test are evaluated by using the energy release rate $G_I$ according to the modified beam theory [5] given by

$$G_I = \frac{3 \cdot F \cdot \delta}{2 \cdot w(a + |\Delta|)}. \tag{1}$$

$\delta$ denotes the crack opening displacement (s. Fig. 1) and $|\Delta|$ is a correction value which is individually determined for each specimen and measurement. The energy release rate $G_I$ is proportional to the squared stress intensity factor ${K_I}^2$ [8] and represents a measure for the crack resistance. In Fig. 3 the results of the DCB-Test are shown for the GFRP reference (#GFRP) at different test conditions. At least 3 specimens were tested for each curve (2 specimens for #Si_80°C and #Ti_aged). The average energy release rate $\bar{G_I}$ is fitted by a power law approach

$$\bar{G_I} = M(a + |\Delta| - a_0)^n + G_0 \tag{2}$$

where $n$, and $G_0$ are fitting parameters, and $a_0$ denotes the initial crack length of $50\,mm$. The fitting parameters $G_0$ and $n$ are given for each set of data within each diagram (s. Fig. 3). The value of the parameter is set to one (1) and compensates only for the units. All sets of data of the GFRP-samples show a good correlation to the power law fit. All specimens shows a strengthening effect which is based on a fiber bridging effect. The magnitude of the strengthening effect is given by the exponent $n$. Here, the specimens tested at room temperature, exhibit the highest value $n = 0.2$ followed by the samples, which are tested at $T = 80\,°C$ with $n = 0.17$. The aged samples exhibit the weakest hardening effect with $n = 0.09$. Hybrid specimens behave differently to the GFRP specimens. The corresponding diagrams are given in Fig. 4 for the silane treated specimens (#Si), in Fig. 5 for the titanium dioxide treated specimens (#Ti), and in Fig. 6. for the grid blasted specimens (#GB), respectively. Surprisingly, the #GB samples, which have been tested at elevated temperature or in an aged state, exhibit a weakening effect contrary to all other samples.

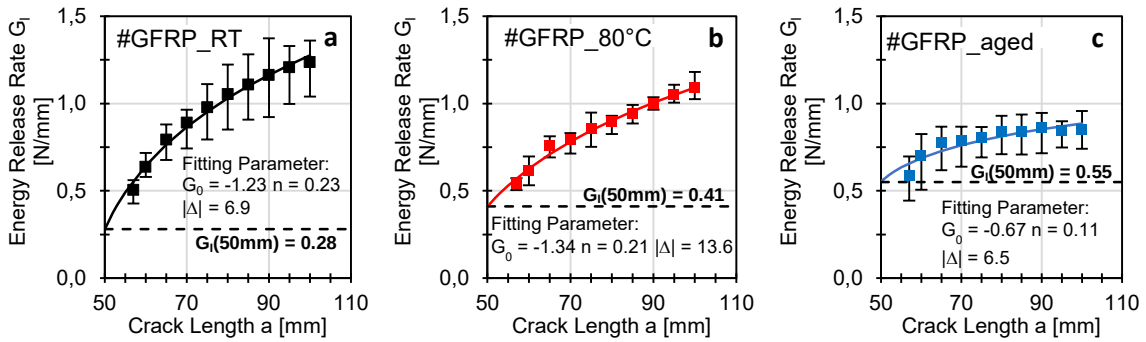


***Fig. 3*** *Energy release rate $G_I$ of the GFRP reference a) at room temperature RT b) at an elevated temperature T = 80 °C and c) for the aged specimens*

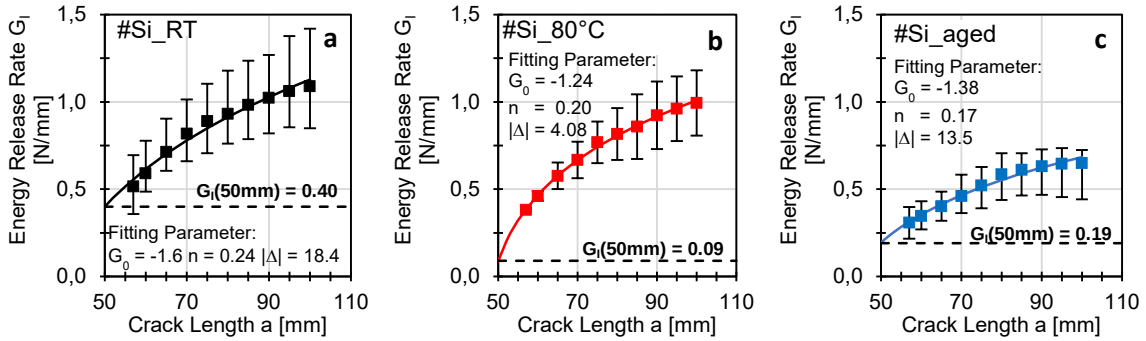


***Fig. 4*** *Energy release rate $G_I$ of the silane treated specimens a) at room temperature RT b) at an elevated temperature T = 80 °C and c) for the aged specimens*

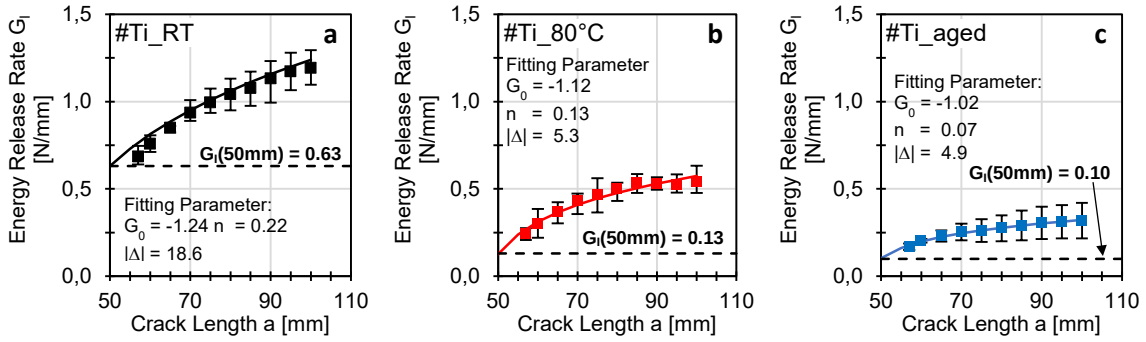


***Fig. 5*** *Energy release rate $G_I$ of the titanium dioxide treated specimens a) at room temperature RT b) at an elevated temperature T = 80 °C and c) for the aged specimens*

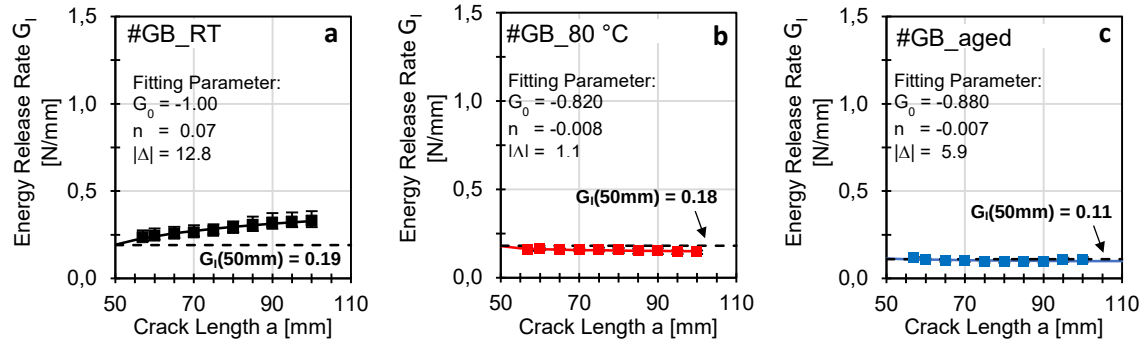


***Fig. 6*** *Energy release rate $G_I$ of the grid blasted specimens a) at room temperature RT b) at an elevated temperature T = 80 °C and c) for the aged specimens*

The shear strength $\tau_s$ of each specimen is evaluated by the maximum force $F_{max}$ of the force-displacement curve and the effective shear area $A_s$ of the specimen by

$$\tau_s = \frac{F_{max}}{A_s}. \tag{3}$$

Fig. 7 shows the corresponding results of the EST. Each group, which is labeled as #GFRP, #Si, #Ti, and #GB, respectively, contains the results for the tests of the as manufactured specimens at both temperatures as well as the result of the aged specimen.

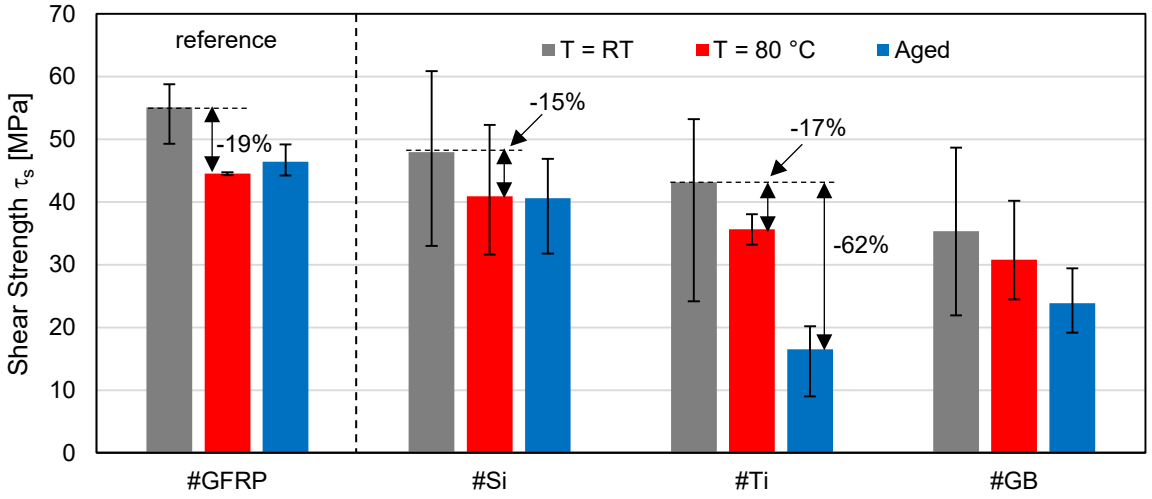


***Fig. 7*** *Shear strength $\tau_s$ of the grid blasted specimens at room temperature RT, at an elevated temperature of T = 80 °C, and for the aged specimens*

The reference specimen #GFRP shows the highest shear strength at room temperature. A drop of 19% occurs under testing at the elevated temperature. Ageing also leads to a comparable drop in shear strength. A very similar behaviour reveals the test for a hybrid laminate with silane primer. Only the magnitude of shear strength is slightly smaller in comparison to the reference. The hybrid laminates, which have been treated with a titanium dioxide primer, behave differently. The tests reveals a drop of 17% by testing the as manufactured specimens at the elevated temperature. However, the performance of the aged samples suffers significantly more by the aging treatment so that a drop of 62% in shear strength is revealed by the test. The test comprises the lowest shear strengths for the grid blasted specimens.

## 5 CONCLUSIONS

The fracture toughness of the hybrid laminates is characterized by the energy release rate, which is determined by means of an extrapolation according to the power law at a crack length $a = 50mm$. All these results are shown in Fig. 8. The $G_{I,a=50mm}$ value for #GFRP_RT is 0.28 $N/mm$, it becomes 0.41 $N/mm$ for #GFRP_80°C, and is highest with 0.55 $N/mm$ for #GFRP_aged. The #Si specimens show the highest value at room temperature and significant drop for #Si_80°C. Even the aged sample shows a higher value than the as manufactured sample at an elevated temperature. It has to mentioned that the decrease of the value of #Si_80°C is maybe affected by the small correction value $|\Delta| = 4.08\,mm$. More tests should be done for this specimen type in order to validate this result. The $G_{I,a=50mm}$ value of specimen #Ti_RT shows the highest energy release rate. In contrast to that, the two other types of specimen #Ti_80°C and #Ti_aged performs rather poorly. All types of specimen #GB show rather small fracture toughness with values between 0.11 $N/mm$ and 0.19 $N/mm$.

The investigation presented in this paper show up that the fracture toughness and the shear strength of the here considered hybrid laminates is severely affected by the ambient temperature and by the aging procedure. The reference type of specimen #GFRP is rather robust against those changes. The here depicted findings of the static mechanical properties indicate a certain weakening of the interface. This has to be investigated more closely by means of fractographical methods. Furthermore, the impact on the fatigue strength is to be considered, too.

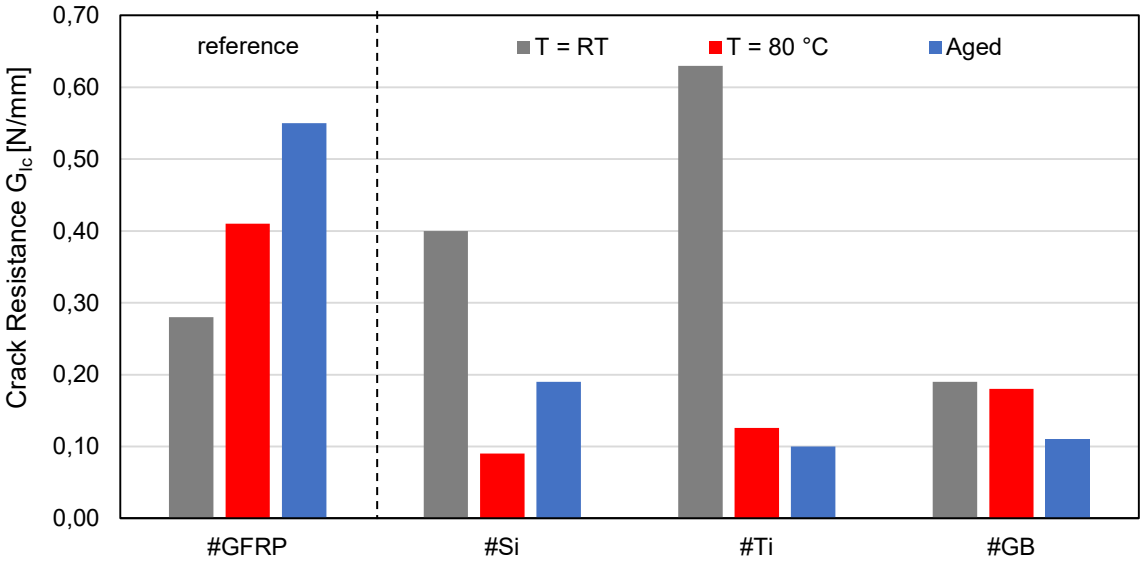


***Fig. 8*** *Calculated energy release rate $G_I$ for a crack length of a = 50 mm for all kinds of specimens*

## 6 ACKNOWLEDGEMENT

This work is funded from the European Union as a part of the competition “Neue Werkstoffe” EFRE.NRW. Further, the authors gratefully acknowledge the co-operation partner Mubea Fahrwerksfedern GmbH.

## REFERENCES

[1] J. C. Both: Tragfähigkeit von CFK-Metall-Laminaten unter mechanischer und thermischer Belastung. Dissertation, München, 2014.
[2] A. Monden, M. G. R. Sause, S. Horn: Surface modified Steel/Epoxy-based CFRP hybrid Laminates under Mode I, Mode II and mixed-mode Load Conditions, ECCM17 - 17th European Conference on Composite Materials, München, 2016.
[3] C. Lauter, T. Tröster, B. Sköck-Hartmann, T. Gries, M. Linke: Höchstfeste Multimaterialsysteme aus Stahl und und Faserverbundkunststoffen, Konstruktion, 2010, pp. 8–9.
[4] A. Monden, M. G. R. Sause, A. Hartwig, C. Hammerl, H. Karl, S. Horn: Evaluation of Surface Modified CFRP-Metal Hybrid Laminates, Euro Hybrid Materials and Structures, Stade, 2014, pp. 32–40.
[5] ASTM D 5528-01: Standard Test Method for Mode I Interlaminar Fracture Toughness of Unidirectional Fiber-Reinforced Polymer Matrix Composites. ASTM International, 2010.
[6] K. A. Weidenmann, L. Baumgärtner, B. Haspel: The Edge Shear Test - An Alternative Testing Method for the Determination of the Interlaminar Shear Strength in Composite Materials, MSF 825-826, 2015, pp. 806–813.
[7] A. Busch, R. Brandt: Characterization of the Bonded Connection in Hybrid-Steel-GFRP-Laminates, KEM 742, 2017, pp. 408–415.
[8] D. Gross: Bruchmechanik: Mit einer Einführung in die Mikromechanik, 6th Ed., Springer Berlin Heidelberg, Berlin, Heidelberg, 2016.

# ADHESION STUDIES OF THERMOPLASTIC FIBRE-PLASTIC COMPOSITE HYBRID COMPONENTS PART 1: THERMOPLASTIC-THERMOPLASTIC-COMPOSITES

**A. Liebsch, R. Kupfer*, M. Krahl, D. R. Haider, W. Koshukow, M. Gude**
Institute of Lightweight Engineering and Polymer Technology (ILK), TU Dresden

## ABSTRACT
Fibre-reinforced thermoplastics are predestined for the automated manufacturing of cost-effective lightweight structures on a large scale. Especially, the combination of different material configurations in one component, e.g. injection moulding compounds, pre-consolidated thermoplastic composite (TPC) sheets or hollow profiles, offers a promising approach for weight reduction. Therefore, hollow profiles are combined with TPC-sheets and overmoulded in an integrated injection moulding process. However, the hollow profile must be in cold solid state and stabilised by an internal supporting structure to prevent collapsing under the high injection pressures.
In order to exploit the lightweight potential, the interfaces between the individual components must be considered more closely. For the efficient integration of thermoplastic hollow profiles, a surface pre-treatment is necessary to achieve adequate bonding strengths. This paper presents experimental studies on the bonding strength between different thermoplastic semi-finished products. Both warm-warm joints and warm-cold joints are investigated. For the warm-warm connections, the influence of the pre-heating temperature is considered in detail. For the warm-cold tested specimens, the effects of both chemical and physical pre-treatment methods are investigated. Both single-lap-shear (SLS) specimens and special rib specimens are used for the examinations.

**KEYWORDS:** joining, hybrid-design, thermoplastic composites, mechanical testing

## 1 INTRODUCTION

The combination of load-adapted substructures, such as torsion- and bend-resistant hollow structures, flat construction elements and three-dimensional knot structures, into highly integrated multi-component structures permit high potentials for weight reduction. In combination with composites and the possibilities of systematic reinforcement of such structures, the lightweight potential can be further increased. Additionally, the use of composites brings up a distinguished degree of manufacturing-, structure- and function-integration, which overcomes many classic construction methods. With typical processing times of less than one minute, composites with thermoplastic matrices are well suited for large series applications [1], [2].

***Fig. 1*** *Generic multi-component thermoplastic composite structure: a) CAE design, b) photography.*

* Corresponding author:
Holbeinstr. 3, 01307 Dresden; phone: +49 351 463-38749; fax: +49 351 463-38143 robert.kupfer@tu-dresden.de

Fig. 1 shows a generic structure which demonstrates the mentioned multi-components design. The sub structures are made of glass fibre (GF) polyamide 6 (PA6) composites. The manufacturing process of such structures is described in detail in [3]. During the manufacturing process, the shaped pre-consolidated TPC sheet is heated above the melting temperature of the matrix. Afterwards, the soft and deformable TPC sheet is placed into the cavity of an injection moulding tool together with a cold and stiff TPC hollow profile. As the tool closes, the TPC sheet is thermoformed and thereby pressed against the hollow profile (interface 1). Immediately after closing the mould, a short fibre reinforced material is injection overmoulded onto both the cold hollow profile (interface 2) and the warm TPC sheet (interface 3) to form a complex rib structure. To prevent the collapsing of the hollow profile under the high injection pressure, it is essential that the profile is stabilised from the inside by a supporting structure [3] and placed into the mould in a cold condition to maximise its stability. During the described process three interfaces between the substructures are developed which influence the overall strength of the structure. As each interface is formed at different processing conditions, it is necessary to consider the single interface strengths in particular. Table 1 gives an overview of the interfaces between the components and their conditions of joining.

***Table 1:*** *Interfaces in the generic multi-component thermoplastic composite structure.*

| Interface | Component 1 | Component 2 | Condition of joining |
|---|---|---|---|
| 1 | hollow profile | TPC sheet | cold-warm |
| 2 | hollow profile | rib structure | cold-warm |
| 3 | TPC sheet | rib structure | warm-warm |

The process of overmoulding warm thermoformed TPC sheets is well known and already established in industrial products [4], [5]. Regarding the interface strength, this technology offers big advantages as the plastic melt directly overflows the already molten surface of the TPC sheet leading to a strong connection between both materials. In [6] shear bonding strengths between PA6 TPC sheets and a PA6/GF30 injection moulding material are analysed. It is shown that the bonding strengths increase significantly with the pre-heating temperature of the TPC sheet.
In contrast to warm-warm interfaces, the bonding strength of cold-warm interfaces with TPC sheets is barely investigated. Previous research has shown, that pre-treatments of polymers with physical methods like plasma, corona, ultraviolet light and ozone increase the wettability and the surface energy of polymers [7]-[13]. As a result, several works demonstrate that the physical surface treatment, especially the use of plasma, can be used to increase the bonding strength of glued polyamide specimens [14], [15].
In the present work the bonding strengths of cold-warm interfaces of pressed TPC sheets are analysed as well as the cold-warm interfaces of overmoulded TPC-sheets. To increase the bonding strengths, the surfaces of the cold specimens are pre-treated with plasma. Additionally, a set of specimens are pre-treated with a $CH_2O_2$ based polyamide solution. For comparison, untreated specimens are fabricated as well. To investigate the resulting bonding strengths, SLS specimens are tested at quasi-static loading. Beside the warm-cold interfaces, the bonding strengths of overmoulded pre-heated TPC sheets are evaluated. Here, an application oriented rib-like specimen design is chosen and the influence of pre-heating temperature on the pull-off force is evaluated.

## 2 SPECIMEN PREPARATION

The structure shown in Fig. 1 consists of three different fibre-reinforced thermoplastic materials. The hollow profile is made of hybrid yarn[1] which is pre-consolidated in a variothermal blow moulding process. The TPC sheet is procured as a fully consolidated semi-finished product of glass fibre and PA6[2] and the rib structure is a glass fibre-reinforced PA6-PA66 blend[3]. Table 2 summarises the material combinations that are tested within this work.
In a first preparation step, TPC sheets with 2 mm thickness are manufactured from 2/2 twill woven ENKA TECTAPE using autoclave technology. Secondly, coupons with the dimensions of 20 x 90 mm are cut out by waterjet cutting from the TEPEX and TECTAPE TPC sheets[4]. These coupons are then used as the first component during specimen manufacturing.

[1] ENKA TECTAPE GF-PA6 1800TEX 6733 by PHP FIBERS, 46 vol% glass fibre content.
[2] TEPEX DYNALITE 102RG600 by BONDLAMINATES, 47 vol% glass fibre content, 2 mm thickness.
[3] EMS GRIVORY GV-5H, 50 % glass mass content.
[4] Reduced specimen width compared to DIN EN 2243-1 standard single-lap-shear tests [16], 12.5 mm overlapping length according to [16].

***Table 2:*** *Material, interface and pre-treatment combinations analysed in the study.*

| No | Component 1 | Component 2 | Interface manufacture | Pre-treatment of component 1 |
|---|---|---|---|---|
| A | ENKA | TEPEX DYNALITE | cold-warm pressing | untreated |
| B | TECTAPE | | | open air plasma |
| C | | | | $CH_2O_2$/PA6-solution |
| D | TEPEX DYNALITE | | | untreated |
| E | | | | open air plasma |
| F | | | | $CH_2O_2$/PA6-solution |
| G | ENKA | EMS GRIVORY GV-5H | cold-warm overmoulding | untreated |
| H | TECTAPE | | | open air plasma |
| I | TEPEX | | | open air plasma |
| J | DYNALITE | | warm-warm overmoulding | pre-heating |

## 2.1 COLD-WARM PRESSING

To manufacture specimens in a defined environment and increase the reproducibility, a manufacturing unit including an IR oven (KRELUS G14-25-2.5 MINI 7.5), an industrial robot (KUKA KR 16-2), a hydraulic press (RUCKS KV275.06) and an atmospheric-pressure plasma unit with a rotating nozzle (PLASMATREAT RD1004 ROTARY NOZZLE) was set up (Fig. 2).

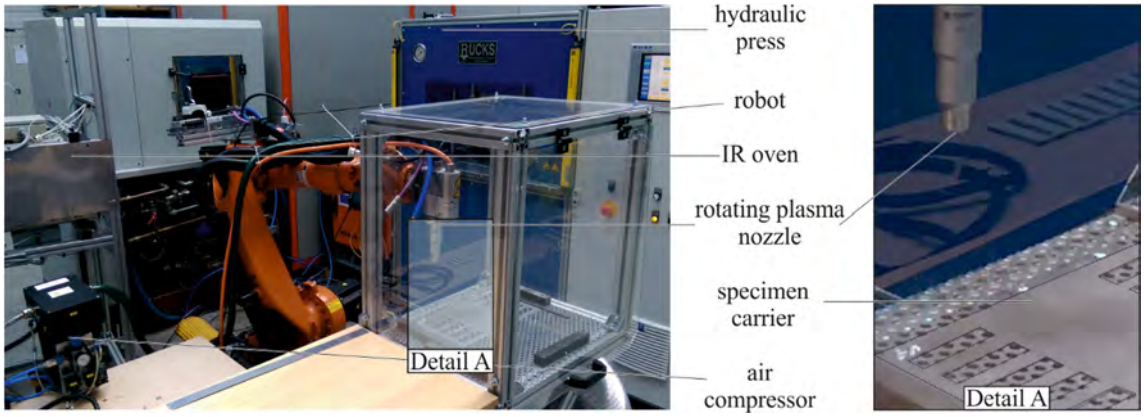


***Fig. 2*** *Manufacturing unit for the fabrication of the pressing specimens.*

Before the manufacturing of test specimens, the influence of plasma treatment parameters on the wettability of the TPC sheets surface is evaluated (Table 3). Therefore, the contact angle between a saturated saline solution and the polymer surface is measured immediately after the treatment procedure. As can be seen in Fig. 3, a reduced translational speed of the plasma nozzle and a small distance between nozzle and specimen surface lead to smaller contact angles and thus to an increased wettability. Indicating a higher surface energy and thus a better suitability for bonding, the highlighted parameters in the right-hand column of Table 3 are used for further specimen preparation.

***Table 3:*** *Test parameters for the plasma surface treatment.*

| Parameter | Values for contact angle study | Values for further testing |
|---|---|---|
| distance nozzle to surface | 2.5/5/7.5/10 mm | **2.5 mm** |
| translational speed of the nozzle | 2.5/5/7.5/10 $^{m}/_{min}$ | **2.5 $^{m}/_{min}$** |
| air pressure | 3 bar | **3 bar** |

Before specimen manufacturing, the TPC coupons for the first component are cleaned with acetone. Afterwards they are inserted into the specimen carrier (cf. Fig. 2 right) and pre-treated with plasma. The carrier with the pre-treated coupons is then placed on the lower plate of the hydraulic press (mould temperature 80 °C). Parallel, TEPEX-TPC sheets for the second component are heated up to 260 °C using the IR oven, transferred into the hydraulic press and then pressed at the coupon carrier with 2 MPa of pressing force for 125 sec. Since the second component TPC sheet overlaps the whole coupon carrier, the individual single-lap-shear specimens have to be cut from the joined structure after cooling and releasing the coupon carrier.

The manufacturing of the chemically treated specimens follows the same process. As known from literature, polyamide can be dissolved in $CH_2O_2$ [17]. Using this effect, a surface treatment of component 1 with a $CH_2O_2$ polyamide solution could potentially lead to a better bonding with the pre-heated TPC sheet. Hence, 10 $\%_{mass}$ of PA6 are dissolved in $CH_2O_2$ (pureness: 98 %) and a film of the solution is applied to the surface of the cold TPC coupons. Afterwards the coupons are placed in the hydraulic press using the specimen carrier and joined with the warm TPC sheet. For comparison, a set of untreated coupons are joined in the same manner.

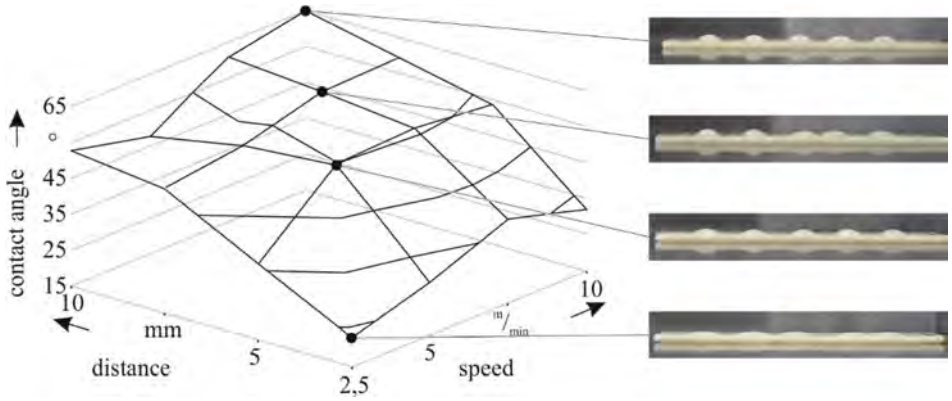


***Fig. 3*** *Contact angle of plasma treated TPC surface.*

## 2.2 OVERMOULDING

For the overmoulding studies two types of test specimens are used. To investigate the cold-warm interfaces, the same SLS specimen preparation procedure as in the pressing trials is applied. The plasma pre-treatment of the coupons is also similar to the pressing process. After surface treatment the specimens are manually placed into the injection mould. The overmoulding parameters can be found in Table 4.

***Table 4:*** *Injection moulding parameters.*

| Parameter | SLS | Rib structure |
|---|---|---|
| mould temperature | 100 °C | 100 °C |
| melt temperature | 300 °C | 330 °C |
| injection speed | 12 $^{cm^3}/_s$ | 6 $^{cm^3}/_s$ |
| packing pressure | 700 bar | 800 bar |
| packing time | 10 s | 6 s |
| cooling time | 25 s | 30 s |

Beside SLS specimens, the testing structure shown in Fig. 4 is used to evaluate the bonding strength of overmoulded TPC sheets. It contains four different rib geometries at the top of a TPC sheet. For the current tests, the TPC sheets are pre-heated between 130 °C and 250 °C in steps of 20 °C. After the injection moulding process, 20 mm segments are cut out of the structure and tested under pull off loading (cf. [5]). Here, rib geometry 4 is used for the tests. The overmoulding parameters can be found in Table 4.

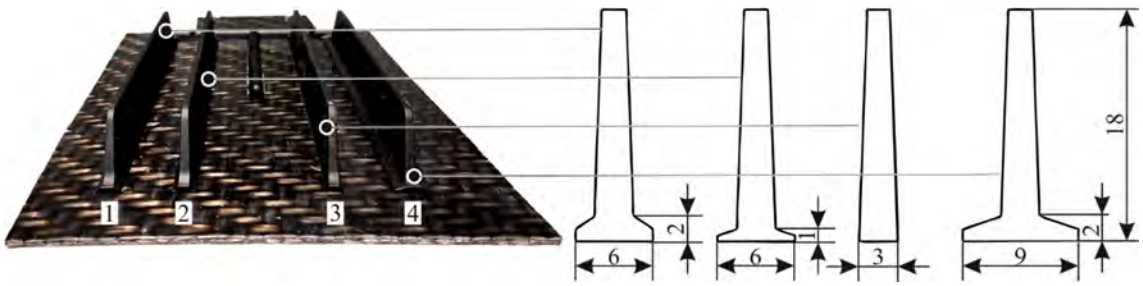


***Fig. 4*** *Rib structure (dimensions in mm).*

## 3 TESTING AND RESULTS

Before testing, the specimens are conditioned according to DIN EN ISO 1110 [18]. All specimens are tested on a standard tensile testing machine (ZWICK 1445) under quasi-static loading (2 $^{mm}/_{min}$). Fig. 5 shows the bonding strengths of the cold-warm joints. In all tests an improvement of the bonding strength by the use of surface treatment is observed. The reference specimens without any surface preparation already fail during demoulding and further handling. With plasma surface pre-treatment, a bonding strength of about 2 MPa is achieved for both TPC sheet variants. The application of the $CH_2O_2$ polyamide dissolution increased the average bonding strength up to 6 MPa for the TECTAPE material and up to 8.5 MPa for the TEPEX material. The results further show, that the bonding strengths of TEPEX are higher than the results achieved with the TECTAPE material.

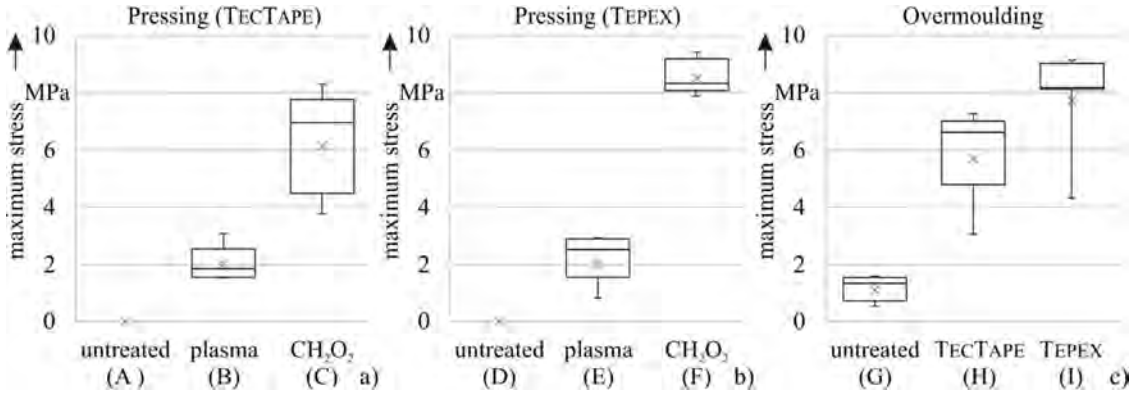


***Fig. 5*** *Bonding strengths of warm-cold joints: a) pressed TECTAPE specimens, b) pressed TEPEX specimens, c) overmoulded specimens.*

The results of the overmoulded cold-warm interfaces show that without surface treatment only low bonding strengths are achieved (Fig. 5c, G). With plasma treatment the bonding strength is increased significantly (H). In the case of the overmoulded TEPEX, bonding strengths equivalent to the 250 °C warm overmoulded specimens reported in [6], can be reached (I).
The results of the warm-warm combinations are shown in Fig. 6. It can be seen, that the average bonding strengths decrease from 250 °C to 170 °C. Between 170 °C and 130 °C the bonding strengths remain at a comparable level.

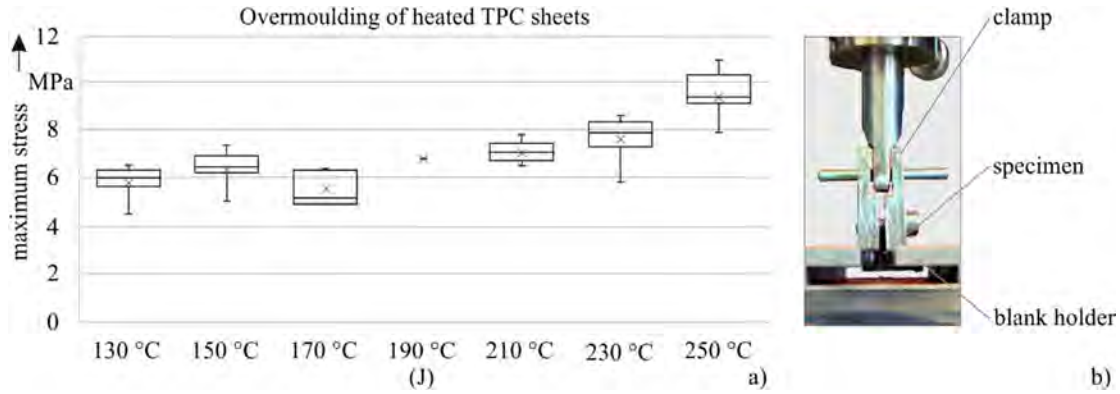


***Fig. 6*** *Rib pull off test: a) temperature dependent bonding strength, b) test set up.*

## 4 CONCLUSIONS

The combination of TPC sheets, hollow composite profiles and injection moulded rib structures offers a high design potential for lightweight engineering. In a new manufacturing approach, consolidated hollow profiles and heated TPC sheets are pressed together and overmoulded in a single process using injection moulding technology. Thereby, different interfaces between the materials are established which have an important influence on the overall structural performance of the lightweight structure. In the present work, the bonding strength of these interfaces is analysed. For this purpose, an automated manufacturing unit for a reproducible surface treatment and SLS specimen manufacturing was set up. The SLS specimens are tested under quasi-

static loading. It was found that the bonding strength can be increased significantly by the use of plasma or even more by $CH_2O_2$ treatment.
Additionally, ribbed specimens were manufactured to investigate the influence of pre-heating temperature on the bonding strength of overmoulded TPC sheets. It is observed, that pre-heating temperatures below the melting temperature of the matrix can lead to bonding strengths similar to the plasma treatment. As expected, the bonding strengths increase significantly at high pre-heating temperatures.

## 5 ACKNOWLEDGEMENT

The research projects are funded by the Federal Ministry of Education and Research (funding ref.: 02P14Z000 – 02P14Z010 and 02P14Z040 – 02P14Z049). Responsibility for the content of this report lies with the author.

## REFERENCES

[1] Kaufmann R., Bürkle E., Bider T.: *Process Integration - Lightweight Parts with a Thermoplastic Matrix*. Kunststoffe International, vol. 03/2011: p. 65-68, 2011.
[2] Hufenbach W., Langkamp A., Adam F., Krahl M., Hornig A., Zscheyge M., Modler N.: *An integral design and manufacturing concept for crash resistant textile and long-fibre reinforced polypropylene structural components*. In: 11th Int. Conf. on the Mech. Behaviour of Materials, p. 2086-2091, 2011.
[3] Liebsch A., Kupfer R., Gude M., Müller P., Andricevic N.: *Hohlprofile, Organobleche und LFT-Knoten – Hybridbauteile aus Faserkunststoffverbunden für die automobile Serienproduktion*. Kunststoffe im Automobilbau: p. 215-226, 2017.
[4] Götze C.: From a Niche Product to Standard Series Production – Highly Resilient Lightweight Components Produced from Organo Sheet. Kunststoffe international, vol. 03/2016: p. 35-38, 2016.
[5] Stegelmann M., Krahl M., Garthaus C., Hufenbach W.: *integration of textile reinforcements in the injection-moulding process for manufacturing and joining thermoplastic support-frames*. In 20th international conference on composite materials (ICCM), 2015.
[6] Al-Sheyyab A.: *Light-Weight Hybrid Structures – Process Integration and Optimized Performance*. Dissertation, Erlangen, 2008.
[7] Labay C., Canal J. M., Navarro A., Canal C.: *Corona plasma modification of polyamide 66 for the design of textile delivery systems for cosmetic therapy*. Appl. Surface Science, vol. 316: p. 251-258, 2014.
[8] Han S. H., Kim B. J., Park J. S.: *Effects of the corona pretreatment of PET substrates on the properties of flexible transparent CNT electrodes*. Thin Solid Films, vol. 572: p. 73–78, 2014.
[9] Tahara M., Cuong N. K., Nakashima Y.: *Improvement in adhesion of polyethylene by glow-discharge plasma.* Surface Coating Technology, vol. 174: p. 826–830, 2003.
[10] Oosterom R., Ahmed T. J., Poulis J. A., Bersee H. E. N.: *Adhesion performance of UHMWPE after different surface modification techniques*. Medical Engineering & Physics, vol. 28: p. 323–330, 2006.
[11] Belmonte G. K., Charles G., Strumia M. C., Weibel D. E.: *Permanent hydrophilic modification of polypropylene and poly(vinyl alcohol) films by vacuum ultraviolet radiation*. Applied Surface Science, vol. 382: p. 93–100, 2016.
[12] Kłonica M., Kuczmaszewski J., Kwiatkowski M. P., Ozonek J.: *Polyamide 6 surface layer following ozone treatment*. International Journal of Adhesion and Adhesives, vol. 64: p. 179-187, 2016.
[13] Balart J., Fombuena V., Espana J. M., Sanchez-Nacher L., Balart R.: *Improvement of adhesion properties of polypropylene substrates by methyl methacrylate UV photografting surface treatment*. Materials & Design, vol. 33: p. 1–10, 2012.
[14] Gao Z., Peng S., Sun J., Yao L., Qiu Y.: *Influence of processing parameters on atmospheric pressure plasma etching of polyamide 6 films*. Applied Surface Science, vol. 255: p. 7683–7688, 2009.
[15] Mandolfino C., Lertora E., Gambaro C.: *Influence of cold plasma treatment parameters on the mechanical properties of polyamide homogeneous bonded joints*. Surface & Coatings Technology, vol. 313: p. 222–229, 2017.
[16] DIN EN 2243-1: *Aerospace series - Non-metallic materials - Structural adhesives - Test method – Part 1: Single lap shear*. Standard, 2005.
[17] Saunders P. R.: *Dilute Solution Properties of Polyamides in Formic Acid. Part I. Repression of Polyelectrolyte Effects by Means of Excess Counterions*. Journal of Polymer Science Part A: Polymer Chemistry, vol. 2: p. 3755-3764, 1964.
[18] DIN EN ISO 1110:1995: *Plastics - Polyamides - Accelerated conditioning of test specimens*. Standard, 1995.

# ADHESION STUDIES OF THERMOPLASTIC FIBRE-PLASTIC COMPOSITE HYBRID COMPONENTS PART 2: THERMOPLASTIC-METAL-COMPOSITES

**D. R. Haider, M. Krahl*, W. Koshukow, M. Wolf, A. Liebsch, R. Kupfer, M. Gude**
Institute of Lightweight Engineering and Polymer Technology (ILK), TU Dresden

## ABSTRACT
In addition to thermoplastic-thermoplastic-composites design, the combination of fibre composites with classical materials such as steel can lead to a significant increasing of the part performance due to using the material-specific advantages. The novel 3D-Hybrid technology combines high-strength steel, endless-fibre-reinforced thermoplastic and long fibre-reinforced thermoplastic compounds to realise cost-efficient light-weight structures for mass production. Extensive researches have shown that the joint strength between the various semi-finished products is a key issue in the component and process development. Therefore, various process-adapted pre-treating methods such as special adhesion promoter systems or surface structuring by means of laser processing were developed and have to be characterised. For the comprehensive analysis of the intrinsically joined hybrid structures, a novel test method and a special hybrid test specimen were developed. These allow reproducing accurately the process conditions of the actual component manufacturing process. Furthermore, the load cases occurring in the hybrid component can be better analysed.

**KEYWORDS:** joining, hybrid-design, thermoplastic composites, mechanical testing

## 1 INTRODUCTION

Novel thermoplastic fibre-reinforced composite-metal-lightweight structures offer a wide range of applications due to a number of combination possibilities. In particular, there is great potential for integrative hybrid design and the use of innovative process technologies in the automotive industry [1], [2]. In this way, the properties of the various materials or material configurations can be used in a targeted manner in order to achieve the best possible utilisation of the entire structure. In modern car bodies, high-strength steels in shell design are predominantly used for crash structures. By combining these classic materials with thermoplastic composite (TPC) sheets and long fibre-reinforced thermoplastic the level of mass reduction and the crash-relevant properties can be increased considerably [3], [4]. Fig. 1 shows the single semi-finished products manufactured in a one-shot process to a hybrid structure of a car body.

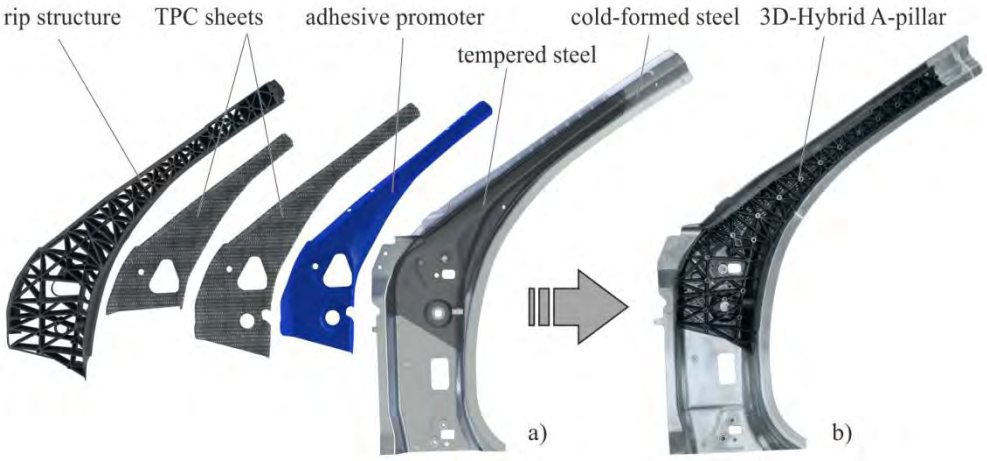


***Fig. 1*** *Components of the demonstrator structure in multi-material-design: a) CAE design, b) photography*

* Corresponding author:
Holbeinstr. 3, 01307 Dresden; phone: +49 351 463-42499; fax: +49 351 463-38143 michael.krahl@tu-dresden.de

A major part in the manufacture process of hybrid structures is the joining of different semi-finished products. Basically, two different process routes can be distinguished. In the in-mould assembly (IMA) process, the materials are joined in the primary shaping or forming process of the final part. No additional joining step is required. In the post moulding assembly (PMA) the components are produced separately from each other and joined in a further process step [5]. The connection between metal and polymer can be realised by form locking, adhesive bonding or non-positive connection. Especially in IMA processes, a combination of the different joining mechanisms is also possible.
Currently there are no standardised test methods and specimen geometries for characterising of intrinsic joined TPC-metal hybrid structures. Depending on the joining mechanism, either modified test specifications from adhesive bonding technology or specimens specially developed for the application are used. Often, it is difficult to compare the properties of the different test methods, because the geometry of the specimens, as well as the joining conditions not defined. The preparation of the test specimens for hybrid structures in an IMA process is particularly very difficult. Especially the cutting of the specimens is time-consuming, because damages in the joining zone caused by the separation process must be avoided. In addition, it is essential that the process conditions of the component manufacturing process, such as heating, transfer, forming, injection moulding and cooling behavior are accurately reproduced. That is while a new test method and an adapted test specimen is necessary, what is presented in this paper.

# 2 SPECIMEN PREPARATION

Based on the KS2 and KS2.5 test specimens developed at the Laboratory for Materials and Joining Technology (LWF) at the University of Paderborn, a novel ILK-hybrid test specimen was developed for analysing of intrinsic joined hybrid structures [6]. The test specimen can be used to reproduce the various manufacturing processes such as pressing, injection moulding and thermoforming. The conditions and process parameters for the production of test specimens can be transferred identically from the original component manufacturing process.
Maximum three different materials can be combined in one specimen (Table 1). A further advantage is the near-net-shape production of the test specimens. This avoids damages in the joint zone as a result of cutting loads during the preparation.

***Table 1:*** *Configuration possibilities for different material and process combinations*

| Configuration | Component 1 | Component 2 | Component 3 |
|---|---|---|---|
| 1 | Metal | TPC sheet | - |
| 2 | Metal | TPC sheet | Injection moulding compound |
| 3 | TPC sheet | TPC sheet | - |
| 4 | TPC sheet | Metal | - |
| 5 | TPC sheet | TPC sheet | Injection moulding compound |
| 6 | Metal | Injection moulding compound | - |
| 7 | TPC sheet | Injection moulding compound | - |

## 2.1 SPECIMEN GEOMETRIES

Depending on the material properties to be tested, suitable test methods are selected for the characterisation of joint strength. For this purpose, mainly the standards of adhesive bonding technology are used. Commonly used is the single-lap-shear (SLS) test according to DIN EN 1465 (formerly DIN 53283) and ISO 4587 (Fig. 2b) [11]. This standard is primarily used for aluminium alloys and materials with the same or higher modulus of elasticity and yield strength. The quotient of the maximum force and the adhesive surface equals the adhesive strength. The adhesive strength therefore corresponds to the bond strength in combination with the respective joining materials and the selected specimen geometry. The SLS specimens are bonded in two overlapping sheets. The result is an offset, which must be compensated that the bonding is in the middle of the direction of force. An additional moment loading is generated in the joining zone. With increasing specimen thickness, the stiffness of the specimen is also increased, which has an influence on the adhesive strength [7]. The bending moment increases linearly while the stiffness of the joining sheet increases with the third potency of the thickness.
Fig. 2 shows the comparison between the ILK-hybrid test specimen and the SLS specimen. The overlap length of the SLS specimen is 12.5 mm. A width of 25 mm results in a joining surface of 312.5 mm². With a length of 50 mm and a width of 16.6 mm, the ILK-hybrid test specimen provides a maximum joining surface of 830 mm². The surface used here is 640 mm² (length: 40 mm, width: 16 mm).

The test specimen with configuration 1 (Table 1) is used in the following tests. In this configuration, the TPC sheet is formed against the metal sheet by the injection moulding machine due to the applied pressing force. Another possibility is shown in configuration 2 (Table 1), in which the pressure between TPC sheet and metal sheet is generated by the injection pressure of the injection moulding compound.

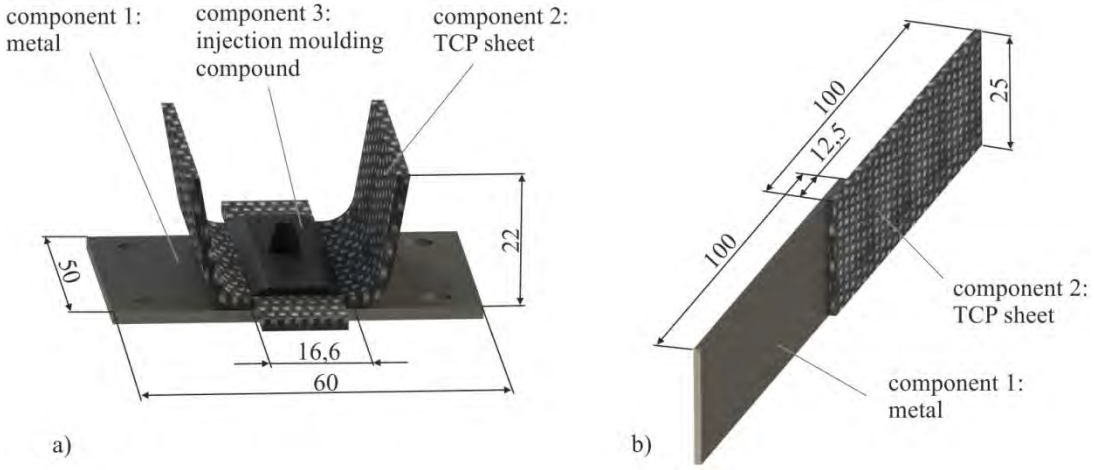


***Fig. 2*** *Test specimen for characterisation of hybrid structures (dimensions in mm): a) ILK-hybrid test specimen, b) SLS specimen (DIN EN 1465)*

## 2.2 ADHESIVE APPLICATION

The bonding strength of the two joining partners is achieved by an adhesive promoter layer, which contains thermoset and thermoplastic ingredients. Depending on the system which is used, the adhesion promoter can be applied by spraying a layer, glueing on an adhesion promoter film or applying adhesive beading. The adhesion promoter systems used here are available as adhesive films, which are applied to the metal surface in a separate process step (Fig. 3a). Two different adhesives were selected and called in the following as system 1 (S1) and system 2 (S2). Before application, the sheet metal is cleaned with acetone. The adhesive promoter layer is applied to the metal sheet and tempered by 130 °C for 5 minutes to start a slight reaction of the thermoset resin.

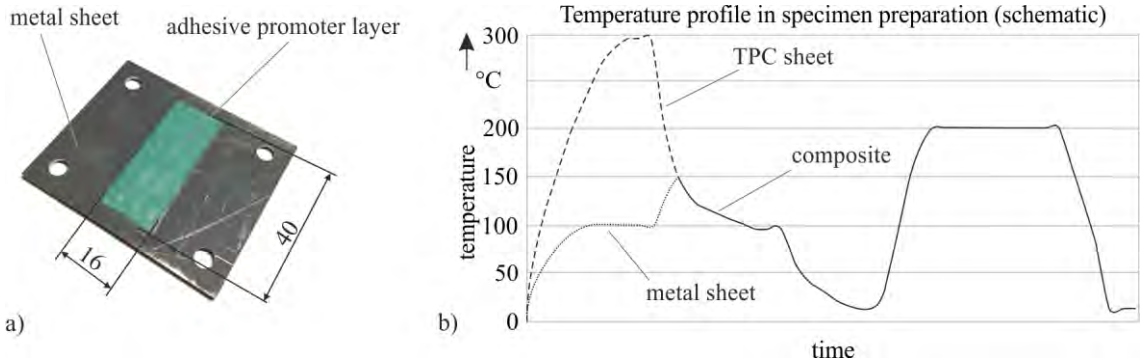


***Fig. 3*** *Joining with adhesive promoter layer: a) Applied adhesive on metal sheet (dimensions in mm), b) Temperature profile during manufacturing process incl. CDP process*

The adhesion promoter system is activated by the TPC sheet heated above melting temperature during the manufacturing of test specimens in the process shown in Fig. 3b. As a result of heat exposure, curing reactions are started from a temperature of 115 °C upwards. The lower mould temperature of 100 °C cools down the joined hybrid structure within the holding time of 3 minutes and is then demoulded. Complete curing is achieved in a further heat treatment process that reproduces the drying process after the cathodic dip painting (CDP) of a car body. That's while a sufficient bonding of the joining partners after the demoulding process is necessary. This requires a very precise temperature control during the manufacturing process, so that the adhesive bond cures in a very short time due to the temperature of the TPC sheet.

## 2.3 MANUFACTURING PROCESS

As joining partners, for the component 1 a tempered steel (22MnB5, 1.5 mm thickness) and for the component 2 a TPC sheet (TEPEX DYNALITE 101-RGUD600, 2 mm thickness) are used. The semi-finished products are cut by waterjet cutting. The adhesion promoter is applied on the metal sheet as described in chapter 2.2. The TPC sheets are dried at 80 °C for at least six hours before processing.
The main difference between SLS specimen and ILK-hybrid test specimen is the manufacturing process. Fig. 4 shows the process chain for SLS preparation. The metal sheet with the applied adhesive promoter layer is inserted in the mould with a temperature of 100 °C. The TCP sheet is heated up externally via an infrared oven (KRELUS G14-25-2.5 MINI 7.5) over melting temperature of the PA6.6 matrix to 300 °C with a heating time of 2 minutes. Both semi-finished products are transferred by hand in the hydraulic press (RUCKS KV275.06). Therefore, reproducible transfer times are difficult to realise. The sheets are joined in a contoured mould with a pressing force of 300 kN. A holding time of 5 minutes and a mould temperature of 120 °C are set. In this way, SLS specimens are made from larger composite and metal panels with the dimensions of 245 x 220 mm. Thus a subsequent cutting of the hybrid plate is necessary. Mechanical processing by cutting grinding is sometimes problematic because the thermoplastic matrix causes the cutting plate to stick together. Therefore, production by waterjet cutting is preferable. However, both cutting technologies can cause damage in the joining zone.

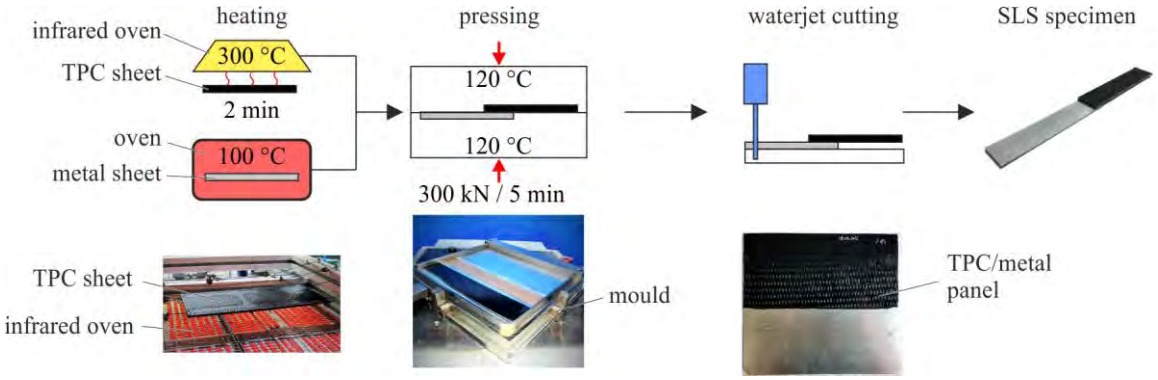


***Fig. 4*** *Manufacturing process of SLS specimens*

The production of the ILK-hybrid test specimen is very close to the original component manufacturing process (Fig. 5). It is of particular importance that not only production parameters but also process sequences such as handling steps are taken into account in the production of test specimens [8]. For this, some process parameters such as the pre-heating of the metal sheet, pressing force, mould temperature and holding temperature had to be adjusted in comparison to the SLS specimen [9], [10]. The TPC sheet is inserted directly in the machine and heated via an infrared oven (KRELUS G14-25-2.5 MINI 7.5) over melting temperature to 300 °C. An external heating process can also be implemented if cooling effects during the transport process are to be represented. The metal sheet can also be pre-heated, but in the following tests it is coldly inserted into the mould. After that, the sheets are pressed with an injection moulding machine (Arburg 270C) and a pressing force of 400 kN. A holding time of 3 minutes and a mould temperature of 100 °C are set. After this process step, the finished specimen can be demoulded.

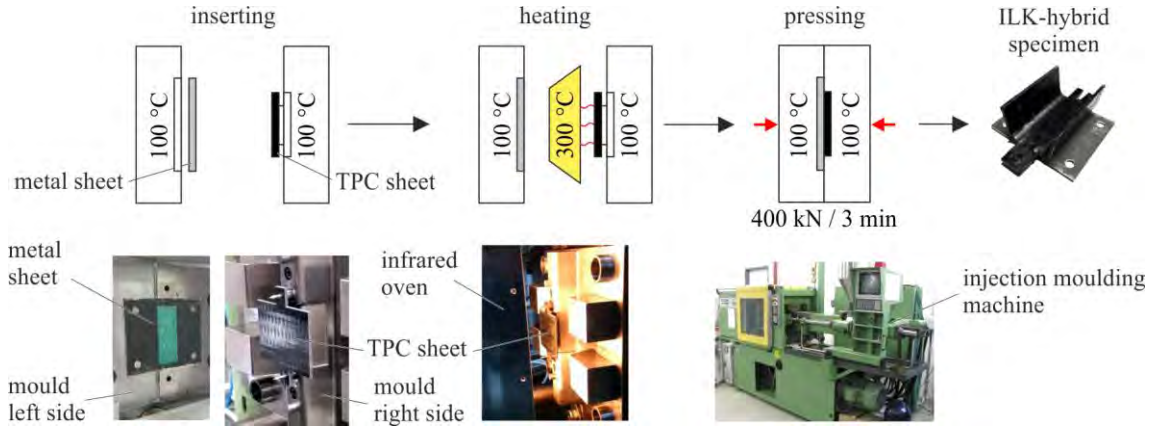


***Fig. 5*** *Manufacturing process of ILK-hybrid test specimens*

Similar to the SLS samples the ILK-hybrid test specimens are tempered at 200 °C for 30 minutes to ensure that the adhesive bond is completely cured. The parameters of manufacturing process of SLS and ILK-hybrid test specimens can be found in Table 2.

***Table 2:*** *Process parameters for test specimens preparation*

| Parameter | SLS specimen | ILK-hybrid specimen |
|---|---|---|
| adhesive application | 23 °C (-) | 130 °C (5 min) |
| metal sheet temperature | 100 °C | - |
| TPC sheet temperature | 300 °C | 300 °C |
| pressing force | 300 kN | 400 kN |
| mould temperature | 120 °C | 100 °C |
| cooling time | 5 min | 3 min |

## 3 TEST AND RESULTS

Before testing, the specimens are conditioned according to DIN EN ISO 1110 [12]. All specimens are tested on a standard tensile testing machine (ZWICK 1465) with quasi-static loading (1 $^{mm}/_{min}$). Fig. 6 shows the joint strength in the tensile shear test of SLS specimens and the ILK-hybrid specimen. Two different bonding agent systems were investigated and referred to system 1 (S1) and system 2 (S2). In all tests higher shear strengths are measured by the different process setup and the developed test method. SLS test reference specimens were obtained for system 1 to 5.1 MPa and system 2 to 3.9 MPa. With the use of the new experimental setup higher bonding strength of system 1 to 6.3 MPa and system 2 to 12.2 MPa are measured. In comparison to the SLS test, the scattering of the maximum bond strength is higher caused by the process, the new specimen geometry or the changed test setup. Nevertheless, the changed process setup and the application of bonding agents also have a considerable influence on the determined properties.

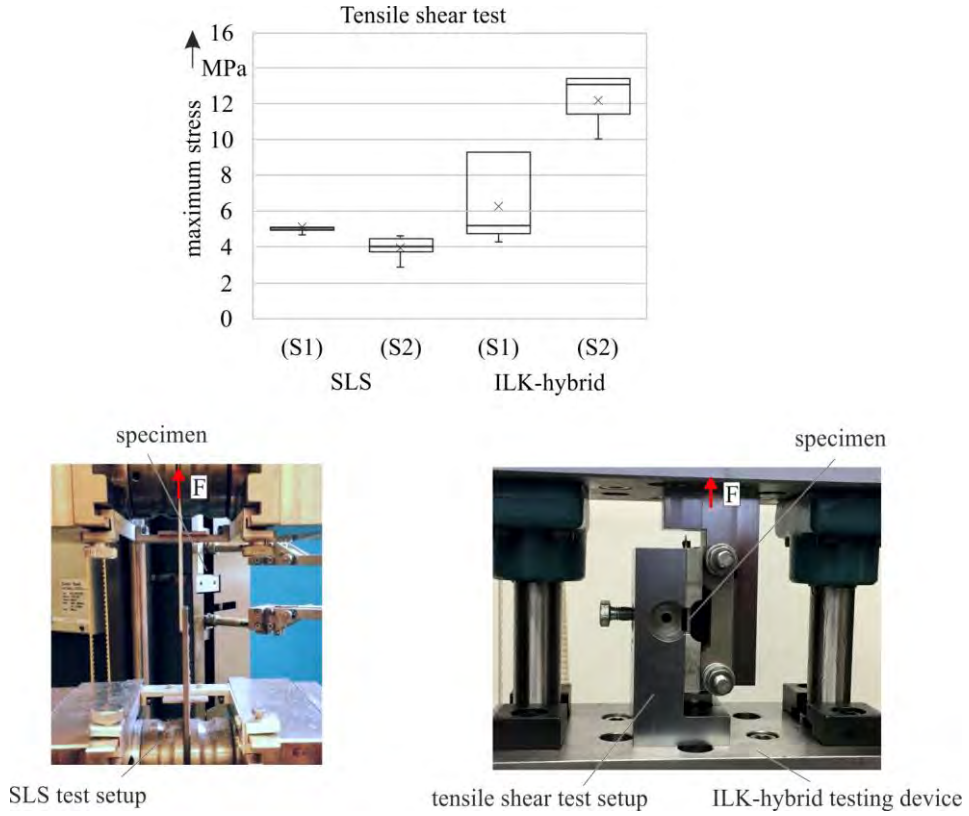


***Fig. 6*** *Comparison of results and test setup between SLS specimen and ILK-hybrid specimen*

## 4 CONCLUSIONS

The combination of thermoplastic fibre-reinforced composites with metal enables new design concepts for lightweight solutions in multi-material-design. The combination of different semi-finished products in a single component requires a material and process adapted joining technology for maximum efficiency. In the present study, different adhesive promoter layers were applied to metal (22MnB5) and joined in a one-shot process with TCP sheet (glass fibre fabric and PA 6.6 matrix). To realise an application-orientated preparation of test specimens a novel specimen design and manufacturing concept is developed and tested. According to the novel specimen geometry a test device for shear testing is designed and experimentally compared to classic SLS specimens. It is proved in first investigations that the specimens can be manufactured near-net shape and very close to the original component manufacturing process with the similar parameters and process sequences. Due to the production close to the final contour, the production of test specimens by cutting is no longer necessary and damage to the joining zone by cutting forces is avoided. Moreover, with one specimen geometry several material combinations, manufacturing technologies and an extensive determination of properties to the different load modes can be realised. In further studies additional investigations need to be made to identify the different influencing parameters in the manufacturing process and the test device.

## 5 ACKNOWLEDGEMENT

The German Federal Ministry of Education and Research (BMBF) funds the research and development project Q-PRO within the Framework Concept ‘Innovations for Tomorrow’s Production, Service and Work’ (funding code 02P14Z040 – 02P14Z049). Q-PRO is managed by the Project Management Agency Karlsruhe (PTKA).

## REFERENCES

[1] Bürkle E., Gude M., Krahl M., Stegelmann M.: *Kunststoffe und Metall - ein unzertrennliches Paar.* Kunststoffe, vol. 12/2017: p. 27-32, 2017.

[2] Gude M., Kupfer R., Krahl M., Liebsch A., Koshukow W.: *Hybridstrukturen für die Großserie.* Jahresmagazin Kunststofftechnik WAK, ALPHA Informationsgesellschaft mbH, p. 80-86, ISSN: 1618-8357, 2017.

[3] Kellner P.: *Zur systematischen Bewertung integrativer Leichtbau-Strukturkonzepte für biegebelastete Crashträger.* Dissertation, Technisch Universität Dresden, 2013.

[4] Kellner P., Steinbach K.: *Die 3D-Hybrid Leichtbautechnologie: Eine neuartige Stahl-GFK-Hybridbauweise für höchstbelastete Karosseriestrukturen.* In: 18. Dresdner Leichtbausymposium, 26./27.06.2014, Dresden.

[5] Endemann U., Glaser S., Völker M.: *Kunststoff und Metall im festen Verbund: Verbindungstechnik für Kunststoff-Metall-Hybridstrukturen.* Z. KU Kunststoffe, vol. 11/2002, p. 110-113, 2002.

[6] Meschut G., Augenthaler F.: *Hybridfügen von Mischbaustrukturen aus faserverstärkten Kunststoffen mit metallischen Halbzeugen.* Abschlussbericht 17617 N, Paderborn, 2015.

[7] Rasche M.: *Der Zugscherversuch in der Klebtechnik.* Z. Adhäsion - Messen und Prüfen, vol. 11, p. 36-43, 1990.

[8] Haider D. R., Krahl M., Gude M., Hengstmann R., Titze S., Haupt M.: *Continuous data measurement and analysis in automated manufacturing processes for hybrid lightweight structures.* In: SAMPE Conference, 14.-16.10.2017, Stuttgart, 2017.

[9] Maaß J., Gude M., Wolf M., Krahl M., Krämer A., Amend P., Roth S.: *Influence of injection moulding process parameters on the joint strength of hybrid fibre-reinforced thermoplastic with laser-structured metals.* In: ECCM - 17th European Conference on Composite Materials, 26.-30.06.2016, München, 2016.

[10] Koshukow W., Krahl M., Gude M., Götz P., Kirchhoff M.: *Influence of laser surface treatment for process-integrated joining of textile reinforced thermoplastic composites to metal sheets.* Key Engineering Materials, vol. 742, p. 366-373, 2017.

[11] DIN EN 1465: *Klebstoffe – Bestimmung der Zugscherfestigkeit von Überlappungsklebungen*. Standard, 2009.

[12] DIN EN ISO 1110: *Kunststoffe – Polyamide – Beschleunigte Konditionierung von Probekörpern*. Standard, 1995.

# THREE-POINT BENDING TEST ON CFRP-STEEL PROFILE HYBRID STRUCTURES

**Markus Muth[1*], Kay André Weidenmann[1]**

[1]Karlsruhe Institute of Technology (KIT), Institute for Applied Materials IAM–WK,

**ABSTRACT:** In lightweight structures the outstanding mechanical properties of carbon fibre reinforced plastics (CFRP) exhibit a high application potential. There are several ways to join structural CFRP parts to other components such as steel profiles without drilling the CFRP. Reasonable joining methods are extrinsic methods like adhesive bonding or embedded metal elements, so called inserts. Another possibility are intrinsic methods where the steel components are embedded in the CFRP during the manufacturing process. In previous studies of the authors, a shape optimized punctiform insert has been subject of research. The insert consists of a threaded shaft and a shape-optimized baseplate which is embedded between the fibre layers. The performance of such inserts under different types of loading has been investigated. In the work at hand, these inserts are used as the connecting element between the CFRP and the steel profile as an alternative to the state-of-the-art adhesive bonded steel profiles. Structures like this represent an option for profiles made out of bulk CFRP or steel. While the metal component introduces ductility and shear stiffness, the CFRP provides the necessary material stiffness and good fatigue properties. Hybrid CFRP / steel structural elements, which are primarily intended to absorb crash loads, are already used in automotive series production. The samples used for the experiments are manufactured by resin transfer moulding (RTM). In addition to the data provided by the testing machine, an inductive position is presented in this work to determine the influence of the connection on to the performance of the samples. So far, no experimental setup to enable complete data collection is available. This work presents an experimental setup and first results for three-point bending of CFRP-steel profile hybrid structures in quasi-static conditions.

**KEYWORDS:** hybrid, CFRP, joining, punctiform inserts, quasi-static bending tests.

## 1 INTRODUCTION

The potential to carry high structural loads whilst keeping the weight of the component low is a property that is met by continuous carbon fibre reinforced plastics (CFRP). With regard to multi material design [1], mechanically fastened joints are well suited for CFRP structures since they offer the possibility of a detachable and inexpensive load bearing structure. Due to the drilling of the CFRP when bolts or rivets are used as the connecting element, the applied local bearing stresses reduce the load bearing capacity significantly [2, 3, 4]. Another possibility of joining avoiding these disadvantages are embedded metal elements which are made of a boundary plate and a bushing welded onto. These metal elements, so-called inserts, are embedded during the preform process of the CFRP. Depending on the type of insert an optimum load path around the insert's stud can be ensured [5]. To ensure an optimum load path, cutting of the fibres has to be avoided and the fibres have to be guided around the insert's stud during the preform process. So-called bighead® inserts have been investigated under tensile (pull-out), compressive (push-in) and bending loads by Ferret et al. [6]. With regard to the size of the inserts boundary plate, it was shown that inserts with a large baseplate show failure around the insert's stud which leads to a reduction of the load bearing capacity in comparison to inserts with a smaller baseplate. Investigations by Fleischer et al. [7] are describing the influence of different surface treatments to the embedded inserts performance. The influence of thickness and diameter of the inserts boundary plate, fibre volume fraction and height of point of application have been carried out by Schwarz et al. [8] under bending loads. Quasi-static tensile, bending, torsion, compressive and shear loads where applied to in CFRP embedded inserts by Gebhardt et al. [9] and they were able to identify tensile loads as the most critical load case. In addition, compressive (push-in) loads have been identified as the second most critical load case. In the work at hand, a shape optimized version of the insert was manufactured by turning and is used as in [5, 7, 9–11]. It has been developed by the Institute of Production Science (wbk) at Karlsruhe Institute of Technology, [12]. The performance of the shape optimized insert under different types of loading and near service loads has been investigated earlier by the authors [13, 14]. The shape optimized insert showed for quasi-static tensile loads a 66% higher load bearing capacity.

In order to pursue the concept of the inserts consistently, in this contribution multiple inserts are embedded in the CFRP and a hat profile is connected to the inserts by use of the inserts threaded bushing. Since there are no investigations on such components a three point bending setup for such specimens had to be designed with an inductive position transducer integrated in the setup to evaluate the different displacements. To gain knowledge about the influence of different numbers of inserts, distributed over the entire length of the hat profile, parts with a minimum of four inserts and a maximum of 14 inserts are tested. As a reference a state-of-the-art adhesive bonded hat profile is investigated. The long-term goal is the development and testing of intrinsic manufactured CFRP/steel hybrid profiles where the steel profiles shoulders are integrated between the CFRP layers during the preforming process. Such profiles combine the feature of both materials without any additional joining process.

## 2 MATERIALS AND SPECIMEN GEOMETRY

The CFRP part of the components with dimensions of 194 x 275 mm² (c.f. Fig. 1) manufactured with eight plies of biaxial non-woven carbon fibre fabric (Hexcel NLT00 series, 0°/90°, 200 g/m²) and an epoxy matrix resin by Sika® (Biresin® CR170/CH150-3) with a resulting fibre volume fraction of 44.4%. For the first parts tested the lowest carbon fibre plie had a 90° angle to determine the influence of the layer structure on the displacement, difference in displacement of the CFRP and the crosshead and the load bearing capacity of the parts.

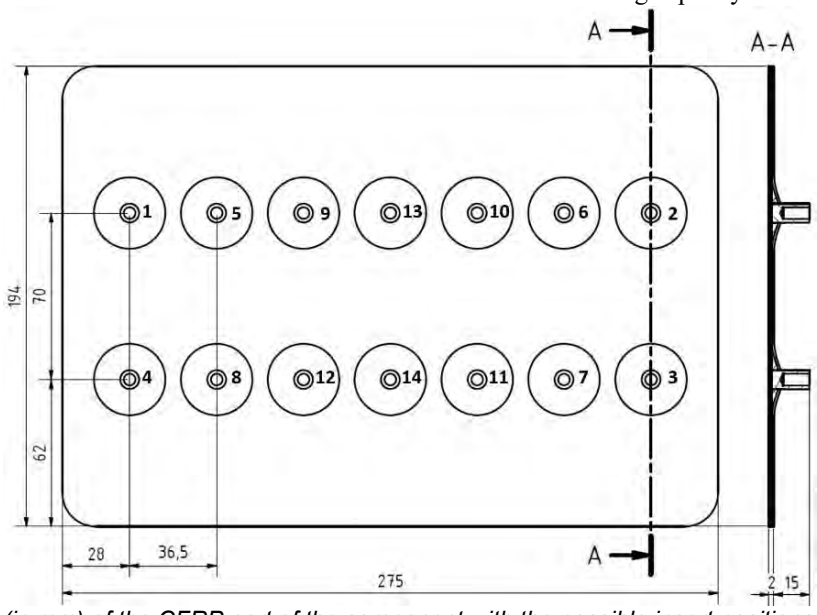


***Fig. 1** dimensions (in mm) of the CFRP part of the component with the possible insert positions*

Fig. 2 shows the shape optimized insert manufactured by turning. If these inserts would be used in larger unit volumes it would decrease the production effort und cost of such inserts when metal powder injection moulding would be used for the production. The hat profile (c.f. Fig. 3) is made from sheet-material which has been formed to the desired shape. All inserts and also the hat profile is made of stainless steel (ANSI 304) to prevent corrosion. The inserts are placed in the middle of eight carbon fibre fabric layers during preforming. Last, the CFRP parts are manufactured by RTM at the Institute for Production Science (wbk) of Karlsruhe Institute for Technology. A hydraulic press (Lauffer type RP 400) and a flow metering and mixing machine (Tartler Nodopur VS-2K) are used to carry out the infiltration of the CFRP parts. The infiltration pressure is 9 bar and the specimens are cured for 60 minutes at 70 °C.

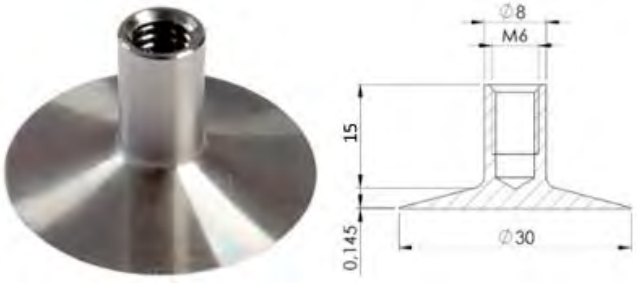


***Fig. 2** representative image and dimensions of the shape optimized punctiform insert*

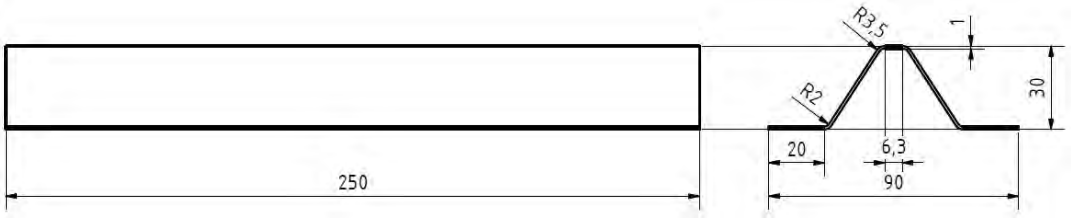


***Fig. 3** dimensions (in mm) of the stainless steel hat profile*

In the tests three different types of components are used. The first type is made out of a CFRP plate without any inserts and an adhesive bonded hat profile (c.f. Fig. 4 a), for these components “UHU Endfest 300”, a 2K-Epoxy adhesive, which is cured for 60 minutes at 70°C is used. For the second type, a CFRP plate with four inserts embedded is used. For the four inserts the positions one to four (c.f. Fig. 1) are used since they represent the minimum number and maximum distance between the inserts possible (c.f. Fig. 4 b). For the components with 14 inserts all possible positions are used which represent the maximum number of inserts and the minimum distance between the inserts (c.f. Fig. 4 c). For both component types, the hat profile is fastened to the inserts thread using screws of strength class 12.9.

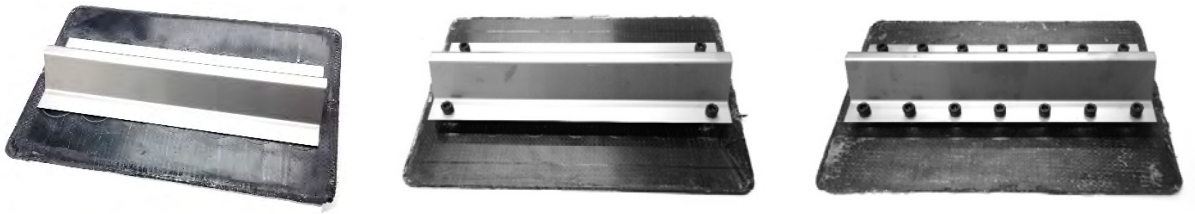

***a)*** ***b)*** ***c)***

***Fig. 4** exemplary images of the components with a) adhesive bonded hat profile, b) component with four inserts and c) component with 14 inserts*

## 3 EXPERIMENTAL SETUP

The expected loads for this structural part are crash scenarios. Thus, testing has to deal with the absorption of crash loads and the test setup and specimen geometry differ from geometries used in [5, 7, 9, 11–14]. Nevertheless, knowledge about the quasi-static bending load case has to be gained first. The dimensions of the three point bending setup are shown in Fig. 5. The crosshead speed used for the tests differs slightly depending on the tested component. The components have been tested under quasi-static conditions with crosshead speeds from 1 to 3 mm/min.

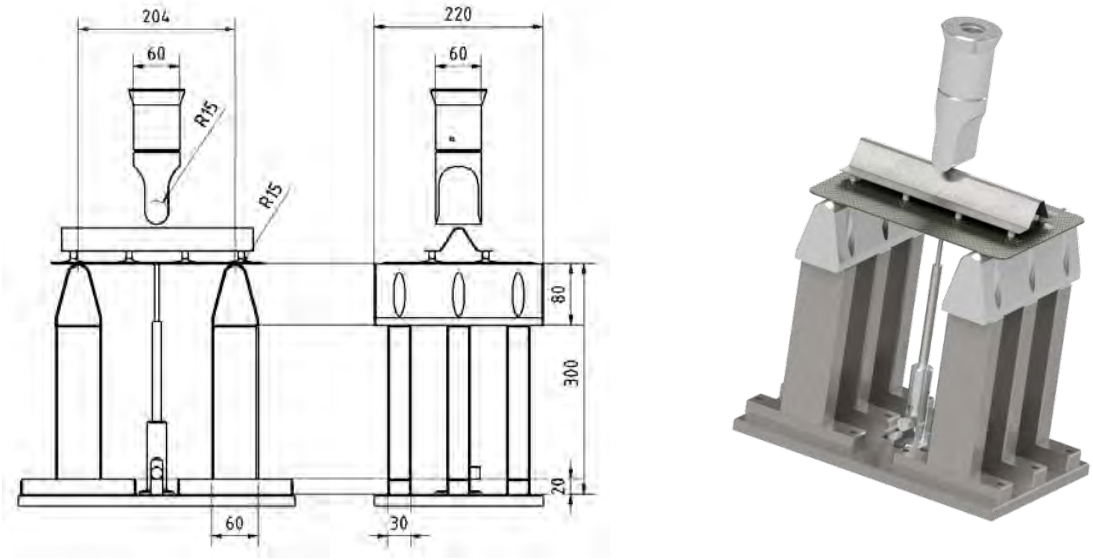


***a)*** ***b)***

***Fig. 5** a) dimensions of the three point bending setup and b) rendered image of the setups CAD-Model*

The quasi-static bending tests were performed on a 100 kN Zwick universal testing machine (c.f. Fig. 6). A peculiarity of this testing machine had to be considered for the digital image correlation (DIC): the upper crosshead is fixed and the lower crosshead is the one that moves.

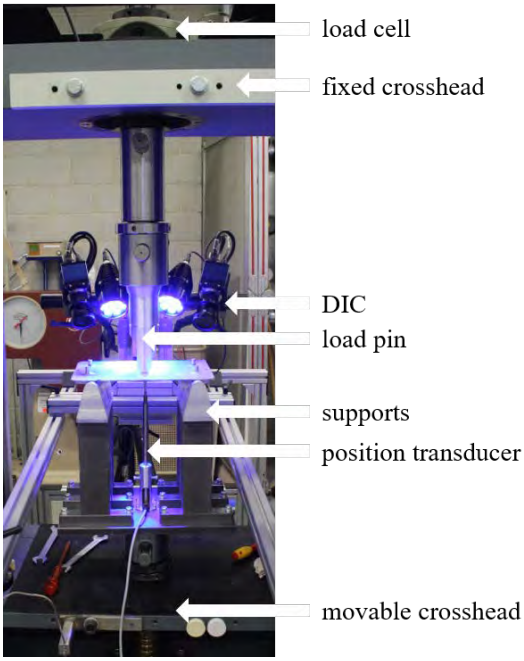


***Fig. 6** test setup in the universal testing machine from Zwick*

## 4 RESULTS AND DISCUSSION

For the experimental setup two different abortion criteria have been chosen. On the one hand, the displacement of the CFRP laminate is limited by the maximum displacement of the position transducer which is 50 mm in total. On the other hand, a load drop of 80% of the maximum applied force aborts the experiment. For all components, the displacements, the applied forces, the displacement of the position transducer and the difference in displacement of the crosshead and the position transducer will be presented. The specimen with the adhesive bonded hat profile serves as a reference for the two other tested component types.

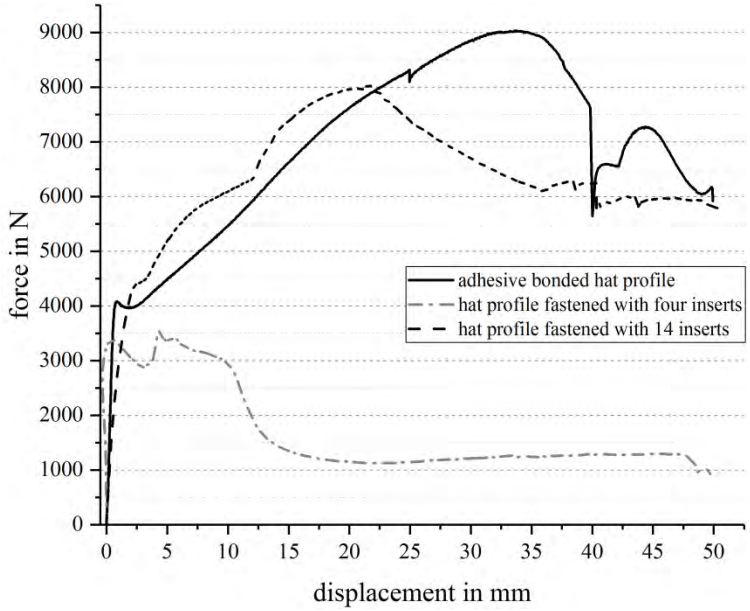


***Fig. 7** force-displacement curves of three point bending tests for the three different component types*

What all tests carried out have in common is, that they had to be aborted when the position transducer on the bottom side of the CFRP reached its maximum displacement. In Fig. 7 the applied forces are shown in reference to the displacement of the CFRP. It can be seen in Fig. 7, that the component with the adhesive bonded hat profile allows the highest absolute applied loads. But with the component whose hat profile is joined with 14 inserts a value which is just 11% percent lower can be achieved. The lowest applicable load is possible with the component with four inserts. The experiment has not been aborted when the applied load dropped by 70% to be able to determine the maximum deflection of the CFRP plate.

The maximum applied forces, the maximum difference in displacements of the position transducer and the crosshead, the component weight and the weight related maximum forces can be seen in Table 1.
The results showed, that the state-of-the-art method to connect a metal hat profile to a CFRP laminate enables higher applicable loads as the other two tested component types. Especially when looking at the weight related values for the three tested components in Table 1 it becomes obvious that the component with the adhesive bonded hat profile shows much better values due to the significantly lower weight of the component.

***Table 1*** *results of the three point bending experiments of the three component types*

| Nb. inserts | Δ displ. (mm) | max. force (N) | weight (g) | F/m (N/g) |
|---|---|---|---|---|
| 0 | 11,8 | 9036 | 399,0 | 22,6 |
| 4 | 38,4 | 3541 | 440,5 | 8,0 |
| 14 | 29,6 | 8035 | 607,5 | 13,2 |

An image of the component with adhesive bonded hat profile after the test is shown in Fig. 8 a. The hat profile is visibly deformed only where the load pin touches its top and in the immediate vicinity. It should be noted that the deformed hat profile detached from the CFRP laminate, which jumped back in the original form without any remaining deformation or visible damage, when the applied load has been reduced to take the specimen out of the experimental setup.

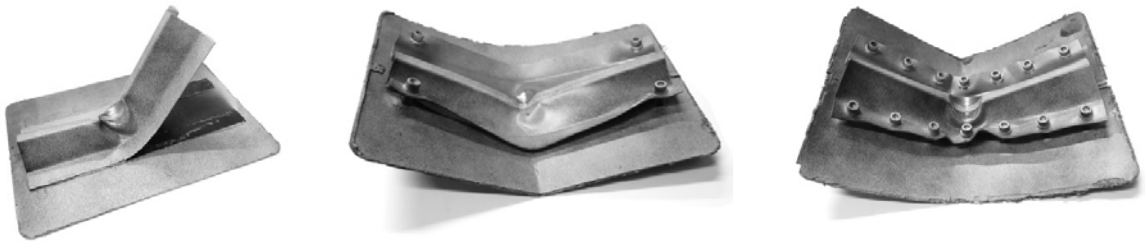

***a)*** ***b)*** ***c)***

***Fig. 8*** *images of the components after the quasi-static three point bending test, a) component with adhesive bonded hat profile, b) component with hat profile fastened by four inserts and c) component with hat profile fastened by 14 inserts*

The component with the hat profile fastened with four inserts after the test is shown in Fig. 8 b. As shown in Fig. 7 the displacement of the bottom of the CFRP of the component with four inserts drops to small negative numbers (approx. 0.30 mm) for loads below 3 kN. The reason for that is, that the force applied to the hat profile is not redirected in the CFRP laminate between the supports so a bending force in the opposite direction as of the applied force is induced. For loads over 3 kN the bending of the hat profile forces the CFRP laminate to bend in the direction of the applied force. After that, the hat profile was flattened during the experiment until its bottom touched the CFRP. In contrast to the component with adhesive bonded hat profile the profile is deformed over the whole length of the profile. A crack, as can be seen in Fig. 8 b emerged right when the position transducer reached its maximum. Therefore, it can be assumed that the maximum possible deformation of the CFRP with the used layer structure and the hat profile joined by the four inserts is in the range of 50 mm. After the component was removed from the experimental setup the deformation stayed as it was when the experiment stopped.
The component with the hat profile fastened by the maximum number of inserts (14) after the three point bending test is shown in Fig. 8 c. The components hat profile has not been flattened during the test because this is prevented by the inserts the profile is fastened to. But due to the distance between the top of the CFRP and the bottom of the hat profiles shoulders they buckled between the points connected to the inserts' studs. In the middle section where the load pin hits the hat profile it is pushed all the way down to the top side of the CFRP but

the deformation of the whole profile is much lower than the one for the components with four inserts which is also indicated in Table 1 where the difference of the displacement is much lower for the component with 14 inserts. A peculiarity for this type of component is, that on the lower side of the CFRP, under baseplates of the inserts, delamination occurs due to the forces applied through the profile which is redirected in the insert's stud and leads to compressive forces in the CFRP laminate. Like for the specimen with four inserts the crack which can be seen in Fig. 8 c emerged when the position transducer reached its maximum displacement. Therefore, also for the component with the hat profile joined by 14 inserts and the used layer structure the maximum deformation of the CFRP is in the range of 50 mm.
Not only for the weight related force values but also for the stiffness the component with the adhesive bonded hat profile shows the highest values (c.f. Fig. 9). The reason for that is, that for the adhesive bonded hat profile the force is redirected through a much higher area as for the component with 14 punctiform load introduction elements. The lowest component stiffness is provided by the component with four punctiform inserts. The reason for that is, that force applied to the hat profile can't be redirected to the CFRP where it is applied because no load introduction element is placed in this area.

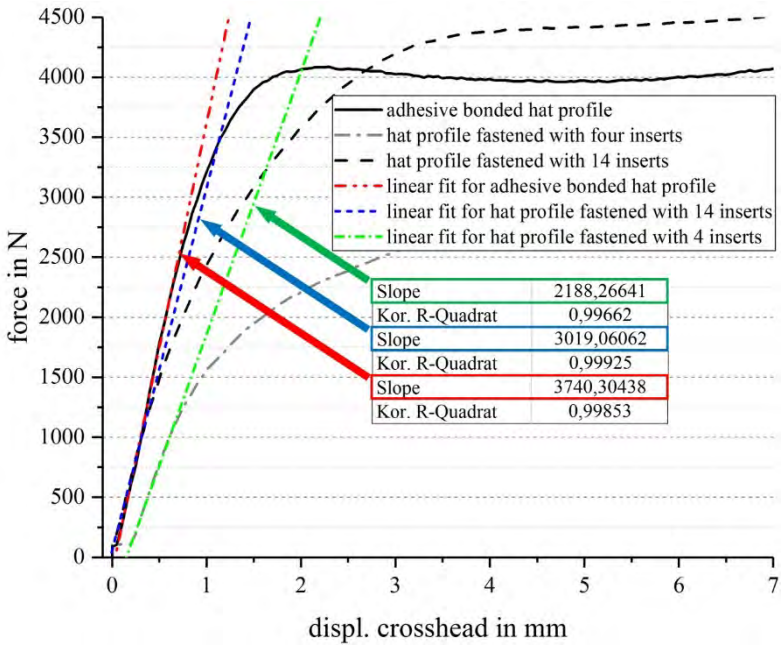


***Fig. 9*** *force-displacement curve to determine the component stiffness (N/mm)*

## 5 CONCLUSION AND OUTLOOK

One goal of the work presented was, to determine whether it is possible to gather all the data needed to evaluate the test on the complex type of component used in the work at hand and to show the differences in the deformation behaviour compared to state-of-the-art hybrid profiles which is represented by the components with an adhesive bonded hat profile. An inductive position transducer was integrated in the experimental setup to evaluate the displacements of the CFRP laminate and the load pin independently.
As expected the component with four embedded inserts showed the lowest values for the maximum applied force and also despite the significantly lower weight, compared to the component with 14 inserts, for the weight related value. The reason for that is that the component with four inserts lacks a load introduction element from the hat profile into the CFRP at the position where the load is introduced from the load pin into the hat profile.
The behaviour and the values of the component with four inserts shows in particular that a load introduction element from the hat profile in the CFRP laminate in the region where the load is introduced from the load pin in the hat profile is of the utmost importance. Nevertheless, the comparison between the other two component types shows, that it is possible to reach values of the absolute applied force near the values of the state-of-the-art component type also with detachable joints like embedded inserts.
For further investigations the setup of the DIC has to be adapted either to cover the whole component or to evaluate individual areas like the CFRP, single inserts, the hat profile or smaller regions of the hat profile separately from each other on different samples. Moreover, an additional video capturing system provided by Zwick will be installed to be able to gather more information about the complex components and they're behaviour. Further

tests should be carried out for more components of the same type as already tested and also with insert numbers between four and 14 inserts. Additionally, test with a layer structure of the carbon fibre fabric with 0° orientation in the outer layers. To determine the crash worthiness and the fatigue strength of such components dynamic test and cyclic tests will be carried out.

## 6 ACKNOWLEDGEMENT

The work at hand is based on investigations of the subproject 3 – „Fundamental research of intrinsically produced FRP-/metal-composites – from embedded insert to load bearing hybrid structure "- of the priority program 1712 „Intrinsic hybrid composites for lightweight load-bearings ", which is kindly supported by the German Research Foundation (DFG). The authors kindly acknowledge the Institute for Production Science (wbk) of KIT for the manufacturing of the specimens within the cooperation in the abovementioned subproject.

## REFERENCES

[1] Eriksson, I.: *On the bearing strength of bolted graphite/epoxy laminates*. Journal of Composite Materials, 24(12):1246 – 1269, 1990.

[2] Camanho, P. P., Lambert, M.: *A design methodology for mechanically fastened joints in laminated composite materials*. Composites Science and Technology, 66(15):3004 – 3020, 2006.

[3] Xiao, Y., Ishikawa, T.: *Bearing strength and failure behavior of bolted composite joints (part I*. Composites Science and Technology, 65(7):1022 – 1031, 2005.

[4] Kolesnikov, B., Herbeck, L., Fink, A.: *CFRP/titanium hybrid material for improving composite bolted joints*. Composite Structures, 83(4):368 – 380, 2008.

[5] Gebhardt, J., Fleischer, J.: *Experimental investigation and performance enhancement of inserts in composite parts*. Procedia CIRP, 23 7 – 12, 2014.

[6] Ferret, B., Anduze, M., Nardari, C.: *Metal inserts in structural composite materials manufactured by RTM*. Composites Part A: Applied Science and Manufacturing, 29(5-6):693 – 700, 1998.

[7] Fleischer, J., Gebhardt, J.: *Experimental investigation of metal inserts embedded in composite parts manufactured by the RTM process*. In: 13th Japan International SAMPE Symposium and Exhibition, Nagoya, Japan, 2013.

[8] Schwarz, M., Magin, M., Peil, C., Schurmann, H.: *Thin-walled FRP-laminates and local bending moments-incompatible or solvable by a skillful design*. Internationale Tagung für Verstärkte Kunststoffe und Duroplastische Formmasse, 28 29, 2004.

[9] Gebhardt, J., Pottmeyer, F., Fleischer, J., Weidenmann, K.: *Characterization of metal inserts embedded in carbon fiber reinforced plastics*. In: Materials Science Forum, 2015.

[10] Wilkening, J., Pottmeyer, F., Weidenmann, K. A.: *Research on the interfering effect of metal inserts in carbon fiber reinforced plastics manufactured by the RTM process*. In: 17th European Conference on Composite Materials, Munich, Germany, 2016.

[11] Pottmeyer, F., Weispfenning, M., Weidenmann, K. A.: *Research of the Load Bearing Capacity of Inserts Embedded in CFRP under Different Loading Conditions*, 2016.

[12] J. Gebhardt: *Strukturoptimierung von in FVK eingebetteten metallischen Lasteinleitungselementen*, Shaker Verlag, 2016.

[13] Muth, M., Pottmeyer, F., Weidenmann, K. A.: *Investigation of the failure behavior of metal inserts embedded in CFRP under cyclic loading*, 2016.

[14] Pottmeyer, F., Muth, M., Weidenmann, K. A.: *Research of the Load Bearing Capacity of Shape-Optimized Metal Inserts Embedded in CFRP under Different Types of Stresses*. In: Key Engineering Materials, Vol. 742, 2017.

# EXPERIMENTAL AND NUMERICAL INVESTIGATIONS ON THE DEFORMATION BEHAVIOR OF FIBER-METAL-ELASTOMER LAMINATES IN 3-POINT BENDING EXPERIMENTS USING DIGITAL IMAGE CORRELATION

**Vincent Sesser[1*], Wilfried V. Liebig[2], Luise Kärger[2], Kay A. Weidenmann[1]**

[1]Karlsruhe Institute of Technology (KIT), Institute for Applied Materials (IAM-WK)
[2]Karlsruhe Institute of Technology (KIT), Vehicle System Technology (FAST)
…

**ABSTRACT:** Compared to conventional fiber-metal laminates (FML) such as GLARE (glass-fiber reinforced aluminum) or CARALL (carbon fiber reinforced aluminum), fiber-metal-elastomer laminates (FMEL) offer the advantage of a structural material with adjustable damping properties. These hybrid laminates are built from sheets of fiber reinforced plastics and metal sheets which are bonded with an elastomeric interlayer. When this laminate configuration is bent, high shear deformation of the elastomer layers occurs. This shear deformation is decisive for the damping behavior of the laminate. In a 3-point bending setup the laminate shows counter bending beyond the outer supports.
In the present study, quasi-static 3-point bending tests are performed on hybrid fiber-metal-elastomer laminates. The elastic deformation behavior is evaluated by means of digital image correlation. The bending line of the samples is monitored, as well as the shear deformation of the elastomeric layers over the laminate thickness. The shear strains are evaluated in laminate direction and over the thickness of the specimens. The results are compared to a numerical model built up in Abaqus which reconstructs the 3-point bending experiment.

**KEYWORDS:** Fiber metal laminate, Fiber metal elastomer laminate, Digital image correlation, 3 point bending

## 1 INTRODUCTION

Common FML such as GLARE can be found in various aerospace applications [1]. Beside their good mechanical properties, they show high fatigue and impact resistance as well as high fracture toughness [2]. CARAL, the combination of carbon-fiber-reinforced plastics (CFRP) and aluminium sheets, however shows mayor disadvantages due to galvanic corrosion in the interface and a big mismatch of the coefficients of thermal expansion [3]. To overcome these drawbacks the metal sheets and the CFRP layers need to be isolated. Therefore, an elastomer interlayer can be introduced between the two constituents transforming the FML into an FMEL. The shear compliant elastomer has mayor influence on dynamic behaviour of the laminate. During bending vibration, the elastomer is deformed in shear which enables these laminates to damp bending vibrations effectively. This damping mechanism, where a relatively soft viscous elastic layer is embedded between two stiff constraining layers, is known as constrained layer damping [4]. Usually this damping mechanism is applied to vibrating structures by adding some sort of damping tape to the surface of the finished product [5]. FMEL however, possess high damping properties due to their enclosed viscoelastic elastomer layers.
As the damping of the laminates is mainly caused by shear deformation in bending loads, it is important to know how big these strains of the elastomeric interlayers are. Therefore, three point bending tests were performed on different FMEL configurations. Due to the shear compliant layer it is also important to evaluate the shear strains in the elastomer layers outside the support span, when damping measurements are done. In order to effectively design structures with these type of laminates a numerical model was built up to simulate the mechanical behaviour. Aim of this study is to quantify the shear deformations of the elastomer layers and see if the numerical model can reproduce the deformations.

# 2 MATERIAL AND METHODS

## 2.1 MATERIAL

For the experimental investigations specimens of 250 x 15 mm² with different lay-ups were cut from plates of 400x400 mm². The FMEL were manufactured from unidirectional CFRP prepreg by Hexcel in a biaxial layup with a ply thickness of 0.15 mm (HexPly M77/38%/UD150/CHS/12K/T700), 2024 aluminium sheets with a thickness of 0.3 mm (2024 T3 ALCLAD AMS-QQA-250/5) and two different elastomers provided by Gummiwerk KRAIBURG GmbH & Co. KG. The batch number of the elastomers are SAA9579-52 and HAA9275-45, respectively. The two elastomers differ in the Young's moduli. Hereinafter, the SAA9579-52 is referred to as the soft and the HAA9275-45 as the hard elastomer. Table 1: shows the tested FMEL configurations. All laminates consist of five layers. For the laminates with CFRP on the outsides the UD layers are stacked in $[0/90]_S$ lay-up. For the laminates with CFRP in the middle the stacking sequence is [0/90/0/90/0/90]. All laminates, except the configuration CFRP-El_soft_thick-AL have a theoretical thickness of 2.5 mm. For the first laminate the theoretical thickness calculated from the manufacturer's datasheet is 2.8 mm. The laminates were consolidated in a hot mold with a pressure of 40 bar at a temperature of 150 °C for 300 s, as dictated by the datasheets of the manufacturer.

***Table 1:*** *Tested FMEL configurations, with theoretical layer thickness (from the datasheet) in mm in brackets*

| CFRP-El_soft_thick-AL | CFRP-El_soft-AL | CFRP-El_hard-AL | AL-El_soft-CFRP | AL-El_hard-CFRP |
|---|---|---|---|---|
| CFRP (0.6) | CFRP (0.6) | CFRP (0.6) | Al (0.3) | Al (0.3) |
| El_soft (0.65) | El_soft (0.5) | El_hard (0.5) | El_soft (0.5) | El_hard (0.5) |
| Al (0.3) | Al (0.3) | Al (0.3) | CFRP (0.9) | CFRP (0.9) |
| El_soft (0.65) | El_soft (0.5) | El_hard (0.5) | El_soft (0.5) | El_hard (0.5) |
| CFRP (0.6) | CFRP (0.6) | CFRP (0.6) | Al (0.3) | Al (0.3) |

Several quasistatic tensile test were conducted to gain the Young's modulus of the CFRP and the elastomer materials. The results from these test are used for the numerical investigations. Table 2: shows the values of the Young's modulus data for a strain range of 0.25% -1 %. The stiffness of the two elastomers differs in one magnitude. As the elastomers undergo big deformations during the bending test, the material behaviour of the elastomers was fitted to the stress-strain curves from the tensile tests for the numerical model. As the elastomer is mainly deformed in shear during the bending test, the shear modulus is calculated by equation 1 [6] with an transversal contraction coefficient of ν = 0.48.

$$G = \frac{E}{2(\nu + 1)} \qquad (1)$$

***Table 2:*** *Material data used for numerical simulation. Youngs modulus is calculated from 0.25-1 % strain (* from Datasheet)*

| | UD-CFRP | | Elastomer | | Aluminum * |
|---|---|---|---|---|---|
| Young's modulus in GPa | 0° | 90° | soft | hard | 73.1 |
| | 113.74 ± 3.0 | 7.75 ± 0.12 | 0.044 ±0.003 | 0.435±0.014 | |

## 2.2 METHODS

### 2.2.1 EXPERIMENTAL

The setup for the quasistatic experimental three point bending tests is displayed in Fig. 1. The experiments were performed on a 100kN Zwick universal testing machine. The machine was equipped with a 1 kN load cell for the experiments. According to DIN EN ISO 14125 [7] the support span for three point bending test

should be 40 times the specimen thickness for material with unidirectional carbon fibre reinforcement. Therefore, a support distance of 100 mm was chosen for all specimens. To capture the shear strains beyond the lower supports the specimens length was set to 250 mm, so that sufficient material overlap occurs. The crosshead displacement speed was set to 5 mm/min. The deflection of the specimen under the loading nose was measured with a laser triangulation sensor (optoNCDT 20300 by MicroEpsilon). The deformation over the thickness of the specimens was tracked with an Aramis 4k professional system by GOM. In order to measure the deformation precisely the DIC system had to be positioned close to the specimens so that not the whole laminate could be recorded with the camera. Therefore, a second camera was placed behind the specimen which recorded the whole deflection curve.

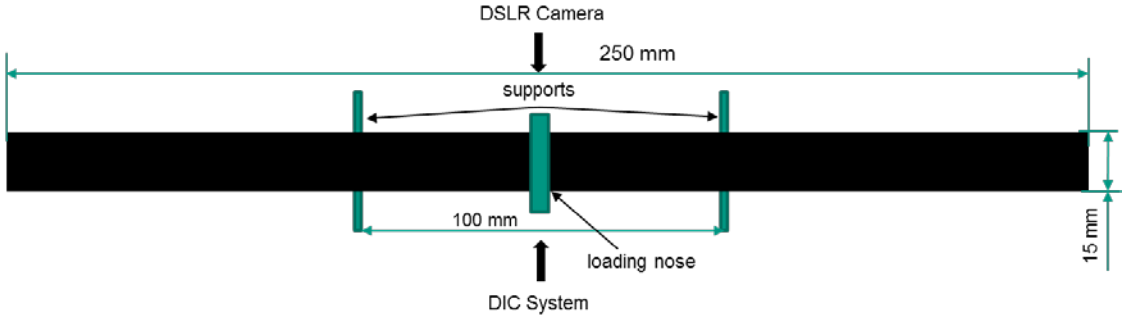


***Fig. 1*** *Setup for tree point bending test with DIC measurement. View from above.*

The specimens were deformed up to a deflection of about 10 mm. The specimens did not fail at this point and showed no signs of failure on visual examination. Thus some specimens were reused for the same bending test when a different positioning of the DIC system was required to measure the deformation behaviour of a different section of the 250 mm long specimen. The picture of the whole bending curve was always taken on the first bending cycle. For evaluation of the shear strains in the elastomer layers three different positions according to Fig. 2 a) were chosen. The Vert_1 axes in thickness direction is placed in the middle between the lower supports and the loading nose. The Hori_1 and Hori_2 directions along the x direction are placed in the middle of each elastomer layer. An example of the $\varepsilon_{xy}$ shear strains measured by the DIC system during an bending experiment can be seen in Fig. 2 b). The specimen was recorded with a resolution of 274 pixels over the thickness, with a facet size of 8 pixels for the evaluation along the Vert_1 direction.

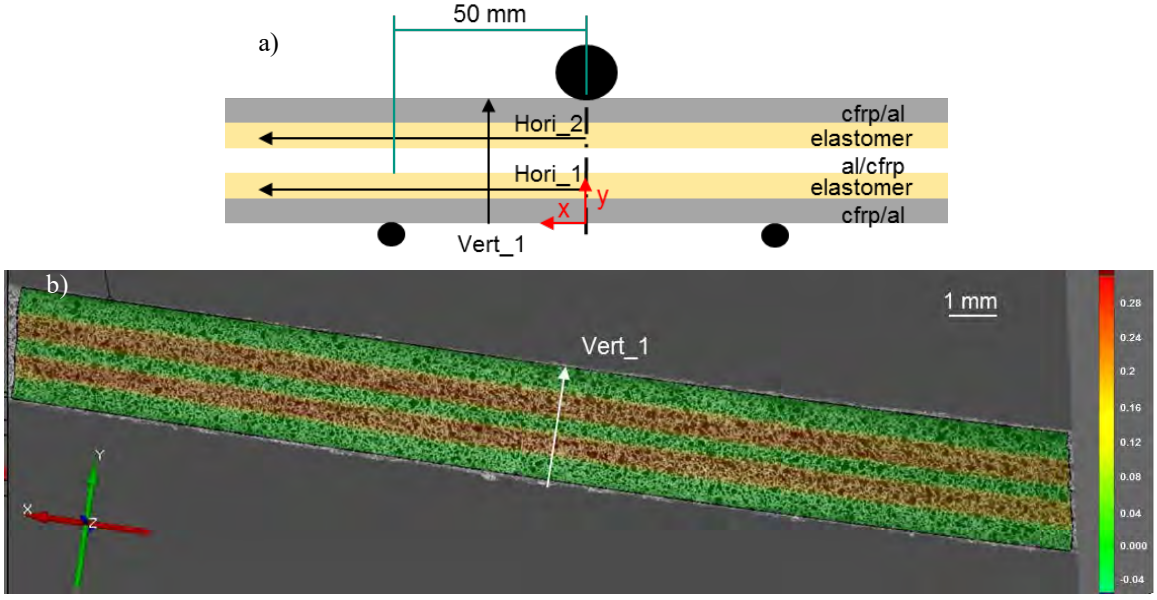


***Fig. 2*** *a) Evaluation of the bending experiments. Arrows show directions along which the shear strains is examined with the corresponding names. b) example of the shear strains between loading nose and supports in an FMEL specimen measured with the DIC system.*

### 2.2.2 NUMERICAL MODEL, BOUNDARY CONDITIONS AND MATERIAL PROPERTIES

For numerical studies, the FE software Abaqus/CAE 2017 is chosen. Based on the geometry of the specimens, a parametric-numerical model was programmed by using implemented Python script language. The

laminate is represented by 3D multi-layer model where C3D20 (20 nodes, quadratic brick) elements are applied. Every layer is captured by three elements through the thickness. For both supports (radius = 2mm) and the loading nose (radius = 5mm) 3D analytical rigid shell elements are utilized to reflect the sliding effect at increasing deflection. Sliding effects itself are assumed to be frictionless, owing to the fact, that the simulation is path controlled and stopped at several values of displacement.
CFRP as well as aluminum is assumed to behave linear-elastic. Whereas the difference in the mechanical tension and compression behavior for CFRP is taken into account by $E_c$=0.85*$E_t$. While the elastomer exhibits a hyperelastic material behavior, which is described by the Bergstrom-Boyces model. The material calibration takes place by using MCalibration V4.6 also providing the user material model for numerical studies for Abaqus.

# 3 RESULTS

## 3.1 EXPERIMENTAL RESULTS

The deflection curves of the specimens at a theoretical strain of ε=1.5% on the outer fibres for an isotropic material is shown in Fig. 3. The specimens with the soft elastomer (black) show counter bending outside the supports, whereas for the specimens with the hard elastomer (orange) this phenomenon could not be seen. It can also be seen that for the specimens with the aluminium layers on the outside the counter bending is lower. It has to be noted that the bending lines are created by using a reverse engineering process, so that there are some variations in the maximum deflections from the measured values with the laser triangulation sensor. However, the difference between the two elastomers can be clearly seen.

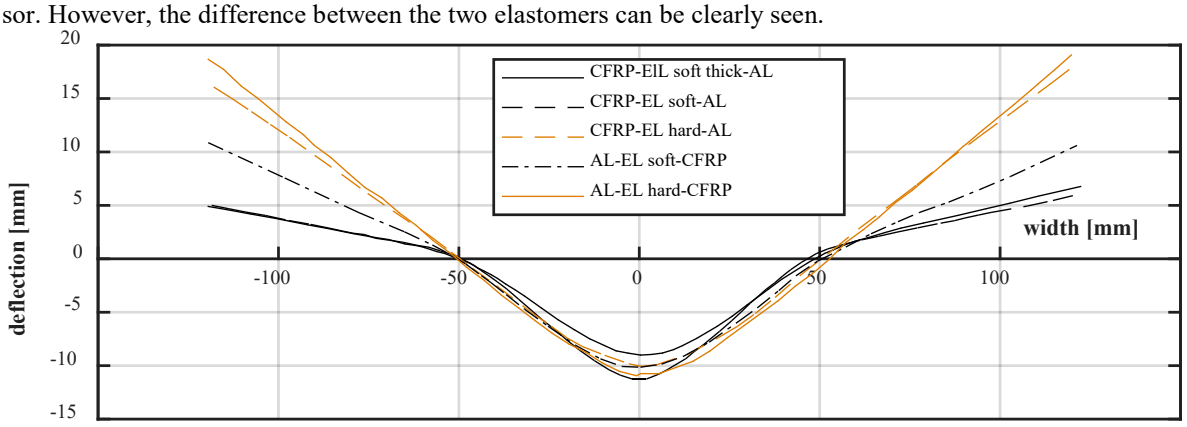


***Fig. 3*** *Deflection curves of the specimen from experimental results*

To understand the ongoing deformations in the FMEL during bending Fig. 4 shows an evaluation along the Vert_1 direction according to Fig. 2. The displacement and the shear strain were measured on a CFRP-El_soft-AL specimen (see Table 1:). Separate, rotated coordinate systems are chosen by the evaluation software for each section, so that it's y-orientation is always along the thickness of the specimens (see Fig. 2 b). Three discrete values (1 mm, 3 mm, 6 mm) of the middle deflection were chosen. One can see that only the elastomer layers are deformed in shear due to their low shear modulus. The shear strain in each elastomer layer (Fig. 4 b) shows two peaks and a small decline in the middle. It is assumed that this behavior is caused by a lack in resolution over the thickness of the specimen. As each elastomer layer is only 0.5 mm thick it is hard to obtain a pattern which is fine enough to measure the shear distribution over each layer with a high resolution.

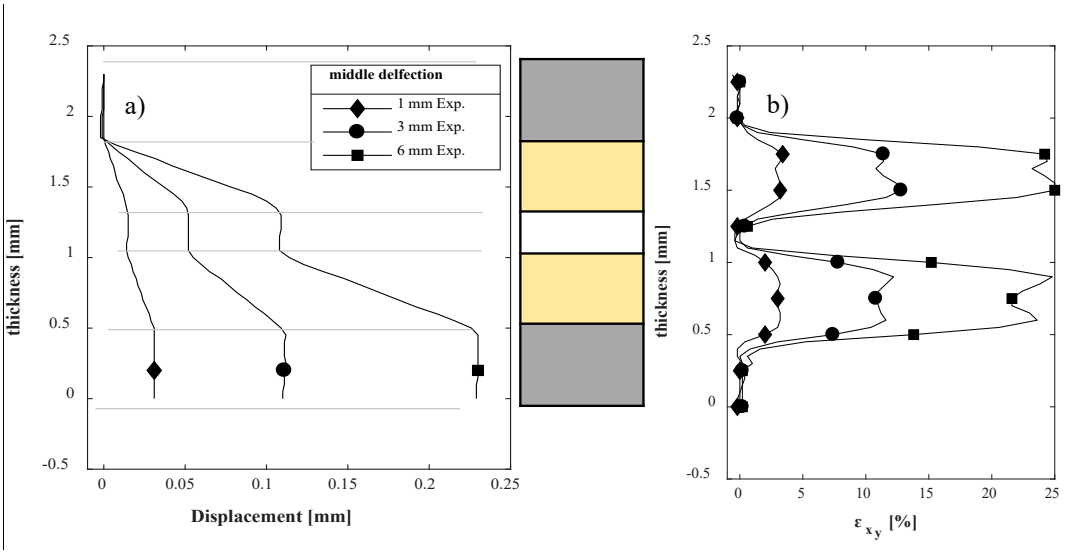


***Fig. 4*** *Displacement (a) and shear strain (b) of each layer of an CFRP-El_soft-al laminate at the position Vert_1 according to Fig. 2 from experimental results.*

To evaluate the shear strain in the elastomer layers along the laminate plane a broader image section was chosen which captures one half of the specimen from the loading nose until 10 mm beyond the lower supports. In Fig. 5 the shear strains along the Hori_1 direction can be seen for all different laminate configurations at different middle deflections. The orange curves mark the specimens with the hard elastomer. The x value is set according to the coordinate system in Fig. 2. A value of 0 mm marks the point under the loading nose, 50 mm represents the supports. It can be seen that for specimens with the hard elastomer (orange curves) the shear strain is much lower compared to the laminates with the soft elastomer. In the range beyond the lower supports (50 mm-60 mm) the hard elastomer is hardly deformed in shear. However, the soft elastomer still has shear strains of 5%-10 % which decreases with further distance from the supports. This decrease in shear strain results in the counter bending of the specimens. The highest shear strains were measured for the specimen with the thicker elastomer layers. To evaluate the shear strains in both elastomer layers of each FMEL configuration the curves from Fig. 5 were smoothed using a cubic spline function, then the fitted curves were evaluated for a x coordinate of 25 mm which marks the middle between the loading nose and the lower supports. Fig. 6 shows the results of the shear strains in both elastomer layers (Hori_1 and Hori_2) for x=25 mm. This point marks the maximum shear strain in the specimens as it can be seen in Fig. 5. A linear increase of the middle deflection (from 1 mm to 6 mm) leads to a linear increase in shear strain in the elastomer. It can also be seen that for all specimen the shear strain of the upper elastomer layer (Hori_2) is slightly higher than in the lower layer (Hori_1).

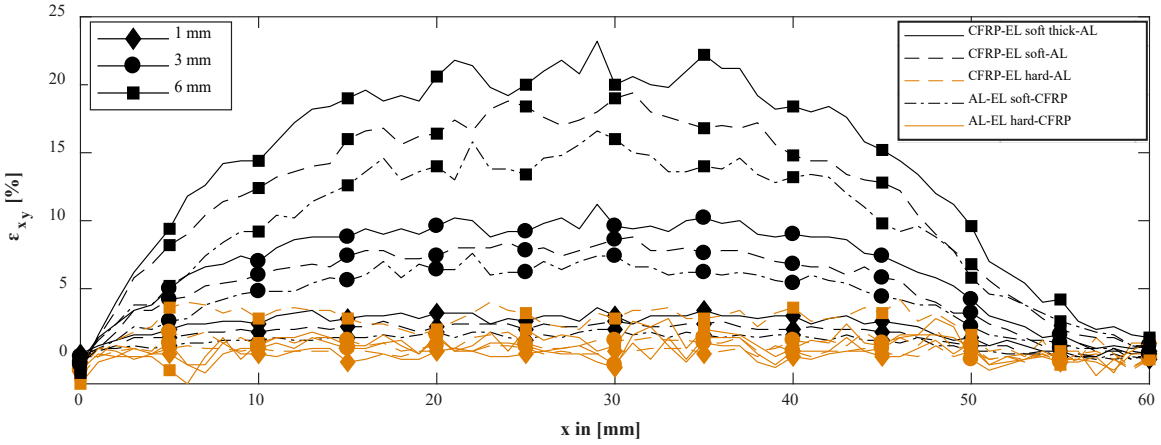


***Fig. 5*** *Shear strain along the Hori_1 axes according to Fig. 2 from experimental results. The shear strain is evaluated for different middle deflections of 1, 3 and 6 mm.*

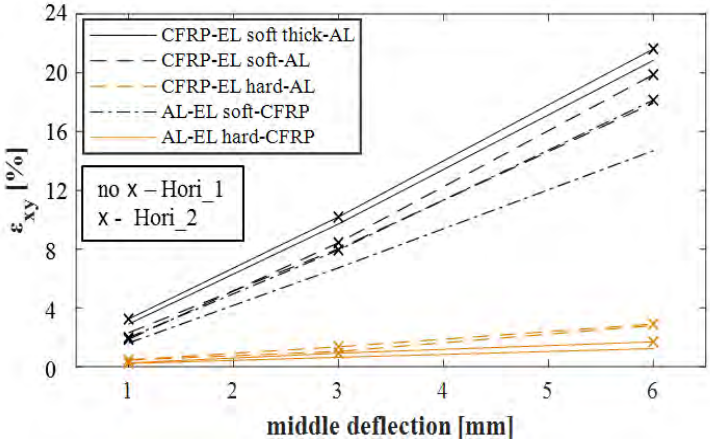


***Fig. 6*** *Shear strain in the elastomer layer in the middle between loading nose and lower support from experimental results. (x=25 mm)*

### 3.2 NUMERICAL RESULTS

For the numerical investigations the same evaluation as in Fig. 4 of the experimental results was conducted. The comparison of experimental and numerical results can be seen in Fig. 7. The numerical results show the same behavior as the experimental, but have smaller values of displacement and shear strain. The maximum displacement of the experimental results is approximately 30% higher. Possible reasons for the deviations of the experimental and numerical results will be covered in chapter 4. The different shear strains can be seen even more precisely in the simulation, as the values for $\varepsilon_{xy}$ are almost at zero for CFRP and aluminum layer and show a sudden increase for the elastomer layers.

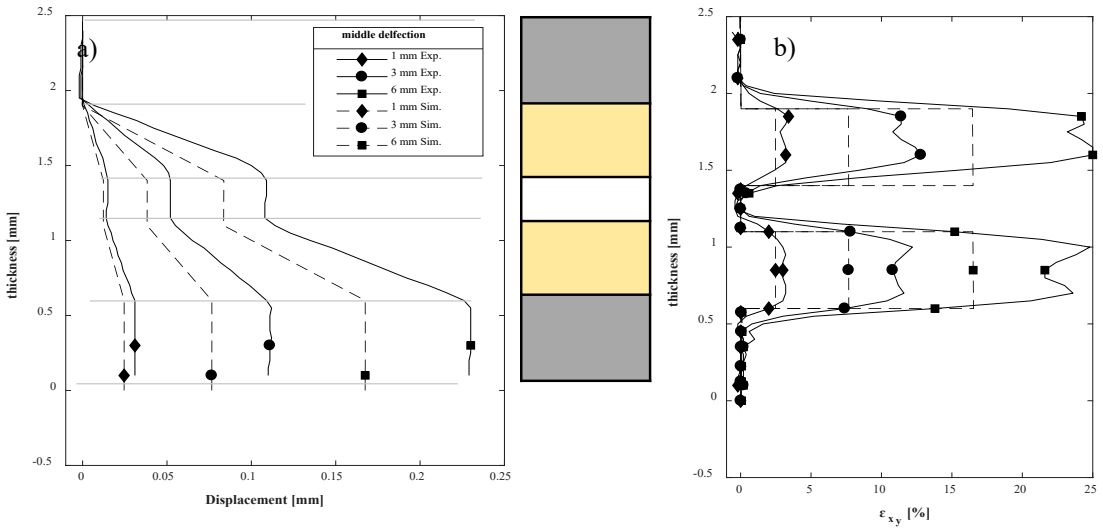


***Fig. 7*** *Experimental and numerical results for displacement (a) and shear strain (b) of each layer of an CFRP-El_soft-al laminate at the position Vert_1 according to Fig. 2.*

## 4 DISCUSSION

The deformation behavior of the FMEL is strongly influenced by the modulus of the elastomer. The displacement curve in Fig. 4 shows that almost no deformation occurs in the CFRP and aluminum layer. This means that the outer fiber strain is much lower when compared to an isotropic material with the same thickness, as each layer is only bent around its own centerline. The counter bending beyond the lower supports, which can be seen in the deflection curves in Fig. 3 is represented by an decreasing shear strain in Fig. 4. At a distance of 10 mm beyond the lower supports the remaining shear strain has decreased to about 4-8% of the maximum value. This means that the overhang of the specimens has an influence the bending stiffness or

damping characteristics of the specimen when measured in three point bending setups. It is assumed that this effect has a higher impact with a softer elastomer as hardly no counter bending can be observed for specimens with the hard elastomer. The counter bending comes from the fact, that if the overhang of the specimen beyond the supports is long enough no displacement of the layers can be seen at the end. The reduction of displacement of the layers results in the counter bending.
Owing to the linear dependency of the shear strains in the elastomer layers with the middle deflection it is easy to calculate a shear strain for a given middle deflection. This is important for further characterization of the dynamic behavior of the elastomer in the correct strain range. The maximum shear strains for the FMEL with the hard elastomer is about 10 % of the maximum shear strains with the soft elastomer. This also reflects the modulus difference of the two elastomers and leads to different deformations behaviors.
The deviation of the experimental and numerical results cannot be clearly traced back to a certain reason. It is assumed however, that the characterization of the elastomer might not precisely depict the ongoing deformations in the FMEL. The shear modulus of the elastomer was calculated from tensile tests by using equation 1 which might lead to an error. Also the fact, that the specimen were tested more than once, to cover different areas of the laminates with high resolution, might have led to a stress relaxation known as Mullins effect [8]. This effect might also appear on the elastomer used in this study. In addition, thermal stresses due to the mismatch of the CTE can affect the deformation behaviour which was neglected until now.

# 5 CONCLUSIONS

A DIC system was used to characterize the elastic deformation behaviour of different FMEL in a three point bending experiment. The bending line of the specimen was analyzed and the deformation behaviour was attributed to the shear strains in the elastomer layers. High shear strains of up to 25% were measured for the soft elastomer whereas for the hard elastomer the maximum strain is only around 1 to 2%. Counter bending of the specimens with the soft elastomer was detected whereas no counter bending beyond the supports of the three point bending setup was seen for the specimens with the hard elastomer. The deformation behaviour was also modelled numerically, and the three-point bending experiment was reconstructed. The same characteristics could be seen from the results. The values of layer displacement and shear strains of experimental and numerical investigations differ approx. 35 %.
Further experiments should be done to characterize the mechanical behaviour of the elastomer in depth. Therefore cyclic tensile tests should be performed to evaluate the Mullins effect and the shear modulus of elastomer layer in an FMEL specimen should be characterized using shear edge experiment.

# 6 ACKNOWLEDGEMENT

The research of this paper is kindly supported by the Deutsche Forschungsgesellschaft (DFG). It is part of project: „HyCEML - Hybride CFK/ Elastomer/ Metall-Laminate mit Elastomerschichten für die gezielte Einstellung des Dämpfungsverhaltens“ under the priority program SPP 1897: Calm, Smooth and Smart - Novel Approaches for Influencing Vibrations by Means of Deliberately Introduced Dissipation". The authors kindly acknowledge the Gummiwerk Kraiburg as part of the Kraiburg Holding GmbH & Co. KG for providing the elastomers used in this study.

# References

[1] E.C. Botelho, R.A. Silva, L.C. Pardini, M.C. Rezende, A Review on the Development and Properties of Continuous Fiber/epoxy/aluminum Hybrid Composites for Aircraft Structures, Mat. Res. 9 (2006) 247–256.
[2] T. Sinmazçelik, E. Avcu, M.Ö. Bora, O. Çoban, A review: Fibre metal laminates, background, bonding types and applied test methods, Materials & Design 32 (2011) 3671–3685.
[3] R. Alderliesten, Fatigue and fracture of fibre metal laminates, Springer, Cham, 2017.
[4] A.D. Nashif, D.I.G. Jones, J.P. Henderson, Vibration damping, Wiley, New York, 1985.
[5] M.D. Rao, Recent applications of viscoelastic damping for noise control in automobiles and commercial airplanes, Journal of Sound and Vibration 262 (2003) 457–474.
[6] M. Stommel, M. Stojek, W. Korte, FEM Zur Berechnung von Kunststoff- und Elastomerbauteilen.
[7] DIN, EN ISO 14125: Bestimmung der Biegeeigenschaften.
[8] J. Diani, B. Fayolle, P. Gilormini, A review on the Mullins effect, European Polymer Journal 45 (2009) 601–612.

# EVALUATION OF BONDING BEHAVIOR IN HYBRID INJECTION MOLDED COMPONENTS BY RIP SHEAR TESTING

**Anne Geyer[1*], Thomas Gläßer[1], Dr. Ralf Schlimper[1]**

[1]Fraunhofer Institute for Microstructure of Materials and Systems IMWS, Halle, Germany

**ABSTRACT:** Due to their excellent specific properties, fiber-reinforced plastic composites as modern lightweight construction material play an increasingly important role for economic and ecologic engineering standards. In order to enable an economical production of lightweight thermoplastic structures, the hybrid injection molding process was developed, which combines the advantages of mass production and design freedom of the plastics processing process with the high mechanical properties of fiber reinforced plastics (FRP). For example, TPC structures such as unidirectional tapes (UD tapes), woven fabrics or organic sheets can be optimally functionalized and produced near net shape by the injection of, for example, ribs or load introduction elements. For the reliable design of such lightweight components, the knowledge of the influences of the individual process parameters on the local component properties, as well as their consideration in the context of coupled process and structural simulations is necessary. To evaluate the bonding performance of injection molded materials to TPC inserts, a rib shear test was developed. In the process, the molded ribs are sheared off from the insert structure and the shear stress is correlated with the bond. In order to be able to evaluate the microstructural influences of the specimens better, morphological analyzes from CT and SEM images of the specimens were compared. In various test series, an influence of the process parameters on the interfacial properties could be determined.

**KEYWORDS:** Thermoplastic Composite, Hybrid Injection Molding, Rib Shear Test, Bonding Behavior

## 1 MOTIVATION

Since hybrid injection molding represents a relatively new manufacturing technology, only a few systematic investigations of the bonding behavior in hybrid injection molded components are known jet. However, numerous studies on process related influencing factors in the conventional polymer injection molding process show that the production parameters significantly influence the bonding properties in multi-component injection molding. Among others, Carella [1], Schuck [2] and Härtig [3] dealt with the influence of manufacturing parameters (for example temperature, injection pressure or holding time) on the bond strength of injection molded tension rods made of two different materials. Based on these and similar investigations [4, 5, 6], it can be assumed that the production parameters in the hybrid injection molding process also have an influence on the bonding behavior in hybrid injection molded components. Compared to multi-component injection molding, a pre-impregnated thermoplastic insert made of organo-sheet (with fabric reinforcement) or a laminate of UD individual layers is integrated into the hybrid injection molding process. Due to these integrated inserts, it is not possible to characterize the bonding behavior with injection molded tensile test bars such as in multi-component injection molding. Test specimens for testing connection behavior are therefore either taken from existing hybrid injection molded components, such as those shown in Figure 1, or fabricated in custom-made hybrid injection molds.

***Fig. 1*** *Demonstrator Components: Composite Carrier (left) and Front End Carrier (right,) both with continuous fiber-reinforced inserts (black)*

* Corresponding author: Walter-Hülse-Straße 1 06120 Halle, +49 345 5589-438, anne.geyer@imws.fraunhoder.de

Recent studies by Tanaka [7] and Giusti [8] are investigating the connection of a rib molded onto a laminate insert. In the experiment, the insert structure is fixed and the molded rib pulled off perpendicularly thereto. The obtained strength values can be used for the comparative evaluation of the connection behavior. In actual component use, however, it has been shown that components with a molded-on rib structure are usually designed for bending and torsional loads. Unlike the tensile loading in these experiments, the connection between the rib and the insert is then primarily subjected to shear. In the present work, the evaluation of the bonding behavior is therefore performed with a rib shearing test in which the rib is sheared off from the insert structure.

# 2 RIB SHEAR TEST

## 2.1 MATERIAL AND PROCESS PARAMETERS

For the rib shear tests, demonstrator components are manufactured on a Krauss Maffei KM 200 injection molding machine. Figure 2 shows the process flow starting with the heating of the pre-consolidated insert structure and the robotic transfer and insertion into the injection molding cavity. In a first process step, the insert is reshaped and in a second process step functionalized by insert molding with a rib structure and a rim. The Composite Carrier, as shown in Figure 1 left, consists of a polypropylene (PP) / glass fiber (GF) fabric insert from Bond Laminates and polypropylene with 30% glass fiber mass fraction injection molding material, which is sold under the name PP/GD301 FE sw. Borealis.

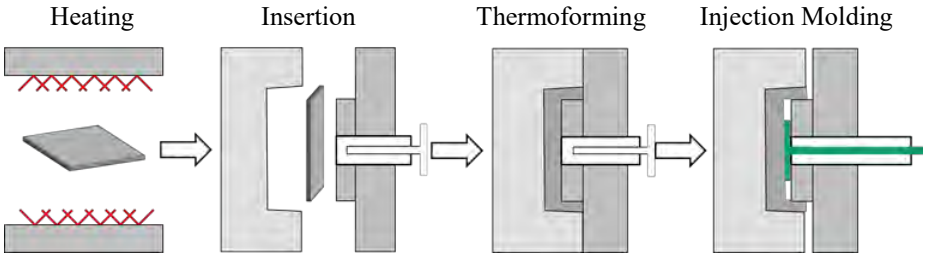


***Fig. 2*** *Schematic process flow of hybrid injection molding process*

Four different series of composite carriers with different gate systems were produced for the trials. Series 1452 is injected with three gates (one each side and one centered) and without an insert. As it is a full thermoplastic component, it is used as reference component in which the shear strength of the pure injection molding material can be examined. For test series 1453, 1454 and 1455 a fabric insert is used. Thereby the gate system varies from center to one-sided to both sides. This leads to change in the mold filling behavior of the injection molding cavity. In the test series, the influence of these changes on the bonding behavior between rib and insert is examined. Therefore the main process parameters like insert temperature or melt temperature of the composite carriers are kept constant. Table 1 shows how the process parameters, injection time and the holding pressure, vary with the changing gate system.

***Table 1:*** *Designation of testing structures and their processing parameters*

| Series | Gate | Temperature Insert [°C] | Temperature Melt [°C] | Injection Time [s] | Holding Pressure [bar] | Cooling Time [s] |
|---|---|---|---|---|---|---|
| 1452 | Reference | 165 | 260 | 4,0 | 300 | 30 |
| 1453 | Center | 165 | 260 | 2,3 | 250 | 30 |
| 1454 | One side | 165 | 260 | 2,6 | 350 | 30 |
| 1455 | Two sides | 165 | 260 | 2,2 | 250 | 30 |

## 2.2 SPECIMEN EXTRACTION AND GEOMETRY

All test specimens are cut out of a hybrid injection molded composite carrier. As shown in Figure 3, the test specimens are taken from the middle rib of the composite carrier according to the extraction plan. The test specimen removal is performed with a diamond-tipped cutting disc or by water beam cutting. In each case, 8 T specimens are prepared from one composite carrier.

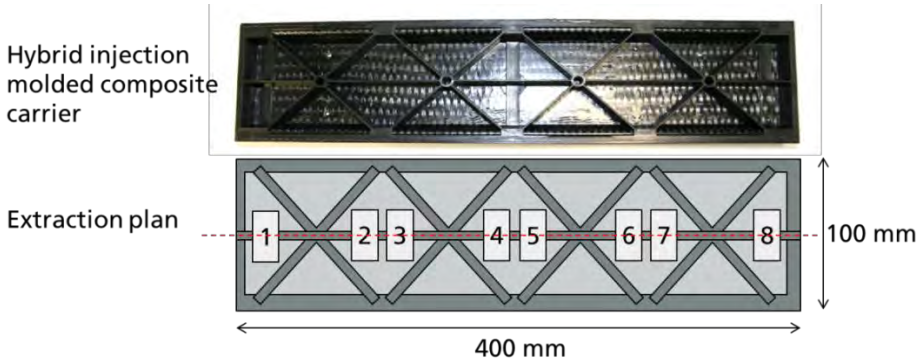


***Fig. 3*** *Hybrid injection molded composite carrier (top) and extraction plan for specimen collection (below)*

Since the rib structure is in principle orthogonal to the insert structure there, the test specimen geometry is T-shaped. The dimension of the T specimens, shown in Figure 4, approximates the specimen used by Tanaka [7] and Giusti [8] to characterize the tensile bond.

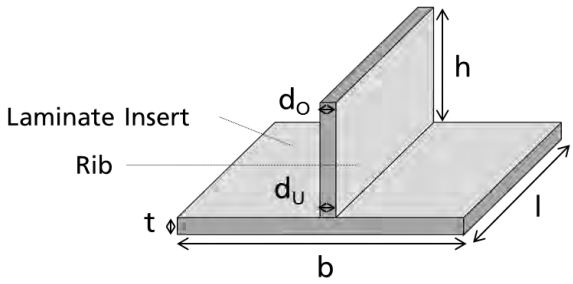


| | |
|---|---|
| length: | l = 20 mm |
| width: | b = 40 mm |
| laminate thickness: | t = 2 mm |
| rib height: | h = 18 mm |
| rib thickness top: | $d_O$ = 1,6 mm |
| rib thickness bottom: | $d_U$ = 2,6 mm |

***Fig. 4*** *Geometry and dimensions of the T-shaped specimen*

## 2.3 TESTING CONCEPT

The rib shear test represents a new test concept for evaluating the bonding behavior in hybrid injection molded components. Starting from bending-loaded components with molded ribbed structure, this concept is based on the realization of a shear load between the ribs and insert as the predominant load type. To create primarily shear in the bond between the insert structure and the rib both the rib and the insert must be clamped. The rib is moved vertically downwards by an applied force while the insert is immovable. In the schematic diagram in Figure 5, it is shown that the insert is pressed against a shear edge in an attempt to allow the rib to be sheared downwards. This creates a shear zone in which the shear deformation takes place. As smaller the height of the shear zone, the higher is the resulting shear stress in the material theoretically.

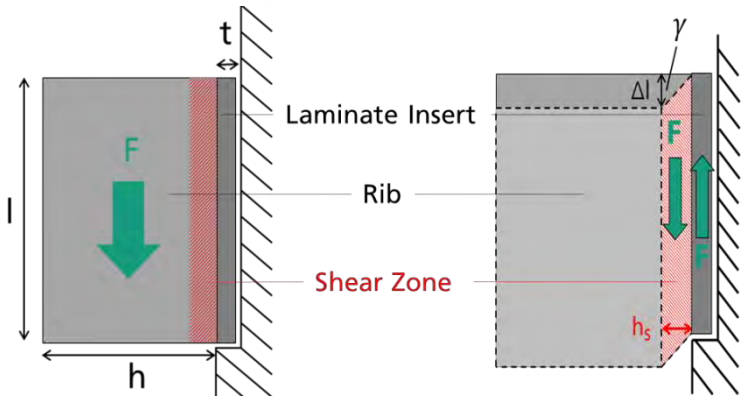


***Fig. 5*** *Schematic sketch of the rib shear test: unloaded (left) and loaded (right)*

The evaluation of the tests is carried out via the determined force-displacement curves of the testing machine. The shear stress τ is calculated with $\tau = F/d_u * l$ (1), from the test force F, the thickness of the rib at the insert du and the length l of the test specimen. The shear strength calculated from the maximum force in case of failure reflects the connection behavior between rib and insert. The shear deformation γ is calculated according to formula $\gamma = \tan\gamma \approx \Delta l/h_s$ (2) with the displacement Δl and the height of the shear zone $h_S$.

## 2.4 EXPERIMENTAL SETUP

In the experimental setup shown in Figure 6, the developed test concept was implemented. The testing stand consists of a linearly mounted traverse and support, which are both arranged in a rigid test frame. The support consists of two mutually displaceable blocks, which on the one hand forms the shear edge and on the other serves to guide the specimens. Depending on the specimen geometry, distances and gaps can be set and fixed. The movable part consists of a load application and a linear guided vise, in which the rib of the T specimen is clamped. This assembly guides the tightly clamped specimen along the traverse to the support and shears off the rib from the insert. Vise, insert, and the support are designed so that a tilting of the insert structure and thus the emergence of a moment during the test can be prevented. The radii between the rib and the insert on the vise define a shear zone in which the shear deformation takes place.

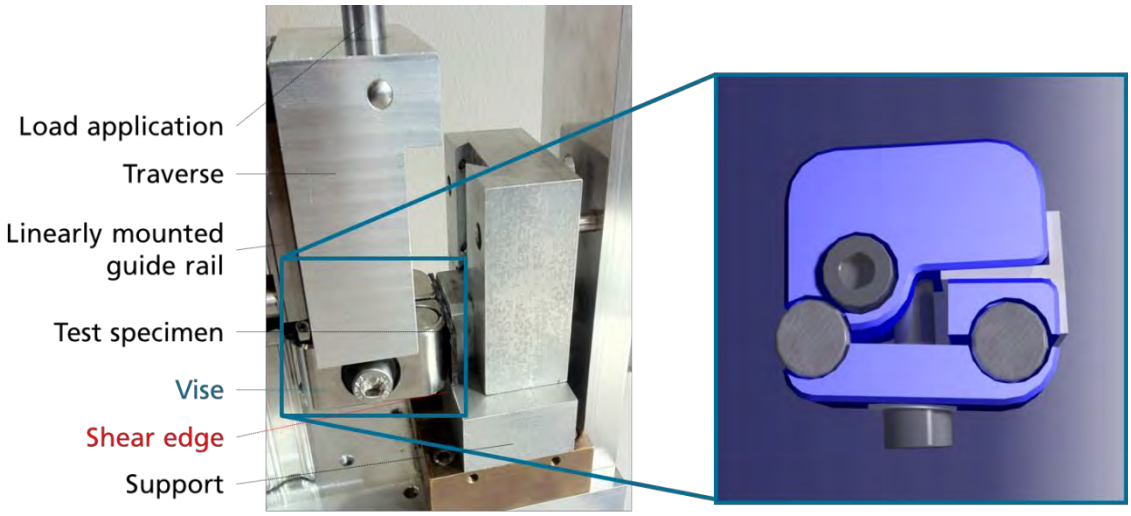


***Fig. 6*** *Experimental setup with an enlarged view of the vise*

All tests are carried out on a universal testing machine with a 10 kN load cell and took place in an air-conditioned testing laboratory with a temperature of 23 °C and a relative humidity of 50.1 %. After application of a preliminary force of 10 N, testing is performed at a speed of 1mm/min. The failure of the samples occurs after 2 to 4 min.

## 3 RESULTS AND DISSCUSION

For each tested composite carrier, consisting of 8 test specimen, shear stress-shear deformation curves can be calculated, using the force-displacement curves measured by the testing machine and the equations shown in Section 2.3. The most characteristic series is series 1454 with only one gate. Figure 7 shows, as an example, the results of test series 1454-1. Looking at the shear stress-shear deformation diagram, the course of the curves seems to be similar for all 8 specimens. When the pre-load is reached, the stress in the samples initially increases linearly followed by a non-linear increase until the sample fails. After a damage initiation, the shear stress drops suddenly. Figure 7 also shows the maximum reached shear stress of each specimen over their former position in the composite carrier. It can be seen that the measured shear strength changes with increasing distance from the gate, which was at a position of 15 mm. The maximum shear strength of the 8 specimens is reached by sample 3 with 22.7 MPa.

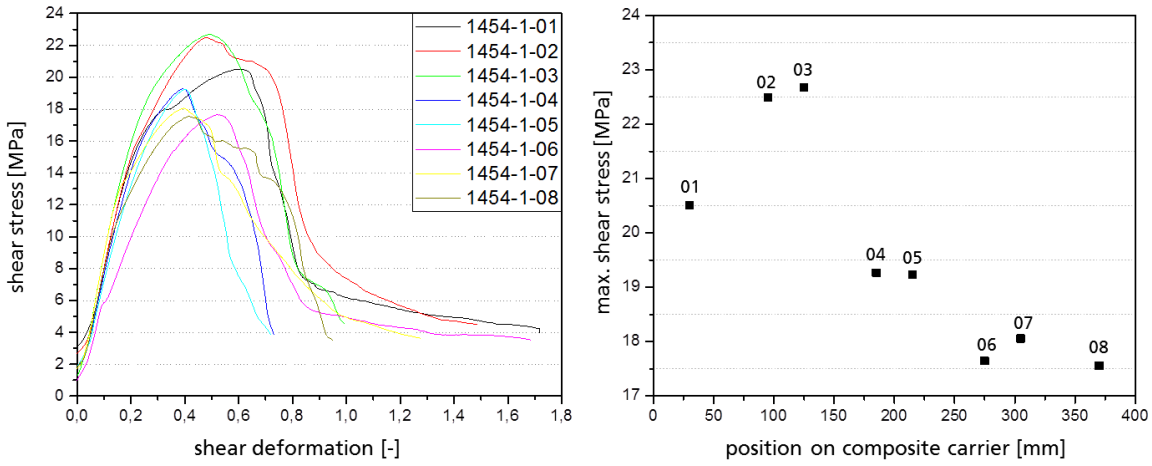


***Fig. 7*** *Shear stress-shear deformation diagram (left) and maximum shear stress over specimen position in the composite carrier (right) of test series 1454-1*

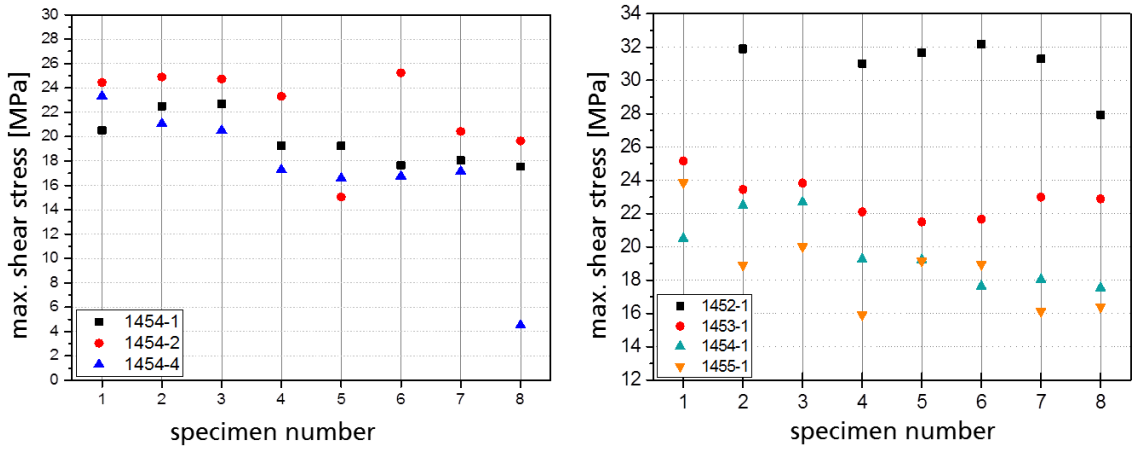


***Fig. 8*** *Comparison of shear strength of series 1454 (left) and of all four series (right)*

Comparing the specimen of three different composite carriers of the same series in Figure 8 left, it can be seen that the tendency of shear strength behavior is the same, except some outliers. The variation of the values is between 0.4 MPa and 2.5 MPa (excluding specimen 1454-2-6 and 1454-4-8). To ensure that the recognized course of the measured shear strength along the composite carrier is not caused by scattering of the testing method, microstructural analyses were performed. On the one hand, the specimens were analyzed by x-ray computed tomography (CT) to assess the porosity content in the shear zone area which could promote damage. And on other hand scanning electron microscopy (SEM) was used to evaluate the bonding between injection molding material and the insert. Figure 9 left shows a virtual three-dimensional image of the scanned specimen. Here the injection molding material is visualized highly transparent to see the loca-

tion of the measured voids. All voids in the shear zone area are highlighted by a different color which corresponds to the void size. The measured voids are all minimal and located mainly at the sides of the rib. In the plane where injection molding material and insert are combined no voids can be found. In total, the porosity amount in the shear zone is 0.22 %, so voids properly do not cause the scattering in the results. Figure 9 right shows an SEM picture of the cross-section of a T-shaped specimen. More significant voids are also visible in microscopy images (small red circle). As the darker parts are the matrix material and the lighter parts the glass fiber reinforcement, it can be seen that the injection molding material reaches the fabric structure of the insert. That implies a melting of insert matrix. A fusion with the injection molding material does not take place. The insert matrix is displaced to the left side of the rib (big red circle). How this affects the bonding is not entirely clear yet, but as there is no matrix material building a separating layer the bonding should not be decreased.

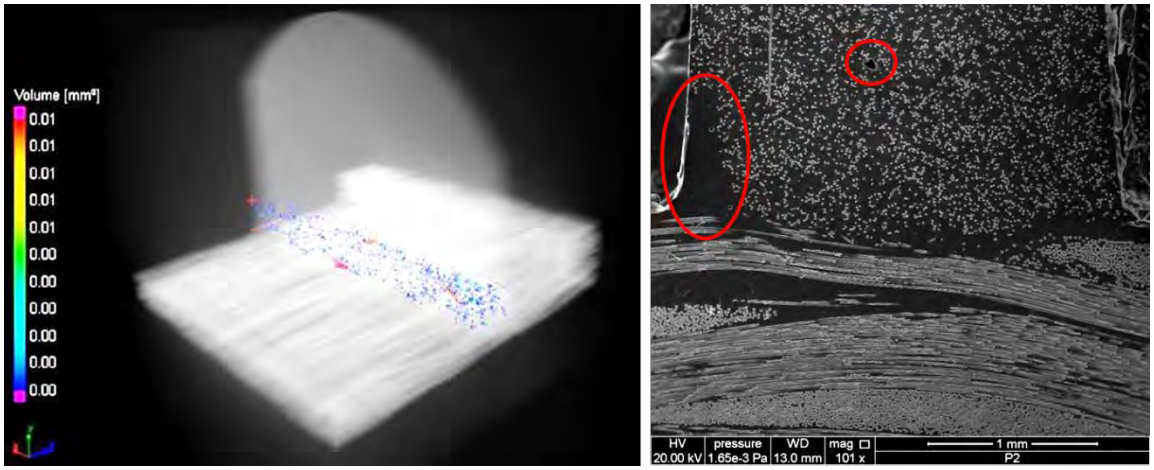


***Fig. 9*** *CT porosity analysis in the shear zone (left) and SEM picture of the shear zone cross-section (right) of specimen 1454-4-1*

Comparing the measured shear strength of all test series in Figure 8 right, it can be stated that the reference specimen without inserts with 27.9 MPa to 32.2 MPa have a significantly higher shear strength than the samples with insert structure. Even in the test series with a different gate system, differences in shear behavior can be recognized, but they are much less noticeable. With the reference studies 1452 (injection molded composite carrier without insert structure), a comparison of the measured shear strength with the shear strength of pure injection molding material is made. Since this composite carrier consists only of injection-molded material, an ideal bonding (based on the used production parameters) in the T-test specimen can be assumed, so that the determined shear strength should correspond to the shear strength of the pure injection molding material. The measured shear strength of 27.9 MPa to 32.2 MPa, which was determined as a parameter for the bonding behavior, corresponds well with the shear strength level of the injection molding material PP/GF30 of 27 MPa [9], so it can generally be assumed that the experimental setup for the evaluation of the bonding behavior is suitable in principle.

The final point to discuss is the significance of the results regarding the influence of the gate system on the bonding behavior. The starting point is the assumption that the choice of a gate system influences the bonding behavior. The reason for this is the different course of the melt front during the mold filling process. The longer the melt flows; the lower is its temperature. Various studies have already shown the influence of the melt temperature on the bonding behavior [7, 8, 10, 11]. Figure 10 shows a comparison of the filling behavior of the injection molding cavity calculated from MOLDEX3D with three gate points (Fig.10 left) and a central gate point (Fig.10 right). Early filled shapes are displayed in red, and later filled areas are shown blue. It turns out that especially the ribs are filled at different times, and thus the bonding takes place at slightly different temperatures of the melt. Hence a progression of the shear strength over the composite carrier should theoretically be discernible in the rib shear tests, as well as a different shear strength level between the test series.

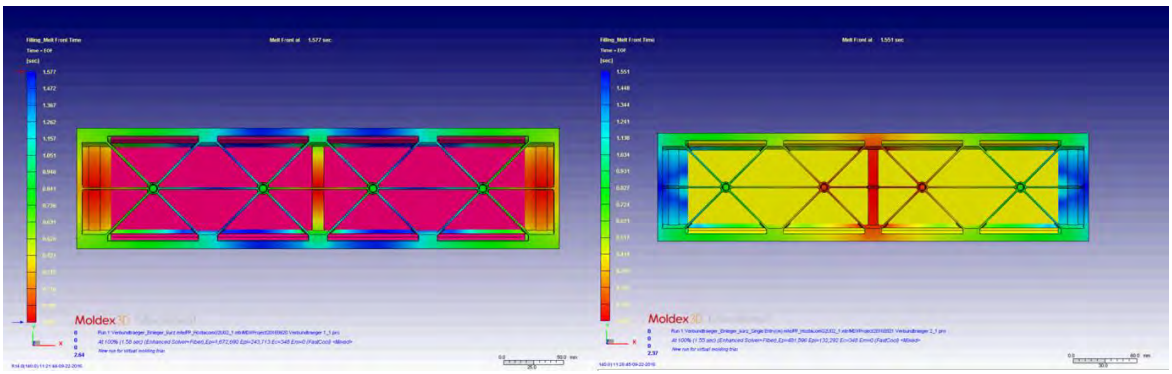

***Fig. 10*** *Comparison of mold filling behavior: three-sided gate (left) and central gate (right)*

As shown in Figure 8, a progression of the shear strength over the composite carrier length is generally recognizable in the experiments. Also, different levels of shear strength can be seen. In general, the influence of the gate systems can be determined so that further investigations can refer to these results.

## 4 CONCLUSIONS

The results of the present work show the basic structure and the performance of a rib shear test to evaluate the bonding behavior in hybrid injection molded components. It is shown that the developed test concept is suitable to evaluate the bonding behavior in hybrid injection molded components. In a reference experiment with a presumed ideal bonding, the shear strength of the injection molding material was determined in good agreement. Compared to samples made of the composite carrier, which were manufactured with different gate systems, the influence of the gate system on the bonding behavior was clearly shown by different shear strength levels. In order to gain a deeper understanding of the processes in the hybrid injection molding process and to improve the statistical evaluation of the investigation, further experiments are planned. In addition, a detailed microstructure investigation will be carried out in parallel, which allows conclusions to be drawn from the process-induced microstructure of the test specimens on their influence on the bonding behavior.

## 5 ACKNOWLEDGEMENT

The present work was carried out as part of the research project "ThermoLeibaS". The Project is part of the High-Performance Center Chemical and Biosystems Technology and supported by the European Regional Development Fund (ERDF) under the award no. 1604/00079.

## REFERENCES

[1] CARELLA, A. R., et al. Sequential injection molding of thermoplastic polymers. Analysis of processing parameters for optimal bonding conditions. Polymer Engineering & Science, 2002, 42. Jg., Nr. 11, S. 2172-2181.

[2] SCHUCK, Marcus: Kompatibilitätsprinzipien beim Montagespritzgießen, Universität Erlangen-Nürnberg, Diss., 2009

[3] HÄRTIG, Thomas: Stoffübertragung beim Spritzgießen, Technische Universität Chemnitz, Diss., 2013

[4] AURREKOETXEA, J., et al. Failure of multimaterial fusion bonding interface generated during over-injection molding/thermoforming hybrid process. Journal of applied polymer science, 2006, 102. Jg., Nr. 1, S. 261-265.

[5] HARTE, A. M.; MC NAMARA, J. F. Overinjection of thermoplastic composites: I. Processing and testing of components. Journal of materials processing technology, 2007, 182. Jg., Nr. 1, S. 12-20.

[6] SCHELL, J. S. U., et al. Computational and experimental analysis of fusion bonding in thermoplastic composites: Influence of process parameters. Journal of Materials Processing Technology, 2009, 209. Jg., Nr. 11, S. 5211-5219.

[7] TANAKA, K.; FUJITA, Y.; KATAYAMA, T. Press and injection hybrid molding of glass fiber reinforced thermoplastics. WIT transactions on engineering sciences, 2015, 90. Jg., Nr. 7, S. 225-232.

[8] GIUSTI, Ruggero: Experimental Investigations and Numerical Modelling of the Bonding Strength of Full-Thermoplastic Hybid Composites. International conferenz and Exibition on Thermoplastic Composites, 2016
[9] WONGPAJAN, Rutchaneekorn, et al. Interfacial shear strength of glass fiber reinforced polymer composites by the modified rule of mixture and Kelly-Tyson model. Energy Procedia, 2016, 89. Jg., S. 328-334.
[10] PFEFFERKORN, Tobias, et al.: Vom Laminat zum Bauteil. Kunststoffe, 2013, Nr. 12, S. 94-100. Dokumentennummer KU111540
[11] FIOROTTO, Marco; LUCCHETTA, Giovanni. Experimental investigation of a new hybrid molding process to manufacture high-performance composites. International journal of material forming, 2013, 6. Jg., Nr. 1, S. 179-185.

# COMPONENT TESTING OF CONTINUOUSLY AND DISCONTINUOUSLY REINFORCED HYBRID SHEET MOLDING COMPOUNDS (CODICOSMC)

**Anna Trauth[1], André Schubert[1], David Bücheler[2], Kay A. Weidenmann[1,2*]**

[1]Karlsruhe Institute of Technology (KIT), Institute for Applied Materials (IAM-WK), Karlsruhe
[2] Fraunhofer-Institut für Chemische Technologie (ICT), Pfinztal

**ABSTRACT:** In order to simultaneously achieve cost savings in addition to the known positive lightweight effect of fiber reinforced plastics, attempts are made to combine continuous and discontinuous fiber reinforcement to achieve a targeted increase of the rigidity of components. Within the scope of this contribution, a four-point bending test on hybrid continuous-discontinuous SMC components was performed to characterize the effect of hybridization on mechanical properties. The components made from a discontinuous fiber sheet molding compound (SMC) featured a locally introduced continuous carbon fiber reinforcement. The matrices of both the continuous and the discontinuous component are based on a novel unsaturated polyester-polyurethane two-step curing resin system which ensures the chemical compatibility of the two constituents. As reference, SMC components of the same resin system with exclusively discontinuous glass fiber reinforcement were considered. The components were subjected to cyclic bending loads to measure the damage-related stiffness reduction. It has been demonstrated that the continuous carbon fiber reinforcement has a positive effect on the stiffness as well as the damage evolution of the reference structures without increasing the weight of the components.

**KEYWORDS:** bending testing, GFRP, CFRP, component testing, damage evolution

## 1 INTRODUCTION

Sheet Molding Compounds were first used in the 1960s. One of the biggest buyers is the automotive industry. In 1999 alone, 66 000 tons were considered for vehicle construction, which accounts for around 35% of total SMC consumption [1]. One of the main reasons for the widespread use of SMC is its excellent design freedom combined with an outstanding surface quality which is well suited for painting. The SMC itself can also be colored. These aspects are an important factor for high surface quality components (so-called Class A components). The development of SMC has been directly designed for high automation, which brings an economic advantage. Compared to steel sheet forming, tools are up to 40% less expensive [2, 3].
Another advantage of SMC is its lightweight potential. The resin system can be modified in a way that it can be adapted to virtually any application [4]. Unsaturated polyester resins are most commonly used as they are inexpensive and cure quickly [2]. But other resins systems, for example vinyl ester resins or epoxy resins can be considered as well [3]. In general, discontinuous glass or carbon fibers are used as reinforcement with glass fibers being the most widespread. However, carbon fibers have been used more and more frequently lately, and also natural fibers are increasingly being considered for SMC [3]. Typical fiber contents are 15% by weight to 30% by weight. In the case of the so-called structural SMC or Advanced SMC, however, the fiber contents are more than 50% by weight. The fiber length can vary between 0.5 and 2 inches [5].
Regarding the generation of hybrid SMC, Cabrera-Ríos and Castro [6] carried out an experiment in which carbon and glass fibers were mixed as discontinuous fibers in the material. This mixing can be achieved by two different methods of preparation: On the one hand, the fibers can already be mixed during the production of the SMC semi-finished sheets or, on the other hand, can be mixed during molding, in which carbon fiber and glass fiber reinforced semi-finished products are inserted in layers. It could be shown by the “layer by layer” method that not only the respective proportion of fiber is important, but also how the stack is arranged during molding. It could be confirmed that the variation of the fiber composition and arrangement

has an influence on the tensile strength, Young's modulus and bending strength. Another approach is to combine discontinuously reinforced SMC with pre-impregnated continuous carbon fibers, as demonstrated by Wulfsberg et al. [7] to develop hybrid SMC material mainly for the aircraft industry .The experiment shows that by adding the continuous fiber reinforcement the flexural modulus as well as the tensile modulus can be increased. The integration of unidirectional carbon fiber layers increases the tensile strength twice compared to the SMC without continuous reinforcement. Another finding is that the impact strength is particularly positively influenced by a combination of discontinuous glass fibers and a woven carbon fiber fabric. However, no improvement can be observed when using discontinuous carbon fibers. According to Wulfsberg et al. this may be due to the poor interlaminar shear strength between carbon fibers and the HUP 27 resin considered within this study. Even SMC with 50% discontinuous carbon fiber in combination with carbon fiber fabric, deterioration of impact resistance is observed. In addition, partial delamination occurred. This proves that in the hybridization of SMC, the resin systems of the continuous and discontinuous phase must be compatible with each other. The International Research Training group on the "Integrated engineering of continuous-discontinuous long fiber reinforced polymer structures" (GRK 2078) focus on the development of a structural hybrid continuous-discontinuous SMC (CoDiCoSMC), whereas the use of a novel UPPH resin system for both the discontinuous SMC and the continuous fiber reinforcement considered within this study offers the possibility to be hybridized in a one shot compression molding process [8].

# 2 MATERIAL AND METHODS

## 2.1 MATERIAL

SMC consists essentially of two components, the resin system and the fibers. A detailed description if the individual components of the resin system of the one-inch fiber length discontinuous glass fiber reinforced SMC and the continuous carbon fiber prepreg used for the local reinforcement are listed in Table 1. The individual components are first mixed under vacuum and then further processed on a conventional SMC conveyor belt plant by Schmitt&Heinzmann (Bruchsal, Germany) at the Fraunhofer ICT (Pfinztal German). Next, the glass fiber reinforced semi-finished product was stored to matured for several days at approximately 30 °C. The nominal fiber content was set to 41 wt.%. The carbon fiber-based prepregs featuring a nominal fiber content of 60 wt.% were produced on the same conveyor belt. Both components were automatically cut to size on a cutting table. The continuous fiber inserts were cut directly to the final geometry, the SMC semi-finished product was cut to 249 x 280 mm².

***Table 1:*** Individual resin components and fiber type of investigated glass and carbon fiber SMC

| Component | | Discontinuous glass fiber SMC | Continuous carbon fiber SMC | Supplier |
|---|---|---|---|---|
| Resin | | Daron ZW 14141 | Daron 41 | Aliancys |
| Additives | Release agent | BYK 9085 | BYK 9085 | BYK |
| | Inhibitor | pBQ | pBQ | Fraunhofer ICT |
| | De-airing | BYK A 530 | | BYK |
| | Impregnation additive | | BYK 9076 | BYK |
| Peroxide | | Trigonox 117 | Trigonox 117 | Akzonobel |
| Thickener | Isocyanate | Lupranat M20R | Lupranat M20R | BASF |
| Styrol | | | Mono Styrol | BASF |
| Accelerator | | | BorchiKat0243 | Borchers |
| Fiber | | MultiStar 272 | | Johns Manville |
| | | | PX3505098T-13 | Zoltek |

The molding steps for the manufacturing of components made from CoDiCoSMC is depicted in Fig. 1.
Since the carbon fiber inserts should stay in place during molding, they are directly put at its final position in the mold. This position is located on the longitudinal slopes of the reference structure. The glass fiber reinforced SMC semi-finished sheets are placed on the insert. To be able to achieve the same flow conditions, the SMC discontinuous semi-finished sheets are also placed in the same position for the non-locally reinforced structures.
SMC plaques with a section of 800 mm × 250 mm, featuring the component in the middle, were molded in a press type: COMPRESS PLUS DCP-G 3600/3200 AS by Dieffenbacher (Eppingen, Germany) at 125 bar at

approximately 150 °C and 112s mold closing time. The reference structure was then extracted from the molded plaque by milling. Figure 2 shows the final parts with and without local reinforcements.

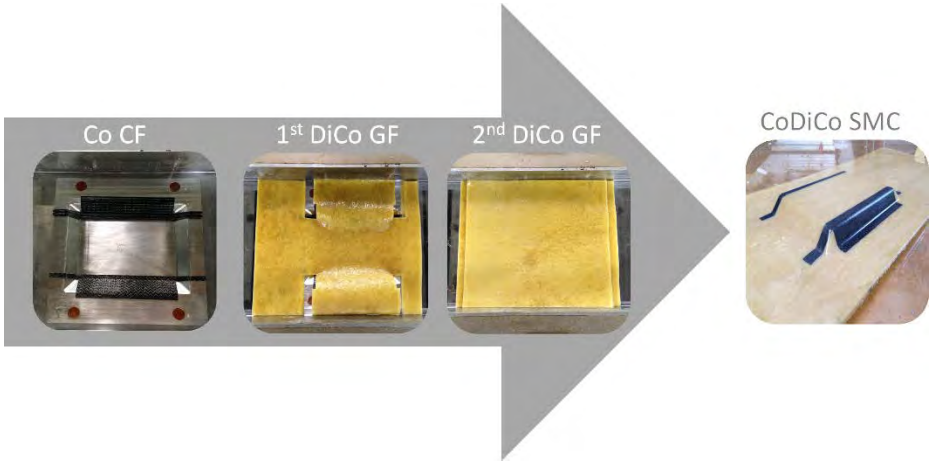


***Fig. 1*** *Molding steps to manufacture hybrid continuous-discontinuous SMC reference structure*

a) b) c)

***Fig. 2*** *SMC reference structure considered for testing. Discontinuous glass fiber SMC specimen (a), locally reinforced specimen (b) and schematic CAD sketch (c)*

## 2.2 METHODS

### 2.2.1 EXPERIMENTAL

The component test was performed on a Zwick Roell Universal testing machine with 500 kN load capacity. As shown in Fig. 3, the specimens were placed on two lower supports, which were aligned at a distance of 120 mm. The supports themselves were mounted on a cage made of aluminium extrusions to be able to measure the deflection directly below the sample with a tactile transducer. The specimens were loaded by two upper supports, having a distance of 40 mm (Fig. 3). The testing machine was controlled by the testXpert II software, which also performed the cyclic test sequence described below (Fig. 4). In addition to the load cell of the testing machine, displacement of the specimens was measured by means of a stereo digital image correlation (DIC) system (GOM 4M). With the aid the software ARAMIS resulting strains at each point in the measuring range could be calculated. After reaching a preload of 100 N, the DIC system was started and images were captured with a frame rate of 1 HZ up to final fracture. The 4-point bending test was carried out cyclically with a constant nominal crosshead speed of 2 mm/min. Each cycle consisted of a maximum deflection (Table 2) and four subsequent stages of descent from 30% to 70% of this previous maximum value. Between different cycles, a force of 100 N was maintained for 90 seconds. After eight cycles, the deflection has been increased until fracture of the specimen.

***Fig. 3*** *Setup of four- point bending test with DIC measurement.*

***Table 2:*** *Cycle number and maximum deflection*

| Cycle | 1 | 2 | 3 | 4 | 5 | 6 | 7 | 8 |
|---|---|---|---|---|---|---|---|---|
| Max. deflection in mm | 0.5 | 1.0 | 1.5 | 2.0 | 2.5 | 3.0 | 4.0 | 5.0 |

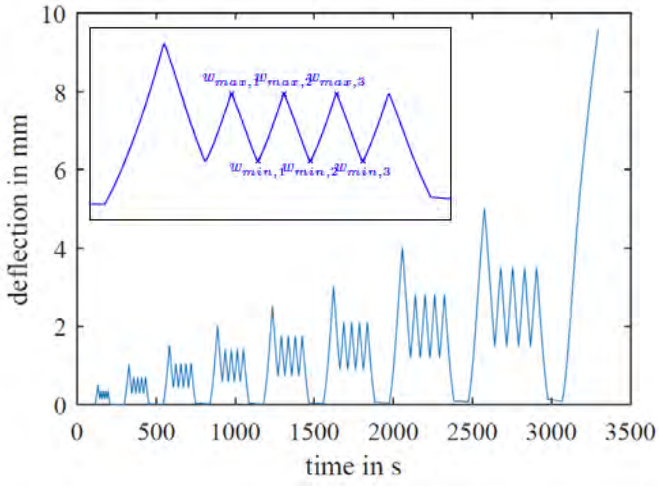


***Fig. 4*** *Cyclic deflection-time evolution of four-point bending tests.*

The global stiffness $S$ of the specimen is calculated from the load $F$ and the deflection $w$ as follows:

$$S = \frac{F_{max,i} - F_{min,i}}{w_{max,i} - w_{min,i}} \tag{1}$$

with $i \in \{1, 2, 3\}$

Locations of $w_{max}$ and $w_{min}$ for a cycle are depicted in Fig. 4. They refer to the maximum and minimum deflection reached within the 30%-70% cycle after the maximum deflection of the cycle. $F_{max,\min}$ is the force at this point. The stiffness was calculated over the unloading phases and the arithmetic mean value of the three calculated stiffness values considered for one cycle was evaluated for the specimens with and without local reinforcement.

The decrease in stiffness can furthermore be represented as damage $D$, with D equal to:

$$D = 1 - \frac{S}{S_0} \tag{2}$$

and D ∈ [0,1].
$D = 0$ means that there is no damage ($S = S_0$) and $D = 1$ means that the stiffness has dropped to $S = 0$ and thus there is complete damage of the structure. The stiffness from the first cycle is defined as $S_0$

# 3 RESULTS

## 3.1 BENDING TESTS

As explained in sub-chapter 2.2, the load data from the load cell, strain data from the digital image correlation and deflection data measured via a tactile transducer were recorded. These data are presented and evaluated in the following. Since the test was carried out deflection-controlled, the deflection data of the specimens are among themselves identical, except for the maximum deflection at breakage. The measured force, however, differed and will be discussed in the following.

In Fig. 5, the force values at the maximum deflection per cycle for reference structures solely made of discontinuous glass fiber SMC (DiCo GF) and specimens featuring an additional local reinforcement (DiCo GF with Co CF reinforcement) are compared with each other. It is clearly visible, that for components with local reinforcement the load increase over deflection is higher, i.e. the stiffness of the parts significantly increases due to the incorporation of a local reinforcement. At the last loading stage (8), the specimens with continuous carbon fiber reinforcements carry an average load surplus of 946 N in comparison to specimens without local reinforcement. That corresponds to an increase in strength of 32 %. Looking at the fracture strength at failure, the specimens with local reinforcement averaged 739 N higher than those without local reinforcements. That corresponds to approx. 17 %. Additionally, the deflection of specimens with local reinforcement at fracture is 15 % less compared to pure SMC parts. The scatter of the fracture strength is significantly reduced for parts featuring a local reinforcement. This is a first hint regarding the fact that the local reinforcement has an impact on the damage evolution.

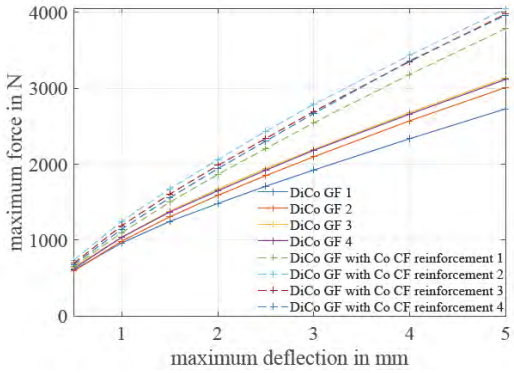


***Fig. 5*** *Evolution of maximum force during cyclic four-point bending test evaluated at maximum deflection of each cycle*

Figure 6 summarizes the corresponding stiffness of the two different specimens calculated from eq. 1. It is obvious, that the stiffness is significantly increased (approximately 250 to 300 N/mm) by the local reinforcement for every cycle.

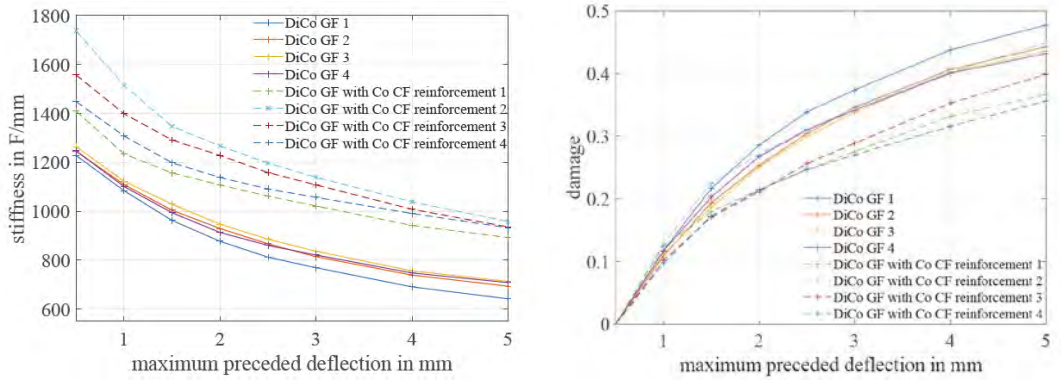


***Fig. 6*** *Stiffness and damage evolution due to cyclic four-point bending.*

Regarding the quantitative damage evolution, no significant difference can be expected. This assumption is proven by Fig. 5, which shows, that the stiffness loss for both configurations is comparable, whereas a certain tendency to lower damage parameters at equal stages for the reinforced parts is visible.

To analyze the data from the DIC system, a surface element was defined on the specimen via the software ARAMIS, which can be seen in Fig. 7 and Fig. 8. The surface element is the same for all specimens and the following results always refer to this surface element.

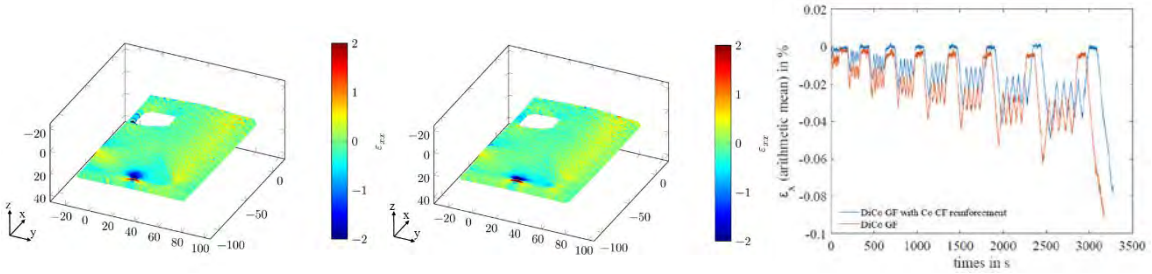


a) b) c)

***Fig. 7*** *Resulting strain field $\varepsilon_{xx}$ (in %) corresponding to maximum deflection of cycle number 8 for reference structure (DiCo GF) (a) and reference structure with local reinforcement (DiCo GF with Co CF reinforcement) (b). Evolution of $\varepsilon_{xx}$ during cyclic four-point bending test (c).*

Figure 7a and Fig. 7b shows the strain fields evaluated by ARAMIS for two exemplary specimens with and without local reinforcement. For both configurations the strain in the x direction at load stage 8 is shown. The large strain in the region of the supports is remarkable. At this point, significant differences between the two specimen types can be seen. In this respect, the reference part features a much larger area around the support with higher strain than the specimen with a continuous carbon fiber reinforcement. There are no significant differences on the remaining area. For these two specimen types, the arithmetic mean value of the strain is plotted for the entire test procedure (Fig. 7c). It can be seen that the part with reinforcement evolves lower average strain on the entire defined area in the x-direction than the reference specimen (DiCo GF). For the same specimen configuration, the strain on the same area in the y-direction is shown in Fig. 8a and Fig. 8b. Here, the higher strain in the region of he supports for the reference part extends to a larger area, too. Additionally, high strains stretching to the edge are visible, while for the specimen with reinforcements, the region with higher strains is localized to region of the lower support. The strain field on the remaining surface, however, hardly differs from each other. The averages over the whole region of interest show that the component with reinforcement elongates less than those without reinforcement, despite the same displacement (Figure 8c)

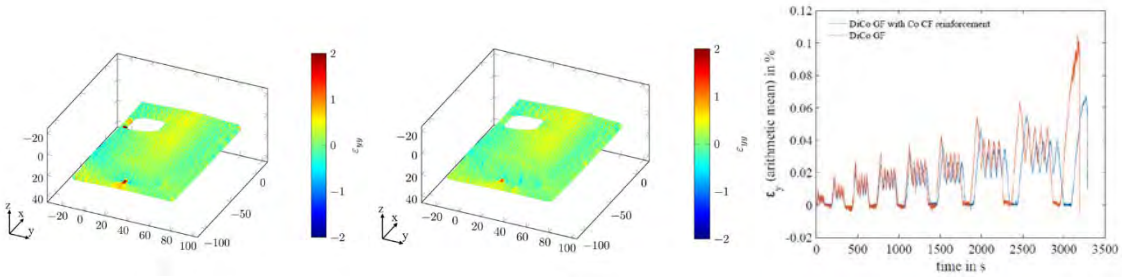


a) b) c)

***Fig. 8*** *Resulting strain field $\varepsilon_{yy}$ (in %) corresponding to maximum deflection of cycle number 8 for reference structure (DiCo GF) (a) and reference structure with local reinforcement (DiCo GF with Co CF reinforcement) (b). Evolution of $\varepsilon yy$ during cyclic four-point bending test (c).*

### 3.2 DAMAGE BEHAVIOUR

The damage evolution for the specimen with local reinforcement does not differ significantly from those without local reinforcement. Both specimen types show a starting crack near an upper support point which propagates along the edge. This is shown in Fig. 9. Instable crack propagation after the last loading stage at very high deflection explain the sudden failure in the end of the testing sequence. Although the part is not symmetrical, no tendency for one certain side regarding the crack occurrence could be observed. In general, the cracks did not start at the same support point.

Nevertheless, taking a detailed view, it can be seen, that delamination occurs at the support points. For the locally reinforced part, this delamination is also occurring and even leads to a delamination of the continuous reinforcement from the surrounding matrix. This indicates that the interface between the continuously and the discontinuously parts of the component may be a weakest link although the chemical composition of the matrix is identical.

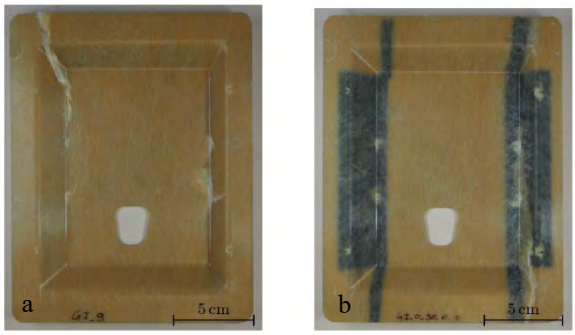


***Fig. 9*** *Damaged reference structures: discontinuously reinforced reference structure (DiCo GF) (a) and locally reinforced reference structure (DiCo GF with Co CF reinforcement) (b).*

## 4 DISCUSSION

The components with local continuous carbon fiber reinforcement feature superior mechanical performance both regarding the component stiffness and the stiffness decrease due to damage. However, there is a certain scatter in the initial value of the stiffness in comparison to pure discontinuous SMC parts. This may be a process-induced difference based on a misalignment of the local reinforcement. Of course, the relatively low number of investigated specimens has also to be taken into account. Looking at the average strains, it is noticeable that hardly any differences between the specimen types can be observed. Nevertheless, regarding the local strain evolution around the support, there is a certain difference between the locally reinforced structure and the pure DiCo GF SMC component. The heterogeneous strain field around the support is limited to a smaller region for parts featuring a local reinforcement. Consequently, the damage evolution for both configurations is also comparable except the fact, that samples with local reinforcement may show a delamination of the reinforcement from the surrounding matrix. Unfortunately, a direct comparison of the results presented here with the experiments carried out by Wulfsberg et al. [7] is not possible, as this preset contribution focused on a structural specimen instead of coupon specimens. However, it can be proven, that it is feasible to reinforce SMC parts regarding the overall stiffness with local reinforcements based on continuous carbon fibers in a one shot process.

## 5 SUMMARY AND CONCLUSIONS

The aim of this contribution was to determine the influence of continuous carbon fibers (Co CF), which were introduced as local reinforcement on a discontinuous glass fiber SMC component, on the stiffness and damage behaviour of the final component. It was shown, that components with local Co CF reinforcement offer significant advantages. The parts are stiffer without sacrificing the benefits of discontinuously reinforced SMC regarding the design freedom. Additionally, the material and manufacturing costs are lower in comparison to components manufactured solely from continuous fibers. As SMC is already widely used, this hybridization option enlarges the area of application of these components. In order to further characterize the material, other load cases must also be investigated in future. The shape of the specimen was designed for a bending load, but in reality often combinations of different types of stress occur. Further investigations with regard to realistic loads can show how the component geometry and shape of local reinforcement, or its position, can still be optimized for practical use.

## 6 ACKNOWLEDGEMENT

The research documented in this manuscript has been funded by the German Research Foundation (DFG) within the International Research Training Group "Integrated engineering of continuous-discontinuous long fiber reinforced polymer structures" (GRK 2078). The authors would like to thank the companies Aliancys for providing the resin as well as Johns Manville and Zoltek for providing glass fibers and the carbon fiber fabric, respectively.

## REFERENCES


[1] J. Sauer, Automobilkarosserien kleben. Kunststoffe 93.3 (2003), A35–A39.

[2] H. Schürmann, Konstruieren mit Faser-Kunststoff-Verbunden. 2., bearb. und erw. Aufl. VDI-Buch. Berlin: Springer, 2007.

[3] L.Orgéas, P. J. J. Dumont, L. Nicolais, Sheet Molding Compounds. Wiley Encyclopedia of Composites. John Wiley & Sons, Inc, 2011.

[4] H. G. Kia, Sheet Molding Compounds: Science and Technology. Munich: Hanser, 1993.

[5] K. Sawallisch, Compounding of Sheet Molding Compound. Polymer-Plastics Technology and Engineering 23.1 (2006).

[6] M. Cabrera-Ríos, J.M. Castro, An Economical Way of Using Carbon Fibers in Sheet Molding Compound Compression Molding for Automotive Applications. Polymer Composites 27.6 (2006).

[7] J. Wulfsberg, A. Herrmann, G.Ziegmann, G.Lonsdorfer, N.Stöß, M.Fette, Combination of Carbon Fibre Sheet Moulding Compound and Prepreg Compression Moulding in Aerospace Industry. Procedia Engineering 81 (2014).

[8] A. Trauth, K.A.Weidenmann, Continuous-discontinuous Sheet Molding Compounds – Effect of hybridisation on mechanical material properties, 20th International Conference on Composite Structures, Paris, 2017.

# ROBUST AND ADAPTIVE NON DESTRUCTIVE TESTING OF HYBRIDS WITH GUIDED WAVES AND LEARNING AGENTS

**Stefan Bosse[*1], Michael Koerdt[2], Axel von Hehl[3]**

[1] University of Bremen, Department of Mathematics & Computer Science, Germany
[2] Faserinstitut Bremen e. V., Bremen, Germany
[3] Leibniz-Institut für Werkstofforientierte Technologien - IWT, Bremen, Germany
…

**ABSTRACT:** Monitoring of mechanical structures is a Big Data challenge concerning Structural Health Monitoring and Non-destructive Testing. The sensor data produced by common measuring techniques, e.g., guided wave propagation analysis, is characterized by a high dimensionality in the temporal domain, and moreover in the spatial domain using 2D scanning. The quality of the results gathered from guided wave analysis depends strongly on the pre-processing of the raw sensor data and the selection of appropriate region of interest windows (ROI) for further processing (feature selection). Commonly, structural monitoring is a task that maps high-dimensional input data on low-dimensional output data (feature extraction of information), e.g., in the simplest case a Boolean output variable "Damaged". Machine Learning (ML), e.g., supervised learning, can be used to derive such a mapping function. But quality and performance depends strongly on feature selection, too. Therefore, adaptive and reliable input data reduction (feature selection) is required at the first layer of an automatic structural monitoring system. Assuming some kind of one- or two-dimensional sensor data (or n-dimensional in general), image segmentation can be used to identify ROIs. Major difficulties in image segmentation are noise and the differing homogeneity of regions, complicating the definition of suitable threshold conditions for the edge detection or region splitting/clustering. Many traditional image segmentation algorithms are constrained by this issue. In this work, autonomous agents are used as an adaptive and self-organizing software architecture solving the feature selection problem. Agents are operating on dynamically bounded data from different regions of a signal or an image (i.e., distributed with simulated mobility), adapted to the locality, being reliable and less sensitive to noisy sensor data. Finally, adaptive feature extraction (information of structural state and damage) is performed by numerical algorithms and Machine Learning based on ultrasonic measurements of hybrid probes with impact damages.

**KEYWORDS:** Adaptive Image Segmentation, Feature extraction, Autonomous Agents, Self-organizing systems, Machine Learning and Clustering

## 1. INTRODUCTION

Monitoring of mechanical structures is a Big Data challenge that addresses Structural Health Monitoring (SHM) as well as Non-destructive Testing (NDT) methods. Trends poses the integration of sensor networks towards the design of self-aware structures, increasing the sensor density significantly and increasing the complexity of applications [1]. The sensor data produced by common measuring techniques, e.g., guided wave propagation analysis, is characterized by a high dimensionality of data in the temporal and spatial domain. There are off- and on-line methods applied at maintenance- or run-time, respectively. On-line methods (SHM) usually are constrained by low-resource processing platforms, sensor noise, unreliability, and real-time operation requiring advanced and efficient sensor data processing [5]. Commonly, structural monitoring is a task that maps high-dimensional input data on low-dimensional output data (information, that is feature extraction), e.g., in the simplest case a Boolean output variable "Damaged". Machine Learning (ML), e.g., supervised learning, can be used to derive such a mapping function, and reinforcement learning or unsupervised learning (clustering) can be used to improve information extraction. The development of hybrid and composite materials leads to new challenges in component testing and damage diagnostics. In

contrast to mono materials, hybrids suffer from well known and complete models. With a combined effect of several factors on guided wave propagation in hybrids and lamninates (e.g., fibre metal laminates), there is no clear determination of the cause of a change in wave propagation to the reference state is possible because the effects interfere. Commonly the effect of damages on the signals of detected guided waves are known effecting the signal processing.

The signal processing methodology shown in this work is the basis for the damage characterization and the description of the damage behavior of fiber composite metal laminates with different hybrid transition structures and in different states under quasi-static and cyclic loading conditions [15].

Numerical analysis of measuring data as well as ML quality and performance depends strongly on the input data size and feature variable selection (quality). Therefore, adaptive and reliable input data reduction (that is feature selection) is required on the first layer of an automatic NDT or structural monitoring system (regardless if it applied at run- or maintenance time).

Assuming some kind of one- or two-dimensional sensor data (or n-dimensional data in general), image segmentation can be used to identify Regions of Interest (ROI), e.g., of wave propagation signals and fields. A ROI is characterized by its relevance for further data processing, and can be recognized by specific patterns or by heuristic knowledge (e.g., the third wave of a recorded ultrasonic signal delivers information about a damage that is demonstrated in the experimental section). Wave propagation in materials underlie reflections that must be distinguished, especially in hybrid materials (e.g., combining metal and fibre-plastic composites) there are complex wave propagation fields. The image segmentation is one of the most crucial part of image processing [3]. Commonly used approaches are edge detection by finding abrupt changes in the signal field suffering from a high sensitivity to noise and inhomogenities [2].

General difficulties in image segmentation are noise and the differing homogeneity (fuzziness and signal gradients) of regions, complicating the definition of suitable threshold conditions for the edge detection or region splitting/clustering. Many traditional image segmentation algorithms are constrained by this issue. Artificial Intelligence can aid to overcome this limitation by using autonomous agents as an adaptive and self-organizing software architecture, presented in this work. Using a collection of co-operating agents decomposes a large and complex problem in smaller and simpler problems with a Divide-and-Conquer approach. Related to the image segmentation scenario, agents are working mostly autonomous (de-coupled) on dynamic bounded data from different regions of an image (i.e., distributed with simulated mobility), adapted to the locality, being reliable and less sensitive to noisy sensor data. Agent-based approaches can be used to enhance classical edge-based approaches, e.g., applying edge regularization using Bayesian methods [2]. A review of agent-based image segmentation approaches can be found in [3]. Applying artificial intelligence approaches using autonomous agents and data marking to edge detection, clustering, and region growing was introduced in [6], featuring reduced computational costs and a wide application field (due to its self-adaptation feature). Random behaviour can aid finding regions and clusters more accurately, efficiently, and faster [4]. This technique is applied in this work to (virtual) agent migration decisions.

In this work, a simple but powerful agent-based segmentation approach combined with Machine Learning (ML) is introduced and evaluated with measured high-dimensional data from piezo-electric acusto-ultrasonic sensors that recorded stimulated wave propagation in plate-like structures. Commonly, SHM deploys only a small set of sensors and actuators at static positions delivering only a few spatially resolved sensor signals (1D), but with high temporal resolution, whereas NDT methods additionally can use spatial scanning to create images of wave signals (2D). Both one-dimensional temporal and two-dimensional spatial segmentation is considered to find characteristic ROIs automatically.

## 2. NON-DESTRUCTIVE TESTING (NDT) OF STRUCTURES AND SHM

NDT usually performs only a few point-to-point measurements to detect damages. The two-dimensional recording of the wave propagation and interaction of guided waves can be performed by using laser vibrometry [8], [9] or an airborne ultrasonic testing technique [10]. In order to be able to excite guided waves, an actuator, usually made of piezo-ceramic materials, must be applied to the structure. By adjusting the geometry of the actuator [10] or its electrode configuration [7], the amplitudes of individual modes can be amplified or attenuated to emphasize specific wave interaction. The identification of damages is made by wave interactions, such as reflection, scattering, mode conversion and wave number changes, in wave propagation.

At delaminations or thicknesses these wave interactions can be determined using wave number spectroscopy (2D-FFT of the wave propagation) [12]. However, these methods require a locally resolved scan of the

wave propagation, producing wave propagation images with only a few regions of interest. The entire measuring setup and the synopsis with this work performing feature selection and extraction is shown in Fig. 1.

A locally resolved segmentation and clustering of sensors and their sensory data as a precursor of SHM and ML methods have so far only been inadequately addressed, but it is an important sensor fusion and feature selection instrument. Here we analyze the wave propagation and interaction using air-ultrasound technology and identify features to the damage interaction of different modes in the time and wave number domain.

Because of the risk of externally invisible damage in laminates (e.g., fibre metal laminates), integrated component monitoring (Structural Health Monitoring) also plays a key role for such hybrid materials. The goal of component monitoring is to answer the following questions: Is there a damage? Where is the damage? Of what kind is the damage and how big is its extent?

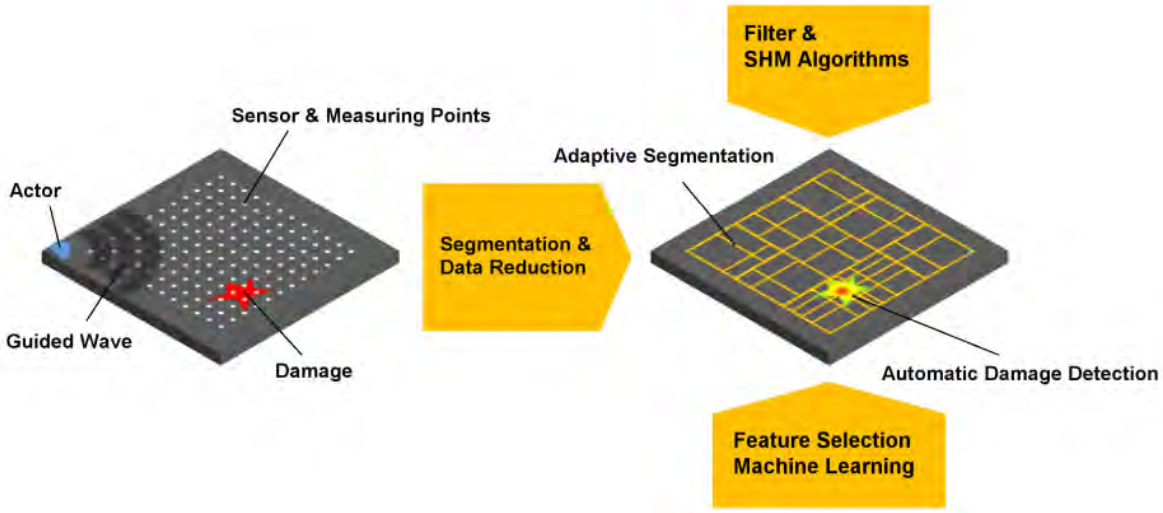


***Fig. 1*** *Automated, model-free damage detection with guided ultrasonic waves and 2D scanning*

In particular, when detecting the type of damage and size of damage there is still considerable, fundamental issues for components made of layered materials with anisotropic layers and high impedance differences between the layers. The high impedance differences lead to previously unknown wave propagation behavior in laminates. This complicates the evaluation of measurement signals of guided waves for detecting damages. The data processing methods introduced in this work address NDT and SHM, too.

## 3. HYBRID MATERIALS: THE CHALLENGE

Hybrid materials combine dissimilar materials of different material classes in a way that the individual material-specific advantages become effective in an optimal manner within the whole lightweight structure. Owing to their outstanding lightweight potential hybrid materials penetrate more and more into applications in transportation.

Since hybrid materials combine dissimilar materials, the structures made of such materials are characterized by complex, multiphase bonding zones whose strength depends to a great extent on their dimensional as well as material design, the applied production techniques and the resulting material and interface properties at local level.

Hence, the destructive analysis and evaluation of the failure behavior of these structures with the intention of deepening the understanding of their loading capacity in order to improve their design and production techniques, and to make their strength and survival probability predictable are extremely challenging compared to monolithic structures.

For instance, the failure mode of a failed structure is result of the failure mechanisms leading to a propagating degradation of the structure. The failure mechanisms themselves again are strongly depending on both the design and dimensioning of the structure, but particularly on the defects caused by the involved production techniques.

For example three different failure modes occurred in hybrid CFRP-Titanium-Aluminum transition structures are shown in Fig. 2 [17].

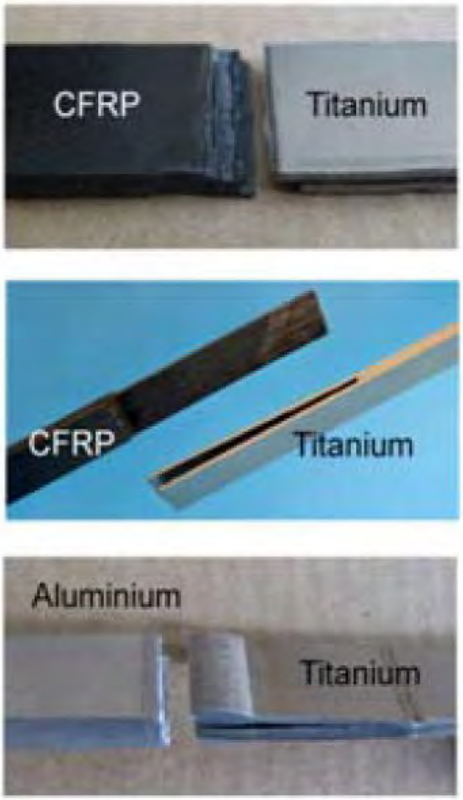


***Fig. 2*** *Different failure modes occurring in hybrid CFRP-Titanium-Aluminum transition structures after failure (Top: CFRP; Middle: hybrid laminate; Bottom: Aluminum (width 15 mm))[17]*

In order to help identifying the failure mechanisms a non-destructive detection of the failure propagation in an early stage would significantly improve the understanding of the interrelation between failure mechanisms and failure modes.

Current research is focused on integrated structural health monitoring (SHM) systems that are capable of detecting structural damage via guided ultrasound waves.

To realize this, the effects on the propagation characteristics of piezo-induced guided waves have to be analyzed. In order to enable the identification of a specific failure the correlation of sensor response and the failure propagation is mandatory. This could be arranged by a systematic classification of the failure modes by means of materialographical analysis combined with clustering techniques of AI methods.

## 4. IMAGE AND SIGNAL SEGMENTATION

Image segmentation is a method to divide an image in different regions (clusters) to identify regions of interest, i.e., isolating regions for further processing (feature extraction). In a signal processing system this is the first important feature variable selection (considering each pixel of an image as variable), e.g., using this reduced variable set as an input vector for Machine Learning. In this work, one-dimensional vectors retrieved from time-resolved ultrasonic wave measurement are used for segmentation tasks. The goal is to automatically detect the relevant signal region (Region of Interest, ROI) used for further numerical damage detection and analysis under varying measuring conditions and without the requirement of manual scaling of signal records. The ROI extraction depends on the signal record, geometrical signal sender and receiver positions, signal quality (noise), and the probe geometry.

## 5. THE MULTI-AGENT SYSTEM WITH SELF-ORGANIZATION

The Multi-agent System (MAS) consists of simple agents with different behaviour. The signal segmentation algorithm bases on an event-based divide-and-conquer approach, shown in Fig. 3. Details of the underlying agent behaviour and programming model can be found in [5].The time-resolved signal vector $\boldsymbol{x}(t)$ is reduced to a segment vector $\boldsymbol{s}(n)$ by using a data filter algorithm (peak, arithmetic average, or exponential filter). Each data segment is handled by a segment agent, instantiated by a master agent. A segment agent can create explorer agents to investigate the segment neighbourhood within a given radius. Agents communicate with each other by using signals (lightweight messages). The segment and explorer agents perform the feature variable selection, and the master agent finally performs the feature information extraction delivering ROIs of the signal input vector.

The summary of the behaviour of the different agents is listed below:

**Master Agent**

The master agent controls the divide-and-conquer process and instantiates segment agents (one for each signal data segment). The master agent transforms the input signal vector to a segment vector of fixed length. Each time a new data set is loaded, the segment agents are notified by sending a `LOAD` signal.

The master agent collect all markings from marked data cells and computes ROIs (by using its *gap* and *roiXX* parameters, see below).

**Segment Worker Agent**

Each segment agent is responsible for one data cell and performs a check for an data event if it got a `LOAD` signal, that means, if there is a significant change in its associated cell data value. If an event was detected, an initial explorer agent is created. An explorer agent is created with a specific set of parameters, which can be adapted by the master agent and the segment agent. The segment agent communicates with its explorer child agents and with its master agent via signals.

**Explorer Agent**

The explorer agent has the goal to collect data from the current left and right side neighbourhood within a given radius. The neighbourhood data values are compared with the current associated data value (difference $|\boldsymbol{s}(i\pm\delta)\text{-}\boldsymbol{s}(i)|$ with $\delta=\{-r,..,-1,1,..,r\}$), and differences lying within a given interval $\Delta$ are counted. If the counter lies within another given interval $\{\eta_{min},..,\eta_{max}\}$, the explorer marks the cell and reproduces itself. The clone migrates virtually to another neighbour cell (left or right side). If the counter values is outside of the interval, it migrates (virtually) to another neighbour cell, performing the exploration again. If random walk is enabled, the diffusion and reproduction direction are chosen randomly, otherwise always one more agent is instantiated on diffusion (opposite direction) and two agents are reproduced (moving in opposite directions).

The explorer agent parameter set consists of the following variables: $\{i, \Delta, \eta_{min}, \eta_{max}, r$, *lifetime* $\tau$, *decay* $\delta$, *randomwalk*$\rho\}$. The segment agent is parameterized by: $\{threshold\zeta\}$. The master agent is parameterized by the set: {*gap*, *roiMin*, *roiMax*, *roiWeightMin*, *roiWeightMax*}.

A signal segmentation and ROI feature extraction delivers the following output variables (delivered by the master agent) enabling the calculation of a quality measure of the extraction: {*agentsTotal*, *markings*, *roi*, *roiWeight*}.

Initially there is a pre-defined table of parameter sets that must be mapped on different signal properties (i.e., sensitivity, noise, signal shape). The success of the ROI feature extraction is sensitive to the proper choice of a parameter set for a specific signal record. The selection of a suitable parameter set is performed by a machine learner introduced in the next section.

Initially there is a pre-defined table of parameter sets that must be mapped on different signal properties (i.e., sensitivity, noise, signal shape). The success of the ROI feature extraction is sensitive to the proper choice of a parameter set for a specific signal record. The selection of a suitable parameter set is performed by a machine learner introduced in the next section.

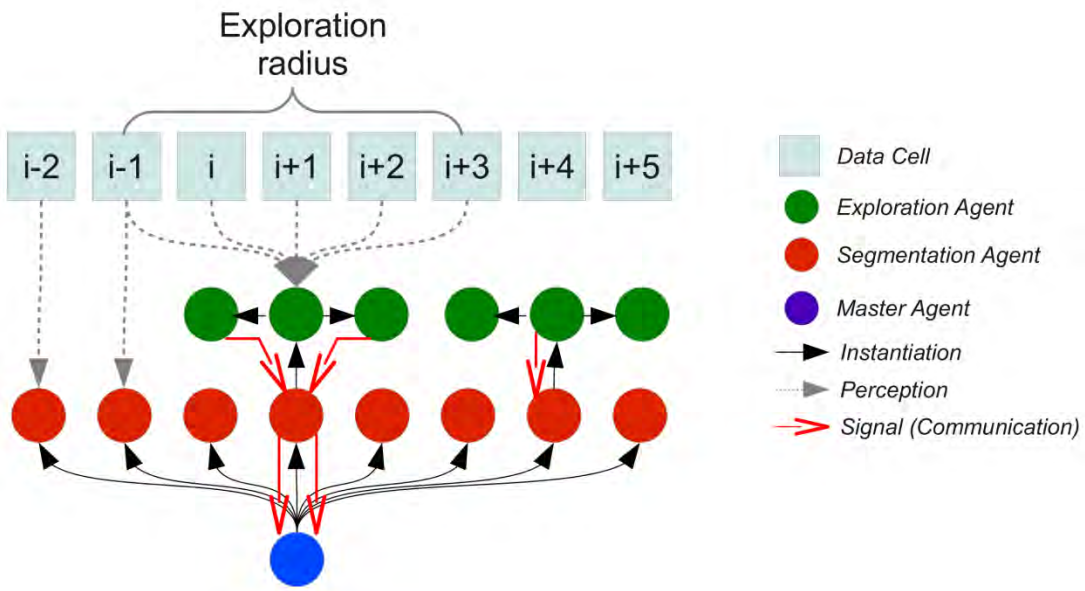


***Fig. 3*** *The MAS: Perception; Event-based instantiation of explorer agents; Diffusion and Reproduction; Communication via signals*

## 6. AUTOMATIC PARAMETER SELECTION

Signal records from acoustic measurements can differ significantly with respect to amplitudes, the frequency spectrum, and noise. The MAS introduced in the previous section used for signal segmentation and ROI extraction relies on parameter sets. Different signal records require different parameter sets for optimal ROI extraction and minimal computational costs. Among auto-adaptation of parameter sets by back-propagation and reinforcement learning based on on quality-of-service evaluation of the ROI extraction, supervised learning can be used to predict an optimal parameter set for a specific signal record to be processed, shown in Fig. 4.

The initial high-dimensional sensor data record is down sampled. Relevant features are extracted from the original and down-sampled record to provide a signal characterization: Constant offset $s_0$ (filtered mean value); Standard deviation $s_1$; Peak amplitude (positive & negative) $s_2$,$s_3$; Frequency distribution ranges ($f_1$,$f_2$,$f_3$,$f_4$); and the Histogram distribution ($h_1$,$h_2$,$h_3$,$h_4$).

The signal record feature vector $\boldsymbol{sf}$=($s_0$,$s_1$,$s_2$,$s_3$,$f_1$,$f_2$,$f_3$,$f_4$, $h_1$,$h_2$,$h_3$,$h_4$) is the input for a Decision Tree learner used to predict a suitable parameter set at run-time (see Fig. 4). The learning task is performed with a known training data set with different signal records providing a relation between a specific measured signal record and the best matching parameter set for ROI feature extraction determined automatically. Initially an Interval Decision Tree Learner (DTL) providing noise stability was used [14].

But the training data delivers signal feature vectors very close to each other and the feature vector consists of different variable types (with respect to their value range and noise characteristics) preventing any suitable variable separation and leading to overall wrong predictions at run-time. Therefore, a simple Multi-layer Artificial Neural Network (ANN) classifier is used instead. The ANN implementing the classification function $f(\boldsymbol{sf})$: $\boldsymbol{sf}\rightarrow P$ requires a normalization of all input variables to the range [0,1] independently. Each parameter set is represented by one output node of the ANN. Hidden layers can be required to implement a proper classification function.

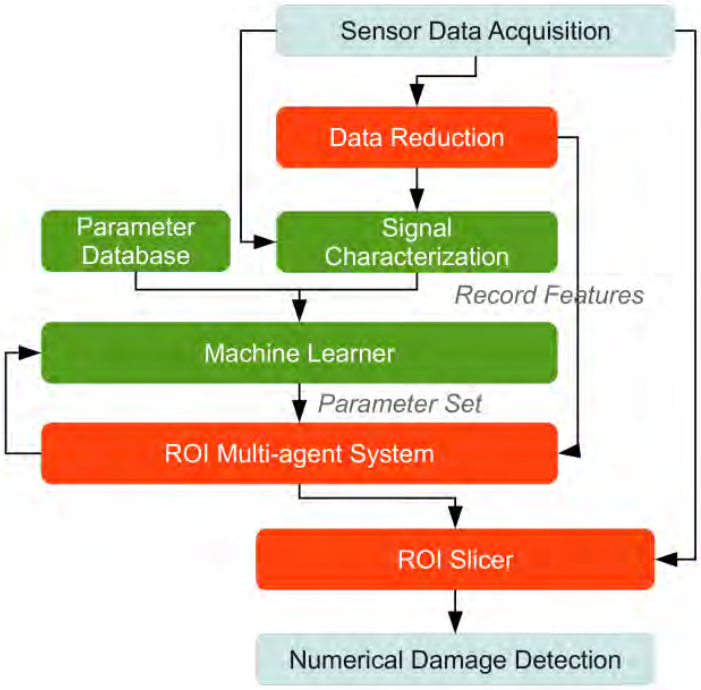


***Fig. 4*** *Sensor data pre-processing using a multi-level architecture and Machine Learning providing an automatic and adaptive MAS parameter selection.*

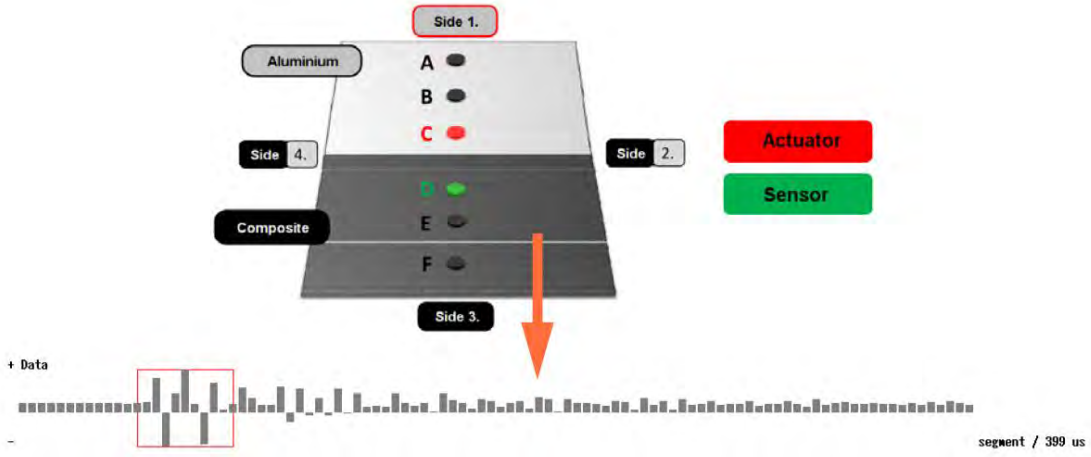


***Fig. 5*** *(Top) Experimental setup and placement of PWAS; in this case the transmitted signal from position C to position D is measured (Bottom) Down-sampled segmented signal record and result of the agent-based ROI feature extraction (red rectangle).*

## 7. EXPERIMENTAL ULTRASONIC MEASUREMENT

The experimental setup for guided-wave propagation consists of a digital oscilloscope Tektronix DPO 5054 and an arbitrary signal generator Hewlett Packard HP 33120A connected to a wideband amplifier Falco Systems WMA-300. The input signal is a Hann-windowed 200 kHz sinusoidal burst of three counts.

Fig. 5 shows the principle experimental setup delivering the signal vectors used by the MAS and analyzed in Sec. 8.. 512 values of the sensor responses with a time resolution of 8 ns are averaged for the signal vectors. The device under test (DUT) is a hybrid structure consisting of a metal (Aluminum) plate and a quasi-isotropic carbon fiber reinforced plastic (CFRP) composite plate. Each plate has a thickness of 4 mm and overall dimensions of 300 mm x 300 mm.

The plates are butt-coupled and an ultrasonic couplant gel is between the coupling edges of the plates. In this way the acoustic interface between the plates is realized by the ultrasonic couplant gel.

Along the vertical axis (side 1 - side 3) ultrasonic round piezoelectric wafer active sensors (PWAS) with a thickness of 0.2 mm and a diameter of 10 mm are placed at different positions A–F. The distance between the positions C and D is 150 mm. The distance between the positions C and B is 100 mm. The PWAS are bonded on the plate surface with Z70 cyanoacrylate adhesive. The piezoelectric material of the PWAS is the ceramic lead zirconatetitanate (PZT) PIC255 from PI Ceramic GmbH with the notation PRYY+0412.

In the measurements the PWAS at position C is used as an actuator (and for some experiments at position D). As a sensor for the reflected ultrasonic signal at the interface the PWAS at position B is used. Finally, as a sensor for the transmitted ultrasonic signal through the interface the PWAS at position D is used. In order to simulate and create definite damages in the interface the ultrasonic couplant gel is removed over definite lengths and positions.

The signals recorded under different settings (transmission or reflection measurement) differ significantly with respect to their dynamic range, base-line offset, and noise.

## 8. SIMULATION AND ANALYSIS

The sensor data recorded in the experiments from Sec. 7..was used to simulate and evaluate the hybrid approach consisting of the SoS MAS and ML and using the JavaScript Agent Machine (JAM) platform (details can be found in [13]). Monte carlos simulation was used in all MAS/ML experiments applying 10% noise to each signal record. Each experiment was repeated ten times to get an average result.

An example ROI marking using the MAS is shown in Fig. 5. Experiments are made with different DUT configurations: (105) Aluminum only without coupling layer; (108) Hybrid structure with actuator pos. C; (110) Hybrid structure with actuator pos. D (details are shown in [16]). Furthermore, different MAS parameter sets were investigated (P1-P10, details are shown in [16]). Using random walk behaviour reduces the number of required (and created) agents on the order of a decade compared with the non-random walk behaviour.

The master agent observes the number of created agents (*agentsTotal*), the number of found ROIs (defined by the markers set by the explorer agents and a gap parameter), and the ROI weight (i.e., the mean width of the ROIs) to compute a quality measure of the self-organizing ROI detection. The higher the number of created explorer agents is, the higher is the number of markings (under the assumption there is the condition satisfied required to detect a region boundary).

The quality $Q$ of the ROI detection computed by the master agent is given by Eq. 1.

$$Q = \left\{ \begin{matrix} 0, \#roi \neq 1 \\ 1, \#roi = 1 \end{matrix} \right\} - \left| roiw - w_0 \right| / k - \left| (roi_0 + roi_1)/2 - c_0 \right| / k \quad (1)$$

with $\#roi$ as the number of detected ROIs (must be one), $roiw$ as the ROI weight (width, i.e., $roi_1$-$roi_0$), $roi_0$ and $roi_1$ are the start and end time of the detected ROI, and $c_0$ is the expected center position of the ROI (based on export knowledge), and $k$ is an error weight factor in the range $k$=[5,50]. The last term $|roi_0+roi_1|/2$-$c_0$ is only used for the evaluation of these ROI detection approach in this work, but not used for the on-line quality estimation at run-time (the expected center point of the ROI $c_0$ is unknown).

The first evaluation was performed with signals having a high signal-to-noise ratio (resulting from reflection signals). The DUT was the aforementioned Aluminum-Composite hybrid structure with an additional gap between the material boundaries. All parameter sets uses random walk behaviour that requires about 20 times fewer agents, but with comparable quality of the ROI detection in all evaluated data sets. Commonly only about 20-30 agents are required for a high-quality detection, shown in Fig. 6 (Bottom). The settings of these parameters depend on the overall signal strength and noise.

The second evaluation uses signals with a low signal-to-noise ratio making the ROI feature selection more difficult and unreliable (resulting from transmitted signals). The choice of appropriate parameter sets with signals having a high signal-to-noise ratio is less critical. Here the choice of an appropriate parameter set is crucial and parameter values must be chosen from narrow ranges for a specific signal. As more as the parameter set is unmatched to the signal as higher is the agent creation rate (or zero), though this primarily correlates with the delta $\Delta$ and threshold $\zeta$ parameter values.

In most cases the agents were able to find the relevant main ROI with a quality factor $Q$>0.5 based on a parameter set delivered by a previously trained ANN using the signals record feature vectors ***sf***, requiring typically less than 40 explorer agents (see Fig. 6).

The configuration of the ANN is crucial. One hidden layer with 8 nodes was added to improve the prediction results (i.e., improvement of the separability of different input-output relations). The learning phase used 2000 iterations to train the perceptron nodes.

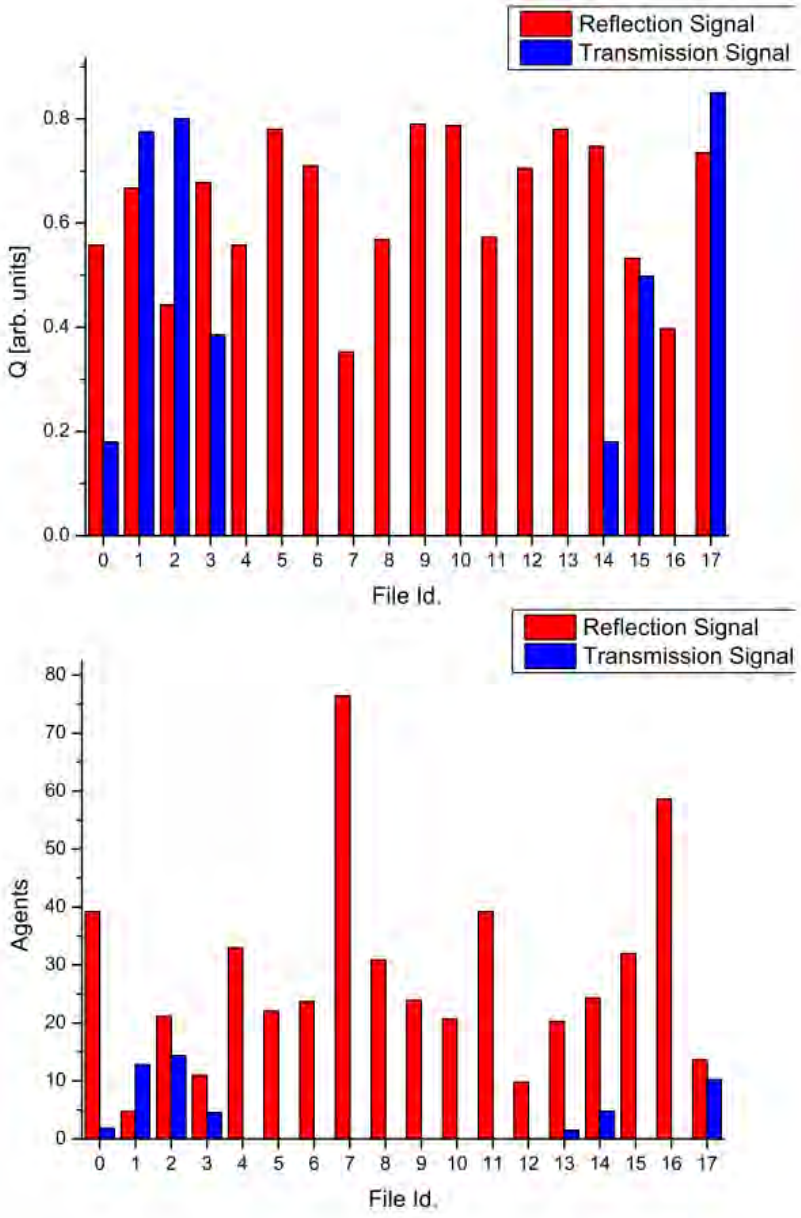


***Fig. 6*** *Evaluation of simulation results: (Top) Automatic ROI feature extraction quality for different signal records (Bottom) Required Explorer Agents*

## 9. CONCLUSION

A self-organizing agent-based approach was used successfully to detect relevant regions in measured ultrasonic wave sensor signals performing a feature selection. With a suitable parameter set controlling the MAS a high quality ROI extraction can be achieved. The bounded regions are used for further processing in a numerical damage detection process (feature extraction). The MAS operates event-based and divides the

input data vector in segments and is populated with agents operating regionally but cooperating to satisfy a global goal (the feature selection generating ROI markers). The self-organizing and parameterizable behaviour capabilities ensure robust feature extraction. In this work, a suitable parameter set for a specific signal record was automatically chosen by an ANN using a signal record feature vector. Most signal records can be processed properly this way. But the evaluation showed a weak correlation between the signal record feature vector and the right parameter set. Further work has to investigate more suitable feature variables able to separate and to identify signal record classes more robustly, eventually based on clustering.

## REFERENCES


[1] V. Di Lecce, M. Calabrese, and C. Martines, *From Sensors to Applications: A Proposal to Fill the Gap*, Sensors & Transducers, vol. 18, no. Special Isse, pp. 5–13, 2013..

[2] S. Mazouzi, Z. Guessoum, F. Michel, and M. Batouche, *A Multi-agent Approach for Range Image Segmentation*, in CEEMAS 2007, LNAI 4696, 2007, pp. 1-10.

[3] P. Mishra, N. Srivastava, A. Singhal, and K. K. Shukla, *Agent based Image Segmentation Methods: A Review*, Int. J. Comp. Tech. Appl.,, vol. 2, no. 3, pp. 704-708, 2011.

[4] K. E. Melkemi, M. Batouche, and S. Foufou, *MRF Model-Based Approach for Image Segmentation Using a Chaotic MultiAgent System*, in WILF 2005, LNAI 3849,, 2006.

[5] S. Bosse, A. Lechleiter, *A hybrid approach for Structural Monitoring with self-organizing multi-agent systems and inverse numerical methods in material-embedded sensor networks*, Mechatronics, (2016), DOI:10.1016/j.mechatronics.2015.08.005.

[6] H. Kagawa, M. Kinouchi, and M. Hagiwara, *Image segmentation by artificial life approach using autonomous agents*, in International Joint Conference on Neural Networks, 1999. IJCNN '99.

[7] D. Schmidt. *Modenselektive Übertragung von Lambwellen in Faserverbundstrukturen*,. Dissertation. Braunschweig, 2014

[8] W. J. Staszewski et al., *Structural health monitoring using scanning laser vibrometry: I. Lamb wave sensing*,. In: Smart Materials and Structures 13.2 (2004), S. 251–260. DOI: 10.1088/0964-1726/13/2/002

[9] L. Mallet, B. C. Lee, W. J. Staszewski und F. Scarpa. *Structural health monitoring using scanning laser vibrometry: II. Lamb waves for damage detection*. In: Smart Materials and Structures 13.2 (2004), S. 261–269. ISSN: 0964-1726. DOI: 10.1088/0964-1726/13/2/003

[10] W. Hillger. *Visualisation of Guided Wave Propagation by Ultrasonic Imaging Methods*. Crete-Greece, 11-14.10.2007.

[11] V. Giurgiutiu. *Tuned Lamb Wave Excitation and Detection with Piezoelectric Wafer Active Sensors for Structural Health Monitoring*. In: Journal of Intelligent Material Systems and Structures 16.4 (2005), S. 291–305.

[12] E. B. Flynn, S. Y. Chong, G. J. Jarmer und J.-R. Lee. *Structural imaging through local wavenumber estimation of guided wave,*. In: NDT & E International 59 (2013), S. 1–10. ISSN: 09638695. DOI: 10 . 1016 / j.ndteint.2013.04.003

[13] S. Bosse, *Mobile Multi-Agent Systems for the Internet-of-Things and Clouds using the JavaScript Agent Machine Platform and Machine Learning as a Service*, in The IEEE 4th International Conference on Future Internet of Things and Cloud , 22-24 August 2016, Vienna, Austria, 2016, DOI: 10.1109/FiCloud.2016.43

[14] S. Bosse, *Structural Monitoring with Distributed-Regional and Event-based NN-Decision Tree Learning using Mobile Multi-Agent Systems and common JavaScript platforms*, Procedia Technology, 3rd International Conference on System-Integrated Intelligence: New Challenges for Product and Production Engineering, June 13th (Mon.) - 15th (Wed.) 2016: Paderborn, Germany, 2016, DOI:10.1016/j.protcy.2016.08.063.

[15] H. Hasselbruch, A. von Hehl und H.-W. Zoch, *Properties and failure behavior of hybrid wire mesh/carbon fiber reinforced thermoplastic composites under quasi-static tensile load*. In: Materials & Design 66 (2015), p. 429–436. ISSN: 02613069. DOI: 10.1016/j.matdes.2014.07.032.

[16] S. Bosse, M. Koerdt, D. Schmidt, *Robust and Adaptive Image Segmentation for Structural Monitoring using Autonomous Agents,* In Proceedings of the 4th Int. Electron. Conf. Sens. Appl., 15–30 November 2017; ; doi:10.3390/ecsa-4-04917

[17] J. Schumacher, B. Clausen, H.-W. Zoch, *Strength and failure behavior of carbon fiber reinforced plastics (CFRP) -aluminum seam structures, Materials* Science and Engineering Technology, Vol. 45 (2014) 12, pp 118- 1115, 2014

# INVESTIGATION OF FAILURE MECHANISMS IN HYBRID FIBER-REINFORCED PLASTICS BY MEANS OF IN-SITU-CT

**Florian Bittner[1*], Hans-Josef Endres[1,2]**

[1] Application Center for Wood Fiber Research HOFZET®, Fraunhofer Institute for Wood Research,Wilhelm-Klauditz-Institute WKI, Hannover, Germany
[2] Institute for Bioplastics and Biocomposites, University of Applied Science and Arts Hannover, Germany

## ABSTRACT:

The failure mechanisms of fiber-reinforced plastics can be studied in detail with a novel In-situ-CT 4-point bending test, based on the testing standard ISO 14125. The 4-point bending test creates a complex load condition under simultaneous influence of tensile and compressive forces. By non-destructive CT measurement at different load levels the origin and development of defects can be traced. Initial tests performed on a natural and a hybrid fiber reinforced plastic reveal significant differences in defect initiation and development. Ruptures of the yarn on the tensile-loaded side characterize the failure process of the natural fiber-reinforced plastic. In the hybrid fiber-reinforced plastic carbon fibers initially show damage on the compression-loaded side followed by fiber breaks on the tensile-loaded side. Matrix failure as well as pores as potentially weak points apparently have no influence in this example. Relevant relaxation effects could be excluded on the investigated macroscopic scale.

**KEYWORDS:** Hybrid fiber-reinforced plastics, failure mechanisms, In-situ-CT

## 1 INTRODUCTION

Novel hybrid fiber-reinforced plastics (FRP) enable to combine the beneficial characteristic properties of different reinforcing fibers, for example carbon and natural fibers. Thereby materials for lightweight construction with high strength can be created which are more cost-efficiently and environmental-friendly then pure carbon materials [1,2].
To specifically optimize the materials a deeper knowledge about the processes under load inside these complex materials – finally leading to part failure – is of major importance. In-situ computed tomography (In-situ-CT) can contribute significantly to this. Beyond classical CT applications, the behaviour of a specimen is monitored dynamically in the course of several consecutive CT measurements, while the specimen is exposed to an increasing external load.
In an innovative 4-point bending test, based on the testing standard ISO 14125 [3], the specimens are exposed to a complex load condition under simultaneous influence of tensile and compressive forces. This reveals extensive and practise-oriented informations about the mechanisms of failure. The material structure is captured 3-dimensionally by CT measurements at different load levels, allowing to detect at which load initial defects such as delaminations or fiber breaks develop, and how they spread until final material failure.

## 2 EXPERIMENTAL

### 2.1 EXPERIMENTAL SETUP

During In-situ-CT measurements specimens are being tomographed under variation of defined exterior influences to track changes inside the specimen induced by the influences. This can mean for example an increasing or cyclic mechanical, thermal or corrosive load [4]. Single research facilities have already conducted In-situ-CT-measurements of FRP to improve the understanding of mechanical failure mechanisms. These studies are mostly restricted to uniaxial loads, i.e. tensile or compression tests [5-8].

* Corresponding author: Heisterbergallee 10 A, 30453 Hannover, Germany, +49 511 9296-2262, florian.bittner@wki.fraunhofer.de

In addition to this, an In-situ-CT 4-point bending test setup for FRP is now available. In contrast to In-situ tensile tests [8] in 4-point bending tests the specimens are exposed simultaneously to tensile and compression forces. In this way, the material failure is investigated in a complex and application-oriented scenario.
The execution of the In-situ test is leant as closely as possible on the testing standard ISO 14125 for the determination of flexural properties of FRP [3]. Instead of the 3-point bending test, which is more common in classical mechanical testing, the 4-point bending test was selected due to two major advantages. Firstly, the 4-point bending test offers the advantage of a constant bending moment between the loading pins, resulting in a larger representative area of defect generation. Secondly, the 4-point bending test supports low-artefact CT measurements of the volume exposed to the highest load, because the potentially disruptive loading pins can be located outside the X-ray beam path.
To realize a measurement setup as small as possible, which is preferable for the execution of the CT measurements, the loading unit and the specimen holding fixture were constructively separated. The specimen is clamped in a stage. In this stage the bending load is applied to the specimen outside the CT system (Fig. 1). The bending test is performed either force- or distance-controlled and is stopped at specific predefined load levels. When a load level is reached the specimen deformation is fixed mechanically inside the stage and the CT measurement is performed. The underlying concept of the 4-point bending test, developed at the Fraunhofer application center CTMT, is described in detail elsewhere [9].

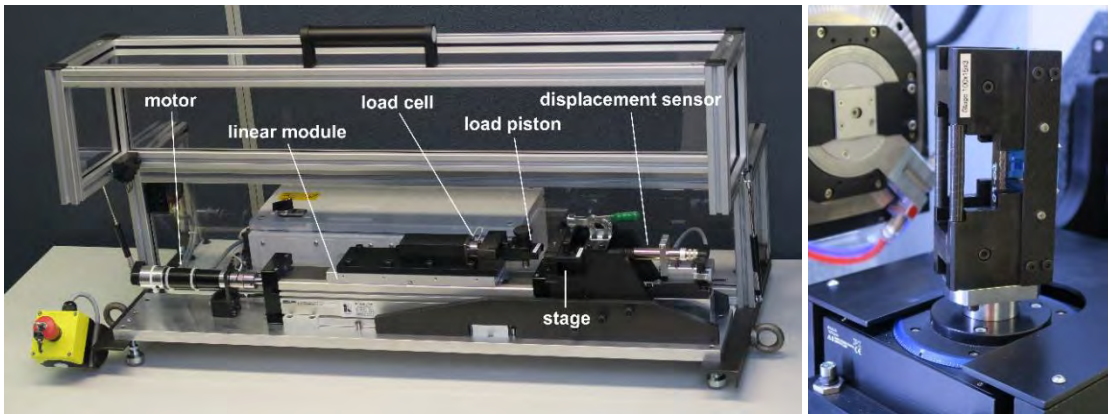


***Fig. 1*** *Total view of the 4-point bending test setup with mounted stage (left); fixture stage inside the CT system with FRP specimen under load (right).*

## 2.2 SPECIMEN PREPARATION

The In-situ bending test was carried out on two different FRP systems, a natural fiber reinforced plastic (NFRP) with thermosetting matrix and a hybrid fiber reinforced plastic (HFRP) combining natural and carbon fibers in a thermoplastic matrix. The NFRP was fabricated in a vacuum infusion process. 6 layers of flax fabric were processed with an epoxy resin. The resulting composite has a plate thickness of about 3.4 mm and a fiber mass fraction of about 43%. For the fabrication of the HFRP PA11 foils were stacked with the reinforcing fiber fabrics and consolidated in a hot press. The symmetrical build-up consists of 2 outer layers of carbon fiber fabric each and a core of 4 layers of linen fabric. The plate thickness and the fiber mass fraction amount to about 4.3 mm and about 40%, respectively.

## 2.3 BENDING TEST

The test samples with dimensions of 100 x 15 mm² were loaded in the 4-point bending test with a supporting width of 81 mm and a testing speed of 5 $mm \cdot min^{-1}$. The bending test was interrupted distance-controlled to acquire CT data of the resulting load levels. The NFRP was loaded in 1 mm steps up to a nominal deflection of 5 mm, subsequently in 2.5 mm steps up to a nominal deflection of 10 mm. The HFRP was loaded in 1 mm steps up to a nominal deflection of 3 mm.

## 2.4 CT MEASUREMENTS

The CT measurements of the samples inside the fixture stage were performed on a CT-AlphaDuo device (Procon X-Ray GmbH, Sarstedt, Germany). As X-ray parameters a voltage of 120 kV and a current of 250 µA were selected. The voxel resolution of the reconstructed volumes amounts to 17 µm, the measuring time for each load level was about 25 min.
Directly before and after the CT measurements single 2D X-ray projections were captured to detect macroscopic relaxation effects.

### 2.5 DATA ANALYSIS

For analysis and visualization of the volume data VGSTUDIO MAX 3.0 (Volume Graphics GmbH, Heidelberg, Germany) was used. To verify the real deflection of the samples opposed to the nominal deflection the volume data were aligned to an assistance structure and the distance between the non-loaded and the loaded sample at the position of maximum deflection was measured. The distance was determined, analogous to the measurement with the displacement sensor inside the 4-point bending test setup, on the support side. The evaluation and quantification of defects inside the composites was performed visually on the basis of CT slice images.
The function "Difference" of the image analysis tool ImageJ 1.48v (National Institutes of Health, Bethesda, USA) was applied to generate differential images of the 2D projections before and after the CT measurements.

## 3 RESULTS AND DISCUSSION

### 3.1 DISPLACEMENT LINEARITY AND NFRP TESTING

Fig. 2 illustrates exemplarily the NFRP's real deflection measured centric between the loading pins. The plotting of real vs. nominal deflection reveals a systematic deviation. Below 3 mm the deviation between real and nominal deflection is positive, above 3 mm the deviation is negative. The reason for this behaviour is presently unknown and is subject to further investigations. Subsequently the real deflection, determined from CT measurements, will be quoted.

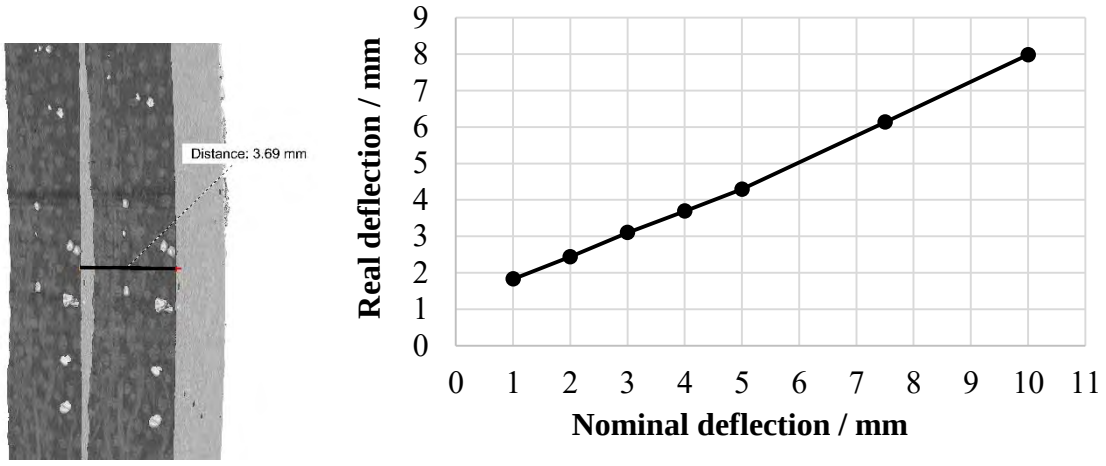


***Fig. 2*** *Exemplary measurement of NFRP's deflection at a nominal value of 3 mm (left); correlation between nominal and real deflection determined by CT measurement (right).*

Inside the NFRP specimen first cracks appear at a real deflection of 3.7 mm. The number of cracks rises substantially with further increasing deflection, as depicted in Fig. 3.

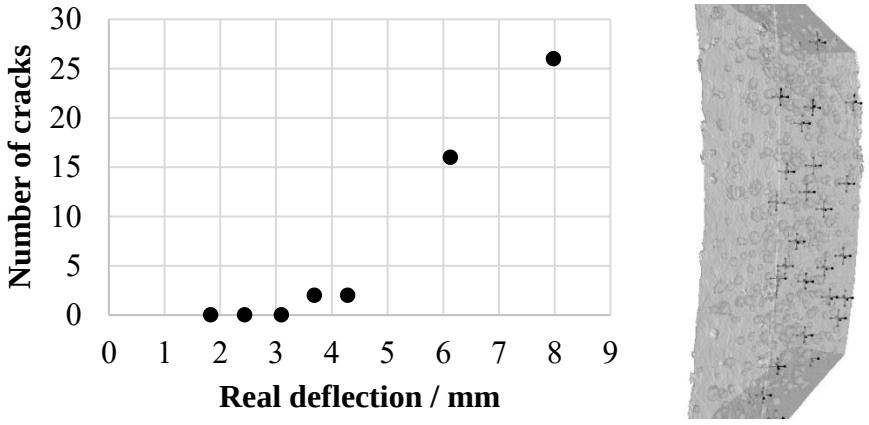


***Fig. 3*** *Number of cracks in the NFRP specimen as a function of real deflection (left); distribution of cracks inside the NFRP specimen at a real deflection of 8 mm.*

The cracks do not originate from pores inside the matrix. Instead, all cracks develop close to the surface of the tensile-loaded outer side. The progression of two exemplary cracks can be observed on the slice images in Fig. 4, starting at a deflection of 6.1 mm. The slice image of the unloaded specimen illustrates the closure of the cracks after disappearance of the load. This invisibility of defects after completion of mechanical testing emphasizes the significance of In-situ-CT measurements for the investigation of failure mechanisms.

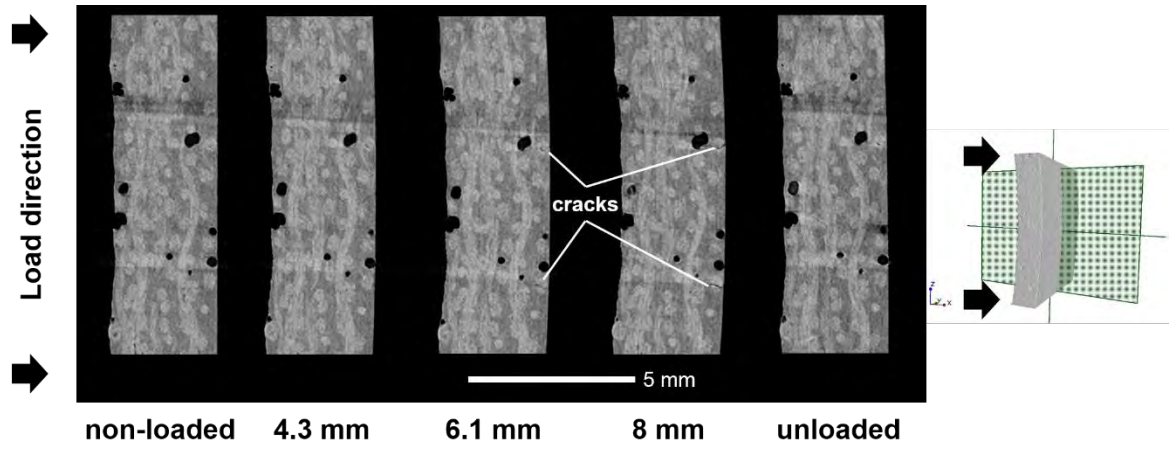


***Fig. 4*** *Defect progression with increasing deflection inside the NFRP and crack closure after unloading.*

As observable in Fig 5, a tensile load at right angle to the yarn direction leads to ruptures inside the yarn. The yarns loaded parallel to the yarn direction show no defects. This can be ascribed to the comparatively high breaking elongation of the natural fibers [10].
On the compression-loaded side of the NFRP no defects are recognizable.

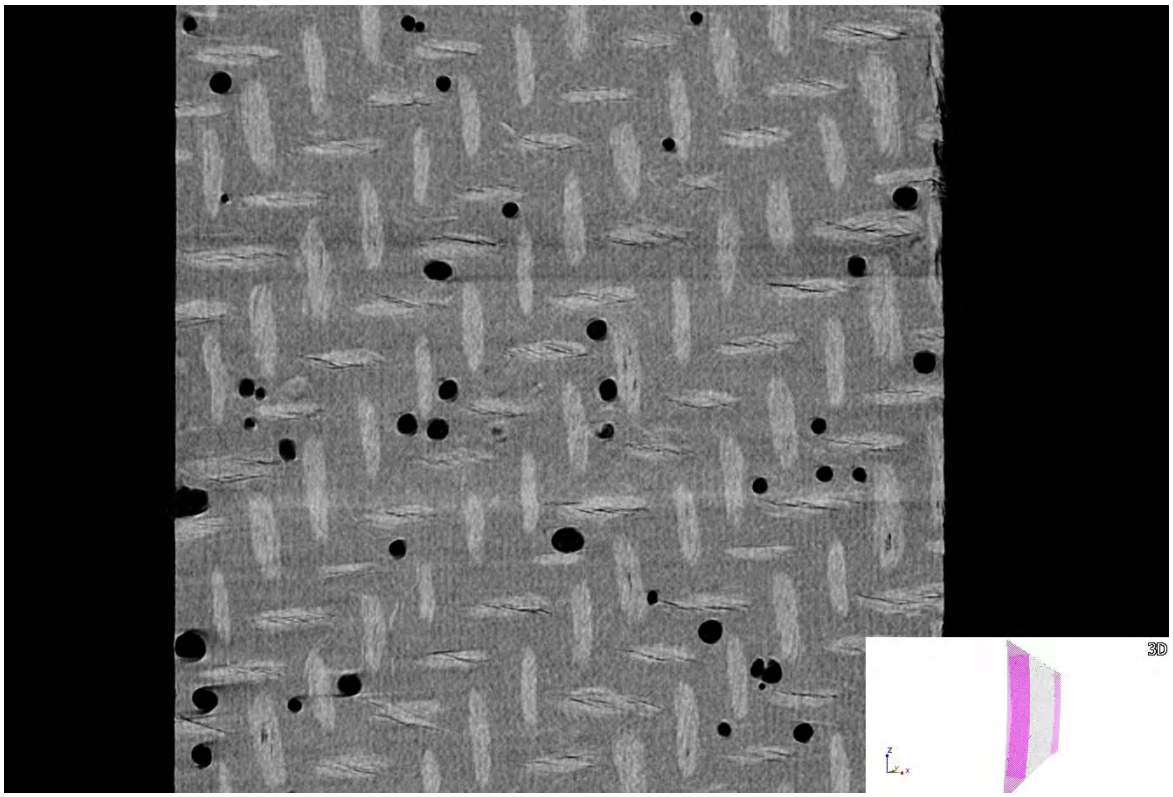


***Fig. 5*** *NFRP at a real deflection of 8 mm. Nonplanar view of a slice parallel to the deformed outer specimen surface under tensile load.*

### 3.2 HFRP TESTING

The HFRP shows a considerably more complex failure behaviour than the NFRP (compare Fig. 6). Already at a deflection of 1 mm an initial damage in the form of a deformation of fiber and matrix at the compression-loaded inner side is visible. With increasing deflection this leads to delamination inside the carbon fiber rovings as well as fiber-matrix failure. At the tensile-loaded outer side, strain-induced fiber breaks develop starting from a deflection of 2 mm. The inner natural fiber layers show no defects. This can be attributed primarily to the low tensile and compressive forces in the core, additionally the high breaking elongation of the natural fibers, which was already of noticeable impact in testing of the NFRP, will have an influence.

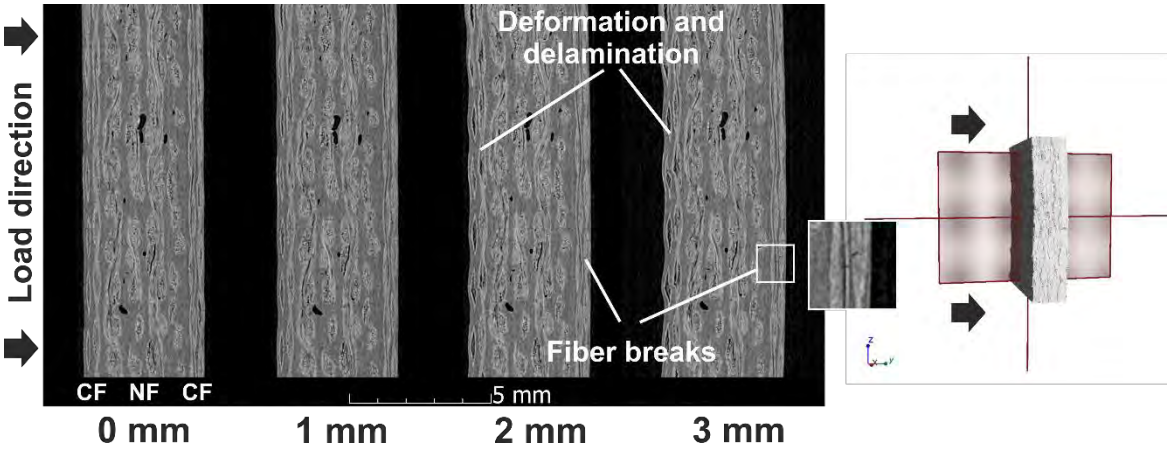


***Fig. 6*** *Defect progression with increasing deflection inside the HFRP. NF: natural fiber; CF: carbon fiber.*

Both the thermosetting matrix of the NFRP as well as the thermoplastic matrix of the HFRP show no damages such as cracks in In-situ-testing, reflecting their high elasticity. Instead, all observable defects originate from the reinforcing fibers.

### 3.3 EVALUATION OF RELAXATION

In comparison to classical mechanical testing In-situ-testing involves a temporal discontinuity. This can falsify mechanical results and structural interpretations due to increasing material relaxation or creeping, respectively. To minimize the relaxation effect, the CT measuring time, which interrupts the mechanical testing, is minimized as far as possible without compromising the interpretability of the CT measurements. To detect potential changes inside the specimen during the CT measurement 2D X-ray projections before and after the CT measurement were captured. Even at the highest deflection of 8 mm (Fig. 7) the differential image of the two projections shows no deviations. Consequently, relaxation is negligible at least on the investigated macroscopic scale.

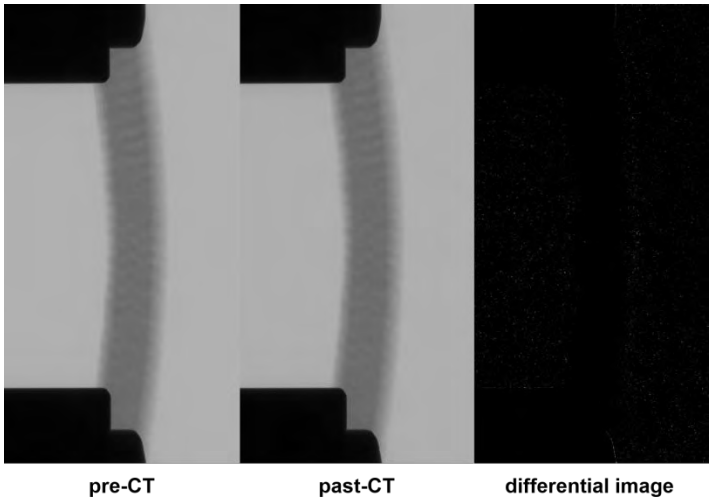


***Fig. 7*** *2D X-ray projections of the NFRP at a deflection of 8 mm before and after the CT measurement; differential image with enhanced contrast shows no deviations.*

## 4 CONCLUSIONS AND OUTLOOK

The presented In-situ-CT 4-point bending test enables the detailed study of failure mechanisms of fiber-reinforced plastics. The two different composites examined showed a diverse failure behavior. In the natural fiber-reinforced plastic failures of the yarn on the tensile-loaded side, initializing only at comparatively high deflections, dominate. In the hybrid fiber-reinforced plastic damage of the stiff carbon fibers on the compression-loaded side develops initially. At higher deflections additionally fiber breaks on the tensile-loaded side appear. Both materials show no matrix failure. Contrary to expectation, the pores inside the matrix of the NFRP did not act as origins of failure.
These initial results provide the basis for more detailed investigations about the failure mechanisms of fiber-reinforced plastics. By improving the understanding of material failure and transferring this to, for example, stacking orders, the benefit of fiber hybridization can be exploited to a larger extent than currently possible. Additionally a prediction of the influence of certain defects, for example pores, on the material performance, and their tolerability, is aspired. To enhance the understanding of processes inside the materials under load the In-situ-CT measurements will be correlated with the stress-strain diagrams in the future.
Due to challenges in measurement technique, the In-situ-CT concept still has a high development potential. This includes the realization of a sufficient CT resolution combined with a measuring time as low as possible, the minimization of measuring artefacts as well as the automated data evaluation.

## REFERENCES

[1] Endres H.-J.: *Vehicle body made from cotton, hemp, and wood*. Research News, Fraunhofer Gesellschaft, 2015(01), topic 4, 2015.
[2] Shamsuyeva M., Endres H.-J.: *Various Sectors Benefit from Bio-Hybrid Fiber Composite*. bio-fibre Magazine 2016(12):218-19, 2016.
[3] *DIN EN ISO 14125:2011-05, Faserverstärkte Kunststoffe – Bestimmung der Biegeeigenschaften*, Beuth Verlag Berlin, 2011.
[4] Liu Y., Kiss A. M., Larsson D. H., Yang F. Pianetta P.: *To get the most out of high resolution X-ray tomography: A review of the post-reconstruction analysis*. Spectrochim Acta B, 117(1): 29-41, 2016.
[5] Whithers P. J., Preuss M.: *Fatigue and damage in structural materials studied by X-ray tomography*. Annual Review of Materials Research, 42:81-103, 2012.
[6] Scott A. E., Mavrogordato M., Wright P., Sinclair I., Spearing S. M.: *In situ fibre fracture measurement in carbon–epoxy laminates using high resolution computed tomography*. Composites Science and Technology, 71(12):1471-1477, 2011.
[7] Böhm R., Stiller J., Behnisch T., Zscheyge M., Protz R., Radloff S., Gude M., Hufenbach W.: *A quantitative comparison of the capabilities of in situ computed tomography and conventional computed tomography for damage analysis of composites*. Composites Science and Technology, 110:62-68, 2015.
[8] Buffiere J.-Y., Maire E., Adrien J., Masse J.-P., Boller E.: *In Situ Experiments with X ray Tomography: An Attractive Tool for Experimental Mechanics*. Experimental Mechanics, 50:289–305, 2010.
[9] Rettenberger S., Bittner F., Endres H.-J., Hiller J.: *Blick in belastete Composite-Bauteile*. Konstruktion 2017(5):IW10-IW13, 2017.
[10] Swolfs Y., Gorbatikh L., Verpoest I.: *Fibre hybridisation in polymer composites: A review*. Composites Part A: Applied Science and Manufacturing, 67:181–200, 2014.

CHAPTER 3

# MANUFACTURING AND PROCESSING

# IN-SITU PROCESSING OF CAPROLACTAM – T-RTM TECHNOLOGY AS A KEY FOR FULLY AUTOMATED PRODUCTION OF COMPOSITE PARTS

**Norbert Müller**[1*]

[1]ENGEL Austria GmbH, Center for Lightweight Composite Technologies, St. Valentin, Austria

**ABSTRACT:** The manufacturing of hybrid components by injection molding, where polymeric and metallic members are combined, and the use of robots for the handling of metal inserts is a well-established technology. However, the fully automated production of composite structures is by far more difficult to perform. Therefore, the processes in industry still are often multi-step sequences and require extensive manual work, particularly when composites based on curing resins are produced.

The in-situ processing of caprolactam (T-RTM technology) enables the production of composite parts, where the matrix is not epoxy resin or polyurethane, but consists of polyamide-6. There is a considerable adhesion potential between the polyamide-based composite and functional elements that can be molded directly onto the composite. Furthermore, even metallic components might be integrated directly during the making of the composite part. This allows completely new concepts for the part design. Dependent on the technical requirements, but also considering the most appropriate materials mix from the economical viewpoint, the resultants components can comprise areas made of metals, continuous fiber reinforced composites as well as injection molded functional elements. Since the processes employed can become fully automated, the way is clear for the efficient and highly integrated production of hybrid lightweight components.

**KEYWORDS:** T-RTM, in-situ processing, caprolactam, composite manufacturing, process automation, multi-stage processes, hybrid structure, in-line inspection

## 1 INTRODUCTION

If a technology comes into consideration for mass production depends on few factors. In the first instance, usually the cycle time and the lowest possible number of process stages are mentioned. However, these simple assumptions are in the most cases kind of an inadequate shortcut. As soon as a technology is in mass production, for example injection molding, then the cycle time really plays a predominant role for further increasing the productivity of a processing setup. Likewise, with the elimination of a whole process step, a significant cost savings can be achieved. However, the actual entry barriers for a novel technology to large-scale production are different ones: the predominant role plays, above all others, whether the whole process chain can be fully automatized or not. Then, the processing system's reliability, availability and repeatability follow. These aspects are discussed for the T-RTM technology leading to thermoplastic based composites with a reactive processing approach.

## 2 HIGH OUTPUT RATES WITH REACTIVE PROCESSING

If a process - cycle by cycle - delivers identical results, without the need for manual interventions, i.e. can be conducted fully automatically, and runs smoothly in a three-shift process, the essential prerequisites for economic mass production are met. With an appropriate processing setup, even cycle times of few minutes can be acceptable. When multi-cavity molds are used and layouts with turntable, rotatable center platen, or sliding table design are employed, then very high output rates can still be achieved.

The in-situ processing of caprolactam still requires a polymerization time of two to three minutes. Furthermore, there are additional time spans necessary for opening and closing of the mold, for component removal and for placement of a new fiber preform in the mold. This results in a total cycle times in the range of three

to four minutes. Nevertheless, a single processing setup for caprolactam based composites can reliably achieve a total output of, for example, 100,000 hybrid components per year.

## 3 CHARACTERISTICS OF THE PROCESSING OF CAPROLACTAM

Caprolactam is a starting material for the manufacturing of polyamide-6. The ring-shaped molecules are opened during the in-situ polymerization and the monomers attach to each other to form long polyamide-6 molecular chains. The special feature of the system is, on the one hand, that no by-products arise, Figure 1. This allows the polymerization to take place directly in the mold. On the other hand, the polymerization is conducted in a temperature of about 120 to 150 °C, in which the polyamide, after completion of the polymerization is in the solid state. Thus, the process can be carried out in a mold that is kept at elevated temperature of to about 140 °C. There is no cyclic heating and cooling of the mold necessary.

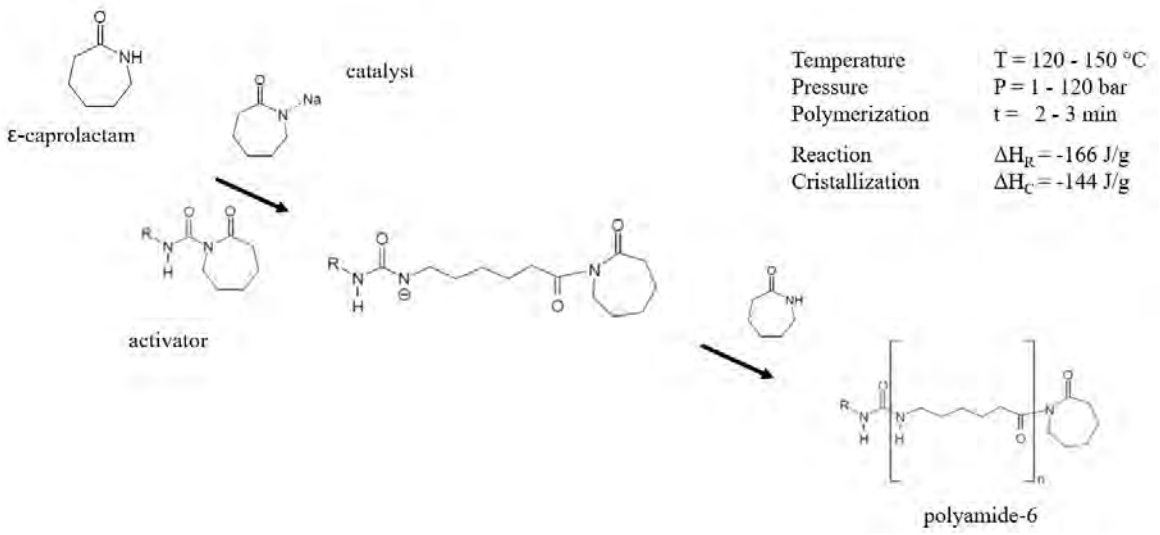


***Fig. 1*** *Anionic ring-opening polymerization of caprolactam resulting in polyamide-6.*

At room temperature, caprolactam is a solid and has a white color. It is supplied as a granule and can therefore be handled quite like a resin for injection molding. The material that is packed in moisture tight bags is filled into material hoppers, which can be hermetically sealed.

For the polymerization reaction to take place, it is necessary to add to the caprolactam, on the one hand, a catalyst and, on the other hand, also an activator. At first, this is done separately for the two components. To facilitate handling and to rule out errors in the recipe, cast-ready mixtures are used. There are two different components delivered in bags. Each of them primarily consist of solid caprolactam, to which the catalyst or the activator, respectively, was added already in small quantities. At 70 °C, the material melts. Then it has a very low viscosity of 5 to 10 mPas.

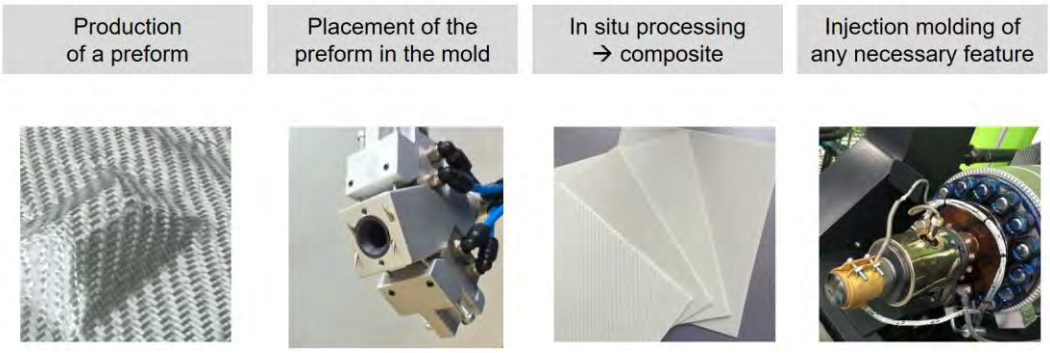


***Fig. 2*** *Process sequence for the manufacturing of hybrid composite parts based on T-RTM technology.*

The subsequent processing is very similar to the conventional RTM method, at least when a basic process variant is considered, Figure 2. The reinforcing materials (glass or carbon fiber fabrics or non-woven plies)

are placed as dry preforms into the mold, the press is closed, and the mold is evacuated. Already this process step, as well as the preform production itself, can be completely automated. The molten caprolactam components with catalyst and activator are mixed in a mixing head and injected into the mold cavity. During the injection, the preform made of glass or carbon fibers is impregnated with the caprolactam. The actual mold filling requires only low pressures. However, at the end of the filling phase, an increased pressure is applied in order to achieve optimal wetting of the fibers and a low residual porosity. The reactive injection unit enables applying an injection pressures of up to 120 bars, Figure 3.

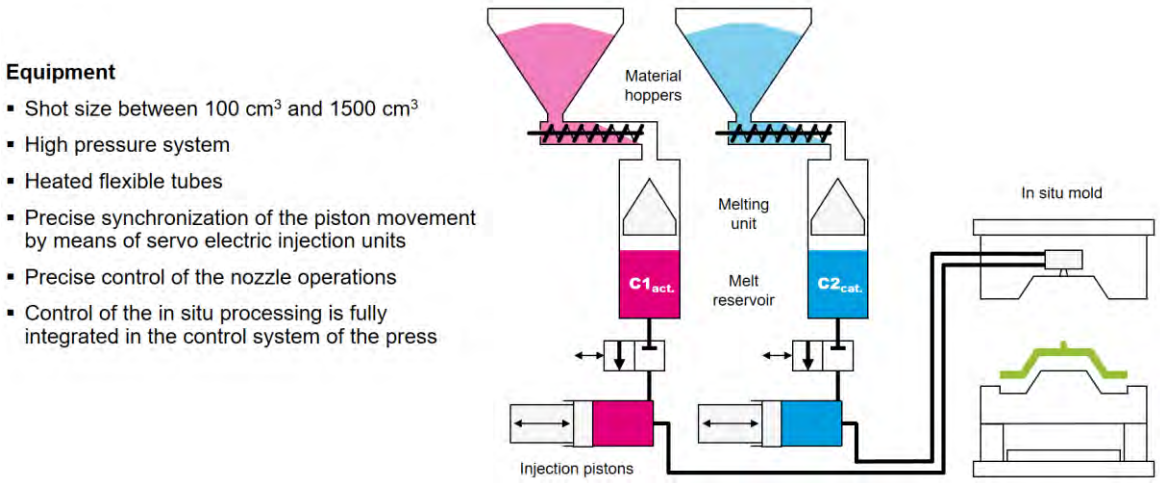


***Fig. 3*** *Equipment setup for the fully automated processing of (epsilon-)caprolactam.*

In contrast to RTM technology, there is no need to pretreat the mold with a release agent, which is an important contribution to optimal preconditions for the automation of the process. From the T-RTM mold, a finished, polyamide-6 based composite component can be removed after two to three minutes of polymerization. The thermoplastic matrix enables subsequent functionalization by injection molding, whereby several process routes exist. The simplest route is the direct placement of the T-RTM composite into the injection molding mold, whereby the composite component from the T-RTM process still exposes a considerably high surface temperature. The reactive process takes place in a mold with a mold temperature of 140 °C and the polymerization itself contributes some additional heat. Correspondingly, the composite components show a quite high surface temperature immediately after demolding. The residual heat can be utilized for the next process step to facilitate adhesive bonding. By means of the injection molding, the component is completed with an edge surround, with ribs and fastening elements and with further detail geometries, which are required, for example, for mechanical functions (guiding elements, bearing seats, etc.).

## 4 MANAGING OUTPUT ISSUES

This T-RTM basic process - preform manufacturing / T-RTM composite / direct functional integration by injection molding - can be fully automated and can run in multi-shift operation. However, a serious concern is the considerable difference in cycle times between T-RTM processing and the injection molding process. While injection molding requires only 30 to 60 s for one production cycle, the cycle time for the T-RTM process ranges between 120 and 240 s. On average, it can be assumed that the injection molding process runs about 3 to 4 times faster than the T-TRM process. In order to actually utilize the high productivity of the injection molding, the number of cavities in the T-RTM process needs to be increased.

Concepts that that are well established in injection molding can be adapted for the purpose of increasing the output of the T-RTM process. These include e.g. 4-cavity molds and dual parting plane molds with 2x2 cavities. Furthermore, turntable machines, rotatable center platen machines, and sliding table layouts can be used to achieve the required production rate with a single processing cell.

## 5 MULTI-STAGE PROCESSING ROUTES

In the case of the most basic approach, the injection molding cycle has the same length as the T-RTM process. Therefore, both processes can be performed on the same machine. The composite component, which comes from the T-RTM mold, is transferred into an injection molding mold. Both molds might be installed in the

same clamping unit, figure 4. In the injection molding mold, the subsequent functionalization takes place and a ready-to-install component is obtained (e.g. a frontend module, a door module, etc.).

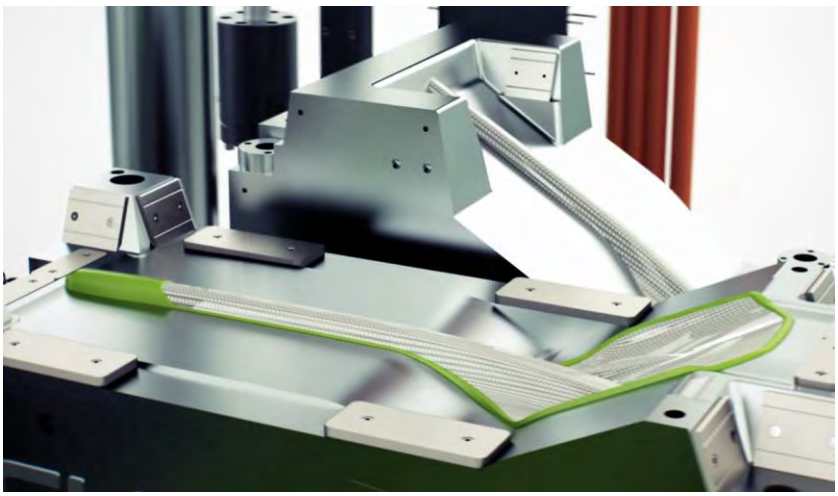

***Fig. 4*** *T-RTM mold (rear) and injection molding mold (front) installed in the same vertical clamping unit.*

In the case of a processing concept with a multi-cavity mold for the composite component and a single-cavity mold for subsequent functionalization, normally it makes more sense to switch to two independent, conventional machines, figure 5. It proves to be advantageous for the T-RTM process to choose a system with vertical clamping unit. The preforms then can easily be inserted into the lower mold half. An extra clamping device in the mold is not required, as it would be the case when a horizontal clamping unit is utilized. The functionalization by injection molding can be performed on a conventional machine with a horizontal clamping unit. For this process step, the vertical closing direction of a press does not provide additional benefits.

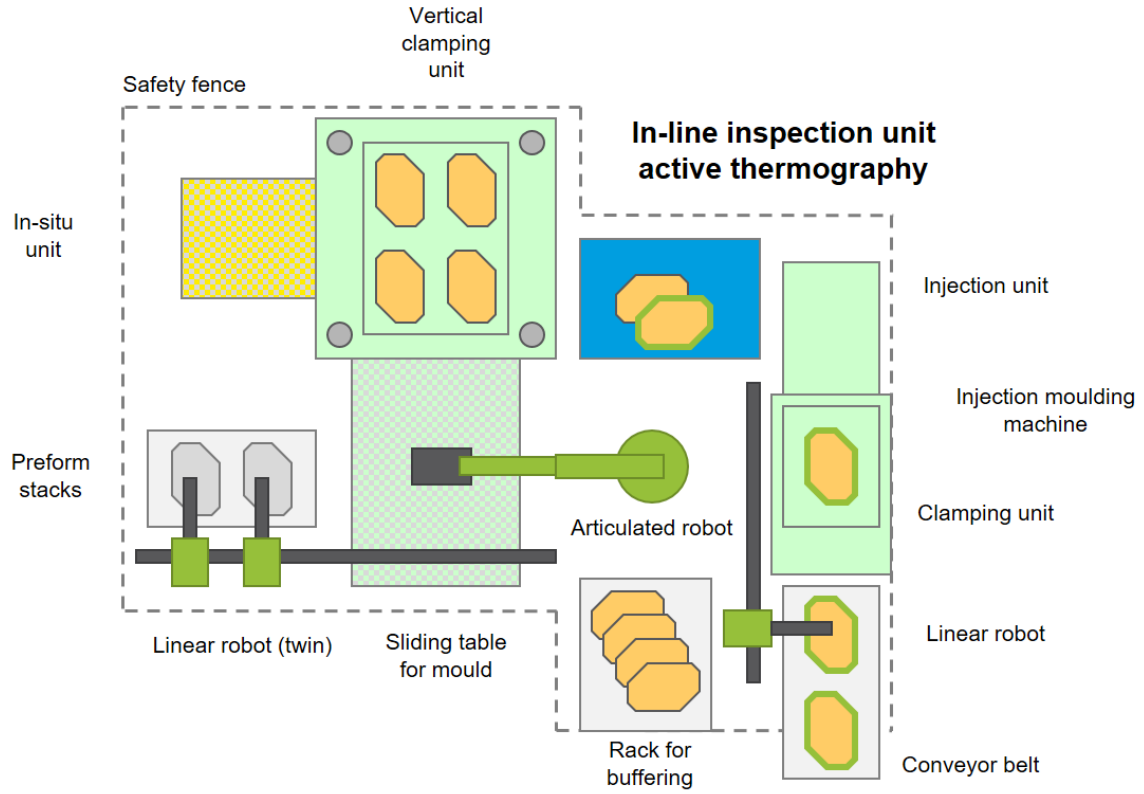


***Fig. 5*** *Multi-stage layout for the manufacturing of T-RTM hybrid components utilizing a vertical press for the composite manufacturing and a conventional injection molding machine for the functionalization.*

If multiple composite components are removed at once from a multi-cavity mold, in order to be functionalized sequentially in an injection molding process, then the composite components cool down to a varying extent before injection molding. Therefore, on the one hand, it must be ensured that the components from the T-RTM process have a sufficiently high surface temperature, so that an adequate adhesion can be achieved. On the other hand, the overmoldings must be created at the same thermal preconditions.

### 5.1 PRE-HEATING OF THE COMPOSITE COMPONENT

From the two-stage processing of thermoplastic composite sheets is known that a rapid and sufficient reheating of already three-dimensionally shapes composite components can be achieved by means of infrared heaters, unless the component does not show very deep and steep flanks and side walls. This concept can be adopted for the process chain T-RTM / functionalizing by injection molding, figure 6.

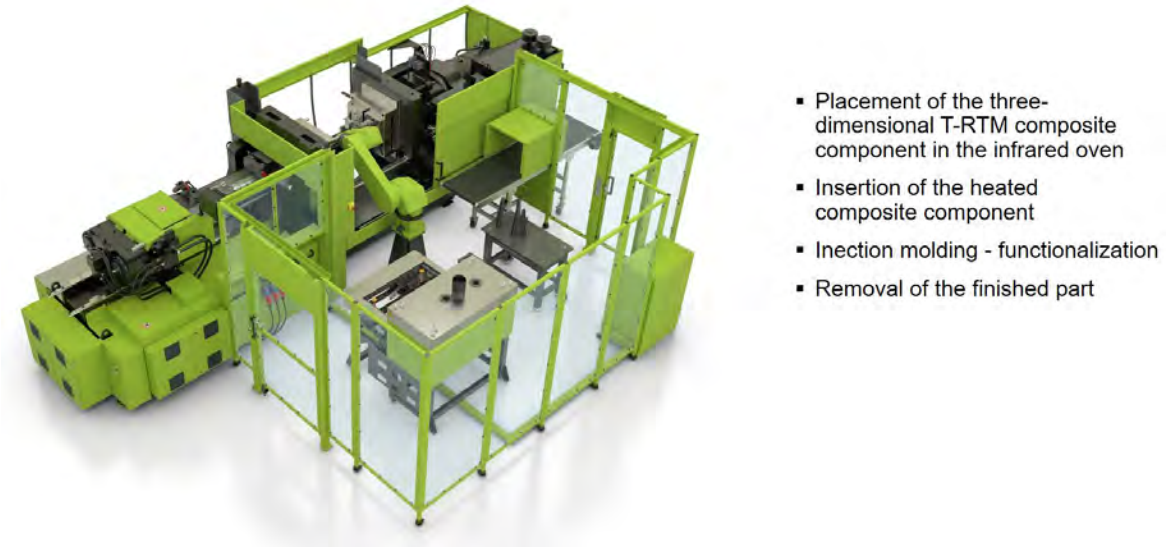


***Fig. 6*** *Functionalization of a three-dimensionally shaped T-RTM component using an infrared oven in combination with a conventional injection molding machine.*

The composite components from the multi-cavity T-RTM mold are reheated in an infrared oven before injection molding to such an extent that the polyamide-6 just does not melt. However, the surface temperature rises even more when the hot thermoplastic melt impinges on composite's surface, so that a good adhesive bond results. Since in infrared ovens for the processing of thermoplastic composites several pyrometers are used even in a standard setup, the measurement and control of the composite's surface temperature is not an issue. In this way, thermally consistent preconditions for the injection molding can be achieved.

### 5.2 TRIMMING OPERATIONS FOR IMPROVED GEOMETRIC PRECISION

The multi-stage approach enables further process variants which on the one hand offer advantages in terms of product design and component precision, but on the other hand also open up cost-saving potentials. If a very precise edge contour or neat breakthroughs are required on the composite components, trimming after the T-RTM manufacturing is a preferable option. For this process variant, a certain projecting edge is provided on the composite component. After the T-RTM process, the three-dimensional composite component is trimmed by water jet cutting or punching. The final functionalization is achieved, after preheating of the composite component in an infrared oven, by means of conventional injection mold.

In the case of a comparatively simple component geometry, the preparation of a three-dimensional preform might even be omitted, employing a quite similar procedure. The flat dry fabric is draped three-dimensionally when closing the T-RTM mold. After injection and polymerization of the caprolactam, a three-dimensional composite component is obtained. This component can be trimmed, preheated and functionalized as described before.

### 5.3 LOAD OPTIMISED BLANKS MADE BY MEANS OF T-RTM PROCESSING

Eventually, the technology also offers the possibility of combining concepts from the processing of thermoplastic composite sheet materials with the T-RTM process. From dry fiber materials, a flat stack is produced

which is locally adapted in thickness, the type of reinforcement and the predominant fiber orientation. By means of the T-RTM processing, this stack is consolidated resulting in a still flat semi-finished product, a blank with load oriented local design. In the next step, heating in the infrared oven follows, in this case up to a temperature clearly above the melting point of the polyamide-6. In the subsequent injection molding step, the shaping and functionalization is achieved, whereby a single-stage or a two-stage process comes into consideration. For the latter, a simple shaping mold and a separate injection molding mold are used in sequence.

The large variety of process variants, all of which are based on the T-RTM process, provides answers to several technical and economical requirements. There are solutions enabling to avoid the effortful and expensive manufacturing of a three-dimensional preform. With multi-step processes, high demands on the precision of the outer edges and on the surface finish of the composite fraction can be covered. Finally, with solutions where first a flat blank is produced and which subsequently is brought into the three-dimensional shape by heating and forming, composites with a load optimized design can be realized at reasonable costs. For this processing route no preforming mold and no extra preforming process is necessary. However, in comparison to the conventional approach with a three-dimensional preform, the possible part complexity is somewhat reduced.

## 6 INSERTS AND METAL-POLYMER HYBRID STRUCTURES

The transfer of high mechanical loads into an injection molded component often is solved using metallic inserts. These inserts usually are anchored only by mechanical interlocking with the thermoplastic material. The inserts are either placed in the mold prior to injection molding or embedded into the final injection molded component, e.g. with the help of an ultrasonic welding device. This concept can be adopted directly for structural components made of a T-RTM composite and an injection-molded geometry. In many cases, this approach is completely sufficient, since the required load transfer from the injection molding into the composite fraction can be achieved by providing correspondingly large contact surfaces.

If the load transfer should reach the composite directly, then the most appropriate approach is embedding the insert between layers of fabric already during the T-RTM processing. However, from the flooding with molten caprolactam and the subsequent polymerization, no direct bonding between the metallic insert and the composite fraction results. An adequate bond strength might be achieved with micro-interlocking, pretreatment/cleaning of the metallic component, and in particular with the utilization of coatings on the metallic component. Hence, current investigations aim on achieving a good adhesive bond strength between the in-situ polymerized polyamide-6 and, for example, a brass insert, a steel sheet or an aluminum foil.

## 7 ACTIVE THERMOGRAPHY FOR IN-LINE INSPECTION

Highly loaded and safety-relevant composite components are for sure supposed to be free of any faults. During component production with manual labor, the component is repeatedly checked by a person. For some industries, especially for aviation, a 100%-inspection of specific components is required after the completion of the component's manufacturing.

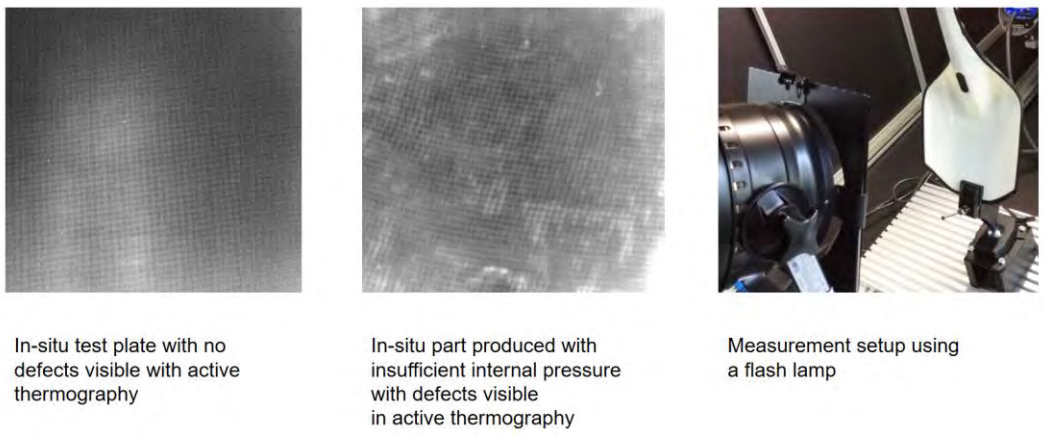


***Fig. 7*** *In-line inspection of T-RTM hybrid structures employing active thermography.*

However, if a production runs fully automatically - although extensive process monitoring is an established standard - the manufactured components themselves are only randomly examined, at least in conventional injection molding.

In the case of hybrid composite components, two additional aspects need to be considered. On the one hand, already the combination of two or more components from different materials (metal, composite, injection molding) leads to a rise of the risk for errors to occur. On the other hand, the demand for a 100%-inspection gains in importance, even in the case of a high-volume production, because these components have to meet even the highest demands in use. Hence, for some novel composite components, there is a need for fully automated in-line inspection of 100% of the produced parts.

By using active thermography directly in the production environment, an inspection can be carried out immediately after component production, figure 7. Furthermore, intermediate products can be examined using active thermography, for example a flat, load optimized semi-finished product from the T-RTM process, or the three-dimensional composite component before the functionalization by injection molding takes place. Thus, for a final component, which has been produced without any manual labor, not only a data log with the process parameters, but also at least one measurement from active thermography is available that contains information on possible faults, which might be seen under the surface. The same thermographic cell, if integrated as a module in a production line, can carry out measurements on a load optimized flat blank, as well as on a composite component and on the finished product, which was completed by injection molding.

# 8 SUMMARY

A multi-stage approach does not have to oppose the economic concerns of a production line. All the process chains described above can run at a fully automatic mode. An additional process stage is associated with a separate investment for the processing module and possibly for an extra mold. However, as long as the entire system, i.e. all process modules, can be operated with high system availability and in the pace of the injection molding machine's cycle time, one often can find an advantageous arrangement with a multi-stage approach. This is, of course, dependent on the component's technical requirements and on the quantity of parts to be produced. This is, on the one hand, due to the fact that the individual process modules consist of well-available standardized components. On the other hand, technically highly sophisticated steps, such as the production of an exact, three-dimensional preform, are replaced by simpler, procedurally far less critical individual processes. These aspects can have a positive effect on the production system's efficiency, on its overall availability and robustness, contributing to high-quality products at a comparatively low part price. Of predominant importance is that all process steps can be carried out fully automatically and can be linked together well using higher-level control systems.

# 9 ACKNOWLEDGEMENT

The Autor gratefully acknowledges the support of the Austrian Research Promotion Agency (FFG), who has funded the work of ENGEL on the processing of Caprolactam under the grant COMPTOOL within the years 2013 to 2015. Furthermore, the author acknowledges the current funding of the ongoing investigations under the FFG grant EVOLVE. Special thanks are addressed to Mr. Gerald Schöfer, M.Sc. (Schöfer GmbH, Schwertberg, Austria) and to Dr. Michael Witt (Lanxess Deutschland GmbH, Dormagen, Germany), who contributed significantly to appropriate mold making solutions and the material recipes, respectively.

# REFERENCES

[1] Müller N., Egger P., Reith L. M., Steinbichler G.: *Controlled Reactivity - In-situ Polymerization for Fully-Automated Production of Lightweight Structures*. Kunststoffe International 10/2016, Carl Hanser Verlag, Munich, 2016

[2] Müller N., Seinsche P.: *T-RTM Components from Caprolactam - Performance Characteristics, Processing Aspects and in-line Testing Employing Active Thermography.* SAMPE Europe Conference 2017, Stuttgart, 2017

[3] Müller N.: *T-RTM Technology and Processing of Thermoplastic Tapes - Two Technologies Managing a Common Challenge.* 17th annual SPE Automotive Composite Conference & Exhibition, Society of Plastics Engineers, Novi/Detroit (MI), USA, 2017

# HYBRID FORMING – A COMBINED DEEP DRAWING AND COMPRESSION MOLDING PROCESS FOR FORMING METAL SHEETS WITH THERMOPLASTICS (LFT) TO HYBRID PARTS

**Prof. Dr.-Ing. Xiangfan Fang[1], Dipl.-Ing. Tobias Kloska[1*]**

[1]Institute of Automotive Lightweight Design, University of Siegen, Germany

**ABSTRACT:** To increase the use of multi-material or hybrid parts in automotive lightweight design, new and efficient production methods have to be developed. With hybrid forming, this paper introduces a cost- and time efficient process for metal sheets and long fiber-reinforced thermoplastics (LFT). The process represents a simultaneous combination of deep drawing (metal) and compression molding (plastic), where the melted LFT behaves like a forming medium, which is similar to hydro-mechanical forming processes. Both materials are formed together in a single step and with only one forming tool. The connection between metal and LFT is also realized during the process by the use of a bonding agent which is previously applied to the metal sheet.
Considering lightweight aspects, it is possible to reduce the sheet thickness of a steel part by a full covering LFT structure with LFT rips and optionally unidirectional reinforced elements instead. A load optimized LFT structure can even lead to improved mechanical properties. The presented FE simulations and optimizations indicate a lightweight potential of more than 20 % for an automotive control arm. Further applications in car body structures or with the use of aluminum as the metal component are conceivable.

**KEYWORDS:** Hybrid forming, Deep Drawing, Compression Molding, Long Fiber-reinforced Thermoplastics (LFT), Multi-Material Design

## 1 INTRODUCTION

Due to the shortage of natural resources and rising limitations for the emission of toxic gases like $CO_2$ or $NO_x$ the automotive industry continuously tries to reduce the fuel consumption through all classes. In this case, material light weight design is only one option to reach these aims or on the example of electrified vehicles to extend the range. Besides lightweight metals like aluminum or magnesium, the use of fiber-reinforced plastics (FRP) becomes more and more important. Despite their advantages of low densities and high weight-specific mechanical properties, the rigidity of metallic materials for local strengths or stiffnesses cannot be waived in many cases. Also the ductile failure behavior of metals has a large importance in automotive applications, especially in chassis applications. For this reason, it is a main aim to combine the advantages of different materials, e.g. the design freedom of plastics and the strength of metals, in a so called hybrid or multi-material design.
Currently, there are different production methods for hybrid parts. Most of the established processes for combining FRPs with metal sheets are executed with the use of injection molding and separate processes for each material. This results in additional costs for the individual process steps and handling operations. Furthermore, at injection molding the length of fibers is limited to 2-3 mm due to the small injectors, which must be passed by previously longer fibers in the compound. In contrast to this long fiber-reinforced thermoplastics with a fiber length up to 25 mm are usually processed in compression molding and keep their length to the component. The fiber length of FRP has a significant influence on the mechanical properties of the component. While the stiffness of FRP cannot be increased significantly from a fiber length of 1 mm upwards, higher strength and impact resistance can be achieved with longer fibers [1]. For these reasons, it is obvious to combine the cold metal forming as an established manufacturing process for metal together with the compression molding of LFT. By using a bonding agent directly in the process hybrid parts with optimized mechanical properties and lightweight potential can be realized by only one process step and in one forming tool. In [2] and [3] the potential of compression molding of LFT to reinforce a hot-formed B-Pillar with an intrinsic LFT structure was already shown.

## 2 PROCESS DESCRIPTION

The usage of plastified FRP to form metal sheets is adopted from hydro-mechanical forming processes. Instead of using a forming fluid (mostly water, oil or a mixture of both) melted LFT is used in the here described and from the authors invented hybrid forming process [4]. In one single tool the forming of sheet metal and LFT can be done simultaneously.
The LFT needed for this hybrid forming can be provided in two different ways. Firstly, LFT is usually compounded in a twin-screw extruder and the fibers are introduced quite at the end to reduce fiber damage and to guarantee a presence of long fibers in the final component. Due to the possibly high fiber lengths and the volume contents the LFT compound has a certain form stability that allows an automated handling via needle grippers or manually by hand. In addition to direct processing, LFT can also be processed by subsequent re-heating, for example by infrared radiation. This independence also applies to the coating of metal sheets with bonding agents. The coating can be done prior to the processing and the sheets can be stored without any specific temperature requirements. To activate the bonding agent right before processing only a preheating is necessary.
Subsequently, the melted LFT and preheated metal sheet can be placed together with optional reinforcement elements like endless fiber-reinforced products (tapes or organo sheets) and directly positioned in the forming tool. The following process scheme (**Fig. 1**) depicts the five process steps of hybrid forming and a u-profile from a research project as a component for example. Not shown is a following cutting operation, which is obligatory for metal forming processes.

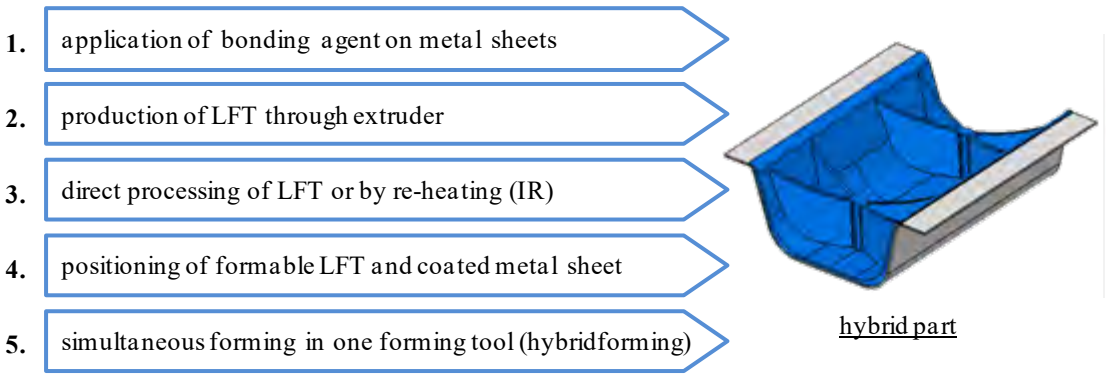


***Fig. 1*** *Process scheme of hybrid forming and a hybrid u-profile*

After a certain cooling time the hybrid part can be ejected as one part from the forming tool. In comparison to injection molding the cooling times at hybrid forming are shorter because of the lower shrinkage and warpage tendency of LFT materials. To ensure a firmly bonded connection between metal and LFT the hybrid components are not only designed with LFT rips, but also with a continuous LFT layer. This connection over the entire part guarantees a reliable connection of the LFT to the metal sheet.

## 3 FORMING TOOLS

The forming tools for hybrid forming have elements of both metal forming and compression molding tools. Besides a punch, blank holder and die a hybrid forming tool also needs a sealing concept when using the melted LFT as a forming medium. On one side, a complete sealing against leakage of the LFT must be ensured within this concept, but on the other a material flow of the metal must not be completely prevented. Therefore, two different concepts for a u-profile and a tub geometry where developed in a research project. These geometries are commonly used in metal forming processes and many structural components are based on these two shapes. Combinations of open and closed profiles are also obtainable, e.g. through a subsequent "opening" of the closed profile in the cutting step.
In contrast to cold metal forming processes, the tools for hybrid forming need be tempered at a constant level of about 80° C. This temperature represents a compromise between long time flowability for the LFT and short times. It is realized by an external water tempering unit and the close-to-contour cooling channels.

### 3.1 U-PROFILE

The configuration of the tool for the u-profile is similar to standard cold metal forming processes. Punch and blank holder are positioned in the movable upper mold half and the die is arranged in the fixed lower half. A special feature of this tool can be seen in the design of the punch. The sealing concept is realized by a three-piece punch, where the lateral elements are attached to gas pressure springs and by an offset to the middle

part of the punch. These elements are the first contact with the metal sheet and enable a complete sealing during the process. Additional sideways sealing (area of metal flow) is guaranteed by the thickness of the blank holder plate and the blank holder contour itself. Both are supported by several gas pressure springs with a slightly progressive spring characteristic (see **Fig. 2**). The number of springs can vary depending on the steel grade to be processed.

### 3.2 TUB GEOMETRY

In comparison to the u-profile, the tool for the tub geometry uses a reverse configuration. Here, the punch is positioned in the lower and fixed mold half while the die is placed in the upper half (see. **Fig. 2**). Furthermore, the blank holder force is realized by the hydraulic die cushion of the hydraulic press system, which allows the force to be controlled during the process. This adjustment is one key aspect for the circumferential sealing and to control the sheet metal flow. By this configuration, the melted LFT cannot be placed on the metal sheet. It must instead be placed directly on the punch and the metal sheet on the blank holder. As a result, the blank holder additionally has an ejector function for the hybrid part.

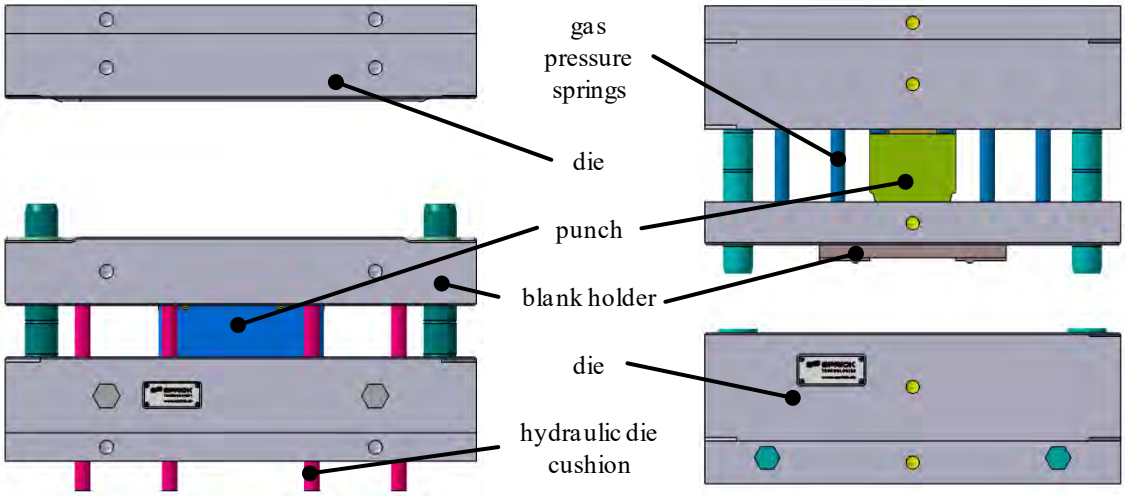


*Fig. 2 Tool concepts of tub geometry and u-profile*

## 4 COMPONENT LAYOUT

In this project, an automotive chassis control arm was chosen as a technology demonstrator. Due to high sheet thicknesses in chassis components there is a large lightweight potential for the hybrid forming process. Furthermore, the positive fail-safe behavior of the metal-LFT combination is a big advantage. With a load adjusted design it is possible to reduce the sheet thickness and replace it by a reinforcement structure of a continuous LFT layer and complex LFT rips. The following optimization was performed with the optimization solver OptiStruct (v.14) by Altair to adopt the original steel design of the control arm into a hybrid design.

### 4.1 OPTIMIZATION AND DESIGN

For the topology optimization it is necessary to define a design space where the LFT rips can be placed. In this case, the whole cavity volume of the control arm was filled with solid tetra elements by an average mesh size of 1.0 mm. This leads to a LFT rip thicknesses between 2-4 mm as a result. The boundary conditions were given in form of six vehicle static load cases and the resulting maximum stresses in the metal sheet. As an objective criterion for the optimization, a minimization of compliance was chosen. **Fig. 3** (left) shows the result of the topology optimization in an isometric view. In this view all elements with low densities and though less stress concentrations were automatically being masked. Visible remains the optimized design for the rip structure.

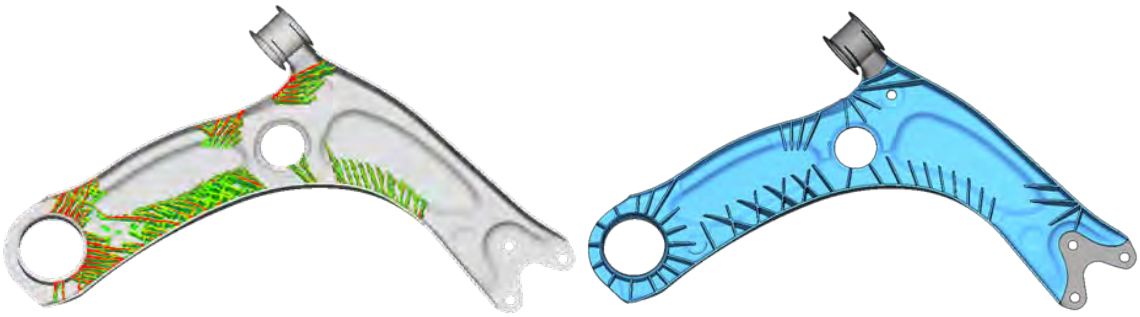

***Fig. 3*** *Result of topology optimization (left) and realized hybrid design (right)*

Due to the design freedom of LFT it is possible to design a LFT rip structure close to the optimization result. To guarantee a homogeneous cooling of the LFT during the hybrid forming process, all rips have a similar thickness of minimum 2.0 mm at their tops and a draft angle of 1° for ejection. The same applies for the continuous LFT layer, which has a constant thickness of 2.0 mm. The final hybrid design (**Fig. 3**, right) leads to a mass reduction of more than 20 % in comparison to the steel counterpart, which is numerically more than 500 g for the whole part. Thereby, the sheet thickness of a DP800 steel was reduced from 3.8 to 2.4 mm [5].

### 4.2 PERFORMANCE

Due to the sheet thickness reduction a change in the stress distribution can be identified for the most critical load case (see **Fig. 4**). For reasons of confidentiality the stress values are given in a normalized manner. Although the stress distribution seems quite similar at first glance, the hybrid part has lower stresses at the right bearing and slightly higher stresses around the middle flange. Of larger importance, however, is the lower maximum stress level at the hybrid design. By the wide-ranging rip structure the new design shows a better material utilization and safes more than 20 % of weight. The life cycle analysis of the control arm in hybrid design and its behavior under cyclic loads is part of current investigations in the project.

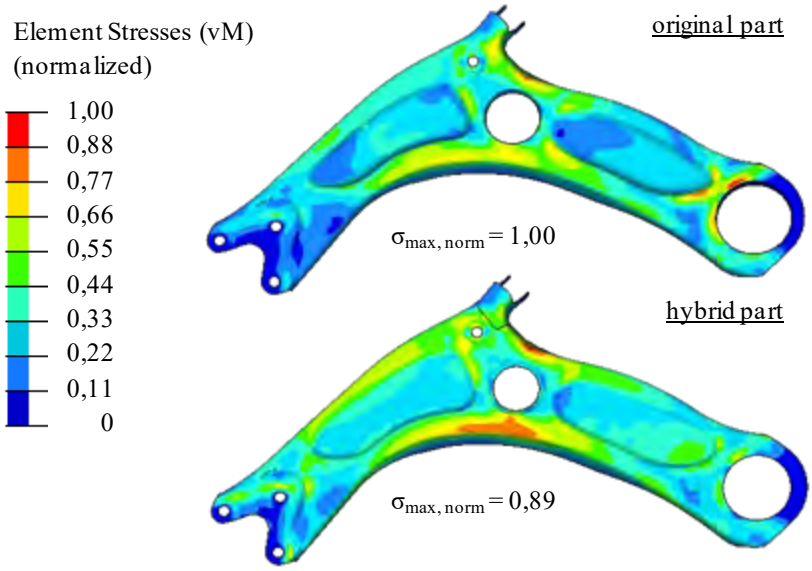


***Fig. 4*** *Comparison of stress distribution in the metal sheet*

## 5 CONCLUSION AND OUTLOOK

The increasing use of multi-material structures in automotive lightweight design requires efficient processes. While most of the established processes for hybrid parts are executed in multi-stage the hybrid forming technology offers a cost and time efficient one-stage process. It can help to extend the application of hybrid parts in car body and even chassis structures by both weight and cost reduction. As shown at the example of an automotive control arm, the weight reduction can reach more than 20 %.

For the future, many applications are imaginable for car body and even crash structures. Also a combination of LFT and aluminum seems practical, because of the positive influence (warm forming) on especially high strength aluminum alloys [6].

## 6 ACKNOWLEDGEMENT

This research is supported by the Federal Ministry of Education and Research (BMBF) in the context of a project named “MultiForm” and with supervision of the Project Management Agency Karlsruhe (PTKA) at the Karlsruhe Institute of Technology (KIT). Additionally, we thank our project partners Weber Fibertech, voestalpine Automotive Components, Sprick Technologies and SimpaTec Simulation & Technology Consulting for the cooperation as well as Altair, Bond-Laminates, Evonik and Volkswagen for their associated partnership.

## REFERENCES

[1] Schemme M.: *LFT – development status and perspectives*. Plastics, Additives & Compounding Vol. 10/2:38-43, 2008 https://doi.org/10.1016/S1464-391X(08)70060-6

[2] Kellner P., Froeschle M., Steinbach K.: *Die 3D-Hybridtechnologie: Eine neuartige Stahl-GFK-Hybridbauweise für hoechstbelastete Karosseriestrukturen*. In: 18. Internationales Dresdener Leichtbausymposium, Dresden, 2014

[3] Modler N., Adam F., Maass J.: *Intrinsic Lightweight Steel-Composite Hybrids for Structural Components*. Materials Science Forum Vols. 825-826:401-408, 2015 10.4028/www.scientific.net/MSF.825-826.401

[4] Fang X.: patent DE102014004359A1, Deutsches Patent- und Markenamt, 2014

[5] Fang X., Kloska, T.: *Hybrid forming – a combined deep drawing and compression molding process for forming metal sheets with thermoplastics (LFT) to hybrid parts*. In: Automotive Engineering Congress, Nuremberg, 2017

[6] Hussain M., Rauscher B., Tekkaya A.: *Wirkmedienbasierte Herstellung hybrider Metall-Kunststoff-Verbundbauteile mit Kunststoffschmelzen als Druckmedium.* In: Materialwissenschaft und Werkstofftechnik Vol. 39/9:585-672, 2008

# DEVELOPMENT OF FIBRE METAL LAMINATES MADE OUT OF HYBRID SEMI-FINISHED PRODUCTS PRODUCED BY A TEXTILE PROCESS

**Jenkel, Sabrina[1*], Schiebel, Patrick[1], Kösters, Robert[2], Herrmann, Axel S.[2]**

[1]Faserinstitut Bremen e. V. (FIBRE)
[2]Universität Bremen

**ABSTRACT:** The combination of fibre reinforced plastic and metal layers results in a lightweight material with high mechanical performances that incorporates the advantages of both components. At the moment the so-called Fibre Metal Laminate (FML) material is used especially by the aerospace industry. Reasons therefore are the high material costs, due to the currently established manufacturing processes and the used prepreg materials. To include FMLs also in cost sensitive sectors, like the automotive industry, an economic production process is needed. The availability of low cost FMLs could open up the market for various new applications. Examples of applications for this puncture-resistant and lightweight material are flat structures of trucks and trailers or side panels of air cargo containers. The aim of the research project "FibMet" is to develop an economic way to produce FMLs. The new approach is to connect fibre and metal layers by sewing and to impregnate these hybrid structures with a thermoset matrix during an infusion process.

**KEYWORDS:** Fibre Metal Laminates, vacuum infusion, textile processes

## 1 INTRODUCTION

A Fibre Metal Laminate (FML) is a combination of different layers of fibre reinforced plastic and metal. The aim of the hybrid materialis to combine the advantages of both base materials. FMLs are characterised by low weight as well as high strength and stiffness [1]. The material the material also shows a high resistance against fatigue crack growth [2]. It offers also a good flame protection, because the fibres slow down the melting of the metal layers [3]. Moreover, the moisture absorption of the material combination is less than the one of every single component, so there is a higher corrosion resistance expectable [3]. Furthermore, FMLs are suitable for applications dealing with high impact loads [4]. An established and commercially available FML material is called GLAss REinforced Aluminium (GLARE), which was developed in the 1980s by members of the TU Delft [5]. This material is often used for large components, especially for flat plate components or large-scale shell structures, for example as fuselage skin material for the airplane Airbus A380 [6].

Today FMLs like GLARE are normally made of prepreg materials with glass fibres and thermoset matrix material, which are combined with aluminium foils. Following the layup procedures the parts are cured in an autoclave [3]. In addition to the costs for the autoclave there are high costs for the cooling of the prepreg material during storage. As a result, the manufacturing of FMLs in this way is associated with high costs, long cycle times and limited part sizes [7]. Hence, FMLs are used more often in aerospace applications than in other industries.

A different approach is to modify a well established fabrication method for fibre reinforced plastics, the vacuum assisted resin transfer molding (VARTM) for producing FMLs. A dry layup made of textile and metal layers is impregnated during an infusion process. The metal layers are perforated to add flow pathways before the layup is stacked. The used perforating methods are dremel drilling, water jet, Nd:YAG laser and precision drilling. The results are perforations with different diameters, for example 0.38 mm for perforation by drilling and diameters variating from 1.52 mm and 3.81 mm for perforation by water jet. [7]

To apply FMLs in cost sensitive industries, such as the automotive or the logistic industry, it is necessary to use manufacturing processes, which allow the producing the FML parts at low costs. This is the aim of the

presented project. Thereby the metal layers are fixed to textiles by sewing to get a dry hybrid semi-finished product. This semi-finished product is formed to the desired shape before it is impregnated by the matrix material during a vacuum infusion process. Subject of the research is to analyse single steps of the production of FMLs in the described way. There are intersections, interdependencies and interactions between the process steps. Additionaly to the analysis of the textile and the infusion process the properties of the material will be tested.

## 2 EXPERIMENTAL PROCEDURE

To analyse the possibilities of the process, the textile and the infusion process are considered in detail for varying parameters.
The chosen textile is a biaxial non crimp fabric (NCF) of glass fibres, while the used metal layers are steel plies (material: 1.0338, thickness: 0.1 mm).
As matrix EPIKOTE™ MGS™ RIMR 035c Resin System and EPIKURE™ RIMH 037 Curing Agent are used.
Each of the produced coupon parts consist of three textile layers and two metal layers. Two different layups are tested, one with alternating textile and metal sheets and the other with the textile sheets sandwiched between the metal sheets, as displayed in Fig. 1.

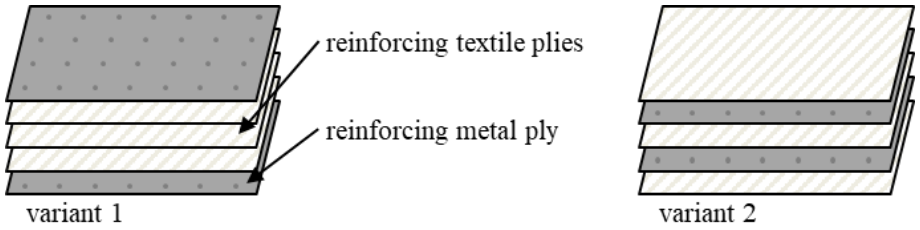


***Fig. 1*** *Variants of two different FML layups*

In different experiments the influence of the layer structure on the textile manufacturing and the infusion process are analysed.

### 2.1 TEXTILE PROCESS

The first step for producing FMLs in the described way is to produce the hybrid semi-finished preform by a textile process. Herein the layer structure is stacked up in a pre-set order before it gets connected by sewing with an industrial sewing machine (see Fig. 2).

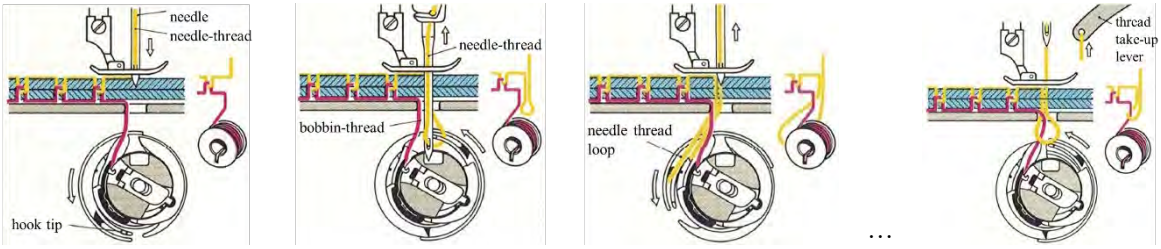


The needle penetrates through the material.

After reaching the deepest point, the needle-thread forms a loop because the needle moves up again.

The hook holds the thread, which opens up by the rotation of the bobbin case. Thereby the needle-thread forms an interlock with the bobbin-thread.

The needle keeps moving up and the thread take-up lever pulls the needle-thread upwards. Thereby the looped bobbin-thread is also pulled into the material.

***Fig. 2*** *Process steps of a double lock stitch [8], [9]*

The textile process is a part of the complete production process. Variations of the parameters in this step will have influences on the textile process. Additionally there are different effects, which are expected for the following process steps and the properties of the produced part. The seam creates a textile connection between fabrics and metal layers and improves the interlaminar shear strength of the laminate. During the sewing process the metal layer is perforated by the needle. This perforation enables the impregnation in the

following process of infusion, like described by [7]. But in this process, there is no need for a step of perforation before the layup is build up, because the perforation is directly integrated in the connection of the layers during the textile process.

### 2.1.1 SELECTION OF A SUITABLE SEWING THREAD AND DEVELOPMENT OF PROPER SEWING PARAMETERS

To find a suitable sewing thread, different types of thread were tested. Most of the tested threads are standard sewing threads, which are mixed threads on basis of polyester fibres and broke just after a few stitches. These threads are Serafil 200/2, Silver-tech 120 and Rasant 75 from Amann & Söhne GmbH & Co. KG. . The reason is the friction of the thread at the edges of the needle hole. While the sewing process the needle punctures the layer stack and leaves perforations in the metal layer. This results in a hole with sharp edges and a devormation of the metal. These sharp edges of the perforations tend to damage the threads. Therefore the used threads have to be resistant to tearing and abrasion. The used thread has to be resistant to tearing and abrasion. The thread proven to fulfil these requirements is the K-tech 75 from Amann & Söhne GmbH & Co. KG. It is made of long stapled para aramid fibres from the brand Kevlar® DuPont™ and has a linear density of approximately 207 * 2 dtex [10].
Before the layers can be sewn to coupon parts, the challenge is to find suitable sewing parameters for a clean seam pattern. Especially the thread tension of the needle-thread and the bobbin-thread are cruial parameters.

### 2.1.2 NUMBER, SIZE AND SPACING OF THE PERFORATION

The influence of the different paramters of the seam patterns to the following process steps has to be analysed. For this purpose, the size and the spacing of the perforation are varied. The diameter of the holes is defined by the size of the needle. Different round-shank needles have been used in the sewing process.
The machine used for producing the coupons is an industrial embroidery machine of type Tajima TMLH-G108 Typ D3-1.

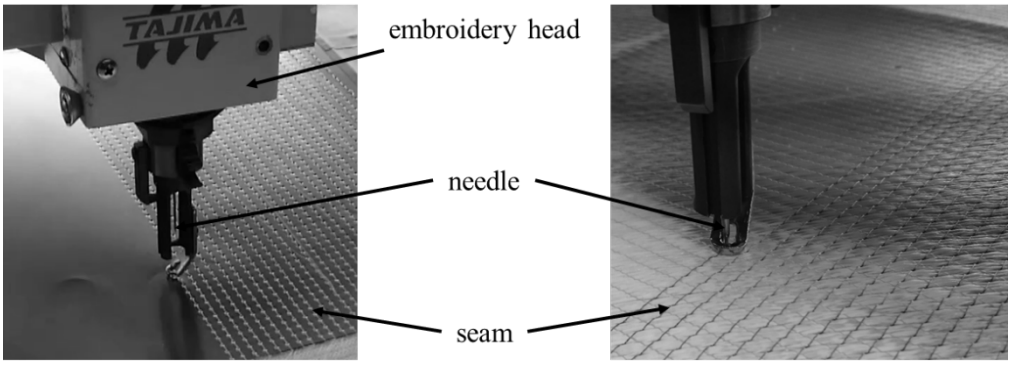


***Fig. 3*** *Sewing of the hybrid semi-finished material, left: layup 1, right: layup 2*

The chosen needles have diameters of 0.7 mm, 0.9 mm and 1.1 mm. Needles with a small diameter are sharper than the ones with greater diameters but they are also more prone to breakage. The distance between the holes are variated between 5.0 mm and 20.0 mm.
To analyse the influence of the size and the spacing of the perforation at the same time, the parameters have to be combined. Changing only one parameter at a time means a high number of combinations to be tested. To reduce the number of tests, significant combinations are found in a Design of Experiments (DoE), which is shown in Table 1:.

***Table 1:*** *Combinations of size and spacing of the perforation*

| Distance between stitches in mm | | | |
|---|---|---|---|
| 20.0 | x | | x |
| 12.5 | | x | |
| 5.0 | x | | x |
| | 0.7 | 0.9 | 1.1 |
| | Diameter of the needle in mm | | |

It is expected, that the impregnation in the infusion process is easier and has a good quality, if the needle holes are big with less space between it. However, it should be noted that the perforation damages the metal ply and creates undulations and gaps within the textile material, so less mechanical strength is associated with a higher number and size of perforations. Just the interlaminar shear strength is expected to be higher with more points connecting the layers.

### 2.2 INFUSION PROCESS

Following the successful textile process, the sewn structure is infiltrated with a thermoset matrix during an infusion process. The hybrid semi-finished product is therefore cut and draped into the proposed shape and included in an infusion assembly.

#### 2.2.1 PROCESS OF VACUUM INFUSION

The sewed hybrid preforms were impregnated with the matrix material during a conventional vacuum infusion process. The used vacuum assembly is illustrated schematically in Fig. 4. The FML preform can be integrated in the assembly like a normal textile layup.
In several iterative steps, the infusion parameters (like the ideal size and material of the flow aid and the ideal vacuum pressure) will be found.
Following to the infusion with the resin/hardener system the infiltrated assembly is cured in the oven for eight hours by 70 °C.

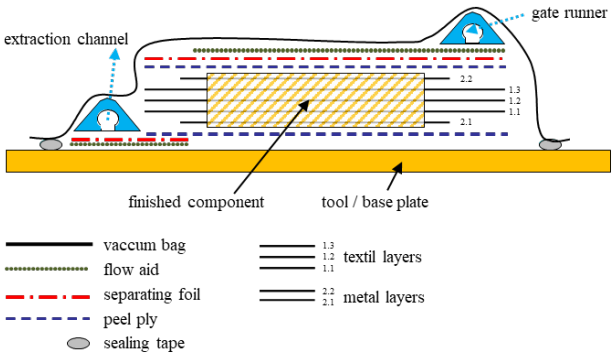


***Fig. 4*** *Vacuum infusion assembly*

For the experiments with coupon scaled parts the vacuum assembly is made on a glass tool. This allows to observe the infusion process from both sides of the manufactured parts.

#### 2.2.2 ANALYSIS OF THE INFUSION QUALITY

The first step is to produce different semi-finished products with different sewing parameters. The infusion properties are observed and documented with the help of video analysis. Top and bottom are observed at the same time, because a mirror is placed under the assembly. In this way, it is possible to monitor the position of the flow front.
To evaluate the quality of the infusion process the laminate quality (delamination and pores), the fibre volume fraction the impregnation properties are to be characterised.

## 3 RESULTS AND DISCUSSIONS

FMLs in coupon size with a variation of the mentioned parameters were produced as described in chapter 2. At first the hybrid structure was sewn to a semi-finished product, which was impregnated with a thermoset matrix material during a vacuum infusion process.

### 3.1 PROCESS RESULTS FOR THE TEXTILE PROCESS

It was possible to connect the metal and the textile with all chosen needles and the selected aramid thread. Thereby could be seen, that the sewing is easier with a needle with a big diameter than with a needle with smaller diameter. The thread also has a diameter which is added to the diameter of the needle. A small needle creates a small hole and the thread rubs at the edges of the hole. This effect increases the smaller the diameter of the needle gets.
The chosen aramid thread makes it possible to sew the structure with a low number of breaks in the thread. By the correct setting of the parameters a regular seam pattern can be produced, shown in Fig. 5 and Fig. 6,

which show two examples of sewn materials of layup 1. On the bottom sharp edges at the needle holes can be identified.

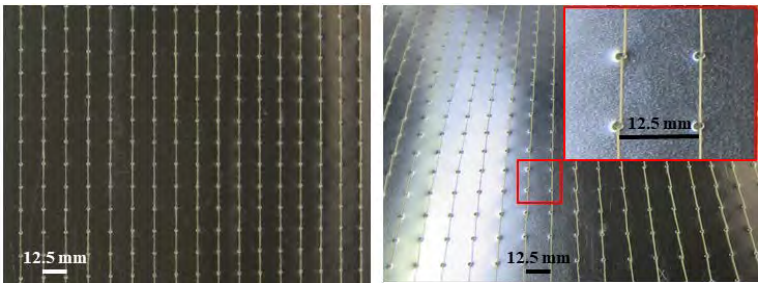


***Fig. 5*** *Seam pattern of a sewn hybrid layup, distance between the stitches: 12.5 mm, diameter of the needle: 0.9 mm, right: top, left: bottom*

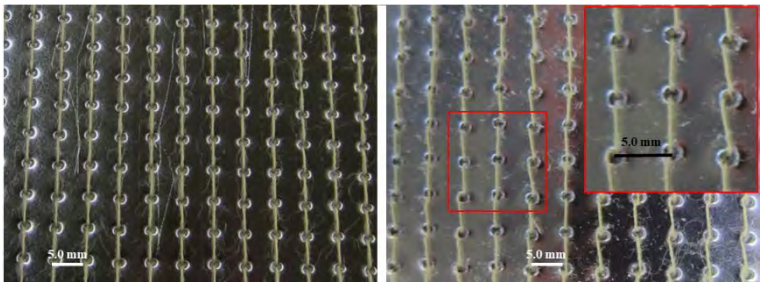


***Fig. 6*** *Seam pattern of a hybrid layup, distance between the stitches: 5.0 mm, diameter of the needle: 1.1 mm, right: top, left: bottom*

### 3.2 PROCESS RESULTS FOR THE INFUSION PROCESS

The sewn coupons have been impregnated with a thermoset matrix system during an infusion process. Thus the expansion of the flow front and the impregnation was observed during the process by a video analysis. At first the resin runs through the flow aid at the upper side of the infusion assembly. After this dark wet points can be spotted at the lower side of the laminate. In these areas, the matrix saturates the laminate. Thus, the resin spreads out form the perforations in the metal to the remaining areas of the laminate until it reaches the extraction channel of the vacuum assembly. Approximately seven minutes after the first resin reaches the gate runner, there are no dry areas in the laminate any more, but there are still air bubbles in the extracting resin, so the infusion can not get stopped at this time. The Table 2: shows the infusion at different times.

***Table 2:*** *Infusion of a FML, layup 2, needle-diameter: 0.7 mm, distance between the perforations: 20 mm, *: the time measured after the first resin reaches the gate runner*

| | | | | | |
|---|---|---|---|---|---|
| top-view | 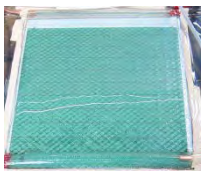 | 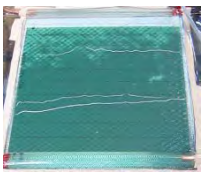 | 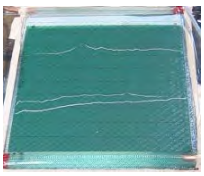 | 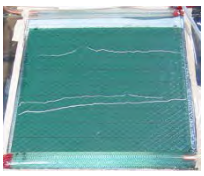 | 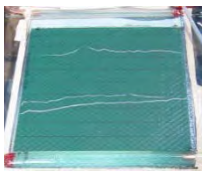 |
| bottom-view | | 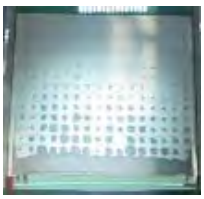 | | 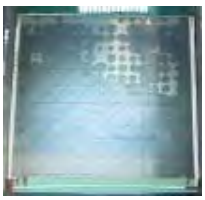 | |
| t* | 30 s | 2 min 30 s | 4 min 30 s | 5 min 30 s | 7 min |
| | The white lines show the position of the flow front at the flow aid. | The flow front at the top has reached the end of the flow aid. | The textile on the top is impregnated. There are wet areas all over the | Most of the laminate is impregnated with matrix material. | There are no dry areas at the bottom any more. |

| | | | | | |
|---|---|---|---|---|---|
| | First wet areas can be spotted at the bottom. | | bottom, which rise and combine to a flow. | | |

The overview shows that the flow front at the top side moves on much faster than the impregnation of the lower layers. The impregnation trickles in thickness direction. There is no continuous flow front between top and bottom of the laminate like it should be monitored during a normal infusion process. This means, that the infusion parameters have to be optimised to get a slower flow front at the top and a consistent impregnation of the whole laminate. This could be reached by using a flow aid, which induces a slower expansion of the flow front at the upper side of the laminate.
A microsection of the laminate is shown in Fig. 7. At the upper side of the laminate a pore is localised under the metal sheet. There this indicates a need for optimization.

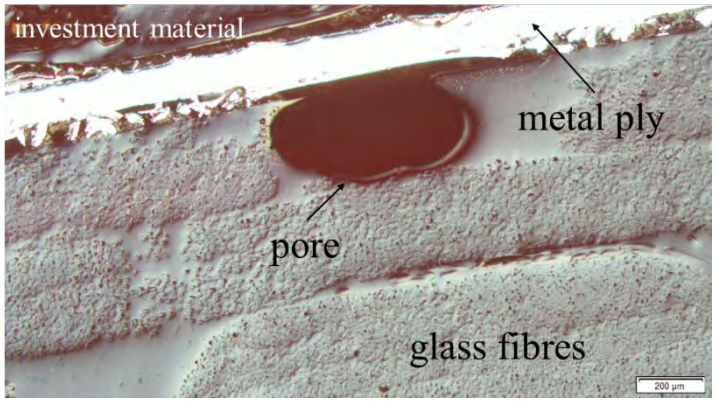


***Fig. 7*** *Microsection of a FML, produced during an infusion process*

Other microsections of a FML with the reinforcing metal plies at the outside of the laminate are shown in Fig. 8 and Fig. 9. A cross section along the seam was prepared to take these figures. The impregnation in this part shows no pores or other failures like delaminations. Furthermore, in these figures show, how the metal layer is deformed at the needle hole. At the edges, the thread rubs during the sewing process, as described in chapter 3.1.

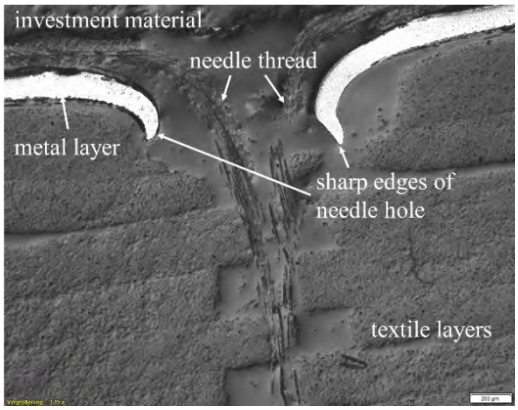


***Fig. 8*** *Upper section of the FML*

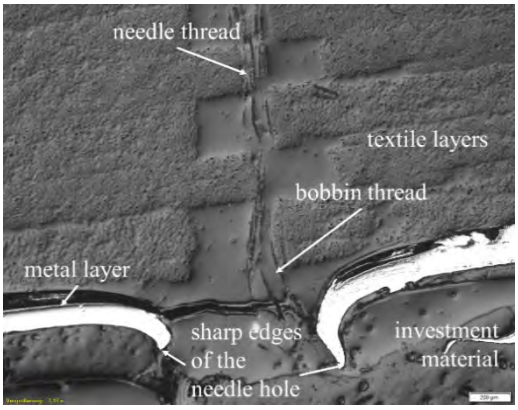


***Fig. 9*** *Lower section of the FML*

## 4 CONCLUSIONS

The study has shown that it is possible to produce FMLs based on pre-assembled hybrid semi-finished products during an infusion process.
Textile and metal layers were sewn to hybrid structures by using an aramid thread. The semi-finished products were impregnated by a vacuum infusion process with a thermoset matrix. The textile process was successful with different needle diameters and different seam patterns.

Two different layups were connected by sewing for every chosen combination of seam pattern and needle diameter. After the textile process the sewn structures were impregnated with a thermoset matrix system during a vacuum infusion process.
The next step is the characterisation of the laminate properties. On this occasion the quality of the infusion process and the mechanical properties are to be defined. The quality of the infusion process is defined by the laminate quality, the fibre volume fraction and the impregnation properties. The mechanical tests will provide clarification about the shear strength, resistance to pullout, Young's modulus and bending stiffness and the impact resistance of the material. All properties of the developed materials should be considered with regards to the influence of the metal layers and the applied perforation scheme.
The aim of the research projects is, to develop an economic procedure for producing FMLs. This material can be used in various areas, e.g. in box bodies of closed trucks or for air cargo containers. The sewn layer structure allows a preforming before the infusion process and can be offered as a semi-finished product by enterprises of the textile industry.

## 5 ACKNOWLEDGEMENT

The research project “Entwicklung von Faser-Metall-Laminaten aus Hybridtextilien (FibMet)” is funded by the German Federation of Industrial Research Associations (AiF) as part of the Industrial Collective Research (IGF) through budgetary resources from the Federal Ministry for Economic Affairs and Energy (BMWi) on the basis of a decision by the German Bundestag to whom we would like to express our sincere thanks. (IGF Project Number: 19300 N; Funding period: 02/2017 – 01/2019)

## REFERENCES

[1] Bienias J., Jakubczak P., Surowska B.: *Properties and characterization of fiber metal laminates.* Hybrid Polymer Composite Materials. Properties and characterisation, Lublin, Elsevier (Woodhead Publishing Series in Composites Science and Engineering), 253–277, 2017.
[2] Schijve J.: *Development of fibre-metal laminates, ARALL and GLARE, new fatigue resistant materials.* Fatigue 93: proceedings of the fifth International Conference on Fatigue and Fatigue Thresholds held 3-7 May 1993, Montreal, Quebec, Canada, Warley, 1993.
[3] Vlot A., Vogelesang L. B., de Vries T. J.: *Towards application of fibre metal laminates in large aircraft.* Aircraft Engineering and Aerospace Technology, 71(6): 558-570, 1999.
[4] Jakubczak P., Bieniaś J., Surowska B.: *Impact resistance and damage of fiber metal laminates.* Hybrid Polymer Composite Materials. Properties and characterisation, Lublin, Elsevier (Woodhead Publishing Series in Composites Science and Engineering), 279–309, 2017.
[5] Vogelesang L. B., Vlot A.: *Development of fibre metal laminates for advanced aerospace structures.* Journal of Materials Processing Technology, 103(1): 1-5, 2000.
[6] Vlot A., Gunnink J. W.: *Fibre Metal Laminates: An Introduction*. Dordrecht: Springer Netherlands, 2001.
[7] Jensen B. J., Cano R. J., Hales S. J., Alexa J. A., Weiser E. S., Loos A. C., Johnson W. S.: *Fiber metal laminates made by the VARTM process.* 17th International Conference on Composite Materials, Edinburgh, Scotland, 2009.
[8] Eberle H., Hermeling H., Hornberger M., Kilgus R., Menzer D., Ring W.: *Fachwissen Bekleidung.* 7 ed., Haan-Gruiten: Verlag Europa-Lehrmittel, 2003.
[9] Ogale A., Mitschang P.: *Tailoring of Textile Preforms for Fibre-reinforced Polymer Composites.* Journal of Industrial Textiles, 77-96, 2004.
[10] Amann & Söhne GmbH & Co. KG: *Produktdatenblatt K-tech 75.* Bönnigheim, 2014.

Supported by:

Federal Ministry
for Economic Affairs
and Energy

on the basis of a decision
by the German Bundestag

# SUITABLE PROCESS FOR MASS PRODUCTION OF HYBRID LAMINATES WITH SENSOR FUNCTIONALITY

**Alexander Graf[1*], Ricardo Decker[2], Verena Kräusel[1], Dirk Landgrebe[1], Lothar Kroll[2]**

[1] Professorship for Forming and Joining, TU Chemnitz
[2] Department of Lightweight Structures and Polymer Technology, TU Chemnitz

**ABSTRACT:** Previously, component production and functional integration were two separate discontinuous processes. It will be presented a continuous large-scale production process for the manufacture of hybrid laminates with sensor functionality in contrast to the classic processes. The functional component of the laminate produced is a thermoplastic film which is electromechanically functionalized by the addition of piezoceramic powder and carbon nanotubes. This foil is joined between an aluminum sheet as a structural component and copper electrodes. Properties such as permittivity and electrical conductivity, toughness, sufficiently good adhesive strength and optimum processability are of great importance for a maximum sensor effect for the conversion of structure excitations into electrical signals. In the first step, the joining process was examined by means of varying parameters with regard to the maximum achievable adhesive strength. The transfer to a continuous process with subsequent forming process is the subject of current research work. Furthermore, it is necessary to polarize the piezoceramic compound in order to activate the sensor effect. To this end, a concept for in-line polarization during forming is presented. As an example of an application, a cladding element is presented in the interior of the car, which is triggered by touch, e. g. to control functions. The hybrid laminate with sensor functionality also enables structural health monitoring in structural components.

**KEYWORDS:** hybrid assembly composite, piezoceramic compound, sheet metal forming, active thermoplastic foil, bivalent resource efficiency

## 1 INTRODUCTION

A recent development of innovative products for the aerospace [1] and the automotive sector, consumer electronics as well as plant and equipment engineering is the use of new lightweight materials with additional sensor functions. This development means that more and more "intelligent" components are used. Current systems are a hybrid combination of a component and a sensor unit, as shown by the example of a shaft seal with integrated sensors [2].
In order to increase the functional integration in lightweight components, sensor materials must be placed directly on or into the structure. In this paper, we present merged technologies for the integration of piezoelectric sensor materials in metal/plastic lightweight parts. The objective is to improve the performance and functional density of hybrid components through functionalization with sensors, actuators and electronics. Therefore, we apply innovative continuous manufacturing technologies for embedding active systems into semi-finished products and preforms based on micro- and nanoeffects with special advantages [3]. In order to reliably integrate additional functionality, we will develop special methods for the design and integration of active transducer elements in lightweight structures.
With the development of integrative extrusion molding processes in association with roll-press technology, a vital contribution is made to the reduction of resource and energy consumption, especially for the areas of metal/plastic composites. These hybrid materials and their production technologies have been under intensive scientific investigation for many years. The development of manufacturing technologies for active and semi-active polymer-based systems with mechatronic and electrical properties is still being researched. Such function-oriented structures have great potential for functionalized lightweight components with energy harvesting, structural health monitoring or vibration and noise damping [4].
Extrusion-molding technology facilitates the efficient, large-scale manufacturing of electromechanical systems by using piezoelectric nano-composites for the production of active thermoplastic foils (ATF). The

* Corresponding author: Alexander Graf, Reichenhainer Straße 70, D-09126 Chemnitz, phone: +49 371 531-39938, fax: +49 371 531-839938, alexander.graf@mb.tu-chemnitz.de

ATF is suitable for embedding into semi-finished metal sheets by merging the extrusion-molding technology with the roll-press technology. Therefore, issues concerning material characteristics, process technologies and metal forming will all be clarified. These intelligent metal sheets can be manufactured more efficiently, due to decreased production times and costs in comparison to classic sequential technologies. Furthermore, this process is the first to allow the in-line production of a lead zirconate titanate (PZT) based transducer system on a large scale, without the use of energy-intensive sintering processes. Thus, embedded sensor system platforms and corresponding measurement approaches will be developed for local signal processing and wireless data exchange.

## 2 PROCESSING CHAIN

After obtaining the optimal process parameters in terms of joining and forming from investigations with separate samples we designed the process chain for the continuous manufacturing of the hybrid assembled composite as shown in Fig. 1:
The optimised piezo-compound is subjected to a foil extruder (1) and then processed in a continuous rolling procedure. In order to meet the required roughness for roll-bonding of the aluminium strip with the piezo-compound as the preferred joining solution, the sheet metal is structured before the joining process, then heated up and joined with the functionalised foil (2). After joining with the copper electrode the semi-finished sheet product can be cut to form as a contoured blank before proceeding the final forming operation (3) in order to manufacture the desired component – the centre console of a car. The subsequent polarisation (4) and the electro-mechanical characteristics of the qualified piezo-sensor will form the base for signal processing and conditioning (5).

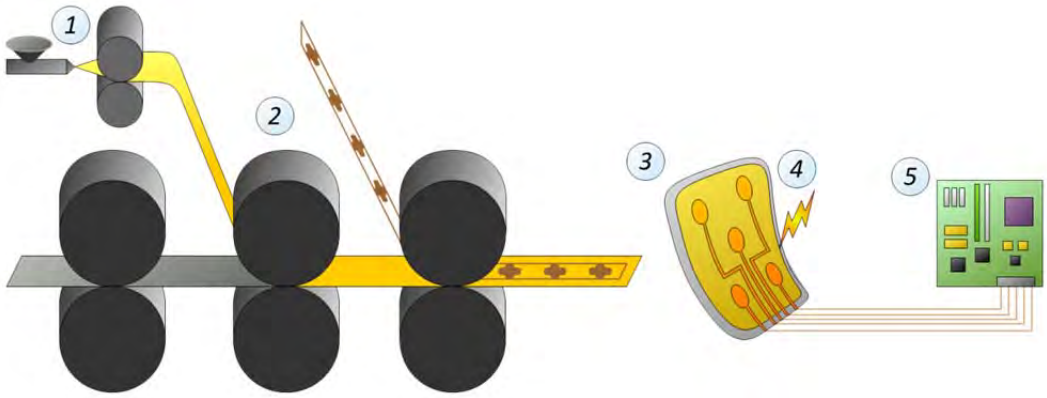


***Fig. 1*** *Process chain for a mass production enabled manufacturing of hybrid laminates*

### 2.1 FOIL EXRTUSION

In order to generate the sensor effect of the hybrid laminate by means of impact induced voltage generation, we functionalized the thermoplastic polymer with piezoceramic powder (lead zirconate titanate – PZT) and electrically conductive filler (carbon nanotubes – CNT). The PZT (NCE55, Noliac A/S, Kvistgård, Denmark) facilitates the voltage generation of the compound and the CNT (NC7000, Nanocyl S.A., Sambreville, Belgium) lowers the electrical resistivity of the matrix polymer. This leads to higher electrical fields in the piezoceramic particles during the polarisation process, whereby the piezoelectric effect is enhanced [5]. Based on previous experiments we chose a filler composition of 70 wt% PZT and 0.5 wt% CNT as a compromise between good electromechanical properties and good processing. Higher PZT loadings generate a higher piezoelectric effect. In addition, the viscosity of the compound increases significantly, resulting in lower processability [6].
We continuously blended the fillers with the matrix polymer polypropylene (Moplen HP501H, LyondellBasell, Rotterdam, the Netherlands) using a twin-screw extruder at 240 °C. For the subsequent calendering operation (Fig. 2) the molten compound was sent to the calender unit through a wide slot die with a cross section of 350 mm x 0.5 mm. The tempered rolls pull off and consolidate the thermoplastic foil. The rolls close to the die have a temperature of 120 °C and the ones farther away have a temperature of 80 °C. We varied the roll circumferential speed from 0.9 m/min to 3.0 m/min in order to control the stretching and thereby the thickness of the foil. This resulted in a reduction of thickness from about 325 µm to about 100 µm [7].

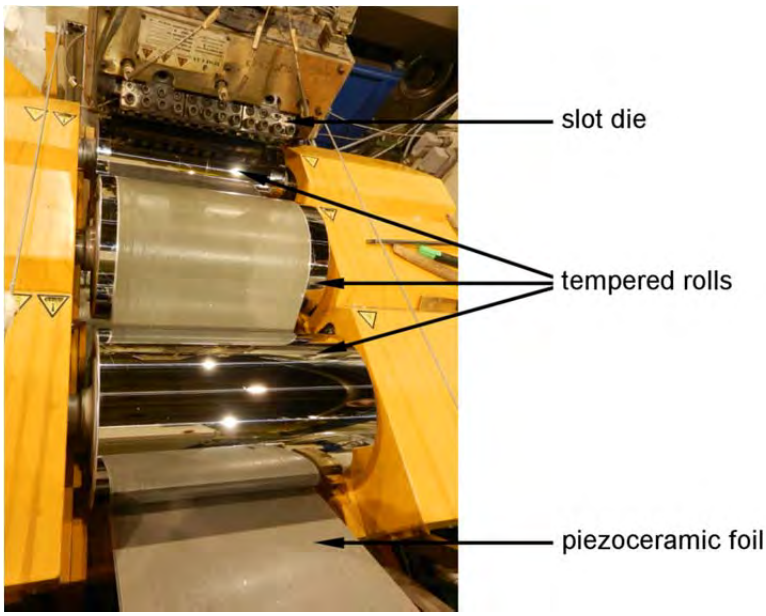


***Fig. 2*** *Foil extrusion*

## 2.2 CONTINUOUS JOINING BY ROLL BONDING

The first experiment of joining of the piezo-compound with the aluminum sheets was a discontinuous process. Its main goal was to determine the best joining parameter (surface preparation, temperature and pressure) to reach the maximum interlaminar shear strength [8]. In the next step we developed a test bench for continuously joining the piezo foil with aluminum sheets. Fig. 3 shows the assembly. In the first step the aluminum sheet is led through an infrared radiator and heated up. The temperature is controlled by thermocouples during heating and by a pyrometer before joining, respectively. After heating, the aluminum is merged with the piezo-compound foil and joined by subsequent roll bonding. In the sheet outlet the hybrid assembled composite is then cooled down. The main parameters for the first examination were the distance between the infrared heater and the aluminum, the rolling speed and power of the infrared radiator [7].

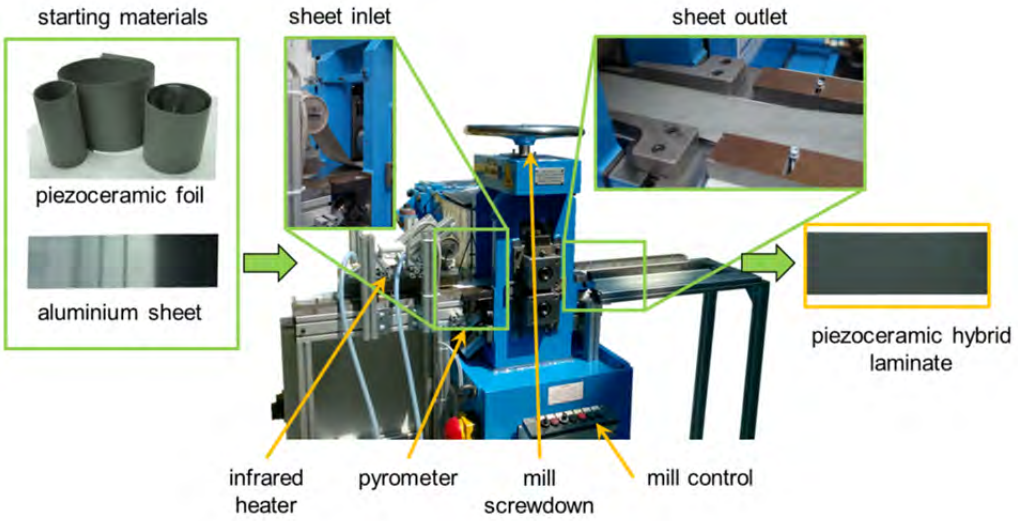


***Fig. 3*** *Pilot plant for the continuous joining of piezoceramic foils with aluminium sheets [7]*

By using a PID controller it is possible to directly control the temperature in front of the sheet inlet. This is an important step for process monitoring and for a robust process. The controller setting is based on iteration so that a slight overshoot is permissible and the controller reacts to changes very dynamically. Subsequently, we were able to examine how the temperature under the radiator affects the joining result, whereas all other parameters remained constant. Table 1 shows the investigated temperatures with the associated optical results in the second column and the measured surface defects. We scanned the parts with an optical measuring system (GOM ATOS Core 200) and the surface defects were displayed using the GOM Inspect software.

Due to the high temperatures (390 °C), the surface melts heavily and parts of the plastic remain attached to the roll. The best joining results have been determined between 250 °C and 300 °C. If the temperature is too low (220 °C), there is significant delamination in some areas.

***Table 1:*** *Influence of the heating temperature on the joining result*

| heating temperature | result (top view) | surface defects | legend |
|---|---|---|---|
| 390 °C | | 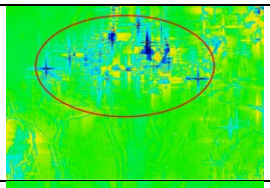 | 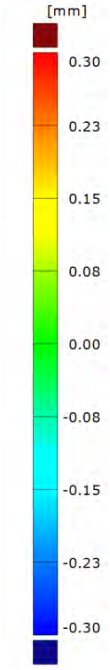  |
| 300 °C | | 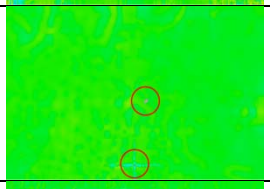 | |
| 250 °C | 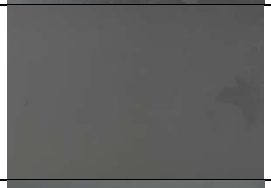 | 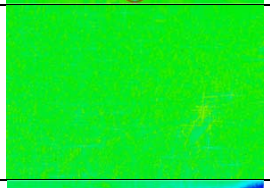 | |
| 220 °C | 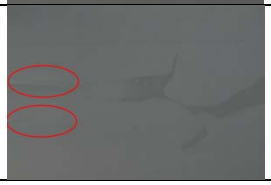 | 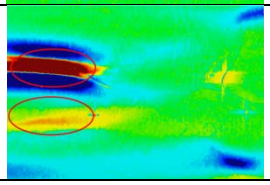 | |

## 2.3 FORMING OF A HYBRID CENTRE CONSOLE

We presented preliminary experiments about forming hybrid laminates with sensor function in [8]. It has been found that the forming temperature has a great influence on the result. Furthermore, it is known that the springback can be significantly minimized by cooling in the forming tool [9]. Based on this, the logical next step would be the development of a tool that can both heat and cool. This technique is widely used in injection molding and is called variotherm tempering. Its implementation as a forming tool for the cover of the center console of an automobile is shown in Fig. 4.

The two essential tool parts (upper and lower tool) each consist of two active elements. For the production of the center console, the outer geometry is preformed by a double bending process in the first step. In the second step, the inner contour is produced by a deep drawing process. All active elements are connected to a variotherm circuit. Thus, the component can be cooled down after deep drawing.

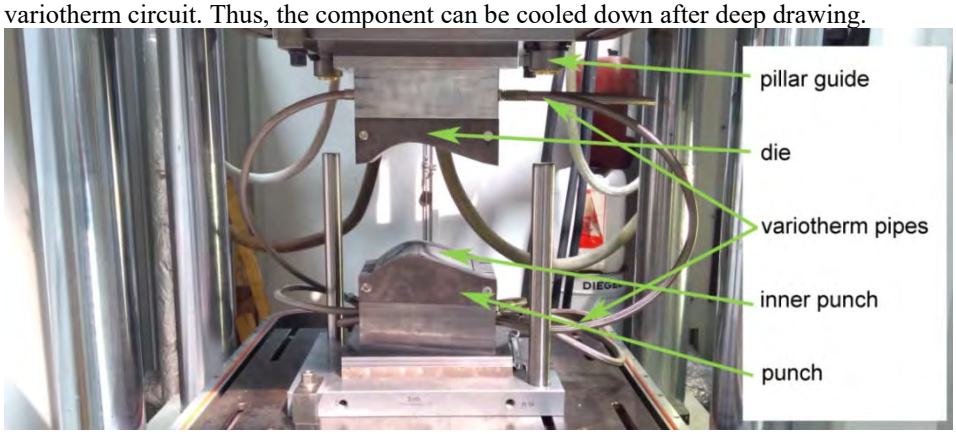


***Fig. 4*** *Variotherm forming tool for the centre console*

First, we conducted experiments on double bending, looking at the preheating temperature and duration, cooling temperature and duration and position of the composite in relation to the active tool part. Our result

at optimal parameters (preheating 220 °C for 5 minutes; forming with 400 kN and cooling in the tool for 4 minutes) is shown in Fig. 5. A distinction is made concerning the position of the composite in relation to the active tool part. In the second row we list the results comparable to the CAD model. The forming without a composite (aluminum only) in column 1 shows a relatively large springback. When the composite is placed in the die, the springback is significantly reduced. In contrast, the springback increases when the composite is placed in the punch.

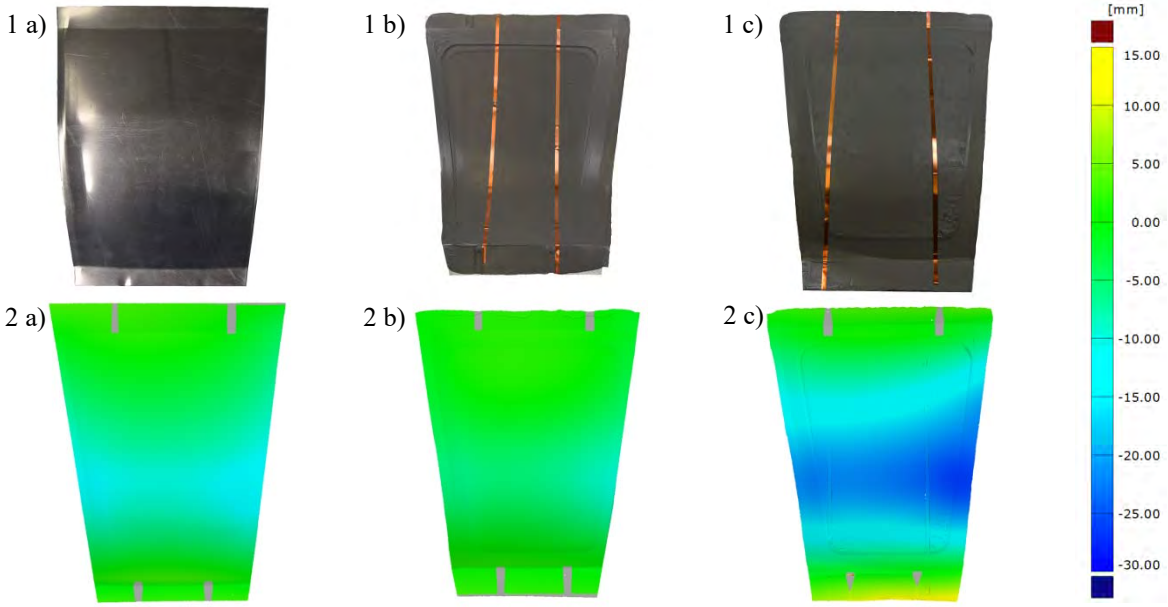


***Fig. 5*** *1) Optical forming result a) without composite, b) composite placed in the die and c) in the punch; 2) surface compared to CAD model*

### 2.4 IN-LINE POLARISATION CONCEPT

In order to activate the sensor effect of the hybrid laminate it is necessary to polarize the piezoceramic compound. Due to the extrusion temperature of 240 °C, the joining temperature of 250 °C and the forming temperature of 180 °C, that are higher than the Curie temperature of the piezoelectric ceramic, the piezo-compound would depolarize thermally during this process steps. Therefore, the polarization process has to take place after the forming of the hybrid laminate. In previous experiments Fraunhofer Institute for Ceramic Technologies and Systems (IKTS) analyzed the polarization behavior of the piezoceramic compound at different temperatures. At lower temperatures of 20 °C and 50 °C the piezoceramic compound could not be polarized. The polarization process is practicable at an elevated temperature of 100 °C, but it is necessary to hold the polarization voltage for long time. We determined the best polarization results at elevated temperatures about 120 °C with a holding time of 5 min. Based on these results we will be able to polarize the hybrid laminate during the cooling in the forming process. The electrical connection to the metallic electrodes can be realized via the die and the punch of the forming tool using the clamping force. Through this approach, we will be able to use the residual heat of the forming and save energy by omitting the reheating in the polarization process. In addition, the cycle time can be reduced significantly by the combination of forming and polarization in one process. A special challenge in this combined process is the precise temperature control and the electrical insulation of the forming tool. This combined forming and polarization process will be part of our future investigations as well as continuing measurements for the characterization of samples polarized in-line.

## 3 CONCLUSION AND VISION

An active thermoplastic foil highly filled with PZT and CNT can be manufactured continuously using the foil extrusion technology. We produced foils with 70 wt% PZT and 0.5 wt% CNT with a decreased thickness of 100 µm. This foil can be joined continuously to an aluminum sheet by roll bonding. By means of a controlled system, the optimum joining temperature could be adjusted and the robustness of the tests increased. In a subsequent forming process the hybrid laminate can be formed using a variotherm forming tool. The positioning of the composite to the active forming elements has a great influence on the springback behavior. We plan further investigations of a possible combination with deep drawing. During cooling at the

end of the forming process the piezoceramic foil can be polarized using the residual heat and hence the sensor function of the hybrid laminate is provided.
The combination of the four processes foil extrusion, roll bonding, forming and polarization allows us to reduce resource and energy consumption due to the use of the residual heat of the upstream processes. The reheating between the process steps can be minimized and the cycle time can be reduced significantly. In future this will lead to a novel merged machine concept for manufacturing complex lightweight structures made of sensor hybrid laminates in one heat only.
An application field for the developed hybrid laminate is the interior of vehicles, e.g. a center console with touch functionality. The required impact localization for this purpose is implemented by means of machine learning algorithms. First experiments show the use of split linear regression is a good choice. It has a better [7] or nearly as good [10] performance as previously investigated methods but is less complex due to its linear nature. Detailed investigations and increasing of the localization accuracy will be part of future research activities.

## 4 ACKNOWLEDGEMENT

We gratefully acknowledge the cooperation of our project partners and the financial support of the DFG (Deutsche Forschungsgemeinschaft) within the Collaborative Research Center/Transregio 39 ‘‘PT-PIESA’’ and the Federal Cluster of Excellence EXC 1075 ‘‘MERGE’’.

## REFERENCES

[1] Das A., Ormbrek G., Obal M.: *Adaptive Structures for Spacecraft – A USAF Perspective*. AGARD Conference: Smart Structures for Aircraft and Spacecraft, Lindau, 1992
[2] *Integration von Sensoren mit autarker Energieversorgung in einen Simmerring*. Chemnitz: Fraunhofer Institut für Elektronische Nanosysteme ENAS Produkt-Datenblatt, 2010
[3] Kräusel V., Graf A., Heinrich M., Decker R., Caspar M., Kroll L., Hardt W., Göschel A.: *Development of hybrid assembled composites with sensory function*. In: CIRP Annals - Manufacturing Technology, 64 (1): 25–28, 2015, doi: 10.1016/j.cirp.2015.04.054
[4] Schulze R., Heinrich M., Nossol P., Forke R., Sborikas M., Tsapkolenko A., Billep D., Wegener M., Kroll K., Gessner T.: *Piezoelectric P(VDF-TrFE) transducers assembled with micro injection molded polymers. Sensors and Actuators.* A: Physical, 208:159–165, 2014, doi: 10.1016/j.sna.2013.12.032
[5] Ounais Z., Park C., Harrison J., Lillehei P.: *Evidence of Piezoelectricity in SWNT-Polyimide and SWNT-PZT-Polyimide Composites*. Journal of Thermoplastic Composite Materials 21 (5):393–409, 2008
[6] Decker R., Heinrich M., Tröltzsch J., Rhein S., Gebhardt S., Michaelis A., Kroll L.: *Development and Characterization of Piezo-active Polypropylene Compounds Filled With PZT and CNT*. In: 5th Scientific Symposium CRC/Transregio 39, Dresden, 2015
[7] Ullmann F., Decker R., Graf A., Kräusel V., Heinrich M., Hardt W., Kroll L., Landgrebe D.*: Continuous Manufacturing of Piezoceramic Hybrid Laminates for Functionalised Formed Structural Components*. Technologies for Lightweight Structures 1 (1), 1–13, doi: 10.21935/tls.v1i1.64
[8] Graf A., Kräusel V., Landgrebe D., Decker R., Kroll L.: *Joining and forming of hybrid assembled composites with sensory function*. In: Euro Hybrid – Materials and Structures 2016 – Proceedings, 118–124, 2016 ISBN: 978-3-88355-414-3
[9] Neugebauer R. , Kräusel V., Graf A.: *Process Chains for Fibre Metal Laminates*. Adv. Mater. Res. 1018:285–292, 2014, doi: 10.4028/www.scientific.net/AMR.1018.285
[10] Ullmann F., Hardt W., Zhmud V.: *Machine Learning Algorithms for Impact Localization on Formed Piezo Metal Composites*. In: 2017 International Siberian Conference on Control and Communications, 2017, doi: 10.1109/SIBCON.2017.799855

# EVALUATION OF RELEVANT PROCESS PARAMETERS FOR DIRECTLY CURED THERMOSET COMPOSITES ON METAL PARTS

**Robert Thomas[1*], Simon Wehler[1], Sören Handtke[1], Wilhelm Großmann[1], Fabian Fischer[1]**

[1]Volkswagen AG – research group – materials and manufacturing processes

**ABSTRACT:** By combining metal structures locally with fibre reinforced plastics, the mechanical performance of the component can be improved by adding a minimum of weight. Still composite manufacturing techniques have deficits in terms of their productivity referring to a high volume car market (cycle time < 50 seconds) and manufacturing costs. This paper focusses the impact of the reduction of cycle time and moulding pressure on the mechanical performance of unidirectional glass fibre reinforced epoxy prepregs and the adhesion of these composites on metallic structures. At first, the reactivity of an epoxy matrix material will be characterized and this data will be used to set up a kinetics model to determine the degree of cure for user-defined temperature profiles. Following the influence of press time and manufacturing pressure on the performance of the composite laminate and the composite-metal joint will be examined and compared with progress of degree of cure. The gathered information regarding the epoxy prepreg material can be used to define the operating point for following manufacturing trials and optimize the cycle time of the manufacturing process. By reducing the moulding pressure, the investment costs of the press technique can be reduced and the manufacturing process can be more efficient.

**KEYWORDS:** co-cured, metal-composite hybrid technology, thermoset prepregs, bonding strength, adhesion built-up

## 1 INTRODUCTION

The usage of battery electric vehicles in road traffic is continuously increasing [1], therefore also the Volkswagen Group is extending their product portfolio of electric cars. A relevant disadvantage of nowadays electric cars regarding to combustion vehicles is the relatively low range, which is compensated by integrating a large number of battery cells and thus increasing the overall weight of the car. In case of a car accident, this increase of weight leads to higher energies which have to be absorbed by the car structure. Beside the safety of the passenger, a high priority is seen in the protection of the battery. The common metal design of these highly loaded body-in-white car structures reaches their limits. An innovative solution is seen in combining metal parts locally with fibre reinforced plastics to increase the mechanical performance (i.e. stiffness, strength, energy absorption) by adding a minimum of weight. These metal-composite-hybrid parts can be joined conventionally in the body-in-white manufacturing process by using state-of-the-art technologies like welding, gluing or riveting.

The Volkswagen Research Group is developing a manufacturing process, where the fibre reinforcement (pre-impregnated, unidirectional glass-fibre-reinforced fabric with epoxy matrix) is directly pressed and cured onto metallic structures. This manufacturing process uses down-sized press technique to reduce the pressing force and therefore the machinery investment. Furthermore a high volume car application with a car cycle time < 60 seconds is focused, so a curing time of the thermoset material < 30 seconds is mandatory to ensure sufficient transfer- and handling time. The challenge is to use the matrix material of the reinforcement to directly bond on the metallic surface and therefore to forgo elaborated pre-treatments or an additional gluing processes. The bonding on a dual-phase steel with zinc-coating (DP980+Z100), contaminated with deep-drawing oil (0,9 g/m²) was examined.

This review is structured into the following major subjects. Firstly, the curing of the chosen thermoset matrix material will be evaluated and a kinetic model will be established. Following, the influence of press time an pressure on the quality of the composite laminate will be examined. These results will then be used to evaluate the influence of these process parameters on the bonding strength of directly pressed prepreg mate-

rial with metallic structures. Furthermore, the adhesion built-up during the curing on the metal surface will be characterized.
The impact of the temperature profile, pressure and press time on the quality of composite laminates is widely investigated for the autoclave manufacturing process of aerospace use-cases. Apart from a not sufficiently cured material, the development of voids in the composite is the main defect as a result of an inappropriate curing cycle which reduces the mechanical performances. The void content is directly linked to the applied pressure on the composite. A reduction of curing pressure from 0,7 MPa to 0,1 MPa reduces the interlaminar shear strength by 23 % and the flexural strength by 22 %, the flexural modulus decreases by 18 % [2-4]. Also an increased humidity of the prepreg or residual solvent in the matrix material can lead to voids in the cured laminate [5,6]. Still the autoclave technology is a vacuum assisted process, which favours a minimal void content. The process parameter of press-formed carbon fibre reinforced specimen made out of pre-impregnated material (so called prepreg) has been investigated. Also the bonding strength of directly cured prepreg material on zinc-coated metallic structures was examined. It was shown that appropriate material quality can be achieved with a pressure of 0,3 MPa and a press time of 90 s. The bonding strength was characterized with 18,1 MPa. [7] The bonding strength of carbon fibre prepreg directly cured on unalloyed heat treated steel was examined by using double lap shear specimen. Values of 25 MPa were achieved. [8]. The adhesion of metal-composite-hybrid specimen, manufactured by autoclave was evaluated by single lap shear characterization. It was shown that a higher pressure increases the bonding strength from 8 MPa to 10 MPa which can also be achieved by a higher surface roughness. [9]. The adhesion of specimen, which were directly manufactured by resin transfer moulding process on the metallic structure was characterized with 14,5 MPa [10]. No relevant literature regarding the adhesion built-up of epoxy prepregs directly cured on metal structures were found. Though the interlaminar shear strength and compression strength of an epoxy prepreg was characterized in dependence of the degree of cure. It was shown that at a cure of 78 %, the mechanical properties are comparable to completely cured laminates. [11]
In contrary to the presented literature, this presence work focusses shorter curing times and also lower manufacturing pressures which is unique.

## 2 EXPERIMENTAL

At first, the reactivity of the epoxy matrix material was examined by differential scanning calorimetry (DSC) according to DIN EN ISO 11357. The specimens (10 mg – 15 mg) were heated up with various heating rates and the exothermal reaction of the thermoset material was recorded. These data was then applied to establish a kinetics model to predict the degree of cure for various temperature routes for following trials. For that, a Netzsch DSC 204 F1 Phoenix in combination with the software Netzsch Kinetics Neo was used. The focused manufacturing process requires reduced pressure and press time. Thus, a parametric study was performed to investigate in the dependency of these process parameters regarding to the quality (micro cut) and mechanical performance (interlaminar shear strength – DIN EN ISO 14130 and 3-point-bending – DIN EN ISO 14125) of the pressed and cured laminates. These plates were manufactured on a heated plate to plate tool mounted in a parallel guidance. The stroke was performed by a hydraulic cylinder. The prepreg stack with the associated sealing was placed on a thin transfer foil for quick transferring into and out of the press area.
A further demand is a sufficient adhesion of the prepreg material directly cured on metallic structures. The bonding strength of metal – composite-joints was characterized by single lap shear-specimen (according to DIN EN 1465). In these tests, the influence of pressure and press time on the shear strength was determined. A heated pneumatic press was used for the manufacturing. At first, the metal sheet was placed magnetically in the mould to heat up to the specified temperature. The prepreg material was then placed in a separate jig and inserted into the mould. The first layer of prepreg regarding to the metal sheet was aligned as 0°. The layup of the composite was adjusted to a bending stiffness, which was similar to the metallic partner. The jig allowed an exact positioning of the composite and also a demoulding of the specimen within short time and without inadvertent loads. Following the hybrid plates were heated up to 180°C for 35 min to simulate the e-coat-drying of nowadays body-in-white manufacturing processes and to take into account the resulting thermal stress due to different thermal expansion coefficients of the joining members. The plates finally were cut by water-jet to the specific single lap shear test geometry and tested by using a Zwick 050 tensile machine.

Another issue focused the adhesion build-up during the curing process. To characterize this effect, test-setups for two load cases (single lap shear and perpendicular) were developed (see Fig. 1 and Fig. 2).

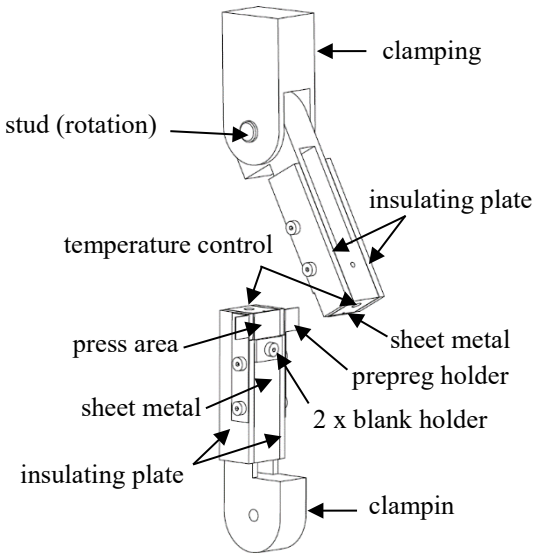


***Fig. 1** test device for characterizing the shear strength of metal-composite-hybrid joints during the curing*

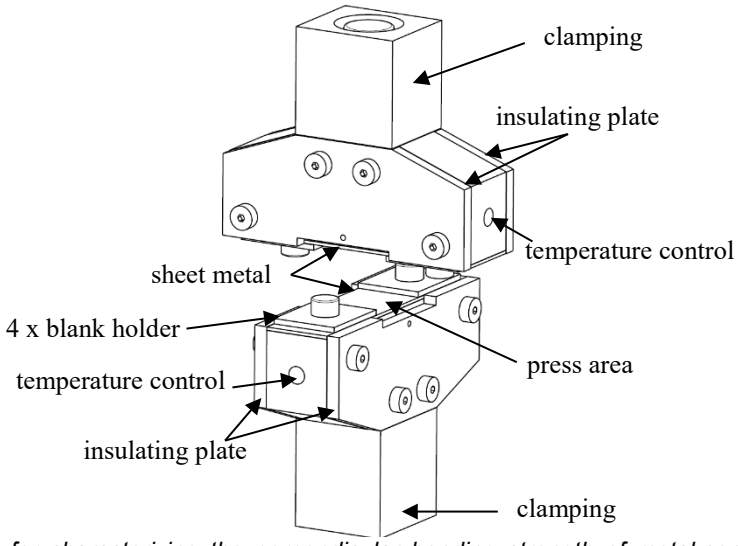


***Fig. 2** test device for characterizing the perpendicular bonding strength of metal-composite-hybrid joints during the curing*

With these temperature controlled devices, prepreg material was directly pressed and cured between two braced sheet metals. The prepreg was positioned in front of the press area. By using spacer lateral to the composite, a heating of the material and thus a premature curing was prevented. While closing of the device, the material was then transferred to the press area and a defined pressure was applied to cure the prepreg and enable an adhesion between the specimens. Subsequently the bonding was tested after defined time steps. The temperature of the composite in the press area was logged to later on calculate the degree of cure depending on the press time. These trials were performed on a Zwick Z050 testing machine. A simplified test sequence of the perpendicular test setup is shown in Fig. 3.

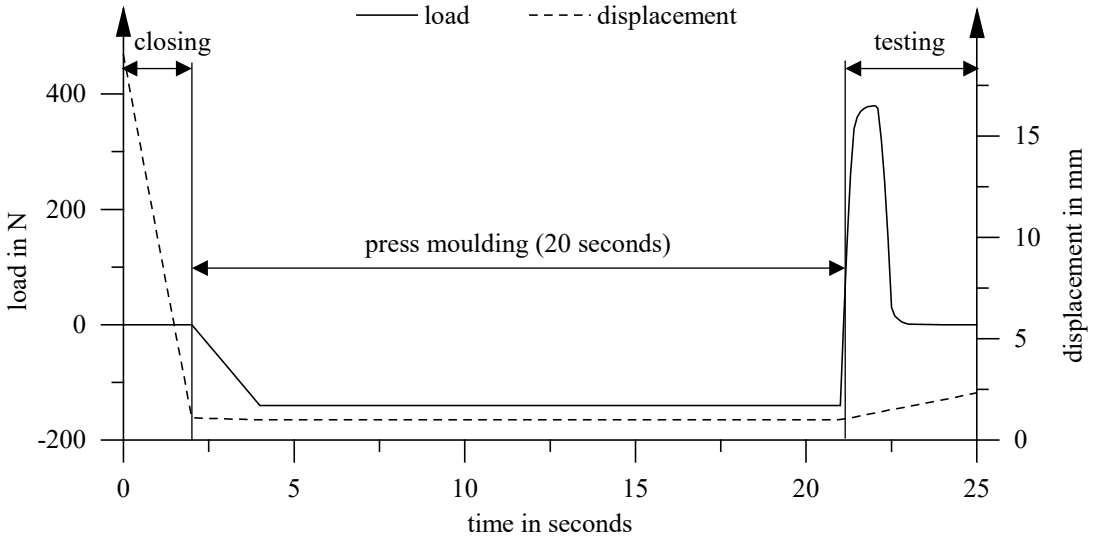


***Fig. 3*** *simplified test sequence of the perpendicular test setup*

# 3 RESULTS AND DISCUSSION

## 3.1 VARIOTHERMAL DSC-STUDY AND DETERMINATION OF KINETICS MODEL

The results of the variothermal DSC-trials with the five different heating rates are shown in Fig. 4. Five experiments for each heating rate were run and a mean value graph was calculated.

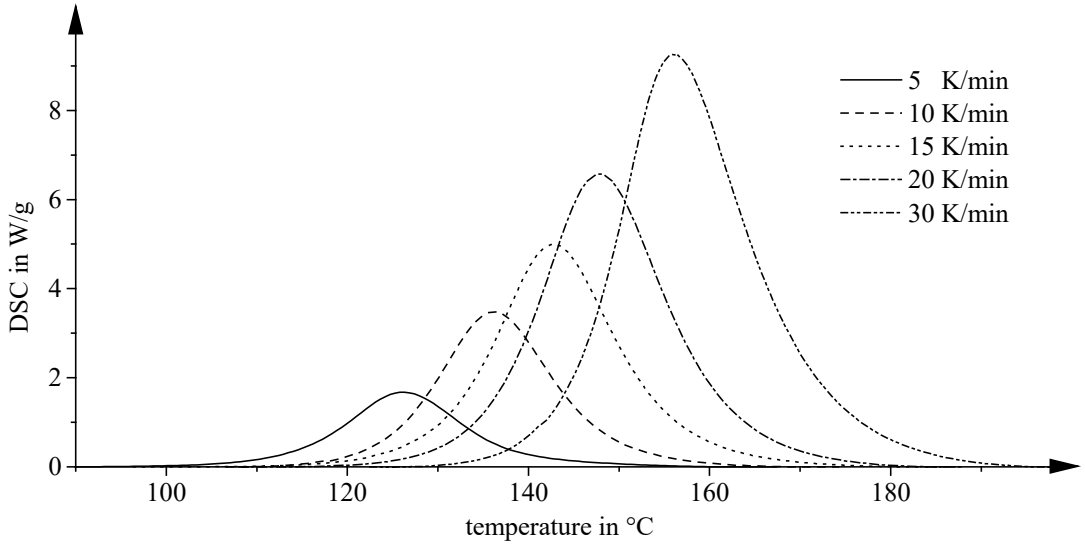


***Fig. 4*** *Results of the variothermal DSC study for five different heating rates*

The starting point of the reaction swifts to higher temperatures with increasing heating rates. Also the curing speed of the matrix material increases. These effects were expected and extensively described in literature [12,13]. Below 90°C a curing of the material has not been observed. This data was then used to establish the kinetics model and to calculate the degree of cure for various user defined temperature curves.

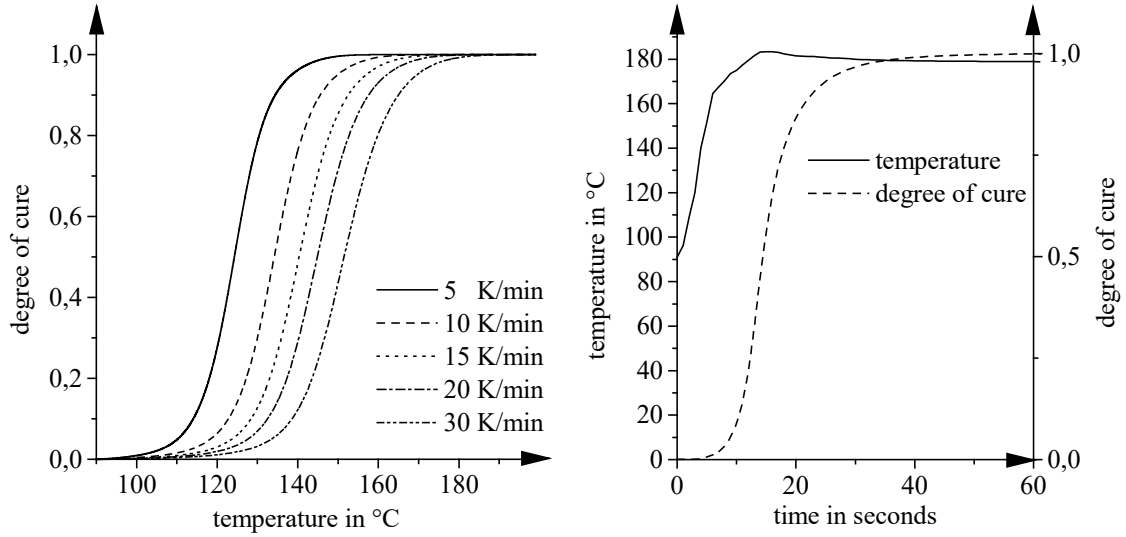


***Fig. 5*** *Degree of cure for defined temperature profiles; left: variothermal DSC-trials, right: temperature of press moulding experiment*

The degree of cure for the variothermal DSC-tests is shown on the left side. The curing speed increases with enhanced heating rates. This course of the degree of cure is calculated by Netzsch Kinetics Neo, but could also be directly calculated [14]. The graph on the right side shows a realistic temperature profile of a prepreg material during the press process and the resultant profile of the degree of cure. The mould temperature was adjusted to 180°C, this curing temperature was defined through preceded studies. The temperature of the material was rapidly rising over 180°C (exothermal reaction) and then converging at 180°C. Equivalent also the degree of cure increases and achieves 100% within 40 seconds. The kinetics model is based on experimental data, which was determined on pure matrix material. It is also applicable for fibre reinforced structures, but it must be assured that the temperature profile of the pressed composite is comparable to pure matrix. This is true for thin composite structures and constant moulding temperatures during the press process. The focused composite reinforcement of metal parts will have reduced thicknesses of 1 mm to 2 mm, a constant moulding temperature is guaranteed by using heated steel tooling with a high thermal capacity.

### 3.2 INFLUENCE OF PRESS TIME AND PRESSURE ON THE LAMINATE QUALITY OF MANUFACTURED COMPOSITE SPECIMEN

Composite plates were pressed with selected process parameters to evaluate their influence on the mechanical properties. From 0,04 MPa the manufacturing pressure was gradually increased up to 0,3 MPa, additionally 0,6 MPa and 1 MPa was adjusted to take into account common moulding pressures of state-of-the-art manufacturing processes. Based on the DSC-results, the press times of 20 s, 30 s and 40 s was chosen. Plates with press times below 20 seconds couldn´t be manufactured due to insufficient curing. A selection of micro cut sections of these trials are shown in Fig. 6.

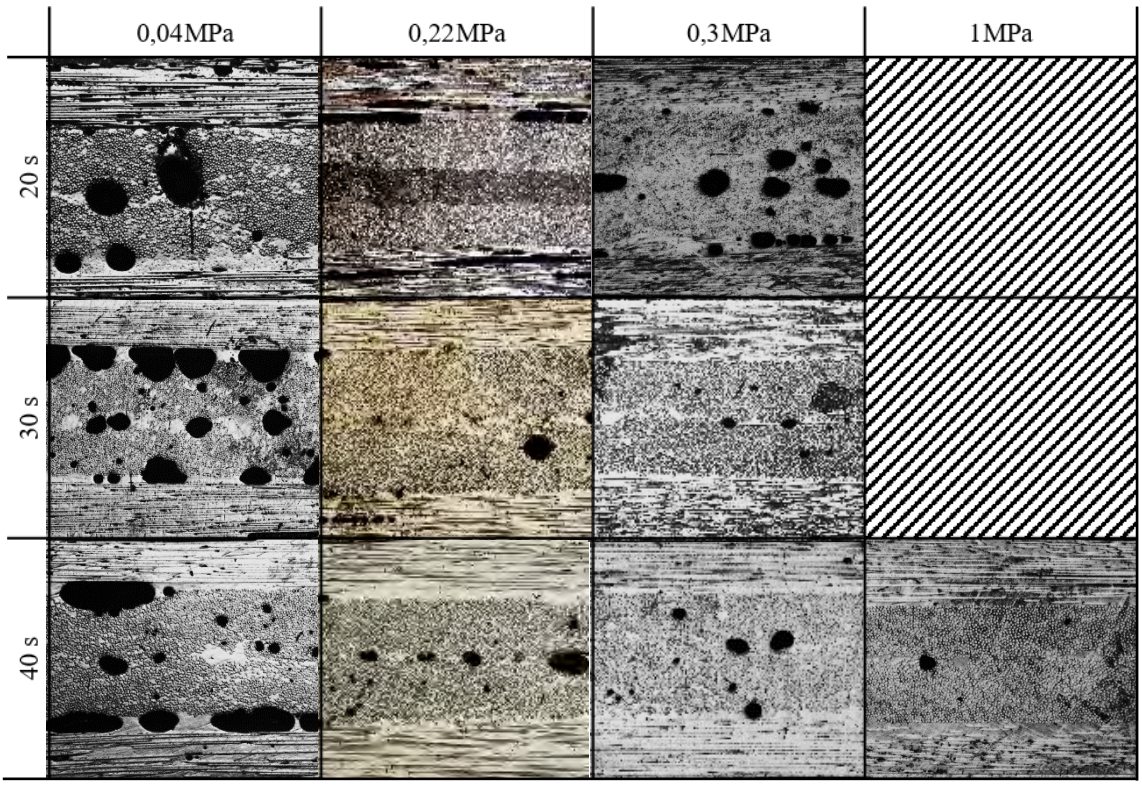


***Fig. 6*** *Micro cut section of plates manufactured with different process parameters*

Specimen, manufactured with a press time of 20 seconds show an increased proportion of voids and porosities, partially no bonding between two layers was built up. These defects occur because of the insufficient degree of cure and therefore slightly cohesion while and after demoulding. A difference between 30 seconds and 40 seconds cannot be identified. A moulding pressure < 1,8 MPa also leads to an enhanced degree of voids in the laminate, a further increase enhances the laminate quality insignificantly. The results of the interlaminar shear test and 3-point-bending test are shown in Fig. 7 and Fig. 8.

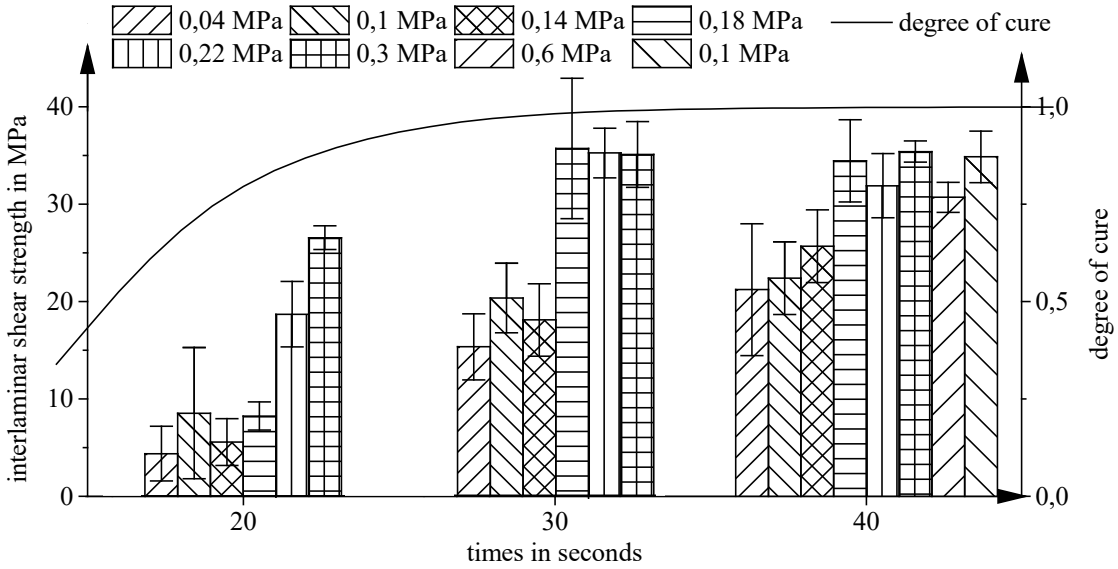


***Fig. 7*** *Results of parametric study regarding to the influence of press time and pressure on the interlaminar strength of cured composite specimen according to DIN EN ISO 14130*

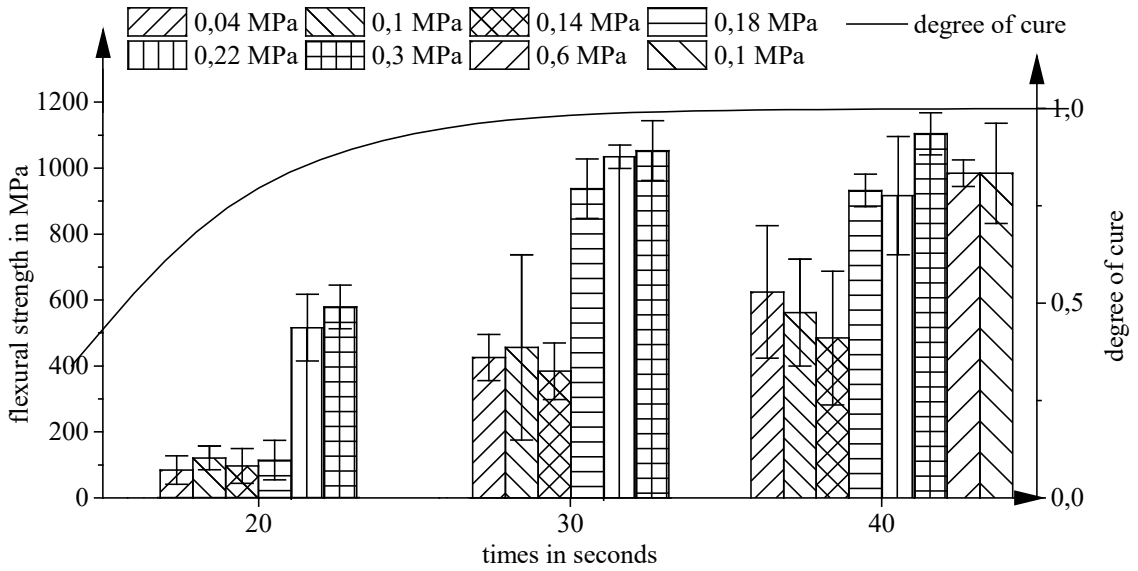


***Fig. 8*** *Results of parametric study regarding to the influence of press time and pressure on the flexural strength of cured composite specimen according to DIN EN ISO 14125*

The diagram shows the degree of cure of the directly demoulded specimens. Because of the residual heat of this material after demoulding, they post-cure completely through the cooling process – so the tested specimen are completely cured. Both studies show a similar results. The interlaminar shear strength and the flexural strength of the specimen, pressed with 20 seconds show insufficient characteristics compared with the results at 30 seconds and 40 seconds. A significant difference between 30 seconds and 40 seconds couldn´t be determined. This is explicable by the nearly fully cured matrix material after 30 seconds. By applying a pressure higher than 0,18 MPa, mechanical properties were characterized, which are comparable with plates pressed with 1 MPa. For following trials, a preferential pressure of 0,22 MPa was defined.

### 3.3 INFLUENCE OF PRESS TIME AND PRESSURE ON THE BONDING STRENGTH OF DIRECTLY CURED PREPREG ONTO STEEL

Single lap shear specimen were manufactured by varying pressure (0,14 MPa, 0,22 MPa and 0,3 MPa) and press time (20 seconds, 40 seconds, 60 seconds). These results were compared with specimen, which were pressed with a higher pressure of 1 MPa and a press time of 60 seconds to illustrate the influence of reduce pressure and time. Furthermore, the temperature profile of the composite was logged and these data was used to plot the degree of cure when demoulded and the dependence regarding to the bonding strength. After manufacturing and demoulding, the specimen were heated up according to the e-coat-drying process (35 min @ 180°C) and cut by water jet machine. The results of the characterization are shown in Fig. 9.

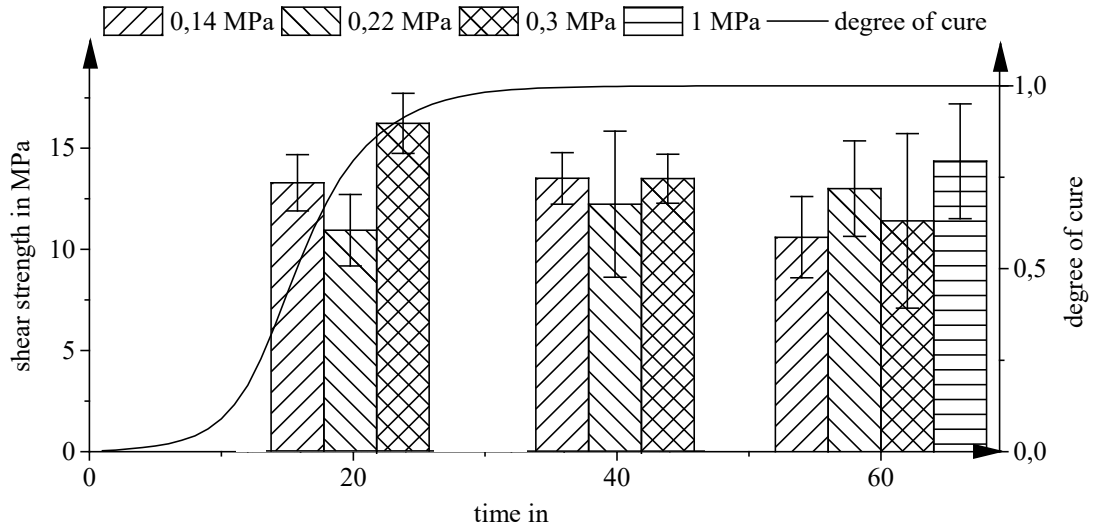


***Fig. 9*** *:Results of parametric study regarding to the influence of press time and pressure on the bonding strength of cured single lap shear specimen according to DIN EN 1465*

The parametric study shows no dependence of press time or pressure on the bonding strength of the directly cured metal-composite hybrid joint. Eight specimen were used for every measurement series, an adhesive failure between steel and composite was investigated. Even though the standard deviation of the results are certainly higher, they are in the scatter range of the experimental data. Therefore no relation between the specified process parameters and the bonding strength is considered. When completing the press process after 20 seconds, the material has a degree of cure of around 75 %. Apparently this is sufficient to build up an adequate adhesion, the further cure up to 100 % occurs without pressure during the cooling of the specimen outside of the press. Specimen with a press time below 20 seconds couldn´t be manufactured due to an insufficient curing of the prepreg material.

### 3.4 CHARACTERIZATION OF THE ADHESION BUILT-UP OF DIRECTLY CURED THERMOSET PREPREG MATERIAL ONTO STEEL

The influence of press time and pressure on the quality of the laminate and the shear strength of composite-steel joints was presented. For an improved understanding of the bonding mechanism of the thermoset matrix material on the selected steel, the adhesion built-up while curing was characterized by using the introduced test devices. The results of the single lap shear experiments are shown in Fig. 10 and Fig. 11.

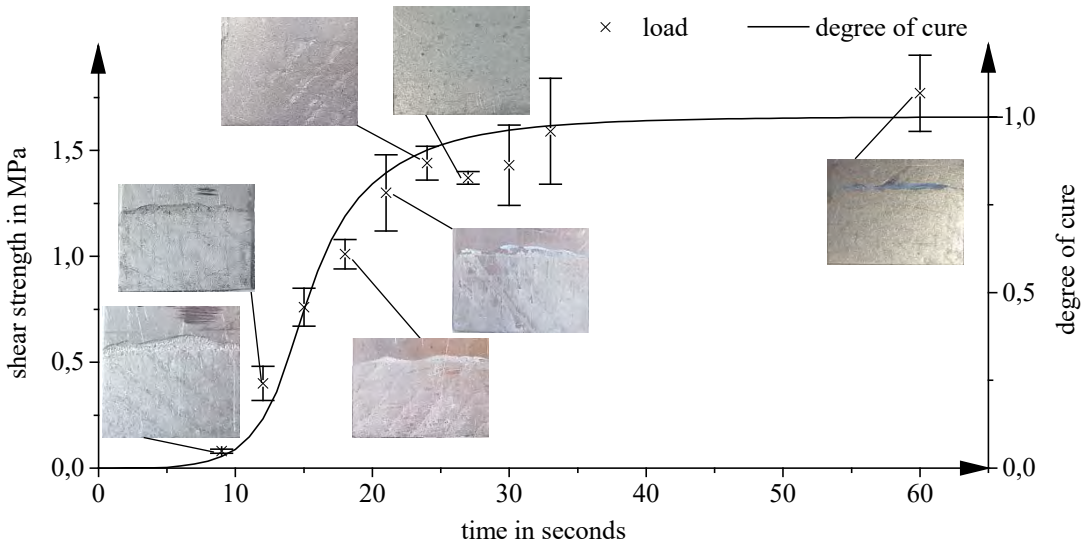


***Fig. 10*** *Characterization of the adhesion built-up of a directly cured prepreg on metal depending on the degree of cure characterized by using a test setup with a single lap shear load case on the bonding joint*

The diagram shows the development of the adhesion between a thermoset prepreg and a zinced and oiled steel for a perpendicular load case on the bonding joint depending on the degree of cure. The temperature of the press area was set to 180°C, the curing pressure was set to 0,22 MPa according to the results of the laminate characterization. The degree of cure was calculated with the logged temperature profile of the composite by using Netzsch Kinetics Neo. A first adhesion is characterized after 9 seconds, then the single lap shear strength is continuously increasing equivalent to the progress of degree of cure. After 21 seconds, the matrix material has achieved a degree of cure of 84 %, the bonding strength was characterized with 1,3 MPa. Subsequently with increasing curing time, the adhesion just slightly increases up to 1,59 MPa (33 seconds). After 60 seconds a shear strength of 1,77 MPa was identified. The fracture pattern of specimen cured for < 19 seconds have a major substrate failure of the composite. The metallic joining member showed matrix residues in the joint area. With an increasing press time, the proportion of adhesive failure grows and finally replaces the substrate failure.

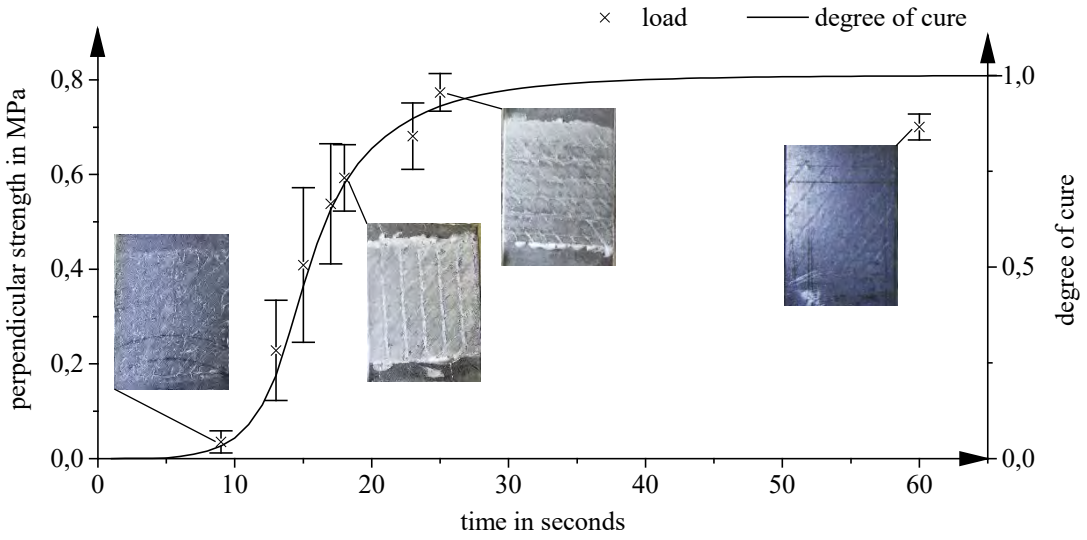


***Fig. 11*** *Characterization of the adhesion built-up of a directly cured prepreg on metal depending on the degree of cure characterized by using a test setup with a perpendicular load case on the bonding joint*

The boundary condition of this characterization is comparable to the shear load case. A minimal adhesion was verified after 9 seconds, where the degree of cure was calculated with 3 %. The fracture pattern shows that the matrix material is completely fluid. With an increase of press time, subsequently also the perpendicular strength increases. After 25 seconds a maximum of 0,77 MPa was characterized, the matrix material had a degree of cure of 92 %. During the curing, also the fracture patterns shifts from fluid (9 seconds) over substrate failure of the composite between fibre and matrix (18 seconds) to adhesive failure (> 25 seconds). It is also shown, that the increase of bonding strength is directly linked to the increase of degree of cure. A press time of 60 seconds (degree of cure of 100 %) showed a complete adhesive failure, a strength of 0,7 MPa was characterized.

## 4 CONCLUSIONS

This work examined the influence of press time and pressure on the laminate quality of epoxy based glass fibre reinforced materials and the adhesion of these materials directly cured on zinced and oiled steel sheets. With a differential scanning calorimetry, the epoxy matrix material and its curing abilities were at first characterized. The results were used to establish a kinetics model and to determine the degree of cure for various user defined temperature profiles. By using a logged temperature profile of a press trial at 180°C mould temperature it was shown, that after 20 seconds a degree of cure of 84 % and after 27 seconds a degree of cure of 95% was established. Flat composite sheets were pressed with different pressures and press times at 180°C mould temperature and tested via 3-point-bending, interlaminar sheer strength and micro cut. A pressure of 0,22 MPa and a press time of 30 seconds are sufficient to manufacture specimen with equivalent properties compared to specimen with higher pressure (1 MPa) and increased press time (40 seconds). Also the influence of press time and pressure on the bonding strength of cured metal-composite joints was evaluated by single lap shear test according to DIN EN 1465. No dependency of these two parameters on the adhesion in the contemplated area was observed. The shear strength was characterised with 11 MPa to 16 MPa. Furthermore two test devices were design and put into operation to characterize the adhesion built-up of directly cured thermoset composites on metal sheets during the press process. It was shown, that the adhesion built-up is directly linked to the progress of the degree of cure. Also the fracture pattern shifts from fluid over substrate failure of the composite to adhesive failure. These information about the material and its process parameters will be used to optimize further manufacturing trials of metal-composite hybrid structures regarding manufacturing speed and mechanical performance.

## 5 ACKNOWLEDGEMENT

We would like to thank the Bundesministerium für Bildung und Forschung (BMBF) for supporting the research project “PROLEI”, which is part of the BMBF lighthouse project FOREL (Forschungs-und Technologiezentrum für ressourceneffiziente Leichtbaustrukturen der Elektromobilität)

## REFERENCES


[1] Kraftfahrtbundesamt*: www.kba.de* (last checked: 30.01.2018).

[2] Olivier P., Cottu J. P., Ferret B.: *Effects of cure cycle pressure and voids on some mechanical properties of carbon/epoxy laminates*. Composites 26, 509-515, 1995.

[3] Liu L., Zhang B., Wu Z., Wang D.: *Effects of Cure Pressure Induced Voids on the Mechanical Strength of Carbon/Epoxy Laminates*. Journal of Material, Science and Technology, Vol. 21 No.1, 2005.

[4] Liu L., Zhang B., Wang D., Wu Z.: *Effects of cure cycles on void content and mechanical properties of composite laminates*. Composite Structure, Vol. 73, 303-309, 2005.

[5] Hayes B.; Seferis J.; Edwards R.: *Self-adhesive honey comb prepreg systems for secondary structural application.* Polymer composites, Vol. 19, 54-64, pages: 54 – 64, 1998.

[6] Grunenfelder L., Nutt S.: *Void formation in composite prepregs – Effects of dissolved moisture*. Journal of Composites, Science and Technology, Vol. 70, 2304-2309, 2010.

[7] Lauter C.: *Entwicklung und Herstellung von Hybridbauteilen aus Metallen und Faserverbundkunststoffen für den Leichtbau im Automobil*. dissertation, Fakultät für Maschinenbau, Universität Paderborn, 2014.

[8] Kim H., Park S., Lee D.: *Smart cure cycle with cooling and reheating for co-cure bonded steel/carbon epoxy composite hybrid structures for reducing thermal residual stress*. Composites Part A, Vol. 37, 1708-1721, 2006.

[9] Shin K., Lee J.: *Effects of manufacturing parameters on the tensile load bearing capacity of a co-cured single lap joint*. In: 13th international conference of composite materials, ID 1515, 1999.

[10] Wang Z., Bobbert M., Dammann C.: *Influences of interface and surface pretreatment on the mechanical properties of metal-CFRP hybrid structures manufactured by resin transfer moulding*. In: International Journal of Automotive Composites, Vol. 2, Nos. 3/4, 2016.

[11] Vora K.: *Mechanical properties evolution during cure for out-of-autoclave carbon-epoxy prepregs*. thesis, department of mechanical engineering, Wichita state university USA, 2012

[12] Fava R.: *Differential scanning calorimetry of epoxy resins. Journal of Polymer*, Vol. 9, 137-151, 1968

[13] Lee W., Loos A., Springer G.: *Heat of Reaction, Degree of Cure, and Viscosity of Hercules 3501-6 Resin*. Journal of Composite Materials, Vol. 16, 510-520, 1982

[14] Mutlur S.: *Thermal Analysis of Composites Using DSC*. In: Advanced Topics in characterization of composites, 11-33, 2004

# ALCUNNECT - A NEW BIMETAL COMBINATION OF ALUMINIUM AND COPPER

**Daniel Schindler[1*], Uwe Dreißigacker[1], Dr. Joachim Ganz[1], Helena Tribus[1]**

[1] Process Development Solutions, DODUCO Solutions GmbH, Pforzheim, Germany

…

**ABSTRACT:** AlCunnect is a new bimetal combination of aluminium and copper for various electrical and thermal applications.

AlCunnect especially is suitable as interface material between aluminium- and copper-based electrical conductors. By the substitution of copper through aluminium within the cable harness the overall weight is reduced by 50 % and comparable electrical conductivity. The aluminium alloy has a level of purity of 99.5 %. The copper alloy has an electrical conductivity of min. 58 MS/m. With the currently available combinations…

- Overlap-single
- Overlap-multiple
- Inlay
- Overlay

several applications are possible.

As production process the combination of roll cladding and additional heat treatment to create a mechanically stable intermetallic compound will be described.

An optional corrosion protection and its structure will be described. The results of its qualification where shown.

**KEYWORDS:** aluminium, copper, aluminium-copper, roll-bonded, corrosion protection, intermetallic compounds; diffusion; corrosion protection,

## 1 INTRODUCTION

Current trends in the market, such as light weight construction in automotive applications or the rising cooling requirements in power electronics are requesting the use of Aluminium in combination with Copper. DODUCO produces Copper clad bands with bondable Al-strips as an inlay for more than twenty years in a volume of about 250 metric tons per year. In the following text the material properties, the new manufacturing process, the test procedures and the final corrosion protection of the new material combination AlCunnect will be described.

## 2 ALCUNNECT - TYPES

Based on the know-how of the above mentioned cladding process the manufacturing of the four materials referred to as “overlap-single”, overlap-multiple, “overlay” and “inlay” type has been recently developed. The products and the typical achievable dimensions are listed in Tab. 1-3.

The overlap-single and overlap-multiple type is a combination of the two materials, Al and Cu, in a side-by-side configuration, as shown in Tab. 1. The maximum strip width, which can be manufactured, is 120 mm with a thickness up to 2 mm. The width of the overlapping area between Al and Cu is about 5 mm. The proportion of the Al to Cu band size can be adjusted to product needs and the final band can be delivered as a coil, e.g. for further stamping or coating processes. The material selection leads to Al 99.5 (EN AW 1050A) because of its availability on the market, electrical and mechanical properties, and the capability of electroplating this material. The pure Cu-PHC (CW020A) was selected because of its electrical and mechanical properties.

The Inlay type is an aluminium clad band with a copper inlay for several applications with the advantage to apply copper only on places where it is needed.

* Corresponding author: DODUCO Solutions GmbH, Im Altgefäll 12, D-75181 Pforzheim,
Phone: +49 (0) 7231 602-256, e-mail: dschindler@doduco.net

In the case of the overlay configuration, Al and Cu are connected across the total contact surface as shown in Tab. 3. The resulting matched material combination can have dimensions up to 200 mm on each side and 10 mm in thickness. The proportion of the Al to Cu thickness can be adjusted to product needs to a large extent.

***Table 1:*** *Typical dimensions of AlCunnect*

| Type | Overlap-single | Overlap-multiple |
|---|---|---|
| Picture | 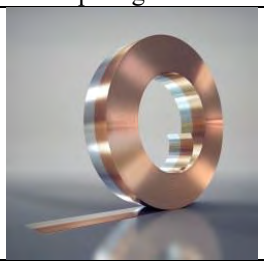 | |
| Total width | Up to 120 mm | Up to 120 mm |
| Thickness | Up to 2 mm | Up to 2 mm |
| Width of overlap | Approx. 5 mm | Approx. 5 mm |
| Width ratio Al/Cu | Different combinations possible | Different combinations possible |

***Table 2:*** *Typical dimensions of AlCunnect*

| Type | Inlay |
|---|---|
| Picture | 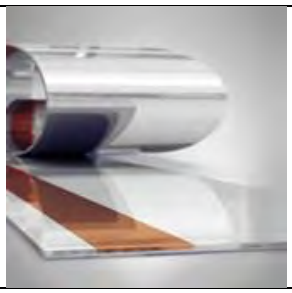 |
| Total width | Up to 120 mm |
| Total thickness | Up to 2 mm |
| Width of inlay | Min. 5 mm |
| Thickness of copper inlay | Min. 20 µm, max. approx. 25 % of total thickness |

***Table 3:*** *Typical dimensions of AlCunnect*

| Type | Overlay |
|---|---|
| Picture | 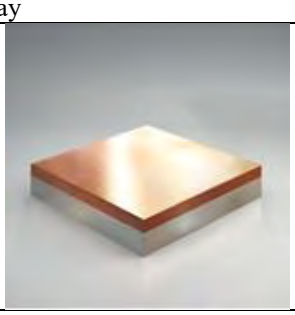 |
| Total width | Up to 200 mm |
| Total thickness | Up to approx. 12 mm |
| Thickness ration Al/Cu | Different combinations possible |

## 3 MATERIAL PROPERTIES

Copper is well known for its very high conductivity. But its price has been increasing throughout the years. Aluminium on the other hand is lightweight and cheap compared to Cu. Finally Al has the fourth highest electrical and thermal conductivity. The comparison of the materials properties are summarized in Tab. 4.

***Table 4:*** *Data of the Materials*

| | **Data of the Materials** | |
|---|---|---|
| | ***Aluminum (Al)*** | ***Copper (Cu)*** |
| Price (USD/t) on Jan. 17th 2018 [7] | 2.187 | 7.047 |
| Electrical conductivity | 37.7 MS/m | 58 MS/m ≙ 100 % IACS[a] |
| Density (g/cm³) | 2.7 | 8.92 |
| Thermal conductivity (W/mK) | 237 | 401 |
| Melting Point (°C) | 660 | 1084 |
| Modulus of Elasticity (GPa) | 65 | 115 |
| Linear Expansion Coeff. (10-6/K) | 23.6 | 16.5 |
| Standard | EN AW-1050A (Al99.5) | Cu-PHC (CW020A) |
| Chemical Composition | Acc. DIN EN 573-3 | Acc. DIN EN 13599 |
| Mechanical Properties | Acc. DIN EN 485-2 | Acc. DIN EN 13599 |

[a] IACS: International Annealed Copper Standard

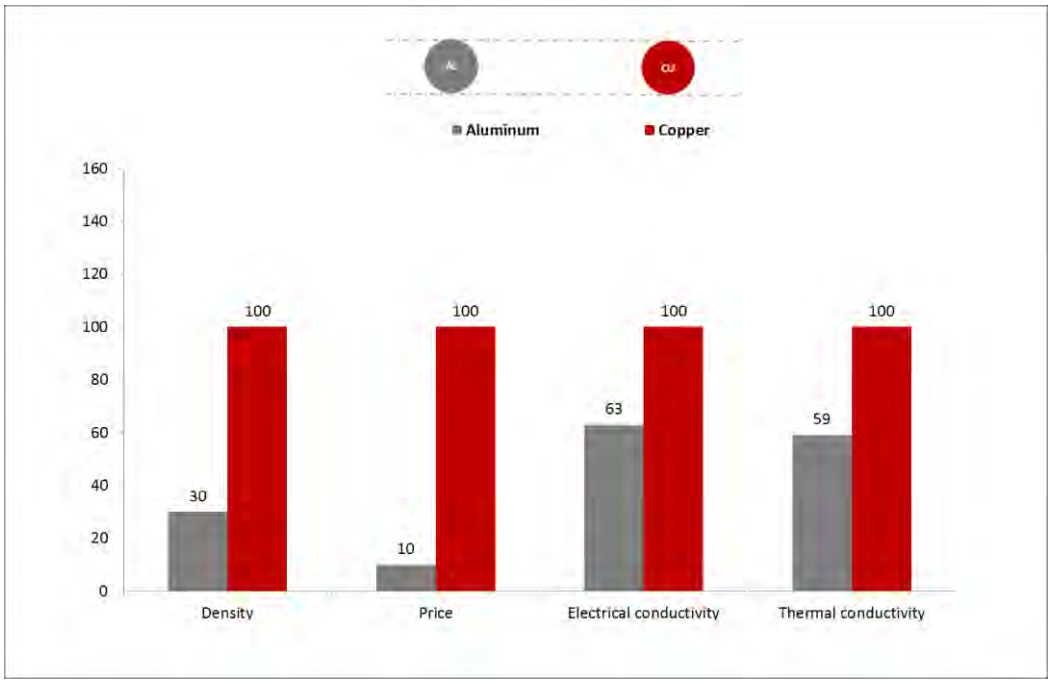


***Fig. 1*** *Comparison for same cross section*

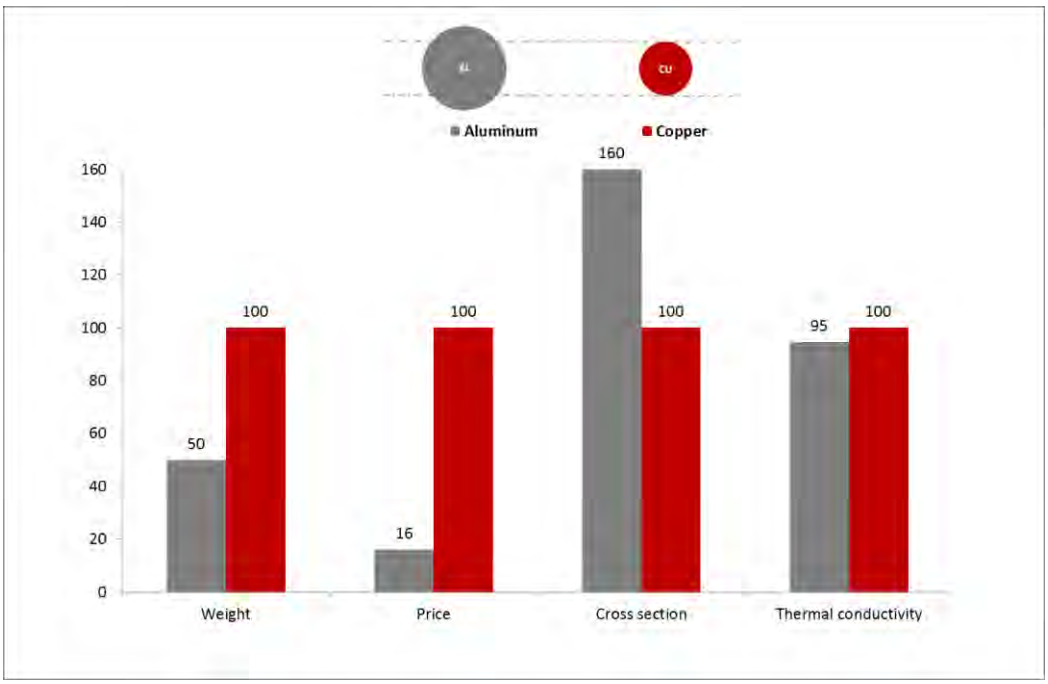


***Fig. 2*** *Comparison for same electrical conductivity*

In Fig. 1 the parameters density, price and electrical and thermal conductivity for Cu and Al are compared under the precondition of equal cross sections of the conductor. Fig. 2 shows the same for the parameters weight, price, cross section and thermal conductivity under the precondition of equal electrical conductivity.

## 4 TECHNICAL CHALLENGES

The technical challenges, which had to be solved during the development of the manufacturing process, are caused by the different properties of five potential equilibrium phases in the Copper-Aluminium system [1 - 5], which can arise during annealing. They exhibit varying brittleness, strength and electrical resistance. In the cross section of a laser welded Cu/Al join in Fig. 3 the formation of the IMCs are visible [6]. As a result, direct welding causes reliability problems because of micro-cracking at the seam. Therefore AlCunnect uses an ultra-thin IMC layer, as shown in Fig. 4, to connect Copper and Aluminium without these negative properties.

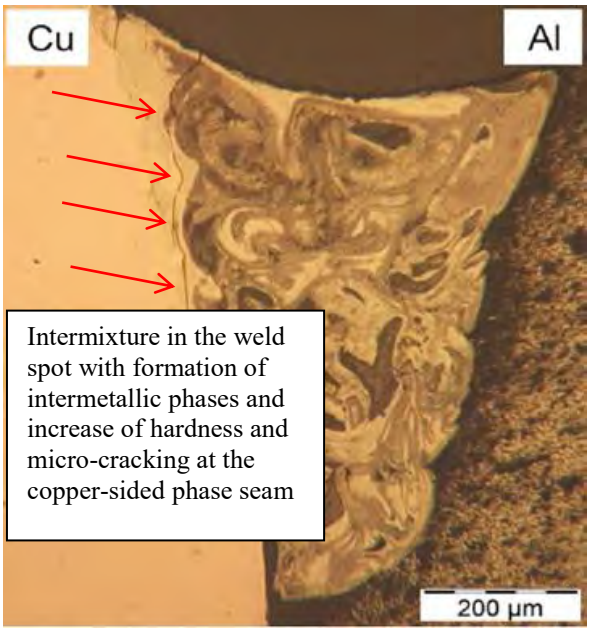


***Fig. 3*** *Cross section of laser welded Cu-Al*

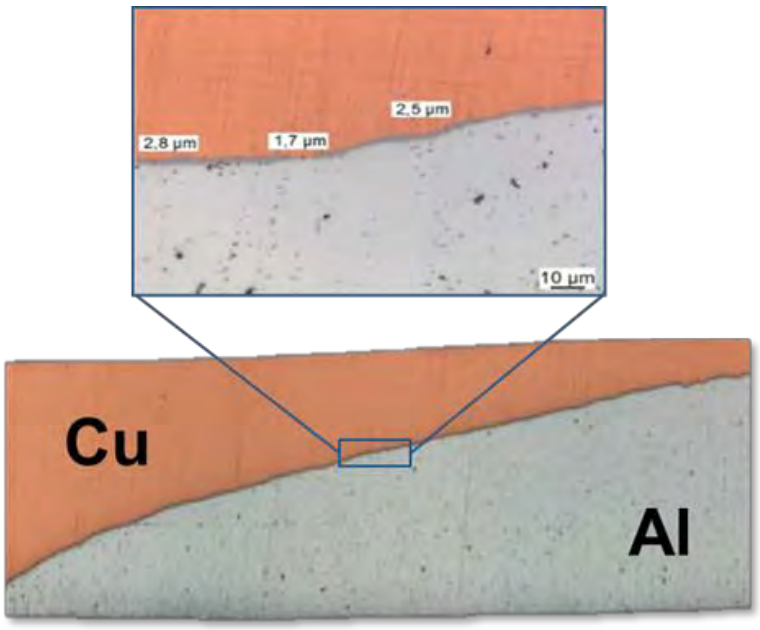


***Fig. 4*** *Cross section of AlCunnect interconnection zone*

The used cladding process is shown schematically in Fig. 5. Two bands of preconditioned material are cladded mechanically by thickness reduction of more than 50 % during one pass through the rolling mill. To achieve a long time stability of this cold welded adhesive connection after cladding a heat treatment in a continuous furnace is applied afterwards. The temperature (400 - 500 °C), the time (15 - 25 min) and the atmosphere (reducing) in the furnace have to be adjusted to create the favoured IMC in the desired thickness. A typical result is shown in the cross section in Fig. 4

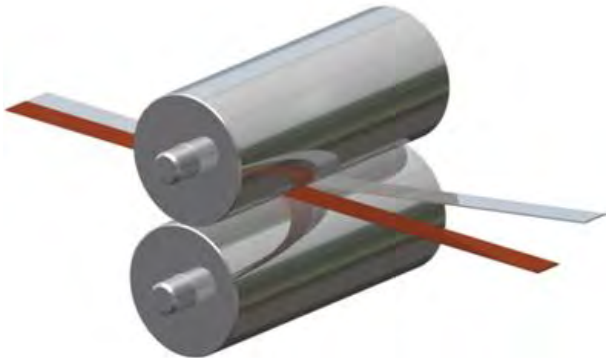

***Fig. 5*** *Cladding process (schematic)*

## 5 ALCUNNECT - PROPERTIES AND MATERIAL TESTING

The material combination AlCunnect is a very mechanically stable composite with high electrical conductivity and can be used in temperatures up to 200°C. It is able to connect the two contact worlds of Copper and Aluminium together. This opens new potentials of cost and weight reduction, especially in automotive applications.
To check the stability of the interconnection zone tensile and bending tests have been performed. During the tensile test a specimen is stretched up to breakage and the applied tensile stress is measured in relation to the elongation (Fig. 6). The visual result of the tensile test is shown in Fig. 7, which always shows cracking in the Al, due to it´s lower modulus of elasticity in comparison to Cu.
During a bending test the specimen will be stressed to the maximum compressive value at the inside of the bend and to its maximum tensile value at the outside. In Fig. 8 the result of the bending test at an angle of 90° with a radius of 1mm is shown. No cracks can be observed in the bending area, which indicates a very good connection at the Al-Cu interface.

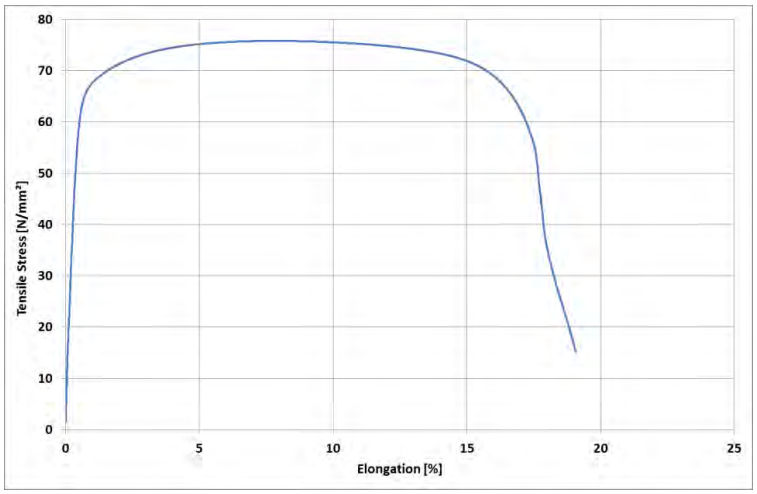


***Fig. 6*** *Diagram of tensile stress versus elongation of the specimen*

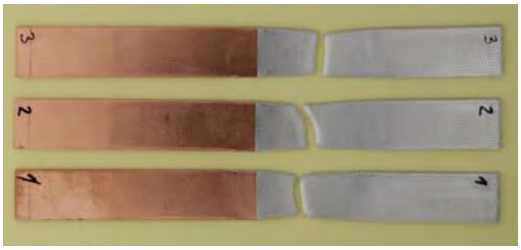

***Fig. 7*** *Specimens after tensile test (dimensions of specimen: 114 mm x 12,9 x 1,9 mm)*

***Fig. 8*** *Specimen after 90°-bending test (R = 1 mm)*

## 6 CORROSION PROTECTION

The electrochemical potential of $Cu/Cu^{2+}$ is +0.34V and for $Al/Al^{3+}$ is -1.66V. Therefore, the combination of the two materials will end up with an electrical potential difference of 2.0V. Thus, a blocking layer is needed to protect against mass transport to the phase boundary interface in the case of humidity exposure. To assure this corrosion protection for the AlCunnect composite, DODUCO developed special coating processes. The protection against environmental influences can be accomplished with an organic as well as an inorganic sealing (Fig. 9).

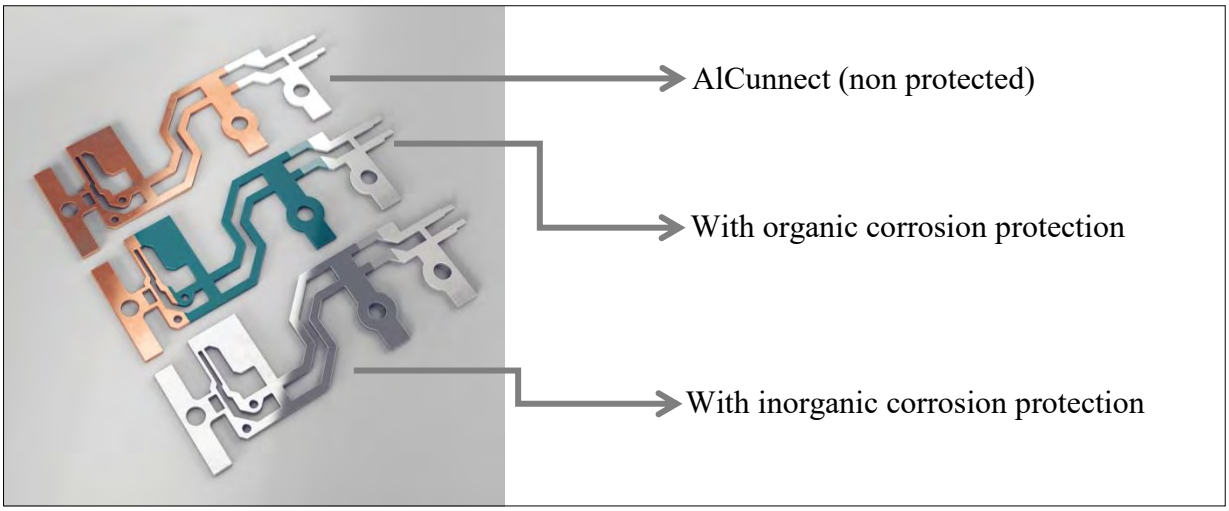


***Fig. 9*** *AlCunnect samples after stamping and application of organic and inorganic coating*

For the organic coating with an insulating lacquer, a special spray coating process was developed, which can be applied full faced or selective in a reel-to-reel setup. The very short curing time after application and the wide range temperature options in use are both outstanding special features of this process.
Another option to avoid corrosion of the AlCunnect composite is an inorganic coating by electroplating. The coating can also be applied full faced or selective in reel-to-reel electroplating equipment.
The salt spray test procedures according to DIN EN 60068-2-11 (severity level 3) have been used to proof the corrosion resistance of the protective coatings. As shown in Fig. 10 the tin surface coating as well as the organic coating show constructive and reliable protection after the corrosion test, when compared to the non-protected specimen.

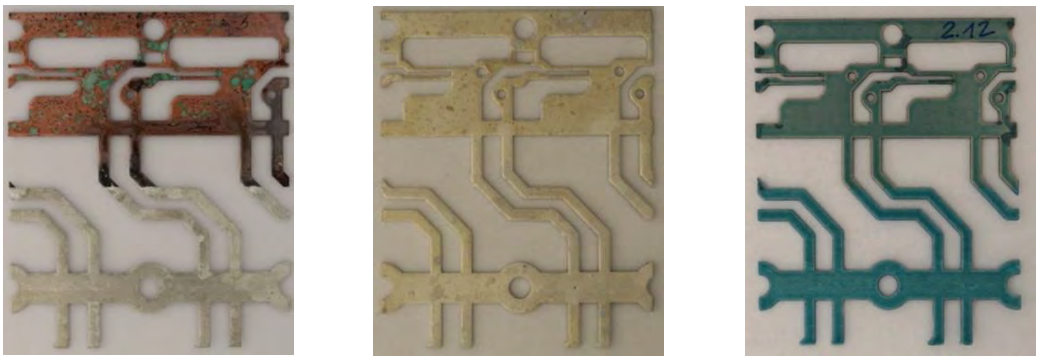


non protected electroplated Ni + Sn organic coating

***Fig. 10*** *Specimens after salt spray testing*

## 7 SUMMARY OF TEST RESULTS

Fig. 11 shows a survey of all test procedures performed and the results achieved.

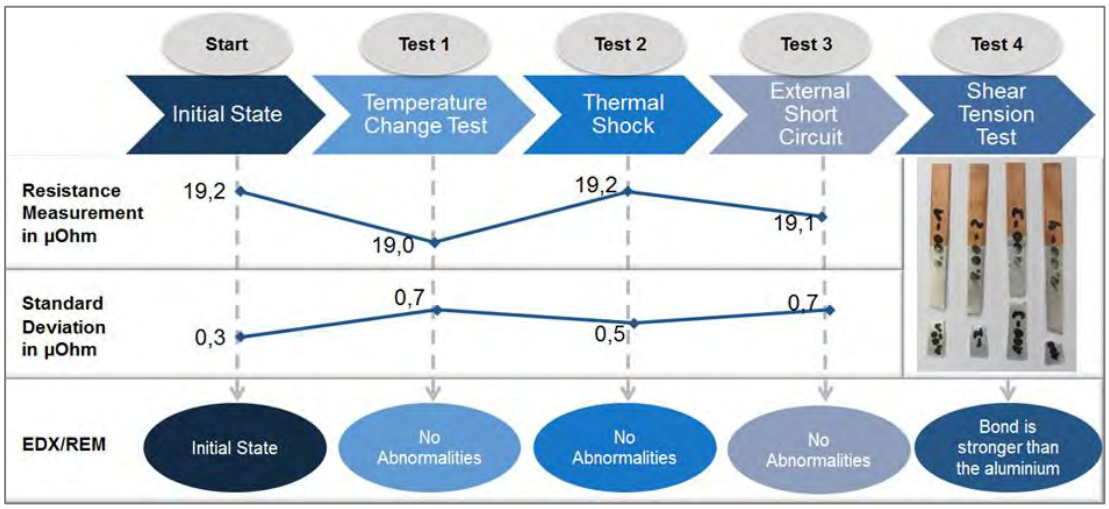


***Fig. 11*** *Overview of applied tests and summary of test results*

## 8 EXAMPLES OF APPLICATION

The three following examples show the variety of applications, which can be utilized with the new AlCunnect material. Using the overlay configuration (copper with overlay plated aluminium) heat sinks for power electronics can be manufactured using an impact extrusion process to form the pin fin structure at the aluminium side (Fig. 12)

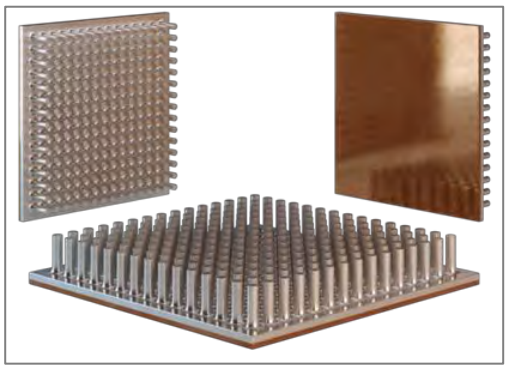

***Fig. 12*** *Al/Cu heat sink with pin fin structure*

The overlapping clad metal can be used as plug connectors or cable lugs to join aluminium with copper for different applications, especially for the automotive industry (Fig. 13).

***Fig. 13*** *Al/cu cable lugs*

Additionally, the overlap and also the inlay clad material can be used in realizing individual connecting solutions for lithium-ion cells systems and BMS-Systems (Battery Management Systems). The overlap type is the ideal cell connector due to the combination of materials. Since in lithium-ion cells the anode is made out of copper, the cathode is made out of aluminium. See Fig.14. The inlay type can be used as connector for BMS-Systems. See Fig. 14.

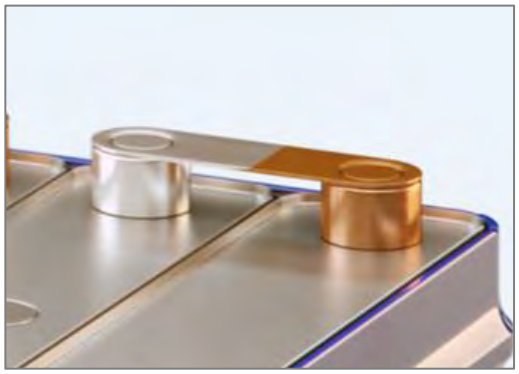

***Fig. 14*** *Cell connector* *BMS-System*

## 9 CONCLUSIONS

The present investigation shows a new method to generate roll bonded Cu-Al bands in overlap as well as in overlay and inlay configuration. The growth of the intermetallic phase has been analysed, and the mechanical and electrical parameters of the AlCunnect material investigated. To assure the corrosion protection of the material combination of Al and Cu two different coating processes have been developed. An organic lacquer or a Ni/Sn electroplated coating is proofed as a reliable corrosion protection in the salt spray test procedure. A few examples for the application of the AlCunnect material are described illustrating the new options opened by this innovative new material combination.

## REFERENCES

[1] E. Hilz, S. Dudziak, R. Schmid-Fetzer, “Formation and properties of intermetallic compounds in an Al-Cu roll-bonded connection” 27th ICEC, Dresden, pp. 163-168, 2014.
[2] C. Chen, W. Hwang, „Effect of annealing on the interfacial structure of Aluminum-Copper joints“, Mat. Trans. Vol. 48, No. 7, pp. 1938-1947, 2007.
[3] C. Chen, H. Chen, W. Hwang, „Influence of interfacial structure development on the fracture mechanism and bond strength of Aluminum/Copper bimetal plate“, Mat. Trans. Vol. 47, No. 4, pp. 1232-1239, 2006.
[4] Y. Funamizu, K. Watanabe, „Interdiffusion in the Al-Cu system“, Trans. JIM, Vol. 12, pp. 147-152, 1971.
[5] R. Schneider, H. Löbl, S. Großmann, T. Schoenemann, M. Holdis, „Langzeitverhalten von Aluminium-Kupfer-Verbindungen in der Elektroenergietechnik“, Metall 63, pp. 591-594, 11/2009.
[6] M. Weigl, A. Grimm, T. Frick, M. Schmidt: „Laser welding of dissimilar copper-aluminium connections by means of roll cladded inserts“, Proc. 29th Int. Congress on Appl. of Lasers & Electro-Optics ICALEO, 2010.
[7] http://www.wieland.com/internet/de/services/metallinfo/metallinfo.jsp, 18.01.2018

# MANUFACTURING OF BRANCHED STRUCTURES FOR FIBRE-REINFORCED PLASTIC-CONCRETE-HYBRID COMPOSITES

**Claudia Möhl[1*], Larissa Born[1], Simon Küppers[2], Florian A. Jonas[3], Jan Knippers[3], Markus Milwich[2], Götz T. Gresser[1,2]**

[1]Institute for Textile and Fiber Technologies (ITFT), University of Stuttgart, Germany
[2]German Institutes of Textile and Fiber Research (DITF), Denkendorf, Germany
[3]Institute for Building Structures and Structural Design (ITKE), University of Stuttgart, Germany

**ABSTRACT:** In modern architecture branched supporting structures are increasingly used. Until now, these branched columns can only be produced in an extensive and cost-intensive way. A new concept made of fibre-reinforced plastic (FRP) serving as a formwork and a load-bearing hull for a concrete core makes it possible to produce a wide variety of different forms and geometries. To enable the potential of complex branched geometries, especially continuous load-confirming fibre arrangements over the entire braiding hull and large diameters, an advanced braiding technique to create triaxially braided preforms is required.
This paper focuses on recent developments of an advanced braiding process to fabricate a multi-layered complex structural geometry on a 144 bobbins radial braiding machine and the adaptation of stationary threads until now regulated by spring force into ones operated electronically.
With the new braiding technique, branched performs with triaxial braids were produced. Subsequent to impregnation with a thermosetting resin and annealing, the FRP-hull is poured with concrete. To evaluate a potential load increase of load capacity of the concrete core due to the confinement of FRP-hulls compression tests are conducted. In comparison to plain concrete specimens the mechanical parameters of fibre-reinforced plastic-concrete-composites show a significant increase in compression strength.

**KEYWORDS:** branching, braiding, fibre-reinforced plastic, confined concrete, hybrid composite, supporting structures, stationary thread, carbon fibres, glass fibres, load-bearing branching

## 1 INTRODUCTION

Components made of fibre-reinforced plastic are widely and increasingly used to enhance and to retrofit structural elements, like beams, columns and slabs. Reasons for this are distinguished mechanical properties like low self-weight, handling, the resistance of carbon against alkaline concrete and the possibility to produce textile preforms cost-efficient.
The manufacturing of complex three-dimensional geometries like branched nodes of supporting structures is a time consuming and expensive process, if several sections of fabric are placed into moulds without a continuous fibre course and impregnated with resin. This method cannot tap the full potential of fibre reinforcement. One of the most important preform technologies for complex three-dimensional forms is braiding, which allows larger variations of cross-section diameter along a curved axis and therefore more sophisticated 3D parts than for example filament winding [1]. Thus a special field of application is the fabrication of branches.
As an alternative to expensive manual sequential work process, branches can be produced directly in the braiding process without interruption. For braiding cables, a special braiding technique is used: The braid core is passed through the braiding point so it is braided from one arm to the main arm, while leaving open the third arm. Finally, the branch is completed by over-braiding the main arm in reverse direction across to the second arm [2]. It is geometrically unavoidable that an arm is double braided and the direction of fibres is non-ideal regarding load path.

* Corresponding author: University of Stuttgart, Institute for Textile and Fiber Technologies (ITFT),
Pfaffenwaldring 9, 70569 Stuttgart, Germany, +49 (0) 711 9340 337,
claudia.moehl@itft.uni-stuttgart.de

In [3] a T-shaped braided bifurcation is produced by moving a rigid T-shaped core back and forth by a robot and rotated accordingly in a braiding machine with corresponding rotation-linear kinematics. Under condition of a flat braiding angle Y-junctions with small cross-section diameter could be produced as well.
To produce Y-shaped branchings without having to braid a branch twice a variation braider equipped with 4 x 4 impellers and 32 braiding bobbins of August Herzog Maschinenfabrik GmbH & Co. KG was modified [4-6]. The impellers touch each other and cross the paths of the bobbins, four points are provided in the centre of the machine for the change of the bobbin course. This way it is possible to choose between circulation and transfer. In case of circulation the bobbin remains in contact of the respective impeller and for transfer the bobbin is moved over to adjacent impeller. The main arm of a branching is braided with all 32 braiding threads and the other two arms with respectively 16 braiding threads.
Based on biological bifurcations as well as insights gained from their analysis a new and biomimetically optimised braiding method was developed [4, 7]: On a circular braiding machine equipped with 48 bobbins the main branch of a bifurcation is braided and afterwards it is transferred to another braiding machine with two braiding circles running, each with 24 bobbins. Thus, the two arms can be braided simultaneously. A disadvantage of this process was a hole of the textile preform in the gusset. It can be closed by intertwining the braiding threads [6].
Summarising the literature published on braiding techniques and developments on braiding machines significant effort has been undertaken to produce branched structures, to close the gusset and to place braid threads along the load path. Only little work is available on bifurcations with a load-adapted fibre orientation, continuous fibre course and larger cross-section diameters.

# 2 MANUFACTURING AND TESTING OF FIBRE-REINFORCED PLASTICS-CONCRETE-HYBRID COMPOSITES

## 2.1 BRAIDING TECHNIQUE

Based on the theoretical model about fibre orientation of branches and a first demonstrator with a small cross-section diameter developed within the research project „Entwicklung einer neuen, wirtschaftlichen Flechttechnik zur Herstellung von kraftflussgerechten Verzweigungen“ (ZIM, KF2009119LK9) the process for braiding branched structures for FRP-concrete-hybrid composites with fibre alignments along the load path, a continuous fibre orientation across the entire mandrel and a cross-section diameter exceeding 100 mm was further developed and adapted. With this method braided Y-junctions as well as symmetric branches with two layers’ of triaxial braid and various cross-section diameters were produced. It is possible to keep the braiding angle almost constant on the arms as well as in the gussets. The fibres in 0° direction (stationary threads) run along the outside of a mandrel. They are serving as an axial reinforcement for the braided hull. In case of branches they transfer forces passing from one arm to another, for example if bending occurs. Due to their crossing in a branch point they also close the hole in the gussets and improve the force path in these areas. The braided fibre-reinforced hull serves as formwork, reinforcement and confinement of the concrete core and the load-adapted fibre orientation results in an increase of compressive strength of braided branches [8]. The fibre orientation on one arm is identical to the other two. Every arm has the same amount of braid threads as well as stationary threads and is connected with another arm by the full amount of their threads. In contrast the described braiding processes before there is no main arm, where all threads emerge. Instead all arms equal regarding amount of fibres, fibre alignment, transition zones between the arms and braiding angle.
All three arms are braided starting with arm 1 to arm 2 (Fig. 1): To ensure a clean depositing of fibres on a mandrel a correct position in front of the braiding ring and a certain initial tension of braid threads is required. If the mandrel is not exactly in horizontal position and in the middle of the braiding ring, with the axis normal to the braiding ring’s plain, shear forces are induced into the braid core. This results in deviation of braid angle, variations in load-confirming fibre arrangements and eventually in limited confinement on concrete as well as a restricted reinforcement capability.
Once the second arm of the branching is parallel to the braiding ring, some braiding threads as well as stationary threads are manually split to open a hole for the third arm (Fig. 2). The position of the opening is always between two specific stationary threads. Thus, every time the hole is in the same vertical position. Without being braided the third arm is moved by the robot through the opening. After finishing the second arm, all threads are cut and the mandrel is turned to start braiding from arm 2 to arm 3 in an identical manner. Repeating these steps for arm 3 to arm 1 the process of braiding a branched geometry with nearly identical laminate set-up in all three arms (two layers of triaxal braid) and the centre of the bifurcation (up to four layers of triaxial braid), a continuous load-adapted fibre arrangement over the entire braiding hull and cross-section diameter is with up to 125 mm is achieved. The difference in the laminate set-up is only the stacking of the layers, whereas the first layer from arm 1 to arm 2 is underneath the second, the second layer from

arm 2 to arm 3 is above the first and below the third and the third layer from arm 3 to 1 is above both other layers. The laminate set-up is adjustable, so that the set-up of the whole branching has not to be symmetrical. To double the layers (Fig. 3) in the branched structure (four layers at each arm) the process can be repeated.

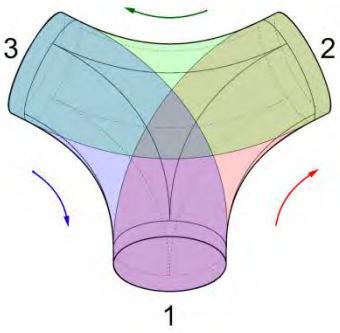


***Fig. 1*** *Schema of braiding technique for branched FRPs [adapted 9]*

***Fig. 2*** *Opening for the third arm during braiding process*

***Fig. 3*** *Branched braided structure made of glass (braiding threads) and carbon fibres (stationary threads)*

## 2.2 STATIONARY THREAD HOLDERS

The tension of braiding threads and stationary threads determines the quality of braid directly: Minor changes can induce optical as well as structural defects like friction between threads, waviness, crimp, loops, displacement and damaging of threads. Consequently, these discontinuities affect the capability of reinforcement as well as the mechanical properties of the later FRP significantly. For this reason, an accurate and definite thread tension is necessary during braiding, especially for the manufacturing of complex structures.
Regulating tension of the bobbins of stationary threads by springs (Fig. 4) is state-of-the-art. Drawbacks of this kind of construction on a 144 radial braiding machine are the manually adjustment of spring length for every single stationary thread on the entire circumference as well as the thread tension is equally to the force of the spring and therefore not adjustable during braiding process. By this a spring can compensate only the difference in haul-off speed from a bobbin and not the changing momentum caused by the decreasing cross-section diameter of threads on a bobbin or other influences. Additionally, the position of every bobbin is locked in horizontal direction. Thus, the relief point of a stationary thread from a bobbin is not ideal in the straight direction of the thread guiding eye of the braiding machine and further friction occurs, which will have an effect on position of the stationary thread in the braid as well as on pretensioning of the thread which might affect the final FRP-component itself.

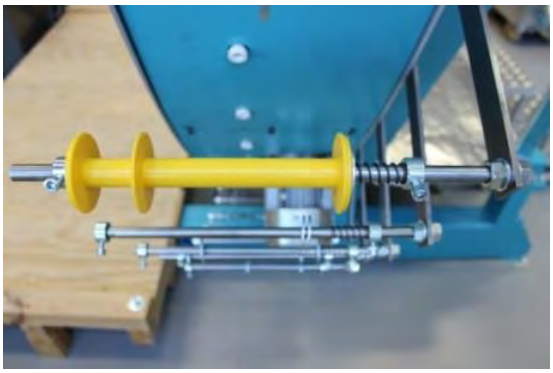

***Fig. 4*** *Spring tensioning system of regulated stationary thread holder*

***Fig. 5*** *Electronical stationary thread holder*

To ease the adjustment and to raise the precision of stationary thread tension electronic stationary thread holders were engineered. Each of them was extended by a motor and an Arduino based self-developed controller. They all were operated by an industrial PC with self-written software (Fig. 5). With a mechanical gear ration of 1 to 3 a breaking power is converted from motor to the particularly stationary thread holder.
After a successful integration of the electronical stationary thread holders the tension of the stationary threads was measured constrained to specific motor control points. Based on the results at halt and in opera-

tion a general formula was determined to regulate thread tension in dependency to diameters of bobbins and the relation to the motor rotation speed during braiding process.

## 2.3 MATERIAL SYSTEMS

The triaxial braided preforms were manufactured from Toho-Tenax STS40 F13 24K (1600 tex) untwisted threads as braiding threads and Toho-Tenax STS40 F13 48K (3200 tex) as stationary threads in combination with Hexion MGS RIM135 epoxy resin and hardener MGS RIMH137. The braids with a nominal braiding angle of 60° were manufactured on a radial braiding machine with 144 bobbins of August Herzog Maschinenfabrik GmbH & Co. KG. Triaxial braids with four layers were produced by over-braiding a branched cylindrical mandrel with a cross-section diameter of 125 mm and an angle between the arms of 120° which was guided through the braiding machine by a robot at a feeding rate of 0,6 m/min and an impeller speed of 55 $min^{-1}$.
After braiding, the hulls were impregnated by hand, cured first for 24 hours at room temperature and second in an annealing oven at 80° for 16 hours.
For the filling of FRP-hulls, concrete C50/60 (EN 206) with a target cylinder strength of 50 $N/mm^2$ was used. Two open ends of the hull were closed by additional formwork (Fig. 6). After short compaction on a vibrator table all samples are cured at room temperature and part-time under water for 28 days.

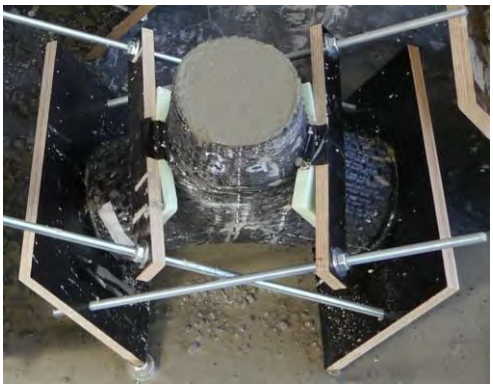

***Fig. 6*** *Concrete filled FRP-branch in a formwork after pouring*

## 2.4 TEST SET-UP AND RESULTS

For compression tests two different types of samples were prepared: A plain concrete branchings without any FRP-reinforcement and FRP-concrete-hybrid composites with 4 layers (double pass braiding) as well as stationary threads.
An experimental test rig for testing branched structures in compression and bending was developed (Fig. 7). In case of compression tests the supports of the lower arms are fixated in a manner that vertical and horizontal movement as well as rotation is hindered. A sample is placed with two arms downwards into the rig (Fig. 8) and is strained from above with an initial load of 5 kN via the third arm. All samples are loaded until a significant drop of the maximum force. Measured are force and deformations by linear variable differential transformer as well as strains by up to six strain gauges.

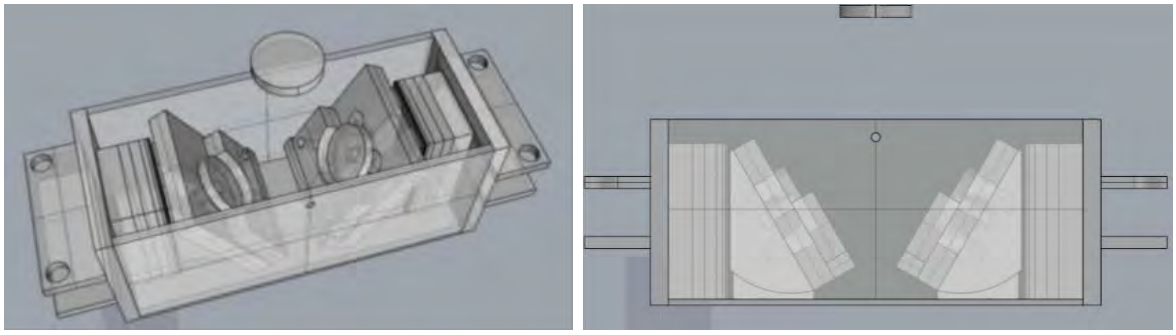

***Fig. 7*** *Multifunctional experimental test rig*

***Fig. 8*** *Experimental steel test rig with a sample of FRP-concrete-hybrid composite*

In Fig. 9 the average maximum force for plain concrete and FRP-concrete-hybrid composite branchings are presented. Due to the FRP-hull with stationary threads, the load capacity could be nearly doubled compared to a plain concrete branching. The effect of strength increase due to development of a multi-axial stress state in concrete is well known. Several authors prove this also for FRP-confined concrete cylinders and it is also evident for cylindrical concrete cylinders with braided hulls [10].

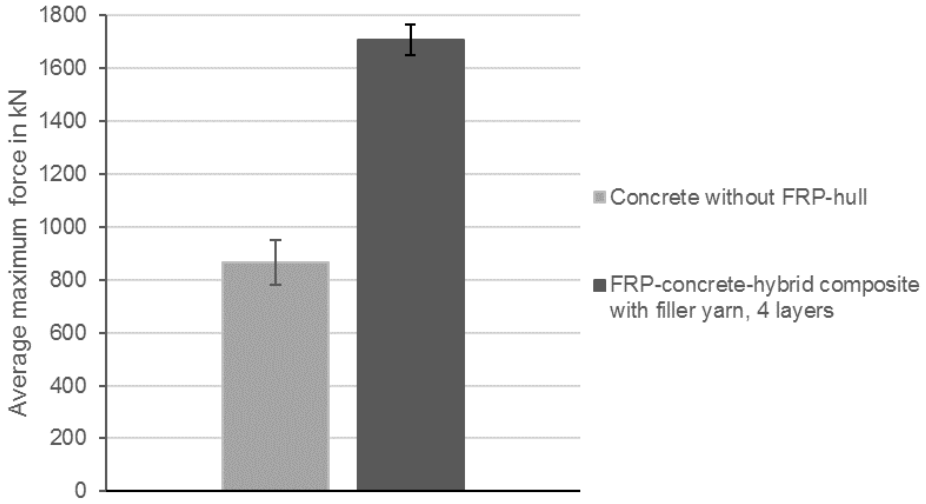


***Fig. 9*** *Average maximum force of plain concrete and FRP-concrete-hybrid composite branchings in compression test*

## 3 CONCLUSIONS

In architecture and civil engineering high load-bearing branchings for branched columns and grid shell constructions with varying knot geometries are of increasing importance. With the developed braiding technique branches for supporting structures with large cross-section diameters up to 125 mm as well as load-adapted fibre alignment and fibre orientation can be produced as hulls for FRP-concrete-hybrid composites. The further development of the braiding process with stationary thread holders to ensure a constant stationary thread tension through electronically controlled stationary holders on a 144 bobbin radial braiding machine is the basis for precise and reproducible manufacturing in a constant quality of the braided hull. As shown by the mechanical tests the compression strength of plain concrete could be increased by an FRP-hull indicating that the fibres serve as an effective confinement to create a beneficial multi-axial stress state in concrete.
Continuative investigations on FRP-concrete-hybrid composite branchings like the upscaling of the diameter, to extend the applicability on bigger constructions, the bonding between hull and core as well as variable geometries are of interest for future research.

## 4 ACKNOWLEDGEMENT

The authors would like to thank the German Research Foundation (DFG) for funding this work as part of the Transregional Collaborative Research Centre (SFB/Transregio) 141 'Biological Design and Integrative Structures'/project A06. Furthermore we would like to thank all collaborating partners from the University of Freiburg (PBG) and Stuttgart (ITFT and ITKE) as well as DITF Denkendorf.

## REFERENCES

[1] Cherif C., *Textile Werkstoffe für den Leichtbau*. Springer-Verlag Berlin Heidelberg New York, 2011
[2] Uozumi T., Hirukawa M.: *Braiding technologies for Commercial Applications*. In: 6th International SAMPE Symposium & Exhibition, Tokyo, 1999.
[3] Miravete A.: *3-D Textile Reinforcements in Composite Materials*. Woodhead Publishing Limited Abington Hall, 1999.
[4] Küppers S., Thumm J., Müller L., Ewert D., Gresser G. T.: *Braiding of branches for the fiber composite technology.* In: Materials Science Forum, Vols. 825-826, pp. 749-756, 2015.
[5] Grave G.: *Flechttechnologie bietet Lösungen für den automatisierten Leichtbau von morgen: Nichts ist leichter als ein geflochtenes Teil*. In: Industrie Anzeiger 33: 22, 2011
[6] Thumm J.: *Wirtschaftliche Herstellung geflochtener Verzweigungen an einer Radialflechtmaschine mit einem methodischen Ansatz für kraftflussgerechte Fadenverläufe*. Diplomarbeit Universität Stuttgart, 2012
[7] Müller L., Milwich M., Gruhl A., Böhm H., Grude M., Haushahn T., Masselter T., Schwager H., Neinhuls C., Speck T.: *Biomimetisch optimierte verzweigte Faserverbundstrukturen mit hoher Tragfähigkeit*. Melliand Textilberichte, 2: 88-93, 2013
[8] Born L., Jonas F. A., Bunk K, Masselter T., Speck T., Knippers J., Gresser G. T., *Branched structures in plants and architecture*. In: Knippers J., Nickel K. & Speck T. (eds) Biomimetic Research for Architecture and Building Construction, Springer International Publishing Switzerland, p 195-216, 2016
[9] Patent DE 10 2017 008 661.3 (pending), *Tragfähiger Verzweignungsknoten aus Beton und faserverstärktem Kunststoff (FVK) für Fachwerk- und Rahmenkonstruktion*, 2017
[10] Jonas F. A., Knippers J., *Tragverhalten von Betondruckgliedern mit Umschnürung durch geflochtene und gewickelte Carbonrohre*. Beton- und Stahlbetonbau, Vol. 112, Nr. 8, 517–529, 2017

# SUSTAINABLE HYBRID COMPOSITES OF CARBON AND NATURAL FIBERS FOR LIGHTWEIGHT COMPONENTS

**R. Rinberg[1*], R. Svidler[1], A.-A. Ouali[1], M. Klaerner[1], L. Kroll[1]**

[1]Department of Lightweight Structures and Polymer Technology, Chemnitz University of Technology (CUT), Reichenhainer Str. 31/33, 09126 Chemnitz, Germany

**ABSTRACT:** In engineering science and technology the development of lightweight structures increases exponentially. The research group of Prof. Lothar Kroll combined for the first time a flax-fiber-reinforced thermoplastic (FFRTP) core with top layers of carbon fiber reinforced thermoset (CFRP) to the hybrid laminate without using further bonding agent. Furthermore, they molded it in just one process step into a three-dimensional component. In this way, the main load paths can be reinforced by CFRP and the lower load paths by natural fibers composite. Due to the material substitution, 50% of the cost-intensive carbon fibers can be substituted by the use of cost-effective natural fibers which means a high increased economic efficiency of these new hybrid lightweight materials compared to conventional carbon-fiber composites. The applied natural fibers feature a very good carbon footprint and very low manufacturing energy demand in comparison to carbon or glass fibers. Furthermore, the flax fibers are not toxic, not respirable, and do not cause skin irritations which is beneficial for the workers who produce the components. Moreover, the carbon fibers within these hybrid composite materials can be reclaimed by suitable pyrolysis and reused as a secondary material. An end-of-life option of these new composite materials is the thermal utilization which is not possible with glass-fiber-reinforced plastics. There is a big potential for these novel materials for the transport sector (especially electro mobility) and aeronautics.

**KEYWORDS:** Flax fiber, polyamide, unidirectional reinforcement, carbon-flax composite, bio-based composite, thermoset and thermoplastic composite, hybrid composite, vibration damping

## 1 INTRODUCTION

For some years, lightweight design has been gaining more and more influence in engineering. Thus, dimensioning of structure, used materials, and manufacturing technologies are changing. For components with high structural and safety requirements metallic structures of steel, titanium, and aluminum are commonly used. Nowadays, also lighter hybrid constructions from plastics and metal are deployed. Examples of the implementation in mass production can be found at Elring Klinger AG in Fig. 1 (left) [1]. They produce modern injection-molded hybrid automotive parts like front-ends and cockpit beams from short glass fiber reinforced polyamide (PA) and formed steel tubes.

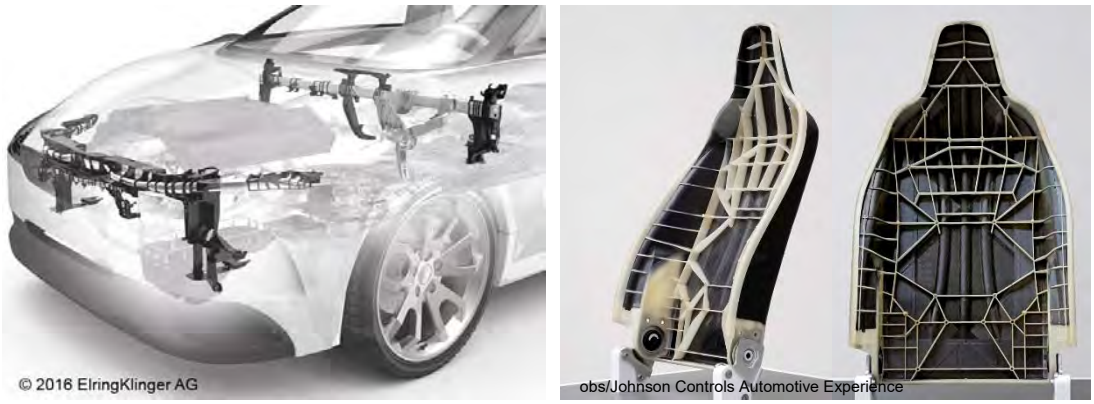


***Fig. 1*** *Front-end und cockpit beam (left) and (right) as examples of automotive hybrid parts*

* Corresponding author: Chemnitz University of Technology, Department of Lightweight Structures/Polymer Technology, Reichenhainer Str. 31/33, D-09126 Chemnitz, Germany, +49 371 531-32359, roman.rinberg@mb.tu-chemnitz.de

When the requirements in stability and stiffness are higher, for example in aeronautic components, the properties of short-fiber-reinforced thermoplastic and thermoset are not sufficient. To increase specific structural properties continuous fiber rovings are used. The reinforcing fibers can be arranged according to the distribution of forces and the strength reserves of material can be exploited. At the same time, there is comparably low material density of the hybrid construction. When using unidirectional reinforced carbon-fiber semi-finished products with PA matrix and optimized metallic inserts at the positions of load application in the seat shell CAMISMA in Fig. 1 (right) [2], there is a mass reduction of more than 40% compared to the reference structure. So far, the use of natural fibers in structural parts with high structural requirements is little-known. Mainly, the specific strength and stiffness of natural fiber-reinforced composites using thermoset or thermoplastic matrix are not sufficient for highly loaded structural components. Further problems are the mechanical fatigue, the variance of parameters, which can be due to the growing of natural fibers, and the tendency to moisture absorption which are not yet solved.

Mostly, structural components from high-performance lightweight materials are loaded along few load paths. Wide areas of the component are structurally not exploited. Therefore, it is interesting to use renewable materials for these areas and to develop hybrid composites, where high performance fibers represent the main load paths and natural fibers represent the secondary load paths.

# 2 MATERIALS AND METHODS

The following sections describe the materials, tests, and analysis which are performed in this work. Firstly, the materials, consisting of fibers and matrix, and the processing parameters are characterized. Afterwards, hybrid thermoplastic-thermoset laminates and one-shot formed hybrid part with thermoplastic core and thermoset covers were made and tested on mechanical, vibration damping, and sound reduction properties.

## 2.1 MATERIALS

For this project, commercially available materials were chosen. As high performance semi-finished product a prepreg from unidirectional non-woven fabric with a grammage of 125 g/m$^2$ made of carbon fibers (CF) type TENAX HTS 40 (Co. Haufler Composites) with thermosetting epoxy matrix (EP) was used. This CF-EP-prepreg shows in bonded state a fiber mass content of 60 wt%, depending on processing parameters and corresponding to an averaged fiber volume ratio of around 50 vol%.
As natural reinforcing component, a dry unidirectional flax-fiber fabric (FF) from Co. Lineo, with a grammage of 110 g/m$^2$ was selected. The quality of natural fiber non-crimp fabrics is not equivalent to the one of carbon fiber non-crimp fabrics, in terms of fiber direction and homogeneity of fiber distribution along the whole width of the semi-finished product. This fact leads inevitably to higher statistical variances of the specific values within the tested laminates.
As thermoplastic matrix for flax-fiber fabric, a completely bio-based PA 11 (PA) type Rilsan® BESNO P20 TL (Co. Resinex) with half-flexible adjustment was used. First, a thin layer of 100 µm thickness was produced in the technical center of Department of Lightweight Structures and Polymer Technology to process to fibers composites using film-stacking method.

## 2.2 MANUFACTURE OF NATURAL-BASED HYBRID LAMINATES

To determine the potential application of bio-based hybrid materials, symmetrical laminate structures based on above mentioned components FF, EP, CF-EP, and PA were made (Table 1). Here, the objective was to combine the advantages of a thermosetting matrix and a thermoplastic matrix in a composite structure.

***Table 1:*** *Structure of testing laminates*

| Marking according to [3] | Laminate structures (C-Carbon fibers, F-Flax fibers, EP-Epoxy resin) |
|---|---|
| CF-EP ‖ | $(0_4)_S$ |
| FF-PA ‖ | $(0_4)_S$ |
| CF-EP+FF-PA ‖ | $((0^C/0^C)EP+(0^F/0^F/0^F)PA)_S$ |
| CF-EP+FF-PA _‖_ | $((0^C/0^C)EP+(90^F/90^F/90^F)PA)_S$ |

To produce hybrid thermoplastic/thermosetting composites, a new one-shot hot compression molding technology was developed. This is a combination of film-stacking and prepreg process (Fig. 2). In the first step, layers, composed of flax-fiber fabrics, polyamide films and CF-EP-prepregs (outer layers), were stacked as described in Table 1. In the second processing step, the stack is heated by a contact heating station (210–220°C) for the duration of 60–120 s. The thermoplastic matrix melts and the flax fibers are impregnated with

molten polyamide under low pressure. In a third processing step, the hot pre-compressed stack is transported into a forming mold (80–120°C) and the hybrid composite gets consolidated by closing the mold. Thereby, the FF-layer impregnated with epoxy resin on the one side and polyamide on the other side works as bonding agent between CF-EP and FF-PA. By using this technology, test laminates and 3D molded components were produced.

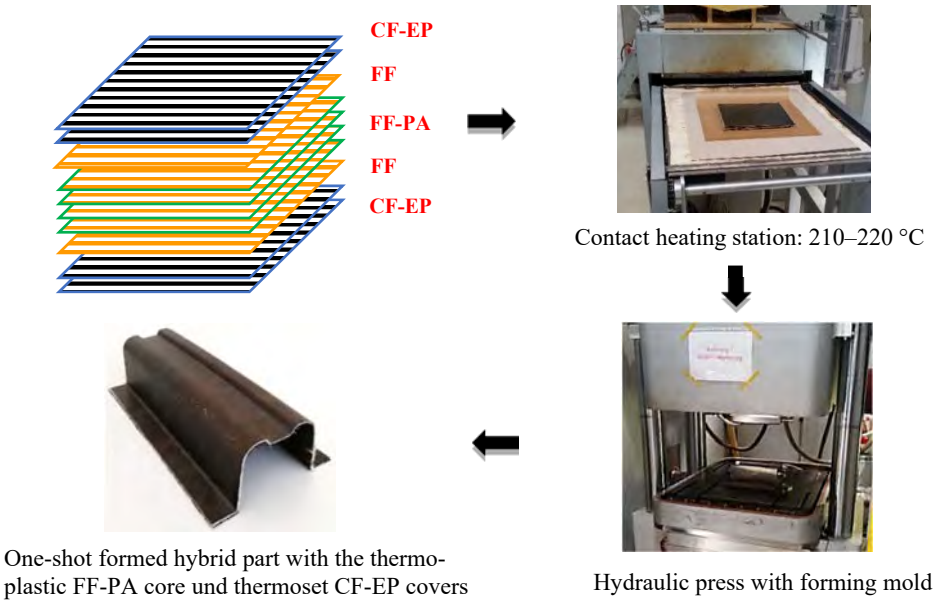


***Fig. 2*** *One-shot hot compression molding process of three dimensional molded hybrid part with the thermo-plastic core and thermoset covers*

# 3 RESULTS

## 3.1 MECHANICAL PROPERTIES

To characterize the mechanical properties of UD laminates, specimens from CF-EP, FF-PA plates and CF-EP+FF-PA hybrid laminates were tested in the tensile test according to DIN EN ISO 527-5. The fiber volume content was calculated from the mass fractions and densities of the respective components, due to the fact that the determination of the volume fraction of flax fibers in the incineration test is not possible. The fiber volume ratio of FF-PA composite reaches 41%. The corresponding characteristic values of the test laminates and the associated standard deviations are given in Table 2.

***Table 2:*** *Density and tensile properties of the tested laminates*

| Tested laminates | | FF-PA | | CF-EP | | CF-EP+FF-PA II | | CF-EP+FF-PA _I_ | |
|---|---|---|---|---|---|---|---|---|---|
| | | value | st. dev. | value | st. dev. | value | st. dev. | value | st. dev. |
| Density | g/cm³ | 1.17 | - | 1.53 | - | 1.33 | - | 1.32 | - |
| E1-Modulus | GPa | 20.007 | 1.268 | 119.970 | 1.254 | 66.764 | 1.236 | 45.257 | 0.558 |
| Specific E1-Modulus | GPa/(g/cm³) | 17.042 | - | 78.412 | - | 50.198 | - | 34.286 | - |
| Max. Strength | MPa | 219 | 46.6 | 1500 | 145 | 674 | 27.0 | 481 | 75.6 |
| Specific max. Strength | MPa/(g/cm³) | 186.5 | - | 980.4 | - | 506.8 | - | 364.4 | - |
| Deformation | % | 1.3 | 0.3 | 1.2 | 0.1 | 1.0 | 0.0 | 1.0 | 0.2 |

The stiffness and strength of FF-PA are significantly lower than the values of CF-EP, although the fiber volume content of CF-EP samples is higher. Therefore, a direct substitution of CFK with NFK is hardly possible. The aim is rather to identify advantageous material combinations for the hybrid laminates. The mechanical properties of produced mixed composites were examined by tensile testing, flexural testing, and impact strength testing, respectively according to DIN EN ISO 527-5, DIN EN ISO 14125 and DIN EN ISO 179-2. The selected results of these investigations are summarized in Fig. 3 and Fig. 4.
For a relevant comparison, the specific characteristics were calculated. Fig. 3 illustrates specific tensile and flexural modulus as well as absolute bio-based content for all tested composites. From a structural-mechanical

and environmental point of view, the hybrid composite CF-EP+FF-PA, having a bio-based content over than 55 wt%, is particularly interesting due to its specific flexural modulus, which performs only 10% to 14% lower than CF-EP laminate. In particular, the properties of CF-EP+FF-PA _I_ in the plane perpendicular to the fiber direction of the CF-EP cover layers are dominated by the FF-PA and are clearly superior to the unidirectional CF-EP composite. The bio-based content of this laminate can be further increased if a bio-based epoxy resin would be used in the CF-EP prepreg instead of the petrochemical one.

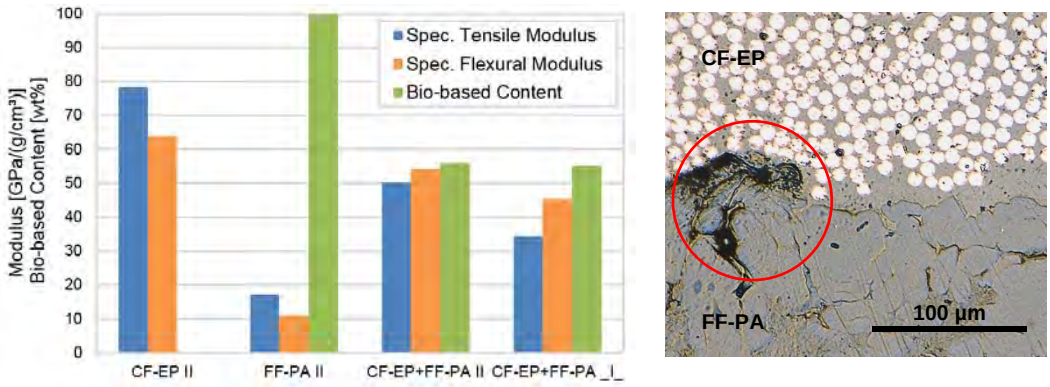


***Fig. 3*** *Specific stiffness characteristics and bio-based content of the tested laminates (left), microstructure of the hybrid composite CF-EP+FF-EP II at 1000x magnification (right)*

Due to flax fiber reinforcement, the hybrid composite CF-EP+FF-PA _I_ has a 14 times higher specific tensile strength than the CF-EP laminate in the plane perpendicular to the fiber direction of the CF cover layers. Compared to that, the specific tensile strength of CF-EP+FF-PA II represents approximately 25–32% of the value of CF-EP laminate. It should be noted that premature failure of the laminates can be attributed to structural defects such as voids or surface defects. Such structural defects can be seen in the example of CF-EP+FF-PA II in Fig. 3 (left) in the form of dark areas, especially at the boundary between CF-EP cover layer and FF-PA core.

Furthermore, the highly dynamic properties of the investigated laminates are technically interesting because they do not exceed the damage tolerance. In the instrumented impact test, the thin composite specimens were placed in the sample holder so that the impact of the pendulum was on the broadside. Fig. 4 shows the impact values of the tested composites. Accordingly, the tested hybrid composite CF-EP+FF-PA has an impact strength at least as high as CF-EP laminate. The material variant CF-EP+FF-PA II has in comparison to the CF-EP composite even about 25% better impact resistance which may be due to the flexibility of the used PA matrix.

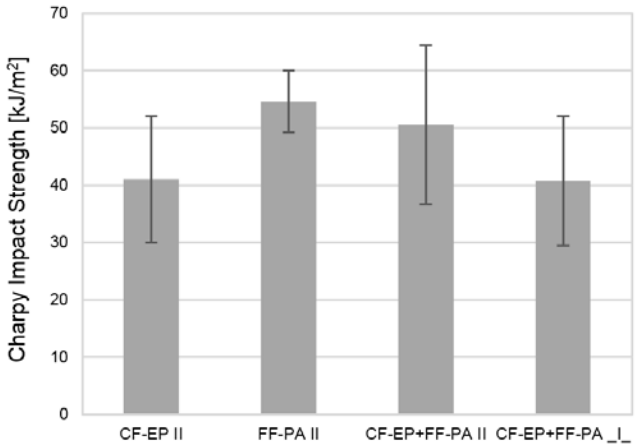


***Fig. 4*** *Charpy impact strength of the tested laminates*

### 3.2 VISCOUS DAMPING AND SOUND REDUCTION

Fiber-plastic composites show a pronounced anisotropic material behavior with regard to material stiffness, strength, and damping properties. The damping of laminates can be described with approaches, similar to the classical laminate theory at the layer level, and can be determined for composites which are dependent on the

direction. The mathematical formulations were first developed by ADAMS and BACON for cantilever beams under flexural load and based on vibrations which are proportional to velocity in the fiber direction and in the fibre transverse direction, and under shear stress [3]. The approaches were extended for two-dimensional calculations [4], [5] and can be implemented in FEM programs based on modal damping [6–8].
The present laminates were examined by cantilever beams. The test setup is based on DIN EN ISO 6721 and VDI Guideline 3830. All specimens were stimulated by induction in their first bending mode, and the velocity in time range was measured using a laser Doppler vibrometer. The Lehr's damping Ratio D was determined after switching off the harmonic stimulation with the aid of the exponential envelope of the decay curve and the flexure proper frequency. In order to have a simple qualitative comparison, all materials samples with only one fiber direction of the cover layers were produced. In Fig. 5, the thermoplastic-bonded flax fiber composite FF-PA shows a pronounced damping behavior of D = 0.0064. Due to the laminate structure of the hybrid composites with outer carbon fiber layers, an increase of the attenuation by 77–106% compared to pure CF-EP is carried out. The fiber orientation of the core materials influences the dissipation properties only slightly. As expected, the damping of the hybrid composites is dominated by the cover layers, which also indicates small inter-laminar shear stresses into the composite.

***Fig. 5*** *Lehr´s Damping Ratio D, measured in the vibration test on cantilever beams*

To determine the airborne sound reduction, circular samples with a diameter of 40 mm were measured in the transmission tube under the action of a direct sound field in the frequency range from 100 Hz to 4000 Hz (white noise). Airborne sound reduction index R was determined using the Song and Bolton transfer matrix method. For the measurements of this small sample size, the influence of the fiber orientation in the core layers of CF-EP+FF-PA laminates was not considered. All laminates with flax fiber reinforcement show a significant increase of the sound reduction index R in the measured frequency range (Fig. 6, left). In addition, the positive influence of the material mix is clearly evident.

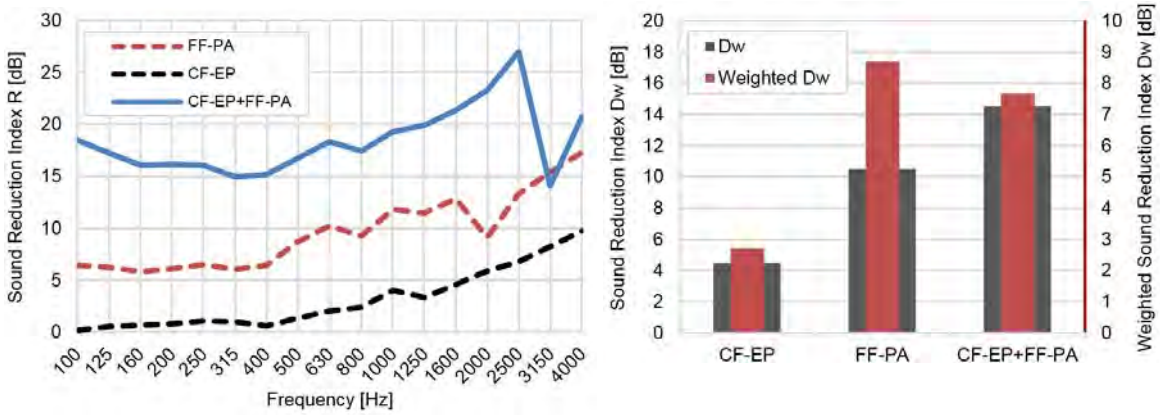


***Fig. 6*** *Results of sound reduction tests (left) and comparison of sound reduction index R and $D_w$ which refers to the basis weight of laminates (right)*

The evaluation of the third-octave band values according to DIN EN ISO 717-1 in Fig. 6 (right) shows the comparison of the weighted and non-weighted sound reduction index Dw. It is evident that the hybrid thermoset-thermoplastic composite CF-EP+FF-PA has significantly higher weighted sound reduction values than

CF-EP. The increase is about 220%. Referred to the basis weight, the values are smaller than of FF-PA, but by a factor of 2.5 higher than of CF-EP.

# 4 CONCLUSIONS

The application of bio-based materials for lightweight structures can provide a lot of special advantages, but involve many risks due to the not yet fully developed semi-finished products and material concepts. A direct substitution of thermoset CFRP with thermoplastic NFRP will hardly be conceivable in the near future even with a successful further development of NFRP. Nevertheless, the potential of bio-based material systems for lightweight applications can be exploited by tailor-made hybrid materials by combining thermoset CFRP and thermoplastic NFRP in load-bearing lightweight structures. In our work, the developed and tested hybrid composites made of carbon prepreg and flax fiber tape with a completely bio-based polyamide matrix gather many interesting features such as a lightweight structure, a high-performing stiffness, and a high content of sustainable materials (about 56 wt%). Furthermore, the impact strength could be improved by 25%. The vibration damping increases by 77%. The airborne sound absorption even increases about 250% compared to classic CFRP composites, even though the specific flexural modulus remains nearly similar.
To achieve the high requirement profile for lightweight structures, e.g. for aerospace applications or components in rail transport, bio-based hybrid composites require intensive investigations at all technological levels, including material development, component simulation, handling of textile semi-finished products, and finishing of the component. In the near future, other important investigations on material behavior under fire conditions and on toxical effects are planned.

# 5 ACKNOWLEDGEMENT

The authors are thankful to German Federal Ministry for Economic Affairs and Energy (BMWi) for financial support by the LUFO-V2 research program.

# REFERENCES

[1] Schuck M.: *Automobiler Leichtbau mit Faserverbundwerkstoffen*. GAK, pp. 144–147, Jahrgang 69 3 2016
[2] Evels S., Jonas J., Nuyan V.: CAMISMA - Carbonfaser/Amid/Metall-basiertes Innenstruktur-Bauteil im Multimaterialsystem-Ansatz. Abschlussbericht, 2015, DOI: 10.2314/GBV:865239010.
[3] Schürmann H.: *Konstruieren mit Faser-Kunststoff-Verbunden*. Berlin, Heidelberg: Springer, 2005.
[4] Adams R. D., Bacon D. G. C.: *Effect of fibre orientation and laminate geometry on the dynamic properties of cfrp*. Journal of Composite Materials, 7 (4), pp. 402–428, 1973.
[5] Berthelot J.-M., Assarar M., Sefrani Y., Mahi A. E.: *Damping analysis of composite materials and structures*. Composite Structures, 85 (3), pp. 189–204, 2008.
[6] Billups E., Cavalli M.: *2D damping predictions of fiber composite plates: Layup effects.* Composites Science and Technology, 68 (3–4), pp. 727–733, 2008.
[7] Klaerner M., Wuehrl M., Kroll L., Marburg S.: *Modelling and FEA-Simulation of the Anisotropic Damping of Thermoplastic Composites*. Advances in Aircraft and Spacecraft Science, 3 (3), pp. 331–349, 2016.
[8] Maheri M. R.: *The effect of layup and boundary conditions on the modal damping of FRP composite panels.* Journal of Composite Materials, 45 (13), pp. 1411–1422, 2011.

# FIFDM – MANUFACTURING PROCESS FOR 3D PRINTED FIBER REINFORCED POLYMER COMPOSITES

**Matthias Domm[1*], Jens Schlimbach[1]**

[1] Institut für Verbundwerkstoffe GmbH, Kaiserslautern (Germany)

**ABSTRACT:** Additive manufacturing processes make it possible to produce very complex structures without the need for special tools. However, the low strength and stiffness of pure polymers prevent the use of additives in structural applications. A new additive manufacturing process for fiber reinforced polymer composites based on the Fused Deposition Modeling (FDM) process is presented. Special features of the FIFDM process are the processing of continuous fibers, the use of fully impregnated semi-finished products, and the placement of fibers in all spatial directions without support materials. To characterize the Fiber Integrated Fused Deposition Modeling (FIFDM) process and to optimize process performance and stability as well as the quality of the printed parts, a theoretical process evaluation was carried out to identify relevant influencing parameters. In addition, a test methodology was developed to quantify and compare process and print quality for different parameter settings. Tensile and three-point flexure tests of printed laminates are performed and compared with autoclave laminates to obtain an initial classification of the mechanical properties of such printed structures. In addition, a parameter study shows the influence of conveying speed, nozzle displacement, and nozzle temperature on the quality of printed laminates. The results flow directly into the further development of the technology. Finally, an outlook on possible fields of application will be given using the example of a process chain including injection molding.

**KEYWORDS:** Additive Manufacturing, Fused Deposition Modeling, Thermoplastic Composites, Continuous Fiber Reinforcement

## 1 INTRODUCTION

Fiber Reinforced Polymer Composites (FRPC) have a great lightweight potential. The highest reinforcement effect is achieved when fibers are continuously present in the component. Due to the strong anisotropy of the fibers, it is very important to know how the fibers in the component are oriented. In the direction of the fiber, reinforcing fibers can absorb forces more than 10 times [1] higher than transverse forces. To obtain the full potential of this material class, it is important to orientate the fibers in load direction. Since the exact and often individual fiber alignment is difficult to implement and automate in production, it is often necessary to use flat semi-finished products such as organic sheets. With the help of organic sheets, however, load paths in a component can only be mapped very rudimentary. In addition, organic sheets are usually very expensive.

In contrast, 3D-printing methods enable automated production of very complex and individualized structures without the need for a specific tool. In recent years, additive manufacturing has become increasingly important for industrial applications. According to a recent study by Ernst & Young [2], 24% of the companies surveyed already use additive manufacturing in various applications. Whereas 38% want to introduce additive manufacturing into serial production in the next few years, this figure is currently only 5%. However, when it comes to polymers, only neat or short fiber reinforced polymers can be processed by 3D-printing. The subsequent low strength and stiffness prevents the use of 3D-printed polymers for structural applications.

Hence, the objective of this work is to combine manufacturing advantages of 3D-printing processes and material advantages of FRPC by developing a 3D-printing process for continuously fiber reinforced polymer composites, enabling an automated and load optimized orientation of the reinforcing fibers.

## 2 APPROACH AND RESEARCH OBJECTIVES

There are several 3D-printing processes for polymers. The processes can be categorized into radiation-curing processes (e. g. stereolithography), sintering and binding processes (e. g. selective laser sintering), and ex-

trusion-based processes (e. g. fused deposition modeling) [3]. Extrusion-based processes are best suited for the integration of continuous fibers, since the raw material is already a continuous polymer filament that is processed in a semi-continuous process. Efforts in this research work have therefore been made to additively produce continuously reinforced thermoplastics based on the FDM method [4, 5]. In the FDM process, a polymer filament is pressed through a heated nozzle and thereby melted. The extruded material is then placed on a printing bed and builds-up the component geometry layer by layer. For the integration of continuous fibers into the new FIFDM process, an impregnated, continuous, Fiber Reinforced Polymer Strand (FRPS) was identified as most suitable, which is aimed at fast process speeds with simultaneously high fiber volume content and high impregnation quality. [4, 5]
There are already possibilities to reinforce 3D-printed polymer parts with short fibers and fillers [6 -11]. In addition, initial efforts have been made to integrate continuous fiber reinforcement into the FDM process [12-28]. An unique feature of the FIFDM process presented here is the processing of fully impregnated, FRPS, so that the impregnation originates from the printing process. Furthermore, except for [26], the screened processes are only able to place the extruded material in the plane. To exploit full potential of the continuous fiber reinforcement, two key challenges arise:

- Load-specific orientation of the fibers
- High laminate quality

The first challenge was approached in an earlier study [4]. To enable a load-specific three-dimensional orientation of the fibers in the final part, the process was further developed to print not only layer by layer but also out-of-plane in all spatial direction without support materials. The results of the study were implemented in new production equipment such as extrusion unit, cooling system, and cutting device for an X400 FDM-printer from German RepRap.
Based on the preliminary developments, aim of this research work is the mechanical characterization and benchmarking of FIFDM printed samples. Based on this, appropriate provisions to optimize the process stability and component quality of FIFDM printed structures as well as to broaden the application spectrum of the process are being derived from.

# 3 MATERIALS AND SETUP

The samples for the required tests were produced using a modified X400 FDM printer with a new extrusion unit for processing continuous fibers. The printer with a print space of 400 x 400 x 380 $mm^3$ is shown on the left in Fig. 1.On the right side, the semi-finished product that was used as FRPS is shown. It is a continuous, glass-fiber reinforced polypropylene (GF-PP) strand. The FRPS has a diameter of approx. 1.89 mm ± 0.4 mm, a fiber volume content of approx. 30 vol%, and a void content of 6.04 ± 1.4 vol%.

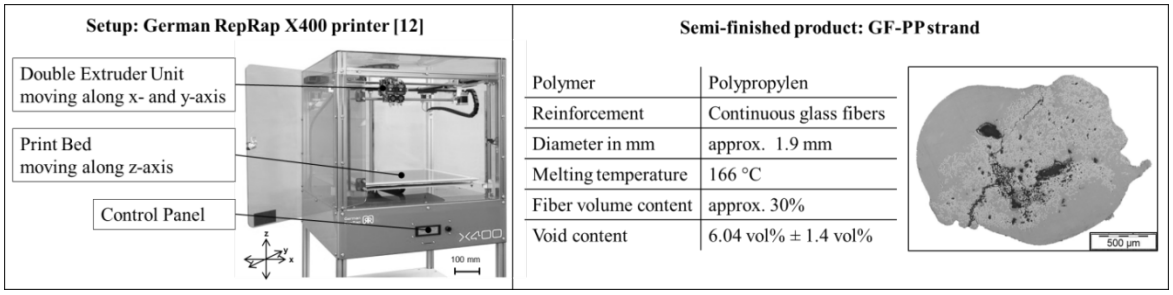


***Fig. 1*** *German RepRap X400 FDM-printer (left side), GF-PP strand (right side)*

# 4 RESULTS AND DISCUSSION

In this chapter the results of theoretical process evaluation, test methodology, mechanical characterization of printed laminates, process optimization and possible applications are discussed.

## 4.1 THEORETICAL PROCESS EVALUATION

To optimize the FIFDM process in terms of stability and print quality, the relevant process variables and influencing factors were identified. Fig. 2 shows the schematic structure of the FIFDM process. The process is divided into several steps: preheating, conveying, extruding, and placing. During preheating, the FRPS is heated to a temperature close to the melting point ($T_m$). This reduces the temperature gradient in the print nozzle, allowing higher process speeds. The process speed is defined by the conveying process, where the force is applied to pull-off the FRPS from the material storage and also to push it through the print nozzle.

The actual extrusion process takes place in the print nozzle. Here, the FRPS is heated to process temperature ($T_P > T_m$). After extrusion, the material is placed either on print bed, in free space or on already placed structures, respectively. A cooling unit and intelligent temperature management helps to control the outer contour, and positioning deviation of the extruded FRPS. All process steps and, of course, the semi-finished product used have several variables that influence process output and stability as well as print and part quality. Relevant influencing factors are shown in Fig. 2.

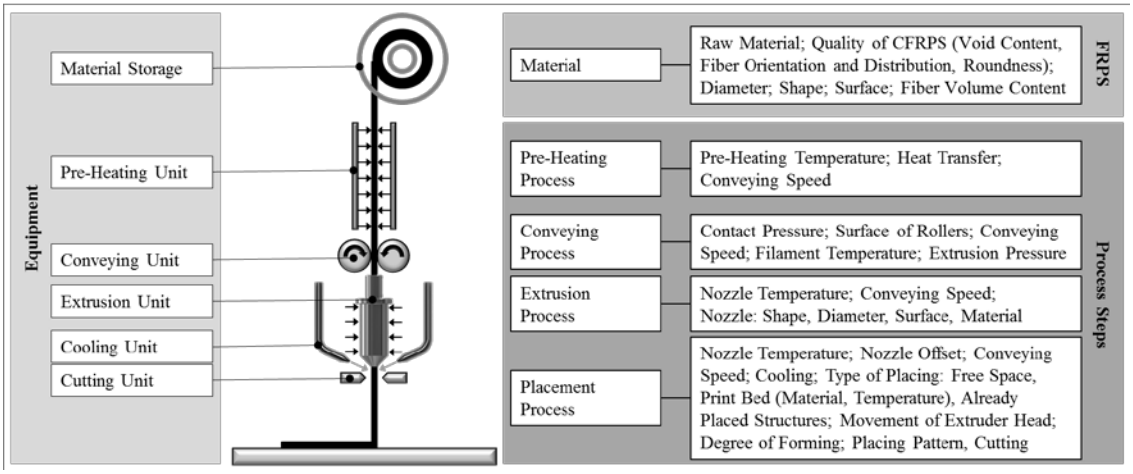


***Fig. 2*** *Process steps and influencing parameters*

In addition, known effects on the print quality characteristic of the FDM process and also new, expected effects resulting from the continuous fiber reinforcement were identified (Table 1).

***Table 1:*** *Known FDM effects and expected FIFDM effects on print quality*

| Known FDM Effects | | Expected FIFDM Effects | |
|---|---|---|---|
| Missing adhesion during placing on print bed | → Incorrect placing on print bed | Increase of friction in print nozzle due to fibers | → Slippage in conveying unit |
| Shrinkage due to cooling | → Warping | Relaxation of melted strand after leacing the print nozzle | → Expansion of cross section of strand |
| Round shapes of strands | → Gaps between placed Strands<br>→ Wavy surface | Low contact pressure during bonding of strands (applied by print nozzle offset) | → Poor bonding of strands and consolidation of laminate |
| | | Reinforcement fibers are inelastic | → Relocation of fibers,<br>→ blurred edges |

In the present paper, the bonding of the extruded FRPS during placement process is analyzed. Since time, pressure, and temperature play a major role for consolidation and thus for the quality of the laminate structures, the influence of the following parameters on laminate quality was investigated:

- Conveying speed: determined by conveying rollers
- Nozzle temperature: controlled temperature of print nozzle
- Nozzle offset: distance from print nozzle to printing bed respectively already placed structures

## 4.2 TEST METHODOLOGY FOR INVESTIGATION OF EXTRUSION AND PLACEMENT PROCESS

To receive optimal comparability of the examined print parameter settings, the test methodology consists of microscopic and macroscopic analysis as well as mechanical experiments. A distinction is drawn between analysis of the extrusion process, the placing of single FRPS, and the placing of coherent structures, like laminates. Table 2 gives an overview of the determined characteristics and the considered test methods.

***Table 2:*** *Test methodology for investigation of extrusion and placement process*

| Influence on | Quantification | Test Methode |
|---|---|---|
| Print quality<br>➢ Extrusion process<br>➢ Placing of single extruded filaments | Quality of Single Extruded FRPS | |
| | • Void content<br>• Fiber orientation<br>• Fiber distribution<br>• Outer Shape | • Micrograph: grayscale analysis<br>• Computer tomography<br>• Micrograph: center of fibers<br>• Micrograph: roundness |
| Part quality<br>➢ Placing of laminates | Outer Shape | |
| | • Dimensions, Warping<br>• Surface | • Caliper<br>• White-light interferometer |
| | Mechanical Properties | |
| | • Tensile performance<br>• Bending performance<br>• Consolidation/ layer bonding | • Tensile test<br>• 3-Point bending test<br>• Bending test (3-point o. 4-point), short bending test (ILSS), peel test |
| | Analysis of Results | |
| | • Void content<br>• Fiber orientation<br>• Fiber distribution | • Micrograph: grayscale analysis<br>• Computer tomography<br>• Micrograph: center of fibers |

Hereafter, the focus will be on analysis of mechanical characterization of printed laminates, supported by microscopic test methods like light microscopy and micro computed tomography. First mechanical characteristics are determined and compared to autoclave reference. Furthermore, a parameter study on 3-point bending specimens was carried out to investigate the influence of the major process parameters on laminate quality. For the characterization of the laminate consolidation 4 different test methods were considered: Peel, short beam, 4-point and 3-point bending tests.
3-Point bending test showed the highest reproducibility and the lowest variations with minimal testing effort. Although, results of the 3-point bending tests cannot directly be addressed to the bonding of the laminate layers, they are a good indicator for laminate quality.

## 4.3 DETERMINATION OF TENSILE AND BENDING CHARACTERISTICS

Tensile and bending characteristics are determined by following the common standards for FRPC DIN EN ISO 527-5 (specimen type A) and DIN EN ISO 14125 (specimen type IV). The specimen geometry was adjusted to height restriction for the FIFDM process, resulting from the dimension of the FRPS. Tests were carried out with an universal testing machine by Zwick (type 1474, max. 10 kN) and 5 repetitions each. The print parameter settings were determined in pre-studies [3], ensuring a stable process also for large specimens. To enable a top benchmark, the mechanical characteristics are compared to an almost idealized laminate produced by autoclave. Tensile and bending specimens were cut out of the plate following dimension specifications of above listed common standards. Table 3 shows process parameters and average specimen dimensions of tensile and bending tests.

***Table 3:*** *Process parameters and average specimen dimensions of tensile and bending tests*

| | | | | |
|---|---|---|---|---|
| **FIFDM** | • Nozzle temperature: | 235 °C | **Autoclave** | • Temperature: 190 °C<br>• Pressure: 25 bar<br>• Holding period: 20 / 60 min |
| | • Nozzle offset: | 1.2 mm | | |
| | • Process speed: | 60 mm/min | | |
| **Tensile Tests** | • Following DIN EN ISO 527-5<br>• FIFDM: 250 x 14.56 x 1.54 $mm^3$ (1 layer à 6 strands)<br>• Autoclave: 250 x 14.47 x 1.5 $mm^3$ | | **3- Point Bending** | • Following DIN EN ISO 14125<br>• FIFDM: 60 x 14.94 x 2.88 $mm^3$ (2 layers à 6 strands)<br>• Autoclave: 60 x 14.93 x 2.3 $mm^3$ |

The diagram in Fig. 3 compares the results from the tensile experiments for printed (FIFDM) and autoclave samples showing maximum tensile strength and tensile modulus. In addition, representative pictures of printed and autoclave specimens before and after testing are presented.

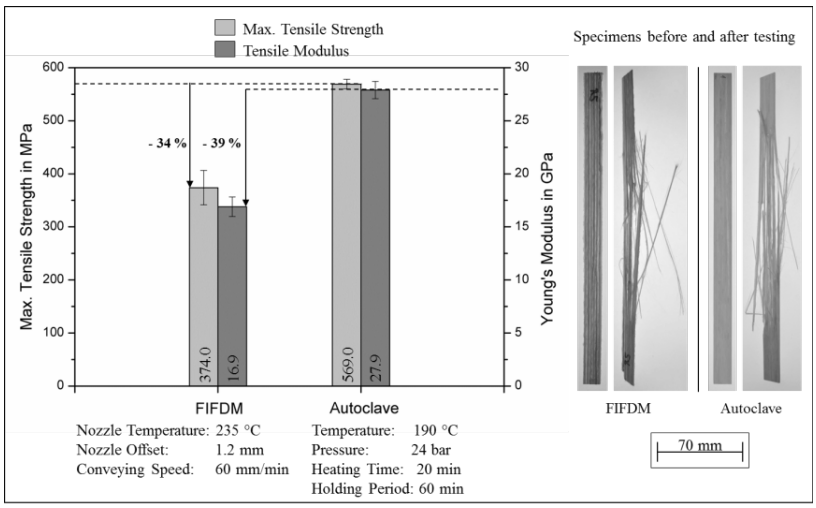


***Fig. 3*** *Comparison of tensile tests between FIFDM and autoclave specimens*

The tested specimens in Fig. 3 show a mechanical failure in the center, representing a valid tensile test. Both printed and autoclave specimens have a separate FRPS failure. In the pictures of the tested specimens the initial FRPS can be detected. It is also noticeable that the tensile strength of the printed sample is 34% and stiffness 39% lower than for the autoclave samples.
The diagram in Fig. 4 compares the results from the 3-point bending experiments for printed (FIFDM) and autoclave specimens showing maximum bending strength and flexural modulus. In addition, representative pictures of printed and autoclave bending specimens before and after testing are presented.

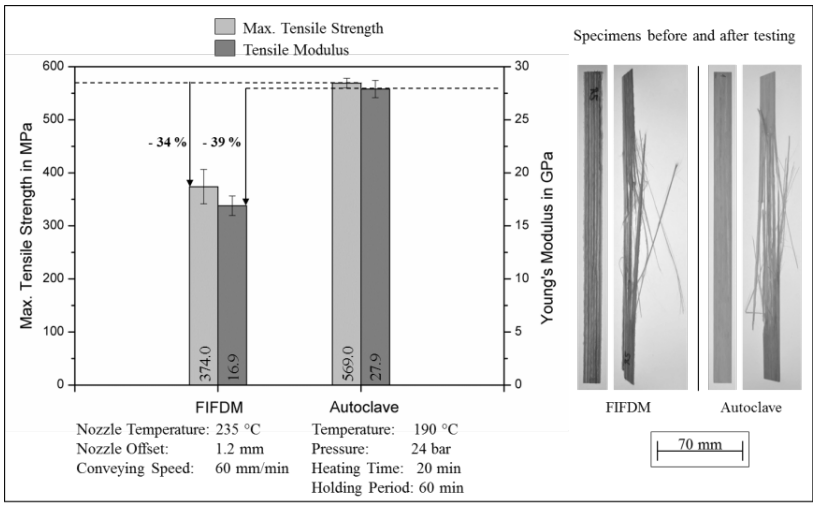


***Fig. 4*** *Comparison of 3-point bending tests between FIFDM and autoclave specimens*

The bending specimens in Fig. 4 also show a mechanical failure in the center, representing a valid 3-point bending test. While printed specimens failed by pressure load on the top side of the specimen, autoclave specimens show a combined failure of pressure and tensile load on top and bottom side. Beyond that, for several of the printed specimens, cracks occur between the two layers (Fig. 4 side view).
The influence on the mechanical properties turns out stronger for bending than for tensile experiments, considering that the maximum bending strength of the printed structure is 79% and flexural modulus 80% lower compared to the comparative autoclave values.

## Analysis of the Laminate

To explore the big difference between the tensile and bending results of printed and autoclave specimens, the specimens are analyzed by optical test methods. Especially for bending characteristics, the difference is significant. Therefore, in the following the results for bending specimens are given. Fig. 5 shows the micrographs of an untested autoclave and printed 3-point bending specimen.

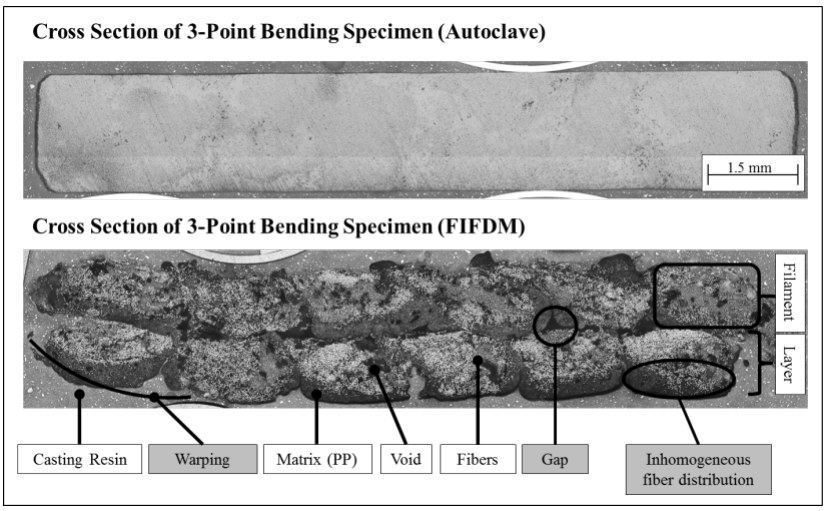


***Fig. 5*** *Micrographs of 3-point bending specimens manufactured by autoclave and FIFDM*

The cross section of the autoclave specimen shows an almost homogeneous and consolidated structure with a minor proportion of small voids. Only on closer inspection, the single FRPS becomes apparent by the distribution of fibers. This is an indication for the separated FRPS failure of the autoclave tensile specimens, which was detected for the tensile tests in Fig. 3.
However, in the cross section of the FIFDM printed specimen, all FRPS still exist as separate unit. Therefore, as expected in Table 1, the surface is significantly rougher compared to autoclave specimen. Warping perpendicular to fiber direction can be detected on the left side of the micrograph. In addition, the void content about 9.6 vol% is also much higher, consisting of voids inside the FRPS, which could not be closed during the extrusion process, and also voids and gaps between the FRPS resulting from the round shape of the FRPS. The observations indicate a worse bonding between the placed FRPS and therefore also a worse consolidation of the laminate. This strongly affects the mechanical properties of a printed product and lead to lower strength and stiffness values. Beyond that, it can be detected that the fibers in most of the extruded FRPS are shifted to the top of the FRPS. The reason for this effect is assumed in the fact, that the FRPS is temporarily bended by an angle of 90 ° during placing. As mentioned in Table 1 the fibers are not elastic and therefore the fibers following a smaller radius are crimped while fibers following a larger radius are shifted to smaller radii. Crimped fibers are straightened again when the FRPS is aligned on the print bed. Fibers shifted to the top of the extruded FRPS remain in their position because of a missing restoring force.
To get a better impression of the fiber orientation and distribution Fig. 6 presents views out of the investigation of a printed, but untested 3-point bending specimen by computer tomography.

***Fig. 6*** *Micro-computer tomography images of 3-point bending specimens*

The images following view direction 1 demonstrate that the round shape of the GF-PP FRPS leads to an inhomogeneous fiber distribution. In addition, the image following view direction 2 clearly shows that a considerable amount of fibers is not orientated straight in FRPS direction but following undulated paths. Since an analysis of the FRPS prior to printing showed that only 3% of the fibers have a deviation of more than 5 ° to FRPS direction, the printing process induces the fiber deviation.

### 4.4 PARAMETER STUDY

Following the test methodology, 3-point bending experiments were carried out to investigate the influence of process parameters on quality of laminates printed by FIFDM. In a parameter study, conveying speed, nozzle offset, and nozzle temperature are varied based on reference settings (conveying speed: 60 mm/min; nozzle offset: 1.2 mm; nozzle temperature: 235 °C). The 3-point bending characteristics were determined by following the common standards for DIN EN ISO 14125 (specimen type IV). The specimen geometry was adjusted to height restriction. The tests were carried out with an universal testing machine by Zwick (type 1474, max. 10 kN) and 5 repetitions each.

Fig. 7 shows a comparison of the results in terms of maximum bending strength and stiffness. Besides the reference two faster speeds at a distance of 30 mm/min each, two larger offsets at a distance of 0.5 mm each and two higher temperatures at a distance of 20 °C each were tested.

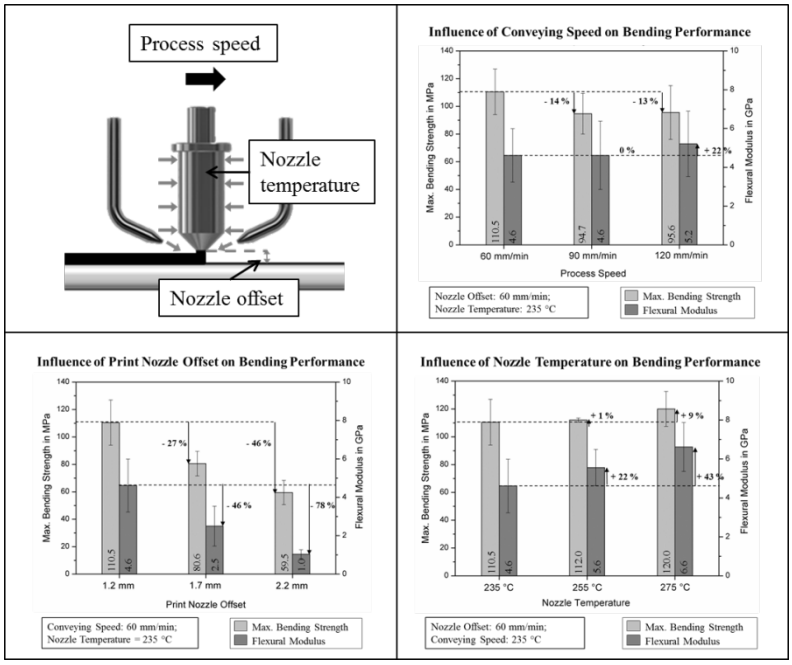


***Fig. 7*** *Bending performance for FIFDM printed specimens with different process parameters*

No definite trend of the bending properties can be detected regarding the variation of speed shown in Fig. 7. While the strength decreases for higher conveying speeds, the stiffness even increases for 120 mm/min. In addition, high standard deviation complicates to define a conclusion.

As expected, both, the bending strength and stiffness, decrease with an increasing print nozzle offset. The results indicate, that the higher nozzle offset induce a decrease of pressure which leads to a worse consolidation of the laminate. An increasing void content for higher offsets (9.6 vol% for 1.2 mm, 13.3 vol% for 1.7 mm, and 26.6 vol% for 2.2 mm) supports this statement.

Furthermore, the results in Fig. 7 show a small dependency of higher bending strength for increasing nozzle temperatures, but a significant growth of flexural modulus. Hence, better consolidation of the laminate for higher temperatures can be assumed. One reason for this is the decreasing viscosity of the PP melt for increasing extrusion temperatures. Also, the already placed FRPS can be heated to higher temperatures, supporting a better bonding.

## 5 DISCUSSION AND POSSIBLE PROCESS APPLICATIONS

The mechanical characterization of FIFDM printed specimens shows a huge gap compared to almost idealized autoclave specimens, especially when it comes to bending performance. Considering all mentioned observations by optical test methods, it becomes obvious, that the loss in tensile and bending characteristics compared to autoclave structures can be explained by a worse bonding of the FRPS, lower consolidation quality of the laminate, and disorientation of the fibers. It is assumed that the displacement of the fibers is caused by differences in the conveying and traversing speed. Reason for this can be for example slippage in the conveying unit due to the fluctuating outer contour of the FRPS material. Main cause for the worse consolidation of FIFDM compared to autoclave specimens is the lower pressure and pressure time that can be

applied in the FIFDM process. A possibility to compensate this drawback could be the increase of process temperature, as in a further tape placement study a decline of pressure influence for higher tape temperatures on consolidation quality has been found [29]. Additional solutions like consolidation devices or squared FRPS result in a limitation of process and geometry flexibility.
Even if additional process optimization can further improve the consolidation of printed laminates, it is not expected that the level of an autoclave or tape laying process can be reached. This means that the range of applications for the FIFDM process is limited. To avoid the disadvantage of lower consolidation, however, it would be conceivable to integrate the FIFDM into a process chain in which the 3D-printed structures are processed as an intermediate product in a second process, such as injection molding or pressing. Investigations in this direction have already been carried out. As a demonstrator, a bending carrier from the automotive industry was designed and a corresponding reinforcing frame made of FRPS was encapsulated with pure PP or LFT made of PP-GF in an injection molding process, see Fig. 8.

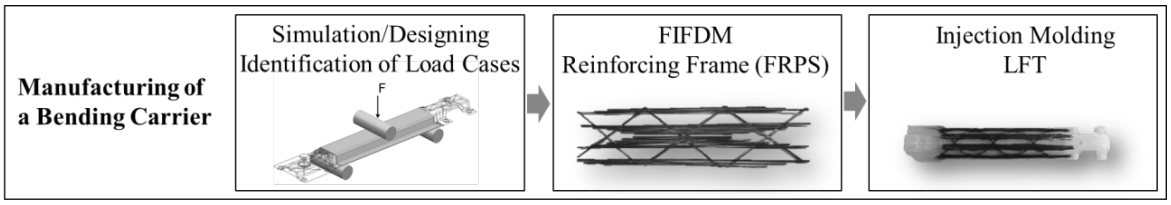


***Fig. 8*** *Manufacturing of a bending carrier by FIFDM and injection molding*

The advantage of such a process variant is that the low level of consolidation in the 3D-printing process can be compensated for by a further process step. In addition, much higher material outputs can be achieved by injection molding or pressing processes than in the 3D-printing process, but using the individualized reinforcement structures through the use of FIFDM. As a result, the FIFDM process, which is also limited in its application possibilities due to its low output, would also qualify to produce higher quantities. At the same time, injection molding or press components could be reinforced very efficiently, as the anisotropic and comparatively expensive continuous fiber reinforcement could be optimally aligned to the stresses on the component. The biggest disadvantage, however, is the loss of the individualized component geometry. Geometry-dependent tools become necessary again due to a subsequent forming process.

# 6 CONCLUSIONS

Based on a novel 3D-printing process for the processing of continuous fiber reinforced thermoplastics investigations are done to characterize mechanical performance and optimize process output and stability as well as quality of the printed parts. Therefore, theoretical process evaluation and the development of a test methodology were carried out to identify relevant influencing parameters and compare different parameter settings. An initial classification of tensile and bending characteristics show a big gap compared to autoclave reference. Main reason is the worse consolidation of the printed structures due to lower process pressure and pressure time. A parameter study was carried out to investigate the influence of conveying speed, nozzle offset, and nozzle temperature on laminate quality. Greatest opportunity to increase mechanical properties is promised by investigation of the temperature profile of the FRPS during extrusion and placement process. Further remedy could be achieved by integrating the FIFDM process in a process chain with a subsequent forming process, such as injection molding or pressing.

# 7 ACKNOWLEDGEMENT

We thank the Federal Ministry of Economic Affairs and Energy (BMWi) for funding the project EntHyLT („Development of hybrid components made of long-fibre reinforced thermoplastics and tapes") as part of Zentrales Innovationsprogramm Mittelstand (funding reference: KF2088337EB4).

## REFERENCES


[1] Ehrenstein, G. W.: *Faserverbund-Kunstoffe, Werkstoff - Verarbeitung – Eigenschaften; 2. völlig überarbietete Auflage*. Carl Hanserverlag, München, 2006.

[2] "Ernst & Young", *How will 3D printing make your company the strongest link in the value chain*. EY's Global 3D printing Report 2016, April 2016.

[3] Gebhardt, A., *Generative Fertigungsverfahren: Additive Manufacturing und 3D Drucken für Prototyping - Tooling – Produktion; 4., neu bearbeitete und erweiterte Auflage*. Carl Hanser Verlag, München, 2013.

[4] Domm, M.; Fischer, J.; Mitschang, P.: *Development of an Additive Manufacturing Process for the Processing of Continuous Fiber Reinforced Polymers*. ECCM17 - 17th European Conference on Composite Materials, München, June 26th-30th, 2016.

[5] M. Domm, J. Schlimbach and P. Mitschang: *Optimizing Mechanical Properties of Additivly Manufactured FRPC*. 21st International Conference on Composite Materials, Xi'an, August 20th-25th, 2017.

[6] Ning, F.; et al.: *Additive manufacturing of carbon fiber reinforced thermoplastic composites using fused deposition modeling*. Composite Part B 80, pp. 369-378, 2015.

[7] Tekinalp, H. L.; Kunc, V.; Velez-Garcia, G. M.; et al.: *Highly oriented carbon fiber-polymer composites via additive manufacturing*. Composites Science and Technology 105, pp. 144 -150, 2014.

[8] Nikzad, N.; Masood, S.H.; Sibarski, I.: *Thermo-mechanical properties of a highly filled polymeric composite for Fused Deposition Modeling*. Materials and Design, Vol. 32, pp. 3448-3456, 2011.

[9] Shofner, M.L.; Lozano, K.; Rodrìguez-Marìas, F.J.; et al.: *Nanofiber-Reinforced Polymers prepared by Fused Deposition Modeling*. Journal of Applied Polymer Science, Vol. 89, pp. 3081-3090, 2003.

[10] Zhong, W.; et al.: *Short fiber reinforced composites for fused deposition modeling Material*. Science and Engineering A301, pp. 125-130, 2001.

[11] Gray IV, R. W.; Baird, D. G.; Bohn, J. H.: *Thermoplastic Composites Reinforced with long fiber Thermotropic Liquid Crystalline Polymers for Fused Deposition Modeling*. Polymer Composites, Vol. 19, No. 4, August 1998.

[12] Julius, A.; Lutz, M.; Finsterbusch, K.: *Integration von Gewebe in 3D gedruckte Bauteile zur Verbesserung der mechanischen Eigenschaften*. Technische Textilien, Vol. 2, pp. 84-85, 2016.

[13] G. Schirtzinger, W. Twelves and E. Butcher: *Continuous Fiber-Reinforced Component Fabrication*. USA Patent US/2016/0114532 A1, April 28th, 2016.

[14] Fischer, A.; Rommel, S.; Bauernhansl, T.; et al.: *New Fiber Matrix Process with 3D Fiber Printer – A Strategic In-process Integration of Endless Fibers Using Fused Deposition Modeling (FDM). Digital Product and Process Development Systems*. Springer Berlin Heidelberg, p. 167–175, 2013.

[15] Prüß, H.; Vietor, T.: *Design for Fiber-Reinforced Additive Manufacturing*. Journal of Mechanical Design, Vol. 137, November 2015.

[16] Omuro, R.; Ueda, M.; Matsuzaki, R.: *Three-Dimensional Printing of Continuous Carbon Fiber Reinforced Thermoplastics by In-Nozzle Impregnation with Compaction Roller*. 21st International Conference on Composite Materials, Xi'an, August 20th-25th, 2017.

[17] Matsuzaki, R.; Ueda, M.; Namiki, M.; et al.: *Three-dimensional printing of continuous-fiber composites by in-nozzle impregnation*. Scientific Reports, March 11th, 2016.

[18] Christian, P.; Jones, I.A., Rudd, C.D.; et al.: *Monomer transfer moulding and rapid prototyping methods for fibre reinforced thermoplastics for medical application*. Composites: Part A, Vol. 32, pp. 969-976, 2001.

[19] Tian, X.; Liu, T.; Wang, Q.: *Manufacturing and Recycling of 3D Printed Continuous Carbon Fiber Reinforced PLA Composites*. 21st International Conference on Composite Materials, Xi'an, August 20th-25th, 2017.

[20] "3. Print.com": *Orbital Composites to Make 3D Printing 100 Times Faster Using Carbon Fiber, Fiber Optics, Injection & More*. April 28th, 2015. [Online]. Available: https://3dprint.com/60662/orbital-composites/. [Accessed May 28th, 2017].

[21] G. Mark: *Methods for Fiber Reinforced Addditive Manufacturing*. USA Patent US 2014/0361460 A1, December 11th, 2014.

[22] G. Mark, D. Benhaim and A. Parangi: *Methods for Fiber Reinforced Addditive Manufacturing*. USA Patent US 2015/0165691 A1, June 18th, 2015.

[23] Sugiyama, K.; Matsuzaki, R.; Ueda, M.: *3D Printing of Integrated Composite Honeycomb Sandwich Structures with Continuous Carbon Fiber*. 21st International Conference on Composite Materials, Xi'an, August 20th-25th, 2017.

[24] Zhuo, P.; Li, S.; Ashcroft, I.: *3D Printing of Continuous Fibre Reinforced Thermoplastic Composites*. 21st International Conference on Composite Materials, Xi'an, August 20th-25th, 2017.

[25] Blok, L.G.; Woods, B.K.S.; Yu, H.: *3D Printed Composites – Benchmarking the State-of-the-Art*. 21st International Conference on Composite Materials, Xi'an, August 20th-25th, 2017.
[26] Eichenhofer, M.; Wong, J.; Ermanni, P.: *Experimental Investigation of Processing Parameters on Porosity in Continuous Lattice Fabrication*. 21st International Conference on Composite Materials, Xi'an, August 20th-25th, 2017.
[27] "Anisoprint", October 2016. [Online]. Available: http://anisoprint.ru/en/. [Accessed October 21st, 2016].
[28] B. Jang, E. Ma and C. Wang: *Apparatus and Process for Producing Fiber Reinforced Composite Objects*. USA Patent 5,936,861, August 10th, 1999.
[29] Kahn, M.A.; Mitschang, P.; Schledjewski, R.: *Identification of Some Optimal Parameters to Achieve Higher Laminate Qualityx through Tape Placement Process*. Advances in Polymer Technology, Vol. 29, No. 2, pp. 98-111, 2010.

CHAPTER 4

# JOINING AND MACHINING

# SURFACE PREPARATION OF STEELS BASED ON TUNGSTEN INERT GAS ARC PROCESSING FOR LASER-BASED JOINING OF METAL-PLASTIC COMPONENTS

**Kohl, M.-L.[1,*], Schricker, K.[1], Bergmann, J. P.[1], Lohse, M.[2], Hertel, M.[2], Füssel, U.[2]**

[1]Technische Universität Ilmenau, Production Technology Group
[2]Technische Universität Dresden, Chair of Joining Technology and Assembly

**ABSTRACT:** The purpose of this research paper is to investigate the surface conditioning by TIG processing and the effect on the joining performance of plastic metal hybrids. Surface preparation by continuous-wave and pulsed-wave laser processes have been used in comparison to the TIG process. The focus of this research represents the comparison between different surface preparations based on tensile strength.

**KEYWORDS:** laser, TIG, dissimilar materials, surface preparation, structural steel, structural analysis

## 1 INTRODUCTION

In order to reduce the emission of $CO_2$, light weight constructions become more interesting, especially for the automotive industry. The weight reduction offers high potential to be used in numerous different applications and can be realized based on combinations of different materials, especially metal-plastic joints. Thereby, thermal joining provides a technology for a direct connection between both materials. The metal sheet is heated and the plastic gets molten due to the heat transfer at the boundary layer between both materials. The molten plastic wets the metal surface. After the solidification of the plastic material, a hybrid joint is formed.

Referring to the welding of plastics, the heat input can be performed by different processes, e. g. ultrasonic welding [1], induction welding [14, 16] and laser welding [13]. Laser-based thermal joining shows advantages over competitive processes by enabling an areal bonding with a high load capacity by using the laser as contactless tool. In general, regarding an overlap joint, laser based thermal joining can be classified in heat conduction joining and laser transmission joining [2, 7]. In heat conduction joining, the laser beam is focused on the surface of the metal part. Due to the heat conduction in the metal, the thermoplastic is molten at the interface and a joint can be formed [7, 15]. In contrast to transmission joining, which is also known from welding plastics, the thermal load of the plastic part is significantly reduced.

According to the literature, the joint strength can be increased significantly by surface pre-treatment of the metal joining partner. Therefore, publications show different structuring processes, e. g. laser based with continuous-wave (cw) laser [6, 12] and pulsed-wave (pw) laser [5]. High joint strength, high reproducibility and short processing times are advantages of laser surface treatment on the one hand. On the other hand, a high area output requires a high invest for an appropriate laser source. The surface preparation by tungsten inert gas (TIG) arc processing is a novel approach in order to realize a high area output by low invest costs in a short time. The TIG preparation can be realized, using a conventional welding machine as well as standard welding torches. The TIG structuring process is carried out with anodic polarized welding torch. This enables a surface cleaning as well as a surface structuring due to the punctual attachment of the arc on the metal surface.

In the literature the resulting surface topography after structuring was examined concerning roughness [4], structure distance [10, 11, 13], aspect ratio [9, 10], undercuts [3, 13], surface enlargement [8] as well as the

inspection of microsections [13]. A further characterization of a specific TIG preparation or a comparison between laser and TIG processing does not exist.

The purpose of this paper is to show a correlation between characteristic values of different structuring processes for steel and resulting tensile strength. The surface preparation was realized using arc-based surface treatment as well as pw- and cw-mode laser structuring processes. The structures were characterized using metallography cross-sections, laser scanning microscopy and SEM inspections. Those methods provide several information concerning structure topography, like structure depth, structure width as well as the area of undercuts and the surface enlargement. The tensile strength of the joint was evaluated by a pure pull-off-test. This test generates a uniform evaluation for the comparison between different surface preparations. Furthermore, tensile shear tests were implemented especially for overlap joints.

## 2 Material and experimental setup

### 2.1 MATERIALS

For the experimental investigations, an unalloyed steel (1.0330) as well as a galvanized steel (1.0322 Z100) were used. Before surface structuring the metal surfaces were cleaned with isopropyl. The metal joining partner has a dimension of 75 mm x 75 mm x 1.5 mm. Polyamide 6 (PA6) in a cylindrical form (polyamide rod) was applied as the thermoplastic joining partner (Ø10 mm x 75 mm).

### 2.2 SURFACE STRUCTURING

The surface conditioning via tungsten inert gas arc process was carried out on a partially automated setup. This setup includes a 6-axis robot, a vacuum clamping device, a welding torch and a welding machine (EWM AG). The welding torch is in anodic polarized configuration. The vacuum clamping device has the dimension of 600 mm x 800 mm and shows an integrated cooling device. For the TIG process a constant arc length (3 mm), distance arc jet (4.5 mm), electrode diameter (4 mm), electrode angle (120), distance gas diameter (15 mm), inert gas flow rate (15 l/min) and a variable electric current rate (10 A to 70 A), inert gas (Ar, Ar + 30 % He, Ar + 5 % $H_2$) as well as a variable process rate (2 mm/s to 250 mm/s).

For the laser structuring as a reference to the TIG structure, two solid state lasers were used for the preparation of the metal joining partner. Using the single mode fiber laser Trumpf TruFiber 400 ($\lambda$ = 1070 nm, $P_{L,max}$ = 400 W, $Ø_{focus}$ = 16.5 µm) in cw operation mode, the structures are generated due to the selected laser power (100 W to 400 W) and the number of repetitions (n = 1 to 6). For the pw-structuring, the Rofin PowerLine F20 ($\lambda$ = 1064 nm, $P_{L,max}$ = 20 W, $f_{pulse}$ = 20 kHz – 100 kHz, $Ø_{focus}$ = 30 µm) was used with varied laser power (12 W to 20 W) and the frequency (20 kHz to 80 kHz) as key parameters for adjusting the structures.

All structures were metallographically analyzed according to structure depth and width. Furthermore, the metallographic examination provides two-dimensional information about the presence of undercuts at the position of the microsection. In addition, laser-scanning-microscopy (LSM, Olympus LEXT OLS4000 LSM) and scanning electron microscope (SEM, Hitachi S4800-II) inspections were used for the characterization of surface structures. A special software tool enables a contour reproduction of the prepared surface, based on a black and white two-dimensionally cross-section. Thereby, the values of the surface enlargement and aspect ratio were calculated. Fig. 1 shows the measurement of a surface enlargement, based on the contour reproduction. Thereby, a segmentation in a structure area below surface baseline (structure depth) and area above surface baseline (ejection of molten steel) is possible, based on the unstructured original surface. The total measured surface enlargement results from the combination of those two area types.

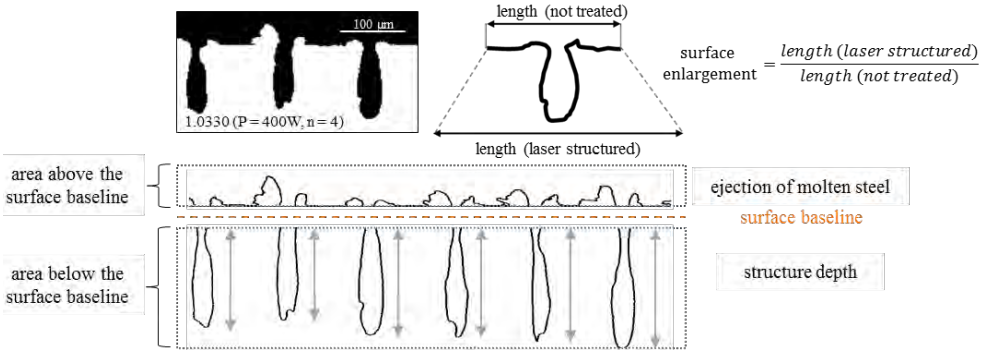


***Fig. 1*** *Experimental setup for laser based joining and tensile shear tests*

### 2.3 LASER BASED JOINING

For the laser-based joining, a diode laser Laserline LDM 1000 ($\lambda = 980$ nm, $P_{max} = 1000$ W, $Ø_{focus} = 5.7$ mm) was used. The nominal contact area between the joining partners metal and polyamide is given by the diameter of the PA6 rod ($Ø_{PA6} = 10$ mm, $A_{contact} = 78.54$ mm). In order to allow a pure pull-off-test for joining characterizing, a novel experimental setup was realized (Fig. 2, left).

For the laser based joining process, structured sheets are positioned on a holder. The setup allows a transmission of the laser beam through a recess towards the metal surface. Thereby, the laser spot is focused on the center of the sheet's bottom surface. On the top surface, the PA6 rod is fixed within the center position, using two spacers and positioners. The setup enables a heat conduction joining process by an evenly distributed joining pressure. This pressure can be adjusted by different masses placed on the top of the rod.

### 2.4 MECHANICAL TESTING

Regarding the determination of the tensile strength, a test device was realized (Fig. 2, right). This device enables a pure pull-off-test (v = 10 mm/min), whereby different surface preparations of the interface can be characterized and compared. Furthermore, tensile shear tests were implemented for the mechanical evaluation of overlap joint samples (125 mm x 25 mm).

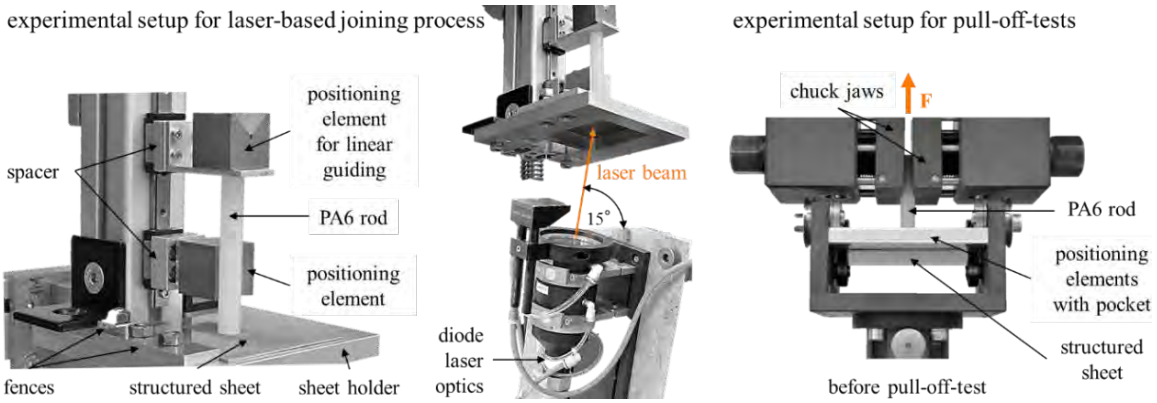


***Fig. 2*** *Experimental setup for laser based joining and pull-off-tests*

## 3 Results and discuss

### 3.1 SURFACE CONDITIONING BY TIG AND LASER PROCESSING

Considering the TIG process, the influence of process parameters, e. g. current, travel speed and the composition of shielding gas, was investigated. As a result of the input parameters from the TIG process and the used metal, different surface modifications were obtained. Fig. 3a shows an example of TIG surface structures without melting areas. In general, the observation of the surface structure depicts a stochastic distribution of grooves in sub-µm range.

In contrast to the appearance of the TIG structured surface, the laser prepared surface have a regular structure of line-shaped grooves using the pw and cw operation mode (Fig. 3a). Based on the increasing numbers of repetitions per line, the structure depth was increased as well as an enlargement of the surface area was determined next to the grooves. The number of repetitions for cw laser structure was limited to six, because the grooves were closed by material bridges due to the melt pool movement. In opposite to cw structures, the pw structuring produces wide and flat structures without undercuts, for relatively high laser power and low pulse rate. In contrast, high pulse rates in combination with high laser power generate a melt pool ejection, which results in a large number of undercuts. In contrast to microsections, the SEM and LSM inspections of surface preparation offers the possibility to provide information of the whole structured area. On this basis, structure profiles were generated at selected positions (Fig. 3a). The obtained surface geometry reveals high homogeneity and reproducibility only for laser structures.

In order to compare the structuring processes, another aspect is the area output per time. The area output is an important parameter for the efficiency and the evaluating cycle time. The TIG structuring process shows an area output up to 1800 $mm^2/s$ (Fig. 3b). This value is e. g. 10 times higher, than the cw laser structuring process for 400 W and 1 repetition.

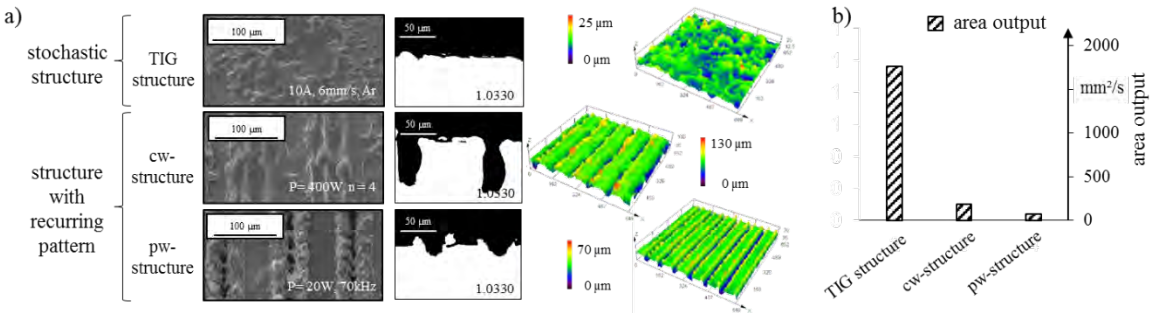


***Fig. 3*** *a) Microsections, laser-scanning-microscopy (LSM) as well as scanning electron microscope (SEM) inspections of TIG and laser structured surfaces b) area output for TIG and laser processing*

### 3.2 SURFACE ENLARGEMENT AND TENSILE STRENGTH

The resulting surface enlargement was investigated by microsections and image processing. Compared to LSM and SEM inspections, this method is more precise regarding to the illustration of undercuts. The measured surface enlargement results from the sum of the surface area below and above the surface baseline. It should be noted, that the resolution of the profile and the investigated surface enlargement is limited on microscopic structures.

Using TIG structuring, the surface enlargement rises slightly for TIG structure, compared to unstructured material (Fig. 4). In this case, only a surface enlargement of the structure area below the surface baseline is detected. The surface enlargement of the TIG structure increase minimal to a value of 2.5 (40 A, 150 mm/s, Ar) for structure type 1 and 2.8 (10 A, 150 mm/s, Ar) for structure type 2. In reference to the unstructured steel, the tensile strength of TIG structure type 1 ($2.51 \pm 0.2$ N/mm²) and type 2 ($2.79 \pm 0.39$ N/mm²) follows the minimal increase of the surface. The tensile strength is calculated with the nominal contact area (78,54 mm²). Dependent on the rise of surface enlargement, the evaluation of the value of tensile strength shows an increase for all kinds of structures in reference to unstructured 1.0330 ($2.3 \pm 0.4$ N/mm²). The results of the pull-off-test depicts an increase of tensile strength, e. g. for TIG structure type 2 up to factor 1.09, also in interaction with a surface enlargement.

The tensile strength of pw structures increases linearly depending on surface enlargement. For pw structuring, the surface enlargement increases in reference to unstructured 1.0330 (1.03) up to 1.88 ($P_L$ = 100 %, $f_{Laser}$ = 60 kHz) and 1.33 ($P_L$ = 100 %, $f_{Laser}$ = 70 kHz). The increase of the area above as well as below the structure baseline is not linear. Further the tensile strength of pw structure increase up to $10 \pm 0.7$ N/mm² ($P_L$ = 100 %, $f_{Laser}$ = 60 kHz) and $8.4 \pm 0.5$ N/mm² ($P_L$ = 100 %, $f_{Laser}$ = 70 kHz), also dependent on the surface enlargement.

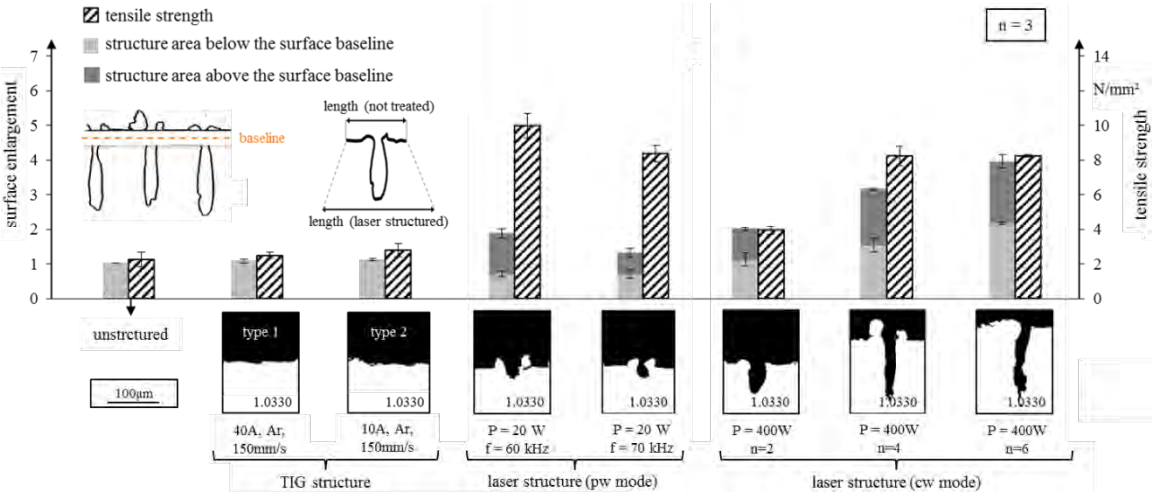


***Fig. 4*** *Examples of the surface enlargement according to tensile strength (1.0330)*

In contrast to TIG and pw structures, the cw structure shows a linear increase of the surface enlargement, dependent on the number of structuring replicates (n). Those replicates result in different structure depths and widths. Furthermore, a linear enlargement of the area below as well as above the surface baseline is

generated up to 4 replicates. For example, up to 2 replicates (n = 2), the surface area enlarged by a factor of 1.1 (1.13) for the area below and 0.9 for the area above the surface baseline, in comparison to unstructured surface (1.03). After the number of 4 replications, a surface enlargement only increases for the structure area below the surface baseline and the tensile strange stagnates. A stagnation of tensile strength is reached because the PA6 is not able to fill the whole structure depth based on a short process time.

In summary, the tensile strength increases for all structures, depending on surface enlargement. It should be noted, that the structuring process as well as the used material is decisive for the increase of the tensile strength. Further investigations were carried out for 1.0322 Z100, whereby an increase of tensile strength (unstructured: 3.1 ± 0.13 N/mm², TIG structured: 6.86 ± 1.38 N/mm²) is much higher in contrast to 1.0330 (unstructured: 1.62 ± 0.11 N/mm², TIG structured: 2.64 ± 0.28 N/mm²). Thereby, the zinc layer at the surface generates a benefit for the hybrid joint [17], wherefore the zinc coated steel 1.0322 Z100 will be used for further investigations.

### 3.3 TRANSFER OF THE RESULTS ON OVERLAP JOINTS AND TENSILE-SHEAR STRENGTH

Based on the industrial application of plastic metal hybrids, the results of the investigations of PA6 metal point joints are transferred to overlap joints. Next to the single matrix material PA6 as a joining partner for the metal 1.0330 and 1.0322 Z100, glass (PA6GF50) as well as carbon fiber reinforced polyamides (PA6CF50) are used. Thereby, the evaluation of pull-off-tests is changed in tensile shear tests. Fig. 5 shows the tensile shear strength using the material combination 1.0322 Z100 – PA6 and 1.0322 Z100 - PA6CF50. In contrast to unstructured metals, the surface preparation enables an increase of tensile shear strength for all investigated surface pretreatments and used polyamide joining partners.

Compared to unstructured 1.0322 Z100 (3.12 ± 0.31 N/mm²), the tensile shear strength of TIG structured joints increases up to 6.25 ± 0.6 N/mm² (1.0322 Z100 – PA6) and 12.38 ± 0.85 N/mm² (1.0322 Z100 - PA6GF50), dependent on the structure type (20 A, 3 mm/s, Ar). In contrast, the cw-structure exhibits a value of 7.9 ± 0.23 N/mm² (1.0322 Z100 – PA6) and 17.39 ± 0.67 N/mm² (1.0322 Z100 - PA6GF50) as well as 7.82 ± 0.17 N/mm² (1.0322 Z100 – PA6) and 17.39 ± 0.81 N/mm² (1.0322 Z100 - PA6GF50) for pw-structure. In contrast to PA6 metal hybrids, using fiber reinforced polyamides enables an increase of tensile shear strength up to factor 5.6 for laser structures and factor 4 for TIG structures. Under the use of fiber reinforced polyamides, the tensile shear strength is getting double in comparison to the use of the matrix material PA6 for all kinds of structures. The penetration of fibers into structures generates a benefit regarding to the increase of tensile shear strength. Further, for all measured tensile shear strength the standard deviation is negligibly small.

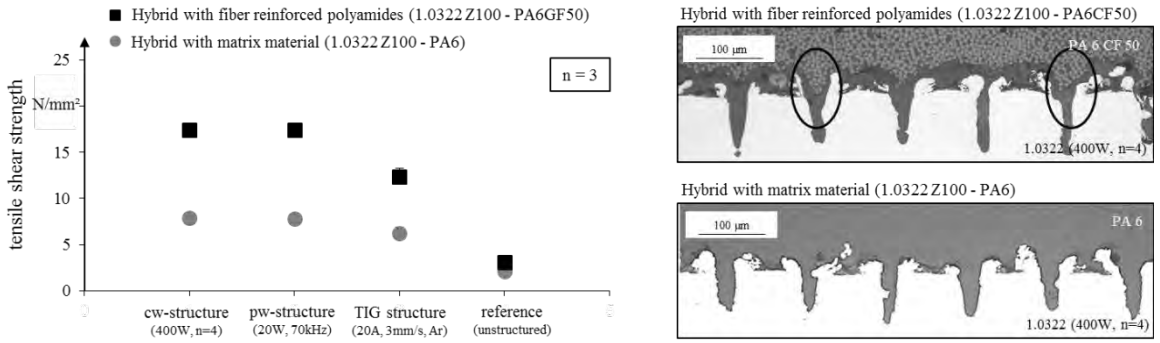


***Fig. 5*** *Examples of the tensile shear strength based on different polyamide joining partners (1.0322 Z 100)*

## 4 CONCLUSIONS

In this paper, investigations were carried out concerning polyamide-steel hybrid joints. Focus of the examination was the characterization of different structured steels. Therefore, micrographs, laser scanning microscopy and scanning electron microscopy inspections were applied. On this basis, the surface enlargement was determined as a characteristic value and correlated to tensile strength due to pull-off-tests.

In summary, the structuring of steel allows an increase of tensile strength as well as tensile shear strength, dependent on the used structuring process. Whereby, cw and pw structures show a higher level of tensile strength compared to TIG structures. The maximal tensile shear strength for cw, pw and TIG structure are 7.15 ± 1.28 N/mm², 15.88 ± 0.8 N/mm² and 3.25 ± 0.69 N/mm² (unstructured: 2.21 ± 1.17 N/mm²) using 1.0330. In contrast, the zinc layer of the material 1.0322 Z100 generates a further increase of tensile shear

strength: 17.39 ± 0.67 N/mm² (cw), 17.39 ± 0.81 N/mm² (pw), 12.38 ± 0.85 N/mm² (TIG) and 3.12 ± 0.31 N/mm² (unstructured). Furthermore, in contrast to laser manufactured structures, the characterization of TIG structures is more difficult, based on the stochastic distribution of grooves as well as micro- and nanoscale structures. In further investigations, the TIG structuring process will be optimized for the increase of tensile strength as well as tensile shear strength. Particularly, the producing of undercuts is useful to increase the surface enlargement. For the TIG process, shielding gases with oxygen will be applied to achieve a positive impact on the joint due to the formed oxide layer.

## 5 ACKNOWLEDGEMENT

The investigations were carried out within the project "TIG based surface texturing of steel and laser based joining with fibre reinforced plastics" from the research association for steel application (FOSTA, Research Association for Steel Application). The research project (IGF-Nr. 19042 BR) is supported by the federal ministry of economic affairs and energy within the German Federation of Industrial Research Associations (AiF - Arbeitsgemeinschaft industrieller Forschungsvereinigungen „Otto von Guericke“ e. V.), which is based on a resolution of the German parliament. We would like to thank all funding organizations as well as the project support committee led by Mr. Dipl.-Ing. Rainer Salomon (FOSTA).

## REFERENCES

[1] Balle, F.: *Ultraschallschweißen von Metall/C-Faser-Kunststoff (CFK)-Verbunden.* Kaiserslautern : Techn. Univ., 2009.
[2] Bergmann, J. P.; Stambke, M.: *Potential of Laser-manufactured Polymer-metal hybrid Joints.* Physics Procedia 39, 84–91, 2012.
[3] Engelmann, C.; Eckstaedt, J.; Olowinsky, A.; Aden, M.; Mamuschkin, V.: *Experimental and Simulative Investigations of Laser Assisted Plastic-metal-joints Considering Different Load Directions.* Physics Procedia 83, 1118–1129, 2016.
[4] Fuchs, A. N.; Wirth, F. X.; Rinck, P.; Zaeh, M. F.: *Laser-generated Macroscopic and Microscopic Surface Structures for the Joining of Aluminum and Thermoplastics using Friction Press Joining.* Physics Procedia 56, 801–810, 2014.
[5] Heckert, A.; Singer, C.; Zaeh, M.F.; Daub, R.; Zeilinger, T.: *Gas-tight thermally jointed metal-thermoplastic connections by pulsed laser surface pre-treatment.* Physics Procedia 83, 1083-1093, 2016.
[6] Heckert, A.; Singer, C.; Zaeh, M.F.: *Pulsed laser surface pre-treatment of aluminum to join aluminum-thermoplastic hybrid parts.* Proceedings of LIM 2015, Munich, Germany, 2015.
[7] Heckert, A.; Zaeh, M.F.: *Laser surface pre-treatment of aluminum for hybrid joints with glass fiber reinforced thermoplastics.* Physics Procedia 56, 1171-1181, 2014.
[8] Klotzbach, A.: *Thermal direct joining of metal-polymer connections.* Dresden, 2016.
[9] Rodriguez-Vidal, E.; Lambarri, J.; Soriano, C.; Sanz, C.; Verhaeghe, G.: *A Combined Experimental and Numerical Approach to the Laser Joining of Hybrid Polymer-Metal Parts*. Physics Procedia 56, 835–844, 2014.
[10] Rodriguez-Vidal, E.; Sanz, C.; Soriano, C.; Leunda, J.; Verhaeghe: *Effect of metal micro-structuring on the mechanical behavior of polymer-metal laser T-joints.* Journal of Materials Processing Technology 229, 668–677, 2016.
[11] Roesner, A.; Scheik, S.; Olowinsky, A.; Gillner, A.; Reisgen, U.; Schleser, M.: *Laser Assisted Joining of Plastic Metal Hybrids.* Physics Procedia, 370–377, 2011.
[12] Rodriguez-Vidal, E.; Sanz, C.; Lambarri, J.; Renard, J.; Gantchenko, V.: *laser joining of different polymer-metal configurations: analysis of mechanical performance and failure mechanism*. International conference on photonic technologies, Physics procedia 83, 1110-1117, 2016.
[13] Rösner, A.: *Laserbasiertes Fügeverfahren zur Herstellung von Kunststoff-Metall-Hybridbauteilen.* Aachen, Techn. Hochsch., Diss., 2014. Stuttgart: Fraunhofer-Verl., 2014.
[14] Scheik, S.: *Untersuchungen des Verbundverhaltens von thermisch direkt gefügten Metall-Kunststoffverbindungen unter veränderlichen Umgebungsbedingungen.* Shaker Verlag, Aachener Berichte Fügetechnik 1/2016, 2016.
[15] Schricker, K.; Stambke, M.; Bergmann, J. P.; Bräutigam, K.: *Laser-based joining of thermoplastics to metals: influence of varied ambient conditions on joint performance and microstructure*. International Journal of Polymer Science, 9 p., 2016.
[16] Velthuis, R.: *Induction welding of fiber reinforced thermoplastic polymer composites to metals*. Kaiserslautern, Techn. Univ., Diss., 2007.

[17] Jung, K. W.; Kawahito, Y.; Takahashi, M.; Katayama, S.: *Laser direct joining of carbon fiber reinforced plastic to zinc-coated steel.* Materials and Design 47, 179-188, 2013.

# LASER SURFACE TREATMENT OF CFRP AND TI6AL4V FOR ADHESIVE BONDING OF HYBRID JOINTS

**B. Rauh[1*], S. Kreling[2], H. Fietzek[1], M. Suess[3], M. Geistbeck[1], K. Dilger[2]**

[1] Airbus, Central Research & Technology, Munich, Germany.
[2] Institute of Joining and Welding, Technische Universität Braunschweig, Braunschweig, Germany.
[3] Airbus Defence and Space GmbH, Space Systems, Mechanical Subsystems and R&T FHN, Friedrichshafen, Germany

**ABSTRACT:** In aerospace industry, innovative design concepts which offer weight saving are widely discussed. Advanced lightweight design is often characterized by choosing the right material for the right application. In this context adhesive bonding is recommended to fully utilize the material and joining properties. Laser treatment shows promising results to represent a reliable surface treatment technology to prepare composite and metal surfaces for adhesive bonding. In this study ns-pulsed laser systems are used to remove adhesion-weakening contaminations off composite surfaces and to generate open porous oxide structures on metals. An ultra-violet laser cleaning process, based on 266 nm wavelength, was developed to reduce the exposure of carbon fibres on the CFRP side during pretreatment. Scanning electron microscopy (SEM) and x-ray photoelectron spectroscopy (XPS) investigations of different carbon fibre reinforced thermoplastic and thermoset materials reveal the influence of this laser cleaning process on the chemical composition and the surface morphology. The positive impact of the laser cleaning process on adhesive bonding is shown by an 100 % increase of joint strength compared to the reference process manual grinding. Single lap shear tests of adhesively bonded joints with laser pre-treated Ti6Al4V substrate surfaces, with laser pre-treated carbon fibre reinforced thermoset and thermoplastic substrate surfaces as well as with Ti6Al4V-CFRP hybrid samples demonstrate the high potential of laser technology for surface preparation before adhesive bonding.

**KEYWORDS:** laser; surface treatment; adhesive bonding; cfrp; Ti6Al4V; composites; hybrid joint; cleaning

## 1 INTRODUCTION

Aerospace products are based on advanced lightweight design by choosing the right material for the right application. The use of mix-material concepts requires adequate joining technologies. In this development adhesive bonding is offering promising advantages by reducing induced micro-cracks and weight compared to current riveting processes [1], [2]. In order to enable a reliable bonding process, the substrate surface has to be prepared as surface contaminations or morphology affect the bonding strength [3]–[7]. On Ti6Al4V surfaces, the possibility to generate a stable oxide layer with an open-porous morphology by laser irradiation was already investigated [8]. The surface enlargement as well as the undercuts in the surface pores lead to high joint strength after hot/wet aging [8]. On CFRP surfaces different approaches were made regarding the use of laser technology. The possibility to ablate the epoxy resin to expose the fibres and to bond directly on the fibres was the most often used approach [9], [10]. In recent investigations the opportunity to remove the contaminations without exposing the fibres were examined [5], [11]. It was indicated that a smooth treatment, that does not expose the fibres leads to higher joint strengths [5].
This study examines the influence of IR laser irradiation of different peak powers per area on the Ti6Al4V oxide layer. Furthermore, a UV laser treatment is presented on an epoxy based CFRP and adapted to another epoxy based CFRP as well as a carbon fibre reinforced PPS material. The effect on the substrate bonding performance is evaluated via single lap shear tests.

# 2 EXPERIMENTAL

## 2.1 MATERIALS

For the metal samples, Ti6Al4V alloy according to material number 3.7164 as sheet material with a thickness of 1.6 mm was used. This study, investigates two different carbon fibre reinforced epoxy systems that are used in industry to build e.g. satellite panels. For CF-EP1, YSH70A carbon fibres from Mitsui in combination with LY556/HY906/DY062 epoxy material were used. CF-EP2 builds up of M60J carbon fibres from Torayca and L20/EPH960 epoxy material. Eight uni-directional layers were oriented in quasi-isotropic setup with 0° top-layers and 1.6 mm overall thickness. For both epoxy based CFRPs, the release agent Frekote 44-NC from Henkel was used to allow demoulding from the metallic moulds. For CF-PPS, a quasi-isotropic material with a thickness of 2.17 mm was produced by using T300JB/PPS-fabric and F-based release film. The adhesives EA9321 Aero from Henkel Loctite and the EC9323-2 from Scotch-Weld were used. 1 wt.% of glass bowls with 75-150 µm diameter were added to adjust the bondline thickness.

## 2.2 SURFACE ANALYTICS

In order to evaluate the influence of different laser treatments on the CFRP and metallic materials, the surfaces were investigated with different surface analytics.

**Scanning electron microscopy (SEM)**

A JEOL JSM-6320 and Zeiss Auriga field-emission scanning electron microscope (SEM) with an acceleration voltage of 15 kV was used to evaluate surface morphologies.

**X-ray photoelectron spectroscopy (XPS)**

The Quantum 2000 Scanning ESCA Microprobe from Physical Electronics Inc. has a beam diameter of 200 µm and allows the detection of all elements with an atomic number of 3 and above.

## 2.3 SINGLE LAP SHEAR (SLS)

Single lap shear tests were conducted to evaluate the adhesive bonding strength. These tests were performed acc. to DIN EN 1465 with sample dimensions of 100 mm x 25 mm. In order to evaluate the failure criteria, the following criteria explanations (acc. to DIN ISO 10365, additional CSF-resin, CSF-fibre, CSF-metal added) were used:
AF = Adhesion failure
CF = Cohesive failure in the adhesive
CSF-fibre = Fibre tear out
CSF-resin = Inter-resin failure or interface resin-fibre failure
CSF-metal = Failure in the oxide layer

# 3 SURFACE TREATMENT

## 3.1 LASER SURFACE TREATMENT OF TI6AL4V

Some wet chemical generated oxide layers as pre-treatment for bonding of Titanium materials reveal critical long term durability regarding adhesion [12]. Preliminary studies showed that laser treatment of titanium surfaces can enhance their bonding capabilities especially regarding hot/wet aging [8], [13]. It was shown that the treatment of Ti6Al4V with a ns-pulsed IR-laser (1064 nm) generates an open-porous and stable oxide layer which led to similar bonding strengths in dry and after hot/wet conditioning [8]. The same laser source was used for the treatment of Ti6Al4V in this study. Based on the work done by Kurtovic et al. [8], laser parameters were varied to identify the influence of scanning speed and hatch on the oxide layer. The different laser parameter sets are defined in *Table 1*.

***Table 1:*** *Laser parameter definition for Ti6Al4V ([1] acc. to* [3]*)*

| Parameter [-] | Frequency [kHz] | Pulse duration [ns] | Peak power per area[1] [W/mm²] | Passes [-] |
|---|---|---|---|---|
| IR – LP 1 | 10 | 13 | 1.6 | 1 |
| IR – LP 2 | 10 | 13 | 3.2 | 1 |
| IR – LP 3 | 10 | 13 | 6.5 | 1 |
| IR – LP 4 | 10 | 13 | 13 | 3 |

### 3.2 LASER SURFACE TREATMENT OF CFRP

Due to the light absorbance of epoxy material and of Si-based release agent an UV-laser system is most suitable to treat CFRP surfaces [5]. It allows a very thin ablation of resin material while hardly exposing the embedded carbon fibres [5]. In this study a ns-pulsed UV laser from Coherent is used with 266 nm wavelength.

***Table 2:*** *Laser parameter definition for CF-EP1*

| Parameter [-] | Frequency [kHz] | Pulse duration [ns] | Fluence [J/cm²] | Focus position |
|---|---|---|---|---|
| LP 1 | 30 | 20 | 0.12 | Defocused |
| LP 2 | 30 | 20 | 0.24 | Focused |

Defocusing increases the pulse overlap and thus leads to a higher amount of pulses per surface increment. The parameter LP 1 leads to chipping and peeling off of the surface contaminations while hardly exposing the fibres [5]. The parameter LP 2 is exposing the fibres due to a higher fluence.

On CF-EP2 and CF-PPS, the parameter LP 1 was adapted to generate a clean and smooth surface. For CF-EP2 the hatch distance of LP 1 was decreased by 33 % in order to achieve homogeneous ablation. The average laser power was varied to investigate the ablation behaviour of the topmost epoxy resin layer.

***Table 3:*** *Laser parameter definition for CF-EP2*

| Parameter [-] | Frequency [kHz] | Pulse duration [ns] | Average power [%] |
|---|---|---|---|
| LP 1 | 30 | 20 | 100 |
| LP 1, 50 % | 30 | 20 | 50 |
| LP 1, 6.25 % | 30 | 20 | 6.25 |

***Table 4:*** *Laser parameter definition for CF-PPS*

| Parameter [-] | Frequency [kHz] | Pulse duration [ns] | Average power [%] |
|---|---|---|---|
| LP 1 | 30 | 20 | 100 |
| LP 1, 50 % | 30 | 20 | 50 |
| LP 1, 25 % | 30 | 20 | 25 |

## 4 RESULTS AND DISCUSSION

### 4.1 SURFACE INVESTIGATIONS

**Ti6Al4V**

The surface of the Ti6Al4V sheet material showed a homogeneous surface topology in the initial state (*Figure 1*). During treatments with different laser parameters open porous oxide layers were formed (*Figure 2*). From the top view an increasing coarse of the nanostructure is noticeable for an increasing ratio of peak power per area. Furthermore, the oxide layer is getting thicker for increasing values of the peak power per area: approx. 200 nm for IR-LP 1 and 1.75 µm for IR-LP 4.

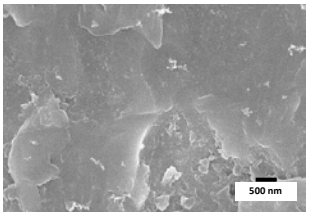


Initial

***Fig. 1*** *SEM- micrograph of initial Ti6Al4V surface*

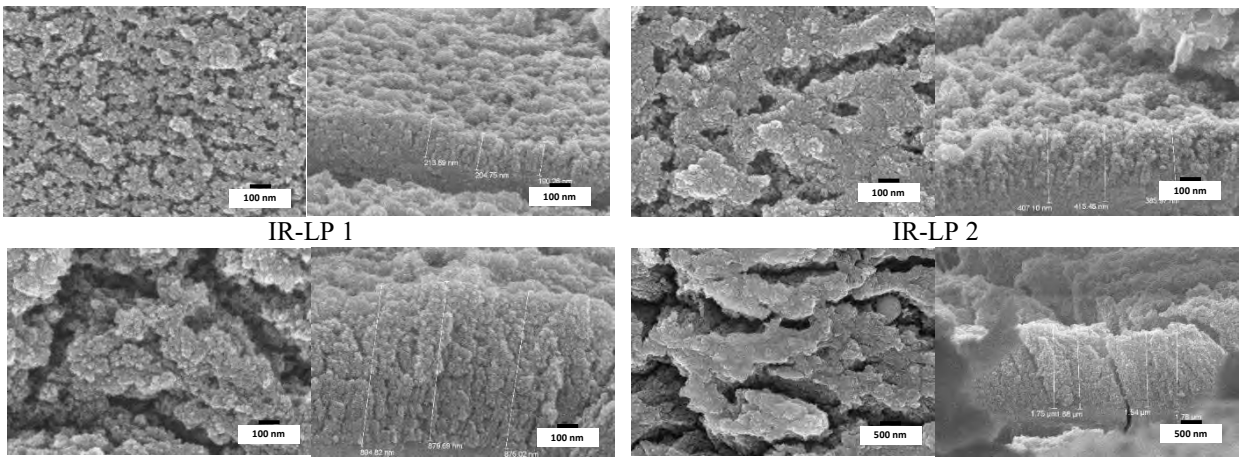


IR-LP 1 IR-LP 2

IR-LP 3 IR-LP 4

***Fig. 2*** *SEM- micrographs of laser treated Ti6Al4V surfaces and cross-sections*

**CFRP**

In the initial state – after production - the CF-EP1 surface is characterized by a rough topology (*Figure 3*). There are carbon fibres observable as well as imprints from the metal mould. XPS-measurements revealed residues of the Si-based release agent with a surface contamination containing 10.9 at.% Si.

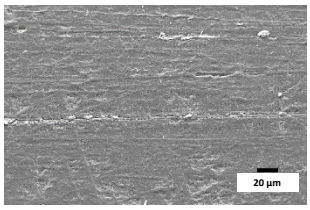


10.9 at. % Si
Initial

***Fig. 3*** *SEM- micrograph of initial CF-EP1 surface*

Laser treatment of CF-EP1 with both parameter sets leads to a significant reduction of remaining silicone on the surface. XPS measurements showed 0.2 at.% Si for LP 2 and 1.0 at.% Si for LP 1 after laser treatment (*Figure 4*). A higher fluence (LP 2) led to exposed fibre surfaces and induced little pits in the interface between the fibres and the surrounding epoxy material. This indicates a thermal impact. LP 1 generated a smoother surface and hardly exposed any fibres. Additionally, the fibre-resin interface showed no sign of thermal influence.

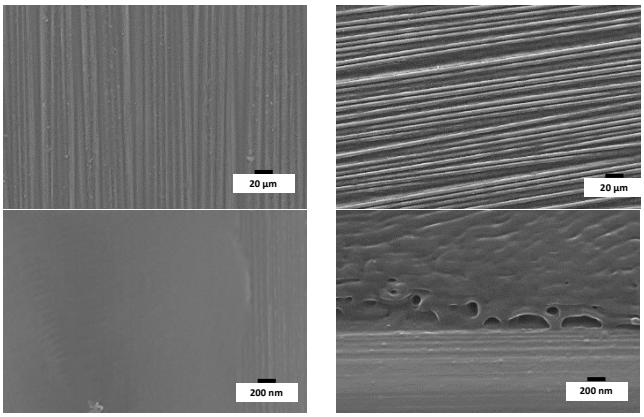


1.0 at. % Si
LP 1

0.2 at. % Si
LP 2

***Fig. 4*** *SEM- results of laser treated CF-EP1*

On the surface of CF-EP2 in the initial state approx. 0.3 at.% of Si are measured via XPS. Although using the same release agent for the manufacturing as for CF-EP1, a significantly lower amount of the release agent is transferred to the CF-EP2 surface during demoulding. This allows the use of lower amount of laser energy to treat the surface. LP 1 led to exposed fibres while with LP 1, 50 % only the tips of fibres were exposed (***Figure 5***). LP 1, 6.25 % led to no observable modification of the surface topology. XPS-measurements showed a cleaning effect for LP 1, while after laser treatment with lower energy the values of silicon had not changed significantly compared to the initial state.

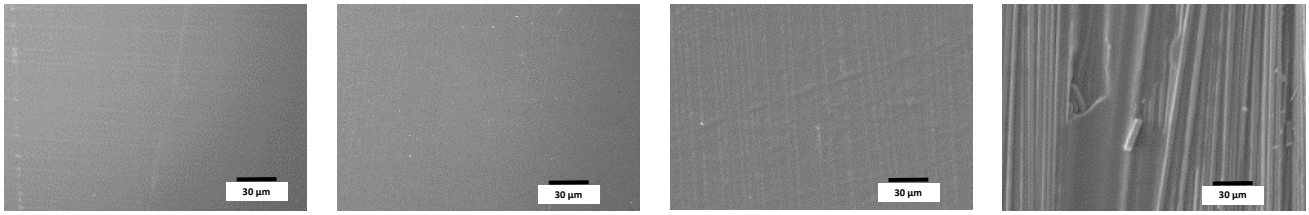


***Fig. 5*** *SEM- and XPS-results of laser treated CF-EP2*

Due to the F-based release film in the production, the CF-PPS material showed a low amount of fluorine in the initial state (0.4 at.% F). After laser treatment with LP 1, LP 1, 50 % or LP 1, 25 % the XPS measurements showed no remaining F anymore (*Figure 6*). Like for CF-EP2 the parameter LP 1 exposed the topmost fibres and the parameter LP 1, 50 % exposed the tips of the fibres. After treatment with LP 1, 25 % no modification of the surface morphology is observable on the SEM images.

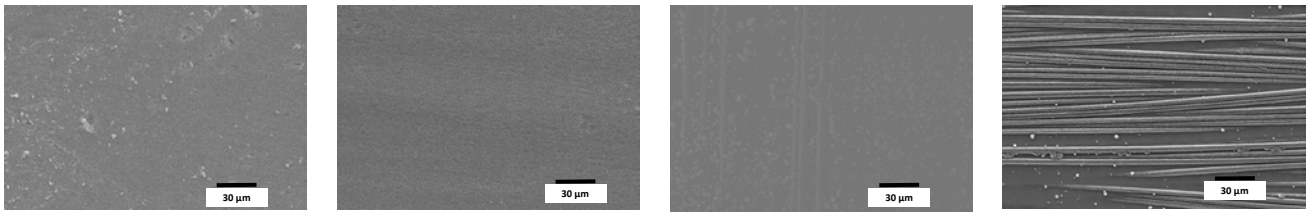


***Fig. 6*** *SEM- and XPS-results of laser treated CF-PPS*

### 4.2 SINGLE LAP SHEAR RESULTS OF SINGLE MATERIAL COMBINATION

IR-LP 1 was already used in [8] and showed high resistance of the substrate surface regarding adhesively bonded Ti6Al4V joints in hot/wet conditions. Thus, the bonding tests in this study were conducted only in dry condition although long-term stability of titanium joints should be tested for further applications. The single lap shear tests of adhesively bonded Ti6Al4V joints showed high shear strength values on comparable levels for all laser treatments (*Figure 7*).

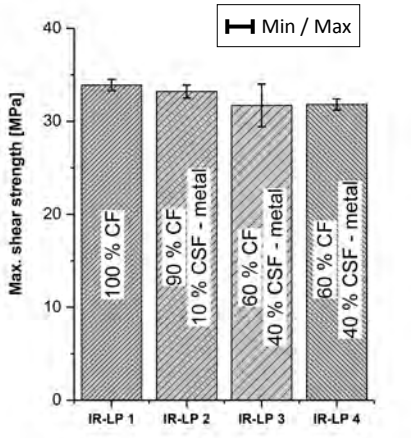


***Figure 7:*** *Ti6Al4V - single lap shear results after different treatments (min/max due to 3 samples per batch)*

The failure criteria of the bondlines reveal an increasing share of failure occurring in the oxide layer with increasing thickness. The thicker the oxide layer the higher the chance that it is breaking. As a result, oxide material was visible in the fracture surfaces, adhering to the adhesive side. The laser parameter with lowest ratio of peak power per area, led to 100 % cohesive failure in the adhesive.

The initial surface of CF-EP1 shows almost no bonding strength with failure occurring in the interface between adhesive and substrate surface (*Figure 8*). This result proves the necessity of surface preparation. Manually grinding the surface changed the failure criteria to failure in the substrate material but revealed only joint strengths of approx. 12.5 MPa. Laser treatment doubled the joint strength. The highest joint strength was achieved by a surface which was treated with the laser parameter LP 1. LP 1 had a lower thermal impact onto the surface than LP 2. Regarding CF-EP2, the initial surface led to high joint strengths due to the low amount of contaminations on the surface. But the standard deviation is relatively high. Grinding the surface reduces the joint strength as it led to fibre tear out. Laser treatment with LP 1 which led to fibre exposure on this material, reduces the joint strength too. Adapting the laser energy to 6.25 % power led to joint strengths of approx. 35 MPa and a bondline failure predominantly between resin and fibres. The surface of CF-PPS showed no bonding strength in initial condition and after grinding. Both sample batches failed due to adhesion failure. This indicates that the PPS material does not build up bonds to the epoxy adhesive. After laser treatment the bonding performance of the substrate changed significantly and led to predominantly failure in the adhesive and joint strengths of approx. 25 MPa.

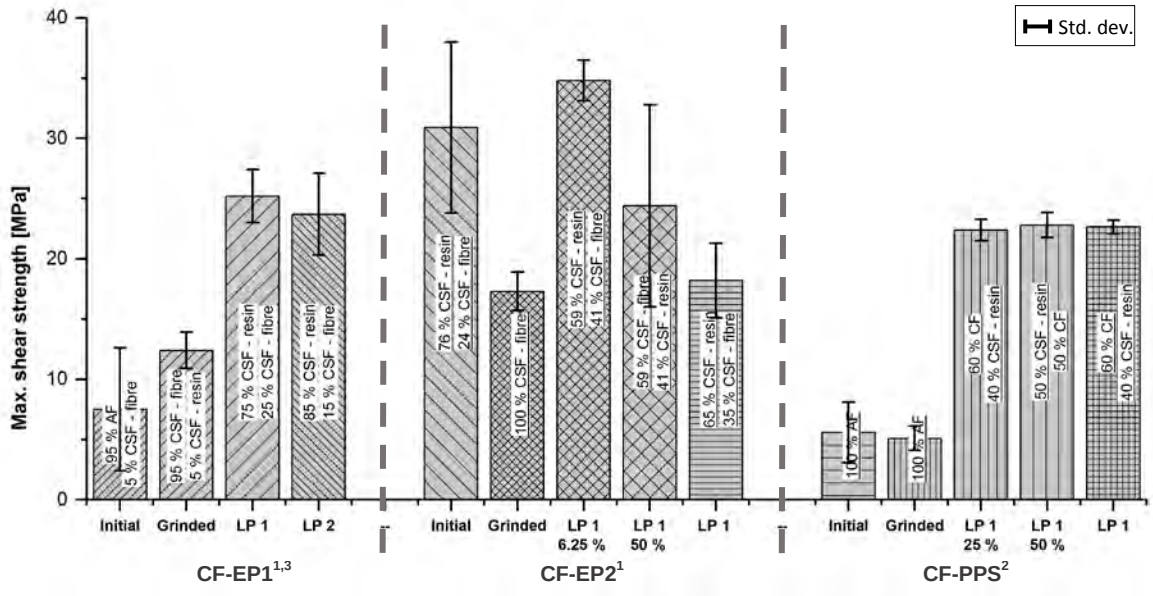


***Fig. 8*** *CFRP - single lap shear results after different treatments ([1] EA9321 Aero, [2] EC9323-2 B/A, [3] reproduced with permission* [5]*)*

### 4.3 SINGLE LAP SHEAR RESULTS OF HYBRID MATERIAL COMBINATION

*Figure 9* shows the results of the single lap shear testing of adhesively bonded CFRP-Ti6Al4V hybrid joints. Whereas for CF- EP1 and EP2 the thickness of the CFRP and metal partner was the same, for CF-PPS the thickness was adapted to gain the same bending stiffness. CF-EP1 showed enhanced joint strength of hybrid joints compared to pure CFRP joints. In contrary CF-EP2 showed significant reduced joint strength. The carbon fibres YSH70A, the fibres of CF-EP1, have approx. 22 % higher tensile modulus compared to M60JB, the fibres of CF-EP2. As this has a strong impact on the bending stiffness, the CF-EP2 samples have a lower stiffness than CF-EP1 samples. Therefore, the bending effect that can occur for the weaker part of a hybrid joint, is intensified for CF-EP2. Beside the shear strength value, the failure criteria for CF-EP2 is changing to fibre tear out. This phenomenon is observable for all hybrid samples, but in comparison between CF-EP1 and CF-EP2 this is intensified for CF-EP2. This is an indication that the bending affects the failure criteria by an occurring peeling effect. Although CF-PPS has the same theoretical bending stiffness as the Ti6Al4V joint partner, the bondline predominantly failed by fibre tear out too. An explanation could be that inhomogeneities of the production process such as ondulation are reducing the stiffness and leading to the phenomenon explained above. Overall the hybrid joints showed strength values between 25 and 30 MPa with a failure in the substrate and the adhesive material.

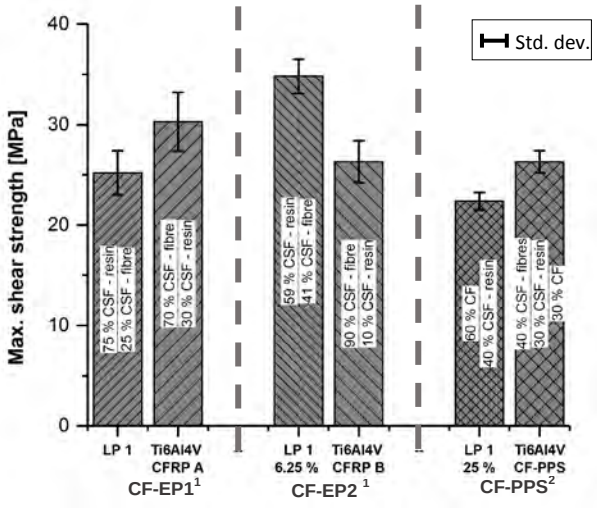


***Fig. 9*** *Single lap shear results of hybrid joints in comparison to CFRP-CFRP joints ([1] EA9321 Aero, [2] EC9323-2 B/A)*

## 5 CONCLUSIONS

For Ti6Al4V it was shown that with IR laser treatment an open-porous oxide was formed with a layer thickness dependent of the peak power per area. Thicker oxide layer failed due to separation of the oxide material but led to only slightly reduced joint strength. For CFRP a laser process was presented that led to a clean and smooth surface on CF-EP1. In order to use the same parameter on CF-EP2, the laser power needed to be adapted to avoid fibre exposure. By treatment with 6.25 % of the laser power, the amount of surface contamination was not changed but the single lap shear strength was significantly improved (up to approx. 35 MPa). The CF-PPS substrate surface led to adhesion failure if bonded on the initial or the manually grinded surface. The laser treatment enabled the adhesive bonding and led to joint strength values of approx. 22 MPa. For all laser treatments of the CFRP the joint strength after laser treatment was at least twice the strength in comparison to manually grinded surfaces. This shows that regarding the investigated CFRP materials, grinding is not an ideal technology to prepare CFRP surfaces prior to adhesive bonding. Single lap shear tests on hybrid samples reveal high strength values and a failure predominantly by fibre tear out. Joint strength values between 25 and 30 MPa underline the high potential of laser technology for surface pre-treatment of Ti6Al4V as well as of CFRP surfaces.

## 6 ACKNOWLEDGEMENT

The German Ministry for Education and Research (BMBF) supported part of the presented work in the project “HyBriLight” (13N12715) and within the Program “Innovations for Tomorrow’s Production, Services, and Work” (funding numbers 02P16Z000 – 02P16Z005) and managed by the Project Management Agency Karlsruhe (PTKA). The authors are responsible for the contents of this publication. The authors thank the following colleagues from the central research department of Airbus: Max Kolb for supporting the surface analytics, Vitus Holzinger, Mehmet Toru and Marinko Rusmir for the lap shear testing. Special thanks go to Airbus Defence and Space for the overall support.

## REFERENCES

[1] S. Kreling, F. Fischer, R. Delmdahl, F. Gäbler, and K. Dilger, “*Analytical characterization of CFRP laser treated by excimer laser radiation,*” Physics Procedia, vol. 41, pp. 282–290, 2013.

[2] M. Nattapat *et al.*, “*Laser Surface Modification of Carbon Fiber Reinforced Composites Laser Surface Modification of Carbon Fiber Reinforced Composites,*” Materials and Manufacturing Processes, vol. 30, no. 12, pp. 1450–1456, 2015.

[3] P. S. Kreling, *Laserstrahlung mit unerschiedlicher Wellenlänge zur Klebvorbehandlung von CFK*. Aachen: Shaker Verlag, 2015.

[4] A. Kurtovic, “*Laserinduzierte Nanostrukturierung von Titanoberflächen für das strukturelle Kleben: Einfluss auf die Oberflächenmorphologie, Ermüdungs- und Adhäsionseigenschaften,*” University of Paderborn, 2014.

[5] B. Rauh *et al.*, “*UV-laser cleaning and surface characterization of an aerospace carbon fi bre*

*reinforced polymer*," International Journal of Adhesion and Adhesives, vol. 82, no. December 2017, pp. 50–59, 2018.

[6] G. D. Davis, "*Contamination of Surfaces: Origin, Detection and Effect on Adhesion,*" Surface and interface analysis, vol. 20, pp. 368–372, 1993.

[7] J. R. J. Wingfield, "*Treatment of composite surfaces for adhesive bonding,*" International Journal of Adhesion & Adhesives, vol. 13, no. 3, pp. 151–156, 1993.

[8] A. Kurtovic, E. Brandl, T. Mertens, and H. J. Maier, "*Laser induced surface nano-structuring of Ti – 6Al – 4V for adhesive bonding,*" International Journal of Adhesion & Adhesives, vol. 45, pp. 112–117, 2013.

[9] D. Hesse, "*Abtragen und Schneiden von Kohlefaserverbundwerkstoffen mit Excimer-Laserstrahlung*." VDI Verlag, Düsseldorf, p. 142, 1995.

[10] F. Fischer, S. Kreling, and K. Dilger, "*Surface Structuring of CFRP by using Modern Excimer Laser Sources*," Physics Procedia, vol. 39, pp. 154–160, 2012.

[11] K. Stefan, D. Blass, and K. Dilger, "*Duroplastische CFK mit dem Laser vorbehandeln,*" adhäsion - Kleben und Dichten, pp. 42–46.

[12] T. Mertens and H. Kollek, "*On the stability and composition of oxide layers on pre-treated titanium,*" *I*nternational Journal of Adhesion and Adhesives, vol. 30, no. 6, pp. 466–477, 2010.

[13] P. Molitor and T. Young, "*Investigations into the use of excimer laser irradiation as a titanium alloy surface treatment in a metal to composite adhesive bond,*" International Journal of Adhesion & Adhesives, vol. 24, pp. 127–134, 2004.

# COMPARISON OF LASER-BASED JOINING APPROACHES FOR PLASTIC-METAL-HYBRIDS – STRENGTH VS. PROCESS SPEED

**K. van der Straeten[1*], C. Engelmann[1], A. Olowinsky[1], A. Gillner[1]**

[1]Fraunhofer Institute for Laser Technology ILT

**ABSTRACT:** Especially in automotive- and aerospace industry saving weight through innovative light-weight designs is an important requirement. The multi-material lightweight construction approach opens up new paths for weight savings by using different materials adapted to local loads and mechanical requirements. While plastics are characterized by low weight, low price and nearly unlimited shaping possibilities, metals can withstand much higher loads due to their mechanical properties. In order to implement multi-material lightweight construction, suitable joining techniques are required to connect plastics and metals. The laser-based joining approach is an innovative joining technique, where no additive materials such as adhesives or fasteners are used. In a first process step laser radiation creates structures with an undercut geometry into the metal surface. In a second process step thermoplastic and metal are thermally joined together by heating up the metal and melting the polymer through heat conduction. The molten polymer flows into the cavities of the microstructured metal surface. After hardening a joint based on mechanical interlocking is created.
Currently, different approaches for microstructuring the metal surface are pursued by using different laser sources and processing strategies. These approaches mostly differ in structure topography and geometry, the resulting joint strengths and processing speeds. In this contribution two different microstructuring processes are compared: The formation of undercut grooves with a continuously emitting single mode fiber laser and the formation of spongy structures with an ultrashort pulsed laser. Advantages and disadvantages of both processes are evaluated and compared regarding structure geometry, joint strength and process speed.

**KEYWORDS:** Laser Joining, Plastic-Metal-Connection, Hybrid-Joint, Lightweight Construction, Thermal Joining

## 1 INTRODUCTION

The reduction of $CO_2$ emissions and energy consumption in general is a challenging topic, particularly in automotive industry and aeronautics. A few years ago the European Commission passed laws limiting the $CO_2$ emissions of new cars, which are registered in Europe, to 95 g $CO_2$/km by 2020. If the average $CO_2$ emissions of a manufacturer's fleet exceed its limit value, the manufacturer has to pay penalty payments for each registered car [1]. This is why automotive industry is particularly interested in reducing weight through innovative lightweight conceptions to comply with these legal regulations.
The combination of different materials, such as fiber reinforced plastics (FRP) and metals, adapted to local loads opens up new paths for weight reduction. While metals can withstand high loads due to their mechanical properties, polymers are characterized by low weight, attractive price and nearly endless shaping possibilities. Though, a direct and strong joint between both materials, e.g. by welding, fails due to their physical and chemical diversity. Up till now joining of fiber reinforced polymers and metals is mostly based on mechanical fastening, riveting or adhesive joining. But these processes have specific disadvantages. Mechanical joining requires drilling holes into the material which destroys fiber bundles inside the FRP and weakens the materials mechanical properties. Additionally the punctual load transfer creates stress concentrations which are not suitable for FRP. On the other hand adhesive joints require extensive surface pretreatments and hardening times which results in high process times. That is the reason why new, reliable joining techniques are required. A promising approach to overcome these problems is a laser based two-step process consisting of metal surface pretreatment and direct thermal joining.

## 2 FUNDAMENTALS

The laser-based process chain is shown in Fig.1. Within the first process step the metal surface is microstructured with laser radiation to create undercut structures for the interlocking of polymer and metal and to enlarge the boundary surface to increase specific adhesion. In a second heat conduction joining process step the metal is heated up and by thermal contact of polymer and metal the thermoplastic composite material melts. An external joining force is applied and the plasticized material flows into the structures. After hardening a strong and durable connection is formed, which is mostly based on mechanical interlocking between the materials.

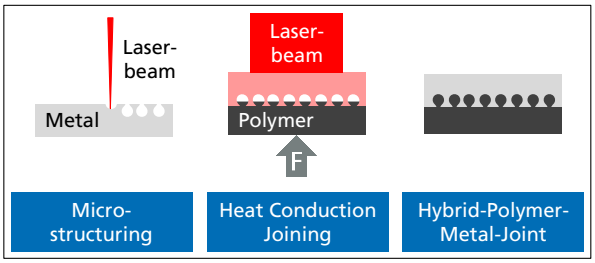


***Fig. 1*** *Process chain of the laser-based polymer-metal connection*

For the metal surface pretreatment different laser-microstructuring approaches are investigated, which are varying in processing strategy, used laser source and resulting microstructure topography. In this contribution two different approaches for microstructuring are compared: The generation of undercut grooves using a cw (continuous wave) single-mode fiber laser [2, 3] and the generation of spongy micro- and nanostructures using an ultrashort pulsed (usp) laser [4, 5].

### 2.1 MICROSTRUCTURING WITH CW SINGLE-MODE FIBER LASER

The first microstructuring approach uses a high-power cw single-mode fiber laser to create grooves with an undercut geometry. The laser beam is moving over the workpiece at high scanning speeds, realized by a galvometric scanning system, which allows scanning variable structure patterns. Due to the high intensity of the beam, metal material is partially sublimated in the centre of the microstructure and the resulting evaporation pressure ejects the surrounding melt from the structure bottom over the edges towards the surface, where some parts of it can solidify. The structuring process is repeated to achieve an undercut structure since more and more generated melt recasts on the surface and on the edges of the structure. Due to the combination of sublimation and melting, the process speed is much faster compared to conventional structuring processes [3, 4].

### 2.2 MICROSTRUCTURING WITH ULTRASHORT PULSED LASERS

The second microstructuring approach is the formation of sponge-like self-organizing microstructures using an ultrashort pulsed laser. During the ablation of metals or silicon with ultrashort laser pulses the formation of numerous self-organized microstructures can be observed e.g. mounds, spikes, micro- and nanoripples or cone-like protrusions (CLP) [6, 7]. The formation of CLP can be observed at medium (~1 J/cm²) and high fluences for example on steel, aluminum, titanium and silicon [8, 9]. Usually the effect starts at grooves, scratches and inhomogeneities after a few layers of ablation with high energy ultrashort pulses in the ablated area. Previous investigations on stainless steel [4, 5] show, that at first some dots and holes appear which grow to small clusters with increasing number of layers. Visually the growth of the CLP can be monitored by a blackening of the surface. The structure is characterized by a random orientation and an extremely enlarged surface with a high surface roughness due to nano-substructures covering the microstructures. Currently processing and ablating with ultrashort laser pulses is a slow process due to the availability of high-power laser sources, suitable equipment und processing strategies.

## 3 EXPERIMENTAL SETUP AND PROCEDURE

### 3.1 MATERIALS AND SAMPLE GEOMETRY

The metal used for the hybrid joint is a regular stainless steel (1.4301). During the joining process the stainless steel is combined with a glass fiber reinforced Polypropylene (PP) for tensile shear tests and an unreinforced PP for tensile tests.
The GFRP used is X111F40-4/1-0/90° (Quadrant Plastic Composites AG, Switzerland), which is a chopped fiber glass mat reinforced PP laminate with randomly oriented glass fibers and additionally reinforced fabric

inside. The material thickness is 3 mm with a glass fiber content of 40 vol.-% (PP/GF40). The unreinforced material is a PP-H at 4 mm thickness.
In this contribution two different load directions are investigated (tensile shear and tensile load). Therefore two different sample geometries are used. The dimensions and the sample arrangement of the joining partners are depicted in Fig. 2.

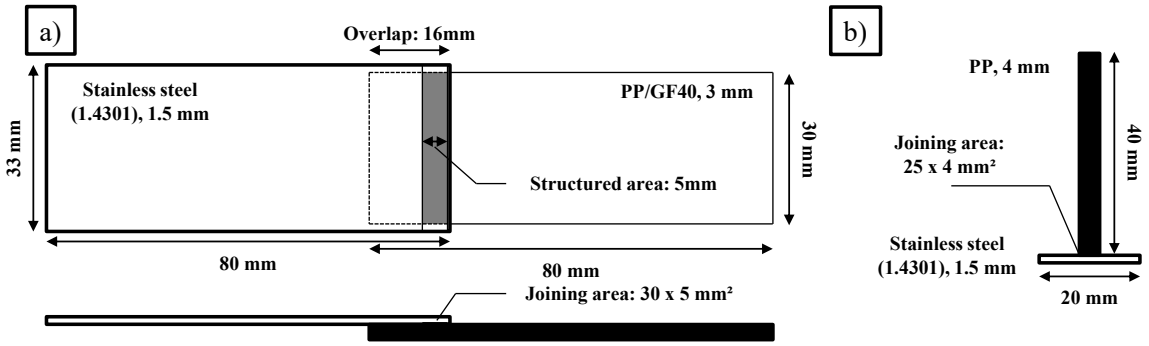


***Fig. 2*** *Sample geometry and arrangement for a) tensile shear tests and b) tensile tests*

For tensile shear tests a 30x80x1.5 mm³ metal sample is arranged in an overlap of 16 mm to the 30x80 mm² PP/GF40 with 3 mm material thickness. To avoid material failure of the fiber reinforced composite outside the joining zone during testing, the joining area is limited to 5x30 mm² (=150 mm²). For tensile tests a 4 mm thick PP plate with 40x25 mm² dimensions is vertically joined onto a 20x25x1.5 mm³ steel plate with a 25x4 mm² joining area.

### 3.2 EXPERIMENTAL SETUP FOR MICROSTRUCTURING

The laser source utilized for the laser microstructuring process of undercut grooves is a water cooled IPG Photonics YLS-1000-SM, 1000 W cw single-mode fiber laser ($M^2 < 1.07$), operating at 1064 nm wavelength. The laser beam is guided through an optical fiber into an Intelliscan25 scanning head (Scanlab), which deflects the laser beam on the metal surface. The metal is positioned in a device within the scan field to ensure reproducible patterns on metal surface. A cross-jet with pressured air prevents the optics from contamination by process emissions. The focusing F-theta optics has a focal length of 330 mm creating a focal diameter of ~40 µm. The system setup is depicted in Fig. 3b). The samples are processed with a scanning speed v = 10 m/s, laser power P = 750 W and N = 4 number of passes. Two different patterns are applied: Crossed lines with a structure distance SD = 300 µm and crossed lines with SD = 400 µm. These parameters have shown high joining strengths in previous tests [2, 3].

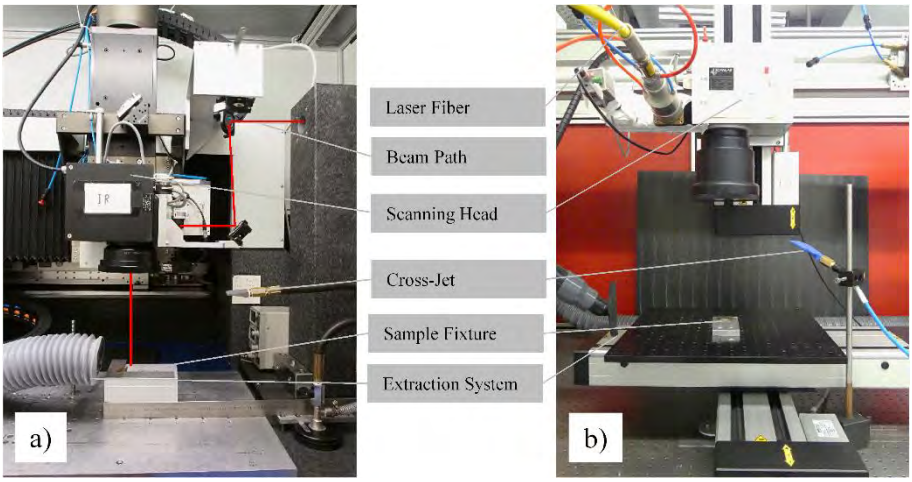


***Fig. 3*** *Experimental setup for microstructuring with a) ultrashort pulsed laser and b) single-mode fiber laser*

The microstructuring process of the sponge-like self-organizing structures is conducted with a laser system consisting of a Kugler Microgantry nano3X (3-axis motion system) with an ultrashort pulsed laser Hyper Rapid 100 (Coherent). The pulse duration is <15 ps at a wavelength of λ = 1064 nm. The maximum average

output power is 100 W at a repetition rate of 400 kHz. After deflection by a galvanometric scanner (IntelliScan14, Scanlab), the laser beam is focused through a lens (f = 163 mm) on the work piece. The system setup is depicted in Fig. 3a). Parameters for microstructuring are chosen based on preliminary tests [5]. The parameters used are scanning speed v = 2 m/s, average laser power P = 57 W, scanning line spacing LS = 8µm and the number of ablated layers N = 30. The samples are processed with a crossed scanning hatch.

### 3.3 EXPERIMENTAL SETUP FOR JOINING

The laser system used for the joining process is a Laserline GmbH LDM 3000-100 continuous wave diode laser combined with a MOTOMAN-HP20-6 robot motion system (Fig. 4). The maximum output power is 3000 W and the laser system is operating at 900-1070 nm wavelength. A zoom optics from Laserline with a focal length of 250 mm forms a square laser spot with a variable size from 5x5 mm² up to 16x30 mm². The variable spot size enables a simultaneous irradiation of the entire joining area with a single pulse. In order to apply pressure and fix the sample arrangement a pneumatic clamping device with a sample holding fixture is used. A pressure of 3 bars is applied.

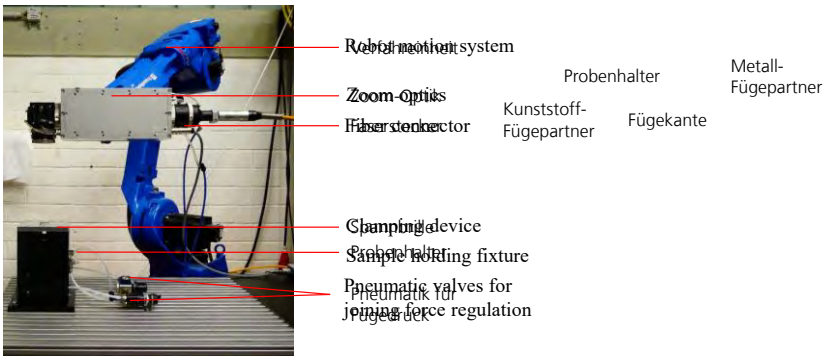


***Fig. 4*** *Experimental setup for joining*

All three types of microstructures are joined with the same parameter settings. The parameter settings for joining are shown in Table 1 based on preliminary tests [5].

***Table 1:*** *Joining parameter settings*

| Sample geometry | Joining Area [mm²] | Laser Power* [W] | Irradiation time [ms] |
|---|---|---|---|
| Tensile shear | 150 | 1956.5 | 2000 |
| Tensile | 100 | 1655.5 | 2000 |

*Laser power before optics and sample holding fixture

### 3.4 TESTING PROCEDURE AND ANALYSIS

The microstructured metal surface is analyzed with a scanning electron microscope (SEM) LEO1455EP and cross-sections are prepared and analyzed under a light optical microscope. The mechanical properties of the joint are tested with a multi-purpose testing machine Z100 from Zwick GmbH & Co. KG. For the shear strength tests a tensile force is applied parallel to the joining area and the breaking force is measured according to DIN EN 1465. The samples are fixed between the clamping jaws in a 50 mm distance. The testing speed is set to 50 mm/min. For tensile and peel tests the force is applied vertically to the joining zone. The distance between the clamping jaws is set to 25 mm and the testing speed is set to 50 mm/min for both tests. For statistical reasons five samples are tested for each parameter setting. Load directions and testing setup are depicted in Fig. 5.

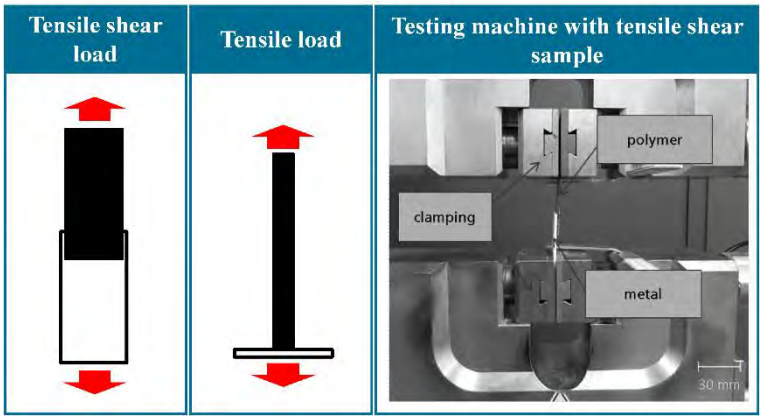


*Fig. 5 Load directions for testing and testing setup*

# 4 RESULTS AND DISCUSSION

## 4.1 MICROSTRUCTURING RESULTS

Microstructuring with a cw single-mode fiber lasers with the given parameters creates undercut grooves with a drop-like shape (see Fig. 6). The undercuts enable a mechanical interlocking between polymer and metal during joining. As the joint strength is depending not only on the structure geometry but also on the structure density [3], crossed lines enable high structure densities. A structure distance SD = 300 µm is the minimum spacing where the structures keep their undercut shape without influencing each other.

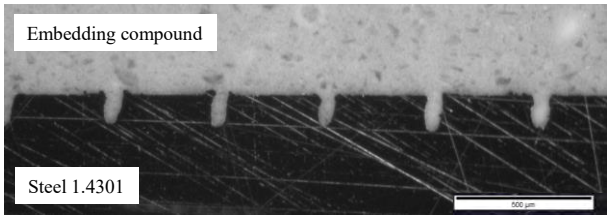


*Fig. 6 Cross-section of linear structures made by cw single-mode fiber laser process on steel*

On the other hand the microstructuring process with an ultrashort pulsed laser generates spongy microstructures so-called CLP, which completely cover the metal surface. Hence the structure density is much higher compared to the fiber laser process. Fig. 7a shows a SEM-picture of the surface which shows the spongy surface of CLP-structures. The cross-section (Fig. 7b) shows small and deep structures, which do have only little undercuts.

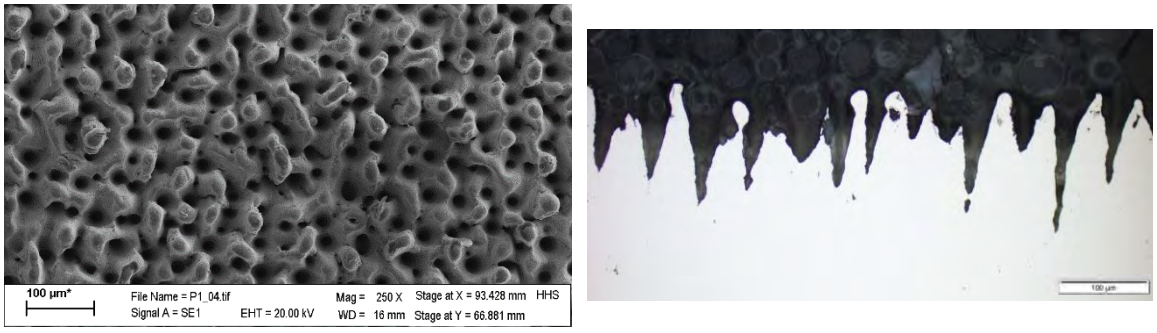


*Fig. 7 CLP-structures on steel: SEM-picture (left), Cross-section (right)*

## 4.2 TESTING RESULTS

After joining, the 5 samples per sample geometry and structuring pattern were destructively tested in a multi-purpose testing machine. The joint strengths are depicted in Fig. 8.

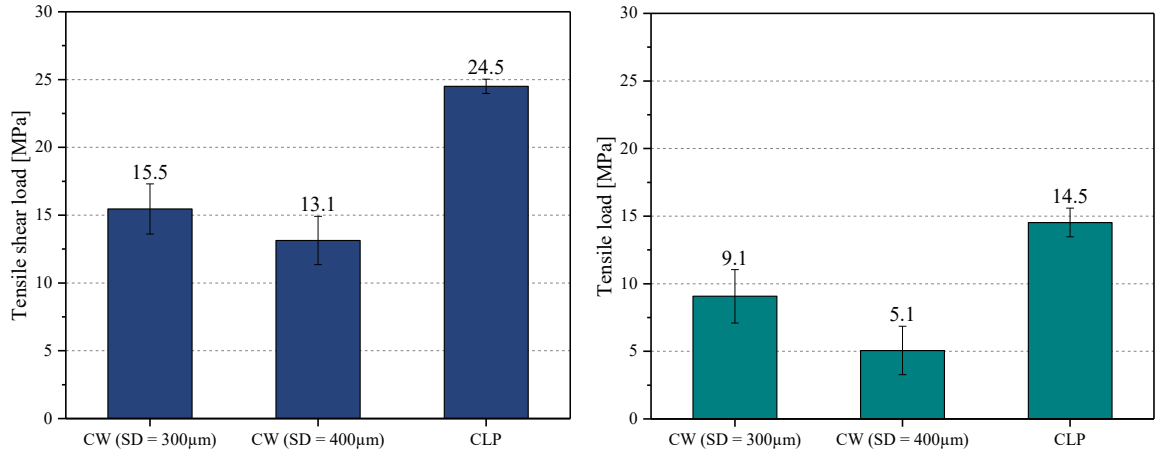


***Fig. 8*** *Joint strengths [MPa] for tensile shear load (left) and tensile load (right)*

The highest loads can be transferred via tensile shear load for all types of microstructures. The tensile shear load between steel 1.4301 and PP/GF40 ranges between 13-15.5 MPa for cw-structures and 24.5 MPa for the CLP-microstructures. For tensile load the joint strength is decreased by approx. 40% to 5.1-9.1 MPa for cw-structures and 14.5 MPa for CLP-structures. For all load directions the highest joint strengths are achieved using the spongy CLP-microstructures (nearly 40% higher strength). For the undercut groove structures the higher structure density with SD = 300 µm also results in higher joint strengths compared to SD = 400 µm. The results indicate, that the structure density has high impact on the joint strength.

### 4.3 PROCESS TIMES

In terms of process speed, there are major differences between both microstructuring approaches. While for the microgrooves only some lines have to be scanned 4 times to achieve an undercut structure, the formation of CLP-structures requires a full-area ablation with a very small line spacing of 8 µm and 30 ablated layers. By neglecting the jump delays during scanning, which means the time the laser beam needs to jump from one end position to the next start position, the time for processing can be calculated as follows:

$$t = \frac{d_{scan} * N}{v}$$

*$t$ = Process time*
*$d_{scan}$ = Scanning distance (distance the laser beam must cover)*
*$N$ = Number of passes/ablated layers*
*$v$ = Scanning speed*

For the described parameters this results in the following process times for microstructuring 1 cm² (see Table 2):

***Table 2:*** *Process times for microstructuring 1 cm²*

| Microstructure | Scanning distance [m] | Number of passes/ablated layers | Scanning speed [m/s] | Process time [s] |
|---|---|---|---|---|
| CW (SD=300 µm) | 0.67 | 4 | 10 | 0.27 |
| CW (SD=400 µm) | 0.5 | 4 | 10 | 0.2 |
| CLP | 12.5 | 30 | 2 | 187.5 |

The process time for microstructuring CLP-structures is with 187.5 s/cm² much higher than for microstructuring of undercut grooves with cw fiber lasers with 0.2-0.27 s/cm². In addition, jump delays that extend the process time must be taken into account.

## 5 CONCLUSIONS

The described laser-based process chain enables a strong and reliable connection between polymers and metals. In a first step the metal surface is modified with microstructures by means of laser radiation. Different

microstructuring approaches are available which mostly differ in processing strategy, used laser source and resulting structure geometry. In a second thermal direct joining process polymer and metal are joint together. Therefore, the metal is heated up by diode laser radiation and through heat conduction the polymer melts and flows into the microstructures.
In this contribution two different laser microstructuring approaches are evaluated regarding joint strength for tensile shear and tensile load and process time. While undercut grooves made by cw single-mode fiber lasers achieve medium joint strengths of ~15 MPa for tensile shear and 5-9 MPa for tensile load, they are characterized above all by their very short process times. On the other hand CLP-structures, created during ablation with ultrashort laser pulses, offer very high joint strengths of ~24.5 MPa for tensile shear and 14.5 MPa for tensile load. Until now, the production of such structures is very time-consuming and therefore not yet suitable for industrial implementation. In recent years, the development of ultrashort pulse laser beam sources has made great progress, so that a reduction in process time seems realistic in the future.
All in all, the user must decide what requirements he has regarding process times and joint strength.

## REFERENCES


[1] European Parliament and Council, *Regulation (EC) No 443/2009 of 23 April 2009 setting emission performance standards for new passenger cars as part of Community's integrated approach to reduce $CO_2$ emissions from light-duty vehicles*, 2009

[2] Engelmann, C., Eckstädt, J., Olowinsky, A., Aden, M., Mamuschkin, V., 2015, *Examination of Bond Strength of Laser Assisted Plastic-Metal-Joints considering Different Load Directions*, Proceedings of LAMP2015, Fukuoka

[3] Engelmann, C., Eckstaedt, J., Olowinsky, A., Aden, M., Mamuschkin, V., 2016, *Experimental and simulative investigations of laser assisted plastic-metal-joints considering different load directions*, Physics Procedia 83 (2016) 1118-1129

[4] van der Straeten, K., Zibner, F., Olowinsky, A., Gillner, A., *Laser-based joining of hybrid plastic-metal-components by increasing specific adhesion*, Proceedings of ICALEO 2016, Paper No. 807, San Diego

[5] van der Straeten, K., Olowinsky, A., Gillner, A., *Laser-based plastic-metal-joining with self-organizing microstructures considering different load directions*, Proceedings of ICALEO 2017, Paper No. 1502, Atlanta

[6] Zuhlke, C.A., Anderson, T.P., Alexander, D.R., 2013, *Formation of multiscale surface structures on nickel via above surface growth and below surface growth mechanisms using femtosecond laser pulses*, Optics express 21, 8460-8473

[7] Raillard, B., Gouton, L., Ramos-Moore, E., Grandthyll, S., Müller, F., Mücklich, F., 2012, *Ablation effects of femtosecond laser functionalization on steel surfaces*, Surface and Coatings Technology 207, 102-109

[8] Eifel, S., Dohrn, A., Gillner, A., 2010*, Quality Aspects in High Power Ultra Short Pulse Laser Ablation*, Proceedings of LPM2010, Stuttgart

[9] Tsukamoto, M., Kayahara, T., Nakano, H., Hashida, M., Katto, M., Fujita, M., Tanaka, M., Abe, N., 2007, *Microstructures formation on titanium plate by femtosecond laser ablation*, Journal of Physics: Conference Series 59 666-669, Eighth International Conference on Laser Ablation

# CHARACTERIZATION OF THE JOINING ZONE IN LASER DIRECT JOINING BETWEEN THERMOPLASTICS AND METALS

**Klaus Schricker[1,*], Jean Pierre Bergmann[1], Marcus Hopfeld[2], Lothar Spieß[2]**

[1]Technische Universität Ilmenau, Production Technology
[2]Technische Universität Ilmenau, Materials for Electrical Engineering and Electronics

**ABSTRACT:** Thermal joining of thermoplastics to metals shows a high potential in terms of light weight constructions. The metal sheet is heated by using laser irradiation and the thermoplastic material gets molten due to the heat transfer between both joining partners. The resulting melting layer is characterized based on its geometrical shape, thermoplastic microstructure and the modification of the material properties due to the thermal joining process based on microscopic investigations, hardness measurements of the metal as well as the thermoplastic joining partner and analysis of melting layer and base material (DSC, XRD).

**KEYWORDS:** melting layer, metal plastic joining, laser joining, thermoplastic morphology

## 1 INTRODUCTION AND STATE OF THE ART

The use of a multi-material design enables a functional design. Thereby, the motivation for the use of hybrid structures depends on the industrial sector. On the one hand, the use of lightweight construction in automotive industry, mechanical engineering and aviation industry is necessary for achieving legal requirements on emissions and fuel consumption. On the other hand, multi-material design allows novel constructions and consequently reduced costs in a large-volume production, e. g. in household appliance industry. Thereby, the joining of thermoplastics to metals has a great potential for the use of the right material at the right place but shows high requirements on the joining technology. Laser-based thermal joining shows advantages over competitive processes without the need of an addition material (e. g. adhesives) or a connecting element (e. g. screws or rivets) and enables a local and areal bonding with a high load capability.

In this process, the thermoplastic gets molten by the energy input, thus wets the metal surface and penetrates the surface structures. A solid joint is formed after solidification. Based on this process, various energy sources, e. g. conductor [1], inductor [2], ultrasonic [3], resistance welding [4] or laser radiation [5, 6], can be used. Hence, the use of a laser-based process shows advantages because of the beam shaping, e. g. rectangle or circular spot geometries, and thereof allows an adjustable temperature-time profile for the joining process and a locally limited energy input. The process can be performed as transmission joining [7] or heat conduction joining [8] for lap joints. In transmission joining, the laser beam passes through the thermoplastic joining partner and is absorbed at the boundary layer between metal and plastic. This leads to a high thermal load of the polymer at the contact area and requires a transmittance of the plastic material within laser wavelength. In heat conduction joining, the laser spot is targeted at the metal surface as upper joining partner and the heat is conducted through the metal sheet into the joining zone. This enables the processing of fiber reinforced plastics or non-transparent materials and induces a reduced thermal load of the plastic joining partner.

The resulting material properties are controlled by time-temperature-regime within the joining process. For welding plastics (e. g. hot gas welding, laser beam welding or heated-tool butt welding), different investigations provide knowledge to microstructure, morphology and materials behavior which can influence weld strength [9, 10]. For polymer-metal joints, changes in crystallinity, bubble formation and corrosion effects were examined [11-14]. Thereby, investigations regarding the influence of microstructural effects and adjusted material properties on hybrid joints do not exist. In this paper, the joining zone of polymer-metal hybrids is analyzed based on spot joints. Starting from the description of the thermoplastic melting layer, further investigations towards the heat affected zone within the metal joining partner, thermoplastic morphology and microstructure as well as crystal modifications were carried out.

## 2 EXPERIMENTAL SETUP

The experiments were carried out using a 1000 W diode laser (Laserline LDM 1000) with a focal diameter of 5.3 mm and top-hat intensity distribution. Heat conduction joining was applied for creating spot joints in overlap configuration (overlap: 75·100 mm²) with joining times ($t_L$) from 1 s up to 10 s. As metal joining partner, Aluminium EN AW 6082 (t = 1.5 mm) was used. The metal surface was prepared by manufacturing grooves in rolling direction using a pulsed fiber laser (Rofin PowerLine F20, $P_L$ = 20 W; f = 50 kHz, v = 0.2 m·s$^{-1}$, see also [15]). On side of the thermoplastics, Polyamide 6 (PA 6), Polyamide 6.6 (PA 6.6) and Polypropylene (PP) were used due to their contrary material properties, especially different melting intervals (PP: 126-178 °C, PA 6: 191-236 °C, PA 6.6 235-270 °C, investigated by differential scanning calorimetry, heating rate: 10 K·min$^{-1}$). The thickness of thermoplastic materials was set to 5 mm in order to avoid heat accumulation within the material which may influence the resulting properties.

The joining zone was characterized regarding geometrical appearance and time-dependent expansion depending on energy input and different material combinations. The heat affected zones in metal as well as thermoplastic joining partner were investigated by hardness measurements (metals: HV 0,2/15; thermoplastics: HV 0.01/60 according to DIN EN ISO 6507-1 [16] and VDI/VDE 2616 [17]). Differential scanning calorimetry (DSC, Netzsch DSC 204 F1 Phoenix, heating rate: 10 K·min$^{-1}$) was utilized to determine the degree of crystallinity and X-ray diffraction (XRD, Bruker Lynxeye XE-T, spot size: 300 µm, testing time per step: 60 s) for evaluating the crystal modification in base material as well as joining zone. For materialographic examinations, sputtering with ionized argon was used for exposing the thermoplastic microstructure followed by differential interference contrast microscopy (DIC).

## 3 RESULTS AND DISCUSSION

### 3.1 THEROPLASTIC MELTING LAYER

The geometrical formation of the thermoplastic melting layer is influenced by the materials and the laser process. The melting layer is bounded to the metal surface and extends towards the thermoplastic base material for increasing energy input. Figure 1 shows the melting layer thickness for PA 6, PA 6.6 and PP depending on joining time and related energy input. For PP, a melting layer thickness between 140 µm at 1 s joining time and 780 µm at 10 s joining time is reached, whereas for PA 6.6 the melting layer achieves thicknesses between 90 µm up to 530 µm. In general, lower temperature ranges of the melting interval result in larger melting layers. This behaviour is characterized by the begin of the melting interval $T_{im}$ ($T_{im,PP}$: 126 °C, $T_{im,PA\ 6}$: 191 °C, $T_{im,PA\ 6.6}$: 235 °C). The resulting melting layer thickness over time follows an exponential function, which can be explained by the heat equation. Further investigations on numerical simulation confirm the dependence of the melting layer from the temperature distribution and melting interval [18]. However, an analytic calculation of the resulting melting layer is not possible due to the mutual influence of phase transition as well as temperature dependent density, thermal conductivity and heat capacity on the result.

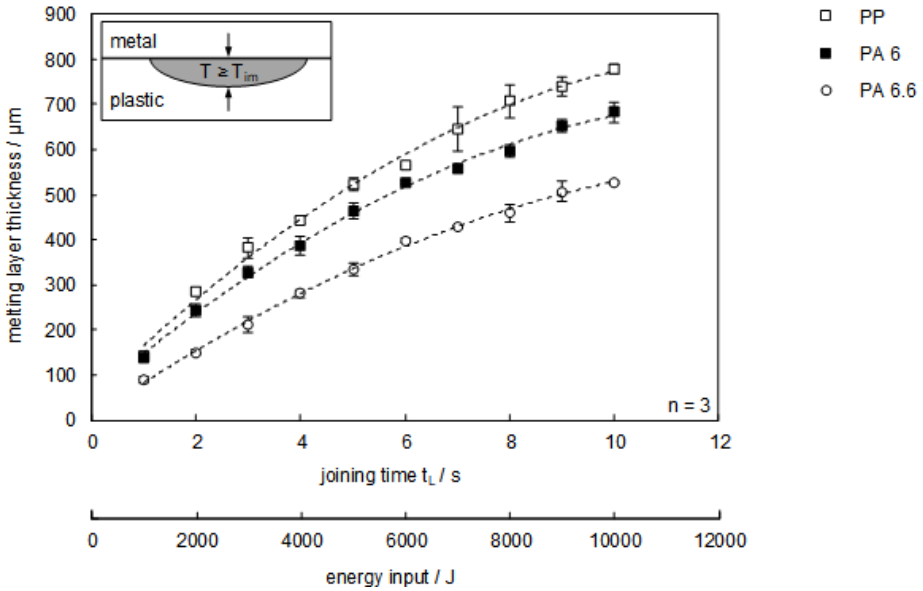


***Fig. 1*** *Melting layer thickness depending on joining time and energy input ($P_L$ = 1 kW)*

The formation and the geometry of the melting layer follows the temperature distribution within the thermoplastic material. Based on the heat transfer over the boundary layer, an axially symmetrical melting layer is formed (Figure 2). The begin of the melting interval $T_{im}$ was identified as characteristically temperature for the melting layer's formation. The growth in radial direction is higher than into the plastic sheet due to the higher thermal conductivity of the metal compared to the thermoplastic. These results were verified by previous investigations on numerical simulation and high-speed recordings in a half-section setup. Some bubbles occur within the melting layer due to dissolved water or thermal degradation. Further investigations on this field were published in [19-20]. Next to the melting layer, a gap between metal sheet and thermoplastic material can be identified. The laser surface pre-treatment ejects some molten material which solidifies at the structures' edge and roughens the surface. On the other hand, a volume increase of thermoplastic material was determined by reorienting macromolecules during the joining process.

Based on the investigations on the joining zone and its formation, the effects on material properties based on the heat treatment of metal and plastic will be investigated.

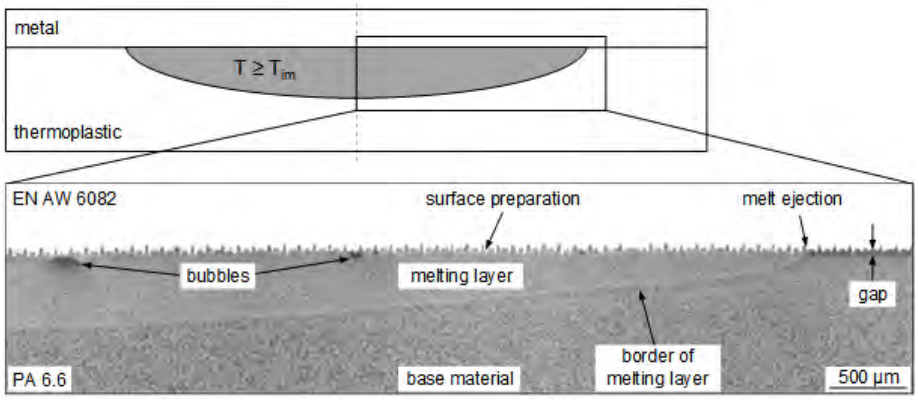


***Fig. 2*** *Melting layer of PA 6.6 – EN AW 6082 joint ($P_L$ = 1 kW, $t_L$ = 5 s)*

### 3.2 EFFECT ON MATERIALS PROPERTIES DUE TO THERMAL JOINING

The laser beam is absorbed at the metal surface and the sheet is heated. The formation of a melt pool in the metal part is avoided due to the industrial requirement for realizing surfaces within the customers field of visibility by this joining process. The heat is conducted throughout the metal towards the interface into the thermoplastic material. Thereby, the metal joining partner receives a heat treatment which changes the materials properties.

Figure 3 shows the hardness measurement map of an EN AW 6082 T6 sheet after joining process. In the interaction area of the laser beam, the hardness level is significantly decreased compared to the base material. Based on numerical simulation, temperatures between 450 °C and 340 °C were determined in this area which shows a relatively equal temperature distribution over sheet thickness. The interaction between this temperature range and the heating rates in laser processing can be correlated to the investigations on aluminium heat treatment for comparable parameters [21]. The softened area might be a weak point in mechanical testing, especially for high strength joints with fibre reinforced polymers. It can therefore be stated, that a heat affected zone in aluminium was identified by hardness measurements.

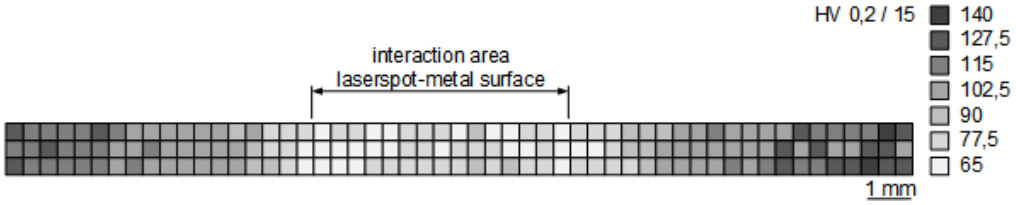


***Fig. 3*** *Hardness measurements for aluminium EN AW 6082 ($P_L$ = 1 kW, $t_L$ = 10 s)*

Further investigations were carried out regarding to thermoplastic microstructure which is influenced by melting and solidification during the joining process. Figure 4 shows the exemplary microstructure for PA 6 based on three positions: The boundary layer (a), the edge of the melting layer (b) and the sideward position (c).

For the boundary layer, no amorphous layer can be detected. The semi-crystalline structure is identified by spherulites within the surface structures and is not influences by bubbles next to the interface (a). At the melting layer edge towards the thermoplastic base material, a fine spherulitic zone is identified for polyamides due to the effect of functional groups and resulting hydrogen bonds on nucleation and solidification (b). Next to the fine spherulitic zone, partially molten spherulites are seen. At the sideward position, the fine spherulitic zone as well as the partially molten spherulites can be detected. Thereby, the melt flow causes a deformation of the partially molten spherulites which is clearly seen within (c). Both zones are located within partially molten material which was proven by investigations with the half-section setup and numerical simulation.

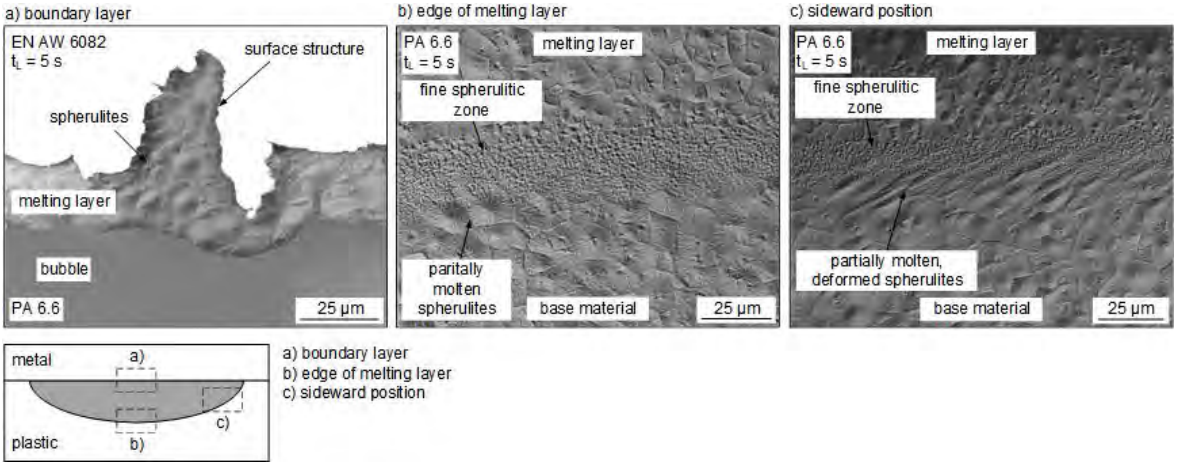


***Fig. 4*** *Thermoplastic microstructure of the melting layer (PA 6, EN AW 6082, $P_L$ = 1000 W, $t_L$ = 10 s)*

Further investigations concentrated on the identification of different zones within the thermoplastic material. The verification of a heat affected zone was in focus of the investigations. Based on the assumption of a heat treatment of material close to the melting layer, secondary crystallization is expected and should be proven by hardness measurements. Figure 5a shows the hardness levels of the melting layer, the fine spherulitic zone, the newly identified heat affected zone and the base material. Thereby, the hardness level of the heat affected zone is significantly increased compared to the other investigated areas. These results were confirmed on PA 6.6 as well.

An additional characterization was provided by DSC analysis. Thereby, the degree of crystallinity between melting layer and base material is comparable, although the curve progression looks slightly different. The temperature of the main peak is slightly shifted to lower temperatures (about 0.5 K up to 0.8 K depending on the investigated material) which indicates a reduced lamellar thickness of crystalline areas respectively less perfect crystal structures. Furthermore, the first peak at about 210 °C is more pronounced within the melting layer compared to base material which indicates an increased presence of γ-PA 6 as crystal modification within the molten polymer.

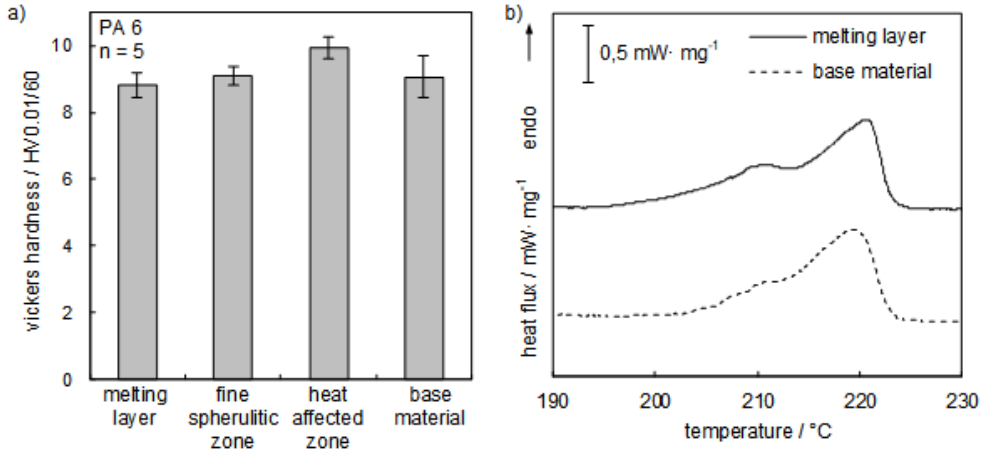


***Fig. 5*** *Identification of different zones within thermoplastic material (a) and comparison between DSC-curves for melting layer and base material (b) (PA 6, EN AW 6082, $P_L$ = 1000 W, $t_L$ = 10 s)*

A verification of this indication was realized by XRD analysis to determine the crystal modification depending on the identified areas within the thermoplastic material. Figure 6 shows five diffractograms for different measurement positions. The base material in a comparable position to the melting layer (0), the base material at the center (1), the heat affected zone (2) as well as the partially molten zone (3) and fully molten zone (4) within the melting layer.

Thereby, the base material (0) shows mainly α-modification characterized by $\alpha_1$ and $\alpha_2$ peak and does not contain strong indications for the presence of γ-PA 6 within this area. In the base material center (1), a comparable diffractogram with slightly increased intensities is shown which indicates a higher degree of crystallinity due to a slower cooling/solidification rate during primary manufacturing process. At position two, a further increase of the peak's intensities is determined and is led back to secondary crystallization. This proves the assumed explanation for the increased hardness level in the heat affected zone. Within the melting layer, the partially molten zone shows a mixture of α- and γ-modification. In this area, some crystallites are partially molten, others are remaining in solid state. During solidification, the molten material forms a new crystal modification whereas the solid crystals does not show a change in modification. This is reasonable due to different cooling rates [22].

In (4), the mostly molten area, mainly γ-modification occurs and just slight shoulders within the diffractogram of α-peaks are noticeable. This could be caused by relatively high solidification rates of the molten material and a completely new formation of all crystals and superstructures.

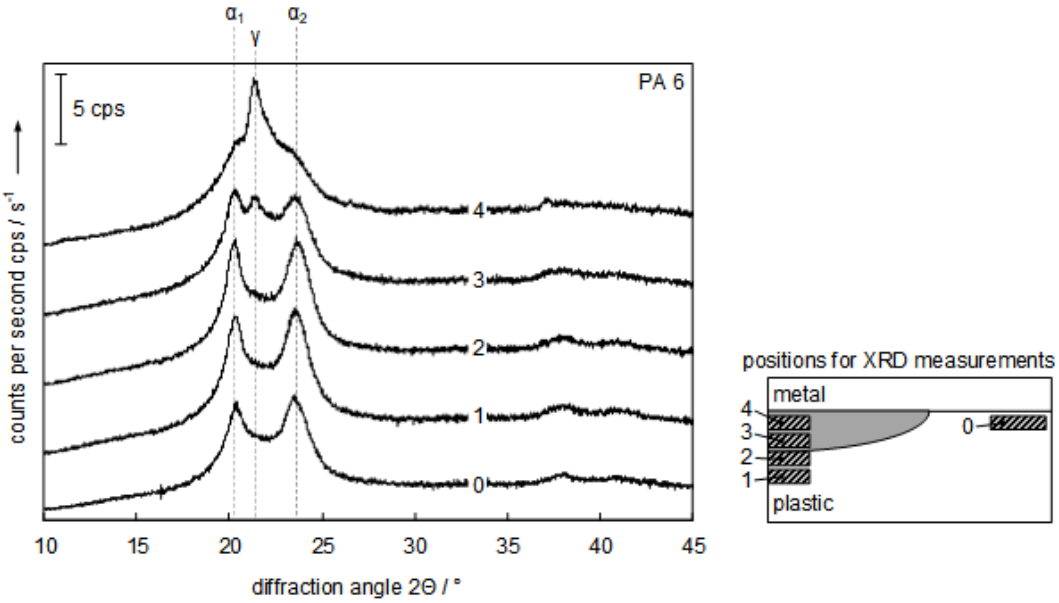


***Fig. 6*** *Comparison of diffractograms for different positions (PA 6, EN AW 6082, $P_L$ = 1000 W, $t_L$ = 10 s)*

## 4 CONCLUSIONS

In this paper, the joining zone of polymer-metal hybrids was investigated regarding changes within materials properties based on spot joints. In aluminum, a heat affected zone with decreased hardness level was detected and a correlation to the temperature field based on numerical simulation was possible. For thermoplastic materials, the resulting melting layer thickness and geometry was investigated for PA 6, PA 6.6 and PP for varied joining times from 1 s up to 10 s. Further investigations were carried out to identify different microstructural zones within the melting layer (fully molten zone, partially molten zone with fine spherulites and deformed spherulites, heat affected zone). XRD- as well as DSC-measurements were performed as additional examinations to provide information on the degree of crystallinity and crystal modification. Thereby, a change in crystal modification from base material to the joining zone was verified.

In further investigations, the influence of the identified zones and their adjustment by the laser joining process will be examined and transferred to industrial relevant overlap joints and applications.

## REFERENCES


[1] Sickert, M.; Haberstroh, E.: *Thermal Direct Joining for Hybrid Plastic Metal Structures.* Proceedings of Euro Hybrid Materials and Structures 2014, 42-45, 2014.

[2] Roesner, A.; Scheik, S.; Olowinsky, A.; Gillner, A.; Reisgen, U.; Schleser, M.: *Laser Assisted Joining of Plastic Metal Hybrids.* Physics Procedia 12, 370-377, 2011.

[3] Balle, F.; Eifler, D.: *Monotonic and Cyclic Deformation Behavior of Ultrasonically Welded Hybrid Joints between Light Metals and Carbon Fiber Reinforced Polymers (CFRP).* Fatigue Behaviour of Fiber Reinforced Polymers: Experiments and Simulations, DEStech Publications, 111-122, 2012.

[4] Ageorges, C.; Ye, L.: *Resistance Welding of Metal/Thermoplastic Composite Joints.* Journal of Thermoplastic Composite Materials, Vol. 14, No. 6, 449-475, 2006.

[5] Katayama, S.; Kawahito, Y.; Mizutani, M.: *Latest progress in performance and understanding of laser welding.* Physics Procedia 39, 8-16, 2012.

[6] Bergmann, J. P.; Stambke, M.: *Potential of laser-manufactured polymer-metal hybrid joints.* Physics Procedia 39, 84-91, 2012.

[7] Arai, S.; Kawahito, Y.; Katayama, S.: *Effect of surface modification on laser direct joining of cyclic olefin polymer and steel.* Materials and Design 59, 448-453, 2014.

[8] Jung, K.-W.; Kawahito, Y.; Takahashi, M.; Katayama, S.: *Laser direct joining of carbon fiber reinforced plastic to aluminium alloy.* Journal of Laser Applications, Vol. 25, No. 3, 2013.

[9] Gehde, M.: *Zum Extrusionsschweißen von Polypropylen.* Universität Erlangen-Nürnberg, Lehrstuhl für Kunststofftechnik, 1993.

[10] Ghorbel, E., et al.: *Laser diode transmission welding of polypropylene: Geometrical and microstructure characterisation of weld.* Materials and Design, 30, 2745-2751, 2009.

[11] Amend, P.; Pfindel, S.; Schmidt, M.: *Thermal joining of thermoplastic metal hybrids by means of mono- and polychromatic radiation.* Physics Procedia 41, 98-105, 2013.

[12] Katayama, S.; Kawahito, Y.; Niwa, Y.; Kubota, S.: *Laser-assisted metal and plasitc joining.* Proc. of 5th Laser Assisted Net Shape Engineering, 41-51, 2007.

[13] Roesner, A. et al.: *Long term stability of laser joined plastic metal parts.* Physics Procedia; No. 41; 169-171, 2013.

[14] Mehner, A., et al.: *Corrosion of Aluminum Alloys in Integral Hybrid Components with Carbon Fiber Reinforced Plastics or Titanium.* Deutsche Gesellschaft für Materialkunde, LightMat, 2013.

[15] Schricker, K.; Stambke, M.; Bergmann, J. P.: *Laser-Based Joining of Thermoplastics to Metals: Influence of Varied Ambient Conditions on Joint Performance and Microstructure.* International Journal of Polymer Science, 9 p., 2016.

[16] Deutsches Insitut für Normung e. V.: *DIN 6507-1: Metallische Werkstoffe - Härteprüfung nach Vickers - Teil 1: Prüfverfahren (ISO 6507-1:2005).* Beuth Verlag, 2006.

[17] Verein Deutscher Ingenieure VDI; Verband der Elektrotechnik Elektronik und Informationstechnik (VDE), VDI/VDE-Gesellschaft Mess- und Automatisierungstechnik: *VDI/VDE-Richtlinie 2616: Härteprüfung an Kunststoffen und Elastomeren.* Beuth Verlag, 2012.

[18] Schricker, K.; Bergmann, J. P.: *Determination of Sensitivity and Thermal Efficiency in Laser Assisted Metal-Plastic Joining by Numerical Simulation.* LANE 2018, 6 p., accepted for publication.

[19] Schricker, K.; Diller, S.; Bergmann, J. P.: *Investigations on bubble formation, flow field and melting/solidification process in laser-based joining of metals to plastics.* IIW Annual Assembly, C-XVI-1004-17, 18 p., 2017.

[20] Schricker, K.; Diller, S.; Bergmann, J. P.: *Bubble Formation in Laser Direct Joining of Thermoplastics to Metals.* LANE 2018, 6 p., accepted for publication.

[21] Graser, M.; Fröck, H.; Lechner, M.; Reich, M.; Kessler, O.; Merklein, M.: *Influence of short-term heat treatment on the microstructure and mechanical properties of EN AW-6060 T4 extrusion profiles—Part B.* Production Engineering 10, 391-398, 2016.

[22] Xie, S.; Zhang, S.; Liu, H.; Chen, G.; Feng, C.; Quin, H.; Wang, F.; Yang, M.: *Effects of processing history and annealing on polymorphic structure of nylon-6/montmorillonite nanocomposites.* Polymer 46, 5417-5427, 2005.

# PROCESS CONCEPTS FOR THE MANUFACTURING OF HYBRID COMPOSITES MADE FROM ALUMINUM AND CFRP WITH A POLYMER-BASED DECOUPLING LAYER

**Armin Schmid[1,3]*, Katharina Arnaut[2], Jan Clausen[3], Maximilian Koerdt[2], Adrian Struß[1,3], Franz-Josef Wöstmann[3], Matthias Busse[1,3]**

[1]University of Bremen, Bibliothekstr. 1, 28359 Bremen, Germany
[2]Faserinstitut Bremen e.V., Gebäude IW3, Am Biologischen Garten 2, 28359 Bremen, Germany
[3]Fraunhofer-Institut für Fertigungstechnik und Angewandte Materialforschung IFAM, Wiener Str. 12, 28359 Bremen, Germany

**ABSTRACT:** Currently, conventional mechanical or adhesive joining technologies are used for the production of hybrid composites consisting of the light construction materials aluminum (Al) and carbon fiber reinforced polymer (CFRP). A direct joining of these materials is, however, problematic due to their electrochemical incompatibility and the resulting corrosive degradation. The aim of the new collaborative research project "Hybrid Casting" funded by the Deutsche Forschungsgemeinschaft (DFG) is to join Al and CFRP in novel ways using the aluminum high pressure die casting (HPDC) process to create an intrinsic hybrid composite with a decoupling and adhesive layer made from thermoplastic polyetheretherketone (PEEK). Two process concepts to produce such a hybrid composite are the primary focus in this investigation.

**KEYWORDS:** hybrid casting, hybrid composite, process combination, HPDC, CFRP, PEEK

## 1 INTRODUCTION

With the aim of the conservation of resources, the minimization of weight is playing a crucial role in many branches of industry. Multi-material construction methods using a combination of the light materials carbon fiber reinforced polymer (CFRP) and aluminum (Al) are already in use today, but will certainly see increased usage in the future [1,2].

A hybrid composite involves the combination of two materials with different material properties, thus the joining technology is of particular importance. The current literature distinguishes between the adhesive, mechanical, and welded joining of hybrid materials. Previously, conventional adhesive joining techniques were used for the joining of polymeric and metallic materials. The disadvantages associated with these are limited application temperatures, time-consuming surface pre-treatments, long curing times of the adhesive component as well as the presence of an irreversible bond [3,4]. Hybrid composites that are adhesively joined can – depending on the quality and strength of the bond – fail cohesively, adhesively, cohesive-adhesively, or within both base materials [5]. As the materials used here also possess very different physical-chemical properties, the joining presents inherent difficulties. For example, the electrochemical potentials of Al and CFRP differ significantly, which promotes corrosion processes and can lead to the failure of the bond [6,7]. Therefore, intensive research is currently investigating new technologies for hybrid joining, whereby the focus should be on the solution to the problem of corrosion. Various innovative joining concepts for Al and CFRP are being investigated by the research group Schwarz-Silber at the University of Bremen. These concepts offer solutions to the different problems of conventional joining techniques [8,9,10].

The aim of this collaborative research project, promoted by the Deutsche Forschungsgemeinschaft (DFG), is to combine the materials Al and CFRP into a hybrid composite using the HPDC process. As already described in previous work by [11], the process concept involves the partial coating of CFRP with thermoplastic polyetheretherketone (PEEK). After the initial experiments, it was suspected that the PEEK is being melted by the process heat, thus joining the CFRP to the Al in the form of an adhesive bond under a process pressure of many hundred bars.

* Corresponding author: Schmid, Wiener Str.12, 28359 Bremen, +4942122467151, armin.schmid@ifam.fraunhofer.de

The adhesive properties of PEEK in a bond with a metal have previously been investigated in experiments by [12] as well as with polyamide 6 and a DC01 steel plate under the term 'fusion bonding' by [13]. PEEK is thus considered a key factor in the realization of such hybrid composites, as it functions both as an adhesive and as an electrochemically decoupling layer between the carbon fibers of the laminate and Al. As shown in [11], a hybrid composite can thus be intrinsically formed using a casting process, demonstrating tensile shear strengths close to those of structural adhesives. Within this DFG-funded investigation, the focus is on another two-step process concept, one that places higher demands on the process technique. In a combination of processes, the consolidation of the CFRP with a PEEK-based matrix occurs in the high pressure die before the composite is cast in Al. Such a process combination is already being individually tested and implemented in various manufacturing processes, demonstrating the feasibility of the direct impregnation and consolidation of the carbon fiber preform with a thermoplastic in conjunction with the plastic injection molding process within a plastic injection molding tool [14].
This study provides a closer examination of two different process concepts for the realization of a hybrid composite made from CFRP and Al with a PEEK decoupling layer.

# 2 MATERIALS & METHODS

Two different process concepts were developed for the production of a hybrid composite of CRFP and Al using the Al HDPC process and with an electrochemically decoupling layer separating both materials. Both concepts are presented in detail in the following. There exist some challenges to a successful implementation of both concepts, and these need to be solved, requiring interdisciplinary cooperative efforts of the project partners in the fields of textile technology (FIBRE Bremen), casting technology and simulation (cooperation of the University of Bremen and Fraunhofer IFAM Bremen). The integration of carbon fiber reinforced composite materials in the Al HPDC process presents the following specific demands:

- The electrochemical decoupling of the carbon fibers
- The temperature resistance of the decoupling layer
- The determination of the process parameters for the realization of a suitable boundary layer with a high bond strength of the composite

In the development of both process concepts, knowledge flowed in from the pre-experiments [11]. Thus, it was possible to develop a hybrid component consisting of a load path oriented CFRP structure combined with an Al cast node modelled after a holding element (bracket) used in aircraft construction (Fig. 1). Besides the process technique and the boundary layer, the focus lay on the realization of a casting structure suitable for HPDC with locally adapted wall strengths as well as on a load path oriented CFRP component realized using the TFP process. This CFRP component has already been the focus of research in preliminary studies [15]. The feasibility and performance of both process concepts could thus be directly evaluated using a technology demonstrator as well as compared with brackets produced using other methods and which are already in use in the industry.

***Fig. 1*** *Technology demonstrator*

In pre-experiments, organic sheets (0°/90°) with the dimensions 100 mm by 40 mm and 2 mm thick with a PEEK matrix (Victrex, type G150/G151) were in addition partially coated over a length of 40 mm with PEEK (Victrex, type: Aptiv 1000), placed in a high pressure casting die in a cold chamber high pressure casting unit from Bühler (SC N/66), and cast in the coated area with the Al alloy SF 36 (AlSi10MnMg). For the evaluation of the process concept, a microsection was taken from the sample cross-section and analyzed. In addition, CT scans were made.

# 3 RESULTS

## 3.1 TFP PROCESS

The side-by-side tailored fiber placement (TFP) process is used for the production of the preform for both process concepts (Fig. 2, A). Special reinforcing fiber rovings made of carbon fibers from Toho Tenax (HTS45, P12, 12K, 800tex) are, together with thermoplastic yarn made of PEEK from Victrex (151 G), laid close to the final outline and fixed with thermoplastic sewing thread from Victrex (151 PF) onto a carrier foil made of PEEK (Aptiv 1000) with a thickness of 50 µm. The preforms are subsequently separated from the carrier foil with a punch. As this process has limitations regarding the individual preform thicknesses, multiple separately finished preforms

(Fig. 2, B) are laid, fixed through sewing, and combined until the desired total thickness of the preform has been achieved.

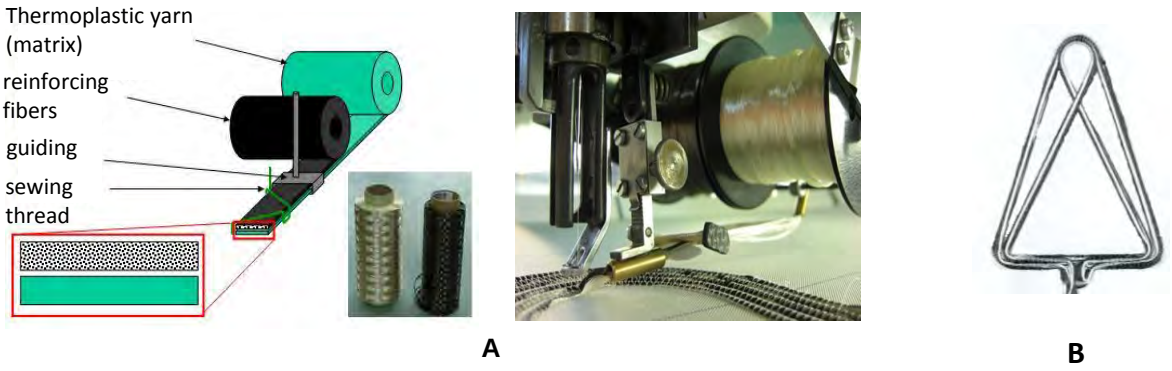


***Fig. 2*** *TFP process (A-B): Stacking of the carbon fibers and PEEK fibers and fixing via sewing thread to a load path optimized flexible preform (A); hybrid flexible preform consisting of carbon and PEEK fibers (B)*

The flexible preform, as described above, forms the basis for both process concepts, which are referred to as "pre-consolidated (PC) and in situ consolidated (ISC)". The further process steps differ according to each process; these are described in the following sections.

### 3.2 PROCESS CONCEPT PRE-CONSOLIDATION (PC)

For the pre-consolidation process concept, the flexible preform is consolidated prior to the actual casting process in an upstream process step. Hereby, the carbon fibers are impregnated with melted PEEK fibers in a press at a temperature of 390° C and a pressure of 60 bar, enabling the subsequent consolidation (Fig. 3, A). In the next step, PEEK (Victrex, type: Aptiv 1000) is partially applied at a temperature of 390° C (Fig. 3**,** B, C). The CFRP inlays are subsequently placed into an in-house developed tool in the cold chamber high pressure die casting machine from Frech (DAK 250) (Fig. 3**,** D**)** and are partially cast in with the Al alloy Silafont 36 (AlSi10MnMg) in the area of the applied PEEK at 700° C and 800 bar holding pressure and close to 20 $ms^{-1}$ gate speed (Fig. 3**,** E).

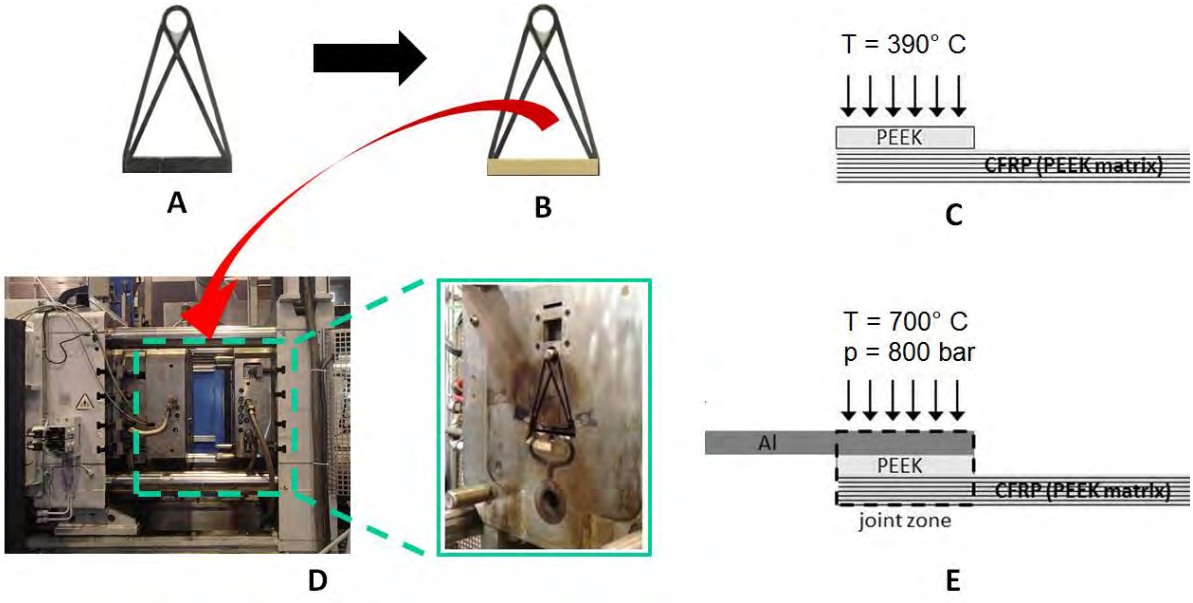


***Fig. 3*** *Process concept PC (A-E): Consolidated CFRP inlay (A) with partially applied PEEK layer (B); Schematic diagram of the PEEK application (C); The partially coated CRFP inlay is placed into the high pressure die (D); Schematic diagram of the hybrid casting process (E)*

### 3.3 PROCESS CONCEPT IN SITU CONSOLIDATION (ISC)

For the ISC process concept, the flexible TFP preform is laid into the high pressure casting die shown above (Fig. 4**,** A). With a closed high pressure casting die, the hybrid preform is then subjected to a temperature of 390° C using heating cartridges, melting the PEEK fibers. Through a defined process management of temperature and pressure (60 bar), modelled on the process parameters of FVK production, after a certain holding time the melted PEEK impregnates the carbon fibers and the preform is pressed into its final contour (Fig. 4**,** B). After cooling to 200° C, the typical temperature in HDPC, the preform consolidates (Fig. 4**,** C). The standard HDPC process is then initiated and the preform is partially cast in with Al (Fig. 4**,** D).

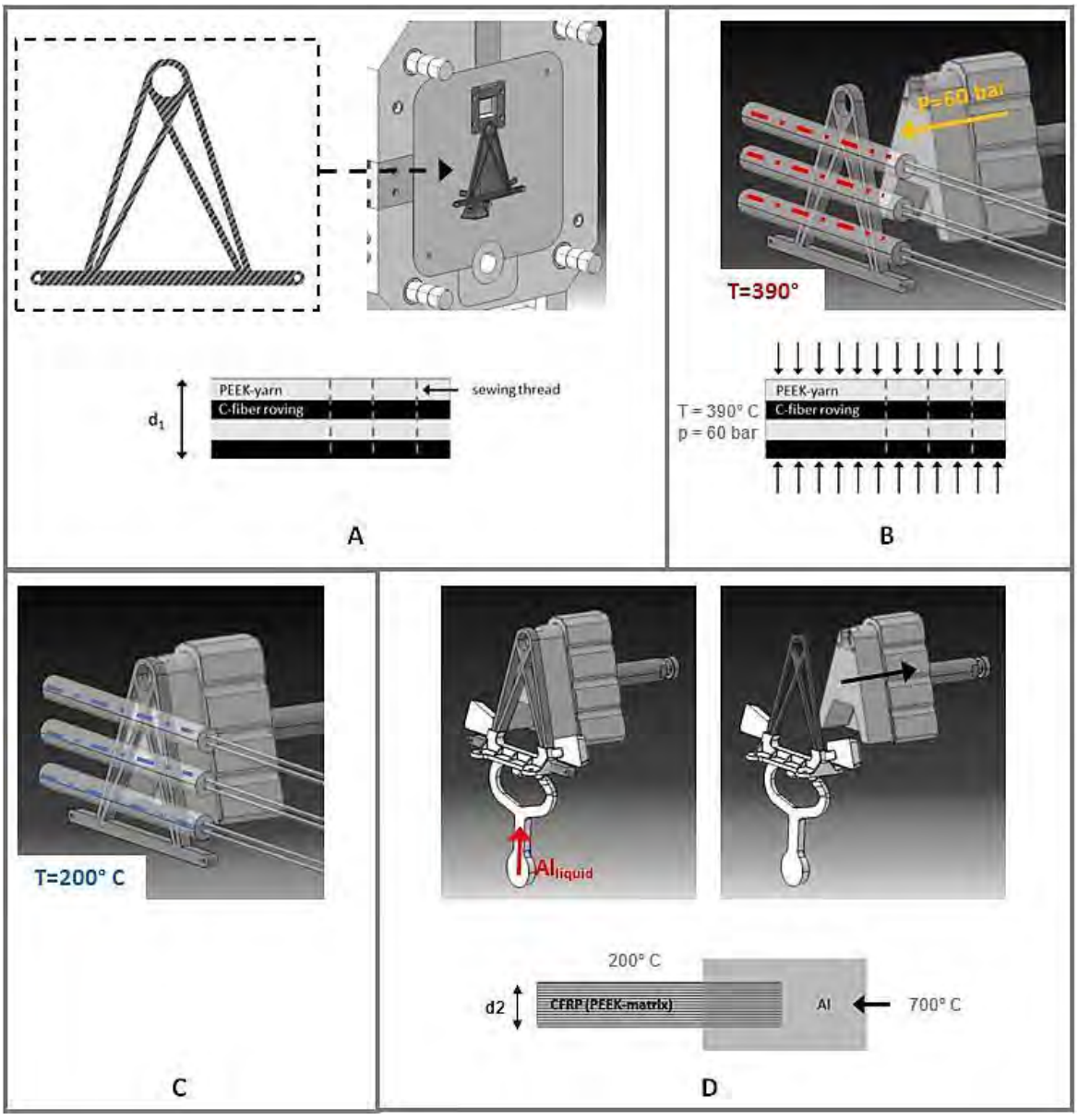


***Fig. 4*** *The preform is placed in the high pressure die at the appropriate position points (A); the preform is heated using heating cartridges and subsequently pressed under a specific pressure (B); under a specific pressure the preform is cooled and consolidated; (C) the consolidated CFRP structure is partially cast in with Al*

### 3.4 ANALYSIS OF THE FRACTURE PLANE

Fig. 5**,** A shows the microsection of a hybrid composite sample that was produced using the PC process concept. It clearly shows that, with the appropriate process parameters, an electrochemically decoupling layer of PEEK, and thus a spatial separation of CFRP and Al, can be achieved. This observation is further underscored with CT imagery (Fig. 5**,** B), which shows that across the entire sample the CFRP is consistently coated with PEEK.

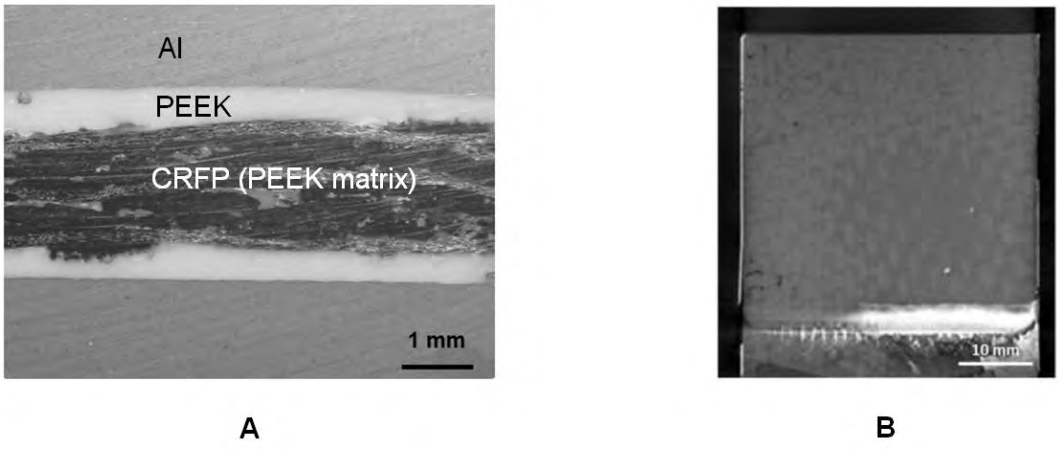


***Fig. 5*** *Microsection hybrid composite sample (A); CT scan of the electrochemically decoupling layer (B)*

## 4 CONCLUSIONS

The PC and ISC process concepts demonstrate new methods wherein CFRP and Al can be joined using Al HPDC. The process concepts presented here combine various manufacturing processes, such as the TFP process and HPDC, both of which are suitable for automated large series production. The short curing time of the PEEK as a thermoplastic further enables the economical production of a hybrid composite. The feasibility of the PC process concept has already been shown in previous studies [11]. Through the use of thermoplastic partially crystalline PEEK with a glass transition temperature (Tg) of 143° C, a melting point of 343° C, and a high strength along a wide range of temperatures [16], a material has been found that can withstand the HPDC process without significant degradation and which can thus be used both as a matrix material for CFRP and an electrochemically decoupling layer in a composite. As has already been shown in [11] for the PC process concept, the use of PEEK between CFRP and Al can enable the production of hybrid composites with tensile shear strengths similar to those of structural adhesives. Based on these results, which are supported by findings in the literature [12,17,18], it can be stated that PEEK thus also takes on the function of an adhesive in a hybrid composite.

The ISC process concept aims to combine different production processes in one tool in order to demonstrate the feasibility, whereby the manufacture of a fiber reinforced composite is combined with the HPDC process. The impregnating of carbon fibers with PEEK and the consolidation of the CFRP is thus shifted into the high pressure casting die, instead of occurring in an additional tool in an upstream work step. This generally has the potential to lower costs in the process chain for the realization of hybrid composites. To this end, unconventional heating cartridges and a pressing unit are additionally integrated into the high pressure casting die in order to melt the PEEK as well as enable the automatic consolidation of the CRFP under specific temperatures, pressures, and holding times.

In summary, it has been shown that the PC process concept is suitable for the production of hybrid composites using the HPDC process, which have both an electrochemically decoupling layer as well as tensile shear strengths comparable to those of conventional bonding techniques such as adhesives. However, further investigations are required in order to verify the previously achieved results for the PC process concept and to further optimize the process and material parameters. Intensive experiments will also be conducted for the ISC process concept, which, on the one hand, offers great potential for process combination and, on the other hand, is presenting challenges for the process technology.

## REFERENCES

[1] Friedrich H. E., Krishnamoorthy S. K.: *Leichtbau als Treiber von Innovationen*. In: H. E. Friedrich, Leichtbau für den Fahrzeugbau, Springer Fachmedien, Wiesbaden, 2013, 1-30.
[2] Hagebeuker L., Seidel K., Eckstein L.: *Composite-intensiver Leichtbau in Fahrzeugmodulen*. Automobiltechnische Zeitschrift, edition 11 (2016) 30-35.
[3] Kah P., Suoranta R., Martikainen J., Magnus C.: *Techniques for joining dissimilar Materials: metals and polymers*. Rev. Adv. Mater. Sci. 36 (2014) 152-164.
[4] Amancio-Filho S.T., dos Santos J.F.: *Joining of Polymers and Polymer–Metal Hybrid Structures: Recent Developments and Trends*. Polymer engineering and Science (2009) 1461-1476.
[5] Kweon J.-H., Jung J.-W., Kim T.-H., Choi J.-H., Kim D.-H.*.: Failure of carbon composite-to-aluminum joints with combined mechanical fastening and adhesive bonding*, Composite Structures 75 (2006) 192-198.
[6] Payan S., Le Petitcorps Y., Olive J.-M., Saadaouic H.: *Experimental procedure to analyse the corrosion mechanisms at the carbon/aluminum interface in composite materials*. Composites: Part A 32 (2001) 585-589.
[7] Wielage, B., Dorner, A.: *Corrosion studies on aluminium reinforced with uncoated and coated carbon fibres.* Composites Science and Technology 59 (1999) 1239-1245.
[8] Clausen J., Van der Auwera R., Lardong M.-C., Pille C., Wöstmann F.-J., Busse M.: *Cast Aluminum – CRFP Composite components with transition layer of a high performance*. International Conference Euro Hybrid, Stade, 10-11 April 2014.
[9] Bitykov V., Jablonski F.: *Failure modeling of hybrid transition structures*. Vol. 831 (2016), 44-53, 1662-7482.
[10] Lang A., Husemann L., Herrmann A. S.: *Influence Of Textile Process Parameter On Joint Strength For Integral CFRP-Aluminum Transition Structures*. Procedia Materials Science 2 ( 2013 ) 212 – 219.
[11] Schmid A., Arnaut A., Clausen J., Koerdt M., Struss A., Wöstmann F-J., Busse M.: *Intrinsic aluminum CFRP hybrid composites produced in high pressure die casting with polymer based decoupling layer*. Key Engineering Materials, 1662-9795, Vol. 742, 197-204.
[12] Suguma T., Carciello N. R., Miura M.: *Adhesion of crystalline polyphenyletheretherketone (PEEK) in metal-to-metal joints*. Int. J. Adhesion and Adhesives, January (1991) Vol. 12, No. 1. 27-37.
[13] Reincke T., Kreling S., Dilger K.: *The Production-Related Influence of Iron Oxides on Steel Surfaces on the Adhesion of Fusion-Bonded Hybrid Structures*. Materials Design and Applications, pp 363-376.
[14] Linn C., Hoffmann L., Müller T., Drummer D.: *Herstellung von CFK-Bauteilen durch Direktimprägnierung mit Thermoplasten in der Spritzgießmaschine*. Lightweight design, Vol. 5, pp 56–61.
[15] Arnaut K., Schiebel P., Lang A., Herrmann A.: *Reinforcement elements aligned with the direction of forces for load transfer areas of long-fiber-reinforced thermoplastic components*. Materials Science Forum, Vol. 825-826 (2015) pp 779-786.
[16] Searle O. B., Pfeiffer R. H.: *Victrex Poly(ethersulfone) (PES) and Victrex Poly(etheretherketone) (PEEK)*. Polymer engineering and science, Vol. 25 (1985) No. 8.
[17] Schulze K.: *Adhäsions- und Degradationsverhalten an der Grenzfläche zwischen Titan und Polyetheretherketon.* Dissertation, Fakultät für Maschinenbau der Technischen Universität Chemnitz, Universitätsverlag Chemnitz 2017.
[18] Ingram C., Ramani K.: *The effect of sodium hydroxide anodization on the durability of poly(etherketonetherketoneketone adhesive bonding of titanium*. Int. J. Adhesion and Adhesives 17 (1997) 39-45.

# BONDING BY MICROBRACING: QUANTIFICATION OF TEMPERATURE INFLUCENCE FOR MULTI-COMPONENT HIGH PRESSURE DIE CASTING

**P. Messer[1*], U. Vroomen[1], A. Bührig-Polaczek[1]**

[1]Foundry-Institute, RWTH Aachen University

**ABSTRACT:** Many industries require highly innovative lightweight construction concepts with specifications which can no longer be met by one material alone. In addition to lightweight construction using fiber-reinforced plastics and aluminum-steel hybrids, a plastic-aluminum hybrid based construction method holds great potential for weight reduction.
There are already many applications for plastic-metal hybrids where the bond is usually realized by macroscopic form-fit connection, which requires appropriate preparation of the metallic semi-finished products. This comprises the consequence of long process chains and the necessity of extensive plant engineering.
The Foundry Institute has at its disposal a high pressure die casting (HPDC)-die that enables the combination of aluminum HPDC and plastic injection molding (IM) within a single die. In a first step, the aluminum component is high pressure die casted and then, after the release of another cavity, the plastic component is injected right onto the aluminum casting. Using this process, metal-plastic hybrids can be formed completely on just one production line in the same die. This shortens the process chain considerably compared to competing processes, such as insert technology.
As part of the "Integrative Production Technology for High-Wage Countries" Cluster of Excellence, the research focus in multi-component high pressure die casting (M-HPDC) is currently on the quantification of temperature influences on the bond strength. In order to meet this requirement, the "Hybrid-III" die is equipped with extensive temperature control technology (variothermal temperature control circuits, high-performance heating ceramics, etc.) and sensors that enable a quantification of the different temperature impacts on the adhesion of the hybrid. The goal is to determine the influencing factors on the bond strength, so that statements can be made as to the conditions under which highly resilient hybrid components are producible.

**KEYWORDS:** hybrid, bond characterization, temperature management, joining method, high pressure die casting, injection molding

## 1 INTRODUCTION

Innovative products often necessitate innovative materials. In multiple cases, the requirements regarding, strength, density, temperature resistance, etc. cannot be provided just by one material resulting in the need for multi-material applications. Accordingly, appropriate manufacturing processes are required which allow the manufacturing of metal-plastic hybrids with a reasonable amount of effort in a reasonable amount of time.

## 2 STATE OF THE ART

As long as HPDC and IM are reviewed independently, several multi-material applications are already in existence. In particular, metal-metal hybrids using combinations of steel and aluminium or aluminium and magnesium are already manufacturable by inserting a sheet metal into a HPDC-die in order to cast the second component using the conventional HPDC-process [1, 2]. However, so far no multi-material-applications are known which consist of more than one high pressure die casted component, manufactured in the same die. At this point, the multi-component IM-technology is already much farther developed, especially concerning the processing of a large number of components on the same IM-machine. Examples of these include items of daily use as for example two-component handles combining hard and soft segments. Another typical two-component process is the combination of metallic inserts and mold-on plastic components. In the procedures described above, a basic distinction can be made between Post-Mold-Assembly (PMA) and In-Mold-Assembly (IMA), which is described in more detail in Chapters 2.1 and 2.2.

### 2.1 POST-MOLD-ASSEMBLY

If joining processes such as bonding, welding, soldering, riveting, etc. are used, this is referred to as PMA. The main difference to the IMA is that both components are manufactured independently of each other and joined together in a subsequent process step. This may be necessary for some applications due to geometric, thermal or other boundary conditions. As a result of the subsequent joining process, the logistics complexity increases and the process chain is prolonged, so that the effort to manufacture components in the IMA described below is often high.

### 2.2 IN-MOLD-ASSEMBLY

All of the processes mentioned in Chapter 2, can be assigned to IMA. The IMA is characterized by the fact that the process forming the second component is also the joining process of the hybrid component [3]. Usually, sheet metals are used for this purpose, but there are also applications where plastics are injection molded onto the castings which were inserted in the IM-die of a separate IM-machine before. As an example of application the production of an antenna base support [4] can be mentioned here.

### 2.3 „ADVANCED“- IN-MOLD-ASSEMBLY

The M-HPDC-process, which has been developed at the Foundry Institute of RWTH Aachen University is the logical continuation of the conventional IMA. In contrast to conventional IMA processes, both the aluminium and the plastic component are produced by primary shaping in the same die, thus eliminating the handling and logistics work involved in preparing metallic inserts and considerably shortening the process chain.

## 3 MACHINERY AND PROCESS FOR M-HPDC

### 3.1 MACHINERY

For the M-HPDC-Process, a HPDC-machine is necessary, which is extended by an IM-unit. The Foundry Institute has a high pressure die casting machine of the type Frech DAK 450, Oskar Frech GmbH + Co KG, Schorndorf, Germany, which is equipped with an IM-unit type Arburg Allrounder 570 S, Arburg GmbH + Co KG, Lossburg, Germany. Figure 1 shows the foundry institute's production cell, which is used for M-HPDC.

***Fig. 1*** *Manufacturing plant for multi-component high pressure die casting (M-HPDC)*

### 3.2 DIE SETUP

The "Hybrid-III" die (figure. 2), designed at the Foundry Institute, is based on the knowledge built with the predecessor die "Hybrid-II". With the Hybrid-II die, it has already been shown that a bond in this process is basically achievable even with more complex geometries [5]. In addition, it is assumed that the main influence for a good bond strength is dependent on the interaction of die, aluminum and plastic temperatures [6].
In order to quantify the influence of temperature, the Hybrid-III die is equipped with extensive temperature control and sensor technology. The specimen geometry in accordance with DIN EN 1465 [7] allows to test the bond strength and compare it directly with competing PMA-methods such as gluing.
As can be seen in figure 2, the die has a vertical slider, which moves into IM-position right after the high pressure die casting process and thus enables injection molding of the plastic components in the same die. The final design and manufacturing of the die was carried out by Heck+Becker GmbH & Co. KG, Dautphetal, Germany.

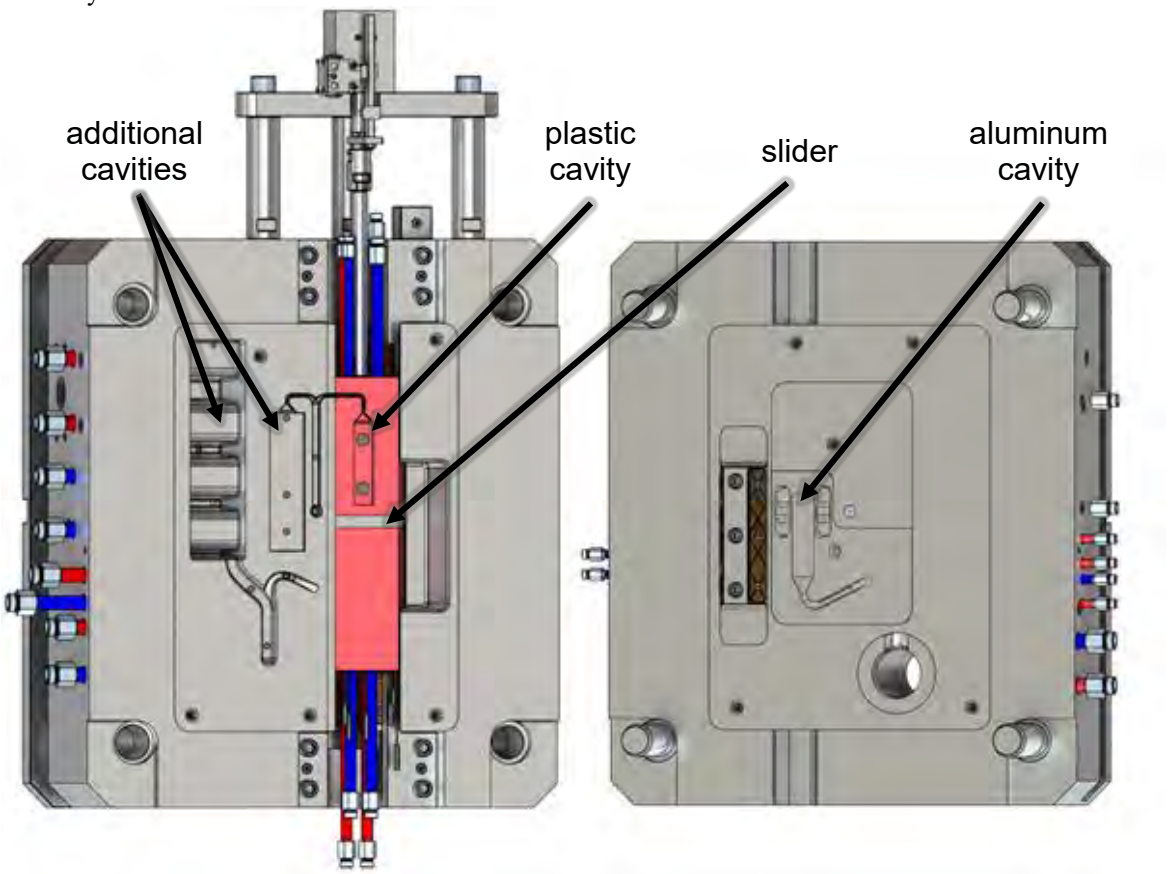


***Fig. 2*** *Setup of Hybrid-III die (Slider in IM-position)*

### 3.3 HEATING EQUIPMENT

Plastics and aluminium have different requirements in terms of die- and processing temperatures. For this reason, the Hybrid-III die is equipped with a variety of temperature control systems. A water temperature control unit, a variothermal oil heating/cooling unit and two conventional oil heating/cooling units are available for fluid based temperature control. A CPH high-performance-heating-ceramic, manufactured by gwk Gesellschaft Wärme Kältetechnik mbH, Meinerzhagen, Germany, is used to ensure high temperature dynamics in the joining area. In addition to the control of the heating ceramics, two additional water circuits are also installed, which allow a shift from heating to cooling at a defined point in time in order to be able to achieve both, high temperatures during casting and high heat flux for cooling and solidification of the hybrid casting.

### 3.4 PROCESS SEQUENCE

The successful formation of a strong bond is highly dependent on the appropriate execution of the process sequence shown in figure 3. The process sequence is explained in the following.

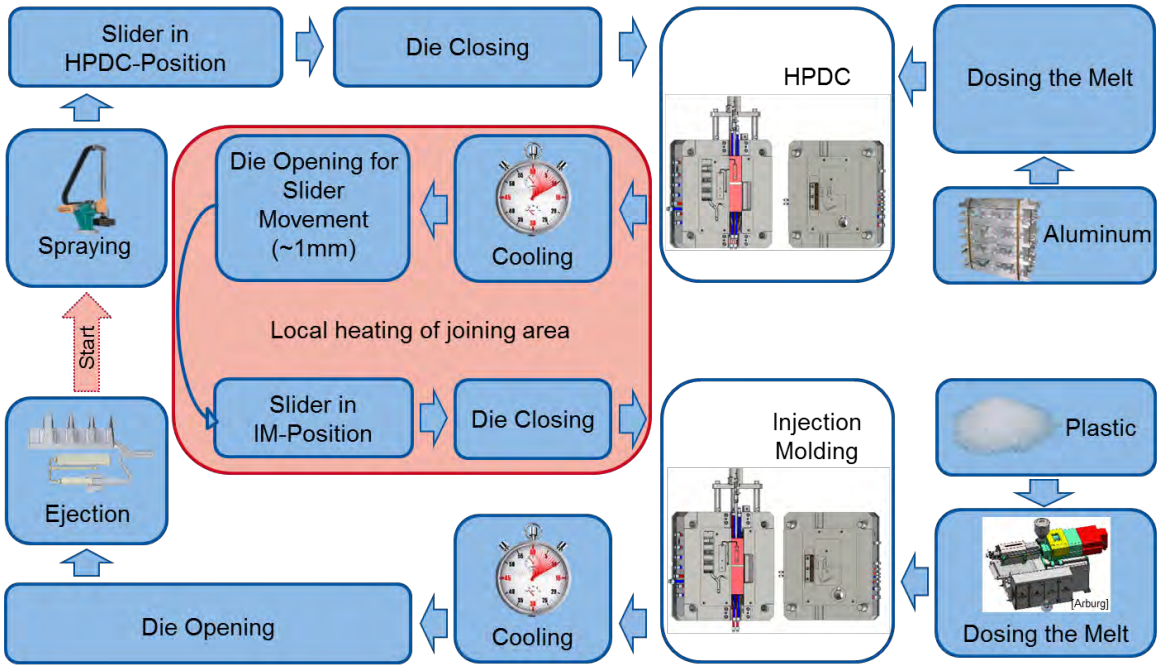


***Fig. 3*** *Process sequence of the M-HPDC-process*

Starting with the open die, the parting agent is first sprayed onto the aluminum cavity's surface, the slider is moved in the following step to the HPDC-position and then the die is closed. This is succeeded by the aluminum shot and a short cooling time in order to ensure that the additional alloy in the aluminum cavity is also sufficiently solidified. In contrast to conventional high pressure die casting, the die does not open completely but only by approx. 1 mm, so that the slider is relieved and can be moved into the IM-position and the die closes again. Parallel to the cooling time of the aluminium component, the joining area is heated by the CPH high-performance-heating-ceramic mentioned in chapter 3.3, so that the temperature in the joining area can be set independently of the cooling state of the remaining aluminium casting. As soon as the target temperature in the joining area has been reached, the plastic component is molded onto the aluminum casting. Finally after the cooling time has elapsed, the die opens completely for ejection of the hybrid casting.

## 4 FIRST SHOTS, CONCLUSION AND OUTLOOK

The Hybrid-III die is currently being put into operation. The goal is to cast a hybrid structure by micro-bracing the plastic with the surface roughness of the aluminium component. As can be seen in figure 4, the first hybrids have already been produced.

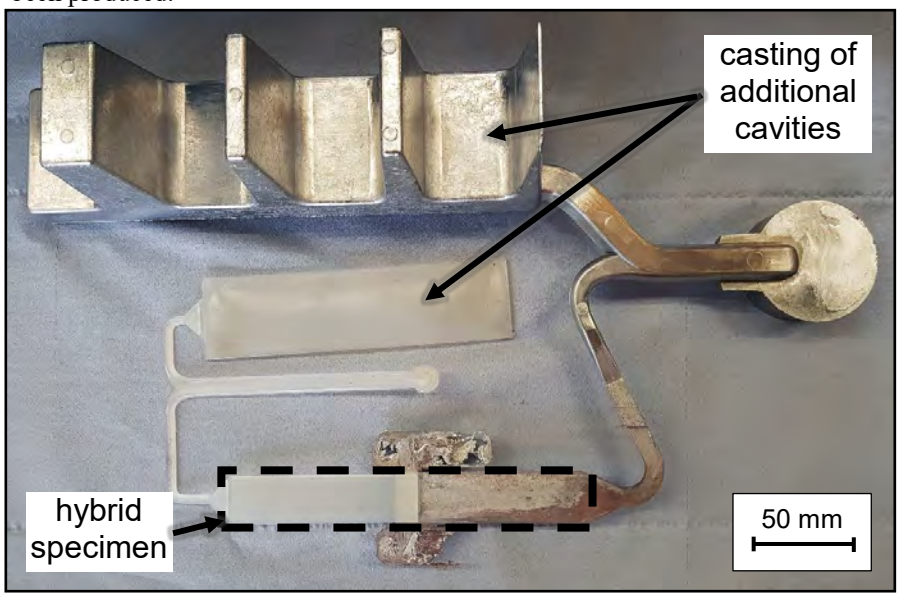


***Fig. 4*** *Hybrid-III: First castings produced in the die*

Commissioning has shown that the Hybrid-III die is suitable for the production of aluminium-plastic test specimens and that in principle a bond can be achieved. Extensive test series are planned in order to determine the influencing factors on the bond strength. The main focus will be to quantify the temperature influence of aluminium, plastic and die temperature.

## 5 ACKNOWLEDGEMENT

The authors would like to thank the German Research Foundation DFG for the kind support within the Cluster of Excellence „Integrative Production Technology for High-Wage Countries".

## REFERENCES

[1] Lao, B., *Druckgegossene Metallhybridstrukturen für den Leichtbau- Prozess, Werkstoffe und Gefüge der Metallhybriden*, in *Fakultät für Georessourcen und Materialtechnik* 2013, RWTH Aachen University.

[2] Schenke, G., D. Joop, and A. Bührig-Polaczek, *Hybride Fertigungsverfahren zur Umsetzung gussintensiver Leichtbaukonzepte - Grundlagenforschung und Prozessentwicklung am Giesserei-Institut der RWTH Aachen University*, in *Verbundwerkstoffe / Werkstoffverbunde 2013*. 2013.

[3] Brecher, C. and D. Özdemir, *Integrative Production Technology*. 2017: Springer.

[4] "Antenna Base Support", http://www.foehl.de/de/technologien/#to-section-51, 21.02.2018

[5] Schenke, G., *New hybrid molding process for good adhesion and increased functions of metal/plastic composite parts*, in *TMS 2014 Annual Meeting & Exhibition*. 2014: San Diego, USA.

[6] Messer, P., U. Vroomen, and A. Bührig-Polaczek, *Multi-Component High Pressure Die Casting (M-HPDC): Influencing Factors on the Material Temperature During the Joining of Metal-Plastic-Hybrids*, in *Light Metals*, A.P. RATVIK, Editor. 2017, Springer. p. 5.

[7] *DIN EN 1465, Klebstoffe –Bestimmung der Zugscherfestigkeit von Überlappungsklebungen; Deutsche Fassung EN 1465:2009*.

# SINGLE SIDE RESISTANCE SPOT WELDING WITH A COAXIAL ELECTRODE ARRANGEMENT FOR JOINING PLASTIC-METAL-HYBRID STRUCTURES

**Konstantin Szallies[1]*, Martin Bielenin[1], Jean Pierre Bergmann[1], Christian Neudel[2]**

[1]Technische Universität Ilmenau, Production Technology Group,
Gustav-Kirchhoff-Platz 2, 98693 Ilmenau, Germany
[2]Audi AG, Predevelopment Department of Joining Technology, 85045 Ingolstadt

**ABSTRACT:** Hybrid joints, such as for polymer-metal components show a high potential regarding to lightweight applications. Due to their fundamental differences in chemical and physical properties, new approaches must be developed for common industrial joining processes. Currently, these joints are usually manufactured by adhesive application or mechanical methods. Challenges for mechanical joining methods are resulting notches and stress peaks. In contrast, the curing time of adhesives causes an increased process time. In this case, thermal direct joining processes show several benefits to the mentioned disadvantages.
A new approach for thermal direct joining is shown in this paper. Based on resistance spot welding a coaxial electrode arrangement was used to join polymer-metal hybrid components in overlap configuration. The impact of the welding parameters as well as different surface conditions (corundum blasting, laser structuring) on the joint strength and joining zone are investigated. It was found that coaxial single sided resistance spot welding of polymer-metal hybrid structures is a method which allows a reproducible joining at low cycle times and low costs.

**KEYWORDS:** design, welding, dissimilar materials, polymer-metal hybrid joint, thermal direct joining, resistance welding

## 1 INTRODUCTION

The use and the advancement of constructive and material lightweight principles are essential in order to achieve the ambitious targets for the reduction of resource consumption in various industries. The current development, especially by the increasing demands in transport applications, shows the importance of the mix of different materials with various characteristics. This engineering approach leads to an enhancement concerning loadability, stiffness or fatigue strength of components without an increase in weight. However, new challenges occur in terms of joining to realize structures with dissimilar materials.
Hybrid structures, in particular through metal-plastic joints, demonstrate a high potential regarding to the mentioned targets. Due to the fundamental differences in chemical and physical properties, the challenge is to find new approaches for common joining processes. Currently, these material combinations are joined by mechanical processes or adhesive bonding. However, mechanical joining processes exhibit several disadvantages, especially notches and stress peaks. Curing times of adhesives are considered as a drawback as well. In contrast thermal joining processes provide several benefits in context to the mentioned disadvantages.
Initially the metal partner is heated until the thermoplastic partner melts at the boundary layer, due to the heat conduction. The molten polymer wets the surface of the metallic partner and penetrates the surface structure. After cooling a solid joint occurs. Therefore, different process strategies for heating can be used to achieve polymer-metal hybrid joints, such as thermal direct joining [1, 2], ultrasonic welding [3, 4], induction welding [5, 6], infrared radiation [7], laser joining [8, 9, 10] or resistance welding [11, 12].
Resistance spot welding is still the most common technology in the sheet-metal working industry for joining. This is caused by a high degree of automation, minor process costs and a short welding time. Conventional resistance spot welding, as is usual in industrial production, requires a both sided accessibility. Therefore, welding of flangeless hollow profiles and the resistance spot joining of polymer-metal hybrid components are limited. [13] This study shows an approach for the resistance welding technology to join polymer-metal hybrid structures.

* Corresponding author: Gustav-Kirchhoff-Platz 2, 98693 Ilmenau, phone: +49 3677 69-2764, fax: +49 3677 69-1660, email: info.fertigungstechnik@tu-ilmenau.de

## 2 EXPERIMENTAL SETUP

The experimental investigations were carried out using an alternating current projection welding machine (Dalex PMS 11-4, Pw-max = 416 kVA) with a special device for welding with a coaxial electrode arrangement designed by the authors within the TU Ilmenau. The schematic configuration of the device is shown in figure 1a. Due to flange geometry used in automotive applications, the outer electrode was arranged as circular ring with an outside diameter of 16 mm. The inner electrode was chosen in F1 geometry, based on DIN EN ISO 5821. As against to standardized diameter, a diameter of 10 mm was required. The electrode working face was scaled, based on 16 mm standardized electrodes. Both electrodes were made from CuCr1Zr in order to use a common electrode material.

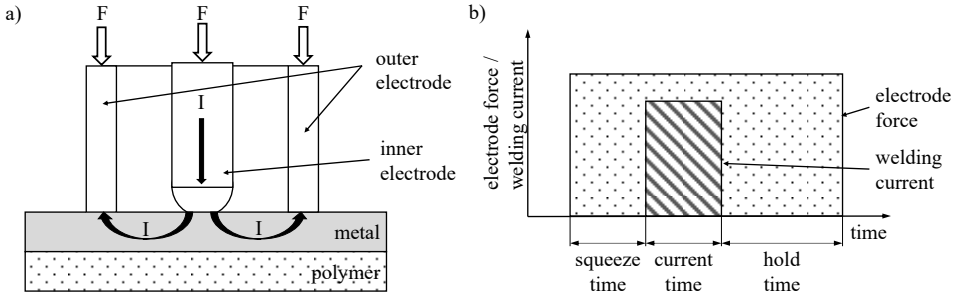


***Fig. 1*** *Schematically arrangement of single-side coaxial resistance spot welding for polymer-metal hybrid joining (a) and principle cycle of welding process (b)*

The welding cycle used in this study is schematically shown in figure 1b. After iterative preliminary investigations, the welding parameters electrode total force (1980 N), squeeze time (200 ms) and hold time (1000 ms) were kept constant.

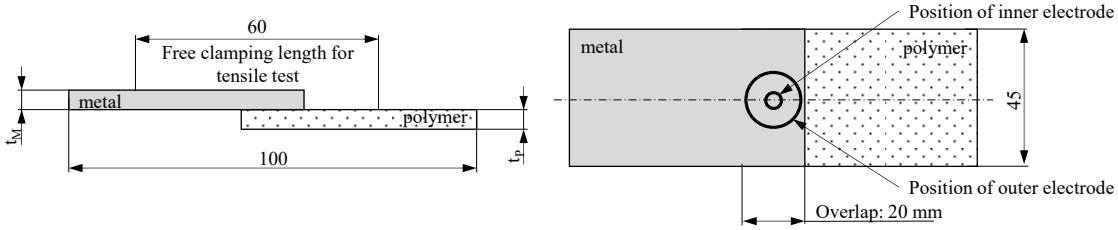


***Fig. 2*** *Specimen geometry*

The specimen were positioned with 20 mm overlap. The joint configuration is shown in figure 2. For the metal joining partners a steel DX56D+Z100MB with a thickness of 1.0 mm and an aluminum EN AW 6016 T4 with a thickness of 1.15 mm were chosen. The used polymer materials were Polyamide 6.6 as well as endless fiber reinforced polyamide PA 6 GF 47 with a thickness of 2 mm. The process configuration was carried out as heat conduction joining. The influence of the metal surface treatment was evaluated with different preparations. After preliminary investigations the corundum blasted (grain size F54, cleaned with isopropyl) and laser-based surface structuring evidenced the advantageous results. For laser-based surface treatment, a 20 W fiber-laser (Rofin PowerLine F20) was used in order to generate line-shaped structures. The line structures were applied perpendicular to the load direction of the following tensile test. In order to realize a high structure aspect ratio, the surface was structured with periodically recurring line-pattern.
The mechanical properties were examined in a standardized tensile test with testing speed of 10 mm/min. For adequate statistical validation all experiments were repeated at least 3 times.

## 3 RESULTS AND DISCUSION

### 3.1 JOINT FORMATION AND WELDABILITY LIMITS

Figure 3 shows coaxial single sided resistance spot welds of DX56D+Z100MB and transparent PA6.6 in overlap configuration for increasing welding currents. The area of the visible joint zone depends particularly on welding current and welding time. This indicates that process conditions value influences the joint zone formation. In Figure 3 the visible melting layer under the electrodes by means of a discoloration of the polymer

is shown. For increasing welding currents, the fusion area simultaneously increases, due to a higher resistance heating in the metal.

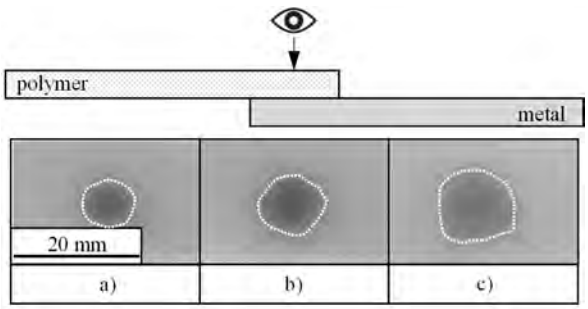


***Fig. 3*** *Joint zone formation for increasing welding currents a) 4.6 kA, b) 5.5 kA, c) 6.4 kA using DX56D and transparent PA 6.6 (welding time t = 200 ms)*

Figure 4 shows the cross section micrographs for two different welding times. The polymer adheres to the metal in the region of the melting layer (symbolized with the while line). This can be shown by the polymer penetrating the surface structure. In this case, the melting layer does not form a spot shape, like conventional resistance welding, due to the one sided heating. By using low welding currents and welding times, a flat planar melting layer obtains. For increasing welding currents and times, a wave-shaped thermal influenced zone of the polymer appears between the inner and the outer electrode. Thus, it can be concluded that the major heating is not centered in the middle, as in case of conventional resistance welding. This zone occurs circular inside the coaxial electrodes, schematically shown in figure 5. Furthermore, in this area a bubble formation can be observed. This formation is additionally facilitated due to, that no resinking of the electrodes is possible in this region.

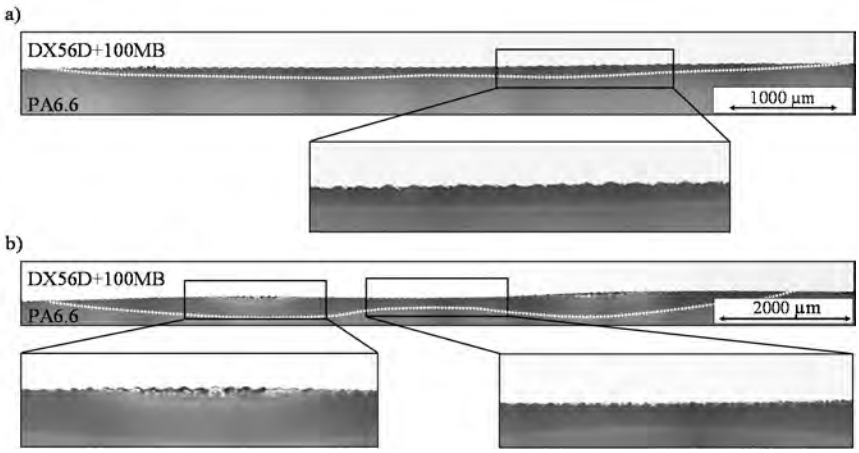


***Fig. 4*** *Joint zone micrographs in cross sections of different welding times a) 200 ms ; b) 1800 ms*

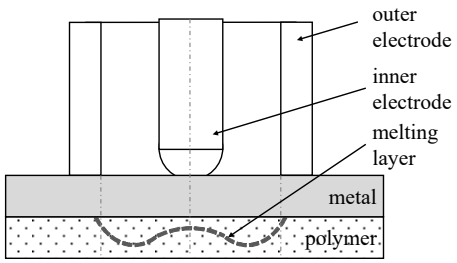


***Fig. 5*** *Characterisation of the melting layer*

In order to investigate the capacities of the single-sided coaxial resistance spot welding process concerning to the metal-plastic hybrid joints weldability studies were carried out and the process limits were specified. To determinate the weldability lobes, common test and documentation guidelines could not be applied. However, in deviation to DIN EN ISO 14327 the limits of the weldability lobes were defined by a minimal tensile force

of 500 N. As characterized in figure 6 the maximum process limit represents a melt ejection of the polymer out of the overlap zone. Due to preliminary investigations, the electrode force of inner electrode was specified to 435 N. The characteristic weldability lobe shows that both, aluminium and steel, have a pronounced welding current range of at least 2 kA in the range of 200 ms to 1800 ms welding time (Figure 6). Compared to the steel DX56D, aluminium (EN-AW 6016) exhibits a significantly higher thermal and electrical conductivity, higher welding currents causing equivalent joints.

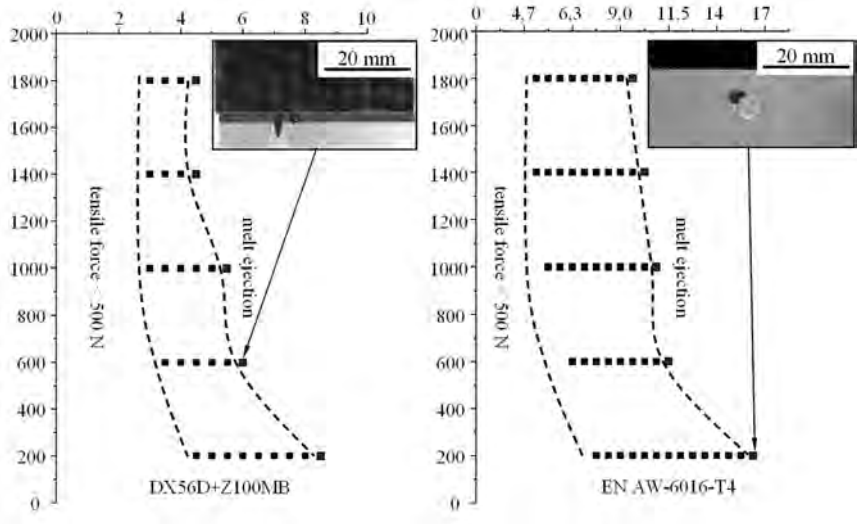


***Fig. 6*** *Weldability lobes for DX56D and EN AW 6016 joined with PA6 GF 47*

### 3.2 SURFACE PRE-TREATMENT

In order to improve the mechanical properties of the joint, the influence of different surface pre-treatments was investigated. The surface of both joining partners was cleaned respectively using isopropyl before welding. The surface of the metal joining partner was pre-treated by corundum blasting and laser structuring with line-shaped patterns. These surface conditions were used in order to investigate their impact on the strength and failure mechanism.

After pre-treatment the welding process was carried out. Therefore, the welding time und the electrode force were kept constant. The electrode force of the inner electrode was 435 N and the welding time was 600 ms. The welding current was adapted to the respective thermosphysical properties of the metallic joining partner. Based on the weldability lobe (figure 6), a welding current of 5.0 kA for the steel (DX56D) and 9.0 kA for aluminum (EN AW-6016) was selected.

Characteristic force-crosshead displacement graphs of the joint specimen depending on to the surface conditions are shown in figure 8. Both materials behave similarly and a minor standard deviation is possible. The laser-structured specimens show a significant increased tensile force and crosshead travel compared to the corundum blasted samples. This effect is explained by an increased load bearing surface due to the increased surface area of the laser-structured partner. On the other hand, a possibility of mechanical interlocking of the thermoplastic matrix is provided by the implied undercuts. Furthermore, it can be seen, that the sandblasted specimen failed abruptly, achieving a maximum load of approximately 2.0 kN and a crosshead displacement of 0.3 mm. The failure surface of the metal shows mainly adhesion failure with residues of polymer matrix. The laser structured specimen, however, achieve a load of at least 3.0 kN at a significant increased crosshead displacement. Related to the outer electrode with an outer diameter of 16 mm a tensile strength of approximately 10 MPa results by using the sandblasted surface. In this context, the laser structured surface enables a tensile strength of approximately 15 MPa. The enhanced load capacity during the test and the increased crosshead travel resulted in an advanced amount of absorbed energy caused by the mechanical interlocking structures. In this case residues of PA6 matrix and ripped glass fibers can be identify on the failure surface, shown in figure 8.

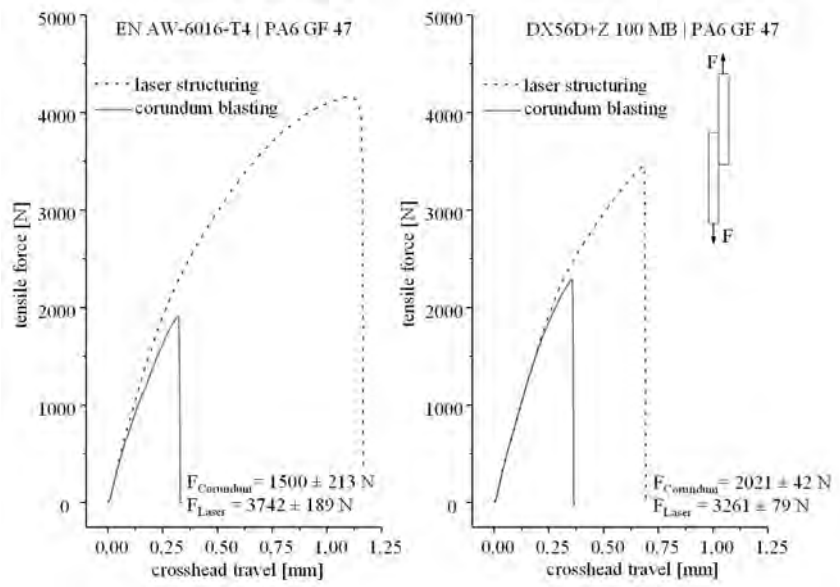


***Fig. 7*** *Load-strain diagram of pre-treated EN AW 6016 and DX56D*

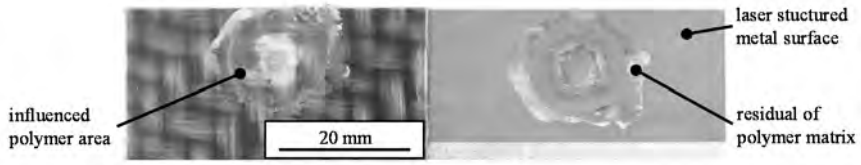


***Fig. 8*** *Fracture behavior of laser structured DX56D and PA6 GF47 joints (I = 5.0 kA, t = 600 ms)*

## 4 CONCLUSIONS

In this paper, a new approach regarding resistance spot welding of polymer-metal hybrid joints in a coaxial electrode arrangement was shown. Coaxial single sided resistance spot joining of polymer-metal-hybrid structures is a method which allows a reproducible joining at low cycle times and low costs compared to conventional methods. Based on preliminary investigation, the joint was characterized. Thereby, the penetration behaviour as well as the mechanical properties were examined depending on relevant process parameters. For given welding parameter combinations, weldability lobes with high current ranges for polymer-metal hybrid joints were developed.

Moreover, the influence of the surface condition on the joint was shown, based on a comparison between different surface preparations (corundum blasted and laser structured). It could be determined that an optimized surface pretreatment improves the shear strength in tensile testing up to 100 %. By using a laser-based surface preparation the mechanical properties, concerning crosshead load displacement and joint strength could be significant increased.

The presented results regarding single side resistance spot joining of polymer-metal-hybrid structures prove that this method has potential to be exploited and contribute to a better understanding of the influence of process parameters on the quality of the joint. For current investigations, the correlation of wetting behaviour and mechanical interlocking must be investigated. In addition the influence of deviations and different polymers is necessary.

## REFERENCES

[1] Sickert, M.; Haberstroh, E.: Thermal Direct Joining for Hybrid Plastic Metal Structures. In: Proceedings of Euro Hybrid Materials and Structures, (2014) pp. 42-45.
[2] Flock, D.: Wärmeleitungsfügen hybrider Kunststoff-Metall-Verbindungen. Aachen: Rheinisch-Westfälische Technische Hochschule. Dissertation, 2011.
[3] Balle, F.; Eifler, D.: Monotonic and Cyclic Deformation Behavior of Ultrasonically Welded Hybrid Joints between Light Metals and Carbon Fiber Reinforced Polymers (CFRP). Fatigue Behaviour of Fiber Reinforced Polymers: Experiments and Simulations. In: DEStech Publications, (2012) pp. 111-122.
[4] Balle, F.; Wagner, G.; Eifler, D.: Ultrasonic spot welding of aluminum sheet/carbon fiber reinforced polymer-joints. In: Materialwissenschaft und Werkstofftechnik. Bd. 38, Nr. 11, (2007) pp. 934-938.
[5] Bobzin, K.; Theiß, S.; Poprawe, R.; Roesner, A.; Haberstroh, E.; Flock, D.; Reisgen, U.; Wagner, N.: Der Exzellenzcluster "Integrative Produktionstechnik für Hochlohnländer" der RWTH Aachen University - Herstellung hybrider Metall-Kunststoffbauteile durch moderne Fügeverfahren. In: Joining Plastics, 3 (2008) pp. 210-216.
[6] U. Reisgen, S. Olschok, N. Wagner: Neue Entwicklungen zu Verbindungen von Kunststoff und Metall unter Zuhilfenahme thermischer Fügeprozesse. In: 17. Symposium Verbundwerkstoffe und Werkstoffverbunde, (2009) pp. 542-548.
[7] Amend, P.; Pfindel, S.; Schmidt, M.: Thermal joining of thermoplastic metal hybrids by means of mono- and polychromatic radiation. In: Physics Procedia 41, (2013) pp. 98-105.
[8] Bergmann, J. P.; Stambke, M.: Potential of laser-manufactured polymer-metal hybrid joints. In: Physics Procedia 39, (2012) pp. 84-91.
[9] Schricker, K.; Stambke, M.; Bergmann, J. P.; Bräutigam, K.; Henckell, P.: Macroscopic Surface Structures for Polymer-Metal Hybrid Joint manufactured by Laser Based Thermal Joining. In: Physics Procedia 56 (2014) 782-790.
[10] Katayama, S.; Kawahito, Y.; Mizutani, M.: Latest progress in performance and understanding of laser welding. Physics Procedia 39, (2012) pp. 8-16.
[11] Ageorges, C.; Ye, L.: Resistance Welding of Metal/Thermoplastic Composite Joints. Journal of Thermoplastic Composite Materials, Vol. 14, No. 6, (2006) pp. 449-475.
[12] Reisgen, U.; Schiebahn, A.; Schönberger, J.: Innovative Fügeverfahren für hybride Verbunde aus Metall und Kunststoff. In: Lightweight Design, Bd. 7, No. 3 (2014) pp. 12-17.
[13] Neudel, C.: Mikrostrukturelle und mechanischtechnologische Eigenschaften wider-standspunktgeschweißter Aluminium-Stahl-Verbindungen für den Fahrzeugbau. Erlangen: Meisenbach. Dissertation, 2013.

# WIRE ARC ADDITIVE MANUFACTURING OF WEAR RESISTANT COMPOUND STRUCTURES BY GAS METAL ARC WELDING

**Philipp Henckell*, Yarop Ali, Jan Reimann, Klaus Schricker, Jean Pierre Bergmann**

[1]Technische Universität Ilmenau, Production Technology Group, Gustav-Kirchhoff-Platz 2, D-98693 Ilmenau

**ABSTRACT:** A novel strategy for producing wear resistant compound structures is provided by the layer-by-layer production of hybrid 3D-structures by means of additive manufacturing. Thereby, the base and functional materials can be applied parallel or layer wise to one another depending on the desired application. Arc welding processes represent a resource-efficient and economical method for the production of large volume metallic components. In particular, gas metal arc welding is characterized by high deposition rates of up to 5 kg/h and a wire based feedstock, that enables the production of composite structures with little material loss. This article shows the potentials and challenges of additive manufacturing of wear-resistant composite structures based on the materials ferrite steel / FeCrC-alloy. In particular, geometric properties such as near net shape or distortion were investigated. Furthermore, metallurgical properties in the transition area of the base material and functional coating were analyzed.

**KEYWORDS:** Wire Arc Additive Manufacturing, WAAM, Hardfacing, Wear resistance, Gas metal arc welding, Compound structures, Hybrid materials

## 1 INTRODUCTION AND STATE OF THE ART

A novel strategy for producing metallic free form parts with adapted functionality (e.g. integrated wear resistance) is the additive manufacturing (AM) of work pieces consisting of compound materials. Thereby, occurring challenges in manufacturing such as undercuts can be avoided by a layer wise build up strategy. Especially wire based additive manufacturing (WAAM) with arc welding processes has become more important for industrial areas such as plant engineering or pipeline construction. Compared to laser based additive manufacturing, high deposition rates can be achieved, enabling a fast production of high volume parts. Furthermore, the easy and uncomplicated handling as well as low investment costs of the welding equipment are reasons for an increasing industrial interest in this technology. Investigations on additive manufacturing with TIG- and Plasma welding processes with different materials were carried out on robotized handling systems within numerous publications [1] – [4]. Compared to low deposition rates of TIG- and Plasma based welding processes, gas metal arc welding (GMAW) is a highly productive additive manufacturing technology, enabling further scaling with deposition rates up to 9 kg/h [5]. Researches on process technological features, such as experimental determination of residual stresses and the prediction by simulation modelling were carried out by Cranfield University [6] – [8]. Investigations of Kah et. al. [9] showed an improved weld bead stability in constraint positions using controlled short arc welding processes. Furthermore, near net shaped structures with high geometric complexity were manufactured with a maximum difference in layer width of 0,2 mm [10] – [11].

However, only few investigations are correlated to material scientific characterizations of additive manufactured structures. In this context, the use of energy reduced short arc welding regimes [12] – [14] or novel gas cooling strategies [15] – [16] are described in order to influence microstructural and mechanical properties. So far, most of the investigations are correlated to aerospace materials [17] – [18]. Industrial areas like pipeline construction or mining with the use of hard facing materials are not considered. In the field of wear protection, the combination of base material (e.g., ferrite steel) and hard facing material (e.g., FeCrC alloy) results in an increase in wear resistance. Particularly relevant parts for this purpose are delivery pipes in the area of open-

cast mining, which are subject to high abrasive wear. So far, these components have been coated internally by welding processes like plasma transferred arc welding or gas metal arc welding. Yet, occurring undercuts such as bends or radii in pipe systems cannot be edited with this process strategy further. In this case, single segments of plates need to be coated with hard facing alloys and welded together in the desired shape afterwards, resulting in an uneconomic amount of processing steps and time. In this connection, wire arc additive manufacturing is a novel way of building compound structures efficiently.

## 2 EXPERIMENTAL SETUP

The experimental trials were carried out with a six-axis industrial robot KUKA type KR15-2 handling device. As a welding power source, the EWM Alpha Q 552 was used in combination with a Binzel Robo water cooled welding torch. The substrate plates (material compare table 1, thickness of 5 mm) were mounted onto a water cooled clamping device. Additionally, a Dewetron DEWE PCI-16 DAQ-system was used for measuring arc voltage and current. The experimental setup is shown in figure 1.

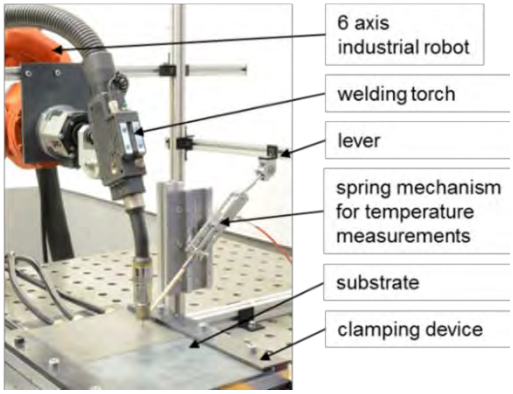


***Fig. 1*** *Experimental setup on 6-axis industrial KUKA robot*

The manufacturing process of hybrid 3D-structures can be carried out with different build up strategies that are shown in the following picture 2. The main target is the application of an efficient coating with increased resistance against wear. Therefore, a layer wise processing strategy describes the additive manufacturing of the functional hard facing layers on top of a base structure. Compared to this, a parallel manufacturing strategy is characterized by generating a functional coating next to a base structure. The experimental trials were carried out in the short arc welding regime constantly with neutral welding torch position.

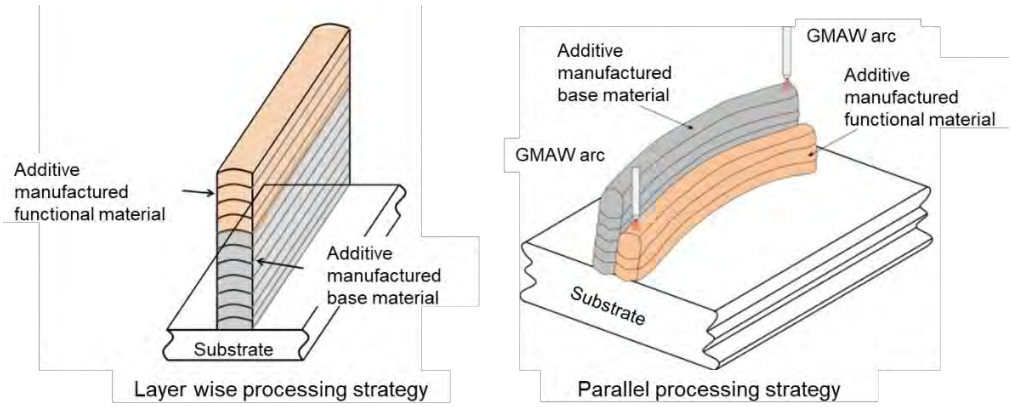


***Fig. 2*** *Processing strategies for additive manufacturing of 3D compound structures*

The used materials for the additive manufacturing of hybrid structures can be seen in the following table 1. The base materials of low and high alloyed steel were processed with solid wire, whereas the functional hard facing layers were set throughout the feeding of filler wire.

***Tab. 1*** *Used materials for additive manufacturing of compound 3D-structures*

| **Material type** | **Material** | **Wire diameter** |
|---|---|---|
| Base material | Low alloyed steel G4Si1 (1.5130) | 1,0 mm |
| | High alloyed steel G 19 9 L Si | 1,0 mm |
| Hard facing material | FeCrC alloy | 1,2 mm |

# 3 RESULTS AND DISCUSSION

## 3.1 NEAR NET SHAPE ANALYSIS

Referring to the state of the art, the energy input is a key factor to affect geometrical properties of additively built structures as well as microstructural characteristics. Regarding a generally valid welding process, the energy input per unit length ($E_s$) was deployed. For arc based processes, $E_s$ can be described by the power input throughout arc voltage $U$ and arc current $I$, divided by welding speed $v_{weld}$.

$$E_S = \frac{P}{v_{weld}} \ (kJ/cm) \quad with \quad P = \int_0^t \frac{U * I}{dt} \ (W)$$

In the first step, the focus of the investigations was based on additive manufactured wall structures with near net shaped geometrical characteristics. Different layer widths were manufactured with a common wire diameter of 1,0 mm by adjustment of the welding velocity. Simultaneously, the energy per unit length was analysed. The following figure 3 shows the resulting wall structures with homogeneous layer width as well as the measured energy input on low alloyed steel G4Si1.

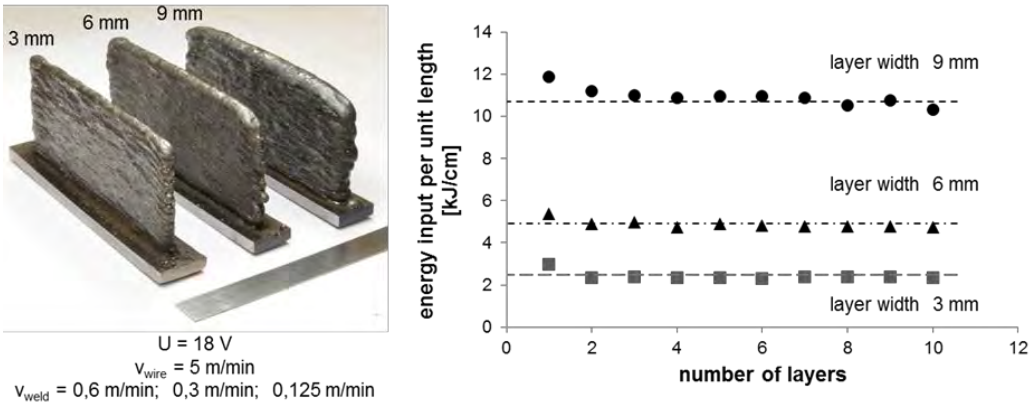


***Fig. 3*** *Correlation of resulting structure width and energy input per unit length on low alloyed steel G4Si1*

The diagram shows a nonlinear correlation between the energy input per unit length and the resulting layer width (see figure 3, right). A structure thickness of 3 mm can be achieved with an approximate energy input of 2,5 kJ/cm. Whereas, the manufacturing process of a tripled structure width of 9 mm requires an energy input of nearly 11 kJ/cm. Due to high heat conduction to the substrate and a base material at room temperature, the first layer of the built wall structures was commonly welded with increased energy per unit length in order to increase the weld bead width and to obtain a homogeneous layer thickness. The following layers were set with constant but decreased processing energies due to the heat affected substrate and preheated layers. These investigations show the relation between energy input and resulting layer width and build the basis for further analysis.

Furthermore, the near net shape of additively built structures of high alloyed steel G19 9 L Si was analysed. Exemplary cross sections in figure 4 show again the correlation between the energy input per unit length and the resulting structure width.

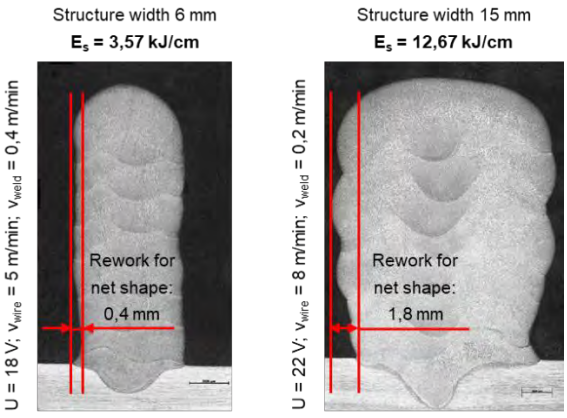


***Fig. 4*** *Correlation of energy input per unit length and necessary rework on high alloyed steel G19 9 L Si*

Additionally, the necessary rework for the finishing of the built part to near net shape geometry is visualized. Low energy input per unit length thereby leads to a homogeneous layer geometry by means of layer height and width. As a result, little material removal is required to obtain the near net shape. In comparison to this, high energy input leads to an increased weld bead width and differing layer geometries.

### 3.2 ADDITIVE MANUFACTURING OF COMPOUND STRUCTURES

In industrial areas like mining or plant engineering the manufacturing process of spare -, respectively wear parts can last up to two years. This is due to the conventional production chain including the construction process, the manufacturing of tools and casting molds to the actual manufacturing process of the part. Additionally, production steps like coating and finishing increase the manufacturing time further.
A novel way of reducing processing time of wear resistant parts like pipelines is the additive manufacturing of compound structures consisting of a base and functional material. The following figure 5 shows additive manufactured compound structures of low alloyed steel 1.5130 and FeCrC hard facing alloy with parallel build up strategy. The energy input during the WAAM process differs from 2 kJ/cm to 12 kJ/cm according to chapter 3.1 and in order to achieve wall widths from 3 mm to 9 mm. The welding direction was changed after each layer. The shown compound structures have a length of 300 mm and a height of 100 mm.

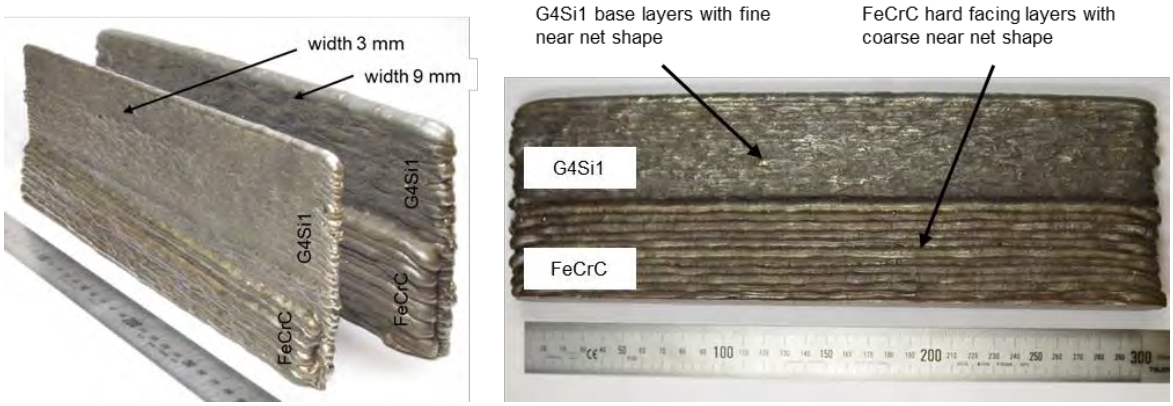


***Fig. 5*** *Additive manufacturing of compound structures with parallel processing strategy*

Figure 5 shows a differing surface structure of the two materials. Though, the base material of low alloyed steel 1.5130 exhibits near net shape surface roughness. In contrast, the wear resistant functional coating of FeCrC-alloy shows a coarse structure of the set layers. This relates to the chrome content of the material, leading to a decreased weld bead viscosity [19] and increased structure roughness. Yet, in industrial areas like open-cast mining, surface finishing of wear strained parts is not desired due to high abrasive exposure.
The wear resistant FeCrC-coating of the shown compound structures in figure 5 was additively manufactured after the ferrite base structure was deployed. Especially thin wall structures show angled distortion due to the reheating of the base structure and differing cooling conditions of the materials. In this case, an alternating welding sequence of base and functional material would lead to less distortion.

### 3.3 INVESTIGATIONS ON METALLURGICAL PROPERTIES

A main focus of this study is the analysis of metallurgical properties of additively manufactured hybrid structures. Therefore, the transition zone between the base and functional material was investigated. The following figure 6 shows a macroscopic view of a parallel built compound structure of G4Si1 / FeCrC-alloy, where the transition zone does not show lack of fusion.

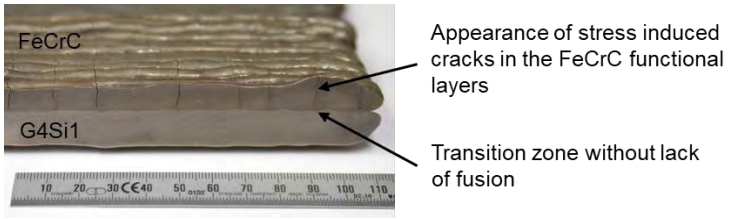


***Fig. 6*** *Macroscopic view of the fusion zone between low alloyed steel G4Si1 and FeCrC-alloy*

In figure 6, the effect of stress induced cracks in welded hard facing layers is visualized. The combination of high hardness properties in the FeCrC-coating and shrinkage of the consolidated weld bead leads to the formation of cracks in the functional layer. However, fine cracks in hard facing layers are accepted. This can be

explained by the application of high load during the industrial use. Thereby, fine cracks lead to a segmental break out of the functional coating without the loss of the entire hard facing layer. These fine branched cracks can be achieved throughout a layer wise additive manufacturing process with gas metal arc welding.
Additionally, the shown investigations on parallel built G4Si1 / FeCrC-alloy were complemented by analysis of layer wise built austenite base material and FeCrC functional alloy. The following figure 7 shows a cross section of an additively built compound structure and the investigations on microstructural properties in different layer heights. In the $10^{th}$ layer of the G 19 9 L Si base material a typical austenite microstructure (white) with delta ferrite content (black) of approximately 15-20% is shown, which is the characteristic appearance in multi-layer welds with austenite filler material. The boundary line is characterized by a soft transition between base material and functional coating with a fully austenite area due to high austenite content of both materials. In the first layer of the functional hard facing material a primary dendritic solidification with austenite phase (white) as well as eutectic phase of austenite and chrome carbides (black) can be seen. This microstructure can be explained by the dilution of base material and functional coating. In the sixth layer of the hard facing material spicular grains of primary $M_7C_3$ chrome carbides are embedded in an eutectic matrix of austenite and chrome carbides. This characteristic microstructure leads to a high wear resistance.

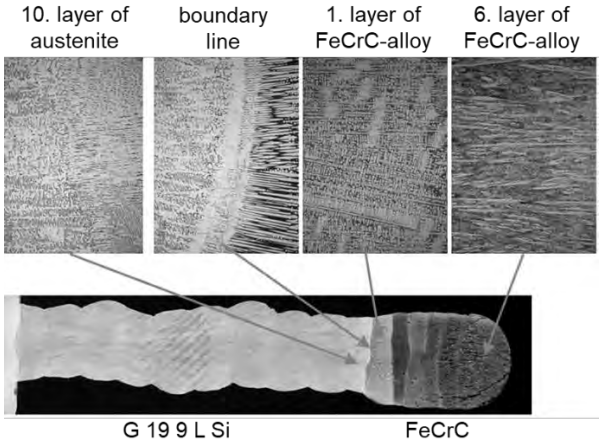


***Fig. 7*** *Microstructural analysis of a layer wise built Ferrite / FeCrC-compound structure*

## 4 CONCLUSION

Wire based additive manufacturing of compound structures is a novel way of producing large volume parts with adaptable function. In the field of wear part production, process time can be reduced significantly due to reduced production steps and decreased manufacturing time. In this article, low and high alloyed steels were used for the manufacturing of base structures with a coating of FeCrC hard facing alloy. It could be shown that functional hard facings can be processed by WAAM efficiently. Analysis of the near net shape were carried out in the first step. Thereby, low energy input per unit length leads to little material removal during the finishing of the manufactured part. In the next step, compound structures with parallel or layer wise additive manufacturing strategies were built. As a result, near net shape structures without lack of fusion in the transition zone were processed. Finally, microstructural analysis of layer wise manufactured Austenite base material and hard facing FeCrC-alloy were showing characteristic properties of multi-layer welds.
In further investigations, high stress wear resistance tests with international standard method ASTM B611 will be carried out. Though, a correlation between differing energy input in the welding process and resulting wear resistance can be deviated. Moreover, the additive manufacturing with Ni-FTC electrodes will be analysed. This filler material increases wear resistance throughout a Nickel matrix with embedded fused tungsten carbides.

## 5 ACKNOWLEDGEMENT

The IGF-project 18585 BR of the research association Welding and related Procedures e.V. of DVS, Aachener Str. 172, 40223 Düsseldorf was funded by AiF within the program “Förderung der industriellen Gemeinschaftsforschung (IGF)” of Federal Ministry of Economic Affairs and Energy, which is based on a resolution of the German Parliament. We would like to thank all funding organizations.

## REFERENCES


[1] Baufeld B., van der Biest O., Gault R.: *Additive manufacturing of Ti–6Al–4V components by shaped metal deposition*. In: Materials and Design 31 (2010).

[2] Baufeld B., et. al.: *Mechanical properties of Inconel 718 parts manufactured by shaped metal deposition (SMD)*. In: Journal of Materials Engineering and Performance 12 (2012).

[3] Martina F., Mehnen J., Williams S. W., Colegrove P., Wang F.: *Investigation of the benefits of plasma deposition for the additive layer manufacture of Ti–6Al–4V*. In: Journal of Materials Processing Technology 212 (2012).

[4] Skiba T., Baufeld B., van der Biest O.: *Microstructure and mechanical properties of stainless steel component manufactured by shaped metal deposition*. In: Journal of the Iron and Steel Institute of Japan 49 (2009).

[5] Günther, K., Bergmann, J.P., Suchodoll, D.: Hot wire-assisted gas metal arc welding of hypereutectic FeCrC hardfacing alloys: Microstucture and wear properties. In: Surface & Coating Technology 334. p.420-428 (2018).

[6] Spencer J. D., Dickens P. M., Wykes C. M.: *Rapid prototyping of metal parts by three-dimensional welding*. In: Journal of Engineering Manufacture 212 (1998).

[7] Mughal M. P., Fawad H., Mufti R. A.: *Three-dimensional finite-element modelling of deformation in weld-based rapid prototyping*. In: Journal of Mechanical Engineering Science 220 (2006).

[8] Ding J., Colegrove P., Mehnen J., Williams S., Wang F., Almeida P. S.: *A computationally efficient finite element model of wire and arc additive manufacture*. In: International Journal of Advanced Manufacturing Technology 70 (2014).

[9] Kah P., Suoranta R, Martikainen J.: *Advanced gas metal arc welding processes*. In: International Journal of Advanced Manufacturing Technology, 67 (2013).

[10] Almeida P. M. S.: *Process control and development in wire and arc additive manufacturing*. Dissertation, Cranfield University (2012).

[11] Adebayo A., Mehnen J., Tonnellier X.: *Limiting travel speed in additive layer manufacturing*. In: 9th International Conference on Trends in Welding Research, Chicago (2012).

[12] Hartke M. A., Günther K., Bergmann J. P.: *Untersuchung zur geregelten, energiereduzierten Kurzlichtbogentechnik als generatives Fertigungsverfahren*. In: Fachbeitrag zur „Großen Schweißtechnischen Tagung“, Berlin (2014).

[13] Hartke M., Günther K., Ali Y., Bergmann J. P.: *Schweißtechnische Herstellung komplexer 3D-Freiformflächen mittels geregelter MSG-Kurzlichtbogentechnik*. In: Tagungsband zur 4. Fachtagung „Verarbeitung von Stählen im Kraftwerksbau“, Duisburg (2014).

[14] Suryakumar S., Karunakaran K.: *A study of the mechanical properties of objects built through weld deposition*. In: Journal of Engineering Manufacture 227 (2013).

[15] Henckell, P.; Günther, K.; Ali, Y.; Bergmann, J. P.; Scholz, J.; Forêt, P: *The Influence of Gas Cooling in Context of Wire Arc Additive Manufacturing - A Novel Strategy of Affecting Grain Structure and Size*. In TMS 2017 146th Annual Meeting & Exhibition Supplemental Proceedings (pp. 147-156). Springer International Publishing (2017).

[16] Henckell, P.; Günther, K.; Ali, Y.; Bergmann, J. P.; Scholz, J.; Forêt, P: *Improving productivity and microstructural properties of wire arc additive manufactured parts by implementing a gas cooling strategy*. In: Konferenzbeitrag International Congress on Welding, Additive Manufacturing and associated Non Destructive Testing, Metz (2017).

[17] Almeida P. M. S., Williams S.: *Innovative process model of Ti–6Al–4V additive layer manufacturing using cold metal transfer (CMT)*. In: Fachbeitrag zum 21th Annual International Solid Freeform Fabrication Symposium, Texas (2010).

[18] Clark D.; Bache M. R.; Whittaker, M. T.: *Shaped metal deposition of a nickel alloy for aero engine applications*. In: Journal of Materials Processing Technology 203 (2008).

[19] Leitner, F.; Plöckinger, E.: *Die Edelstahlerzeugung: Schmelzen, Giessen, Prüfen*. Springer-Verlag (2013).

CHAPTER 5

# MATERIAL MODELLING AND SIMULATION

# OPTIMIZATION-BASED MATERIAL DESIGN OF TAILORED STACKED HYBRIDS FOR FURTHER IMPROVEMENT IN LIGHTWEIGHT CAR BODY STRUCTURES

**Alan A. Camberg[1*], Thomas Tröster[1]**

[1] Automotive Lightweight Design, Paderborn University, Pohlweg 47-49, 33098 Paderborn, Germany

**ABSTRACT:** In latest body-in-white (BIW) concepts, engineers take into account a wider range of different materials to pursue a multi-material design approach. However, the lightweight potential of common materials like steel, aluminum or even fiber-reinforcement plastics (FRP) is limited. In keeping with the motto "the best material for the best application", a new approach for a top-down material design is introduced. With the aim to develop an application tailored material, the multi-material concept is adapted for the thickness dimension of the component. Within this contribution, a new numerical design methodology is applied on a stiffness and crash relevant car body structure. The identified demonstrator components are subdivided into layers and submitted to a first optimization loop in which the algorithm can freely parametrize the material parameters for each single layer. After finding an optimum, further optimization loops with concrete material pendants and manufacturing restrictions are carried out. The result is a hybrid laminate consisting of steel and FRP plies. Finally, the tailored hybrid stacks are validated in BIW and full vehicle simulations and compared with the reference. The optimization-based approach allows a weight reduction of at least 20% while maintaining or even improving the BIW properties.

**KEYWORDS:** hybrid materials, optimization, lightweight design, finite elements analysis, fiber-metal-laminates

## 1 INTRODUCTION

Automotive lightweight design is a considerable measure to meet the worldwide need for reducing CO2 emissions. In the past, this led to an excessive portfolio development of conventional metals like steel or aluminum. However, the lightweight potential of common materials like steel, aluminum or even fiber-reinforcement plastics (FRP) is limited. High strength steels play a significant role in the design of safe and light car body structures. Nevertheless, the high density and buckling problems related to reduced sheet thicknesses limit the achievable mass reduction. Aluminum alloys are well known for the potential to improve the strength to weight ratio of car bodies. Nonetheless, in terms of stiffness aluminum has a clear disadvantage due to a relative low Young's modulus. Even FRP components, which have superior lightweight characteristics, show limitations for the car body design, as catastrophic failure or high production costs. Hybrid materials combine metals and FRP in a manner to offset the drawbacks of every single material and reach an optimum of mechanical properties and costs. Nonetheless, the achievable lightweight potential of such materials heavily depends on the loading situation, geometry or cross section of the chosen material design.

## 2 THE APPROACH

To account for these limitations, a novel approach is necessary. The "LHybS" (Lightweight Design with Novel Hybrid Materials) project aims high to design a material, which different than usual is not developed in a bottom-up way, but rather in a top-down manner. Within the scope of the project a new numerical process is developed, which provides for the first time a methodology that allows the design of sophisticated requirement-optimal layered materials. The through thickness property profile of the material takes into account not only loading dependent requests, but also demands that are related to the direct application of the material in the vehicle. The goal of the project is to develop a lightweight hybrid material with processing characteristics similar to materials conventionally used in body-in-white production plants.

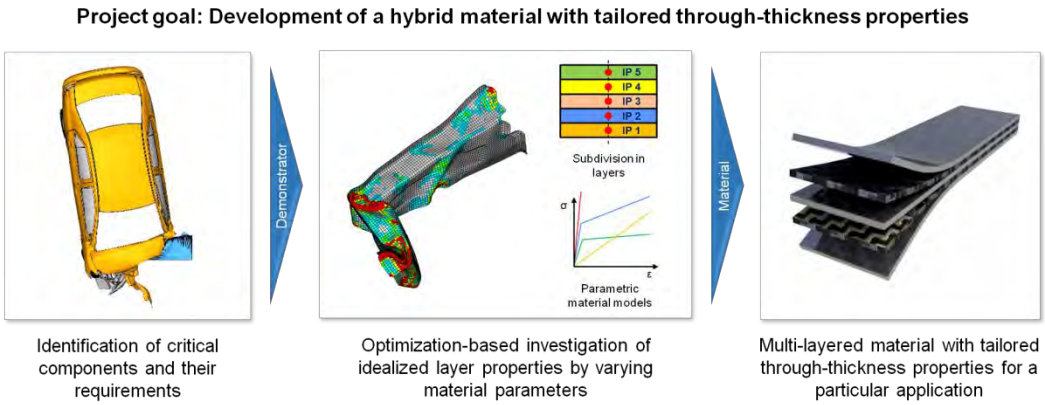


***Fig. 1*** *The approach of the LHybS project: from the application to the material profile*

## 3 BENCHMARK

As a basis for the material development the thyssenkrupp InCar®plus model is used. The InCar project started back in 2006 as a customer-independent car body structure project. The goal of the InCar project was to develop a basis for the potential analysis for new material grades and processing concepts. A further development and an adjustment to newest crash safety demands was realized in 2014 as InCar plus. The steel-intensive structure of the InCar plus represents the current state of the art by utilizing the usage of hot formed, ultra-high and high strength steels [1], [2]. The crash, stiffness and noise-vibration-harshness (NVH) properties of the InCar plus are investigated in latest crash assessment tests, stiffness load cases and OEM specific methods to set a benchmark for the development of the new tailored hybrid materials. The benchmark analysis was carried out by tests presented in figure 2.

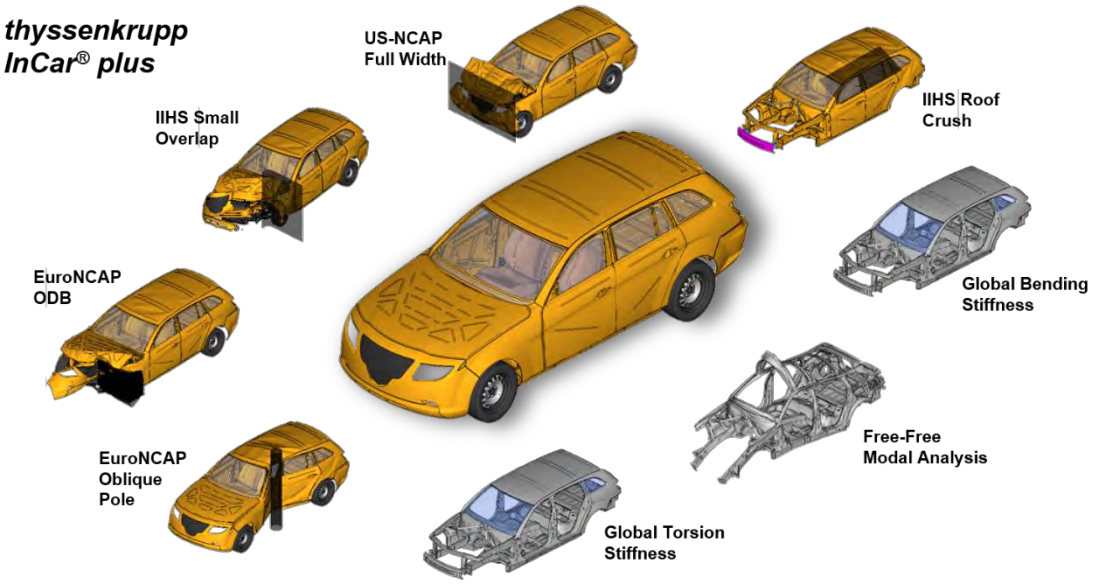


***Fig. 2*** *Assessment of the InCar plus characteristics as a benchmark for the material development*

## 4 COMPONENT CLASSIFICATION

The investigated body-in-white properties result from an interaction of all car body components. Every single part accomplish in terms of a body structure a particular function and contributes with its specific characteristics to the global body-in-white properties. Depending on the external load, singular parts and component groups could be more or less involved in the deformation resistance of the body structure. To classify the BIW parts in load case relevant groups and evaluate their importance, a strain energy based method is introduced. In case of the stiffness relevant part the assessment of potential components is further supplemented by a

sensitivity analysis to identify structural parts with a great impact on the global stiffness. In that manner, it can be ensure that the material improvement will be realized on parts that show a high relevance for the global BIW properties and so, additional costs can be justified by better overall vehicle characteristics.

### 4.1 COMPONENT SPECIFIC PRORATE STRAIN ENERGY

With the aim to quantify the relevance of structural BIW parts for particular load cases, a classification method is necessary. Within this contribution a strain energy based method, henceforth referred to as component specific prorate strain energy, is developed. The strain energy is a side product of any finite element analysis, so it can be used almost without any additional computational effort. The fundamental idea of that method is trivial - if an external force is deforming a component, the conducted work is saved within the former as strain energy. Considering an infinitesimal small element $e$ of the deformed component it follows:

$$W_{i,e} = \frac{1}{2}\underline{\sigma} dA \underline{\varepsilon} dt = \frac{1}{2}\underline{\sigma}\underline{\varepsilon} dV \qquad (1)$$

From the statement presented in equation (1) an approach for the classification of structural car body components is developed. Hereto, the strain energy of every single finite element $W_{i,e}$ is calculated and summed up over all BIW elements of the domain $\theta$ to the BIW strain energy $W_i$. Subsequent, a ratio between the element strain energy and the BIW strain energy is calculated and expressed as a percentage value, following equation (2):

$$W_{i\%,e} = \frac{W_{i,e}}{\sum_{e\in\Theta} W_{i,e}} * 100\% \qquad (2)$$

In the next step a specific prorate strain energy of all BIW components is calculated by adding up the elements percentage strain energy over the component sub-domains $K$. The specific prorate strain energy for a component follows to:

$$W_{i\%,\mathrm{K}} = \sum_{e\in\mathrm{K}} W_{i,e} \qquad (3)$$

While for the domain of elements $\{e_a\}_{a=1,\dots,m}$ and the domain of components $\{K_b\}_{b=1,\dots,n}$ the following conditions apply:

$$\forall a = \{1,\dots,\mathrm{m}\}\ \exists!\ b = \{1,\dots,\mathrm{n}\} \text{ mit } e_a \in \mathrm{K}_b, \qquad a \geq b\,,\ \mathrm{K}_b \cap \mathrm{K}_m = \emptyset \quad \text{and}$$

$$W_i = \sum_{\mathrm{K}\in\Theta} W_{i,\mathrm{K}} = \sum_{e\in\Theta} W_{i,e} \qquad (4)$$

By applying this method on a particular load case, a specific prorate strain energy value will be attributed to each BIW component. This approach allows to identify components which are eminently involved in the deformation resistance of the car body structure. Linked with a graphical output in a post-processor relevant parts can be easily highlighted, see figure 3.

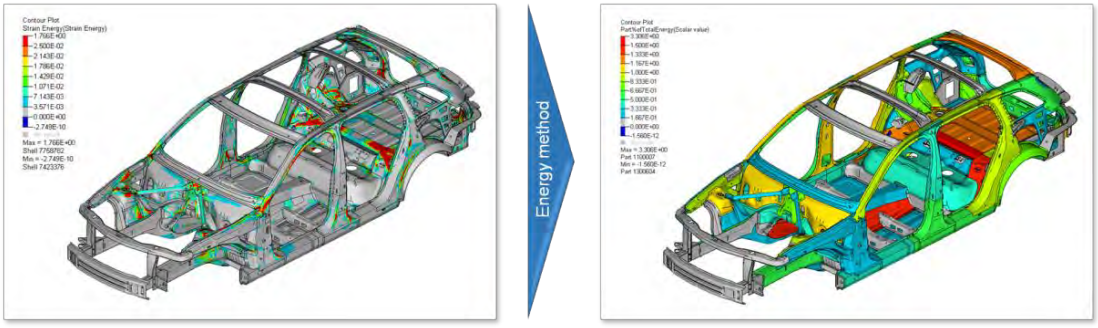


Element-wise strain energy distribution

Component-wise prorate strain energy distribution

***Fig. 3*** *Application of the component prorate strain energy method on the load case "global torsion"*

### 4.2 SENSITIVITY ANALYSIS

In terms of cost-efficiency a material substitution should be at least related to a weight reduction or a performance improvement. Thus, the specific characteristics of the chosen demonstrator components ought to be enhanced in general. Whereas the energy absorption is a complex mechanism where no clear impact factor can be identified, the crash relevant demonstrator is chosen by adding up all component and load case specific prorate strain energies and selecting the part with the highest value. In case of the stiffness relevant part a rigidity improvement is easy to simulate by scaling up the Young's modulus. For that reason a sensitivity analysis of ten preselected components with highest prorate strain energy values is carried out. By increasing the Young's modulus of particular components the influence of an improved material on the global characteristic can be evaluated. Since the global stiffness is directly affecting the "lightweight index" $L$ of a car body, see equation (5), the load case "global torsion" is defined as design relevant. As reported in [3], an improvement of the torsion stiffness usually leads concurrently to an improvement of other stiffness properties of the BIW.

### 4.3 IDENTIFIED COMPONENTS

As a result of the numerical procedures described in section 4.1 and 4.2, two demonstrators - one crash and one stiffness relevant part - were selected for a tailored material design trail. The crash relevant component represented by a front longitudinal member is manufactured in the baseline design of a tailored dual-phase steel blank. The rear cross member, which embodies the stiffness demonstrator, consists of three individual steel parts. In addition to mechanical requirements that have to be satisfied by the material the demonstrators are manufactured of, there are secondary demands as for example damping characteristics, corrosion protection or joinability that have to be taken into account within the material design process. These needs are investigated and defined in a specific requirement catalogue for each of the new hybrid materials.

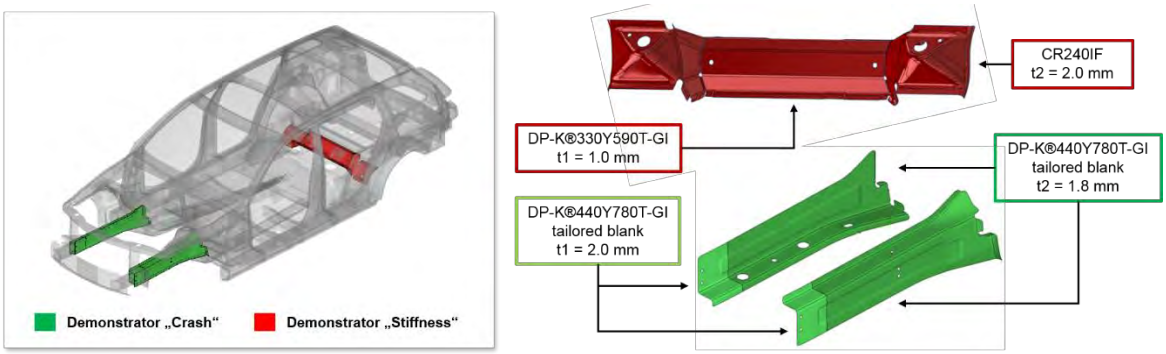


***Fig. 4*** Selected components on which the tailored material design process will be examplified

## 5 TAILORED MATERIAL DESIGN

In general, the developed material design process is uniform for both components and consists of four main stages. In the first step, the part is subdivided into at least five layers and the objective is defined. Then a first optimization loop follows in which the algorithm can freely vary the material parameters for each single layer. Once an optimum was found, the still idealized material properties of each layer are compared with a material database to select a concrete pendant. In the last optimization loop, real materials are used and the layers are optimized in terms of thickness and material orientation. Nevertheless, in detail there are substantial differences between the "stiffness" and "crash" material design processes. Different boundary conditions lead to different time integration methods and by reasons of result data characteristics, different optimization algorithms are needed. Since the stiffness load cases are mainly linear and static, an implicit time integration method and gradient-based or local search algorithms can be used [4]. By contrast, the crashworthiness issue is highly transient and non-linear what makes the optimization more challenging. Due to high non-linearity, numerical noise and non-convex objective functions with numerousness extrema the optimization is often conducted by surrogate models, as for example by response surface models (RSM) [4]. In consequence of that, the demonstrator materials have to be optimized in two different ways.

### 5.1 STIFFNESS

The tailored property profile of the stiffness component is identified by an approach based on topology optimization. In topology optimization, it is common to couple every single finite element to a Young's modulus – density-scaling function with the aim to control the stiffness and mass of every element. The possibility of

an element-wise variation of these properties allows to find a load-optimal component topology. This approach is revisited in the developed method, but instead of a strictly monotonically increasing function, a higher order polynomial is used to describe the Young's modulus - density relation of technical materials. Furthermore, the property variation does not take place only on element-basis but on clustered through-thickness integration point (IP) layers of each element. That in turn enables to realize layers of different properties within the investigated component and the design of an application-optimal hybrid material.

### 5.2 CRASHWORTHINESS

The crashworthiness material profile was investigated by a response surface model. Similar to the stiffness profile, also here a layer-wise modeling is used. Every single IP layer has its own fully parametrized bilinear material model which allows to emulate any material behavior between ideal plastic and ideal elastic. Owing to computation time and available technical materials, the parameters where restricted within physically reasonable bounds. Since an objective for crashworthiness is hardly to define in numbers, the increase of the specific energy absorption (SEA) was set as a target for the optimization.

### 5.3 OPTIMIZED MATERIAL DESIGN

The optimization led in both cases to an initially unexpected material profile. In spite of different loading conditions and demands, as well as free material parameters the algorithms proposed in both cases a quite similar profile design consisting of steel top layers and a FRP core. However, due to different component requirements the material profiles are distinct. In detail different steel grades, as well as different FRP matrixes and bonding agents are used. The developed application-tailored hybrid materials are presented in figure 5.

***Fig. 5*** *Developed hybrid materials with an application-tailored material profile*

Finally, the developed materials undergo a series of full vehicle and BIW simulations. The results are compared with the InCar plus reference to highlight the potentials of the tailored material design. In both cases, a redesign of the through thickness properties by a tailored hybrid stack leads to an at least 20 % weight reduction for each part while maintaining or even improving the overall vehicle properties (see table 1 and 2).

***Table 1:*** *Stiffness and NVH values of the InCar plus BIW with a steel and hybrid stacked rear cross member*

| BIW characteristic | Baseline | Hybrid | Units |
|---|---|---|---|
| Global bending stiffness | 100 % | 99.28 % | [N/mm] |
| Global torsion stiffness | 100 % | 100.44 % | [kNm/°] |
| Lightweight index | 100 % | 99.57 % | [kgm$^2$/(kNm/°)] |
| First bending mode | 100 % | 100 % | [Hz] |
| First torsion mode | 100 % | 100.33 % | [Hz] |
| Second bending mode | 100 % | 100.04 % | [Hz] |

***Table 2:*** *Maximum firewall intrusion of the InCar plus with a steel and a hybrid stacked front long member*

| Crash Test | Baseline | Hybrid | Units |
|---|---|---|---|
| EuroNCAP ODB | 100 % | 97.45 % | [mm] |
| US-NCAP Full Width | 100 % | 88.82 % | [mm] |

## 6 CONCLUSIONS AND OUTLOOK

Numerical processes introduced within the scope of this contribution allowed to design novel requirement-optimal hybrid materials. These materials led to a weight reduction of at least 20 % and hold further light-weight potentials. To ensure that the new materials can be manufactured to parts by conventional production processes, as for example deep drawing, special tooling or process routes shall be developed too. The developed materials were hitherto investigated only in numerical simulations and coupon based experimental tests. The experimental validations on real component geometries are still pending. The hardware tests are in preparation right now. The chosen demonstrator components will be subjected to a series of crash, stiffness and durability tests to point out the qualification for automotive applications. Further, the developed approach will be consolidated to a user-friendly numerical tool to provide usability in the serial development of mechanical systems. Distal the automotive field the approach could be used for other disciplines, as for example in the aeronautical or energy sector.

## 7 ACKNOWLEDGEMENT

The authors would like to give thanks to the European Regional development Fund and the State of North Rhine-Westphalia for funding the research project “LHybS” (www.tecup.de/lhybs/) and the lead partner PTJ. Sincere thanks also to all of the industrial partners, especially to the thyssenkrupp Steel Europe AG for providing the InCar®plus model. On a final note, we would like to give thanks to Ina Stratmann and Patrick Besting for the assistance in simulation and evaluation of some of the data presented within this contribution.

## REFERENCES

[1] ATZ extra: Das Projekt ThyssenKrupp InCar plus. Lösungen für automobile Effizienz. Springer Vieweg Verlag, October 2014.
[2] Pohl B., Rützel S.: *The all new Opel Insignia – Body development and manufacturing.* In: Conference Proceedings of Aachen Body Engineering Days 2017, 2017.
[3] Braess H.-H., Seiffert U. (ed.): Vieweg Handbuch Kraftfahrzeugtechnik. Springer Vieweg Verlag Berlin, 2013.
[4] Duddeck F.: *Multidisciplinary optimization of car bodies.* Struct Multidisc Optim 35, 375-389, 2008.
[5] Malen D. E.: *Fundamentals of Automobile Body Structure Design.* SAE International, 2011.
[6] Kiani M., Shiozaki H., Motoyama K.: *Simulation-based design optimisation to develop a lightweight Body-In-White structure focusing on dynamic and static stiffness.* Int. J. of Vehicle Design, Vol.67, No.3, 219-236, 2015.
[7] Helsen J., Cremers L., Mas P., Sas O.: *Global static and dynamic car body stiffness based on a single experimental modal analysis test.* In: Proceedings of ISMA2010 including USD2010, 2505-2521, 2010.

# COUPLED PROCESS AND STRUCTURE ANALYSIS OF METAL-FRP-HYBRID STRUCTURES

**Daniel Weck[1,*], Bernd Grüber[1], Minh Quang Pham[2], Alexander Wolf[3], Sven Bräunling[3], Jean-Paul Ziegs[4], Thomas Gereke[2], Franz Hirsch[4], Markus Kästner[4], Alexander Brosius[3], Chokri Cherif[2], Maik Gude[1]**

[1] Institute for Lightweight Engineering and Polymer Technology, TU Dresden
[2] Institute of Textile Machinery and High Performance Material Technology, TU Dresden
[3] Institute of Manufacturing Science and Engineering, TU Dresden
[4] Institute of Solid Mechanics, TU Dresden

**ABSTRACT:** Multi-material design aims at the targeted combination of materials with different characteristics in order to meet technical requirements. Especially the combination of metals and fibre-reinforced plastics has led to innovative lightweight structures with high load-bearing capacity and ductility in recent years. The process chains required for the production of such structures are more complex and therefor characterized by a variety of process parameters. They possess a significant influence on the performance of such hybrid components.
For the theoretical consideration of these process chains, simulation methods for the involved individual process steps and their connection towards a coupled process and structure analysis are described in this paper. Besides of the analysis of the sub-models, the layout of the interfaces between them is also considered. In addition, experimental methods are described which are used to determine the required input parameters, also under process conditions. In particular, parameters are addressed here that cannot be realistically calculated or can only be calculated with increased effort. The overall goal of this approach is the continuous numerical analysis of the manufacturing process and its impact on component quality and performance, in order to obtain indications for the favourable setting of process parameters.

**KEYWORDS:** process simulation, structural simulation, experimental methods

## 1 INTRODUCTION

In recent years, innovative lightweight structures in multi-material design have been generated by the targeted combination of materials with different property profiles. Especially the combination of metals and fibre-reinforced plastics has opened up new potentials for the generation of structural components with high load-bearing capacity, high ductility and minimum mass [1, 2]. The development process of such components places high demands on the engineer due to the complex interactions between design, dimensioning and manufacturing [3, 4]. Adapted models for geometry, material and process can provide a significant contribution to the efficient development of hybrid structures made of metal and fibre-reinforced plastics (FRP). Initial modelling approaches are already available for the individual steps of the manufacturing process of such metal-FRP-hybrid components. These models have to be combined into a coupled analysis of process and mechanical structure in a modular way. In doing so, the system behaviour can be determined based on the real material and component conditions arising from the manufacturing process. The aim of this procedure is, on the one hand, the comprehensive observation and assessment of manufacturing influences on component quality and performance in order to obtain indications for a favourable setting of process parameters. At the same time, the described procedure allows the definition of permissible tolerance ranges for the process parameters within which a sufficient component quality is achieved. Furthermore, this integrative approach including the structural analysis also allows for the holistic adaptation of material, geometry and process according to the component requirements [5, 6].
In order to achieve this goal, the submodels of the individual process steps metal forming, textile forming and consolidation are first analysed. Particularly for the consideration of the FRP composite, different degrees of detail are compared. Furthermore, the interfaces between the sub-models are described. On the

experimental side, common and newly developed methods for analysing the properties of materials and semi-finished products also under process conditions are explained. Furthermore, the friction behaviour between the components involved is assessed.
In the studies, it is shown that the detailed modelling of the textile structure allows for the mapping of local variations of the composite structure and the corresponding structural properties of the component. The experimental investigations document that the required parameters show partly significant temperature dependence. The use of temperature-dependent data and corresponding material models within the simulation is therefore of crucial importance for high quality results.

# 2 INTEGRATIVE MODELLING APPROACH

For the development of complex lightweight solutions in FRP and metal-FRP-hybrid design, the implementation of an interactive development and design process that takes into account the manifold interdependencies between manufacturing process, material structure and geometrical design has proven its effectiveness. In order to be able to align these three dimensions at an early stage of the development process, simulation approaches for the coupled process-structure-analysis are to be developed. Based on this approach, information regarding existing restrictions and dependencies is gained, which supports the engineer during the interactive and targeted development of lightweight structures.

## 2.1 MODULAR SIMULATION CHAIN

The process chain for manufacturing of metal-FRP-hybrid structures can basically be divided into the individual process steps of metal forming, textile forming and composite consolidation via hot pressing. These steps may be sequentially arranged or combined with each other; two different methods for manufacturing the multi-material work piece will be examined. On the one hand the process starts with the forming simulation of the metal component to its final shape followed by draping the reinforcement onto the semi-finished product. On the other hand, we consider the simulation of the one-step thermoforming process consisting of deep-drawing the metal sheet with a pre-heated fibre-reinforced-thermoplastic composite simultaneously. Accordingly, a modular approach for designing the simulation chain and submodels is necessary. In the coupled process and structure analysis examined here, the manufacturing steps are followed by the numerical assessment of the mechanical behaviour of the virtually manufactured component (cf. Fig. 1). The procedure for modelling the individual modules of this simulation chain is described in detail in the following sections. Within the present investigations, the works regarding metal forming will concentrate on steel (DC06, DX54) and magnesium alloys (AZ31B, WZ73). For modelling the textile forming process, biaxial reinforced weft-knitted fabric made of commingled yarns was used in this study. The reinforcement yarns are made of carbon fibre (CF) and polyamide 6.6 (PA 6.6), while the knitting yarns are doubling yarns from glass fibre (GF) and polypropylene (PP). A summary of the textile material parameters is shown in Table 1. The stress-strain behavior of the yarns was tested on a tensile testing machine according to the standard DIN EN ISO 3341.

***Table 1:*** *Material data of the biaxial weft-knitted fabric*

| Parameter | Value |
|---|---|
| Weft and warp yarn material | CF-PA 6.6 (4 x 300 tex) |
| Yarn distance (weft and warp) | 3.6 mm |
| Reinforcement yarn Young's modulus | 69.7 GPa |
| Knitting yarn material | GF-PP (125.2 tex) |
| Knitting yarn Young's modulus | 68.4 GPa |
| Mass per area of the fabric | 824.2 g/m$^2$ |
| Fabric thickness according to DIN EN ISO 5048 | 1.9 mm |

With regard to the aforementioned interactive development process, the exchange of information between the individual submodels is a key challenge in such a coupled process and structure analysis. For this purpose, the relevant parameters must first be identified. This includes in particular information on component shape (obtained component geometry including elastic recovery and shrinkage effects, wall thickness distribution etc.), material behaviour (thermo-mechanical properties, local hardening, fibre orientations etc.) and physical condition (residual stresses, structural imperfections etc.). In order to transfer this information, the specification for the respective interface is defined and corresponding mapping methods are designed, also between different simulation environments.

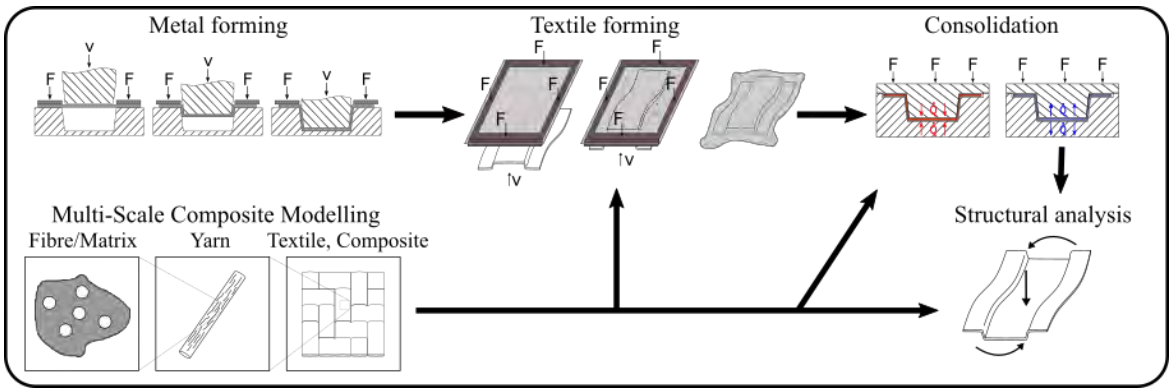


***Fig. 1*** *Schematic layout of the coupled process and structure analysis*

## 2.2 NUMERICAL ANALYSIS OF METAL FORMING

Current developments like lightweight structures, resource efficiency and the often used multi-material mix provide a new situation and advanced methods for the characterisation and modelling are needed [7]. Whereas in the past the error-free feasibility of a simple part was considered separately, today the process needs to be implemented in a complex process chain. The holistic approach of simulating the entire process chain requires several modifications on the numerical analysis regarding the continuous transfer of part properties.

The numerical simulation process of metal parts and structures is widely used in industrial applications. It is used to predict the behaviour of the working piece especially in deep drawing processes regarding thickness development and wrinkling. The accuracy of the simulation logically depends on the used analytical approach for the plastic material behaviour. Different yield criteria were developed in the last years whereas the number increases due to new materials involving complex material behaviour [8]. Together with an anisotropic strain hardening approximation, e. g. by Hockett-Sherby [9] or Swift [10], the development of the yield loci can be described. The yield criteria can be divided into isotropic and anisotropic hardening. The isotropic yield criteria, e. g. like the one from Tresca (1864) or v.-Mises (1913), assume a material behaviour independent from the rolling direction. Therefore, these criteria are not suitable for an accurate prediction of the behaviour of anisotropic materials like magnesium or aluminium alloys. For such material characteristics, various material models are available for nearly each specific demand. The choice mostly depends on the needed accuracy, the possibilities for gaining the needed material parameters and the robustness of the determination process [11]. Models like the widely used Yld2000-2d consider the anisotropy with eight independent parameters, acquired by material testing under uniaxial tension in 0°, 45°, 90° to rolling direction and biaxial tension [12]. Further current developments focus on the development of material models for asymmetric behaviour, which means different reactions for tension and compression. Because of their crystal structure (hexagonal closed-packed – hcp), magnesium alloys show a forming behaviour that implies the use of an anisotropic non-symmetric approach to describe the material behaviour in the forming process. Cazacu et al. evolved C-P-B 06 in 2006 [13], which is taken as the starting point for the present investigations. The model will be adapted for the research of anisotropic metal forming in the process chain. Together with the modelling approach of the hardening behaviour (kinematic, isotropic, distortion) the process of metal forming will be modified and the output will be adjusted for the further simulation chain so that especially potential vulnerabilities can be regarded or remedied early in the stage of process development. Furthermore, the generated information regarding component geometry, local wall thicknesses and altered material properties will be provided for subsequent steps of the simulation chain.

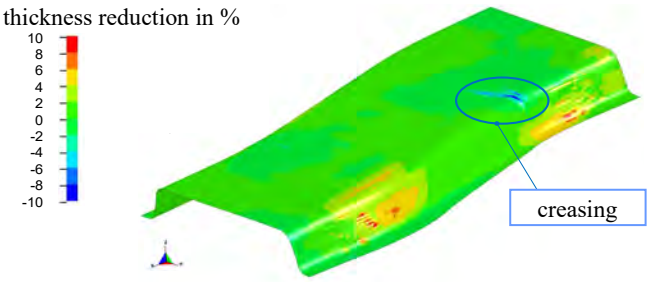


***Fig. 2*** *Results of metal forming simulation: thickness reduction and creasing in critical deformation zones*

## 2.3 NUMERICAL ANALYSIS OF TEXTILE FORMING

The manufacturing of three-dimensional composite structures typically involves the forming of textile semi-finished products. During the forming process, large local and global deformations occur in the textile. The knowledge of these phenomena is a prerequisite for achieving consistently high component quality and the targeted adjustment of the textile's reinforcing effect.

For the simulation of the forming of the weft-knitted fabric macro- and mesoscopic models were developed. While the macroscopic model considers the whole textile fabric as a continuum, the mesoscopic model involves single yarns as the smallest unit modelled. The macroscopic model is based on a laminate formulation, in which the bending behaviour and the membrane properties of finite shell elements are decoupled in order to achieve a correct description of the mechanical behaviour of textiles [14]. The mesoscopic model is based on the simplification of yarn as a chain of single beam elements [15]. In the present paper, Belytschko-Schwer resultant beam element is chosen to model the yarns in LS-Dyna (Fig. 3 left). The mesoscopic model requires more effort for modelling and computation, but has the ability to reflect yarn sliding and failure of textiles at yarn level (cf. Fig. 3 right). Numerical forming analysis of textiles provides insight into the fabric behaviour and yields local fibre orientation, fibre volume fraction and imperfections such as wrinkles and gaps. This information is needed for the following steps of the simulation chain.

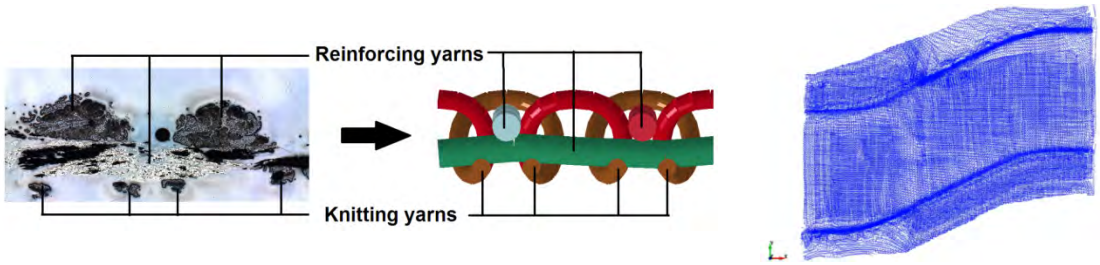


***Fig. 3*** *Mesoscopic model of weft-knitted fabric based on Belytschko-Schwer beam element: cross-section of actual fabric and finite element representation (left), results of textile forming simulation (right)*

## 2.4 CONSOLIDATION VIA HOT PRESSING

For modelling the forming process of the hybrid work piece consisting of metal and FRP material, numerical models for both components are needed. While the mechanical response of the metal part can be modelled according to section 2.2, novel approaches are needed to formulate the thermo-mechanical behaviour of composites during hot pressing. Here, methods based on meso- and macroscopic approaches have to be considered and validated by experimental investigations in parallel.

With the help of these material formulations, the different methods for manufacturing the multi-material work piece can be examined. Also the temperature depending friction between tool and work piece is respected. The implemented consolidation model takes into account anisotropic shrinking of the FRP which may cause residual stresses or even delamination. To consider the bending behaviour of composites, which is different to metals [5], shell element formulations are used to discretize the metal and composite parts separately. A contact formulation including a failure criterion between both materials is initialized before cooling the work piece inside the tool to take into account delamination due to varying thermal expansion of the components and resulting residual stresses.

## 2.5 STRUCTURAL MECHANICAL SIMULATION

Finally, a structural analysis will be performed to predict the mechanical performance of the hybrid component. The geometric properties, material characteristics and internal stress conditions are taken from the upstream simulation models and implemented in a structural analysis of the component. Particularly in view of the composite material, it is necessary to pursue a multi-scale simulation approach. The proposed multi-scale modelling approach for the fibre-reinforced-plastic includes the thermo-mechanical properties of the polymer matrix and the anisotropic elastic response of the reinforcement in order to determine the anisotropic thermo-mechanical behaviour of the composite. Also, the damage behaviour of the composite material is determined based on mesoscalic simulation models. The results of this step of the coupled process-structure-analysis are assessed for different process conditions and materials. In doing so, insights into the interactions are generated and the systematic interactive development of process, structure and material becomes possible.

# 3 EXPERIMENTAL CHARACTERISATION OF MATERIAL AND SEMI-FINISHED PRODUCT

For the individual models used to simulate the process chain, input values must be provided to describe the material and component behaviour. Besides of information transferred from upstream simulation steps, additional experimental investigations are still necessary. Suitable procedures and test methods are presented in the following sections.

## 3.1 METAL

Particularly with regard to material models suitable for magnesium alloys the needed parameters are sketched in Fig. 1. As mentioned in section 2.2., the approach for the yield criteria by Cazacu et al. [13] will be used and further modified by a new determination of the anisotropy factor $k$ [16]. Latest researches for magnesium alloy AZ31B have shown a good accordance of experimental data and the new formula especially in the tension area of the yield surface (see Fig. 4 left).

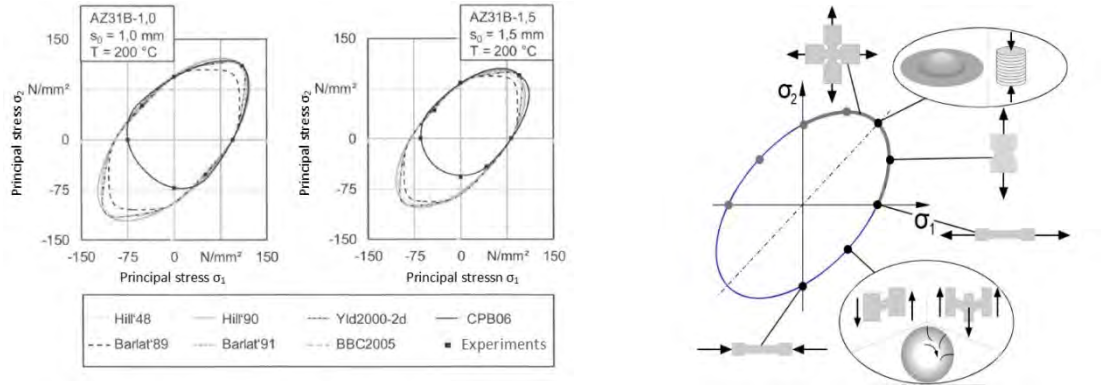


***Fig. 4*** *Material models for metal alloys. left: Comparison of different approaches to depict the yield surface; right: different test methods to assess the characteristic grid points*

Within the simulation of a whole process chain, the accuracy of each model affects the following ones. Therefore, a good material definition with a defined amount of stress points is needed. For the stress acquisition, certain (quasi-)standardized test methods are common (cf. Fig. 4 right). For the described concept, the mostly standardized tests, like the tension test, the biaxial test, a compression test and a tension-pressure test will be performed. Here, a reasonable limitation of tests is tolerable with respect to the number of mandatory tests. The possibility of semi-analytic parameter identification by the use of inverse methods will be checked to minimize the effort for the determination [17]. Knowing the material properties of magnesium alloys, the tests need to be performed at temperatures above $T \geq 200$ °C which activates gliding planes in the material and allows a forming process. The strain hardening behaviour and therefore the development of the yield surface during the forming will be regarded in particular, whereas new research results are taken into account [18]. The customized model will be validated by reference parts. Afterwards, the part properties will be included in the whole process chain for the next steps. Regarding the friction behaviour especially in the planned simultaneous forming of metal and FRP, a determination of the corresponding parameters in a draw-bend-test is suitable in order to detect possible effects for the process [19].

## 3.2 TEXTILE

The forming behaviour of textiles is influenced by the deformation properties of the yarns as well as the specific textile structure, the respective deformation modes and the interactions of the warp and weft yarns. During the forming of a textile into a three-dimensional shape, the three basic deformation mechanisms shear, tension and bending can be observed. When forming textile thermoplastics such as hybrid yarn fabrics, in particular, phenomena occur on several scales that may require a cross-scale approach for characterization and modelling. For this purpose, adapted test methods for yarns and textiles have been developed recently at the Technical University of Dresden. These enable the determination of the characteristic force-deformation-curves of the forming and sliding modes even under process conditions (temperature, pressure, deformation speed) [20]. The main parameters for yarn characterization are the force-deformation curves under tensile, transverse compressive and bending loads as well as the friction properties. For textile analysis, the shear force vs. shear angle curve is required additionally. In the following, only the determination of textile properties is described.

*In-plane shear deformation* is the main deformation mechanism during the forming of typical technical textiles. To model this mechanism, shear force vs. shear angle curves are required, which can be determined

using different test methods [5, 21]. Preferably, the two test methods bias extension test and picture frame test are used. The bias extension test uses a rectangular textile strip with a ±45° yarn orientation. In the testing machine, the specimen is subjected to a longitudinal tensile load and the force-deformation curve is recorded. However, the evaluation of this experiment is very complex. The picture frame test, on the other hand, uses a hinged frame to create a uniform shear strain field in the textile [22]. The textile is clamped into the frame or connected to it via pins. The latter option allows a significant reduction of clamping effects. In both cases, the use of a Digital Image Correlation method to determine the deformation is recommended. By means of hysteresis tests and the use of the results of the third run, the known weaknesses regarding large variation and limited comparability of different shear frame sizes can be compensated [20]. The recorded shear force vs. shear angle curves are typically strongly non-linear, since the shear force increases due to the increasing contact of adjacent yarns and the yarns are compressed laterally at the same time. This behaviour finally ends up in a so-called locking angle, from which no further deformation without wrinkling is possible. The testing of textile thermoplastics in particular shows increased resistance to shear deformation at process temperature due to the temperature-dependent viscosity of the matrix [20].
The characteristic force-deformation relationship for the deformation mechanism *In-plane tension* can be determined according to DIN EN ISO 13934-1 in a basic tensile test on strip specimens, also with temperature superimposition and different deformation speeds. Due to the initially occurring elimination of fibre undulations at comparatively low forces and the subsequent elastic material deformation with correspondingly higher forces, the recorded curves are strongly progressive and show a different behaviour for warp and weft direction. In order to evaluate the interaction of warp and weft direction, biaxial tensile tests are also proposed, which are the subject of current research [5, 20].
The *Out-of-plane bending* behaviour of textiles strongly affects the development of wrinkles and is therefore an important mechanism in textile forming. The bending stiffness depends mainly on the yarns used, namely their mechanical properties, their structural arrangement and their interaction behaviour. Depending on the composition of the textile, lateral asymmetries must also be taken into account. Compared to many other methods used, the gravimetric cantilever bending test according to DIN 53362 is characterized by its simplicity, the good reproducibility and the applicability even at process temperatures. However, this method is based on linear elastic behaviour and therefore allows only the determination of the bending stiffness. The influence of deformation speed cannot be studied.

### 3.3 COMPOSITE

In order to determine the thermo-mechanical parameters required to describe the material behaviour of the composite by the selected material model, appropriate measuring methods like tensile test, compression test, Iosipescu-Test etc. are utilized. Within these tests, digital image correlation is used for non-contact measuring of surface strains as well as out of plain displacements of the specimen. The gathered data is analysed to identify Young‘s modulus, Poisson‘s ratio, shear modulus, bending stiffness and plastic flow for different temperatures and strain rates. Furthermore, the damage behaviour is assessed by in-situ computer tomographic analysis. The thermal material parameters like specific heat capacity or glass transition and melting temperature can be detected by using the differential scanning calorimetry. Furthermore, the dynamic mechanical analysis is applied to determine the viscous behaviour of the specimen.

## 4 ANALYSIS OF INTERACTION PROPERTIES

Besides the mechanical behaviour of the materials and semi-finished products employed, interactions between different materials and components are present in the process as well as the fabricated hybrid component. For their description, input parameters are required, which normally have to be determined experimentally.

### 4.1 ASSESSMENT OF FRICTION PARAMETERS

In order to describe the interaction of different material domains in a finite element analysis by means of contact models, the determination of the friction parameters is of great importance. Standardized frictional examinations of the material contact between sheet metal and tool yield reasonable results. However, changed values are expected for the contact of textile structures under process-induced normal contact stresses, which are unusually high in the combined forming process of sheet metal and textile structure.
In order to determine these friction parameters between textile structure and the forming tool, an adapted test method on a biaxial testing machine is used (cf. Fig. 5 left). For thermoplastic composites, the influence of the process temperature on the viscosity of the polymer matrix and thus on the friction parameters of the textile must also be analysed. Test concepts with heated compression plates have proven their effectiveness in practice [20, 23].

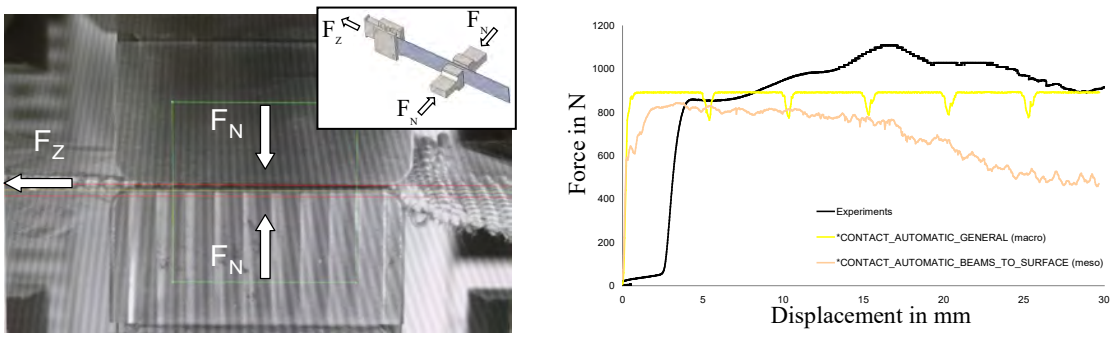


***Fig. 5*** *Determination of friction parameters: friction test setup (left), comparison of experimental and numerical results*

The simulation models, especially the contact formulations, must be subjected to a validation with determined force-displacement curves of the friction experiments. The chart in Fig. 5 right shows results of a first step in this process. When using magnesium sheets, an increased process temperature during the forming process is necessary. In this case, this increased process temperature has to be considered in later investigations of the coefficient of friction.

### 4.2 EXPERIMENTAL ASSESSMENT OF METAL-FRP-INTERFACE PROPERTIES

The load-bearing capacity of the hybrid structures considered here is decisively influenced by the properties of the interface between metal and composite. These are mainly determined by the pre-treatment of the two joining partners. On the one hand, mechanical processing methods are used here to structure and thus increase the joining surface area and to create form closures. Physical methods such as plasma treatment or coating are also used, which aim at increasing the surface energy or applying an adhesion promoting layer. Furthermore, chemical pre-treatment methods are widely used to clean and microstructure the joining surface. Finally, inherent adhesion promoters based on polymers are another technical possibility to improve the interface properties.
In order to evaluate the properties of different interface types, easy to implement test concepts such as peel test or single lap shear test are the first choice. For the determination of input data for the structural simulation which describe the interface properties, tests according to DIN EN 6033 and DIN EN 6034 for the measurement of Mode I and Mode II fracture toughness energies must be carried out additionally. Here, the tracking of the specimen deformation and the crack growth are performed by means of digital image correlation methods. The obtained data is then implemented into the simulation using cohesive zone elements.

## 5 CONCLUSIONS

Metal-FRP hybrid components place increased demands on the development process due to the more complex manufacturing process, the heterogeneous component structure and the interactions of structure, process and material. In this context, simulative approaches can be used specifically to identify existing interactions between individual process steps as well as between process chain and component properties. The gained knowledge fosters the interactive development process.
In the present paper, an approach for a coupled process-structure-analysis is presented. The sub-models used are described as well as the interfaces between the individual models and the parameters to be transferred. In addition, appropriate experimental methods for the determination of required input variables for the simulation models are explained. On the basis of this approach, novel hybrid composites based on magnesium, for example, will be analysed in an interdisciplinary team in further works.

## 6 ACKNOWLEDGEMENT

The „Saxon Alliance for Material- and Resource-Efficient Technologies“ (AMARETO, 100291445) and the collaborative research project “Series-based technologies for highly loaded hybrid multi-layer crash structures” (hybCrash, 100285086) are funded by the European Union (European Regional Development Fund) and the Free State of Saxony.

European Union
Europe funds Saxony.
EFRE
European Regional Development Fund

## REFERENCES


[1] Bürkle, E.; Gude, M.; Krahl, M.; Stegelmann, M.: *Kunststoffe und Metall - ein unzertrennliches Paar.* Kunststoffe, 12:27-32, 2017

[2] Jaschinski, J.: Lightweight floor assembly in multi-material design – Results of the FOREL-Project LEIKA. Materials in Car Body Engineering, Bad Nauheim, Germany, 16.-18.05.2017

[3] Haider, D. R.; Krahl, M.; Gude, M.; Hengstmann, R.; Titze, S.; Haupt, M.: *Continuous data measurement and analysis in automated manufacturing processes for hybrid lightweight structures.* In proceedings: SAMPE 2017, 14.-16.10.2017, Stuttgart

[4] Maaß, J.; Gude, M.; Wolf, M.; Krahl, M.; Krämer, A.; Amend, P.; Roth, S.: *Influence of injection moulding process parameters on the joint strength of hybrid fibre-reinforced thermoplastic with laser-structured metals.* Proceedings of the ECCM - 17th European Conference on Composite Materials, Munich, Germany, 26.-30.06.2016

[5] Gereke, T., Döbrich, O., Hübner, M., Cherif, C.: *Experimental and computational composite textile reinforcement forming: A review.* Composites: Part A, 46:1-10, 2013

[6] Baran, I., Cinar, K., Ersoy, N., Akkerman, R., Hattel, J. H.: *A Review on the Mechanical Modeling of Composite Manufacturing Processes.* Archives of Computational Methods in Engineering, 24(2):365-395, 2017

[7] Brosius, A.; Guilleaume, C.: *hybridn – Werkstoffe, Methoden, Prozesse.* In: Proceedings of 23. Sächsische Fachtagung Umformtechnik SFU 2016, pp. 12-21, Dresden, Germany, 7.-8.12.2016

[8] Schacher, H.-D.: *Entwicklungstendenzen in der Massivumformung für die Automobilindustrie.* In: Seminar proceedings "Neuere Entwicklungen in der Massivumformung", Stuttgart, Germany, 3.-4.6.1997

[9] Hockett, J. E. & Sherby, O. D.: *Large Strain deformation of polycrystalline metals at low homologous temperature*. Journal of the Mechanics and Plastic Solids 23: 87-98, 1975

[10] Swift, H. W.: *Plastic instability under plane stress*. Journal of the Mechanics and Plastic Solids 1: 1-18, 1952

[11] Banabic, D.: *Fließkriterien*. In: Siegert, K. (ed.): Blechumformung : Verfahren, Werkzeuge und Maschinen. VDI Buch, Berlin Heidelberg: Springer Vieweg, 2015, pp. 309-322

[12] Barlat, F.; Brem, J. C.; Yoon, J. W.; Chung, K.; Dick, R. E.; Lege, D. J.; Pourboghrat, F.; Choi, S.-H.; Chu, E.: *Plane stress yield function for aluminum alloy sheets – part 1 : Theory.* International Journal of Plasticity 19(9):1297-1319, 2003

[13] Cazacu, O.; Plunkett, B.; Barlat, F.: *Orthotropic yield criterion for hexagonal closed packed metals*. International Journal of Plasticity 22(7):1171-1194, 2006

[14] Döbrich, O., Gereke, T., Diestel, O., Krzywinski, S., Cherif, C.: *Decoupling the bending behavior and the membrane properties of finite shell elements for a correct description of the mechanical behavior of textiles with a laminate formulation.* Journal of Industrial Textiles, 44 (1):70-84, 2014

[15] Döbrich, O., Gereke, T., Cherif, C.: *Modeling of textile composite reinforcements on the micro-scale*. Autex Research Journal, 14(1):28-33, 2014

[16] Suttner, S.: *Charakterisierung und Modellierung des spannungszustandsabhängigen Werkstoffverhaltens der Magnesiumlegireung AZ31B für die numerische Prozessauslegung.* PhD-thesis, Friedrich-Alexander-Universität Erlangen-Nürnberg, Germany, 2017

[17] Küsters, N. & Brosius, A.: *Semi-analytic parameter identification for complex yield functions.* MATEC Web Conferences 80: NUMIFORM 2016: The 12th International Conference on Numerical Methods in Industrial Forming Processes, 2016

[18] Küsters, N. & Brosius, A.: *An adapted yield criterion for the evolution of subsequent yield surfaces.* Journal of Physics: Conference Series 896: 12-20, 2017

[19] Müller R., Jesche F., Lachmann L.: *Ermittlung von Reibwerten und Verschleißverhalten bei hohen Temperaturen im Streifenzugversuch*. Proceedings of the 25th Tagung Werkstoffprüfung, pp. 317-322, Neu-Ulm, 29.-30.11.2007

[20] Maron, B.: *Beitrag zur Modellierung und Simulation des Thermoformprozesses von textilverstärkten Thermoplastverbunden.* PhD-Thesis, Technische Universität Dresden, Germany, 2016

[21] Sharma, S.; Sutcliffe, M.; Chang, S.: *Characterisation of material properties for draping of dry woven composite material.* Composites Part A: Applied Science and Manufacturing 34:1167-1175, 2003

[22] Cao, J.; Akkerman, R.; Boisse, P. et al.: *Characterization of mechanical behavior of woven fabrics: Experimental methods and benchmark results*. Composites Part A: Applied Science and Manufacturing 39:1037-1053, 2008

[23] Sachs, U.: Friction and Bending in thermoplastic composites forming processes. PhD thesis, University of Twente, Enschede, The Netherlands, 2014

# OPTIMISING MECHANICAL INTERLOCKING INTERFACE OF CFRP-(THERMOPLASTIC/METAL)-HYBRIDS

**Fabian Günther[1]*, Markus Pohl[1], Vanessa Kretschmar[2], Gerik Scheuermann[2], Markus Stommel[1]**

[1]Plastics Technology, Faculty of Mechanical Engineering, TU Dortmund University
[2]Department of Computer Science, Image and Signal Processing Group, University of Leipzig

**ABSTRACT:** This contribution is about the experimental and numerical investigation of cfrp thermoplast interface joint strength. In tensile tests the joint strength of lap-shear-joints with cfrp thermoplast hybrid specimens with different surface structures are investigated. Comparing to a smooth reference, pin structures show the highest increase in joint strength up to 500 %. In FE simulation the optimal geometry for pins is determined to an ellipse. Further, the strengthening effect of pins towards the displacement reduction in joint interface is shown. Here, elliptic pins which are stretched in load direction are found to be most feasible in this application. Finally, three different visualisation techniques are introduced to determine pin's position on interface surfaces.

**KEYWORDS:** cfrp, interface, joint, structural elements, pin, single-lap joint, tensile test, FE simulation, optimisation, Abaqus, visualisation, LIC

## 1 INTRODUCTION

Hybrids combine different materials taking the advantage of individual material's properties to design products particularly suitable to different applications. A well-known example for a hybrid material is the combination of carbon fibre reinforced plastic (cfrp) and metals. The use of hybrid-materials requires a clear understanding of material's behaviour as well as the interface's characteristics.
A general study about surface modification is given in [1]. The interface of hybrids has been studied for different structures and production processes in e.g. [2–5]. These investigations proved an increasing joint strength for structured surfaces.
An alternative approach is the use of an additional plastic interlayer between the metal and cfrp interface [6, 7]. The thermoplastic interface enables a more fibre-suitable design as well as feasibility to mass series production. Further, the thermoplastic surface is easily structured to realize an interlocking on multiple dimensional scales (micro 1-30 µm/meso 0.5-3 mm/macro 10-80 mm).
In this contribution a meso scale optimized interface between cfrp and thermoplastic is investigated by experiments and numerical simulation. In addition to investigations on cfrp-metal hybrids with additional thermoplastic intermediate component done by Kießling *et al.,* Pohl *et al.*[6, 7] the influence of the structural elements on adhesive strength in thermoplastic-cfrp-interface is analysed in tensile tests on specimens. A proper specimen geometry with different interface structure is defined for this purpose. Additionally, FE simulation are done to investigate the effect of structures on the meso scale in hybrid composite joints. Finally, a method is introduced to position and orientate the structural element on the interlocking surface in an optimal arrangement according to the mechanical stresses.

## 2 SINGLE LAP JOINTS (SLJ) –TENSILE EXPERIMENTS

The single lap shear specimens are made of a thermoplastic wedge-shaped part and two carbon-fabric layers. The thermoplastic part consists of a PPA GF30 produced by injection moulding. The surface structure of the overlapping section is varied by using different injection mould tool inserts as shown in Fig. 2. The cfrp thermoplast joint is done intrinsically when producing cfrp with the resin transfer moulding (RTM). Here, two 0.25 mm thick carbon fabric layers (Torayca FT300B [8]) are used with a 0°-90° orientation and an epoxy resin (Biresin CR170 CH150-3 [9]).

## 2.1 SPECIMENS GEOMETRY AND SURFACE STRUCTURES

A single lap joint specimen with an overlapping section of 25 to 12.5 mm [10] is used to analyse the adhesive lap-shear strength between cfrp and thermoplast. To optimize the single lap specimen the geometry can be adjusted to obtain a more uniform stress distribution as discussed in [11]. Considering the lower stiffness the thermoplastic part thickness (H) is changed as depicted in Fig. 1. Further, the shaft angel (R) is varied to gain more shear load and reduce peeling forces in the joint area. Therefore, a FE parametric study is done to find an optimized geometry for the specimen. Here, Abaqus [12] is used with an multi continuum model (MCT) implemented with Helius PFA [13] where matrix and fibres separately considered to describe the composite material (cf. 3.1). The optimal geometry parameters are determined to 5 mm for the specimen's thickness and an angle of 10 degrees.

After the optimal geometry of the lap shear reference specimen with smooth surface is determined the thermoplast surfaces are structured with different patterns as shown in Fig. 2. The geometries are made of 0.5 mm walls/grooves (straight and circular) and pin or hole pattern with diameter of 0.5 mm. The gaps in between of all pattern has a size of 1.5 mm.

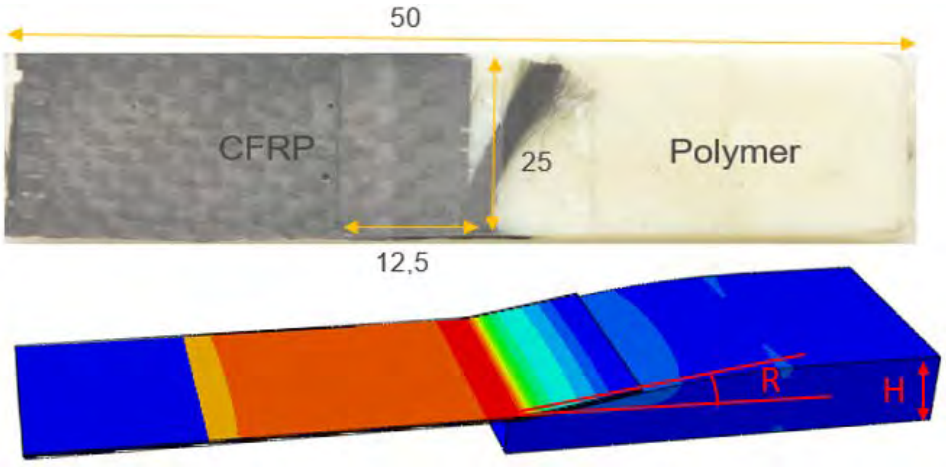


***Fig. 1*** *SLJ-specimen FE model with optimized geometry of polymer part (R and H varied parameters)*

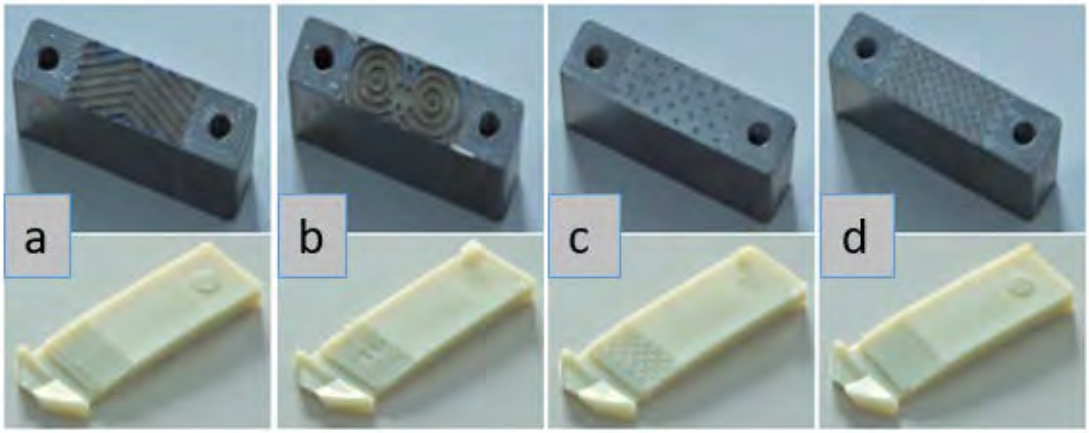


***Fig. 2*** *Injection moulding tool inserts (upper line) and thermoplastic specimen wedges (bottom line) with structured surface a) straight walls/grooves b) circular walls/grooves c) pins d) holes*

## 2.2 TENSILE TEST RESULTS

The tensile tests with SLJ-specimens show the adhesive and interlocking joint strength of the various geometries. The tests are done with an Instron E1000 tensile testing machine. The displacement velocity is 2 mm/min [14]. During the test the forces are recorded by an integrated load cell and the displacement is observed with an external optical measurement system. The maximum mean tensile forces of each geometry is given in Table 1. Here, it can be seen that all geometries have a big effect to the joint strength referring to a specimen with

smooth surface from 200 up to 500 %. The highest maximum forces show the specimens with pins on their surface.

***Table 1:*** *Tensile test maximum mean forces of different geometries*

| | Reference | Straight walls | Round walls | Holes | Pins |
|---|---|---|---|---|---|
| Max. Force [N] | 252,11 | 756,00 | 1092,46 | 1015,06 | 1505,21 |

# 3 FE-SIMULATIONS AND GEOMETRICAL OPTIMISATION

The experiments show the highest increase of connection strength with pins on the thermoplastic surface. Hence, the interlock joint of pins is further investigated with FE simulation. Therefore, an optimized design for pins is introduced. The FE simulation are done with a 3D-model of the SLJ-specimen which shows the load reduction in the interface due to interlocking by pins in the composite layer. Moreover, a 2D-model is used to optimize the pins' shape inside of the composite.

## 3.1 2D GEOMETRIC PIN OPTIMISATION

The optimal pin geometry is determined by a design of experiment (DoE) and a following optimization simulation by Dassault Isight [12] and Abaqus. Here, a 2D-model is used to find the appropriate pin parameter. The initial 2D simplification of the model is feasible due to the composite's size to thickness ratio. The pin is represented by an ellipse with two radiuses. These radiuses are varied in a range of 0.5 to 1 mm to find the optimal design. The load is induced by displacing the centre of the pin for 0.3 mm while the outer frame of the composite is fixed (encastre). The thermoplastic pin has an isotropic elastic material behaviour while the composite has a biaxial (orthotropic/fabric-like) material behaviour. The material parameter of pin and composite are given in Table 2.

***Table 2:*** *FE simulation material parameter*

| | $E_{11}$=$E_{22}$ [MPa] | ν or $\nu_{12}$ | $G_{12}$ [MPa] | $G_{13}$ [MPa] | $G_{23}$ [MPa] |
|---|---|---|---|---|---|
| Thermoplastic pin | 0,0091 | 0.37 | - | - | - |
| Composite | 2.2970 | 0.39 | 731,80 | 636,70 | 636,70 |

A Tsai-Hill-criterion from stress and strength values is used to determine the inner composite loads considering the anisotropic composite behaviour (see equation 1) [15]. Each simulation's maximum Tsai-Hill values are compared to determine the pin parameter with the smallest Tsai-Hill value. An initial DoE of 500 simulations shows a load stress minimum for radius ratios of 1 to 0.71624 mm while the ellipse is stretched into the load direction. In Fig. 3 two ellipses, orientated orthogonal to each other, are shown with the Tsai-Hill response. It can be seen that stress distribution differs and maximum stress values are higher in the simulation where the ellipse is stretched perpendicular to the load direction.

$$\left(\frac{\sigma_{11}}{R_{11}}\right)^2+\left(\frac{\sigma_{22}}{R_{22}}\right)^2-\left(\frac{\sigma_{11}\cdot\sigma_{22}}{R_{11}^2}\right)^2+\left(\frac{\tau_{12}}{R_{12}}\right)^2\leq 1 \qquad (1)$$

($\sigma_{ij}$ stress tensor value in plain given from simulation and composite strength values $R_{11} = R_{22} = 230$ MPa, $R_{12} = 24$ MPa)

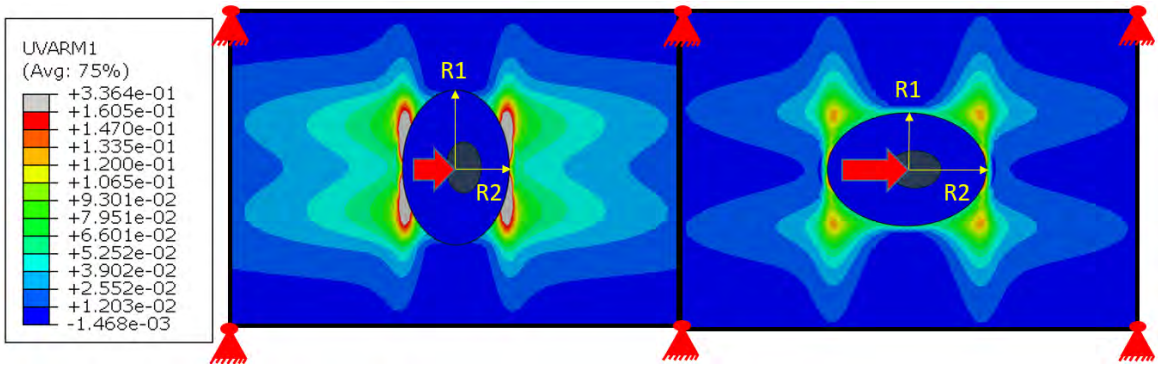


***Fig. 3*** *Tsai-Hill-Values (UVARM1) contour plot of elliptic pins with ratios R1/R2 of 0.72/1 and 1/0.72 (optimum) from 2D optimization simulation*

### 3.2 3D SLJ-SPECIMENS FE MODEL

The 3D simulation model is similar to the 2D FE model used to investigate the optimal SLJ-specimens. As stated in section 2.1 the MCT material model is implemented in Abaqus with Helius PFA which provides material models for composites with a progressive failure behaviour.

The composite consists of two layers of hexagonal elements (8-node linear brick, reduced) with 0.24 mm thickness see Fig. 4, B. The layers have a bi-directional 0°-90° fabric-like orientation. The interfaces between both layers and between composite and the thermoplastic part consists of cohesive elements (three-dimensional, 8-node) with a thickness of 0.01 mm see Fig. 4, C and D. These cohesive elements are necessary to enable delamination in between the materials. The thermoplastic wedge part has the dimension of the original specimen and is built from hexagonal elements (see above) and has a linear elastic material model as shown in Table 1. In the simulation the upper part is fixed with boundary conditions while the bottom part of the composite is displaced by 0.1 mm to induce load.

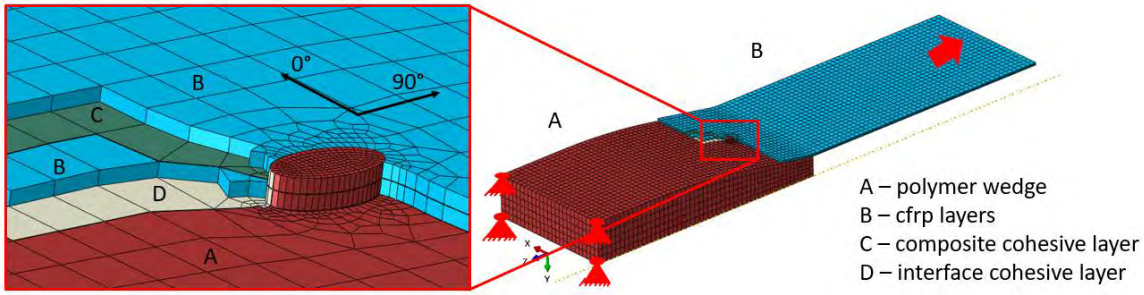


***Fig. 4*** *3D FE simulation model of SLJ specimen with Helius composite material*

### 3.3 SIMUALISATION RESULTS

With the 3D model different pin geometries are studied with a focus on the load reduction inside the composite. The simulation results are shown in Fig. 5. First, a circular pin is compared with a reference simulation without pin (upper line). The displacement in the interface of composite and thermoplastic is used to analyse the effect of the pin in the composite. The less the displacement the lower the load in the interface region. The results show larger displacements in the lower part of the joint interface because the displacement is introduced here. As expected the displacement in the interface decreases going up the interface because of the adhesive joint. Comparing the interface displacement with and without pin it can be seen that a small region behind the circular pin is less displaced. These reductions in displacement is shown through the blue/green region and is even better to observe in simulations with elliptic pins. The perpendicular pin shows an extended region with reduced displacement. Finally, the biggest effect can be seen in the simulation with the elliptic pin orientated in load direction which has the dimension as calculated before with 2D-optimisation. Here, the region with lesser displacement is extended over the whole width of the joint section.

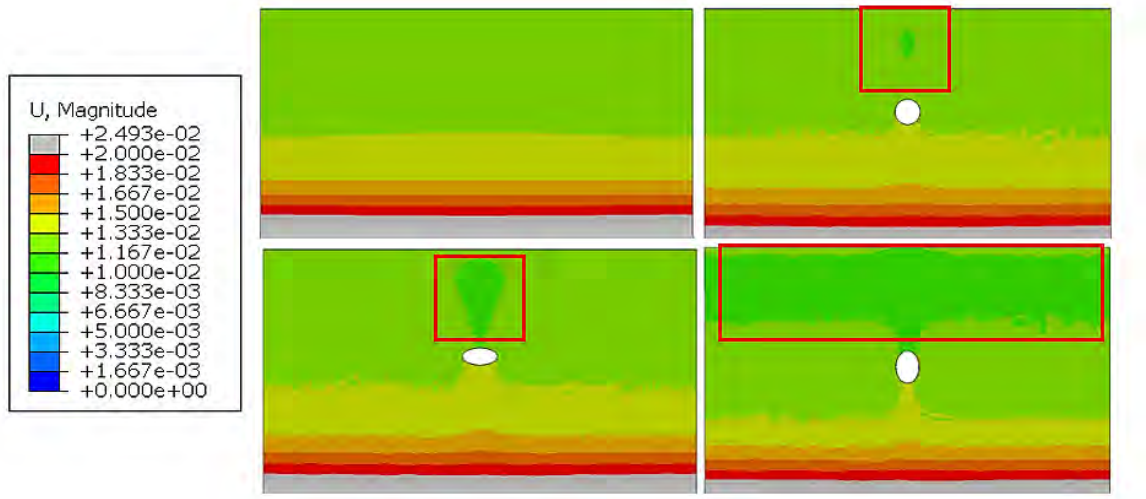


***Fig. 5*** *Displacement in the interface between cfrp and thermoplast with and without pin and different elliptic orientations*

## 4 VISUALISATION

Visualisation is an important part of FE simulation to interpret and analyse the calculated results. Different visualisation techniques can be used to determine position and orientation of geometric surface structures like pins. Contour plots as used in Fig. 3 or Fig. 5 aren't feasible to these applications. Following different visualisation techniques to position pins on interface surfaces will be introduced.

Tensor field lines are non-directional lines which can be calculated by integrating along an eigenvector of a tensor field [16]. To do so seeding points are required to begin with the integration. Therefore, it is important to choose a seeding strategy that matches the data, since only the information along the lines are visible, not in between and to prevent overplotting. The advantage of this method lies in the fact that someone can easily track them and get a good understanding of how a force for example stress is spread inside a material or along an interface. To get a better understanding see Fig. 6 (A) in which lines are integrated along the major eigenvector started at randomly set seeding points.

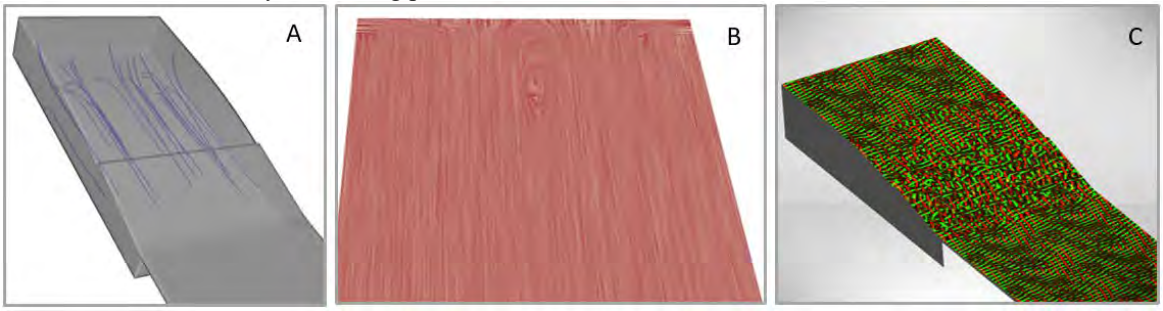


***Fig. 6*** *Visualisation techniques to position pin in interface joint: A: Tensor filed lines integrated inside the polymer part of the 3D FE simulation model, B: Line Integral Convolution applied to the surface of the cfrp layers projected into 2D space, C: Exemplary visualization using a fabric-like texture method based on LIC*

Line Integral Convolution (LIC) [17] is a similar method for visualisation of tensor fields. In difference to the common use case of tensor field lines applying for three dimensional data visualisation, LIC is used for two dimensional fields or sectional planes of 3D data. In general, a texture is applied to the plane and every pixel of the texture is integrated along the tensor field. The resulting picture is a smeared version of it towards the eigenvector. Since it is a texture based technique the quality of information display heavily depends on the chosen texture. Therefore, in most cases a random spot noise is calculated and integrated to generate a line like display shown in Fig. 6 (B) where a change in flow is visible around the pin and the edges of the layer.

In conclusion LIC is used for a detailed view of the data, while tensor filed lines offer a better global understanding and could be used for the analysis of boundary layers. These two methods have in common that they only display data of one eigenvector and thus the need to generate up to three applications for each eigenvector extracted from the tensor field accrues depending on the observation. To solve this problem Hotz *et al.* [18]

developed a fabric-like texturing method based on LIC for displaying the information of two integrations along the tensor field instead of only one. In Fig. 6 (C) the method is applied to a surface part of the presented model.

# 5 CONCLUSIONS

This contribution shows in experiments and FE simulation how structural elements can be used to improve the joint strength of cfrp thermoplastic joints. In tensile experiments pins are found to be most strengthening structure to improve cfrp thermoplastic joints.
Further, simulations are used to analyse the strengthening effect of pin in the interface. In 3D-FE simulations it is shown that interlocking pins reduce the displacement. A 2D simulation is used to determine the optimal elliptic geometry for pins which then are implemented to 3D model. This 2D simulation show a stress reduction around the pin area when it is stretched in load direction. Overall, it can be said that elliptic pins orientated in load direction have a strong joint improving effect. Finally, three different visualisation techniques are introduced which can be used to determine positions of pins on interface surfaces.

# 6 ACKNOWLEDGEMENT

This research was supported by the German National Science Foundation (DFG) within the Priority Program 1712.

# REFERENCES

## 7 References

[1] A.A.G. Bruzzone, H.L. Costa, P.M. Lonardo, and D.A. Lucca, “Advances in engineered surfaces for functional performance,” *CIRP Annals*, vol. 57, no. 2, pp. 750–769, 2008.
[2] Won-Seock Kim, Il-HanYun, Jung-JuLee, Hee-TaeJung, “Evaluation ofmechanicalinterlockeffecton-adhesionstrengthof polymer–metalinterfacesusingmicro-patternedsurfacetopography,” *International Journal of Adhesion &Adhesives*, vol. 2010, no. 30, pp. 408–417, https://www.sciencedirect.com/science/article/pii/S014374961000062X#fig1, 2010.
[3] T. M. Gwon, J. H. Kim, G. J. Choi, and S. J. Kim, “Mechanical interlocking to improve metal–polymer adhesion in polymer-based neural electrodes and its impact on device reliability,” *Journal of Materials Science*, vol. 51, no. 14, pp. 6897–6912, 2016.
[4] S. Ucsnik, M. Scheerer, S. Zaremba, and D.H. Pahr, “Experimental investigation of a novel hybrid metal–composite joining technology,” *Composites Part A: Applied Science and Manufacturing*, vol. 41, no. 3, pp. 369–374, 2010.
[5] X. Wang, J. Ahn, J. Lee, and B. R.K. Blackman, “Investigation on failure modes and mechanical properties of CFRP-Ti6Al4V hybrid joints with different interface patterns using digital image correlation,” *Materials & Design*, vol. 101, pp. 188–196, 2016.
[6] R. Kießling *et al.,* “On the Design, Characterization and Simulation of Hybrid Metal-Composite Interfaces,” *Applied Composite Materials*, vol. 24, no. 1, pp. 251–269, 2017.
[7] M. Pohl *et al.,* “Development structures for intrinsic hybrids,” *WT Werkstattstechnik*, vol. 107, no. 7-8, pp. 546–550, 2017.
[8] Toray Carbon Fibers America, INC., *Technical Data Sheet -Torayca.* [Online] Available: http://www.torayca.com/. Accessed on: Feb. 07 2018.
[9] Sika Deutschland GmbH, *Biresin CR170 mit CH150-3 Härter: Compositeharz-System.* [Online] Available: https://deu.sika.com/dms/getdocument.get/…/Biresin_CR170_mit_CH150-3.pdf. Accessed on: Feb. 08 2018.
[10] *DIN EN 1456 - Klebstoffe – Bestimmung der Zugscherfestigkeit von Überlappungsklebungen; Deutsche Fassung*, 2009.
[11] G. Fessel, J.G. Broughton, N.A. Fellows, J.F. Durodola, and A.R. Hutchinson, “Evaluation of different lap-shear joint geometries for automotive applications,” *International Journal of Adhesion and Adhesives*, vol. 27, no. 7, pp. 574–583, 2007.
[12] Dassault Systèmes, *Abaqus/CAE.* [Online] Available: https://www.3ds.com/de/produkte-und-services/simulia/produkte/abaqus/. Accessed on: Feb. 08 2018.
[13] Autodesk GmbH, *Helius Composite.* [Online] Available: https://www.autodesk.de/products/helius-composite/overview. Accessed on: Feb. 08 2018.
[14] *EN ISO 527 Bestimmung der Zugeigenschaften*, 1997.

[15] Kolios, A. J., Proia, S., “Evaluation of the Reliability Performance of Failure Criteria for Composite Structures,” in *World Journal of Mechanics*, 2012.
[16] David Weinstein, Gordon Kindlmann, and Eric Lundberg, Ed., *Tensorlines: advection-diffusion based propagation through diffusion tensor fields: In Proceedings of the conference on Visualization '99: celebrating ten years (VIS '99)*. Los Alamitos, CA, USA,: IEEE Computer Society Press, 1999.
[17] Brian Cabral and Leith Casey Leedom, *Imaging vector fields using line integral convolution: In Proceedings of the 20th annual conference on Computer graphics and interactive techniques (SIGGRAPH '93)*. ACM, New York, NY, USA,: 263-270, 1993.
[18] Hotz I., Feng L., Hamann B., Joy K, *Tensor-Fields Visualization Using a Fabric-like Texture Applied to Arbitrary Two-dimensional Surfaces: Möller T., Hamann B., Russell R.D. (eds) Mathematical Foundations of Scientific Visualization, Computer Graphics, and Massive Data Exploration*. Mathematics and Visualization. Berlin, Heidelberg, Germany, 2009.

# CHAPTER 6

# DESIGN

# DESIGN AND INTRINSIC PROCESSING OF A HYBRID CFR-TP CONTOUR JOINT WITH A MULTI-SCALE STRUCTURED LOAD INTRODUCTION ELEMENT

**Veit Würfel[1*], Daniel Barfuss[1], Raik Grützner[2], Franz Hirsch[3], Maik Gude[1], Roland Müller[2]**

[1]Technische Universität Dresden, Institute of Lightweight Engineering and Polymer Technology, Holbeinstr. 3, 01307 Dresden, Germany
[2]Fraunhofer-Institute for Machine Tools and Forming Technology IWU, Reichenhainer Straße 88, 09126 Chemnitz, Germany
[3]Technische Universität Dresden, Institute of Solid Mechanics, George-Bähr-Str. 3c, 01602 Dresden, Germany

**ABSTRACT:** In contrast to classical joining technologies for composite/metal hybrid structures like bonding and riveting contour joints prove to be a valuable alternative in terms of manufacturing efficiency and mechanical performance. This paper gives an overview of the design and the intrinsic processing technology of carbon fibre reinforced polyamide 6 with a multi-scale structured aluminium load introduction element. The presented approach combines a high pressure formed metal load introduction elements with an intrinsic bladder assisted blow moulded and braided fibre reinforced thermoplastic tape preform. This enables an industrial scale production of hollow hybrid composite structures with no need of post-processing operations. Design guidelines for principles of transferring high loads by multi-scale structured load introduction elements into composite profile structures are given. Further, the process parameters time, moulding pressure and process temperature are analysed and show a significant effect on the moulding quality of the part. An approach to manufacture a circumferential reinforcing bandage is presented. Additional investigations addressing the electrochemical compatibility of the joining partners are conducted and processing suitable surface treatment methods to minimize corrosion damage of the aluminium load introduction element are determined.

**KEYWORDS:** Intrinsic Hybrid, Contour Joint, Corrosion, Multiscale Structuring, Tape Braiding

## 1 INTRODUCTION

Carbon fibre reinforced polymers (CFRP) present a considerable lightweight engineering potential to save resources. The highest benefit can be achieved in structures with clear loading directions by the use of their anisotropic material behaviour. However, in commonly used differential designs this leads to challenges regarding joining operations, which introduce areas of complex stress and strain states. Thus, a multi-material design with joining strategies that are suitable to the specific material is essential for the efficient application of CFRP. Widely used techniques for joining fibre reinforced materials with metals, like bonding, bolting, riveting or screwing, join after the manufacture of each single component in a subsequent process step [1]. In general, this is often linked to labour intensive operations like surface preparation and machining, which may add extra cost and cause damage to the laminate. In contrast, the here addressed intrinsic production strategy combines joining and consolidation into one process step to reduce cycle times [2]. Within the integral blow moulding process (IBM) as shown in [3] a braided preform consisting of fibre reinforced thermoplastic hybrid commingled yarn material is consolidated and simultaneously moulded into a functional metallic element. The here presented approach enhances the composite performance by braided carbon fibre reinforced polyamide 6 (CF-PA6) UD-tapes and as well as the joint's strength by a load introduction element with a multi scale structured contour design. The interlocking geometries are adjusted to the braiding architecture in order to ensure the desired joining strength of CFRP and metal. In *Figure 1* this

principal is demonstrated for a tension-compression rod for automotive or aviation application. The tape braiding process combines the benefits of pre-impregnated thermoplastic unidirectional fibre reinforced tapes with the highly automated manufacturing advantages of braiding [4].

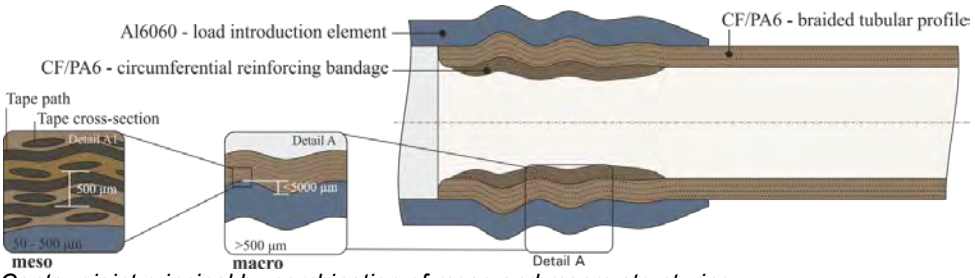


***Fig. 1*** *Contour joint principal by combination of meso and macro structuring*

This paper gives an overview of the design and the intrinsic processing technology of braided CF-PA6 tapes with a multi-scale structured aluminium load introduction element, shows investigations in moulding of thick walled circumferentially reinforced laminates and the electrochemical compatibility of the utilized materials.

## 2 DESIGN OF MULTI-SCALE STRUCTURED LOAD INTRODUCTION ELEMENTS

The design of a contour joint has a significant impact on the load bearing capability of the joint. As the composite is moulded into the contour of the load introduction element undulations are introduced into the laminate and its properties are reduced. Further a complex stress and strain state by tension or compression loading is caused. Thus, analyzation of the failure behaviour of the single parts, the material interaction and the effects of the structuring design are necessary to develop an optimized design of the interface.
In *Figure 2* the overall design approach considering the process induced residual stresses, stiffness gradient of the joining partners and the contour design is shown. At first the laminate in the free zone is defined. The investigated composite tape is made of Celanese, CF-Polyamide (PA) 6 Celstran® CFR-TP PA6 CF60-01 slit tape material with a fibre volume fraction of 48 %. Extensive investigations in the deviation of the coefficients of thermal expansion and the stiffness gradient from the CFRP and the metallic partner were conducted to trigger a cohesive failure behaviour and to improve material utilization for the given materials. A laminate architecture with a $[\pm 30_2° / 0_7° / \pm 30_2°]$ stacking sequence is defined which matches the CTE in the circumferential direction and the longitudinal stiffness of the utilized aluminium material [5].

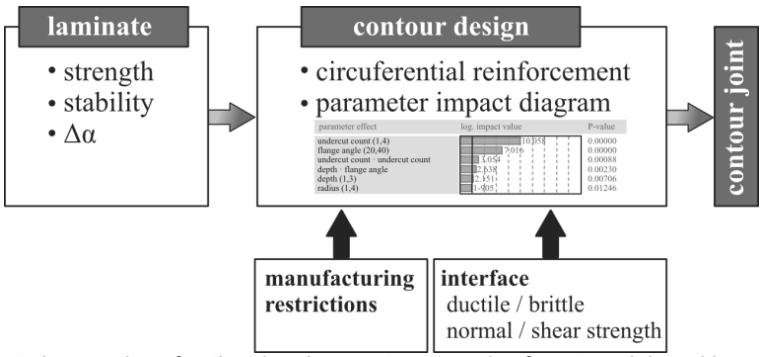


***Fig. 2*** *Demonstrated procedure for the development approach of contour joint with multi scale structured load introduction elements*

Having each bonding partner individually defined the laminate in the interface zone as well as the contour has to be specified. A parameterized model was developed for the optimization of the contour for which the investigated parameter combinations were determined by a design of experiment (DoE) approach to reduce computing effort. The contour parameters are determined by the aid of the derived parameter diagram based on the DoE model and under regard of the interface behavior. Multiple undercuts, big radii and shallow flange angles of the contour improve fibre failure (FF), inter fibre failure (IFF) and interface debonding while a higher undercut depth is beneficial for IFF and interface debonding but influences the FF mode negatively [6]. To achieve high load bearing capabilities [7] suggested the integration of an additional circumferential reinforcement to secure the axial orientated layers within in the undercuts of the contour.

Preliminary tensile tests of integrally blow moulded meso contour joints prove the potential of a reinforcing bandage on the load bearing capability (*Figure 3*). Due to the high transversal strain within braided laminates caused by the trellis effect [8] the CFRP profile is pulled out of the meso contour successively when a tensile load is applied. The load bearing capability gradually decreases after the first slipping in consequence of damage propagation and a decreasing contour length. In contrast with an inner circumferential reinforcement of five braided ±70° layers [$\pm 30_2$° / $0_7$° / $\pm 30_2$°/ $\pm 70_5$] the maximum load of the joint is increased by 66%, leading to a material failure of the aluminum tube.

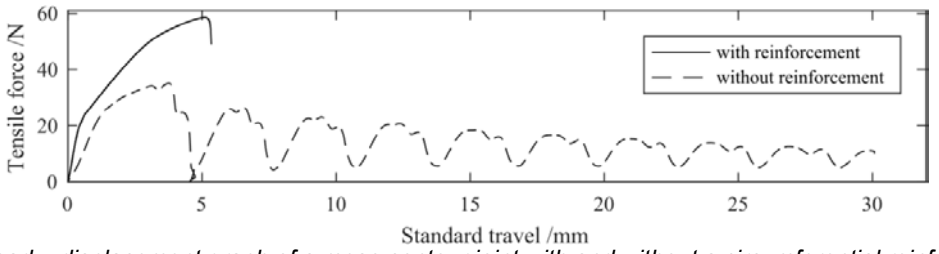


***Fig. 3*** *Load – displacement graph of a meso contour joint with and without a circumferential reinforcement*

With the help of the demonstrated procedure and additional point FE analysis the design of a reliable contour joint according to the application's requirements can be obtained. Due to a maximum expansion rate of a braided preform manufacturing restrictions exist limiting the depth of the undercuts of a macro contour and the thickness of an added circumferential reinforcement. This manufacturing issue is addressed in the following section.

## 3 PROCESS AND MANUFACTURING STUDIES

For the manufacture of the presented hybrid tension and compression rod a braided fibre reinforced thermoplastic tape-preform and an aluminium load introduction element are produced separately and then joined in the intrinsic IBM process. The load introduction element is hydro formed in a two-stepped process by external and internal high pressure to sequentially mould the multi scale structuring. Additional forming technologies like knurling or press forming are used to expand the design space. Three suitable designs of meso structures have been identified: knurled pyramids, press formed pins and press formed rhombs.
In the IBM process the thermoplastic composite is being moulded by an internal pressure bladder against an aluminium tool in the tubular section and into the contours of the load introduction element, which thereby serves as the tool itself. Both the braided preform and the aluminium tool are inductively heated in an induction coil which is specifically tailored to the requirements of heating aluminium. The investigated composite tape has a targeted process temperature of 230°C.

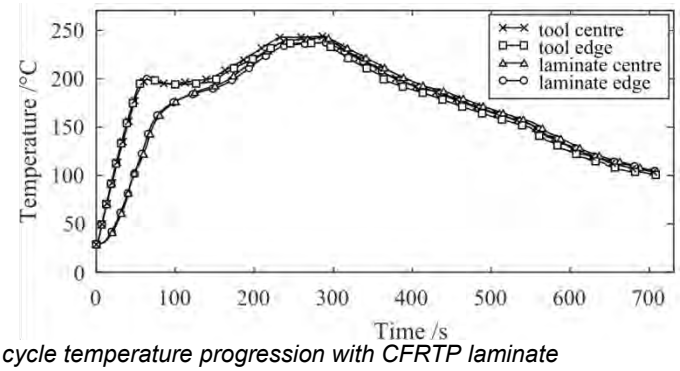


***Fig. 4*** *IBM process cycle temperature progression with CFRTP laminate*

A detailed investigation in the induction heating process with the overall goal of minimizing the cycle time while achieving an equal laminate quality of a variothermal oven process has been conducted. *Figure 4* shows an exemplary temperature curve with an optimized power application cycle, a bladder pressure of 6 bar and a consolidation dwell time of 60 s. The temperature of the laminate aligns very quickly to the temperature of the tooling's inner surface during heat up and the temperature gradient in the longitudinal direction stays almost constant at 6,5°K. A higher pressure during heat up decreases the heating time until 230°C is reached due to an increased contact surface between the individual tapes. Short cycle times of less than 10 minutes are achievable.
*Figure 5* shows the consolidation quality of a reference oven laminate with a 15 minute consolidation dwell time and the laminate after the presented intrinsic IBM process. White areas represent the fibres, the PA6

resin is grey and dark spots are either voids or break out during the grinding process. It shows that 60 s consolidation dwell time in the IBM process is sufficient for full interlaminar adhesion with no visible macro porosity inside the laminate.

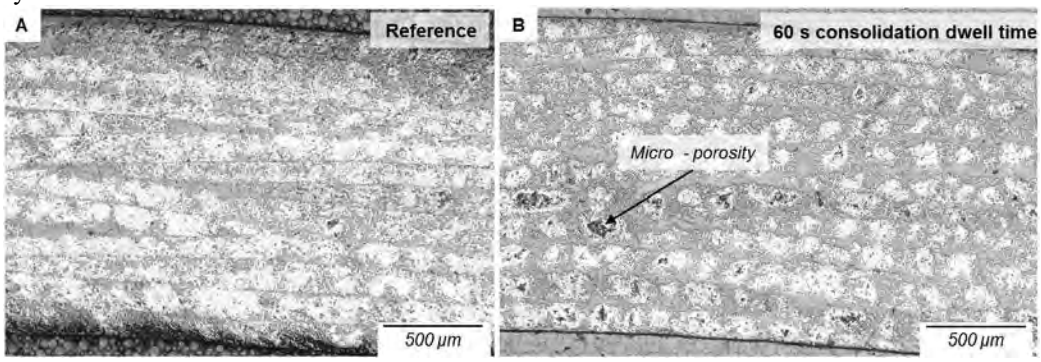


***Fig. 5*** *Consolidation quality evaluation of a reference laminate (A) and the IBM laminate with a 60 s consolidation dwell time*

However, micro porosities inside yarn bundles and an overall less homogenous fibre distribution are present compared to the reference laminate. This is related to the quality of the used Celanese tape material.
The laminate quality in the macro contour of the joint is of particular interest. Moulding of the CFRP into the undercuts of the load introduction is challenging because of the limited expansion capabilities of the braid. Due to the textile architecture of the laminate a defined shear deformation takes place whereby the braiding angle is locally increased and the preform is shortened in longitudinal direction. Based on the findings of [8] the resulting braiding angle as well as the shear locking angle at maximum expansion can be determined with the relationships (1) and (2). Thereby $D_0$ is the original and D the expanded preform diameter, $\theta_0$ is the original and $\theta$ the expanded braiding angle and $\theta_c$ the shear locking angle, while w is the width of the utilized tape and L the distance between the crossing points of two interlacing yarns.

$$\frac{D}{D_0} = \frac{sin\theta}{sin\theta_0} \qquad (1)$$

$$\theta_c = 90° - \frac{sin^{-1}\left({}^{w}/_{L}\right)}{2} \qquad (2)$$

In general a circumferential reinforcing bandage like shown in *Figure 1* is located in the joining area. The initial braiding angle of the preform accounts for the related fibre reorientation after expansion. Considering the bulk of the braided plies of the tubular profile laminate as well as the five plies of the bandage a mandrel diameter of $D_0$ = 35 mm is chosen for the braided bandage. With the help of relationship (1) a braiding angle of $\theta_0 = \pm 50°$ is determined to achieve the desired expanded angle of $\theta = \pm 70°$ at the maximum inner diameter of D = 43 mm. By utilizing the shear deformation capability of the braid the preforming effort is reduced, but it is limited due to friction between separate layers. *Figure 6* shows the manufacturing approach as well as the resulting computer tomography scan of the manufactured specimen and the moulding quality.

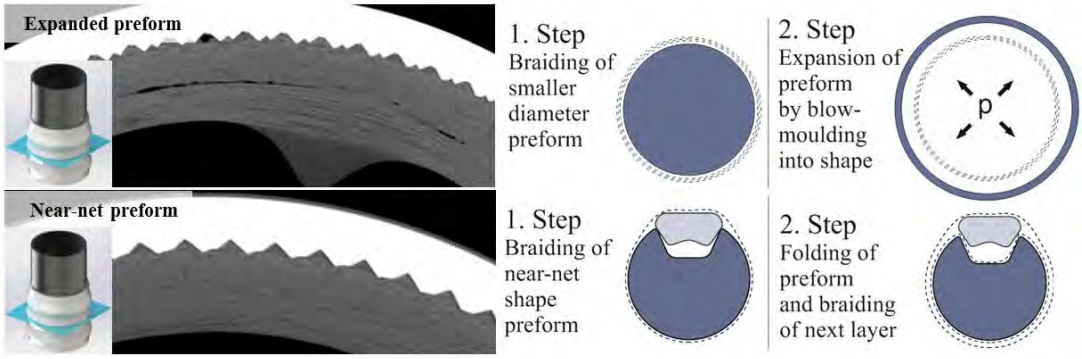


***Fig. 6*** *Computer tomographic (CT) scans of the expanded 50° bandage (top) and the near-net shape manufactured bandage (bottom)*

Even though the shear locking angle $\theta_c$=78° has not been reached the expansion of the whole laminate is limited due to intra- and interply friction of the 50° bandage. The bandage is not fully bonded to the plies of

the tubular profile leaving voids at the interface. Voids are also present in the knurled meso structure of the load introduction element. Additionally, wrinkles are created on the inner surface of the bandage.
An alternative approach has been developed to directly near-net shape manufacture the preform with the right angle and right diameter. This is achieved by a mandrel design with a changeable cross section diameter. The layers of the circumferential reinforcement are braided on a larger diameter, folded inside a groove and then are over braided by the layers of the CFRP profile on a smaller diameter. After consolidation the near-net preform demonstrates the potential for full moulding of the macro and the meso contour as the braided preform does not need to be expanded.
Depending on the design of the macro contour and the needed depth of its undercuts near-net preforming is recommended for the manufacturing of the circumferential reinforcing bandage.

# 4 ELECTROCHEMICAL COMPATIBILITY OF THE MATERIAL COMBINATION

Carbon fibre reinforced thermoplastic polymers generally have excellent resistance to corrosion and chemical attacks which results in a long life expectation without the need for maintenance or repair. Aluminium is also very resistant to corrosion in most environments due to its thin but effective oxide layer. However, both materials paired together cause galvanic corrosion (GC) due to the electrochemical potential difference of carbon and aluminium. This type of corrosion occurs when both materials are in direct electrical contact with each other and when they are bridged by an electrolytic solution. Furthermore, the design of the contour joint can promote crevice corrosion (CC) when the edges of the CFRP laminate debond due to mechanical loads, fatigue or different thermal shrinkage during manufacturing which is worsened due to exposed fibre ends in this area. *Figure 7* shows the types of corrosion in the presented hybrid contour joint which have to be prevented for the long term durability of the structure as well as the four characteristic areas of the joint.

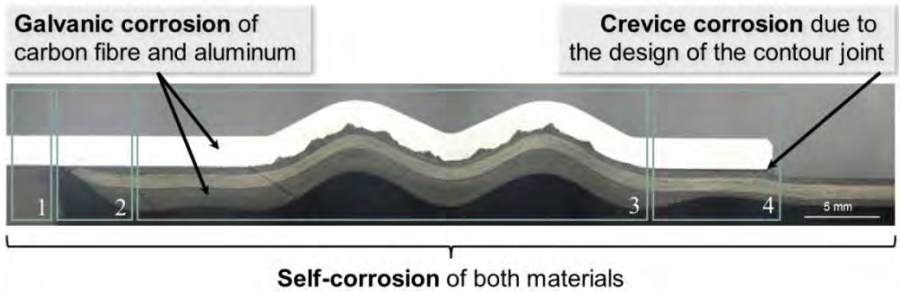


***Fig. 7*** *Types of corrosion in the presented contour joint in 4 different characteristic areas*

To avoid galvanic corrosion both contact partners must be electrically isolated from each other, which is typically achieved by surface coatings, separating layers or the electrolyte access must be prevented. Targeting mass production the following requirements for a corrosion protection of the intrinsic processed hybrid contour joint have to be met: temperature resistance throughout the process, low manufacturing effort, low cost and low layer thickness as well as sufficient strain rates.
Following a cost benefit analysis six anti-corrosion concepts have been selected for an evaluation in a cyclic corrosion test following the VDA 233 – 102 recommendation. The test consists of alternating humidity and temperature as well as salt spray phases, developed in the automotive industry. The concepts are an untreated specimen as a reference (A), edge sealing with silicone on areas 2 and 4 (B), a 1,5 µm Ormosil sol-gel coating (C), a 10 µm anodized layer (D), a 40 µm hard-anodized layer (E) and a 0,5 mm glass fibre (GF)-PA6 organosheet (F). Four specimens per concept remained 18 weeks in the climate chamber and have been cut open and cleaned before inspection. The results of one specimen of each concept are shown in *Figure 8*.

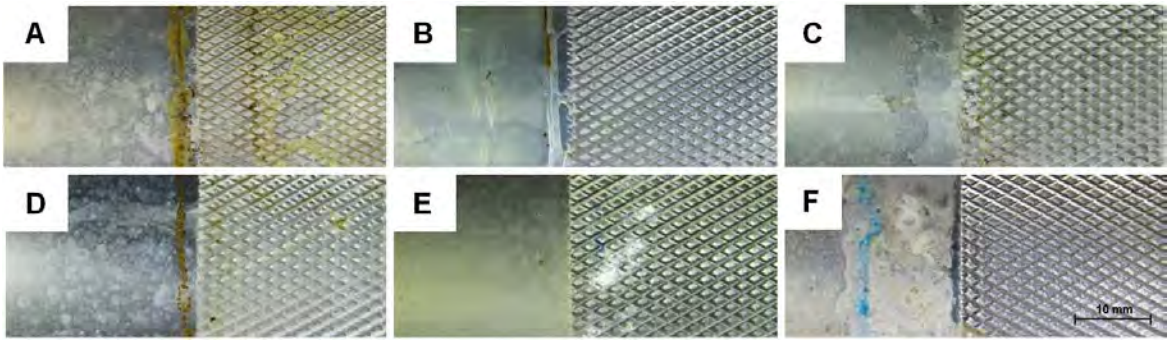


***Fig. 8*** *Macroscopic corrosion damage inspection on different load introduction elements after an alternating climate test*

The untreated specimen (A) is corroded extensively. Large spots of GC within all areas as well as CC at the edge of the CFRP in area 2 are visible. In specimen B CC could be prevented by the silicone sealing which was able to prevent the advance of the electrolytic solution into crevices at the edges of the CFRP. Small amounts of GC are present in area 3 of specimen B. It is assumed, that the high moisture absorption of PA6 still enables a current flow between the two partners of the contour joint by a process of diffusion. This is effect is also present in the specimen with a GF/PA6 insulation layer (F), which shows strong CC in area 2. The Ormosil sol-gel coating (C) shows GC as well as pitting corrosion (PC) in area 3. Small amounts of PC due to CC are present at the edges of the laminate in area 2 and 4 where exposed fibres are visible. The surface coating might have been damaged in the moulding process. The anodized specimen (D) shows similar results to specimen C. The hard-anodized coating (E) proved to be the best protection against GC and CC, but shows strong corrosion damage in very localized areas where the coating might have been damaged. Summarizing the investigation the design of the contour joint proved to be the most challenging aspect due to the crevices at the edges of the CFRP part where crevice corrosion is of great significance. The sol-gel coating, the anodizing layer and the hard –anodizing layer proved to be mostly successful against GC but show strong effects of corrosion once the coating has defects or gets damaged in the manufacturing process. This is related to the resulting ratio of cathodic to anodic area.

## 5 CONCLUSIONS

A design and intrinsic manufacturing approach is presented for hybrid carbon fibre reinforced thermoplastic rods with a multi scale structured load introduction element. A preliminary design guideline for a reliable contour joint according to the application's requirements is presented. Within the IBM process short cycle times of 8 to 9 minutes are obtainable by an inductive heating approach. Investigations in higher pressure levels have to be conducted to improve the quality of micro impregnation while maintaining the fast cycle time. A manufacturing approach for circumferential reinforcing bandages is presented which secures complete moulding of the undercuts in the macro contour of the joint. A study in the electrochemical compatibility of the joint showed the challenges in the design regarding corrosion damage in which hard anodizing proved to be the most promising surface coating. Further investigations in the protection against corrosion have to be conducted, especially combinations of edge sealing with anodizing or a sol-gel coating. The influence of the manufacturing process on the surface coatings as well as the effect of the corrosion damage on the load bearing capabilities of the joint need to be studied further.

## 6 ACKNOWLEDGEMENT

The authors are grateful for financial support through the German Research Foundation, DFG, within the priority program 1712: Intrinsic hybrid composites for lightweight structures - basics of manufacturing, characterization and design.

## REFERENCES

[1] Fischer T., Schürmann H.: *Der Pressverband als Krafteinleitungs-Element in Faser-Kunststoff-Verbund-Wellen*. 11. Nationales Symposium SAMPE Deutschland e.V., 2005

[2] Fleischer J., Ochs A., Dosch S.: *The future of lightweight manufacturing – production related challenges when hybridizing metals and continuous fiber-reinforced plastics*, Proceedings of International Conference on "New developments in Sheet Metal Forming", 51-70. Stuttgart. 2012

[3] Helms O.: *Konstruktion und technologische Umsetzung von hochbeanspruchten Lasteinleitungssystemen für neuartige Leichtbaustrukturen in Faserverbundbauweise*. Dissertation, TU Dresden, 2006

[4] Garthaus C., Barfuss D., Witschel B. et al.: *Tape braiding: high-performance fibre-reinforced thermoplastic profile structures*. JEC Composites Magazine, No 96, 62-64, 2015
[5] Hirsch F., Kästner M.: *Multiscale modelling and simulation of failure in metal composite interfaces*. In proceedings 17th European Conference on Composite Materials, Munich, 2016
[6] Barfuss D., Garthaus C., Gude M. et al.: *Design of multi-scale structured Al-CF/PA6 contour joints*. International Journal of Automotive Composites, Vol. 2, No. 3/4, 2016
[7] Hufenbach W., Kroll L., Gude M. et al.: *Integrated load introduction system for composite lightweight structures in aerospace applications*. 27th SAMPE Europe international conference, Paris, 27th -29th March 2006
[8] Manabe K.-I: *Bulge forming of braided thermoplastic composite tubes under axial compression and internal pressure*, Polymer Composites, Vol. 17, No.1, February 1996

# EXPERIMENTAL INVESTIGATION OF THE DESIGN CONCEPT FOR A NON-ENGAGING BELLOWS COUPLING MADE OF PREPREG-BASED CARBON FIBER REINFORCED POLYMERS

**C. Oblinger[1*], A. Baeten[2], K. Drechsler[3]**

[1]University of Augsburg, Application Center for Materials and Environmental Research, Augsburg, Germany
[2]Augsburg University of Applied Sciences, Augsburg, Germany
[3]Technische Universität München, Institute for Carbon Composites, Munich, Germany

**ABSTRACT:** This paper deals with the experimental investigation of the design concept for a non-engaging bellows coupling made of prepreg-based carbon fiber reinforced polymers. The main task of this shaft coupling is the torsionally stiff torque transmission and the compensation of axial displacement as well as the angular misalignment of the connecting shafts. The presented design concept combines the fulfillment of the compensation and connection functionality. A very high torsional stiffness as well as a certain flexibility of the whole coupling geometry is required due to the connection of two torsion-loaded shafts. For a separate investigation of the CFRP/metal interface different cylindrical CFRP specimens were defined. In order to examine the respective connection functionality the slipping torque of the shaft-hub-joint was determined via a static bracing test bench. Prototypes of the CFRP bellows coupling were manufactured with a new reusable core system. The characteristic load cases were experimentally investigated. These results were compared with previous experimental findings from prototypes made with a different core system. The characterization of the geometric structure was based on the determination of the wall thicknesses and the recording of the contour accuracy using a stereomicroscope.

**KEYWORDS:** Shaft coupling, bellows coupling, design concept, composite, CFRP, prepreg, metal, hybrid, testing

## 1 INTRODUCTION

In contemporary society, weight-reducing and durable components made of lightweight materials are of great importance. Fiber reinforced polymers (FRP), especially carbon fiber reinforced polymers (CFRP), are high-performance lightweight materials with unique properties. They are used where other materials have reached their limits. For example they are broadly applied in aerospace industry, automotive production, shipbuilding and wind energy sector as well as in the sports equipment industry [1 - 3]. Various textile reinforcement materials, resin systems and processing technologies are available for most diverse requirements [4, 5]. For example in mechanical engineering prepregs (pre-impregnated materials) impart high strength, stiffness and good damping property to components subjected to extreme dynamic stresses (e.g. drive shafts, gripper bars). However, the advantage in performance of using prepregs is detrimental to productivity. Therefore this technology is mainly used for very small (prototype manufacturing) to medium-sized production runs. In these scenarios, component performance and production cost can be easily reconciled using prepreg materials [6, 7]. Nevertheless, in many different applications of FRPs, a combination with metallic components leading to so-called mixed material constructions is the key to benefit from the specific properties of both material classes [8 - 10]. In mechanical and propulsion engineering (e.g. rotating machine elements) mixed material constructions lead to a significant increase of efficiency [11 - 13]. In this respect, a shaft coupling between two shafts depicts an exemplary machine element for a possible application of a combination of FRP/metal construction. An approach for the design and optimization of offset-compensating components and their integration into a car drive shaft is shown in [14]. Within a further research work [15], this concept has been extended by the development and optimization of a non-engaging multi-plate coupling made of glass fiber reinforced polymers. The functionality of a shaft coupling can be divided

into a transmission, compensating and switching function [16, 17]. The compensation functionality distinguishes between four types of shaft misalignments: axial displacement, angular and radial misalignment as well as rotational misalignment. For example these misalignments can result from manufacturing, assembly or load-related deviations [18 - 20]. The flexibility of shaft couplings is often achieved by a number of compensating elements. Furthermore, shaft couplings can be distinguished between engaging and non-engaging couplings [21]. This paper presents the experimental investigation of the design concept for a non-engaging bellows coupling made of prepreg-based carbon fiber reinforced polymers. Moreover, the focus lies on the torsionally stiff torque transmission and the compensation capability of axial displacement as well as angular misalignment.

# 2 DESIGN CONCEPT, MATERIALS AND METHODS

## 2.1 DESIGN CONCEPT

The research approach for the design concept consists of designing and realizing a non-engaging shaft coupling with as few single components as possible and using prepregs made of carbon fibers. A small number of components reduces the complexity of the whole shaft coupling and possibly increases the necessary maintenance intervals. The aim of this work is the implementation of a torsionally stiff and frictionally engaged torque transmission device. In addition, the focus is on the compensation capability of axial displacement as well as angular misalignment of the shaft ends. This focus results in two essential requirements for the design concept of the shaft coupling, which shall be simultaneously fulfilled: the compensation and connection functionality. Regarding the realization of the compensation functionality, two partly contrary structure-mechanical requirements were to be fulfilled in one single component: (a) transmission of a specific torque without exceeding a threshold on the torsion angle (high torsional stiffness) as well as (b) compensation of axial displacement and angular misalignment, whereby the resulting load on the bearings shall be within certain limits (low bending stiffness). Within the operation range of drive technology, plain shafts (steel solid shafts) of frequently different diameters should be connected with the hub body detachably and frictionally engaged. In the present research work the reference diameter of the connecting shafts is 60 mm, whereby the maximum outside diameter for the entire system should not exceed 100 mm. After the disassembly of this shaft-hub-joint a repeated assembly (two to three times) should be possible. The research work revealed that a CFRP compensating structure with different diameters could meet these requirements [22]. Therefore in the approach three bellows-shaped elements, each with an identical outside diameter, are used for the realization of prototypes of the CFRP bellows coupling (see figure 1).

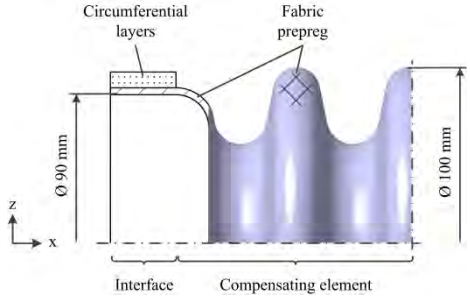


***Fig. 1*** *Schematic of the generic CFRP bellows coupling (¼ segment)*

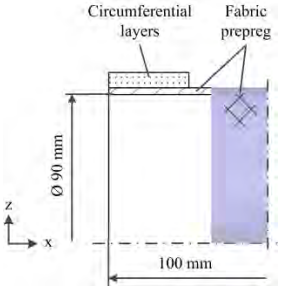


***Fig. 2*** *Schematic of the cylindrical CFRP specimen (¼ segment)*

The fiber orientation of the fabric prepreg layers is ± 45° with respect to the x-axis of the coupling. The detachable shaft-hub-joint based on an internal clamping set between the CFRP/metal interface represents a fiber-compatible design for torsion-loaded structures, especially in machine and plant construction. At the interface circumferential layers of unidirectional prepreg are necessary. Cylindrical CFRP specimens were considered to validate the connection functionality (see figure 2). The required variability with regard to different connection shaft diameters is achieved by using different metallic reducing bushings while maintaining the same internal clamping set. Geometrical design variables were identified using the finite elements method and the design of experiments approach, which have a significant influence on the structure mechanical behavior of the CFRP bellows coupling [23].

## 2.2 MATERIALS

Commercially available epoxy-based prepregs made of carbon fibers were purchased from SGL CARBON SE. The fabric prepreg was CE 8201-200-45S (twill 2/2) with the nominal thickness of 0.19 mm. Moreover, the unidirectional prepreg CE 1250-230-39 with a nominal thickness of 0.22 mm was used for the circum-

ferential layers. Both materials were used for manufacturing sequence I (seq. I). Because of a change in the product segment, comparable successor prepregs were used for the manufacturing of further specimens and prototypes. This fact led to the manufacturing sequence II (seq. II). The components produced within both manufacturing sequences are explained in subchapter 2.3.1. The C W200-TW2/2-E323/45% was used as the successor material for the fabric prepreg CE 8201-200-45S and the C U230-0/NF-E320/39% for the unidirectional prepreg CE 1250-230-39 (manufacturing sequence II (seq. II)). The prepregs are chemically compatible. In addition, they require a low curing temperature, which enhances the economical usage of these materials in machine and plant construction.

## 2.3 METHODS

### 2.3.1 COMPOSITE MANUFACTURING FOR TESTING

The hand lay-up prepreg technology was applied as an appropriate manufacturing method for the realization of the cylindrical specimens and the prototypes of the bellows coupling. Table 1 clarifies the assignment as well as the design and manufacturing parameters of the cylindrical CFRP specimens.

***Table 1:*** *CFRP-specific design and manufacturing parameters of the cylindrical specimens*

| | Fabric prepreg | | Unidirectional prepreg | |
|---|---|---|---|---|
| Specimen No. | Laminate thickness [mm] | Cover per layer [°] | Laminate thickness [mm] | Cover per layer [°] |
| 1-1 (seq. I) \| 1-2, 1-3 (seq. II) | 2.1 | 360 | 4.8 | 360 |
| 2-1 (seq. I) \| 2-2, 2-3 (seq. II) | 2.1 | 360 | 2.4 | 360 |
| 3-1 (seq. I) \| 3-2, 3-3 (seq. II) | 2.1 | 180 (2 x) | 4.8 | 360 |
| 4-1 (seq. I) \| 4-2, 4-3 (seq. II) | 2.1 | 180 (2 x) | 2.4 | 360 |

The cylindrical CFRP specimens have the same connection geometry and material assignment as the prototypes of the CFRP bellows coupling (see figures 1 and 2). However, the configurations of the cylindrical specimens (No. 1 to No. 4) differ in cut size of the fabric prepreg layers and number of circumferential layers. The cylindrical CFRP specimens were consolidated and cured in an autoclave comprising a first dwell phase and a second one at 120 °C for 120 minutes. The temperature program followed the materials supplier's recommendations. A pressure of 0.5 MPa and a vacuum of 0.005 MPa were applied throughout the cycle. The complex bellows geometry was draped in individual layers by segmentation of the fabric prepreg in circumferential direction (6 x 60° segments). The fabric prepreg layers were arranged in x-direction using offset butt joints. One segment covered the complete length of the bellows coupling, whereby the fiber orientation is ± 45° to the x-axis. For the manufacturing of prototypes of the CFRP bellows coupling, a reusable and detachable core concept was realized. Close diameter tolerances within the interfaces could be achieved by using cylindrical metal elements. During a first phase several core segments of ABS (acrylonitrile butadiene styrene) were applied, which were manufactured with the fused deposition modelling procedure. In order to protect the ABS structures from possible damages during the autoclave process, the consolidation and the curing were carried out in an annealing furnace with vacuum bag assembly. Three prototypes of the CFRP bellows coupling (prototype No. EK-1, EK-2, EK-3) were produced using this method concerning the materials from manufacturing sequence I (seq. I). Table 2 declares the assignment as well as the design and manufacturing parameters of the prototypes of the CFRP bellows coupling.

***Table 2:*** *CFRP-specific design and manufacturing parameters of the bellows couplings*

| | Fabric prepreg | | Unidirectional prepreg | |
|---|---|---|---|---|
| Prototype No. | Laminate thickness [mm] | Cover per layer [°] | Laminate thickness [mm] | Cover per layer [°] |
| EK-1, EK-2, EK-3 (seq. I) | 2.1 | 60 | 4.8 | 360 |
| MzK-1 (seq. II) | 2.1 | 60 | 4.8 | 360 |
| MzK-L-1 (seq. II) | 1.3[1] | 60 | 5.7 | 360 |

[1]refered to the basis laminate; additional local reinforcement in the bellows area using fabric prepreg with a width of 20 mm and a total laminate thickness of 1.0 mm

The laminate thicknesses in table 2 were calculated based on the specified thickness of the single layers from the data sheets. A reusable and detachable core system with complete metal elements was used for prototype No. MzK-1 (seq. II) and for prototype No. MzK-L-1 (seq. II). For this purpose the consolidation and the curing were carried out in an autoclave with vacuum bag assembly.

### 2.3.2 MECHANICAL TESTING

All experiments were conducted at room temperature. The aim of the experiments with the cylindrical CFRP specimens was to prove the functional capability of the shaft-hub-joint and to determine the frictionally engaged transferable maximum torque. The investigation was carried out via torsion tests on a static bracing test bench, whereby the specimens were installed in a horizontal position. A shaft diameter of 40 mm as well as a metallic reducing bushing were attached at one side of the specimen. At the opposite side, a shaft diameter of 60 mm was applied. On both connection sides an identical interior clamping set was used. The test preparation comprised degreasing of the CFRP/metal interfaces as well as tightening the interior clamping sets up to their limit. The torque was measured, whereby a digital displacement transducer was mounted on the CFRP structure. The torque was increased until a slipping through of the detachable connection could be detected. In that context, the first load decrease was regarded as indication where the transmittable torque value of the clamping connection ends.

The aim of the experiments with the prototypes of the CFRP bellows coupling was to prove the torsionally stiff torque transmission and compensation functionalities. The torque-torsion-angle characteristic of one single prototype was determined with the same static bracing test bench used for the cylindrical CFRP specimens. The restoring force was determined at an axial displacement of 0.7 mm, whereby the prototype was installed in vertical position in a compression device. Furthermore, the restoring force was determined at an angular misalignment of 1.0°, whereby the prototype was installed in horizontal position in a deflection device. The CFRP bellows coupling was fixed on one side via an internal clamping set. The shaft coupling was loaded with a vertical pin on the opposite interface. The angular misalignment of 1.0° around the y-axis of the shaft coupling corresponds to a free end displacement along the z-axis of 1.33 mm.

### 2.3.3 CHARACTERIZATION OF THE GEOMETRIC STRUCTURE

The aim was to characterize the realized geometric structure of the prototypes of the CFRP bellows coupling. The characterization was based on the determination of the wall thicknesses and the recording of the contour accuracy using a stereomicroscope. For this procedure two segments were separated from the prototypes of the CFRP bellows coupling (No. EK-2 (seq. I) and No. MzK-1 (seq. II)), respectively. The segments extend over the entire length of the structure (longitudinal cuts) and have a center angle of about 23°. Afterwards, the cross-sectional surfaces were ground and polished in several steps with grinding wheels. The wall thicknesses were determined at defined measuring points using a digital caliper gauge. Five individual measurements were carried out at each measuring point to ensure a statistically relevant, quantitative evaluation. Regarding the longitudinal cuts nine measuring points per section plane were defined on one segment of a prototype. Subsequently, the cross-sectional surfaces were observed with an optical stereomicroscope and images were taken with a high-resolution digital camera. Panoramic views were taken for better display, which were automatically composed of several single images.

## 3 RESULTS AND DISCUSSION

### 3.1 MECHANICAL TESTING

The results from the determination of the static slipping torque and the associated torsion angle with respect to the different configurations of the cylindrical CFRP specimens are presented in figures 3 and 4. It can be determined that the respective static slipping torque of all specimens from sequence I (seq. I) is higher than the respective static slipping torque of all specimens from sequence II (seq. II). The specimen No. 4-3 was damaged during assembly of the internal clamping sets at the interfaces, so that a reduced static slipping torque in conjunction with a low torsion angle was achieved. Figure 5 shows the mean value of the static slipping torque and the mean value of the torsion angle of the three cylindrical CFRP specimens per configuration (No. 1 to No. 4) as well as the corresponding mean error. The assumption that the increase in the number of circumferential layers enhances the mean value of the static slipping torque of the specimen configurations (No. 1, No. 3) to a higher mean value than the specimen configurations (No. 2, No. 4) was confirmed. For the specimens with a divided cover (2 x 180°) per fabric prepreg layer, doubling the number of the circumferential layers (No. 3) leads to an increase in the mean value of the static slipping torque by about 50 % compared to configuration No. 4. In contrast, regarding the specimens with a single cover (360°) per fabric prepreg layer, doubling the number of the circumferential layers (No. 1) leads to an increase in the mean value of the static slipping torque by about 15 % compared to configuration No. 2. For the specimens with a thickness of 2.4 mm, the divided cover (2 x 180°) per fabric prepreg layer (No. 4) leads to a decrease in the mean value of the static slipping torque of about 19 % compared to configuration No. 2 (360°). In contrast, regarding the specimens with doubling the number of the circumferential layers, the divided cover (2 x 180°) per fabric prepreg layer (No. 3) leads to a slight increase in the mean value of the static slipping torque by about 10 % compared to configuration No. 1 (360°).

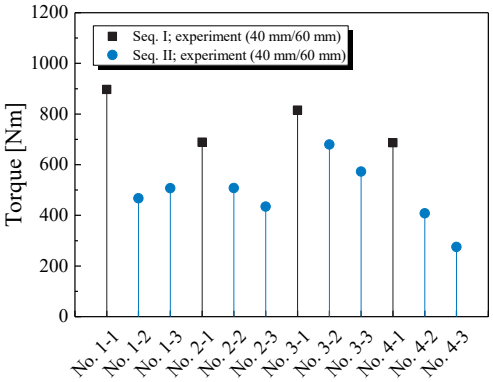


***Fig. 3*** *Static slipping torque of the different cylindrical CFRP specimens*

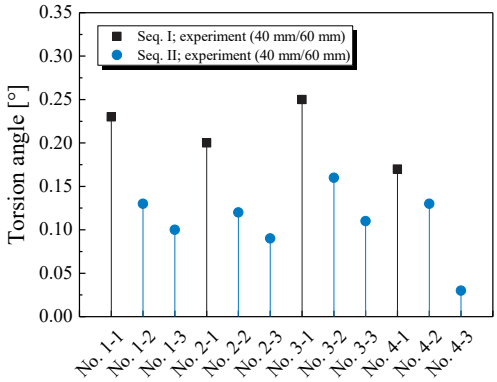


***Fig. 4*** *Torsion angle from the determination of the static slipping torque of the different cylindrical CFRP specimens*

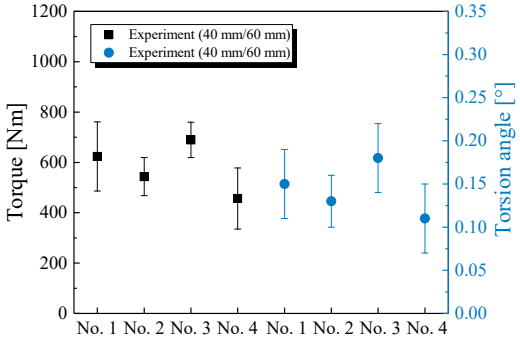


***Fig. 5*** *Mean value of the static slipping torque and the mean value of the torsion angle of three specimens per configuration (No. 1 to No. 4) as well as the corresponding mean error*

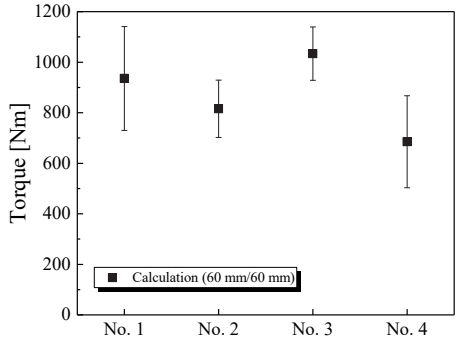


***Fig. 6*** *Calculation of the transferable theoretical torque for the shaft configuration 60 mm/60 mm: mean value of the static slipping torque of three specimens per configuration (No. 1 to No. 4) as well as the corresponding mean error*

The influence of the degree of cover (2 x 180° versus 360°) per fabric prepreg layer with the same number of circumferential layers could not be entirely clarified with the cylindrical CFRP specimens. However, it is assumed that the torque transmission decrease by a further reduction in the degree of cover per fabric prepreg layer. It should be noted that the shaft configuration of 40 mm/60 mm represented a higher load case for the shaft-hub-joint than the shaft configuration 60 mm/60 mm (design configuration). However, for the shaft configuration of 60 mm/60 mm, the transferable theoretical torque was calculated with the help of measured static slipping torque resulting from the shaft configuration of 40 mm/60 mm. The results with regard to the specimen configurations (No. 1 to No. 4) are shown in figure 6. All cylindrical CFRP specimens significantly fulfill the torque transmission of 400 Nm. For the realization of the prototypes the thickness of the circumferential layers was set at 4.8 mm, because the degree of cover per fabric prepreg layer is specified to 6. Figure 7 shows the determined torque-torsion-angle characteristic of prototype No. EK-2 with respect to the shaft configuration of 60 mm/60 mm. It can be seen that there is a linear correlation for the torque with regard to positive and negative direction of rotation. This characteristic is also evident for the other prototypes. For a nominal torque of 400 Nm the resulting torsion angle is 0.36° (prototype No. EK-2). For all prototypes of the CFRP bellows coupling (see table 2) the resulting torsion angle at nominal torque of ± 400 Nm is shown in figure 8. It can be revealed that all prototypes of the CFRP bellows coupling achieve the specified torque transmission of ± 400 Nm with the resulting maximum torsion angle of less than or equal to ± 0.45° (torsionally stiff torque transmission).

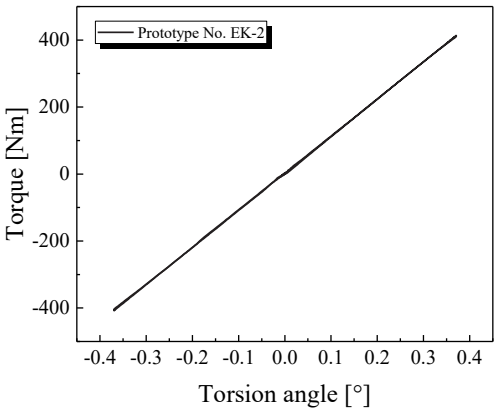


***Fig. 7*** *Torque-torsion-angle characteristic of prototype No. EK-2*

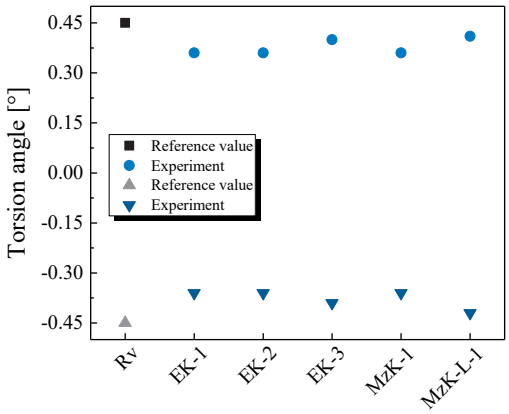


***Fig. 8*** *Torsion angle at nominal torque of ± 400 Nm of the prototypes*

In figure 9 the resulting restoring force for the axial displacement of 0.7 mm is displayed for all prototypes of the CFRP bellows coupling. The measurements were repeated once for each prototype whereby the second measurement marked with an asterisk (*) after the component designation. The restoring force shall be less than or equal to 350 N (reference value) for a maximum axial displacement of 0.7 mm. The restoring force for all prototypes of the CFRP bellows coupling (except No. MzK-L-1) is approximately 2.2 to 2.7 times higher than the reference value. It can be revealed that the modified layer structure of prototype No. MzK-L-1 significantly reduces the restoring force. Thereby the restoring force is only 1.7 times higher than the reference value.

In figure 10 the resulting restoring force for the angular misalignment of 1.0° is shown for all prototypes of the CFRP bellows coupling. The measurements were repeated once for each prototype whereby the second measurement marked with an asterisk (*) after the component designation. The restoring force shall be less than or equal to 197 N (reference value) for a maximum angular misalignment of 1.0°. The restoring force for all prototypes of the CFRP bellows coupling (except No. MzK-L-1) is approximately 1.3 times higher than the reference value. Thereby for prototype No. MzK-L-1 the restoring force is even 0.9 times lower than the reference value. This positive effect can be addressed to the modified layer structure of prototype No. MzK-L-1. On the one hand, the reference values are fulfilled in the case of torsion angle and angular misalignment. On the other hand, exceeding the reference value in the case of axial displacement can be reduced. In this context it should be mentioned that the presented design concept of the shaft coupling had primarily to serve the torsionally stiff torque transmission. Therefore a full adherence to the compensation capabilities had to be compromised.

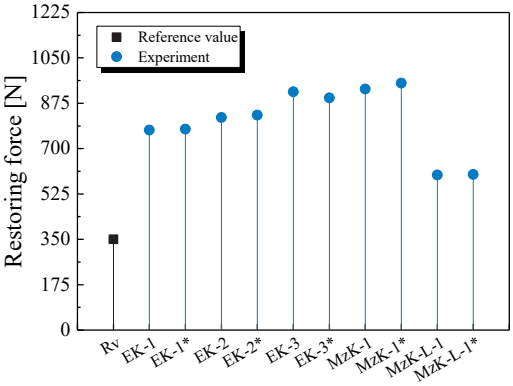


***Fig. 9*** *Restoring force for the axial displacement of 0.7 mm with repeat measurement (*) for the prototypes of the CFRP bellows coupling*

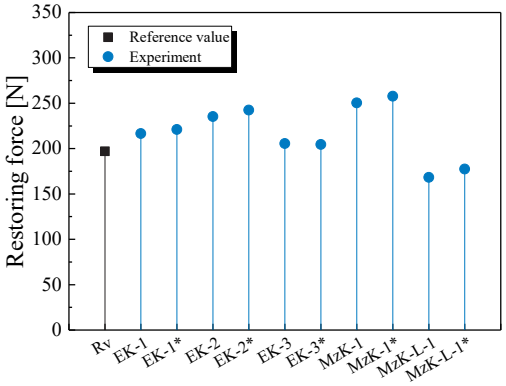


***Fig. 10*** *Restoring force for the angular misalignment of 1.0° with repeat measurement (*) for the prototypes of the CFRP bellows coupling*

### 3.2 CHARATERIZATION OF THE GEOMETRIC STRUCTURE

In the following, a representative microscopic panorama view of a cross-sectional surface is presented regarding prototype No. EK-2 and prototype No. MzK-1 (see figures 11 and 12). The axial position was identical for both views.

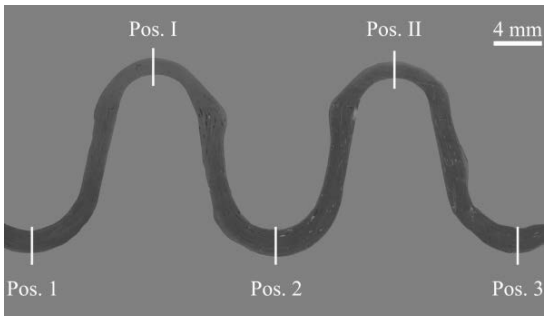


***Fig. 11*** *Microscopic panoramic view of a cross-sectional surface regarding prototype No. EK-2*

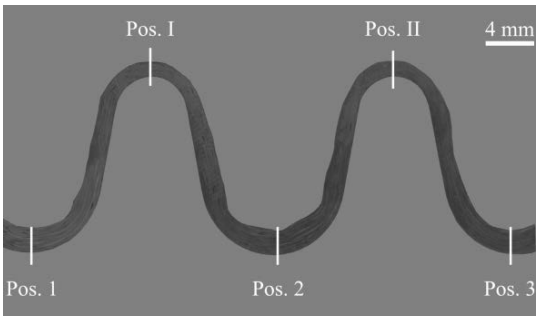


***Fig. 12*** *Microscopic panoramic view of a cross-sectional surface regarding prototype No. MzK-1*

The figures show the longitudinal cuts of two CFRP bellows elements of the compensating structure, respectively. In addition, it can be seen that the fabric prepreg layers on the inside of the bellows elements precisely follow the contour of the core system (open mold). The deviations in thickness and homogeneity of prototype No. MzK-1 are smaller than for prototype No. EK-2. This can be explained by the consolidation and curing in the autoclave with vacuum bag assembly. The fabric prepreg layers are more compacted at the convex features (Pos. I and Pos. II) than at the concave features (Pos. 1, Pos. 2, Pos. 3). This means that the concave features reveal a higher wall thickness than the concave features (see table 3). Moreover, the individual measuring points for determining the wall thicknesses are highlighted in figures 11 and 12.

***Table 3:*** *Wall thicknesses of a cross-sectional surface regarding prototype No. EK-2 and prototype No. MzK-1*

| | Laminate thickness of the fabric prepreg [mm] | | | | |
|---|---|---|---|---|---|
| | Concave features | | | Convex features | |
| Specimen of prototype No. | Pos. 1 | Pos. 2 | Pos. 3 | Pos. I | Pos. II |
| EK-2 (seq. I) | 3.00 | 3.52 | 3.50 | 2.39 | 2.39 |
| | ± 0.05 | ± 0.07 | ± 0.07 | ± 0.01 | ± 0.02 |
| MzK-1 (seq. II) | 3.27 | 3.24 | 3.44 | 2.09 | 2.17 |
| | ± 0.02 | ± 0.02 | ± 0.03 | ± 0.01 | ± 0.01 |

In contrast to the existing core system, the geometry of the compensating structure can be more precisely realized with the metallic core system due to an adapted process technology.

## 4 CONCLUSIONS

The present paper describes the experimental investigation of the design concept for a non-engaging bellows coupling made of prepreg-based carbon fiber reinforced polymers. The design concept of the CFRP bellows coupling combines the connection and compensation functionality in one single structure. Hereby the cylindrical CFRP specimens were used to demonstrate that the CFRP/metal interface realized by a frictionally engaged and detachable shaft-hub-joint meets the requirements. For this purpose, the slipping torque at each specimen was determined via a static bracing test bench. The results revealed that an increase in the number of circumferential layers enhances the static slipping torque.

In addition, it could be experimentally shown that the prototypes of the CFRP bellows coupling realized with the hand lay-up prepreg technology in general fulfill the connection and compensation functionality. Furthermore, a prototype of the CFRP bellows coupling with modified layer structure revealed that it is possible to reduce the respective restoring force from axial displacement and angular misalignment while maintaining the torsionally stiff torque transmission. It was evident that the geometry of the compensation structure can be more precisely reproduced with the aid of a complete metallic core system than with an existing core system due to an adapted process technology.

## 5 ACKNOWLEDGEMENT

The authors would like to thank the Bavarian Research Foundation (Bayerische Forschungsstiftung) for funding this research within the research cluster FORCiM$^3$A.

## REFERENCES

[1] Flemming M., Ziegmann G., Roth S.: *Faserverbundbauweisen – Halbzeuge und Bauweisen.* Springer-Verlag, Berlin, 1996.
[2] Schürmann H.: *Konstruieren mit Faser-Kunststoff-Verbunden.* Springer-Verlag, Berlin, 2007.
[3] Drechsler K., Bockelmann P.: *Produktentwicklung mit neuen Materialien am Beispiel der Carbon Composites.* In: Lindemann U. (Hrsg.): Handbuch Produktentwicklung. 877-904, Hanser Verlag, München, 2016.
[4] Drechsler K., Heine M., Mitschang P., Baur W., Gruber U., Fischer L., Öttinger O., Heidenreich B., Lützenburger N., Voggenreiter H.: *Carbon Fiber Reinforced Composites.* In: Ullmann's Encyclopedia of Industrial Chemistry. 1-120, Wiley-VCH Verlag, Weinheim, 2009.
[5] Henning F., Drechsler K., Chatzigeorgiou, L.: *Faserverstärkte Kunststoffe*. In: Henning F., Moeller E. (Hrsg.): Handbuch Leichtbau. 337-392, Hanser Verlag, München, 2011.
[6] Lengsfeld H., Wolff-Fabris F., Krämer J., Lacalle J., Altstädt V.: *Composite Technology: Prepregs and Monolithic Part Fabrication Technologies.* Hanser Verlag, München, 2016.
[7] Bank L. C.: *Composites for Construction: Structural Design with FRP Materials.* John Wiley & Sons, Inc., Hoboken, 2006.
[8] Fink A., Camanho P. P., Andrés J. M., Pfeiffer E., Obst A.: *Hybrid CFRP/titanium bolted joints: performance assessment and application to a spacecraft payload adaptor.* Composites Science and Technology 70, 305-317, 2010.
[9] Lauter C., Frantz M., Kohler J.-P., Troester T.: *Crash tests of hybrid structures consisting of sheet metal and local CFRP reinforcements.* 15th European Conference on Composite Materials, Venice, 2012.
[10] Kashaev N., Ventzke V., Riekehr S., Dorn F., Horstmann M.: *Assessment of alternative joining techniques for Ti-6Al-4V/CFRP hybrid joints regarding tensile and fatigue strength.* Materials and Design 81, 73-81, 2015.
[11] Hufenbach W., Lenz F., Renner O.: *Welle-Nabe-Verbindungen für Leichtbauantriebswellen in Faserverbund-Metall-Mischbauweise*. In: VDI-Berichte Nr. 2176. 141-153, 2012.
[12] Hufenbach W., Lenz F., Birke M., Spitzer S., Münter S.: *Design, Dimensioning and automated Manufacturing of profiled Composite Driveshafts.* Proceedings of ICCM19, Montreal, Canada, 2013.
[13] Oblinger C., Lang H., Drechsler K.: *CFK/Metall-Mischbauweisen im Maschinen- und Anlagenbau – wichtiger denn je. Nachhaltigkeit und Energieeffizienz durch innovative Leichtbaustrukturen.* In: Umwelt-Technologie und Energie in Bayern. 26-28, 2015.
[14] Tichelmann P.: *Auslegung und Optimierung Versatz-ausgleichender Bauelemente und ihre Integration in eine Antriebswelle.* Diss.-Darmstadt, Shaker Verlag, Aachen, 2009.
[15] Katz J.: *Gestaltung und Optimierung einer nichtschaltbaren Lamellenkupplung aus Glasfaser-Kunststoff-Verbund.* Diss.-Darmstadt, Shaker Verlag, Aachen, 2015.
[16] Niemann G., Neumann B., Winter H.: *Maschinenelemente Band 3.* Springer-Verlag, Berlin, 1986.
[17] Muhs D., Wittel H., Jannasch D., Voßiek J.: *Roloff/Matek Maschinenelemente.* Springer Vieweg, Wiesbaden, 2015.
[18] Kollmann K.: *Grenzen der Drehmomenten- und Leistungsübertragung bei Riementrieben, Kettentrieben und Kupplungen.* In: Riementriebe, Kettentriebe, Kupplungen, Schriftenreihe Antriebstechnik. 1-17, Vieweg+Teubner Verlag, Wiesbaden, 1954.
[19] Pampel W.: *Kupplungen Band I.* VEB Verlag Technik, Berlin, 1958.
[20] DIN 740-1: *Antriebstechnik, Nachgiebige Wellenkupplungen, Anforderungen, Technische Lieferbedingungen.* Beuth Verlag, Berlin, August 1986.
[21] Richtlinie VDI 2240: *Wellenkupplungen – Systematische Einteilung nach ihren Eigenschaften.* VDI-Verlag, Düsseldorf, Juni 1971.
[22] Oblinger C., Jelinek M., Lang H., Baeten A., Drechsler K., Reinhart G.: *Development, manufacturing and testing of a CFRP bellows coupling for powertrain application.* Proceedings of the 2nd International Conference Euro Hybrid Materials and Structures 2016, Kaiserslautern, Germany, 97-104, 2016.
[23] Oblinger C., Baeten A., Drechsler K.: *Numerical Analysis on the Structural Behavior of a Non-Engaging CFRP Bellows Coupling for Propulsion Technology.* Key Engineering Materials, Vol. 742, 723-731, 2017.

CHAPTER 7

# SPECIAL SESSION: MULTI-METAL DESIGN

# INFLUENCE OF PROCESS PARAMETERS ON THE FATIGUE BEHAVIOR OF STEEL/ALUMINUM HYBRID JOINTS PRODUCED BY MAGNETIC PULSE WELDING

**N. Gelinski[1*], D. Huelsbusch[1], E. Schumacher[2], S. Böhm[2], F. Walther[1]**

[1]TU Dortmund University, Department of Materials Test Engineering (WPT), Dortmund, Germany
[2]University of Kassel, Department for Cutting and Joining Manufacturing Processes (tff), Kassel, Germany

**ABSTRACT:** The aim of this study is to optimize the process window for magnetic pulse welding in terms of fatigue properties of hybrid joints made of S235JR and EN AW-1050 (Al99.5). Therefore, the focus lies on a resource-efficient determination of the influence of process parameters, i.e. the discharge energy (9-15 kJ) and the acceleration distance (1-2 mm), on the fatigue behavior and damage mechanisms. The structure-property-relations were evaluated by means of combined instrumented load increase and constant amplitude tests. The experimental procedure was developed by application of different physical measuring technologies, i.e. mechanical, electrical and thermal sensor technology. The results show that the plastic strain amplitude and change in AC voltage are well suited for reliable detection of damage initiation and propagation and allow an estimation of the fatigue limit. It can be concluded that the fatigue properties are mainly determined by imperfections of the welding seam which is directly influenced by the process parameters. For improved process parameters, the fatigue strength is determined by failure of the weaker aluminum.

**KEYWORDS:** Magnetic pulse welding, Hybrid joints of steel/aluminum, Fatigue behavior, Damage mechanisms, Instrumented fatigue testing, Physical measuring technologies

## 1 INTRODUCTION

Multi-metal-design is increasingly gaining importance with regard to lightweight design for enhancement of dynamic range, resource optimization and emission reduction in many fields of traffic engineering. Conventional welding processes, as for example resistance spot welding or friction stir welding are not well suited for multi-metal-design in metallurgical terms as well as from a technological and economic view. Instead, magnetic pulse welding offers the opportunity to produce hybrid joints of steel and aluminum with a low amount of thermal distortion and without temperature-induced microstructural changes [1, 2]. Low cycle times combine these benefits with a high productivity. However, the lack of knowledge about the fatigue behavior and damage mechanisms inhibit a wide-scale industrial use of magnetic pulse welding.
Traditionally information about the fatigue behavior of structural materials and joints is derived from Woehler curves which are generated in highly time-consuming cyclic tests. Advanced short-time fatigue testing procedures allow a resource-efficient characterization of the fatigue behavior and have been validated for a variety of materials, i.e. metallic and polymer materials and hybrid joints [3, 4]. Due to advanced measurement technologies, it is possible to detect early signs of evolving damage by microstructural changes which eventually lead to fatigue failure [5]. This allows a detailed characterization of the process-structure-property-relations through a process- and product-optimized measurement for investigation of the fatigue behavior beyond a mere lifetime-oriented approach.

# 2 EXPERIMENTAL PROCEDURE

## 2.1 SPECIMEN PRODUCTION BY MAGNETIC PULSE WELDING

Hybrid joints of steel (S235JR) and aluminum (Al99.5) were produced by a magnetic pulse welding system (PSTproducts Blue Wave PS48-18). The utilized flat coil (B80/10) had a maximum current of 500 kA and the discharge frequency was around 19.6 kHz. For investigations of different process parameters, the discharge energy E was altered between 9 and 15 kJ resulting in currents I from 267 to 349 kA. Furthermore, different acceleration distances d from 1 to 2 mm between the target (steel) and flyer (aluminum) were evaluated. The dimensions of the hybrid joints are displayed in Fig. 1. The overlap length was chosen to be 30 mm. In order to reduce the bending moment resulting from the asymmetrical structure and different moduli of elasticity of both materials alignment sheets made from glass-fiber reinforced plastic (GFRP) were adhesively bonded to the specimen based on DIN EN ISO 14324: 2003-12 [4, 6].

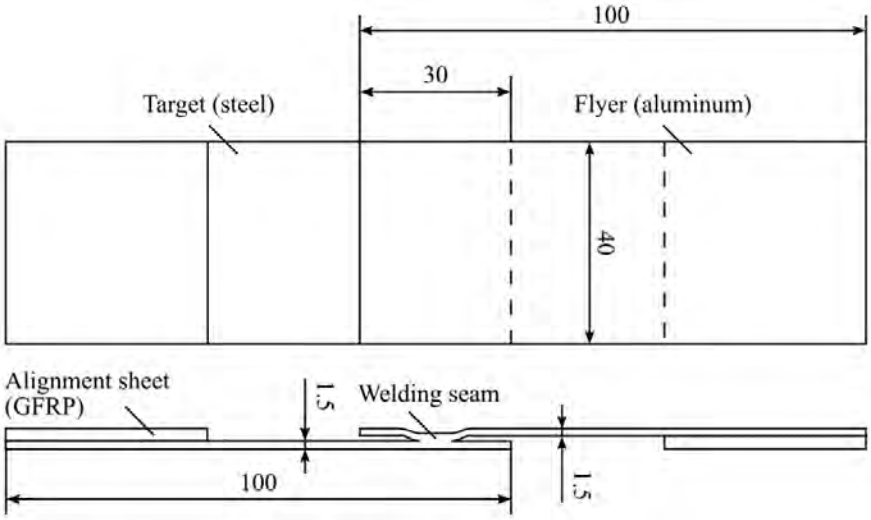


***Fig. 1*** *Dimensions of investigated steel/aluminum hybrid joints produced by magnetic pulse welding*

## 2.2 INSTRUMENTED FATIGUE TESTING

Instrumented continuous load increase tests (LIT) combined with constant amplitude tests (CAT) were performed at a servohydraulic testing system (Schenck PC63M, Fmax = 63 kN, Instron controller) using a sinusoidal time-load-function. The cyclic tests were carried out with a frequency of 10 Hz at ambient temperature under tension-tension loading at a load ratio of 0.1. For the LIT the maximum load $F_{max}$, starting at $F_{max,start}$ = 0.5 kN, was increased continuously by $dF_{max}/dN = 0.4\ kN/10^4$ until failure. A schematic representation of the testing procedure is illustrated in Fig. 2. Physical measuring technologies enable the detection of damage initiation caused by microstructural changes which is used to estimate the fatigue limit $F_{max,e(LIT)}$.

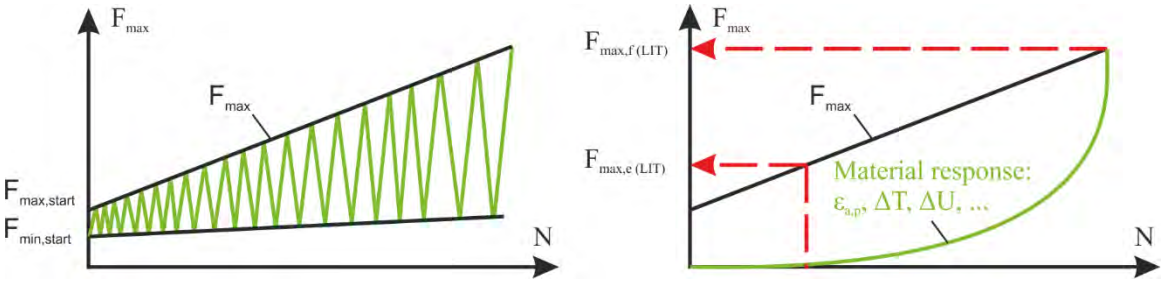


***Fig. 2*** *Experimental procedure of continuous load increase test (left) and corresponding material response for determination of characteristic values (right)*

The experimental setup in Fig.2 includes an extensometer (Instron, $l_0$ = 50 mm) for local strain measurements in the area of the welding seam. Additionally, changes in AC voltage $\Delta U_{AC}$ caused by changes of the specimen's specific resistance were detected by four wire measurement. The current feed was realized by electrical contacts on the clamping jaws while the resulting voltage was tapped by contacts around the overlap. Local temperature changes were measured by three thermocouples (type K) positioned at the overlap ($\Delta T_1$), the

aluminum part ($\Delta T_2$) and the steel part ($\Delta T_3$). In order to take changes in ambient temperature into account and constrain the measurement to heat generation produced by microstructural changes at the welding seam, $\Delta T$ was calculated by equation 1.

$$\Delta T = \Delta T_1 - (\Delta T_2 + \Delta T_3)/2 \qquad (1)$$

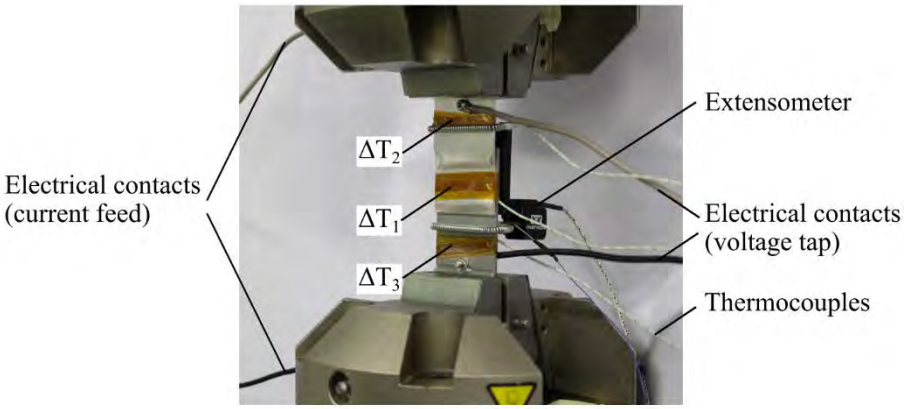


***Fig. 3*** *Experimental setup for instrumented fatigue tests*

### 2.3 FRACTOGRAPHIC INVESTIGATIONS

For determination of the damage mechanisms, fractographic investigations were carried out. For this purpose, the fracture surfaces were analyzed by light microscopy (Zeiss Axio Imager M1m).

## 3 RESULTS

### 3.1 LOAD INCREASE TESTS

Representative results of the LIT in Fig. 4 show the evolution of the plastic strain amplitude $\varepsilon_{a,p,}$ which is determined from stress-strain hysteresis loops, as well as the change in AC voltage $\Delta U_{AC}$ and temperature $\Delta T$ as a function of the load cycles. The plastic strain amplitude and the change in AC voltage show a linear increase about $2.5 \cdot 10^4$ cycles respectively 1.5 kN, followed by an exponential course which indicates damage initiation and thus can be identified as the estimated fatigue limit. Based on the change in temperature no material reaction could be detected.

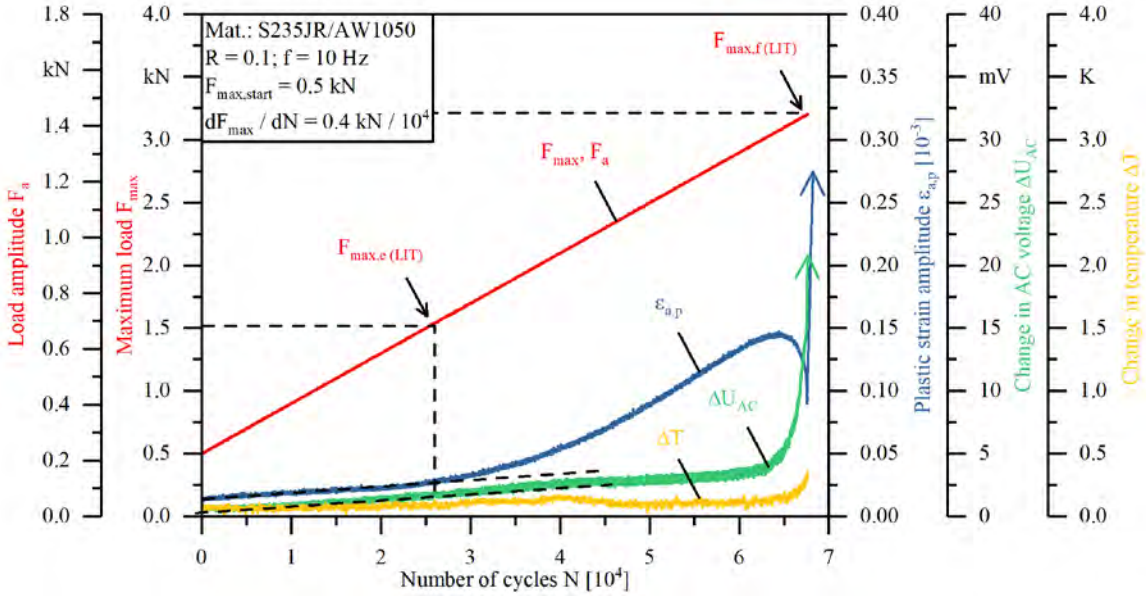


***Fig. 4*** *Results of an instrumented load increase test and estimation of the fatigue limit*

The estimated fatigue limit and the maximum load at failure for specimens produced by varying process parameters are displayed in Fig. 5. It is apparent that a noticeable correlation between the welding current and estimated fatigue limit as well as the maximum strength under cyclic loading exists. A higher welding current leads to a higher maximum load at failure which can be attributed to the formation of the welding seam during the production process as can be seen exemplary in Fig. 6. The fracture surface of the specimen produced with 267 kA shows an imperfectly and asymmetrical bonded welding seam while the specimen produced with 322 kA can be characterized by a significantly superior form. Shear failure can be identified as the dominating failure mechanism in the cyclic tests. At a welding current of 349 kA optimal process parameters with regard to the formation of a perfect welding seam are obtained. This means that the strength of the welding seam is higher than the strength of the weaker material and failure of the aluminum becomes critical. In the case of a perfect welding seam, the crack which leads to failure is initiated at the notched area of the flyer which is caused during production because of the magnetic pressure loading within the flyer acceleration [2]. A significant and consistent influence of the acceleration distance on the strength like reported by Kwee at al. under quasistatic load cannot be concluded from the obtained results under cyclic load [7].

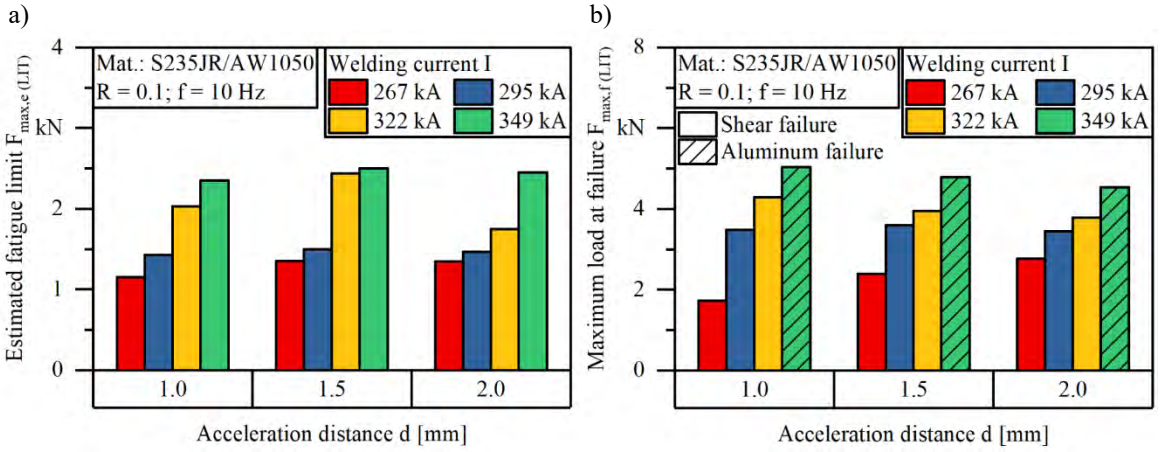


***Fig. 5*** *a) Estimated fatigue limit and b) maximum force at failure in load increase tests*

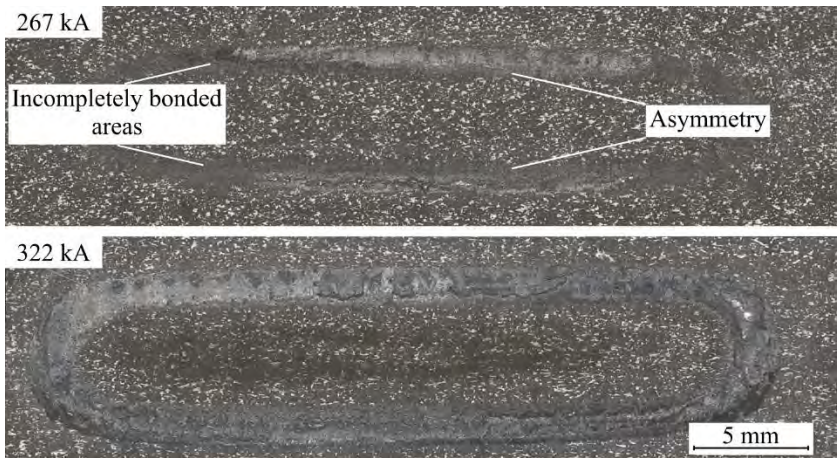


***Fig. 6*** *Fracture surface after failure in load increase tests*

### 3.2 CONSTANT AMPLITUDE TESTS

The results of CAT were conducted on basis of the LIT and are displayed in Fig. 7 for an acceleration distance d = 1.5 mm. It can be concluded that a welding seam area which, as explained earlier, is correlated to a higher welding current leads to a higher bearable load in low-cycle fatigue regime (LCF, $N < 10^5$). For cyclic load reaching high cycle fatigue (HCF, $N > 10^5$) the fatigue life was not only determined by failure of the welding seam but also by failure of the weaker aluminum. For relatively small loads the estimated fatigue limit was in good accordance with the results obtained in CAT reaching $2.0 \cdot 10^6$ cycles.

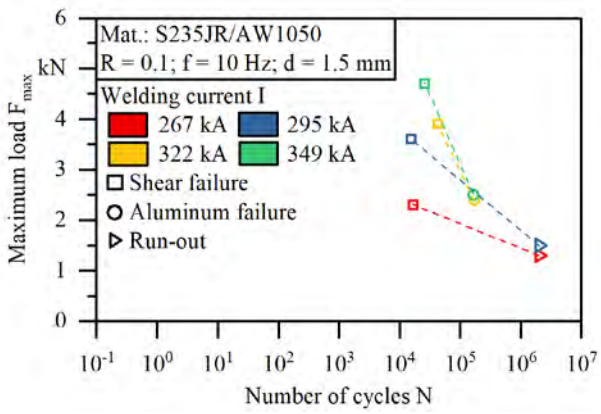


***Fig. 7*** *Results of constant amplitude tests for an acceleration distance of 1.5 mm*

## 4 CONCLUSIONS AND OUTLOOK

The fatigue behavior of hybrid joints of steel and aluminum produced by magnetic pulse welding was evaluated by combined load increase and constant amplitude testing procedure with regard to a resource efficient characterization of the process-structure-property-relations. Instrumented fatigue testing revealed that the plastic strain amplitude and change in AC voltage are well suited for a reliable detection of material damage. Constant amplitude tests showed that, additionally to shear failure at the welding seam in low cycle fatigue, failure of the weaker aluminum becomes critical in high cycle fatigue. This leads to the conclusion that a further optimization of the process parameters to improve the bonding between both materials will not be expedient with regard to fatigue behavior. Instead, the use of high-strength alloys offers the potential for an improvement of the cyclic properties. This will be investigated in future work.

## 5 ACKNOWLEDGEMENT

This work was funded by the Federal Ministry for Economic Affairs and Energy (BMWi) on the basis of a decision by the German Parliament. The authors thank the BMWi, the research association “Welding and Related Procedures” of the DVS and the AiF e.V. for their financial support. The results of this publication were obtained within the scope of the IGF funded research project No. 19396 N "Investigations on the influences of surface topography and corrosion on the fatigue strength of steel/aluminum hybrid sheets produced by magnetic pulse welding – SchwingStAl-K.O.”.

## REFERENCES

[1] Aizawa, T.: *Methods for electromagnetic pressure seam welding of Al/Fe sheets*. Welding International, 18(11):868-872, 2004.

[2] Schäfer R., Pasquale P., Elsen A.: *Material hybrid joining of sheet metals by electromagnetic pulse technology*. Key Engineering Materials, 473:61-68, 2011.

[3] Walther F.: *Microstructure-oriented fatigue assessment of construction materials and joints using short-time load increase procedure*. Materials Testing, 56(7-8):519-527, 2014.

[4] Caspari T., Hülsbusch D., Haack M., Solbach A., Emmelmann C., Walther F.: *Technological and economical aspects of novel hybrid joining strategies based on integrated fibre penetrating reinforcing elements.* In: Euro Hybrid Materials and Structures 2016, 81-85, 2016.

[5] Walther F., Eifler D.: *Cyclic deformation behavior of steels and light-metal alloys.* Materials Science and Engineering A, 468:259–266, 2007.

[6] Imanaka M., Haraga K., Nishikawa T.: *Fatigue Strength of Adhesive/Rivet Combined Lap Joints*. The Journal of Adhesion, 49(3-4):197-209, 1995.

[7] Kwee I., Psyk V., Faes K.: *Effect of the Welding Parameters on the Structural and Mechanical Properties of Aluminium and Copper Sheet Joints by Electromagnetic Pulse Welding.* World Journal of Engineering and Technology, 4(4): 538-561, 2016

# VARIETY OF METAL PROPERTY AND DESIGN COMBINATIONS BY COLD ROLL CLADDING

**Dr. Lutz Hofmann[1*], Dr. Maria Ostafin[2]**

[1/2]Wickeder Westfalenstahl GmbH

**ABSTRACT:** Intelligently combined clad materials – made of different metal layers – are used in many products used in our daily life: automotive, electro(tech)nics, cooking, household appliances, batteries, coins, consumer goods, machinery and energy appliances.
The technological process of cold roll cladding enables the combination of the outstanding properties of different metals in one multi layer material. Metals such as steel, stainless steel, copper, aluminium, nickel, including their alloys, bonded together in one clad strip can offer unique technical and / or cost-optimized solutions. Compared to other cladding techniques an important advantage of cold rolled materials is the variety and ratios of layer thicknesses. Two to five layers with thickness ratios from 2 to 98% are possible.
Recent developments in the lay-out designs offer a comprehensive modular system for advanced material solutions such as Edgelay, Inlay, Corelay, Side-to-Side.
Best practice examples such as hot spot avoidance in smart devices, performance improvement in cell connectors, transition solutions in steel-Al mixed construction, spring strips with a wide range of functionality of strength, conductivity and formability testify to the potential of such multi-metal designs.

**KEYWORDS:** Cold roll cladding, clad material strips, combined metal properties, cladding designs, clad material applications, clad configurator

## 1 INTRODUCTION

Cladding is an long-established and very traditional technology to join different metals by metallurgical bonding and to combine their properties in multi-metal composites. During the time of industrialization cladding technology has been developed to more and more efficient industrial processes.
Cold roll cladding of strips is one of these technologies; it was introduced by Wickeder Westfalenstahl, a member of the Wickeder Group, about 100 yeares ago.
From this point of time a continuous development of clad metal combinations has taken place, including new clad designs in the recent past.
New clad metal configurations have been always driven by the creation of new product properties and functions based on the multi-metal principle.
As typical customized products, clad materials nowadays offer versatile opportunities for the design of state-of-the-art product developments in various industries.

## 2 CLADDING PROCESSES

### 2.1 COLD ROLL CLADDING

The process of cold roll cladding of metal strip can be defined as

- a cold rolling process
- at which two or more metallic strip materials are brought together in front of the roll-bite of a rolling mill,
- bonded together continuously by high rolling pressure and gauge reduction to a material composite,
- in such a way, that the achieved adhesion between the metal layers ensures at least sufficient further processabilty (see fig. 1).

To achieve the required bond strength between the layers, suitable surface cleaning and preparing processes of the input materials are necessary.

* Dr. Lutz Hofmann: 58739 Wickede (Ruhr), Hauptstr. 6, Phone: +49 2377 917 362, Fax: +49 2377 917 733, e-mail: lutz.hofmann@wickeder.de

After the cladding process the bonded coils typically will be heat treated to maintain or improve the bond strength to a permanent non-separable state.

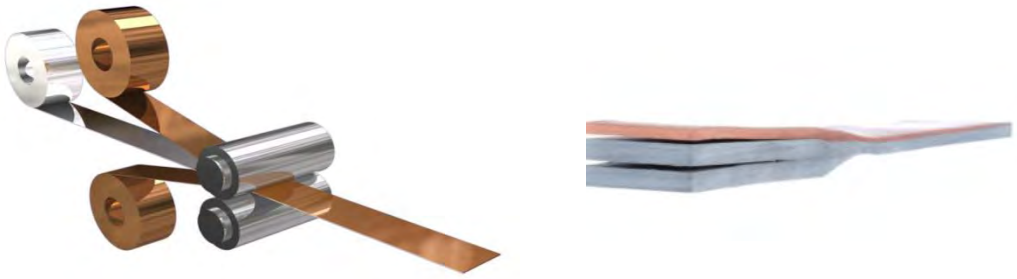

***Fig. 1*** *Principle of cold rolled cladding of different metal strips by high thickness reduction*

### 2.2 OTHER CLADDING TECHNOLOGIES

Alternative traditional industrial cladding technologies for strip or sheet material are hot roll and explosive cladding. Hot roll cladding is characterized by stacking of slabs and hot rolled sheets of different steel grades and hot rolling the package to hot rolled strip gauges. In explosive cladding two or more thick metal sheets are stacked together. An explosive material top layer will be ignited at one end of the sheet stack. The detonation shockwave runs along the length of the sheet , applying high pressure to both sheets and bonds them together.
Induction assisted laser roll cladding is a newer technology using laser beams to heat the material surfaces directly at the entry to the roll bite. Additionally the entry strips can be heated up by induction devices in front of the rolling mill. Both supporting processes enable a reduction in the total gauge reduction during the roll cladding process.
There are further cladding technologies to generate a metallurgical bond such as deposition welding or powder sintering. These are joining processes realized by applying a melt in the liquid state to a carrier material. They are quite different to roll cladding and will not be further considered in this paper.

### 2.3 EVALUATION OF COLD ROLL CLADDING

Based on technological possibilities, flexibility and economic efficiency cold roll cladding has been found to have the broadest usage compared to the alternative cladding technologies described above.
Cold roll cladding allows the combination of metals with different physical and forming properties due to processing at room temperature without any pre-heating. Different material flow behaviour during cladding is often proven to be advantageous. In no way creation of intermetallic phases during cladding is disturbing processability and adhesion of the layers.
By using a larger number of narrower entry strips various geometric arrangements of the clad cross section can be produced.
The biggest disadvantage of cold roll cladding is the requirement for high power load for cold deformation. Based on this there are limitations to join exclusively high strength materials as the necessary reductions to achieve sufficient adhesion between the clad layers may not be achieved.
Otherwise diverse strategies have been developed to overcome these disadvantages, at least in part.

## 3 MATERIAL COMBINATIONS AND CLADDING DESIGNS

Cold roll cladding offers, as already mentioned, a large variety of metal combinations to produce composite strips.
For a more or less systematic overview the most important and commercially used metals and alloys can be divided into 3 categories (see fig. 2)

- Available standard products and metal combinations that have been successfully used (or tested) in industrial applications;
- Combinations producable with no relevant difficulties
- Producable with restrictions based on the exact metal combination. Definitly, there is a potential to shift such combinations to category 1 or 2, should further cladding reseach be required and undertaken

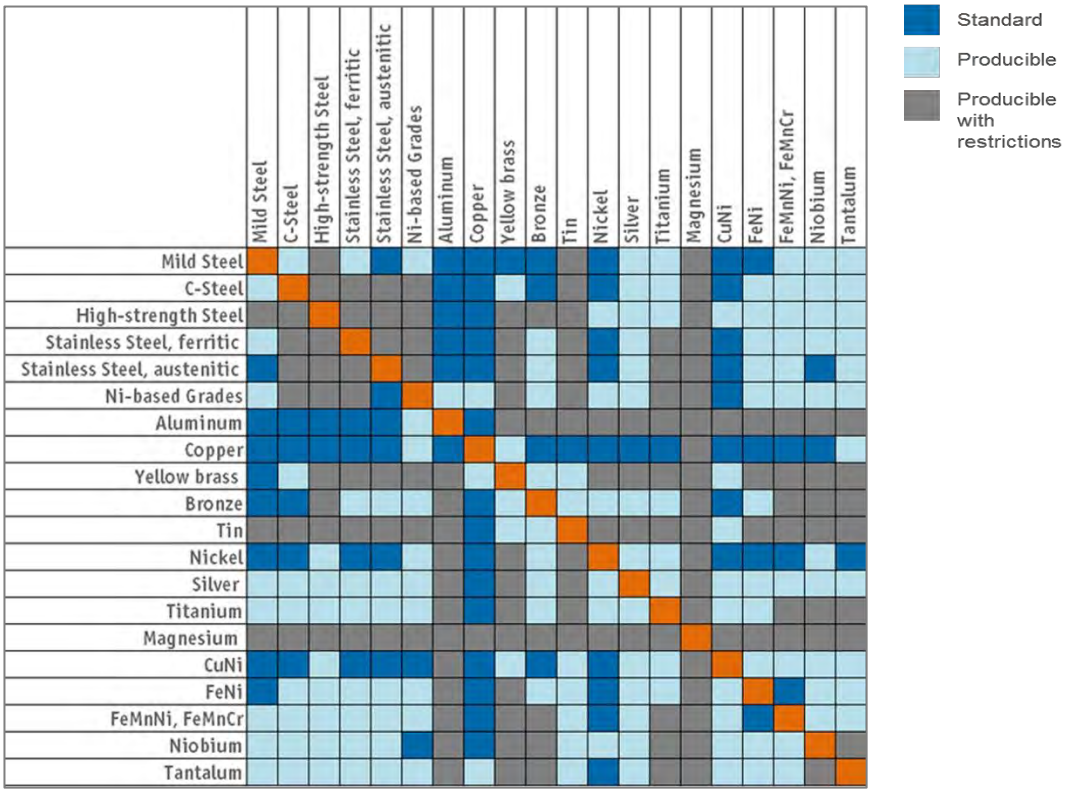


***Fig. 2*** *Producability of metal combinations by cold roll cladding*

The variety of metal combination is enhanced by a number of so-called clad designs, in other words, the ratio and geometrical arrangement of the different metal layers (see fig. 3).
Already the full overlay design offer in combination of number of layers, practicallywise today up to 5 layers with 3 materials, and the technically feasible layer ratios a very flexible design opportunities. Minimum layer ratio is about 2% of the overall composite thickness. This is a function of minimum and maximum input thicknesses based on limitations of the cladding equipment. Compared to other coating systems such as plating or PVD, cladding is (can be seen as) a technology for thicker coating layers.

***Fig. 3*** *Geometrical arrangement of clad designs*

The different, more complex, layer arrangements enlarge the spectrum of applications of clad materials as follows:

- Inlay/Edgelay - Local availability of the inlay materials with a dominant carrier material, i.e. for defined contact requirements.
- Corelay – Modification of the properties of an homogenuous "outside" cross section by a different core material. Latent disadvantages of classic overlay designs due to welding and corrosion issue will be avoided, at least in part.
- S2S-Overlap – The side-to-side arrangement of the materials allows connection of disimilar materials and joining of similar materials at the same time.

# 4 CLAD METAL APPLICATION

Following clad product applications illustrate the property combination of different metals as selected examples:

## 4.1 THERMOSTATIC BIMETALS

Thermostatic bimetals are very traditional and typical clad materials showing impressively how a new application property will be created by combining two extreme different ranges of a physical property - thermal expansion. Heating of the clad composite will lead to a defined bending behaviour, which can be calculated by using CTE´s (coefficient of thermal elongation), Young modulus, part dimension, and temperature change (see fig. 4). Thermostatic bimetals are still widely used today as very robust electrical switches controlled by temperature change.

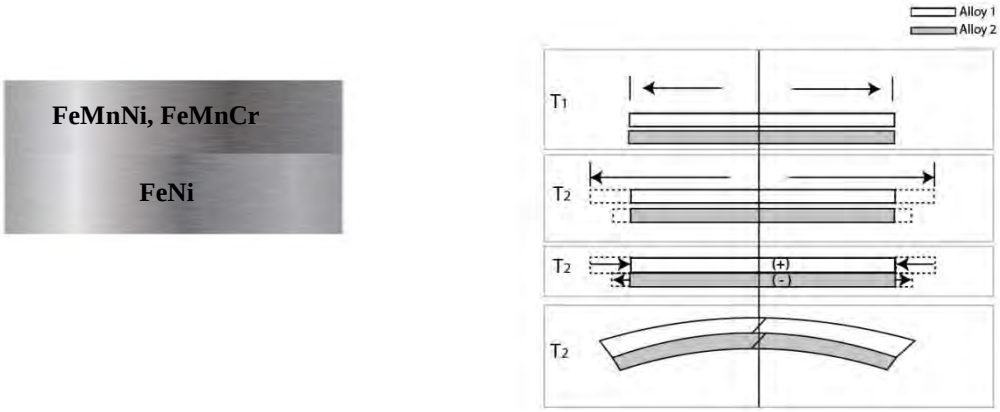


***Fig. 4*** *Layout and functionality of clad thermostatic bimetal*

## 4.2 HEAT SPREADING

Excellent heat spreading property is becoming more and more important, amongst others within sophisticated smart devices to avoid critical hot spots. Using a clad material with a Cu center layer between Stainless Steel cover layers will increase the heat conductivity of a backing plate and dissipate the heat from electrical sources more effectively than pure Stainless Steel (see fig. 5). By varying Stainless Steel and Cu layer ratio the functions of both clad components can be optimized to technical specification.

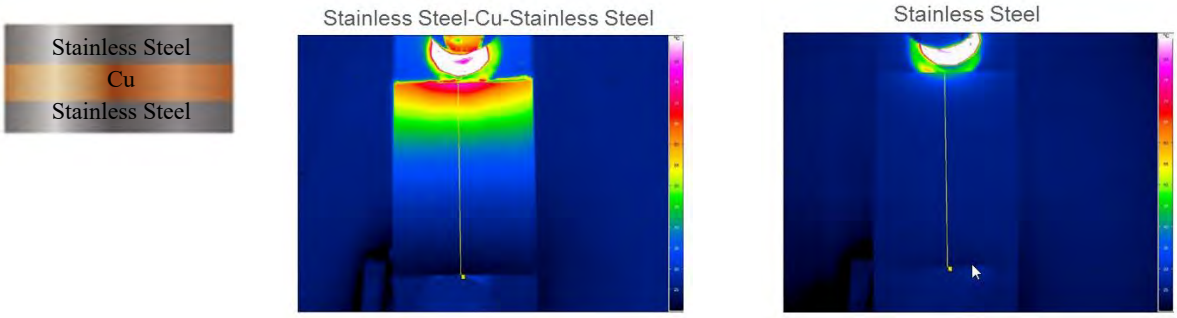


***Fig. 5*** *Layout of Stainless Steel -Cu-Stainless Steel and comparison of head spreading behaviour of Stainless Steel -Cu-Stainless Steel and homogenuous Stainless Steel*

Busbars as power transmission components play an important role in electrical, electronic equipment. Cu with its very high electrical conductivity and excellent contacting properties has been and is the preferred metal for these application. In the recent past Al has had a renaissance in this area because of its light weight potential. Cladding Cu and Al together combines the advantages of both metals to produce a compound material with appropriate reduced weight, high electrical conductivity and good contacting behaviour. Fig. 6 demonstates this property superposition. Depending on the detailed requirements, different cross section designs can be chosen.

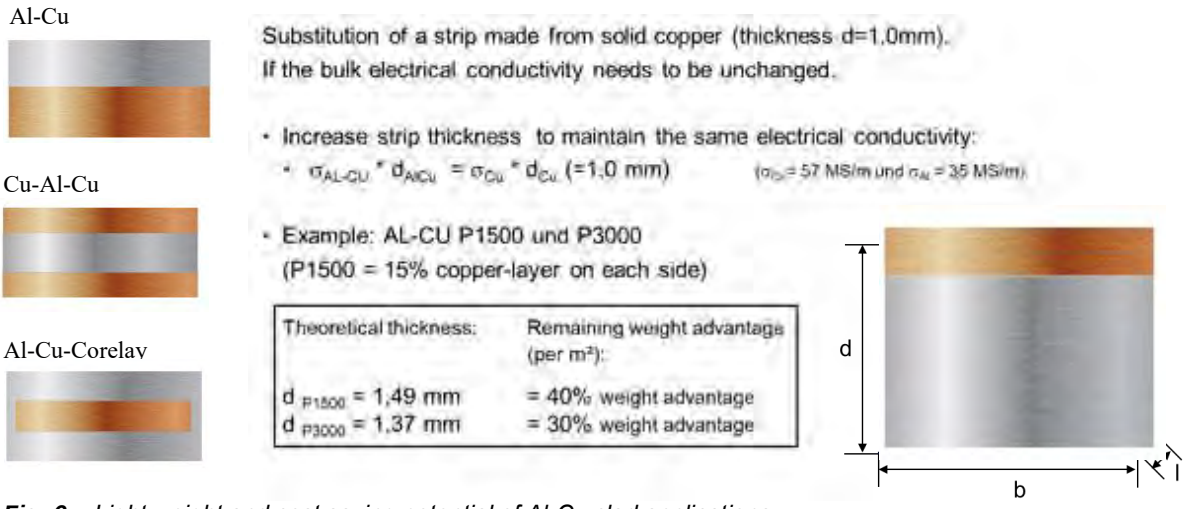


***Fig. 6*** *Light weight and cost saving potential of Al-Cu clad applications*

### 4.3 LIGHTWEIGHT TRANSITION MATERIAL

Lighweight construction in general, and specifically combined material contruction, is one of the most important automotive trends due to fuel saving and environmental protection. Al-Steel clad products can contribute to this development, especially as so-called transition joints between Al and Steel parts. It is well known that metallurgical joining of both metals is a general problem. Placing an Al-Steel clad piece between the Al and steel parts allows welding of similar metals, avoids creation of intermetallic phases and corrosion risk at the joining faces. Resistance and laser trials using al-Steel clad have been done successfully (see fig. 7)

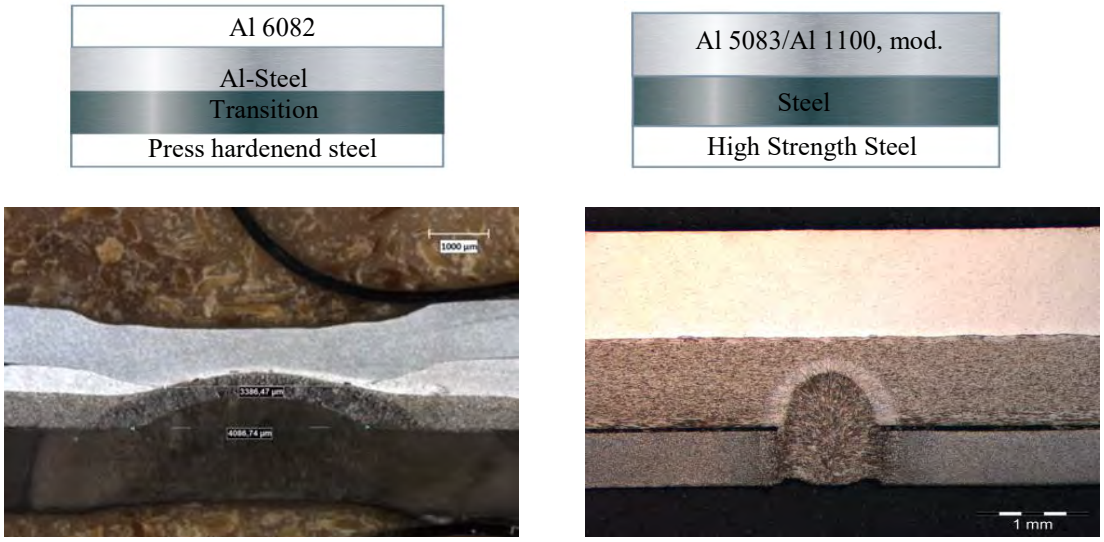


a) Al-Steel resistance welding using Al-Steel transition material

b) Laser welding on an Al-Steel light weight clad material

***Fig. 7*** *Al-Steel clad combination for automotive light weight application as joining transition material (a) and as a light weight sheet direct joint to steel*

### 4.4 SPRING STRIP WITH ELECTRICAL CONDUCTIVITY

Spring strips with increased electrical conductivity are based on special Cu spring alloys or CuBe variants. Alloying elements reduce the conductivity correspondingly. As-rolled and precipitation annealed conditions result in reduced formability. By defined selection of different available high strength steels, using high conductivity pure copper and adapted layer ratios, a wide range of tensile strength (spring property), conductivity and elongation levels can be achieved by varying Copper-Steel/Stainless Steel configurations (see fig. 8). Spring properties of such clad variants have been investigated and are comparable with these traditional alloys.

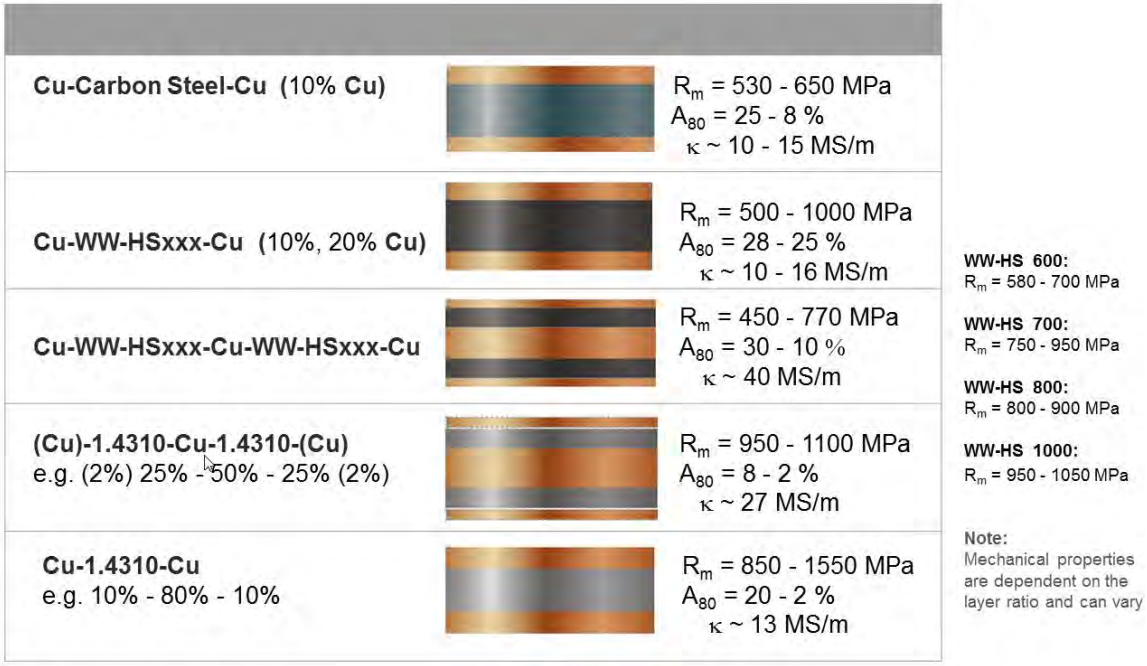


***Fig. 8*** *Different Cu-Steel and Cu-Stainless Steel combinations to create a customized material according to strength, spring properties, formability and electrical conductivity*

## 5 CONCLUSIONS

As at the above very shortly described samples shown clad material composites offer a really wide variety of combined metal properties as traditional and future oriented multi-metal designs.
If interested our on-line “CLADconfigurator” (www.clad-configurator.de) provides the opportunity to design own and customized composites and property combinations. Our materials engineering will support you to find the way from your idea to a real unique product.

# COLD ROLLING OF COATED STEEL SHEETS AS PRETREATMENT FOR HYBRID COMPONENTS

**S. Senge[1*], L. Gerdt[2], S. Wiesner[2], M. Öte[2], K. Bobzin[2] and G. Hirt[1]**

[1]Institute of Metal Forming (IBF), RWTH Aachen University
[2]Surface Engineering Institute (IOT), RWTH Aachen University

**ABSTRACT:** Nowadays the requirements regarding material properties are quite ambitious. It is therefore difficult to find a single material to fulfil all the demands placed on technical components. Hybrid components of different materials are used to meet these demands by combining beneficial material properties, such as chemical resistance, high strength and lightweight. The challenge is to achieve a resilient compound between different materials. This paper deals with the development of a possible process chain to prepare steel sheets, which will be used to produce hybrid components consisting of steel and aluminium inline during high pressure die casting (HPDC) process. First of all, steel sheet is coated with a bonding layer using cold gas spraying (CGS), aiming the achievement of metallurgical bonding between the steel sheet and the molten aluminium. In a second step, the coated steel sheets should be structured by cold rolling, in order to enable an additional form closure between Al-cast and coated steel. Properties of coated steel sheet, such as adhesion strength and bonding quality, are analysed throughout coating deposition and cold rolling process steps. It can be stated that heat treated aluminium coatings can be rolled without delamination, while the adhesion strength stays in the range of as sprayed condition.

**KEYWORDS:** rolling, cold gas spraying, hybrid components

## 1 INTRODUCTION

Hybrid components made of different materials such as steel and aluminium open up new possibilities for designing new parts or assemblies. One of the key challenges in the production of such components is the realization of a reliable bond between the different materials at the whole interface. Established joining technologies in general require a subsequent bonding process to connect sheet metal structures and high pressure die cast parts. Furthermore, it is not possible for arc and laser welding to create a reliable bond not affected negatively by the resulting brittle cast structure [1]. A process suited for the combination of steel and aluminium is friction stir welding (FSW). The major drawback of FSW is the required accessibility of the joint and the sensitivity of the process to the exact positioning of the rotating pin. Consequently, the process is more suitable for joining of flat sheets [2]. A possible attempt for local joints is clinching or roller clinching. These processes create a form closure connection, which do not negatively affect the applicability of the process for the combination of steel and aluminium. The main disadvantage of the process is the resulting global deformation of the sheets [3]. Schwankl [4] investigated a combination of an aluminium insert that was recasted with another aluminium alloy to create a hybrid materials combining benefits of both alloys. In order to avoid an oxidation of the aluminium sheet this component was coated with zinc which acts as an interlayer during casting. Pasligh stated in 2010 [5] that a metallurgical bonding between high pressure die cast aluminium and steel sheets in the desired process chain is not possible or at least not desirable due to the formation of brittle intermetallic phases. As explained before, there is no inline joining process resulting in a reliable metallurgical bond for the combination of steel and aluminium. This paper presents the possibility of applying an interlayer made of AA7075 on the steel sheet enabling metallurgical bonding with the aluminium cast during the HPDC and preventing the formation of brittle intermetallic phases. Structuring of the coating by cold rolling can further improve the bonding by providing a form closure connection during HPDC. However, due to a strong work hardening effect occurring during deposition, cold gas sprayed coatings have low ductility and are difficult to deform plastically. As recently reported by Rokni et al., a heat treatment of the cold sprayed coatings can significantly improve their mechanical properties and the formability in particular [6]. In the present study the formability of the coatings by cold rolling in as sprayed condition as well as after different heat treatments was analysed.

## 2 Experimental Setup

The experimental procedure includes cold spraying, heat treatment, cold rolling and sample analysis. Cold gas spraying (CGS) is used to apply a coating of AA7075 with a thickness between t = 100 µm - 180 µm onto industrial cold rolled steel sheets made of DC04 with an initial thickness of t = 1.92 mm. Afterwards, two different heat treatments are performed to achieve different initial states. Following this, the coated sheets will be rolled with a thickness reduction of 10 % in a single rolling pass and 16 % in two rolling passes to examine how this compound reacts to a forming process. The effect of two different heat treatments on the formability of the coatings during the cold rolling is in the focus of the current study.

### 2.1 COLD GAS SPRAYING

Conventional cold rolled steel sheets made of DC04 were used as substrate material. Prior to cold spraying, the steel sheet was punched to rectangular plates with the dimensions of V = 200 × 30 × 1.92 $mm^3$ and grit blasted with alumina with a grit size of F80. AA7075 alloy was chosen as feedstock material for coating application. The chemical compositions of the materials are given in Table 1.

***Table 1:*** *Chemical composition of the substrate and coating*

| | Si | Mn | Mg | C | S | P | Cu | Al | Fe | Zn |
|---|---|---|---|---|---|---|---|---|---|---|
| DC04 | | 0.4 | | 0.08 | 0.03 | 0.03 | | | bal. | |
| AA7075 | 0.4 | 0.3 | 2.5 | | | | 1.60 | bal. | | 5.5 |

Powder of AA7075 with a size distribution of -63 +20 µm was used for the experiments. The Kinetics 8000 Cold spray system from Oerlikon Metco (Pfäffikon, Switzerland) was used for depositing Al-based coatings with nitrogen as process and carrier gas. The process parameters for the coating deposition are given in Table 2.

***Table 2:*** *Spray parameters for coating deposition*

| Parameter | Value |
|---|---|
| Gas temperature [°C] | 490 |
| Process gas flow [$m^3$/h] | 66 |
| Carrier gas flow [$m^3$/h] | 3.0 |
| Spray distance [mm] | 30 |
| Transverse movement velocity [mm/s] | 200 |

In order to improve the formability of the sprayed coating, some samples were annealed at a temperature of T = 400 °C for t = 3 h or stress relief heat treated at the temperature of T = 150 °C for t = 5 h. The choice of these parameters is based on the analysis of the results presented in the study of Rokni et al. [6] in order to achieve a better formability of the coated samples. The cold sprayed samples were heat treated using a PVA MOV 553 T vacuum furnace (PVA TePla AG, Wettenberg, Germany). In Table 3 the overview of the process parameters for cold rolling as well as for different heat treatments is given. Six different combinations of the process parameters were tested in total.

### 2.2 COLD ROLLING

After heat treatment the coated samples were cold rolled with one or two passes to achieve different thickness reductions. The initial thickness of the sheet as well as after coating deposition was measured with a micrometre screw. Differences in thickness reduction of the coating and the steel substrate as well as changes in adhesion strength and quality of the coating were analysed afterwards. Table 3 gives an overview of all rolling experiments after different heat treatments, the initial and final thicknesses as well as the global thickness reduction of the sheets.

### 2.3 TESTING

In order to characterize the coating, the cold sprayed samples were metallographically prepared and examined in terms of their microstructure. The adhesion strength of the deposited coatings was determined using a PATHandy tester. The measurement principle is described in [7]. Even though this method is primarily standardized for lacquer coatings according to DIN EN ISO 4624 [8], it is industrially deployed for thermally sprayed coatings due to its simple handling and robustness. As it was shown by Schlaefer [9], the measurements by PATHandy are in good agreement with the adhesion tests conducted according to DIN 582 [10]. The microhardness tester Bühler Micromet 1 by ITW Test & Measurement GmbH (Esslingen am Neckar,

Germany) was used for measurements of the Vickers hardness of the coatings. In order to identify a possible formation of cracks in the coating during the cold rolling process, a SEM/EDS analysis was performed by means of the scanning electron microscope Zeiss Leo 1530.

***Table 3:*** *Overview of the performed rolling experiments and the resulting thicknesses in mm*

| Sample | heat treatment | total initial thickness $h_0$ | initial thickness of AA7075 | total final thickness $h_1$ | final thickness of AA7075 | total thickness reduction $\varepsilon_h$ in % |
|---|---|---|---|---|---|---|
| CR10 | no | 2.029 | 0.108 | 1.831 | 0.058 | 9.7 |
| CR16 | no | 2.095 | 0.174 | 1.743 | 0.090 | 16.8 |
| HT400+CR16 | 400 °C, 3 h | 2.066 | 0.146 | 1.746 | 0.089 | 15.5 |
| HT400+CR10 | 400 °C, 3 h | 2.092 | 0.172 | 1.872 | 0.095 | 10.5 |
| HT150+CR16 | 150 °C, 5 h | 2.029 | 0.109 | 1.704 | 0.055 | 16.0 |
| HT150+CR10 | 150 °C, 5 h | 2.025 | 0.104 | 1.822 | 0.059 | 10.0 |

# 3 RESULTS

A coating with a thickness of about s = 120 µm could be deposited with a process gas temperature of T = 490 °C, resulting in an adhesion strength of $\beta_{HZ}$ = 13.8 ± 1.0 MPa. A further increase of the process temperature did not improve the coating properties significantly and led to particles clogging on the nozzle. The process parameters shown in Table 2 were adopted for further investigations.

## 3.1 THICKNESS REDUCTION

Fig. 1 shows the initial and the final thickness for each sample separated into the thickness of the steel substrate and the thickness of the AA7075 coating. Furthermore, the relative thickness reductions of the coating and the steel substrate are given. In comparison to the global thickness reduction shown in Table 3 it can be seen that the relative thickness reduction of the steel substrate is in the range of the global thickness reduction whereas the relative thickness reduction of the AA7075 coating is six times as big as the relative thickness reduction of the steel substrate for single pass rolling and about 3.5 times as big for two pass rolling. This can be attributed to the flattening of the rough surface of the cold sprayed coating as described in previous study for copper coated steel sheets [11]. This phenomenon will be discussed later in the context of hardness and microstructure evolution of coating and steel throughout the process chain.

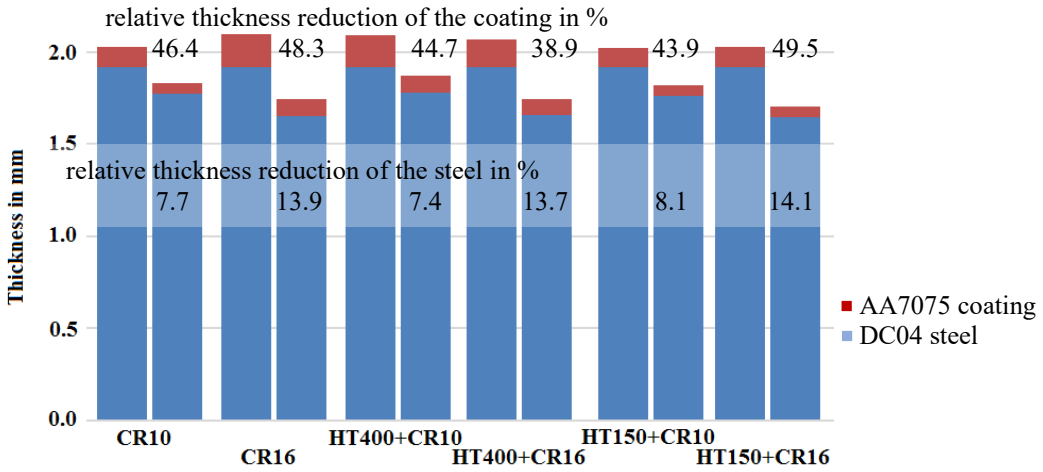


***Fig. 1*** *Initial and final thickness of each sample, separated into thickness of steel in blue and AA7075 in red and the relative thickness reduction of both materials.*

## 3.2 HARDNESS OF THE COATING

The hardness measurement represents a simple method to estimate the extent of strain hardening after cold spraying and cold rolling and, therefore, could give an explanation for the observed thickness reduction. In Fig. 2 the evolution of the Vickers Hardness HV 0.025 of the steel substrate DC04 and the AA7075 coating after each process step is presented. The hardness of the steel in initial state is about 100 HV 0.025. Due to strain hardening the hardness increased to about 120 HV 0.025 at a thickness reduction of 10 % and to about 135 HV 0.025 at a thickness reduction of 16 %. The influence of the performed heat treatment on the hardness of the steel substrate is negligible. The initial hardness of the powder particles was about 118.3 ± 7.6 HV 0.025. After coating deposition, the hardness reached the value of 146.8 ± 3.9 HV 0.025. The

subsequent flat rolling does not contribute to further work hardening of the coating even after two passes. The high degree of the particle deformation during the spraying process possibly leads to the condition, where particles reach their strain limit. This assumption is in accordance with the coating behaviour observed metallographically, indicating the crack propagation or delamination already after the flat rolling process with a thickness reduction of about $\varepsilon = 10$ %. The hardness evolution of the steel and coating confirms the assumptions that the flattening of the roughness peaks mainly contributes to the thickness reduction of the coating, while the steel sheet is deformed plastically with the relative thickness reduction, which corresponds to the thickness changes of the whole compound. Furthermore, the presumed behaviour of both materials during the cold rolling process is in accordance with the fact, that the yield strength of the steel $R_{p0.2} = 210$ MPa is significantly lower than that of the coating $R_{p0.2} = 310$ MPa [6]. After annealing of the cold sprayed samples at the temperature of T = 400 °C for t = 3 h, the hardness of the AA7075 coatings recovers to the level of about 68.8 ± 4.5 HV 0.025. A subsequent cold rolling process leads to an increase of the hardness up to 85.2 ± 5.7 HV 0.025. For the coating of AA7075, however, other common mechanisms like precipitation hardening and solid solution hardening can lead to hardness changes. A stress relief heat treatment at T = 150 °C for h = 5 h did not cause a significant change regarding the hardness of the coating.

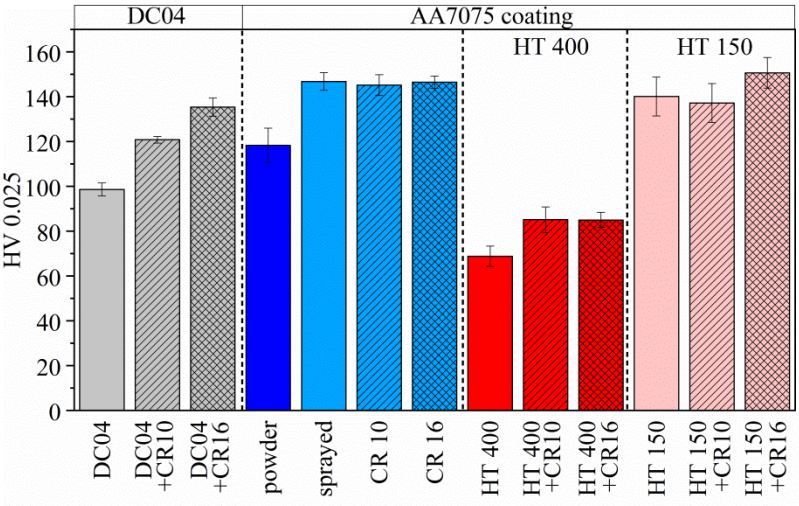


***Fig. 2*** *Vickers hardness HV 0.025 of the steel sheet after cold rolling and the AA7075 coating after deposition, different heat treatments and flat rolling.*

### 3.3 MICROSTRUCTURE

The microstructure of the cold sprayed coating could be a crucial factor regarding the material response to the cold rolling process. In order to investigate the influence of the heat treatments on the microstructure of the cold sprayed coatings, SEM/EDS analysis was performed. The coatings of AA7075 exhibited a low porosity of about p = 1.0 %. The evolution of the coatings microstructure and morphology is shown in Fig. 3. No significant changes of the microstructure could be detected after stress relief heat treatment at T = 150 °C. In contrast, annealing at T = 400 °C led to a densification of the coating caused by the sintering effect at the interfaces between the particles. As a result the interfaces between the particles almost disappeared. Furthermore, annealing led to precipitations coarsening and recrystallization of the grains.

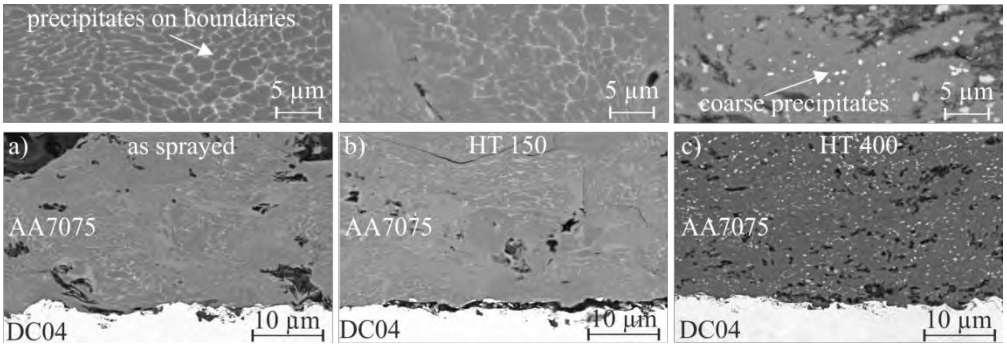


***Fig. 3*** *SEM micrographs of the coating a) after deposition b) after stress relief heat treatment at T = 150 °C for h = 5 h and c) after heat treatment at T = 400 °C for h = 3 h*

Fig. 4 shows micrographs of samples rolled with a total thickness reduction of 16 % after each heat treatment. Some cracks were observed in normal direction/rolling direction (ND/RD) cross sections after the coated samples were cold rolled in as sprayed condition. The crack propagation occurred mainly at the splats boundaries, Fig. 4a. Significantly less crack initiation occurred after stress relief heat treatment at T = 150 °C. No cracks could be identified in the cold rolled coating after annealing at T = 400 °C as the particle boundaries disappeared due to the sintering effect driven by diffusion process.

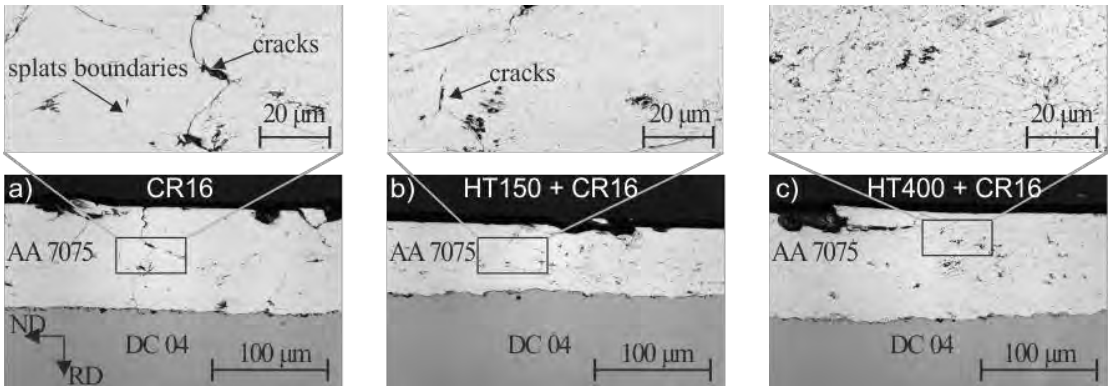


***Fig. 4*** *Confocal laser microscope micrographs of cold rolled coating with thickness reduction of ε = 16 % a) in as sprayed condition b) after stress relief heat treatment at T = 150 °C for h = 5 h and c) after annealing at T = 400 °C for h = 3 h.*

Prior research revealed that one major issue relating to thickness reduction of the coating is the flattening of the surface [11]. Experiments with the same process chain but using copper as coating showed that CGS results in a surface roughness depth of $R_z$ = 100 µm what can be reduced to a roughness of $R_z$ = 44 µm in a single rolling pass and to a roughness of $R_z$ = 26 µm in two subsequent passes [11]. Due to the fact that the initial thickness was measured with a micrometre screw, thus on the top of roughness peaks, it must be assumed that the change of roughness has a major influence on the calculated relative thickness reduction of the coating. Thus the differences in the relative thickness reductions between steel and coating of up to 38.7 % can be explained with this flattening effect. This fits to the observation that the relative thickness reduction of the coating after two rolling passes is nearly the same as after a single pass. .

### 3.4 ADHESION STRENGTH

In order to determine the influence of the annealing and stress relief heat treatments as well as the cold rolling process on the adhesion of the coating to the steel substrate, the bond strengths were measured after corresponding process. The annealing at T = 400 °C for t = 3 h led to an increase of the adhesion strength from $\beta_{HZ}$ = 13.8 ± 1.0 MPa up to $\beta_{HZ}$ = 43.7 ± 3.6 MPa, Fig. 5.

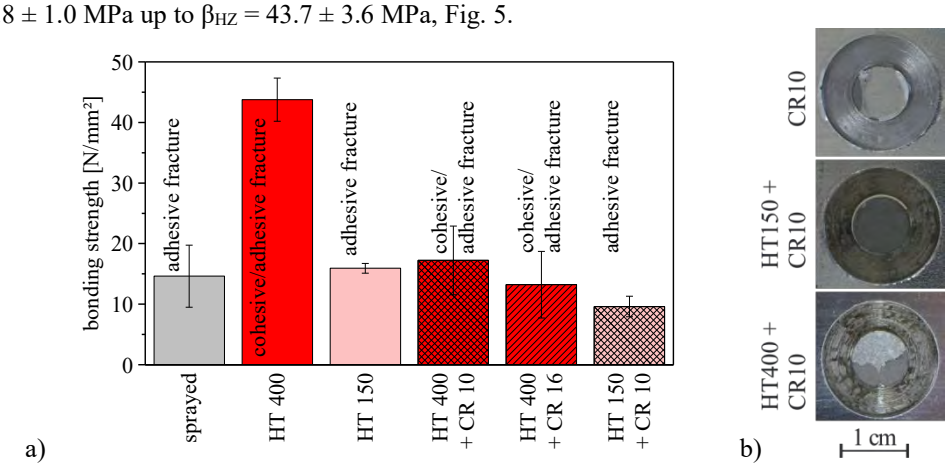


***Fig. 5*** *a)The adhesion strength of the AA7075 coatings after deposition and flat rolling, b) images with the examples for coating delamination during samples preparation for CR10, entirely cohesive fracture and cohesive/adhesive fracture after adhesion test.*

The presumption that this increase was caused by diffusion process at the interface between coating and steel could not be verified by SEM/EDS analysis. The subsequent cold rolling with the thickness reduction of about ε = 10 % caused a decrease in adhesion strength to $\beta_{HZ}$ = 17.2 ± 5.6 MPa. After the second rolling pass with

$\varepsilon = 16$ %, the adhesion strength of the coating has been further reduced to the values comparable with the level of the as sprayed condition $\beta_{HZ} = 13.2 \pm 5.5$ MPa. In the case of annealed samples, the coating failed partly cohesively and partly adhesively at the interface with steel. A stress relief heat treatment did not cause a significant change of the adhesion strength of the coating. Due to the partial coating delamination during sample preparation, adhesion strength could not be determined for cold rolled samples without heat treatment (CR10 and CR16) and for samples after stress relief heat treatment at T = 150 °C for t = 5 h and a thickness reduction of 16 % (HT150+CR16). The damage developed during the cutting of the area for affixing a punch for adhesion test is depicted in Fig. 5b.

# 4 CONCLUSIONS

In the present study the formability of cold sprayed AA7075 coatings during cold rolling was analysed. It was shown that heat treatments can be an efficient tool to increase the formability of the AA7075 coating. A stress relief heat treatment at T = 150 °C for h = 5 h did not cause significant changes of the microstructure of the coating and its mechanical properties. The tolerable thickness reduction without delamination is limited to about $\varepsilon = 10$ %. Furthermore it could be shown, that the annealing of the coatings at T = 400 °C for h = 3 h results in the recrystallization of the microstructure and its softening, leading to a significant improve of the coating formability, as no crack formation was observed after cold rolling of annealed samples. This heat treatment also caused a considerable increase of the adhesion strength compared to as sprayed condition. The coated samples were successfully cold rolled after annealing with thickness reductions of up to $\varepsilon = 16$ %. The influence of cold rolling on the later bonding of die cast aluminium has to be analysed separately. Achieved outcomes open the possibility for structuring of coated steel sheets to combine metallurgical bonding and form closure during the HPDC of Al-steel hybrids. The quality and performance of the joints produced after the application of the proposed surface preparation technique should be analysed. Especially the influence of the change of roughness has to be evaluated.

# 5 ACKNOWLEDGEMENT

The authors gratefully acknowledge the financial support of the “Deutsche Forschungsgemeinschaft” (DFG) received within the research project “Behandlung von Stahlblechen für das Druckgießen spalt- und verzugsarmer Aluminiumguss/Stahlblech-Metallhybriden”. We also want to thank our partners at Foundry Institute at RWTH Aachen University. Special thanks are addressed to our colleagues at Access e. V. research centre for providing SEM analysis.

# REFERENCES

[1] Chen, C.M., Kovacevic, R.: *Joining of Al 6061 alloy to AISI 1018 steel by combined effects of fusion and solid state welding*. International Journal of Machine Tools & Manufacture 44:1205–1214, 2004.
[2] Helal, Y., Boumerzoug, Z.: *Dissimilar friction stir welding of Al-6010 to steel*. AIP Conf. Proc. 1772, 030008, 2016.
[3] Hiller, M., Volk, W.: *Joining Aluminium Alloy and Mild Steel Sheets by Roller Clinching*. AMM Vol. 794 pp 295-303, 2015.
[4] Schwankl, M.: *Al-Al-Verbundguss – Technologische Grundlagen und werkstoffkundliche Charakterisierung der stofflichen Anbindung von Aluminiumknetlegierungen im Aluminium-Druckguss*. FAU University Press, ISBN: 978-3-96147-048-8, 2017.
[5] Pasligh, N.: *Hybrid form closure connections in lightweight-design components of steel sheet and aluminium high pressure die casting*. Foundry Institute RWTH Aachen, 2010.
[6] Rokni, M. R., Widener, C. A., Champagne, V. K., Crawford, G. A., Nutt, S. R.: *The effects of heat treatment on 7075 Al cold spray deposits*. Surface and Coatings Technology 310, 278–285, 2017.
[7] Bobzin, K., Öte, M., Knoch, M. A., Liao, X., Hopmann, C., Ochotta, P.: *Investigation of Influencing Factors on the Transfer of Wire Arc Sprayed Zn Coatings for the Metallisation of Plastic Parts*. ITSC International Thermal Spray Conference & Exposition, 24–29, 2016.
[8] DIN EN ISO 4624:2014-06. *Paints and varnishes - Pull-off test for adhesion*.
[9] Schläfer, T.: *Entwicklung von Verfahren zur Bestimmung der Haftzugfestigkeit von thermisch gespritzten Zylinderlaufbahnen*. 1. Aufl. Shaker, Herzogenrath, 2014.
[10] DIN EN 582:1994-01. *Thermal spraying; determination of tensile adhesive strength*.
[11] Bobzin, K., Öte, M., Wiesner, S., Gerdt, L., Senge, S., Hirt, G.: *Investigation on the cold rolling and structuring of cold sprayed copper-coated steel sheets*. IOP Conf. Ser.: Mater. Sci. Eng. 181, 12028, 2017.

# POWDER METALLURGICAL COMPONENTS WITH RADIALLY GRADED MATERIAL SYSTEM BY SEGREGATION

**Dieter Bohr[1*], Bernd-Arno Behrens[1], Kai Brunotte[1]**

[1] Institute of Forming Technology and Machines (IFUM), Leibniz Universität Hannover, Garbsen, Germany

**ABSTRACT:** This paper deals with a novel powder metallurgical manufacturing process for the production of radially graded MMC components by means of segregation. By superimposing the so-called Brazil nut effect with a rotational movement, the directional gravitational force is substituted by the centrifugal force. As a result, the segregation is no longer vertical but radial, so that a radially graded material system can be generated.
The influence of different material- and process-specific parameters on the segregation behavior was investigated in a special setup using aluminum and silicon carbide powders. The evaluation of the micrographs of the pressed and sintered samples shows that by varying the rotation speed and the grain size ratio both positive and negative gradients can be achieved. The influence of different grain shapes seems to be marginal. Counterproductive effects could be observed by varying the vibration amplitude as an increase of gradient intensity and scattering occurred simultaneously.

**KEYWORDS:** Powder metallurgy, composite materials, functionally graded materials, segregation, Brazil nut effect

## 1 INTRODUCTION

Powder metallurgy (PM) covers different processes like the production and treatment of powders, but also the fabrication of components by shaping and compaction of corresponding materials. Main advantages are high material utilization and low energy consumption. Moreover, the properties of such components can be selectively adjusted which leads to various application possibilities. Typical industrial parts are spur and helical gears with internal or external teeth, connecting rods and shock absorbers [1].
The commonly used PM shaping process is double-sided die pressing, in which the powder is filled into a die cavity and then is compacted by applying mechanical pressure by a simultaneous motion of an upper and a lower punch [2]. After pressing, the green parts are sintered in a (vacuum or protective atmosphere) furnace in order to increase their mechanical properties by diffusion processes and/or further densification (up to 99 %) [3].
Another application of PM is the production of metal matrix composites (MMC). Usually, a powder mixture, consisting of metallic and ceramic (reinforcement) grains, is processed by pressing and sintering. By taking advantage of both mono-materials, components with enhanced mechanical properties (strength, E-modulus, wear resistance) can be produced [4]. In comparison to MMC casting processes, the PM route enables products with a homogenous microstructure [5].
In general, the gradation of powder materials can be stepwise or continuous. The advantage of continuously graded arrangements is a slight change of material properties without any abrupt peaks [6]. The production of such functionally graded materials (FGM) is generally based on separation effects, where it can be distinguished between processes with particle motions in a liquid phase [7, 8] and in a powder mixture [9, 10]. The latter processes are limited to the production of axially graded parts. In this contribution a new powder based method is presented, which allows the fabrication of radially graded MMC components. For this purpose, the so-called Brazil nut effect (BNE) is combined with a rotational motion. As a result, the gravitational acceleration is overlapped with a centrifugal one, which should change the segregation direction from vertical to radial.
The BNE is defined as a vertical segregation of a granular material under a vertical vibration, while the larger particles tend to move upwards and the smaller ones downwards [11]. Despite this effect other segregation states such as reverse BNE (RBNE) or a horizontal (HS) or a periodic (PS) segregation can be established by appropriate adjustment of process and material specific parameters [12]. Besides experimental

* Corresponding author: An der Universität 2, 30823 Garbsen, Germany, bohr@ifum.uni-hannover.de

investigations [13–15], various scientists dealt with numerical simulations concerning segregation by the application of discrete element method (DEM) or molecular dynamics [16–19].
The paper is structured as follows. In Section 2, the theoretical principles of the newly developed process including the dynamics are presented. Section 3 is reserved for the experimental implementation of the segregation process and for the used materials and evaluation methods. Afterwards, the evaluation of the proposed manufacturing method as well as a critical discussion of the experimental results are shown before the paper is closed by the Conclusion section.

# 2 THEORETICAL

## 2.1 PROCESS ROUTE

In Fig. 1 the developed process route is depicted schematically. First, a cylindrical die cavity is filled with a binary powder mixture, which consists of a metal powder and a reinforcement phase. Then the segregation process is applied by combining rotation and vibration. After that, the die is transferred to a press where the mixture is compacted in order to obtain sufficient green strength. Finally, for adequate mechanical properties the green part is sintered in a vacuum furnace.

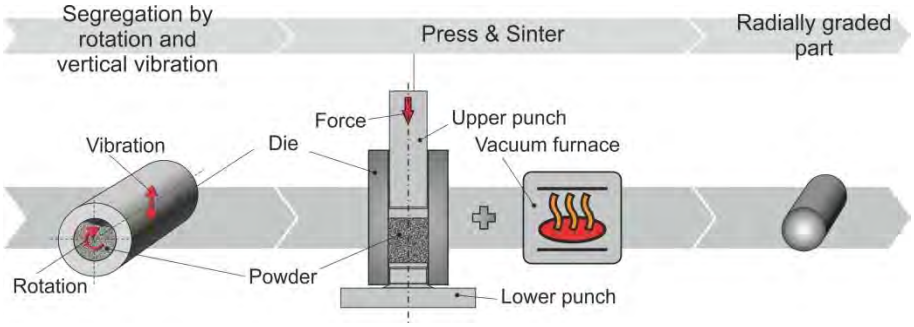


***Fig. 1*** *Schematic process route for radially graded PM components*

## 2.2 DYNAMICS

A vertical vibration of a shaker can be characterized by two parameters $f$ and $\Gamma$, where $f$ is the vibrational frequency, and $\Gamma$ is a dimensionless acceleration given by equation (1) [12].

$$\Gamma = \frac{4A\pi^2 f^2}{g} \qquad (1)$$

This relation describes the ratio of the maximum acceleration of the shaker to the gravitational acceleration g, where A is the vibration amplitude. Here, the vertical vibration is overlapped with a rotational motion in order to transform the vertical segregation to a radial one. Thus, equation (1) is modified to

$$\Gamma_R = \frac{4A\pi^2 f^2}{a_c - g} \qquad (2)$$

where $a_c$ is the centrifugal acceleration with

$$a_c = \omega^2 * r \qquad (3)$$

The centrifugal acceleration $a_c$ depends on the angular velocity $\omega$ and the current radial location $r$, where $\omega$ is a function of the rotation speed $n$ in 1/min:

$$\omega = 2\pi n/60 \qquad (4)$$

In Fig. 2 the centrifugal acceleration for different rotation speeds is plotted as a function of radius. It can be seen, that in order to surpass the gravitational acceleration, and thus change the segregation direction from vertical to radial, the rotation speed has to be greater than 250 1/min. Moreover, the intersection between the gravitational and centrifugal acceleration decreases with increasing rotation speed. As a result, in order to ensure a slighter influence of the gravitational acceleration either the diameter or the rotation speed needs to be increased.

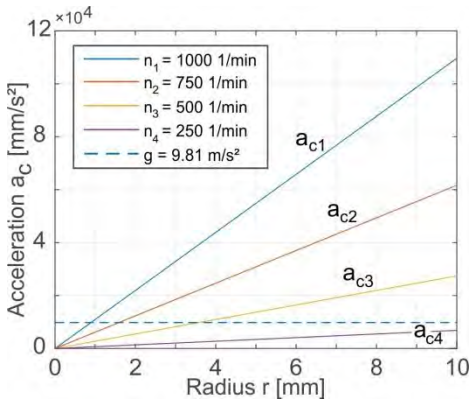


***Fig. 2*** *Centrifugal acceleration as a function of radius and rotation speed*

# 3 EXPERIMENTAL

## 3.1 SEGREGATION SETUP

In Fig. 3 the experimental setup for the segregation is presented. The vibration is established by a vibratory sieve shaker, which amplitude can be adjusted in range of 0.1–2.5 mm while the frequency is not adjustable and depends on the amplitude. On top of the shaker an extension, which consists of a geared motor, supplied by voltage controller, and the die for the powder mixture, is mounted and fixed by tension belts. The side view shows the detailed structure. The powder mixtures were filled to a die height of 40 mm and covered by two cylinders, where the left one (upper cover) can be axially adjusted in process.
In order to calculate $\Gamma_R$ the vibration frequency has to be determined. For this the setup was marked on different positions and was recorded with a high-speed camera varying the vibration amplitude. Subsequently, the recordings were analysed by means of fast Fourier transform (FFT) and the vibration frequency was calculated as a function of amplitude.

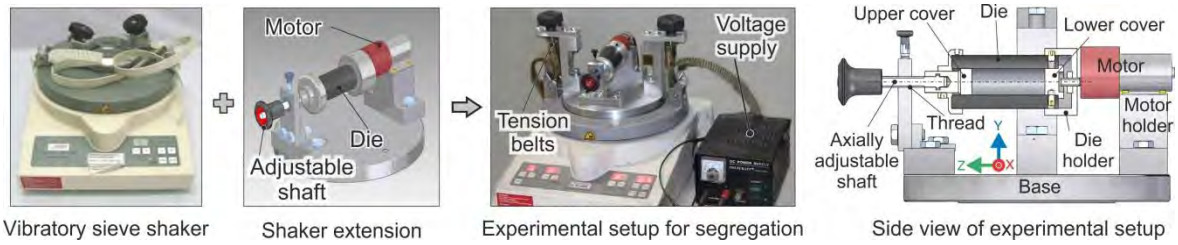


***Fig. 3*** *Experimental setup for radial segregation of binary powder mixtures*

## 3.2 MATERIALS AND DESIGN OF EXPERIMENTS

The investigated powder mixtures consists of cp (99.7 wt.-%) aluminium and silicon carbide with a 85:15 weight-relation, which is the most commercially used powder compound [20, 21]. According to Hong et al. the crossover condition between the occurrence of BNE and RBNE can be described by

$$\frac{d_l}{d_s} \approx \left(\frac{\rho_l}{\rho_s}\right)^{-1} \qquad (5)$$

where $d_l$, $d_s$, $\rho_l$ and $\rho_s$ are the diameter and the density of the large $l$ and small $s$ particles, respectively [17]. With given densities of aluminium (2.71 g/cm³) and silicon carbide (3.21 g/cm³) equation (5) can be transformed to

$$\frac{d_{SiC}}{d_{Al}} > (1.19)^{-1} \qquad (6)$$

which describes the condition of RBNE to take place. Therefore, in order to compel the SiC particles to rise, their size has to be at least 1.19-times greater than the size of the Al particles. Thus, six mixtures were investigated with different aluminium grain sizes. Additionally, in order to influence the friction conditions in the process [22, 23] two different grain geometries were used. The material specification of the used powders are summarised in Table 1. With this information each powder combination can be clearly described by the

grain size ratio, which is defined as the ratio of the mean grain diameter of the SiC to the mean grain diameter of the Al, and the grain geometry of the aluminium.

***Table 1:*** *Grain form and size of used powders*

| | Aluminium | Silicon carbide |
|---|---|---|
| Grain form | Spherical, Spattered | Spattered |
| Grain size | <50 µm, 50-100 µm, 100-200 µm | 100-200 µm |

Because of the large number of possible influence factors a d-optimal DOE-plan was utilised in order to determine the main influences. Moreover, considering the adhesive and abrasive wear due to the MMC the experimental procedure of a full factorial plan would be strongly inefficient. Additionally, in order to verify the theory of radial (R)BNE slow rotation speed were included. The corresponding parameter variations are depicted in Table 2.

***Table 2:*** *Parameter variations for experimental investigations*

| | Aluminium grain form | Grain size ratio | Rotation speed [1/min] | Vibration amplitude [mm] | Sample number |
|---|---|---|---|---|---|
| Parameter variation steps | Spherical | 1.0 | 10 | 0.6 | |
| | Spattered | 2.1 | 250 | 1.0 | |
| | | 6.7 | 750 | 2.3 | - |
| | | | 1050 | | |
| Parameter combinations | Spherical | 6.7 | 1050 | 0.2 | 1 |
| | Spattered | 6.7 | 1050 | 1.0 | 2 |
| | Spattered | 6.7 | 750 | 0.2 | 3 |
| | Spattered | 2.1 | 1050 | 2.3 | 4 |
| | Spattered | 6.7 | 10 | 2.3 | 5 |
| | Spherical | 1.0 | 250 | 1.0 | 6 |
| | Spattered | 1.0 | 10 | 0.2 | 7 |
| | Spattered | 6.7 | 250 | 1.0 | 8 |
| | Spherical | 1.0 | 10 | 0.2 | 9 |
| | Spherical | 6.7 | 10 | 2.3 | 10 |
| | Spherical | 1.0 | 1050 | 2.3 | 11 |
| | Spattered | 6.7 | 10 | 1.0 | 12 |
| | Spherical | 2.1 | 250 | 1.0 | 13 |
| | Spherical | 1.0 | 10 | 2.3 | 14 |
| | Spherical | 6.7 | 1050 | 2.3 | 15 |
| | Spattered | 2.1 | 750 | 1.0 | 16 |
| | Spherical | 1.0 | 750 | 0.2 | 17 |
| | Spattered | 1.0 | 750 | 2.3 | 18 |
| | Spherical | 2.1 | 1050 | 0.2 | 19 |
| | Spattered | 1.0 | 10 | 2.3 | 20 |
| | Spherical | 6.7 | 10 | 0.2 | 21 |
| | Spattered | 1.0 | 1050 | 0.2 | 22 |

### 3.3 EXPERIMENTAL PROCEDURE AND EVALUATION

The samples were produced as follows. First, the die cavity was filled with the corresponding powder mixture. Then vibration and rotation are applied by adjusting the vibration amplitude and rotation speed for two minutes according to relevant literature to ensure a steady state of the segregation process [14, 15]. In the last 10 seconds the left cylinder (upper cover) is moved towards the powder in order to freeze the segregation process. After that, the die is dismounted and transferred to a manual hydraulic press, where a pressure of 300 MPa is applied [24, 25]. Subsequently, the green parts are sintered in a vacuum furnace for 1 hour at 620 °C [20, 24, 25].

The SiC distributions of the sintered samples were analysed by micrographs. For each sample 8 rectangular regions, equidistantly placed in 45° around the circumference, were evaluated by calculating the percentage radial SiC distribution by grey value analysis. Afterwards the least squares method for determination of the slope m of a linear regression was applied. The outcome parameter is used for a quantitative evaluation of the DOE-plan and an algebraic comparison between the results.

# 4 RESULTS AND DISCUSSION

## 4.1 DYNAMICS

The results of the dynamic measurements are depicted in Fig. 4 (left). Three different amplitudes ($A_A$) were examined. It can be seen, that the horizontal vibration (X and Z) are negligible in comparison with the vertical one (Y), which is the main one. In addition, a significant correlation between the vibration amplitude and the frequency is determined. With this relation $\Gamma_R$ can be calculated, which is plotted as a function of rotation speed and vibration amplitude for different radial positions in Fig. 4 (right). The dimensionless acceleration increases with rising vibration amplitude, while it decreases with growing rotation speed. This shows that at high speeds a nearly constant $\Gamma_R$ can be adjusted regardless of the radius, which is important for process control. In contrast, for slow speeds and small radii $\Gamma_R$ changes abruptly. Here, the transition area where the gravitational acceleration converges the centrifugal is approached, which can result in strong distortions and thus an unstable process.

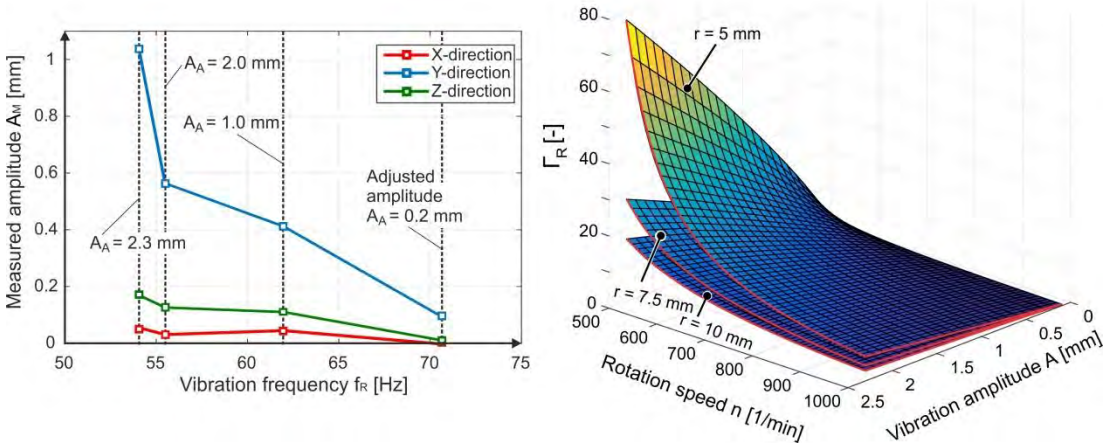


***Fig. 4*** *Vibration amplitude as a function of frequency (left) and dimensionless acceleration as a function of rotation speed and vibration amplitude for different radial positions*

## 4.2 SEGREGATION

In Fig. 5 the results of the DOE experiments are depicted including the effects of grain size ratio, rotation speed, vibration amplitude and grain form on the slope *m*.

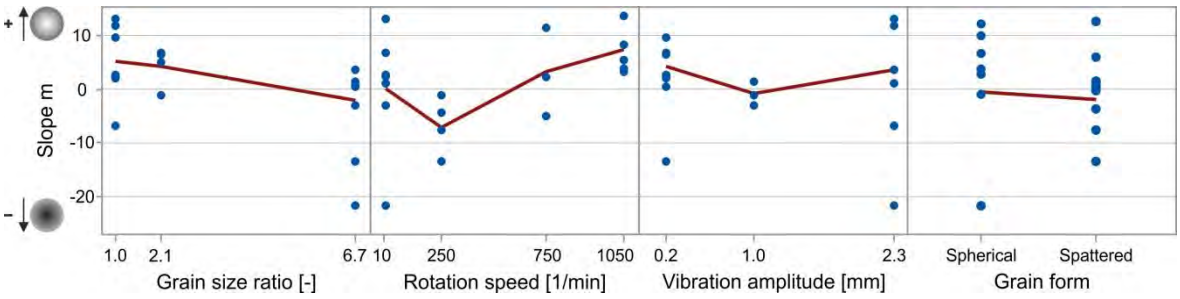


***Fig. 5*** *Effects of grain size ratio, rotation speed, vibration amplitude and grain form on the slope* m

By trend, with rising grain size ratio the slope becomes negative, which means higher Al fractions in the outer shell compared to SiC. This behaviour can be attributed to the mechanism of percolation and convection, which results in BNE, meaning that the smaller particles descend by sieving effects or in this case move outward [17]. At slow speeds ($n \leq 250$ 1/min) the slope varies in a huge range as a result of high sensitivity of the dimensionless acceleration $\Gamma_R$ as described above. Due to the unsteady conversions between gravitational and centrifugal forces the results deviate strongly, while mostly homogenous mixtures ($m \approx 0$) can be observed. With rising rotation speed the centrifugal acceleration increases and surpasses gravity. As a result, the segregation direction of the SiC particles changes from vertical to radial as described above, which can be verified by small deviations. Regarding the effects of the vibration amplitude no clear statement can be made, as both extremes ($A = \{0.2; 2.3\}$) lead to high deviations of the slope while the mean value results in uniform mixtures. The effect of different grain forms seems to be marginal, as both geometries lead to varying slope values. In fact, these deviations can be attributed to the variation of the other three parameters.

## 5 CONCLUSIONS

A newly PM process route was developed to create radially graded MMC components consisting of aluminium and silicon carbide by combining vibrational and rotational motions. The main effects of different material and process specific parameters were determined and analysed by means of a DOE-plan. The rotation speed and the grain size ratio can lead to both positive and negative gradients. The effect of different grain forms seems to be insignificant while the influence of the amplitude needs to be investigated in more detail.

## 6 ACKNOWLEDGEMENT

The presented results are based on the research project “Production of powder metallurgy components with radially graded material system by means of segregation”, Project number Be1691/182-1. The authors would like to thank the German Research Foundation (DFG) for the financial support.

## REFERENCES

[1] W. Schatt, K.-P. Wieters, and B. Kieback: *Pulvermetallurgie*. Springer, Berlin (2007).
[2] O. Beer: *Verdichtung von Metallpulvern*, München (1996).
[3] P. Beiss: Fortschritte bei der Formgebung in Pulvermetallurgie und Keramik, VDI-Verlag, Düsseldorf (1991).
[4] B.-A. Behrens, R. Rolfes, M. Vucetic, J. Reinoso, M. Vogler, and N. Grbic: Procedia CIRP (2014) 18. DOI:10.1016/j.procir.2014.06.140.
[5] W. Weißbach, M. Dahms, and C. Jaroschek: *Werkstoffkunde*. Springer Vieweg, Wiesbaden (2015).
[6] Y. Watanabe and H. Sato (2011. Review Fabrication of Functionally Graded Materials under a Centrifugal Force. In *Nanocomposites with Unique Properties and Applications in Medicine and Industry*, J. Cuppoletti, Ed. InTech. DOI:10.5772/20988.
[7] B. Kieback, A. Neubrand, and H. Riedel: Materials Science and Engineering: A 1-2 (2003) 362. DOI:10.1016/S0921-5093(03)00578-1.
[8] H. Sato, J. Maeda, M. Yamada, and Y. Watanabe: MSF (2016) 879. DOI:10.4028/www.scientific.net/MSF.879.1691.
[9] D. Janković Ilić: *Self formed Cu-W functionally graded material created via powder segregation*. Shaker, Aachen (2008) 11.
[10] Z.-G. Wang, C.-P. Li, H.-Y. Wang, J.-N. Zhu, C. Wang, and Q.-C. Jiang: J. of Materi Eng and Perform 2 (2017) 26. DOI:10.1007/s11665-016-2466-9.
[11] M. E. Möbius, B. E. Lauderdale, S. R. Nagel, and H. M. Jaeger: Nature 6861 (2001) 414. DOI:10.1038/35104697.
[12] A. P. J. Breu, H.-M. Ensner, C. A. Kruelle, and I. Rehberg: Phys. Rev. Lett 1 (2003) 90. DOI:10.1103/PhysRevLett.90.014302.
[13] C.-C. Liao, S.-S. Hsiau, T.-H. Tsai, and C.-H. Tai: Chemical Engineering Science 3 (2010) 65. DOI:10.1016/j.ces.2009.09.065.
[14] X. Yang, N. Zheng, P. Wen, L. Li, and Q. Shi: Powder Technology (2015. DOI:10.1016/j.powtec.2015.08.051.
[15] P. Wen, N. Zheng, L. Li, and Q. Shi: Sci. Rep (2014) 4. DOI:10.1038/srep06914.
[16] V. Garzó: Phys. Rev. E 2 (2008) 78. DOI:10.1103/PhysRevE.78.020301.
[17] D. C. Hong, P. V. Quinn, and S. Luding: Phys. Rev. Lett 15 (2001) 86. DOI:10.1103/PhysRevLett.86.3423.
[18] R. Y. Yang, R. P. Zou, and A. B. Yu: Phys. Rev. E 3 (2000) 62. DOI:10.1103/PhysRevE.62.3900.
[19] H. Zhu, Z. Zhou, R. Yang, and A. Yu: Chemical Engineering Science 23 (2008) 63. DOI:10.1016/j.ces.2008.08.006.
[20] P. Kumar, R. Ranjithkumar, C. Shanmugam, Asst.Professor.M.Jayaram, Dr.Vijayakumar.S, and Dr.V.Karthik: IJIRT (2015).
[21] K. Suryanarayanan, R. Praveen, and S. Raghuraman: International Journal of Innovative Research in Science, Engineering and Technology 2 (2013) 2013.
[22] M. P. Ciamarra, M. D. de Vizia, A. Fierro, M. Tarzia, A. Coniglio, and M. Nicodemi: Phys. Rev. Lett 5 (2006) 96. DOI:10.1103/PhysRevLett.96.058001.
[23] C.-C. Liao, S.-S. Hsiau, and C.-S. Wu: Powder Technology (2014) 253. DOI:10.1016/j.powtec.2013.12.031.
[24] J. Bensam Raj, P. Marimuthu, M. Prabhakar, and V. Anandakrishnan: Int J Adv Manuf Technol 1-4 (2012) 61. DOI:10.1007/s00170-011-3709-4.
[25] B. Leszczynska-Madej: Archives of Metallurgy and Materials 1 (2013) 58. DOI:10.2478/v10172-012-0148-7.

# PUMP-OUT EFFECT REDUCTION OF POWER MODULES BY USING HYBRID HEAT SPREADER PLATES

**Ronald Eisele[1], Stefan Söhl[1]**

[1] University of Applied Sciences Kiel, Institute for Mechatronics

**ABSTRACT:** This report introduces an experimental setup to visualize the "pump-out effect". The physical background of the thermomechanical module movement is explained. As an alternative to the conventional copper base plate, a new type of hybrid heat spreader plate is presented. The hybrid heat spreader plate consists of an asymmetrically designed multilayer composite. The individual layers are joined together using the low-temperature bonding technology (NTV). The combination of different material properties in a multilayer metal composite, results in a thermo-mechanically balanced stack with reduced pumping movement. Using the hybrid heat spreader plate, the CTE mismatch can be minimized, the crowning of the entire power module can be adjusted and the movement under the influence of a thermal alternating load can be reduced.

**KEYWORDS:** multi-layered heat spreader plate, power electronics, pump out effect

## 1 INTRODUCTION

Classical power electronic assemblies consist of a ceramic circuit board (DBC) which is connected to a copper heat spread plate. This design has been a proven thermal solution in the field of power electronics for years. Such modules are usually used in combination with a heat sink to improve heat dissipation. For further optimization of the heat conduction, there is a heat-conducting paste (TIM layer) between the module and the heat sink. This is necessary to compensate unevenness between the components and to avoid air inclusions [1] [2]. However, this type of module structure carries the risk of displacing the TIM layer under the influence of a thermal alternating load. This effect is due to the different thermal expansion coefficients (CTE mismatch) of the components. The CTE mismatch causes a deformation of the stack with every change in temperature, which causes a membrane-like pumping movement [3] [4]. As a result of this movement, the heat-conducting paste is displaced and air inclusions are formed. The use of CTE reduced materials reduces the mismatch and thus the pump out effect. One possibility to achieve the CTE reduction is the use of layered heat spread plates. Laminated heat spreader plates are already used in many technical areas. Mostly, they consist of a symmetrically constructed material composite of copper / molybdenum / copper. The objective of this study is to create the layered heat spreader plate in an asymmetrical material ratio. Due to its asymmetry, the heat spreader plate behaves similarly to a bi-metal strip. A defined crowning occurs. This crowning can be designed in such a way that it counteracts the resulting crowning of the entire power module and thus compensate the deformation. This in turn leads to a reduction of the movement under a thermal load and to a reduction of the pump out effect.

## 2 EXPERIMENT

The specimens, which are used in this study, are based on a Danfoss ECO3 module. The hybrid heat spreader has a thickness of 3mm and is constructed in a 3-layer composite (copper / molybdenum / copper). The heat spreader has a molybdenum amount of 10 vol. %. The components are joined together using the low-temperature bonding technology. The molybdenum layer is integrated asymmetrically into the stack (see Fig. 1). The reference model is a Danfoss ECO3 module with identical design and a standard Cu heat spreader plate.

* Stefan Söhl: Schwentinestraße 24, 24149 Kiel, phone: +49 431 12850285, fax: +49 431 210 2542, stefan.soehl@fh-kiel.de

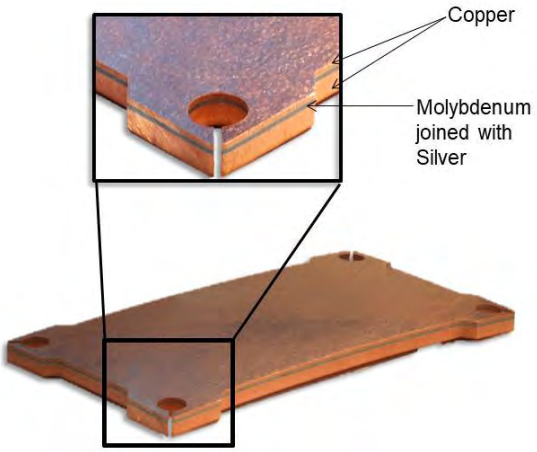


***Fig. 1*** *Asymmetrical hybrid heat spreader*

## 2.1 MEASUREMENT OF THE CROWNING

In the first part of the study, it is to be shown that by using an asymmetric hybrid heat spreader plate, the module movement under a thermal load can be reduced. To calculate the crowning, the base plates are measured by a 3D surface scanner and the differences in height are determined. The specimens are placed on a temperature-controlled heating plate during the examination. The deformation of the modules can be determined under the influence of a thermal load. The difference in height between the center and the edge area is used to assess crowning (see Fig. 2).

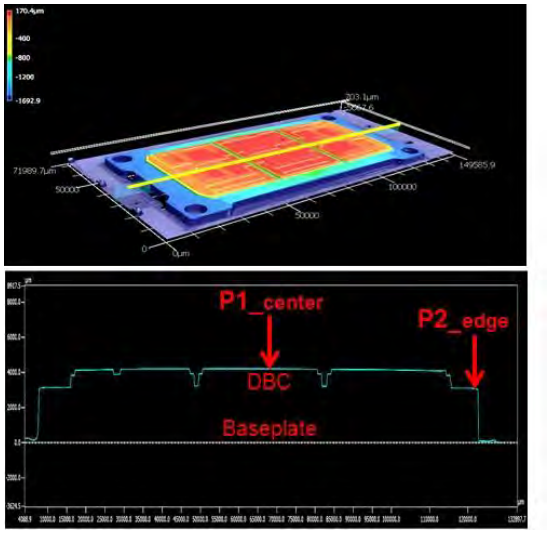


***Fig. 2*** *Height difference measurement*

The reference value is the crowning below room temperature. The module is warmed up to 140°C and the height difference is measured in 20°C steps. The following figure shows the results of the height measurement.

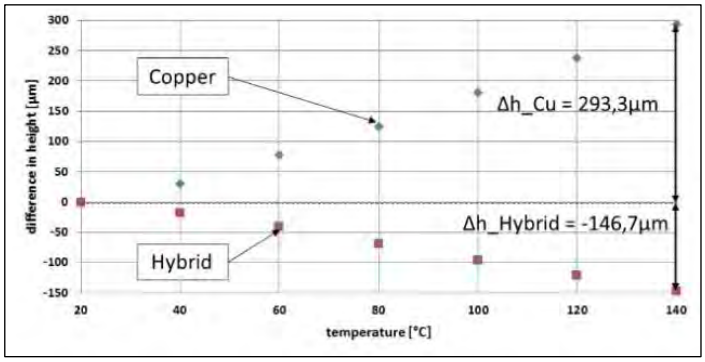


***Fig. 3*** *Height displacement of the samples under a thermal load*

It can be seen that the module with the hybrid heat spread has a 50% lower thermal movement.

## 2.2 PUMP OUT TEST BENCH

The next part of the study will show that reduced thermomechanical movement of the module leads to a reduction of the pump out effect. For this investigation a test bench developed at the University of Applied Sciences in Kiel. The test bench is used to visualize the displacement of the TIM layer. The schematic drawing of the test bench is shown in Fig. 4.

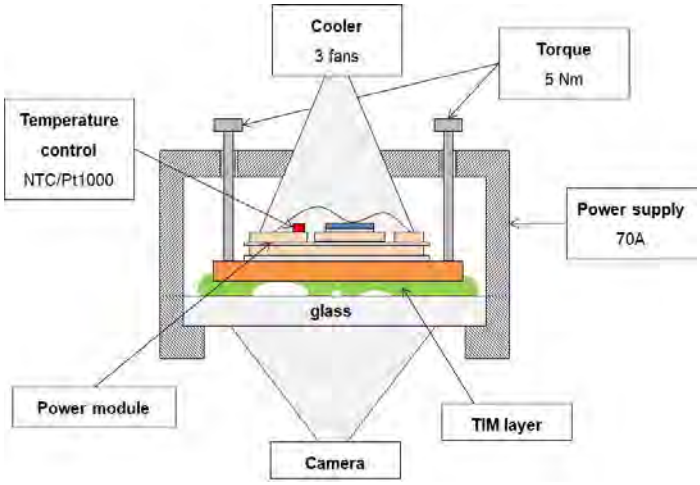


***Fig. 4*** *Schematic structure of the test bench*

The test bench consists of an upper and a lower frame. The lower frame contains a glass bottom, which allows the TIM layer to be visible over the entire surface. The upper frame is used to fix the power module. Below the glass bottom there is a camera which can be used to photograph the TIM layer. The module is heated to a temperature of 130°C via a current source of 70A and then cooled to 40°C by forced convection. This cycle is repeated and every time the temperature limits are reached, an image is captured (Fig. 5).

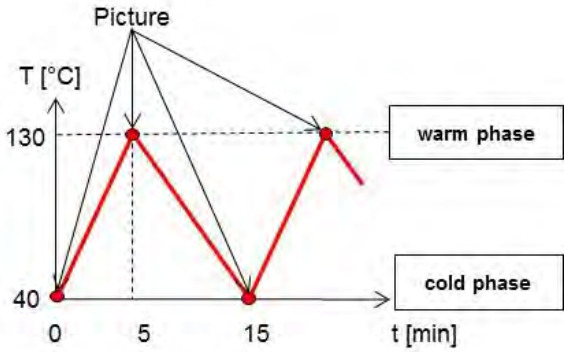


***Fig. 5*** *Sequence of the Pump Out cycle*

## 3 RESULTS

An image processing software is used to evaluate the resulting air inclusions. The software generates a histogram of each recording. The histogram shows the distribution of the gray values of an image. If dark spots appear in an image, the average grey value increases. The change in the gray value is used as a measure of the reduction of the TIM layer.

### 3.1 EVALUATION OF THE REFERENCE MODULE

The following figure shows images taken after 0/50/100/150 cycles of the TIM layer of the reference model.

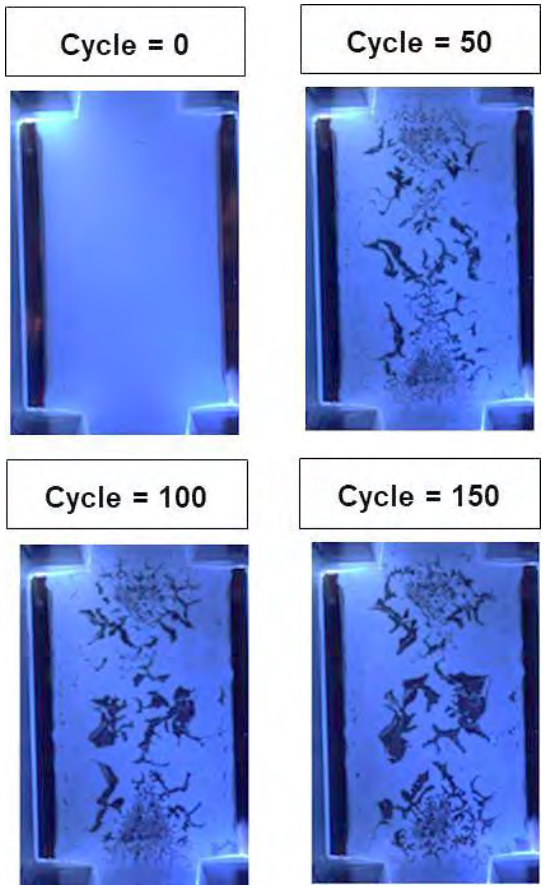


***Fig. 6*** *TIM Layer of reference measurement with Cu heat spread*

It can be seen that after a small number of cycles the TIM layer shows air inclusions.

The initial value for the evaluation is the 0 cycles recording. All further recordings are evaluated in relation to the initial value. The following figure shows the results of the reference measurement.

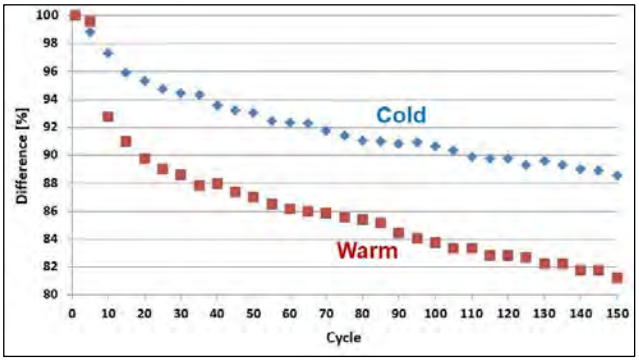


***Fig. 7*** *Reduction of the TIM layer of the reference measurement depending on the number of cycles*

It can be seen that an increasing number of cycles is accompanied by a percentage decrease in the TIM layer. In the warm state, the reduction after 150 cycles is about 20%. Furthermore, even after 150 cycles, the course of the curve is still constantly decreasing.

### 3.2 EVALUATION OF THE REFERENCE MODULE

A reduction of the TIM layer is also visible when using the hybrid heat spreader plate (see Fig. 8).

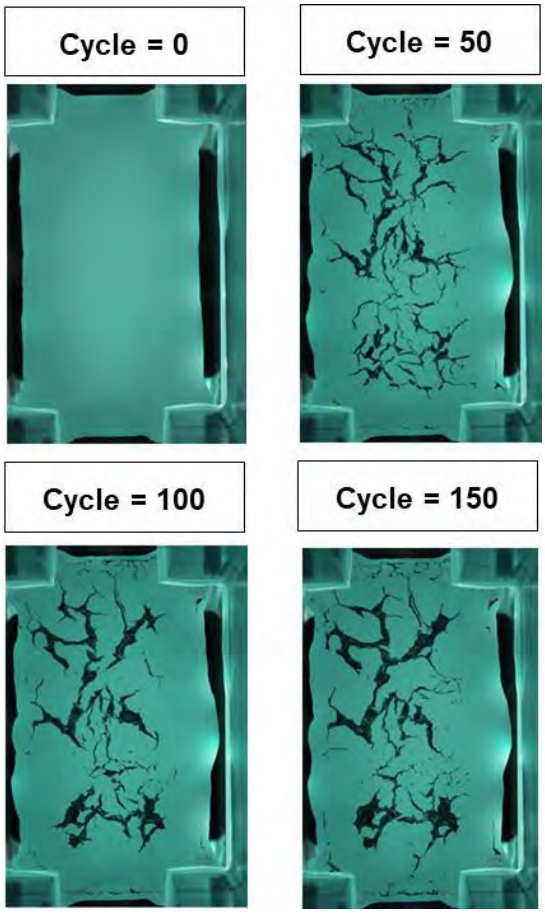


***Fig. 8*** *TIM layer of pump out measurement with hybrid heat spread*

The captured images are evaluated as well as those of the reference measurement. The results are shown in the following figure.

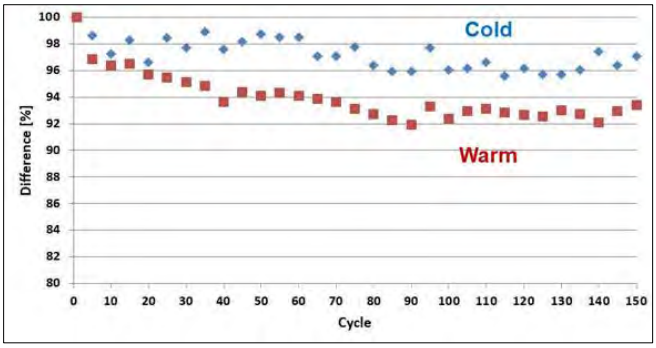


***Fig. 9*** *Reduction of the TIM layer of the hybrid metal measurement depending on the number of cycles*

Compared to the reference measurement, a lower pump out effect can be detected. The maximum reduction of the TIM layer is 8%. This is 12% less compared to a module with a copper heat spreader.

## 4 CONCLUSIONS

The objective of this study was to visualize and evaluate the pump out effect of a power module. Furthermore, this effect should be reduced by using asymmetrically designed hybrid heat spreader plates.
By using the test bench it was possible to visualize and analyze the pump out effect. The use of the hybrid heat spreader plate does not prevent the pump-out effect completely but significantly reduces its effect. By further measurements and adjustments to the simulation models it will be possible to further limit the thermomechanical movement and thus reduce the pump out effect to a minimum.

## 5 ACKNOWLEDGEMENT

This work was carried out and processed as part of a cooperation project with Heraeus Holding GmbH.

## REFERENCES

[1] Klaka, Sven (1997): Eine Niedertemperatur-Verbindungstechnik zum Aufbau von Leitungshalbleitermodulen. Bremen : Cuvillier Verlag Göttingen, 1997. ISBN 3-89588-771-4.
[2] Knörr, Matthias (2011): Verbinden von Leistungshalbleiterbauelemente durch Sintern von nanoskaligen Silberpartikeln. Aachen : Shaker Verlag, 2011. ISBN 978-3-8440-0352-9
[3] Jany, Peter; Langeheinecke, Klaus (Hrsg.); Sapper, Eugen (2001): Thermodynamik für Ingenieure. 3., durchgesehene Auflage. Vieweg Verlag. Braunschweig/Wiesbaden, 2001
[4] Lämmel, Bernd; Will, Peter (2009): Kleine Formelsammlung der Technischen Mechanik. Leipzig: Carl Hanser Verlag München, 2009. ISBN 978
[5] -3-44642166-0

# List of Authors


A

Arnaut, K. **216**

B

Baeten, A. **269**
Barfuss, D. **262**
Behrens, B.-A. **296**
Beitelschmidt, D. **24**
Berger, A. **24**
Bergmann, J.P. **188**, **210**, **227**, **233**
Bielenin, M. **227**
Bittner, F. **114**
Bobzin, K. **290**
Böhm, S. **278**
Bohr, D. **296**
Born, L. **28**, **165**
Bosse, S. **104**
Brandt, R. **34**, **56**
Bräunling, S. **40**, **246**
Brosius, A. **246**
Brunotte, K. **296**
Bücheler, D. **96**
Bührig-Polaczek, A. **222**
Busch, A.B. **34**, **56**
Busse, M. **216**

C

Camberg, A. **240**
Cherif, C. **246**
Clausen, J. **216**

D

Decker, R. **140**
Dilger, K. **48**, **195**
Domm, M. **177**
Drechsler, K. **269**
Dreißigacker, U. **156**

E

Eisele, R. **302**
Endres, H.-J. **114**
Engelmann, C. **203**

F

Fang, X. **128**
Fiebiger, T. **24**
Fischer, F. **146**
Füssel, U. **188**
Fux, V. **24**

G

Gelinski, N. **278**
Gerdt, L. **290**
Gereke, T. **246**
Geyer, A. **88**
Gillner, A. **203**
Gläßer, T. **88**
Graf, A. **140**
Gresser, G.T. **28**, **165**
Großmann, W. **146**
Grützner, R. **262**
Gude, M. **40**, **62**, **68**, **246**, **262**
Gundlach, C. **48**
Günther, F. **254**

H

Haider, D. **62**, **68**
Hartwig, S. **48**
Henckell, P. **233**
Herrmann, A.S. **133**
Hertel, M. **188**
Hirsch, F. **246**, **262**
Hirt, G. **293**
Hofmann, L. **283**

J

Jenkel, S. **133**
Jonas, F.A. **165**

K

Kärger, L. **81**
Kaspar, J. **24**
Kästner, M. **246**
Kawalla, R. **40**
Kloska, T. **128**
Knippers, J. **165**
Koerdt, M. **104**, **216**
Kohl, M.-L. **188**
Koshukow, W. **62**, **68**
Krahl, M. **62**, **68**
Kräusel, V. **140**
Kretschmar, V. **254**
Kroll, L. **140**, **171**
Krüger, L. **40**
Kupfer, R. **62**, **68**

L

Landgrebe, D. **140**
Lange, K. **40**
Liebig, W. **81**
Liebsch, A. **62**, **68**
Lohse, M. **188**

M

Mandel, M. **40**
Mannig, M. **48**
Menzel, M. **48**
Messer, P. **222**
Milwich, M. **28**, **165**
Möhl, C. **28**, **165**
Monden, A. **9**
Müller, N. **121**
Müller, R. **262**
Muth, M. **74**

N

Neh, K. **40**

O

Oblinger, C. **269**
Olowinsky, A. **203**
**283**
Öte, M. **290**
Ouali, A.-A. **171**

P

Pohl, M. **254**

R

Rauh, B. **195**
Rinberg, R. **171**

S

Sause, M.G.R. **9**
Schaper, M. **17**
Scheuermann, G. **254**
Schiebel, P. **133**
Schindler, D. **156**
Schlimbach, J. **177**
Schlimper, R. **88**
Schmid, A. **216**
Schricker, K. **188**, **210**, **233**
Schubert, A. **96**
Schumacher, E. **278**
Seifert, M. **24**
Senge, S. **290**
Sessner, V. **81**
Smatt, T. **48**
Söhl, S. **302**
Stommel, M. **254**
Struß, A. **216**
Svidler, R. **171**
Szallies, K. **227**

T

Thomas, R. **146**
Trauth, A. **96**
Tröster, T. **240**

U

Ullmann, M. **40**

V

van der Straeten, K. **203**
von Hehl, A. **104**
Vroomen, U. **222**

W

Walther, F. **278**
Wang, Z. **17**
Weck, D. **40**, **246**
Weidenmann, K.A. **74**, **81**, **96**
Wiesner, S. **290**
Würfel, V. **262**

Z

Zinn, C. **17**

**IMPRINT - IMPRESSUM**
**HYBRID - MATERIALS AND STRUCTURES 2018 - PROCEEDINGS**
Editors
Joachim M. Hausmann, Marc Siebert, Axel von Hehl
Compilation
Fraunhofer-Institut für Intelligente Analyse- und Informationssysteme IAIS
© DGM - Deutsche Gesellschaft für Materialkunde e.V.

Besucheranschrift:
Wallstraße 58/59
10179 Berlin

Postanschrift:
DGM - Deutsche Gesellschaft für Materialkunde e.V.
c/o INVENTUM GmbH
Marie-Curie-Straße 11-17
53757 Sankt Augustin

T +49-(0)69-75306 750
F +49-(0)69-75306 733
E-Mail: dgm@dgm.de
Web: www.dgm.de

ISBN 978-3-88355-417-4
Das Werk einschließlich seiner Teile ist urheberrechtlich geschützt. Jede Verwertung außerhalb der engen Grenzen des Urheberrechtsgesetzes ist ohne

Zustimmung der DGM und der Herausgeber unzulässig und strafbar. Das gilt insbesondere für Vervielfältigungen, Übersetzungen, Mikroverfilmungen und die Einspeicherung und Verarbeitung in elektronischen Systemen.

This work including all its parts is protected by copyright. Any use outside the strict constraints of the German Copyright Law without the permission of the DGM and the editors is prohibited and liable to prosecution. This applies particularly for reproduction, translation, adaption on microfilm, and storage or processing in electronic systems.